DISS. ETH NO. 17856

Electricity from wood through the combination of gasification and solid oxide fuel cells

Systems analysis and Proof-of-concept

A dissertation submitted to
ETH ZURICH

for the degree of
Doctor of Sciences

presented by
Florian-Patrice Nagel
Dipl.-Ing. Universität Stuttgart
Born 05.12.1977
citizen of
the Federal Republic of Germany

accepted on the recommendation of
Prof. Dr. A. Wokaun, examiner
Dr. F. Maréchal, co-examiner
Dr. S. Biollaz, co-examiner

2008

Für meine Eltern
in Liebe und Dankbarkeit

Danksagung

If we knew what it was we were doing, it would not be called research, would it?

Albert Einstein

Prof. Dr. Alexander Wokaun gilt mein besonderer Dank für die Möglichkeit diese Dissertation anzufertigen und die stets vorzügliche Betreuung dieser Arbeit. Ihr Vertrauen, Herr Prof. Wokaun, in meine Lernfähigkeit und Beharrlichkeit war für mich Verpflichtung und Ansporn zugleich. Die Quartalsbesprechungen haben meine Arbeit wesentlich beeinflusst und bereichert.

Die herzliche Aufnahme in die „Thermal Process Engineering“ Gruppe, die Formulierung des Dissertationsthemas und die Übernahme des Koreferats kann ich Herrn Dr. Serge Biollaz nicht hoch genug anrechnen. Ich danke Dir, Serge, für die vielen anregenden Diskussionen die aufgrund Deiner Erfahrung fast immer zur Verbesserung des Versuchsaufbaus geführt haben. Vielen herzlichen Dank für die freundschaftliche Zusammenarbeit und für die Unterstützung in Zeiten persönlicher Not und Ungewissheit ob ich diese Arbeit gesundheitsbedingt abschließen kann.

Für die Übernahme des Koreferats und interessante Diskussionen zum Thema der Modellierung bedanke ich mich herzlich bei Dr. François Maréchal.

Dr. Tilman Schildhauer könnte ich eine eigene Danksagung widmen und hätte immer noch nicht genug Platz um meinen Dank ausreichend auszudrücken. Die unzähligen Diskussionen, Fragen und Anregungen in allen Bereichen der Dissertation haben mich nicht nur akademisch sondern auch menschlich bereichert. Danke für die viele Zeit die Du, Tilman, in mich und diese Dissertation investiert hast, ohne die diese Arbeit nicht in dieser Form möglich gewesen wäre.

Dr. Samuel Stucki danke ich herzlich für die freundliche Aufnahme in das Labor für Energie- und Stoffkreisläufe und die Einführung in die Welt der Elektrochemie.

Dr. Alexander Schuler von der Hexis AG danke ich für die fachliche Unterstützung und die Bereitstellung mehrerer Brennstoffzellenmodule ohne die der experimentelle Teil dieser Arbeit nicht denkbar gewesen wäre.

Für die entspannenden Gespräche in den Kaffeepausen die mir stets neuen Schwung für meine Arbeit gaben danke ich Gisela Herlein. Ohne Dich, Gisela, wäre meine Zeit am LEM nur halb so schön gewesen.

Ein besonderer Dank gilt dem Technikteam des LEM. Für die Lösung unlösbarer Steuerungsprobleme beim Aufbau des weltweit ersten Vergaser- Brennstoffzellen Systems danke ich Peter Hottinger. Peter, der erste HoVer-BZM Versuch, bei dem wir uns vorkamen wie Spaceshuttlepiloten beim Landeanflug auf den alten Hong Kong Airport werde ich nie vergessen.

Für sein Talent auch die verrücktesten Ideen aufs Papier und zum schlussendlich sogar zum funktionieren zu bringen danke ich Thomas Marti. Thomas, ich werde immer mit einem Lächeln im Gesicht an die Zeit mit dem Schraubenschlüssel in der Hand zurück denken.

Peter Binkert danke ich post mortem für seine Geduld mit meinen Wünschen und die Beharrlichkeit an der Dreh- und Fräsmaschine. Spaß hat es gemacht, Peter.

Die perfekten Zyklone und viele andere Bauteile im HoVex-Veruschsaufbau verdanke ich Marcel Hottiger.

Für die unzähligen Stunden mit dem Schweißapparat in der Hand durch die der HoVex-Aufbau erst Realität wurde danke ich Markus Schriber.

Die Messungen der abstrusesten Gase, die so manche Überraschung an den Tag brachten, hat Herr Jörg Schneebeli durchgeführt. Danke Jörg, für deine stete Bereitschaft mir in Diagnostikfragen zu helfen.

Weiterer Dank gebührt Dr. Frédéric Vogel, Christian Pitta, Dr. Sudip Ghosh, Manuel Damsohn, Markus Jenne, Martin Künstle, Stefan Decker, Mohand Nait-Atmane, Thorsten Schulz, Jan Kopyscinski und Johannes Judex für die Freundschaft sowie allen anderen nicht namentlich genannten LEM-Mitarbeiter mit denen ich arbeiten durfte und die immer noch Zeit für das ein oder andere Späßchen gefunden haben.

Last but not least möchte ich für die außerordentlich entspannte und positive Arbeitsatmosphäre am PSI und dem AXPO Naturstrom Fond für die finanzielle Unterstützung meiner Arbeit danken.

Meine Eltern, Dr. Karl-Heinz Nagel und Chantal Nagel, und meine beiden Schwestern, Nathalie McCaughey und Sandra Nagel Bolliger, haben mich stets unterstützt und mir durch eine unfallbedingte Zeit voller dunkler Zweifel hinweggeholfen. Ihre Liebe und ihr Vertrauen in mich und nicht zuletzt die familiäre Geborgenheit haben mir die notwendige Kraft gegeben meine Reise in die Welt der Wissenschaft fortzusetzen und letztendlich abzuschließen.

Villigen, im Juli 2008
Florian-Patrice Nagel

Abstract

The availability of energy in general and electricity in particular has become a major concern given the growing global population, numerous fast developing nations and depleting fossil fuel reserves. Further, the excessive use of fossil fuels with their attributed carbon dioxide emissions has lead to changes in the global ecosystem with negative consequences for life on earth. Against this background it comes as no surprise that renewable, carbon dioxide neutral energy sources have gained increased interest recently. Biomass has a large potential as renewable and carbon dioxide neutral feedstock for electricity generation but is comparably expensive. An approach to overcome this economical drawback is the combination of high-temperature fuel cells with biomass gasification processes, which is commonly referred to as "Biomass Integrated Gasification Fuel Cell" systems (B-IGFC). Solid oxide fuel cells (SOFC) are considered as promising candidates for the application in B-IGFC system due to their less stringent requirements to the fuel gas quality compared to other fuel cell types and their capability of directly oxidizing carbonaceous fuel gases with high efficiencies at small scales. However, the composition of the fuel gas plays an important role for its conversion through SOFCs which leads to strong system interactions that must be well understood to allow for the exploitation of the full potential of the B-IGFC approach. This thesis presents the demonstration of the B-IGFC technology on kW-scale and a thermo-economic system analysis aiming at the identification of promising B-IGFC systems with power outputs around 1 MW_{el}.

The PSI B-IGFC system concept comprises an updraft biomass gasification reactor, a hot gas cyclone, a catalytic partial oxidation (CPO) unit and a 1 kW Hexis SOFC system. The experiments conducted in this thesis initially concentrated on the characterization of all processes steps in the PSI B-IGFC system. The first milestone was reached with the stable operation of the lab-scale updraft gasifier over 165 h non-stop. Experiments with short stacks showed that tars are to some extent a fuel for SOFCs. A commercial CPO catalyst was investigated, revealing satisfying conversion performance for not only oxygenated tars and aromatics but also organic sulfur compounds. The PSI B-IGFC concept was subsequently operated for 28 h non-stop employing the above mentioned 1 kW Hexis SOFC system. Compared to operation with partially oxidized methane, the SOFC delivered 40 % less current when operated with water and nitrogen diluted producer gas. Overall, the demonstration unit was operated without problems and valuable experience for future improvements was gathered. The application of effective means for the removal of micro particles has been identified as very important in this respect.

The system analysis is based on a finite volume SOFC model developed in this thesis that includes all relevant charge, mass and heat transport processes. Cell internal steam

reforming is considered through a Langmuir-Hinshelwood type applied kinetic model. For the system analysis, the model was applied to anode- and electrolyte-supported planar cell designs with co- and counter-current flow pattern as well as the standard tubular cell design promoted by the Siemens AG. The model was validated against experimental and literature data and proved to behave physically correct with smaller mass and energy balance errors than comparable models. The robustness of the general trends predicted for various fuel gas compositions was attested by means of a sensitivity analysis.

Based on measured producer gas compositions originating from downdraft and updraft gasification processes as well as the fluidized bed steam gasification process, seven B-IGFC systems with different gas processing strategies were defined. The corresponding gas compositions at the fuel inlet of the SOFCs were computed with ASPEN PLUS.

Compared to pre-reformed methane, the power output of SOFCs decreases by 25 to 70 % when operated with producer gases. The magnitude of the power output decrease mainly depends on the degree of dilution of the producer gas and on the anode catalyst activity which both determine the importance of activation losses. The tubular cell design appears to feature a highly active anode catalyst according to the employed model parameters. Diffusion limitations in contrast do not gain importance for any of the investigated producer gases and cell designs. The required air-to-fuel ratio to maintain a given mean cell temperature increases with decreasing internal reforming potential of the fuel gas. This mechanism is considerably less pronounced for counter-current cell designs compared to their co-current correspondents. The thermal stress resulting from the operation of SOFCs with producer gases is generally lower than for operation with pre-reformed methane. This may slow down the corresponding cell degradation processes.

The power outputs predicted by the SOFC model were used as input for overall system simulations performed with ASPEN PLUS aiming at the investigation of the interactions between the gasification processes, gas processing technologies and SOFC designs. The heat integration was conducted by means of a generalized heat exchanger network.

The comparably low operational temperature of the zinc oxide trap beds, generally employed for the removal of hydrogen sulfide, calls for additional humidification of the producer gases to prevent thermodynamic carbon deposition except in the system where a catalytic partial oxidation unit is employed for tar conversion. The net system efficiency is preeminently determined by the cold gas efficiency of the biomass gasification process and the auxiliary power requirements, which directly correlate with the air-to-fuel ratios. The adiabatic methanation and catalytic partial oxidation are effective means to lower the required air-to-fuel ratios by increasing the internal reforming potential of the corresponding producer gases, while simultaneously converting undesired organic species.

Consequently with 32.1 %, the highest net AC system efficiency in the analysis is reached by the combination of the updraft gasification with an adiabatic methanation and the tubular cell design. The updraft gasification yields a producer gas with high cold gas efficiency and considerable internal reforming potential, which is further increased through the adiabatic methanation. The high internal reforming potential leads to a very low air-to-fuel ratio and thus low auxiliary power needs. The steam reforming of the produced methane can be interpreted as the final gasification step using SOFC waste heat.

With the mass and energy flows determined for of the different B-IGFC systems through the overall system simulations, all major equipment pieces were sized and pricewise rated using pertinent cost functions. The fuel cell balance of plant equipment and the corresponding heat exchangers in particular are the most important cost drivers amounting for up to 50 %, while the fuel cell itself accounts for up to 25 % of the total system costs. This emphasizes the importance of the air-to-fuel ratios which together with the operational cell temperatures determine the size of the heat exchangers. The total plant costs were related to the corresponding net system power outputs to yield the specific plant costs. The downdraft gasification based systems have the highest specific plant costs due to costly wood drying, large heat exchangers and low power outputs resulting from high activation losses as a consequence of gas dilution. The fluidized bed steam gasification based systems yield lower specific plant costs, mainly because of low activation losses and thus high power outputs. The updraft gasification based systems feature the lowest specific plant costs as a result of low total plant costs and auxiliary power needs.

The power production costs (PPC) relate the total plant costs to the corresponding system efficiencies. The basis for the calculations was a detailed cost analysis for a given planning horizon including costs not only for operation and maintenance, feedstock and utilities but also capital costs resulting from plant costs depreciation and interests. The annuity method was employed to evenly distribute the net value of all costs throughout the planning horizon. On average, 40 % of the PPC arise from fuel expenses, the remainder being attributed to capital costs. Hence, reduction of the specific plant costs is considerably more effective than system efficiency increases with respect to PPC reduction. With 0.1154 €/kWh$_{el}$, the updraft gasification based system discussed above yields the lowest PPCs in the analysis. Increasing the operational voltage of the SOFC from 0.6 V to 0.7 V results in a net system efficiency increase from 32.1 % to 37.1 %. With 0.1912 €/kWh$_{el}$, the resulting reduced power output yields however considerably higher PPCs. In contrast, reducing the auxiliary power needs by adjusting the air-to-fuel ratio to the lowest possible value leads to higher net system efficiencies and lower specific plant costs, thus considerably lowering the PPCs.

Finally, the revenues from heat sales are crucial for the economical viability of the investigated B-IGFC systems without bottoming cycles. Future systems analysis should focus on B-IGFC systems with bottoming cycles. Therefore, the developed SOFC model has to be integrated in Flowsheeting- Software packages such as e.g. ASPEN PLUS.

Zusammenfassung

Angesichts der wachsenden Weltbevölkerung, zahlreicher wirtschaftlich aufsteigernder Länder und zur Neige gehender fossiler Energiequellen ist die Verfügbarkeit von Energie und besonders von Elektrizität zu einem Besorgnis geworden. Zudem hat der übermäßige Verbrauch fossiler Energiequellen durch die damit verbundenen Kohlendioxidemissionen zu bedenklichen Veränderungen des Ökosystems der Erde geführt. Vor diesem Hintergrund ist es nicht verwunderlich, dass erneuerbare, CO_2-neutrale Energiequellen zunehmend an Interesse gewonnen haben. Unter den erneuerbaren Energien hat Biomasse ein vielversprechendes Potential für die Elektrizitätserzeugung, ist allerdings vergleichsweise teuer. Ein Ansatz um diesen Nachteil auszugleichen ist die Kopplung der Hochtemperaturbrennstoffzellen-Technologie mit der Biomassevergasungstechnologie der gemeinhin als "Biomass Integrated Gasification Fuel Cell Systems" (B-IGFC) bezeichnet wird. Aufgrund Ihrer geringeren Anforderungen an die Brenngasreinheit im Vergleich zu anderen Brennstoffzellen und der Möglichkeit kohlenwasserstoffhaltige Brenngase im kleinen Leistungsbereich hocheffizient direkt zu Strom zu wandeln werden Festkeramikbrennstoffzellen (SOFC) als sehr interessant für den Einsatz in B-IGFC Systemen eingestuft. Die Zusammensetzung des Brenngases spielt eine besonders wichtige Rolle für dessen elektrochemische Umwandlung in SOFCs, was zu starken Wechselwirkungen zwischen den einzelnen Prozessen in B-IGFC Systemen führt. Diese müssen verstanden werden um das volle Potential der B-IGFC Technologie auszunutzen.

In der vorliegenden Arbeit wird über die Demonstration der B-IGFC Technologie im kW-Maßstab berichtet. Zudem wird eine thermo-ökonomische Systemanalyse vorgestellt, die zur Identifikation viel versprechender B-IGFC Systemkonzepte im 1 MW_{el} Leistungsbereich durchgeführt wurde.

Das PSI B-IGFC Systemkonzept umfasst einen Gegenstromholzvergaser, einen Heißgaszyklon, eine katalytisch partielle Oxidationsstufe sowie ein 1 kW SOFC- System der Hexis AG. Zunächst wurden Experimente zur Charakterisierung aller oben genannten Prozessschritte durchgeführt. Ein erster Meilenstein wurde mit dem stabilen und ununterbrochenen Betrieb des Gegenstromholzvergasers über 165 Stunden erreicht. Versuche mit Experimentalzellstapeln haben ergeben, dass Teere bis zu einem gewissen Grad als Brennstoff für SOFCs angesehen werden können. Untersuchungen eines kommerziellen Katalysators für die katalytisch partielle Oxidation haben befriedigende Umsatzraten sauerstoffhaltiger und aromatischer Teere sowie organischer Schwefelverbindungen bestätigt. Das PSI B-IGFC System wurde im Anschluss an die Charakterisierung aller wichtigen Prozessschritte ununterbrochen für eine Dauer von 28 Stunden betrieben. Im Vergleich zum Betrieb des SOFC- Systems mit partiell oxidiertem Methan wurde mit

Holzgas aufgrund dessen Verdünnung mit Stickstoff und Wasser 40 % weniger Strom erzeugt. Insgesamt konnte der Versuchsaufbau ohne nennenswerte Probleme betrieben und wertvolle Erfahrungen für künftige Verbesserungen gesammelt werden. Insbesondere hat sich gezeigt, dass eine effiziente Kleinstpartikelabscheidung für künftige Langzeitexperimente von hoher Wichtigkeit ist.

Die in der vorliegenden Arbeit beschriebenen Ergebnisse der Systemanalyse beruht auf einem eigens dafür entwickelten SOFC Modell. Das Modell wurde nach dem Finite-Volumen-Ansatz aufgebaut und berücksichtigt alle wichtigen Ladungs-, Masse- und Wärmetransportprozesse die in SOFCs stattfinden. Mögliche zellinterne Dampfreformierungsreaktionen werden über eine Langmuir-Hinshelwood Kinetik beschrieben. Für die Systemanalyse wurden planare Anoden- und Elektrolyt-gestützte Zelltypen in Gleich- und Gegenstromausführung, sowie der röhrenförmige Zelltyp der Siemens AG mit dem Modell abgebildet und gegen Messdaten und Literaturwerte validiert. Es konnte gezeigt werden, dass das aufgebaute Model physikalisch sinnvolle Ergebnisse liefert. Die erreichte Schließung der Massen- und Energiebilanzen ist deutlich besser als die vergleichbarer Modelle in der einschlägigen Literatur. Um sicherzustellen, dass die vorhergesagten Trends für verschiedene Brenngaszusammensetzungen nicht die Folge der festgelegten Modellparameter ist, wurde eine entsprechende Sensitivitätsanalyse durchgeführt. Die vom Modell vorhergesagten Trends haben sich als sehr robust erwiesen.

Aufbauend auf gemessenen Zusammensetzungen von Produktgasen aus Gleich- und Gegenstromholzvergasungsprozessen sowie einem Wirbelschichtdampfvergasungsprozess wurden sieben verschiedene B-IGFC Systemkonzepte definiert. Die aus den verschiedenen B-IGFC Systemkonzepte resultierenden Gaszusammensetzungen am Eintritt der eingesetzten SOFCs wurden mittels ASPEN PLUS berechnet.

Im Vergleich zu vorreformiertem Methan ist die Leistung der holzgasbetriebenen SOFCs um 25 bis 70 % reduziert. Die Höhe der Leistungsminderung hängt maßgeblich vom "Verdünnungsgrad" des Holzgases und der Aktivität des Anodenmaterials ab, die beide zusammen die Aktivierungsspannungsverluste bestimmen. Gemäß den verwendeten Modellparametern scheint im untersuchten röhrenförmigen Zelltyp ein hochaktives Katalysatormaterial zum Einsatz zu kommen. Nennenswerte Diffusionslimitierung wurde für keines der untersuchten Holzgase und keinen der untersuchten Zelltypen vorhergesagt. Die zur Einhaltung der vorgegebenen mittleren Zelltemperatur benötigte Kühlungsluftzahl nimmt mit sinkendem Potential des Brenngases für zellinterne Reformierung zu. Dieser Effekt ist für Zelltypen in Gegenstromausführung deutlich schwächer ausgeprägt als für solche in Gleichstromausführung. Die aus dem Betrieb der verschiedenen Zelltypen mit Holzgas resultierenden thermischen Belastungen sind grundsätzlich geringer als die die sich mit vorreformiertem Methan als Brenngas einstellen. Dies könnte sich positiv auf die entsprechenden Zelldegradationsmechanismen auswirken.

Die vom SOFC Modell vorhergesagten Leistungswerte wurden als Eingabewerte für Gesamtsystemrechnungen genutzt. Die Rechnungen wurden mit ASPEN PLUS durchgeführt um die Wechselwirkungen zwischen den verschiedenen Vergasungsprozessen, Gasreinigungsvarianten und Zelltypen zu untersuchen. Die Wärmeintegration der betrachteten Gesamtsysteme wurde über ein verallgemeinertes Wärmetauschernetzwerk abgebildet.

Die vergleichsweise niedrige Betriebstemperatur des standardmäßig zur Schwefelwasserstoffabscheidung eingesetzten Zinkoxids macht eine zusätzliche Befeuchtung der verschiedenen Holzgase zwingend um eine thermodynamisch begünstigte Kohlenstoffbildung zu vermeiden. Einzige Ausnahme ist dabei des B-IGFC Systemkonzept in dem eine katalytisch partielle Oxidationsstufe zur teilweisen Teerumwandlung zum Einsatz kommt. Der Netto-Systemwirkungsgrad wird hauptsächlich vom Kaltgaswirkungsgrad des Vergasungsprozesses und vom Eigenstrombedarf bestimmt, der direkt von der zur Zellkühlung benötigten Luftzahl abhängt. Die adiabate Methanierung und die katalytisch partielle Oxidation sind Prozesschritte, die sich gut für die Senkung der benötigten Luftzahl eignen indem sie das Potential der entsprechenden Brenngase für zellinterne Reformierung steigern und gleichzeitig den Abbau unerwünschter organischer Verbindungen erlauben.

Folglich wurde der höchste Netto-Systemwirkungsgrad von 32.1 % in dieser Systemanalyse von der Kombination der Gegenstromholzvergasung mit einer adiabaten Methanierungsstufe und des röhrenförmigen Zelltyps erreicht. Die Gegenstromvergasung liefert bereits ein Holzgas mit vergleichsweise hohem Potential für zellinterne Reformierung. Dieses wird in der adiabaten Methanierungsstufe zusätzlich gesteigert, was zu einer entsprechend niedrigen Kühlungsluftzahl und geringem Eigenstrombedarf dieses B-IGFC Systemkonzepts führt. Die zellinterne Dampfreformierung des hohen Methananteils im so aufbereiteten Holzgas entspricht im weitesten Sinne dem letzten Schritt der Biomassevergasung unter direkter Nutzung der Hochtemperaturabwärme der SOFC.

Die über Gesamtsystemrechnungen für jedes der untersuchten B-IGFC Systemkonzepte ermittelten Massen- und Energieströme wurden für die Auslegung der wichtigsten Apparate genutzt. Die Gesamtsystemkosten wurden mit Hilfe entsprechende Kostenfunktionen und Wichtungsfaktoren bestimmt. Die Anlagenperipherie der Brennstoffzellen und insbesondere die benötigten Wärmetauscher machen bis zu 50 % der Gesamtsystemkosten aus, während die Brennstoffzellenstapel selbst nur bis zu 25 % der Gesamtsystemkosten verursachen. Dies verdeutlicht nochmals den Stellenwert der Kühlungsluftzahl, aus der, zusammen mit dem Temperaturniveau des entsprechenden Brennstoffzellenstapels, die benötigte Wärmetauscherfläche folgt.

Die Gesamtsystemkosten wurden mit den entsprechenden Gesamtsystemleistungen zu den spezifischen Anlagenkosten verrechnet. Gleichstromholzvergaser basierte Systeme weisen die höchsten spezifischen Anlagenkosten in dieser Systemanalyse auf. Die Gründe dafür sind die benötigte kostenintensive Holztrocknung, große Wärmetauscherflächen und relative geringe Gesamtsystemleistungen, die auf hohe Aktivierungsverluste durch die stark verdünnten Holzgase zurückzuführen sind. Im Vergleich dazu sind die spezifischen Anlagenkosten der B-IGFC Systemkonzepte mit Wirbelschichtdampfholzvergasern etwas geringer. Dies ergibt sich trotz der insgesamt höheren Gesamtsystemkosten aus den deutlich kleineren Aktivierungsverlusten. Die auf Gegenstromholzvergasern beruhenden B-IGFC Systemkonzepte haben die geringsten spezifischen Anlagenkosten dieser Systemanalyse aufgrund der insgesamt niedriger Gesamtsystemkosten und zusätzlich befriedigenden Gesamtsystemleistungen die sich hauptsächlich aus niedrigen Eigenstrombedarfswerten ergeben.

Die Stromgestehungskosten bilden die Synthese aus den Gesamtsystemkosten und den entsprechenden Netto-Systemwirkungsgraden. Grundlage für deren Berechnung war eine detaillierte Kostenanalyse für einen festgelegten Planungszeitraum. Die Kostenanalyse umfasst Betriebs- und Wartungskosten, Brennstoffkosten und Betriebsmittelkosten sowie alle Kosten die aus der Anlagenabschreibung und Darlehnszinsen entstehen. Zur gleichmäßigen Verteilung des Nettobarwerts aller anfallenden Kosten über den Planungszeitraum wurde die Annuitätenmethode angewandt.

Etwa 40 % der Stromgestehungskosten können dem Brennstoffbedarf zugeordnet werden während der Rest im weitesten Sinne von den spezifischen Anlagenkosten abhängt. Folglich ist die Senkung der spezifischen Anlagenkosten wirksamer um geringere Stromgestehungskosten zu erreichen als die Steigerung des Netto-Systemwirkungsgrades.

Das bereits weiter oben beschriebene gegenstromholzvergasungsbasierte System erzielt mit 0.1154 €/kWh$_{el}$ die geringsten Stromgestehungskosten in dieser Systemanalyse. Die Erhöhung der Betriebsspannung des eingesetzten Brennstoffzellenstapels von 0.6 V auf 0.7 V ergibt eine Zunahme des Netto-Systemwirkungsgrads von 32.1 auf 37.1 %. Im Gegenzug steigen die Stromgestehungskosten auf 0.1912 €/kWh$_{el}$, was auf die deutlich reduzierte Gesamtsystemleistung zurückzuführen ist. Dagegen birgt die Senkung des Eigenstrombedarfs durch optimierte Brennstoffzellenstapelbetriebsparameter zur Senkung der Kühlungsluftzahl erhebliches Potential zur Senkung der Stromgestehungskosten. Dies folgt aus der gesteigerten Gesamtsystemleistung und den gleichzeitig reduzierten Kosten für die Anlagenperipherie der Brennstoffzellen.

Schlussendlich sind die Einkünfte aus dem Verkauf von Nutzwärme entscheidend für die Wirtschaftlichkeit von B-IGFC Systemen, falls die Wärme nicht anlagenintern zur zusätzlichen Stromerzeugung verwendet wird. Der Einfluss entsprechender "Bottoming cycles" auf die Wirtschaftlichkeit von B-IGFC Systemen ist in weitererführenden Arbeiten zu untersuchen. Dazu muss das aufgebaute SOFC Modell in Flowsheeting- Programme wie z.B. ASPEN PLUS integriert werden.

Table of Contents

1 Introduction ... 1
  1.1 Motivation ... 2
  1.2 Objectives ... 4
  1.3 Methodology ... 4
  1.4 Organization of the thesis ... 5
2 Technology overview ... 9
  2.1 Biomass ... 10
    2.1.1 Definition ... 10
    2.1.2 Classification ... 10
    2.1.3 Construction ... 10
    2.1.4 Properties ... 12
  2.2 Gasification ... 16
    2.2.1 Biomass conversion overview ... 16
    2.2.2 Fundamentals of thermochemical conversion ... 17
    2.2.3 Wood gasification technology overview ... 21
  2.3 Gas processing ... 31
    2.3.1 Gas cleaning ... 31
    2.3.2 Gas conditioning ... 39
  2.4 Solid oxide fuel cell ... 43
    2.4.1 Fuel cells in general ... 43
    2.4.2 Technology features ... 46
    2.4.3 Working principle ... 47
    2.4.4 Cell designs ... 50
    2.4.5 Support designs ... 52
    2.4.6 Materials ... 54
    2.4.7 Cell failure and performance degradation ... 61
3 Experiments ... 71
  3.1 The PSI B-IGFC system ... 71
    3.1.1 System description ... 71
    3.1.2 Discussion of the chosen approach ... 72

3.2 Gas analysis ... 76
3.3 Proof-of-feasibility tests ... 79
3.3.1 Lab scale tests under load conditions ... 79
3.3.2 Lab scale tests under open circuit conditions ... 81
3.4 Characterization of important unit operations ... 84
3.4.1 Updraft gasification reactor ... 84
3.4.2 Hot gas particle removal ... 88
3.4.3 Catalytic partial oxidation ... 92
3.4.4 Sulfur absorption by zinc oxide ... 96
3.4.5 Solid oxide fuel cell ... 97
3.5 Proof-of-concept of the PSI B-IGFC system ... 103
3.5.1 First demonstration unit tests and derived modifications ... 104
3.5.2 Present demonstration unit configuration ... 106
3.5.3 Long-term test results ... 108
4 Modeling work literature review ... 117
4.1 Modeling approaches for steady-state investigations ... 117
4.1.1 Molecular level models ... 118
4.1.2 Electrode level models ... 118
4.1.3 Cell level models ... 120
4.1.4 Stack level models ... 123
4.1.5 Plant level models ... 124
4.2 Recent studies of biomass fed SOFC cycles ... 124
5 Modeling ... 129
5.1 Overall modeling approach ... 129
5.2 Flowsheeting models ... 131
5.2.1 Biomass gasifier ... 131
5.2.2 Gas humidifier ... 132
5.2.3 Heat integration network ... 132
5.2.4 Steam reforming and methanation reactors ... 133
5.2.5 Catalytic partial oxidation reactors ... 134
5.2.6 Sulfur adsorbent beds ... 135
5.2.7 SOFC ... 135

5.3 ATHENA SOFC model 136
  5.3.1 Model description 136
  5.3.2 Planar model verification 181
  5.3.3 Tubular model validation 186
  5.3.4 Triangular model validation 191
  5.3.5 Sensitivity analysis 193
5.4 Economic model 219
  5.4.1 Equipment purchase cost estimate functions 220
  5.4.2 Equipment sizing and purchase cost estimation 222
  5.4.3 Total investment, direct and indirect plant costs 227
  5.4.4 Net AC power efficiency 228
  5.4.5 Power production costs 229
6 System analysis 235
6.1 Analysis constraints 235
  6.1.1 SOFC simulation assumptions 235
  6.1.2 Overall system simulation assumptions 239
6.2 System definition 240
  6.2.1 Natural gas reference system 240
  6.2.2 B-IGFC systems 241
6.3 Technical evaluation 249
  6.3.1 Simulation results of gas processing sections 249
  6.3.2 Simulation results of SOFC operation with producer gases 253
  6.3.3 System simulation results 270
6.4 Economic evaluation 279
  6.4.1 Direct plant cost estimates 279
  6.4.2 Power production costs 283
  6.4.3 Sensitivity analysis 286
7 Concluding remarks 293
7.1 Conclusions 293
  7.1.1 Experiments 293
  7.1.2 System analysis 294
7.2 Recommendations for future work 297

7.2.1 Experiments 297
7.2.2 Modeling and system analysis 299
Notation 303
References 311

1 Introduction

The on-call availability of energy was a prerequisite for the development of mankind, its culture and technology. After the discovery of fossil fuels and the start of their large-scale use approx. 200 years ago, the development has strongly accelerated. Today, the global energy consumption is primarily covered by fossil fuels, Figure 1-1, and amounts to a yearly average of 17500 kWh per capita translating into a continuous power need of around 2000 W per capita, [1]. However, the majority of people are denied access to their share. For instance, the average person living on the African continent has to content himself with approx. 650 W, while the average Western European resident requires almost ten times as much, 6000 W, and the average North American tops the consumption at 12000 W, [1]. Aggravating the picture many of the fossil fuels are extracted in regions of the world, which are politically unstable und less-developed. These issues combined with the fact that fossil fuel reserves are limited, [2], generate serious conflict potential between the well- and the less-developed nations.

Figure 1-1: Development of global energy consumption during the last 150 years, [1]

Note:
1 Etajoule = 10^{18} J

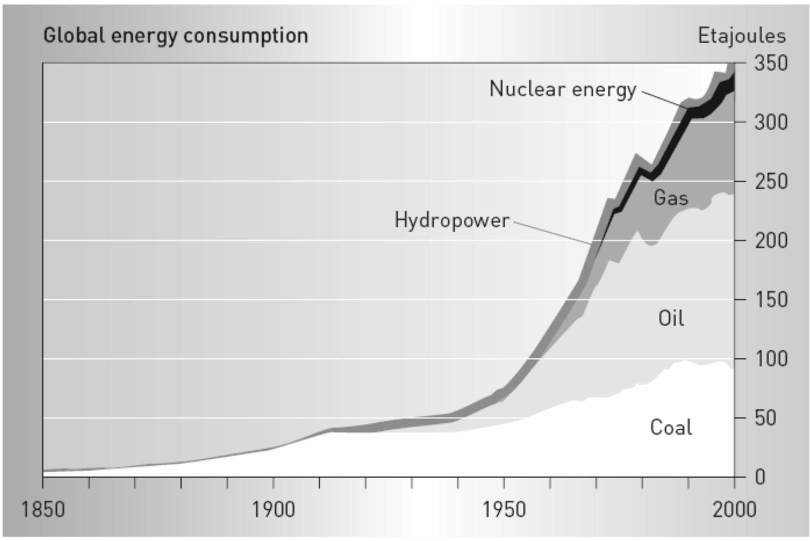

A fairer distribution of the fossils fuels and the foreseeable end of reserves is however only one part of the problem arising from the presently excessive use of fossil fuels, which will only continue to increase due to the rapidly growing global population and numerous fast developing nations. In the year 2000 only, mankind consumed an amount of fossil fuels that took approx. one million years to be formed. The emissions of CO_2 attributed to the combustion of fossil fuels have thus reached levels impacting negatively on the ecosystem, endangering not only the security of food and water supplies but also irreversibly altering the climate conditions on earth. Thus, a continuity of the developed nations currently taken as granted and a fair chance for every human being to relish a comparable quality of life crucially hinges on finding ways to reduce the pace at which global energy consumption increases and to sustainably satisfy the global energy needs. It comes as no surprise then that renewable energy sources such as solar (direct), wind, tide, wave, geothermal and biomass have gained increased interest recently given their time unlimited abundance and global availability. In the ongoing and often controversial debates between citizens, governments, industry and scientists regarding the energy problem, the electricity generation has always played a key role and will continue to gain significance in the near future.

1.1 Motivation

Among the renewable energy sources biomass has a large potential for electricity generation. If the harvest is performed in a sustainable way, wood is a CO_2-neutral energy source. Within the next 20 years, the worldwide installed capacity of biomass power plants is expected to increase by approx. 65 GW, [3]. This forecasted increase however still leaves most of the potential untapped. A prerequisite to achieve this increase and to exploit its full potential is to overcome the economical drawbacks related to biomass as feed stock.

Currently most power plants using wood as feedstock are based on grate firing and steam cycles, where high electrical efficiencies are only possible on multi-MW scale. Wood is an expensive feedstock due to the elaborate harvesting processes. This makes the sale of the produced heat mandatory for the economical feasibility of power generation using wood. Consequently the scarcity of major heat consumers and connection points to large-scale district heating grids limit the number of economically feasible power plant locations. Small-scale wood power plants may overcome the heat sales problem due to comparably small amounts of heat that can be sold to residential heating. However, the low efficiencies of small-scale steam cycles waste this advantage to a major extent.

The gasification of wood instead of its combustion allows the application of more efficient energy conversion cycles than steam cycles such as internal combustion engines (ICE). These ICE based combined heat and power plants (ICE CHP) reach electrical efficiencies up to three times larger than small-scale steam-cycle based wood power plants in the range up to a few MW, [4]. In a first step, the wood is converted to a combustible gas, commonly referred to as producer gas (PG), through a gasification reactor. The composition of the PG depends on the employed gasification reactor type, gasification agent and operating conditions of the gasification process. The PG consists to a major extent of hydrogen and carbon monoxide, the rest being carbon dioxide, methane, water, impurities (e.g. tars, alkali salts, sulfur, particles etc.) and nitrogen. Especially the hydrocarboneous species that are liquid at room temperature, summarized under the term "tars", cause problems in ICE CHP plants. This is because the PG has to be cooled prior to its conversion in the ICE for thermodynamic efficiency reasons. During the cool down, tars condensate and can cause problems for the operation of ICEs. Thus, tars have to be largely removed from the PG. The removal of tars often involves complex and expensive processes, which add to the specific system costs. Nevertheless, the efficiency advantages of ICE CHP plants are high enough to justify this additional effort compared to classical steam-cycle based biomass power plants.

A promising approach to achieve higher electrical efficiencies than those of ICE CHP plants is the use fuel cells (FC) for the conversion of the PG to electricity. This combination is commonly referred to as "Biomass Integrated Gasification Fuel Cell System" (B-IGFC). FCs directly convert the chemical energy of a fuel gas into electricity and heat through electrochemical reactions. Regarding its application in B-IGFC systems, the solid oxide fuel cell (SOFC) has drawn a lot of interest in recent years. SOFCs impose less stringent requirements to the fuel gas quality compared to all other FCs and are capable of directly oxidizing carbonaceous gases with high efficiencies at small scales. Further, SOFCs require fuel gas inlet temperatures well above the dew point of tars and operate at temperatures that are high enough to allow for the conversion of tars and their subsequent use for the electricity production. Ideally, only a particle removal would be required between the wood gasification reactor and the SOFC. Especially with respect to its hydrocarbon, tar, alkali salts and sulfur content, the composition of the PG plays a more important role for its conversion in SOFCs than in ICEs. The interactions between the gasification process and the SOFC need to be well understood to allow for the exploitation of the full potential of the B-IGFC approach.

1.2 Objectives

The present thesis aims at demonstrating the B-IGFC technology on kW-scale and at identifying promising B-IGFC system concepts with power outputs around 1 MW_{el}. With respect to the latter the most important questions are:

- How strongly does the producer gas composition resulting from different wood gasification processes influence the temperature management and the power output of available SOFC designs and what is the impact on the corresponding cooling requirements?
- Are there producer gases that lead to critical operating conditions in SOFCs such as critical temperature gradients and cell temperatures?
- Do different producer gases yield the same effects in SOFCs of different design?
- What role does the eventual treatment of tars and removal of sulfur play for the overall system efficiency and the specific plant costs?
- What are the major cost drivers in B-IGFC systems?
- What power production costs are feasible and what are the cost differences between the different cell designs?

1.3 Methodology

The chosen approach to fulfill the above aims is based on dedicated experiments and numerical systems analysis:

- Investigations of different operational modes of an in-house developed lab-scale updraft gasification reactor are performed aiming at a stable long-term operation and producer gas composition.
- The removal of impurities such as particles and sulfur species as well as the partial degradation of tars are experimentally characterized to explore the performance of state-of-the-art and currently developed gas processing technologies.
- An experimental setup covering the complete chain from wood to electricity is erected and operated to identify the most important technical problems, which may arise in B-IGFC systems.

The knowledge gained from the above mentioned experimental investigations is used for the definition of promising and realistic B-IGFC system concepts including all major equipment pieces. The interactions between different gasification processes, gas processing technologies and SOFC designs are investigated through numerical systems analysis:

- The core of the system analysis is a detailed one-dimensional numerical SOFC model. The model is developed to predict the impact of different producer gas compositions on the power output delivered by state-of-the-art cell designs for power plant applications. Besides, the model shall allow for the identification of critical operating conditions in SOFCs provoked by different producer gases.
- The defined B-IGFC systems are simulated by means of the commercial flowsheeting software package ASPEN PLUS. The system simulations aim at the determination of all relevant mass and energy streams in the investigated B-IGFC systems as well as an approximate sizing of the required heat exchanger network.
- The predicted SOFC power output and the results of the system simulations are the basis for the economic simulation of the defined B-IGFC systems. The economic model is developed to yield plant cost estimates and power production costs.

1.4 Organization of the thesis

Chapter 2 gives an overview of important aspects of the B-IGFC technology. At first, the properties of biomass as feedstock for power generation are explained in section 2.1. Section 2.2 provides the fundamentals of thermochemical biomass conversion processes focusing on the differences between producer gases originating from different biomass gasification processes. The most important technical processes for the removal of impurities and gas conditioning are discussed in section 2.3. Section 2.4 gives a brief introduction to the solid oxide fuel cell technology concentrating on the state-of-the-art, development trends as well as cell failure and degradation mechanisms.

Chapter 3 provides details about the experimental work conducted in the framework of this thesis. The B-IGFC system envisaged for the demonstration of the B-IGFC technology on kW-scale is explained in section 3.1. Further, the experimental setups used for the characterization of different gas cleaning and conditioning technologies are presented and the corresponding results are discussed in sections 3.2 to 3.4. The history of experiments leading to the first-time long-term demonstration experiment of the B-IGFC technology on kW-scale is outlined in section 3.5.

Chapter 4 summarizes the different modeling approaches for steady-state systems analysis of SOFC-based power generation systems in section 4.1. The modeling standard of recently published system analysis dealing with B-IGFC systems is presented in section 4.2.

Chapter 5 explains the numerical model framework developed for the envisaged system analysis. The overall modeling approach is charted in section 5.1 and centers on the data exchange between the detailed SOFC model, the flowsheeting system model and the economic model. Section 5.2 provides a detailed account of the lumped models developed to simulate the gas cleaning and conditioning technologies considered in the system analysis. The detailed one-dimensional SOFC model is explained in detail in section 5.3. Further, the model validation and an extensive sensitivity analysis is presented, the latter being focused on the determination of the impact of important model parameters on the temperature and power output trends predicted for different fuel gases. Section 5.4 explains the economic model built on cost functions, equipment sizing procedures and power production cost calculations.

Chapter 6 addresses the conducted system analysis. The major assumptions made and model settings used for the analysis are summarized in section 6.1. The investigated B-IGFC systems are described in detail in section 6.2. Section 6.3 treats the simulation of the gas processing performed in the various B-IGFC systems. The predicted PG compositions are then investigated with respect to the resulting operating conditions in different SOFC designs. The discussion centers on the impact of the different PGs on the interactions between the heat, mass and charge transport processes taking place in various SOFC designs. The predicted power output of the SOFC designs provides the background for overall system simulations which in turn are the basis for the discussion of the expected system efficiencies and efficiency losses. The results of the economic model are presented in section 6.4. At first, the plant cost estimates are analyzed to appoint the cost drivers of B-IGFC systems. The power production cost structure is explained subsequently. Finally, a sensitivity study of economic model parameters and analysis assumptions is presented.

Chapter 7 summarizes the main findings, gives the resulting conclusions and provides recommendations for future research.

2 Technology overview

The combination of biomass gasification with SOFCs is a highly promising approach to exploit the potential of biomass in combined heat and power generation. The according systems are commonly referred to as "Biomass Integrated Gasification Fuel Cell Systems" (B-IGFC). Figure 2-1 gives an outline of the core components of B-IGFC systems.

Figure 2-1: Technical outline of a B-IGFC system

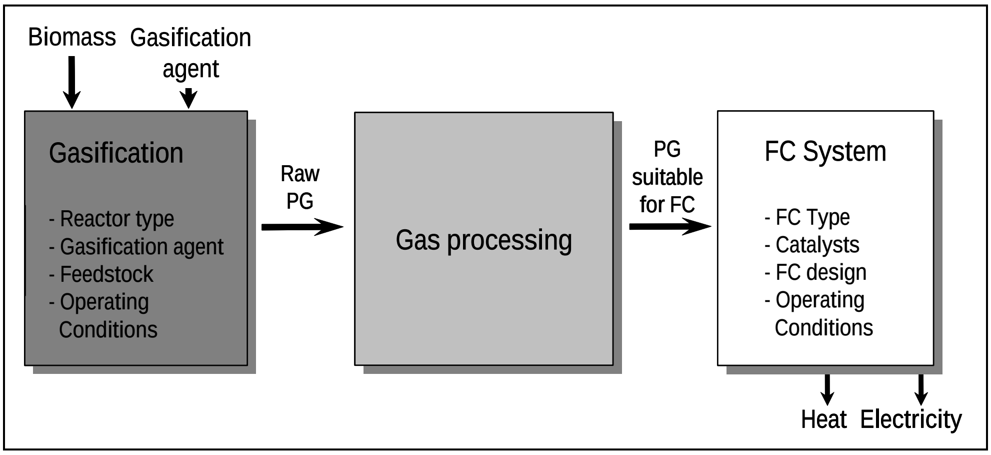
Biomass
Gasification agent
Gasification
- Reactor type
- Gasification agent
- Feedstock
- Operating Conditions
Raw PG
Gas processing
PG suitable for FC
FC System
- FC Type
- Catalysts
- FC design
- Operating Conditions
Heat
Electricity

In a first step the solid biomass is converted to a combustible gas mixture. The composition of the gas mixture depends on the employed reactor type, gasification agent, feedstock and operating conditions of the gasification process. It consists to a major extent of hydrogen and carbon monoxide, the rest being carbon dioxide, methane, other hydrocarbon species, water, diverse impurities (e.g. tars, alkali salts, sulfur, soot particles etc.) and nitrogen in case of air as gasification agent. The impurities are potentially performance degrading and have to be removed to some extent in order to meet the requirements of the employed fuel cell. The requirements depend on the specific fuel cell (FC) type and its design, catalyst materials and the operating conditions.

The strong interactions between the composition of the gas mixture obtained from the gasification process and the fuel cell entail that optimal system integration is crucial for overall energy efficient and cost effective system. The subsequent sections provide an introduction to the most important aspects and components of B-IGFC systems.

2.1 Biomass

2.1.1 Definition

Biomass is a diverse term. In biological and ecological disciplines, the accumulation of all living matter (plants, bacteria, animals and men) or specific species in a given area or of a biological community is referred to as biomass. In contrast, the energy and chemical industry defines biomass as all living or recently deceased biological matter suitable as raw material for industrial processing. In this work, the term biomass refers to plant tissue or more specifically to wood.

2.1.2 Classification

The variety of plant matter can be classified based on the origin and the type of growth of the plants, [5]:

- Terrestrial plants
  - Woody plants, i.e. perennial lignocellulosic crops
    - Long term growth (15-50 year); Short term single stem forestry (6-15 year) and multiple stem plants (3-5 year)
  - Herbaceous plants and grasses, i.e. switchgrass
  - High sugar-/ starch-producing crops, i.e. sugarcane
  - Oil-producing plants, i.e. rapeseed
- Aquatic plants, i.e. algae

Another, more process-oriented, classification is based on the intrinsic moisture content which is that of the biomass material without the influence of weather effects. Plants with an intrinsic moisture content requiring more energy for the drying than their chemical energy content are classified as wet, [6], while wood is classified as dry biomass.

2.1.3 Construction

Plants combine water and carbon dioxide to sugar building blocks, Eq. 1.

$$n \cdot H_2O + n \cdot CO_2 + Light \xrightarrow[Chlorophyll]{} (CH_2O)_n + n \cdot O_2 \qquad \text{Eq. 1}$$

The required energy is produced from light via photosynthesis based on chlorophyll. On average, between 0.1 and 1 % of the available light is stored as chemical energy in plants, [7].

The sugar building blocks are the starting point for the major fractions found in all terrestrial plants, [8], lignin, hemicellulose and cellulose.

- Lignin

  Lignin makes up about 25-35 mass-% (dry) of wood and 10-25 mass-% (dry) of other plants. It is a complex irregular aromatic polymer, often linked to cellulose and hemicellulose compounds in the plant cell walls. The high lignin fraction of wood accounts for its rigidity and slow growth compared to herbaceous plants, Figure 2-2, [6].

Figure 2-2: Molecular structure of lignin, [9]

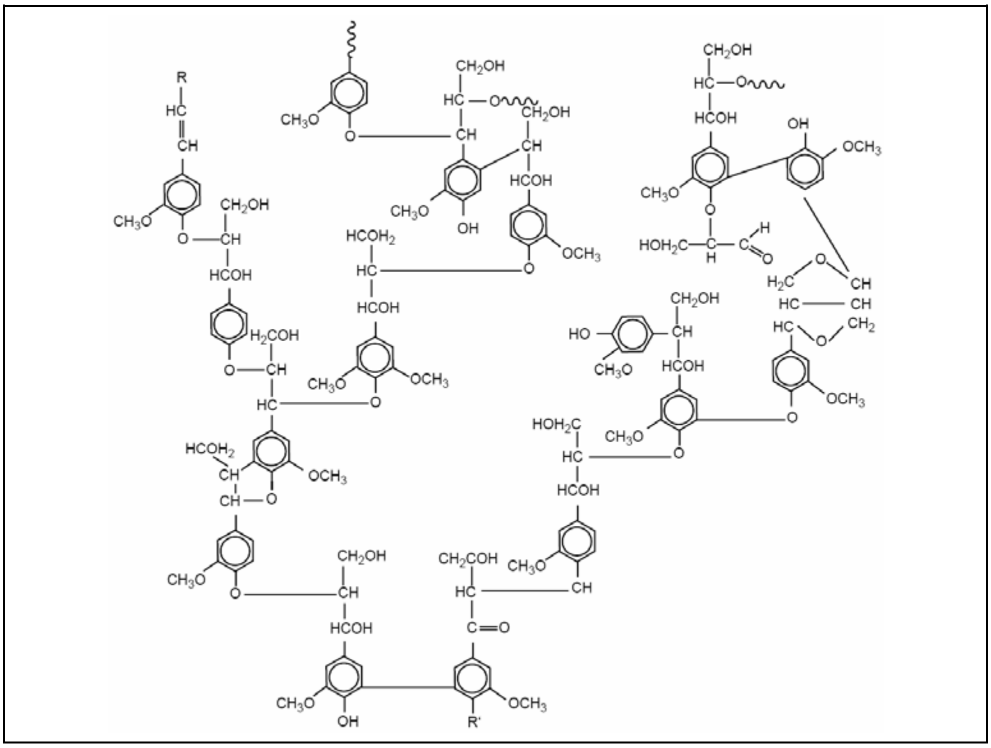

- Hemicellulose

  In contrast to cellulose, hemicellulose comprises five sugars, namely xylose, arabinose, galactose, glucose and mannose. Hemicellulose consists of 50 to 200 sugar units and is amorphous, see Figure 2-3. Plants consist to approx. 15-30 mass-% (dry) of hemicellulose.

Figure 2-3: Molecular structure of hemicellulose, [9]

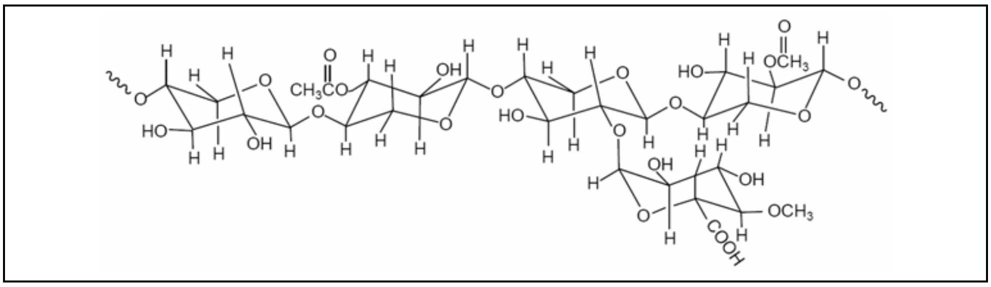

- Cellulose

  Plants consist to approx. 40-80 mass-% (dry) of cellulose, being a linear polysaccaride occasionally made up of over 10000 glucose units, see Figure 2-4. The elemental formula of polymeric cellulose is $(C_6H_{10}O_5)_n$.

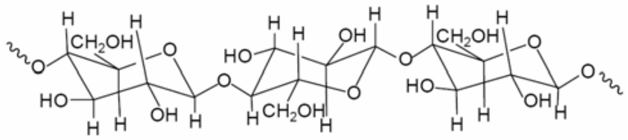

Figure 2-4: Molecular structure of cellulose, [9]

Cellulose, hemicellulose and lignin represent approx. 95-98 mass-% (dry) of woody biomass. The rest can be allocated to extractives and ash, [10]. Extractives are defined as compounds of the biomass that are not an integral part of the plant structure and that are soluble in e.g. water or methanol. Ash is defined as the non-combustible, inorganic fraction of the biomass. It includes alkali salts, heavy metals, sulphur, chlorine and silicates. The ash fraction of wood is mostly below 1 mass-% (dry). Table 2-1 illustrates the variation spectrum.

Table 2-1: Average chemical composition of various terrestrial biomass species, [7]

Dry fraction [mass-%]	Eucalyptus tree	Switchgrass	Corn stover	Corn grain
Cellulose	48	43	36	3
Hemicellulose	14	33	23	6
Lignin	29	9	17	2
Extractives	6	8	6	82
Ash	1	6	10	0
Residues	2	1	8	7

2.1.4 Properties

This work focuses on woody biomass for power generation, the most important material properties of which are discussed in the following.

2.1.4.1 Moisture

The intrinsic moisture content comprises the water in the pores and hydroscopic bound water in the solid structure of the woody material, [10]. The extrinsic moisture content accounts for complementary moisture originating from the weather conditions during harvesting and storage. Regarding wood as feedstock for power generation applications, the extrinsic moisture content, also referred to as water load, is of greater interest than the intrinsic:

$$M = \frac{m_s - m_d}{m_d} = \frac{m_{H_2O}}{m_d}$$

with Eq. 2

M *=water load;* m_s *= moist mass;* m_{H_2O} *= extrinsic water mass*

m_d *= mass of specimen after 24 h drying at 102 °C at 1 atm*

In contrast to the moisture content, the humidity is based on the wet mass of the specimen. It is defines as:

$$w = \frac{m_s - m_d}{m_s} = \frac{m_{H_2O}}{m_s}$$

Eq. 3

with w *= humidity;* m_s *= moist mass*

m_d *= mass of specimen after 24 h drying at 102 °C at 1 atm*

The moisture content can be converted to a humidity value via Eq. 4.

$$M = \frac{w}{1-w} \qquad \text{Eq. 4}$$

2.1.4.2 Proximate and ultimate analysis

The "proximate analysis" of solid fuels is standardized in the ASTM E870-82. The analysis yields information about moisture, volatile matter, ash and residue as well as fixed carbon content of solid fuels. The volatile matter content is determined by heating a fuel sample up to 950 °C without adding oxygen or steam and maintaining this temperature for 7 minutes. The mass difference of the sample before and after the procedure represents the volatile matter content. The volatile matter fraction is calculated as follows:

$$X_{VM} = \frac{m_{start} - m_{end}}{m_{start}}$$

with Eq. 5

m_{start} *= original sample mass*

m_{end} *=sample mass at end of volatile matter test procedure*

The ash content is determined by heating a fuel sample up to 600 °C in air and maintaining this temperature for 4 to 6 hours. The remaining material is considered as ash. The ash fraction is the quotient of ash mass and sample mass before the test procedure.

$$X_{Ash} = \frac{m_{end}}{m_{start}}$$

with

Eq. 6

m_{start} *= original sample mass*

m_{end} *=sample mass at end of ash test procedure*

The fixed carbon fraction is used to estimate the amount of coke that can be obtained from a fuel sample. It is calculated according to:

$$X_{FC} = 100 - X_{VM} - X_{Ash}$$

Eq. 7

The proximate analysis gives a first measure for the suitability of the analyzed material for thermochemical conversion technologies.

The "ultimate analysis" provides information about the elemental composition of solid fuels. Plants mainly consist of carbon, hydrogen, oxygen and nitrogen. Besides, a variety of other chemical elements can be found in biomass with more or less important concentrations. The importance of these trace elements depends on the subsequent processes. For thermochemical conversion, sulfur, chlorine, potassium and sodium are most important. The rest of the biomass material (e.g. heavy metals) is usually summed up under the term ash. Table 2-2 gives the proximate and ultimate analysis of biomass materials in comparison to coal.

Table 2-2: Proximate (italic) and ultimate (bold) analysis for various biomass and fossil fuels, [10]

	M	X_{VM}	X_{FC}	C	H	O	N	S	Cl	K	Na	Ash
	[%]	[mass-% (dry)]										
Average Wood	*20*	*82*	*17*	51.9	6.0	41.8	0.1	0.01	0.02	0.04	0.02	*1*
Corn Straw	*16*	*59*	*21*	50.2	6.7	42.1	0.44	0.44	0.11	-	-	*4*
Lignite	*34*	*44*	*47*	70.0	5.2	22.8	1.99	-	-	-	-	*9*
Bituminous coal	*11*	*39*	*51*	80.9	6.1	9.6	1.55	1.88	-	-	-	*10*

The main difference between biomass and solid fossil fuels can be found in the oxygen to carbon and the hydrogen to carbon ratios, [11].

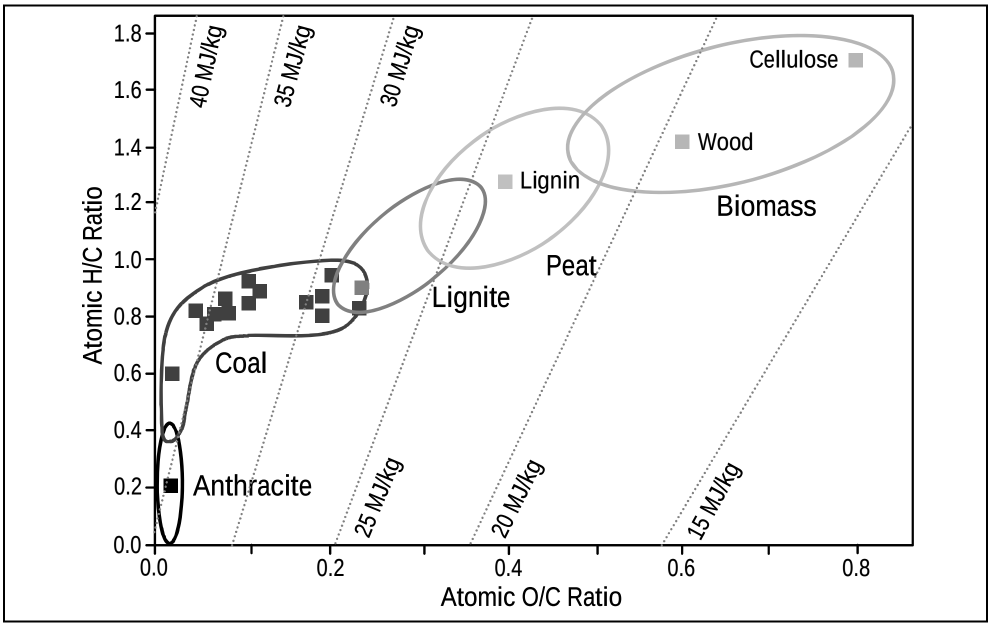

Figure 2-5:
Van Krevelen diagram for various dry solid fuels, [12], with calculated dry-basis iso-LHV lines via Eq. 8 exclusively considering the carbon, hydrogen and oxygen fractions

Figure 2-5 illustrates the significance of these ratios on the lower heating value of young biomass and solid fossil fuels in a so called Van Krevelen diagram. The comparably higher heating value of solid fossil fuels can be explained with the low number of carbon-oxygen bonds, [6], which again is a result of the natural diffusion process of biomass bound oxygen under high pressure and temperature. However, hydrogen also diffuses away under these conditions. Hence, at a certain stage of the process, the heating value begins to decrease asymptotically against the heating value of pure carbon which is 34.8 MJ/kg (daf).

The alkali metal content (Na, K, Ca, etc.) of biomass is of special interest regarding thermochemical conversion processes. Alkali metals can react with silica present in the biomass or originating from soil material introduced into the process during harvesting. The resulting sticky, liquid phase can provoke slagging in furnaces and boilers. Another known problem which can arise from alkali metals is high temperature corrosion of e.g. gas turbine blades. The catalysts employed in fuel cells could be poisoned by alkali metals, [13]. However, alkali metals were also found to have a positive effect as they reduce the tar formation, while increasing the char formation, in pyrolysis and gasification processes, [14, 15].

2.1.4.3 Caloric value

The caloric value (CV) of a material is defined as the heat per mass, volumetric or molar unit which is released during combustion. There are two different expressions for the CV:

- The quantity of heat which is obtained by bringing all the products of combustion back to the pre-combustion temperature, usually standard conditions, is defined as the higher heating value (HHV).
- The lower heating value (LHV) is mostly employed for applications that can not use the heat of condensation of steam. The LHV equals the HHV less the evaporation heat of water at standard conditions.

The caloric value is commonly determined using bomb calorimeters. The LHV of dry wood is typically in the range between 17 and 20 MJ/kg (daf), [16], see also Figure 2-5. The CV is often calculated via empirical correlations based on proximate and ultimate analysis results. In this work, the LHV was calculated using the Boie correlation, Eq. 8.

$$LHV\left[\frac{MJ}{kg}\right] = 34.8 \cdot c + 93.9 \cdot h - 10.8 \cdot o + 10.5 \cdot s + 6.3 \cdot n - 2.44 \cdot w$$

Eq. 8

with c, h, o, s, n, w *: carbon, hydrogen, oxygen, sulfur, nitrogen & water mass fraction on wet, ash free basis*

Besides, the Dulong, Grummel & Davis and Mott & Spooner correlations are used, [17]. The results may significantly diverge. Hence, the correlation choice is usually a question of minimizing energy balance errors.

2.2 Gasification

2.2.1 Biomass conversion overview

The type of biomass has a strong impact on the choice of conversion technology due to varying moisture contents and proportions of the three main components; cellulose, hemicellulose and lignin. In addition, the choice of conversion technology depends on the subsequent energy converting device and its specific requirements.

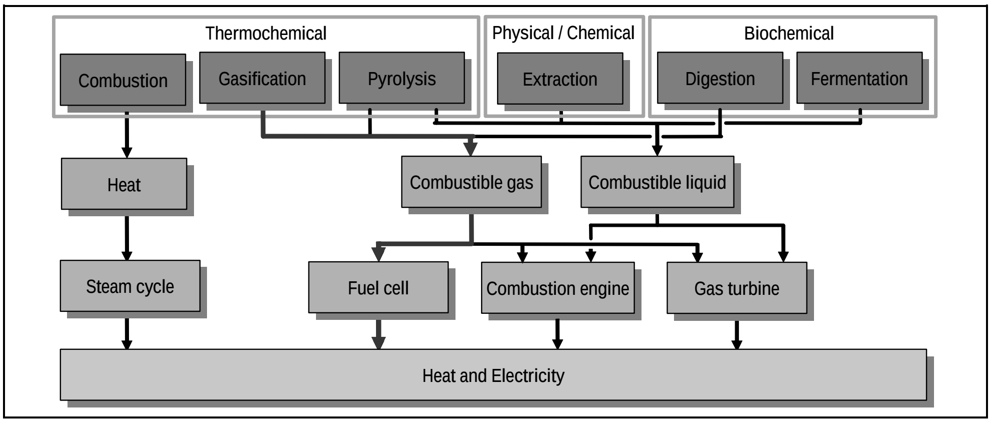
Thermochemical
Physical / Chemical
Biochemical
Combustion
Gasification
Pyrolysis
Extraction
Digestion
Fermentation
Heat
Combustible gas
Combustible liquid
Steam cycle
Fuel cell
Combustion engine
Gas turbine
Heat and Electricity

Figure 2-6: Biomass conversion technologies, intermediate products and end-use applications for the combined generation of power and heat

Figure 2-6 gives an overview of conversion technologies for heat and power generation from biomass with the respective intermediate products and possible end-use energy converting devices. The following three categories of conversion technologies are differentiated:

- Biochemical conversion
- Physical/chemical conversion
- Thermochemical conversion

Digestion and fermentation of biomass are biochemical conversion technologies with an energy efficiency of approx. 20 to 40 %, [18]. Biomass fermentation usually yields liquid ethanol, while digestion yields gaseous methane. The micro-organisms used in both processes can convert the sugar-based cellulose and hemicellulose as well as starch but not stable organic materials such as lignin. Hence, biochemical conversion of woody biomass results in high amounts of residues and is not indicated. In contrast, algae are well suited to biochemical conversion, [18].

Mechanical extraction, as physical/chemical conversion technology, yields a combustible liquid referred to as bio-oil. This oil is usually further processed to bio-diesel via transersterification and used for mobile applications. Plants such as rapeseed, with high moisture and extractible fraction are predestined for mechanical extraction technologies. Physical/chemical conversion of woody biomass is unfavorable due to its low extractible fraction. Thermochemical conversion technologies are discussed in the following sections.

2.2.2 Fundamentals of thermochemical conversion

Thermochemical conversion allows complete conversion of lignin and is therefore mainly indicated for dry biomass such as wood, [6]. The most important thermochemical conversion technologies are combustion, pyrolysis and gasification. The three technologies mainly differ in the product composition and amount of used oxidant if any. The latter is described by either the air-to-fuel ratio, which is the quotient of the effective and the stoichiometric amount of air or oxygen for complete combustion, Eq. 9, or the steam-to-fuel ratio for steam gasification processes.

$$\lambda = \frac{m_{act,oxi}}{m_{stoic,oxi}} \qquad \text{Eq. 9}$$

All thermochemical conversion technologies involve all or some of the sub-processes "oxidation", "reduction", "devolatilization" and "drying".

- Oxidation

  Heat is produced via exothermal partial or total oxidation of carbon, Eq. 10 and Eq. 11, at around 1000 to 1600 °C, [19]. The carbon originates from the devolatilization and reduction sub-processes.

$$C + 0.5 O_2 \rightarrow CO \ with \left(-\Delta H_R^0 = 110.5 \frac{kJ}{mol} \right) \qquad \text{Eq. 10}$$

$$C + O_2 \rightarrow CO_2 \ with \left(-\Delta H_R^0 = 398.8 \frac{kJ}{mol} \right) \qquad \text{Eq. 11}$$

- Reduction

  Most of the hydrogen, carbon monoxide, carbon dioxide and methane found in producer gases from thermochemical biomass conversion is produced in the reduction sub-process at temperatures between 600 and 1000 °C, [19]. The required heat, steam and carbon dioxide is usually produced in the oxidation sub-process. The carbon steam reaction, Eq. 12, is the principal reaction for the gasification of carbon. Besides, carbon can be gasified via the Boudouard reaction, Eq. 13.

$$C + H_2O \leftrightarrow CO + H_2 \ with \left(-\Delta H_R^0 = -131.3 \frac{kJ}{mol} \right) \qquad \text{Eq. 12}$$

$$C + CO_2 \leftrightarrow 2CO \ with \left(-\Delta H_R^0 = -172.5 \frac{kJ}{mol} \right) \qquad \text{Eq. 13}$$

  Another important reaction in the reduction sub-process is the exothermic water-gas shift reaction where carbon monoxide and steam react to hydrogen and carbon dioxide, Eq. 14. The water-gas shift reaction is heterogeneously catalyzed on carbon at temperatures below 1100 °C but may occur homogenously at higher temperatures, [20]. The exothermic hydrogasification reaction yields methane as product from carbon and hydrogen, Eq. 15. Methane can also be produced via the exothermic methanation reaction, Eq. 16. However in sum, the reactions taking place in the reduction sub-process are endothermic.

$$CO + H_2O \leftrightarrow CO_2 + H_2 \ with \left(-\Delta H_R^0 = 41.0 \frac{kJ}{mol} \right) \qquad \text{Eq. 14}$$

$$C + 2H_2 \leftrightarrow CH_4 \ with \left(-\Delta H_R^0 = 74.8 \frac{kJ}{mol} \right) \qquad \text{Eq. 15}$$

$$CO + 3H_2 \leftrightarrow CH_4 + H_2O \ with \left(-\Delta H_R^0 = 206.1 \frac{kJ}{mol} \right) \qquad \text{Eq. 16}$$

- Devolatilization

  Devolatilization denotes the thermal decomposition of biomass without the participation of an oxidant at temperatures between 200 and 600 °C, [19]. The three main constituents of biomass; cellulose, hemi-cellulose and lignin, see section 2.1.3, exhibit different thermal decomposition behaviors which originate from their molecular structure, [5]. Devolatilization yields gaseous, liquid and solid products. Gaseous products are mainly hydrogen, carbon monoxide and dioxide as well as methane and higher hydrocarbons. Liquid products are hydrocarboneous species that condense at room temperature, generally summarized under the term "tars". Non reacted carbon is the main solid product. Due to transport phenomena in pores and on the surface, the kinetics of devolatilization depends on the shrinking behavior and structure of the feed particles, [21]. Further, the heating rate and the heat transfer play important roles. The thermal decomposition reactions are endothermic. A more detailed discussion of the devolatilization of biomass is given in [20].

- Drying

  The moisture of biomass is vaporized in the drying sub-process at temperatures below 200 °C. The amount and nature of moisture determine the required heat quantity. Especially the vaporization of the water bound in the cell walls involves strengthening of the wood fibers and is accompanied by shrinkage of the biomass, [5]. More details on recent developments in biomass drying are given in [22].

Table 2-3 summarizes thermochemical conversion technologies with typical air/steam-to-fuel ratios, process temperatures and products.

Table 2-3: Thermochemical conversion technologies differentiated by air/steam-to-fuel ratio and desired products, [4]

Technology	Temperature [°C]	Air-to-fuel ratio [-]	Product [-]
Pyrolysis	400-700	0	Combustible liquid, gas and solid
Gasification	700-900	Oxidant: Air 0.2-0.5	Combustible gas with low LHV Non combustible solid
		Oxidant: Steam 0.4-3	Combustible gas with high LHV Non combustible solid
Combustion	800-1300	>1	Non combustible gas and solid

The technical pyrolysis process comprises the sub-processes "drying", "devolatilization" and to a minor extent "reduction" which usually occur simultaneously. During the thermal decomposition of biomass at temperatures between 400 and 700 °C without addition of oxygen or steam, a mixture of combustible gaseous, liquid (at room temperature) and solid products is produced. The product distribution as well as the composition of the produced gaseous and liquid species depend on the applied process conditions such as temperature, pressure, heating rate, fuel particle size and composition of the biomass, [20]. The required heat for the pyrolysis is produced via the oxidation of undesired products, mostly the solid fraction. The liquid product, named pyrolysis oil, can contain up to 80 % of the energy originally stored in the converted biomass, [23].

Combustion involves the simultaneously occurring sub-processes "drying", "devolatilization", "reduction" and "oxidation". During the oxidation with air-to-fuel ratios higher than one, the chemical energy of the biomass is entirely converted to sensible heat of exhaust gases consisting of steam, carbon dioxide and nitrogen for air as oxidant. The volatile compounds of the biomass and the products of char reduction are oxidized in the gas phase. However, char may also be directly oxidized in surface reactions which are not well understood yet, [24]. Depending on the biomass humidity, the exhaust gases have a temperature of 800 to 1300 °C. The produced heat can be converted to mechanical work via e.g. steam cycles or Stirling engines, [4].

Gasification comprises the sub-processes "drying", "devolatilization", "reduction" and "oxidation". Depending on the reactor design, the sub-processes may occur simultaneously or sequentially. The desired product of biomass gasification is a combustible gas with high heating value. Its composition is mainly determined by the gasification agent and the process conditions, [25]. Air as gasification agent yields a nitrogen diluted gas mixture which mostly contains hydrocarbons. This gas mixture is commonly referred to as producer gas in contrast to syngas, which stands for nitrogen-free gases from oxygen, steam or hydrogen gasification with negligible hydrocarbon content, [7]. The gasification is autothermal if the required heat is produced via partial combustion of the feed within the same reactor. The gasification is allothermal if the heat is produced in a spatially separated second reactor and introduced to the gasification reactor by means of a bed material, heat pipes etc. The efficiency of a gasification process is given by the cold gas efficiency which relates the chemical energy content of the produced gas to that of the biomass before conversion. Depending on the process conditions, the cold gas efficiencies of today's biomass gasification processes range from 50 to over 90 %, [25].

2.2.3 Wood gasification technology overview

The primary aim of every wood gasification technology is the efficient conversion of the energy content of the wood into the chemical energy content of the produced gas. The gas composition and the impurity signature depend on the gasification agent and the process conditions which are a consequence of the gasification reactor design and vice versa. The impurity signature of a producer gas is principally characterized by six different types of impurities and their phase of appearance, Figure 2-7. The total amount of impurities is independent of the reactor design but depends strongly on the concentration of the according educts in the feedstock.

Figure 2-7:
Types of impurities and their typical phase of appearance in biomass-derived producer gases

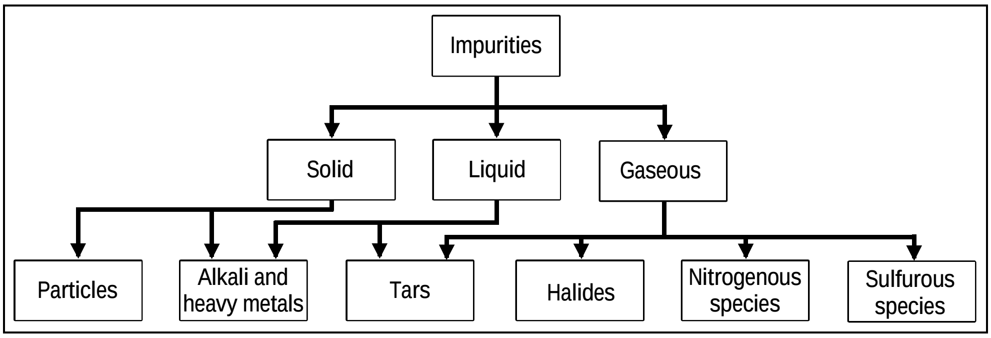

As the gasification is the origin for all impurities found in producer gases, a short summary is given at this point as a basis for the discussion of different gasification technologies. The removal of impurities and their impact on the operation of SOFCs is discussed in the sections 2.3.1 and 2.4.7. As can be seen in Figure 2-7, impurities can be present in the produced gas in the solid, liquid and gaseous phase. Following types of impurities can be distinguished:

- Particles are solid agglomerations of unreacted carbon and ash.
- Alkali metals can be present in the solid state condensed on particles at temperatures below 600 °C, [26], and in the liquid phase as aerosols or even gaseous phase at temperatures above 800 °C, [25].
- Tars are a mixture of diverse organic species of oxygenated and aromatic character formed during the thermal decomposition of the biomass in the devolatilization sub-process and subsequent reactions with reactive char. The complex mechanisms of primary and secondary tar formation are discussed in depth in [20, 27]. Depending on their molecular structure, tars may be in the liquid state as aerosols

up to temperatures around 400 °C, e.g. the boiling point of benzanthracene is approx. 435 °C.

- Halides, of which hydrochloric acid (HCl) is the most important representative, originate from the chlorine content of the biomass. Hydrochloric acid is in the gaseous phase due to its boiling point at 57 °C.
- Nitrogenous species such as ammonia (NH_3) and hydrogen cyanide (HCN) are typically in the gaseous phase due to their boiling point below 30 °C and originate from the nitrogen content of the biomass. Between 50 and 80 % of the nitrogen originally bound in the biomass are released as gaseous species during gasification, [25].
- Sulfurous species in producer gases are generally in the gaseous phase with hydrogen sulfide (H_2S) as most prevalent species. However, carbonyl sulfide (COS) and organic sulfur species, of which thiophene (C_4H_4S) is an important representative, can also be present in producer gases.

More generally, fixed bed, moving bed and entrained flow biomass gasification reactors can be distinguished. Figure 2-8 outlines the most important gasification reactor designs. The main difference is the gas/solid flow pattern which in return determines the sequence of the above described sup-processes of gasification.

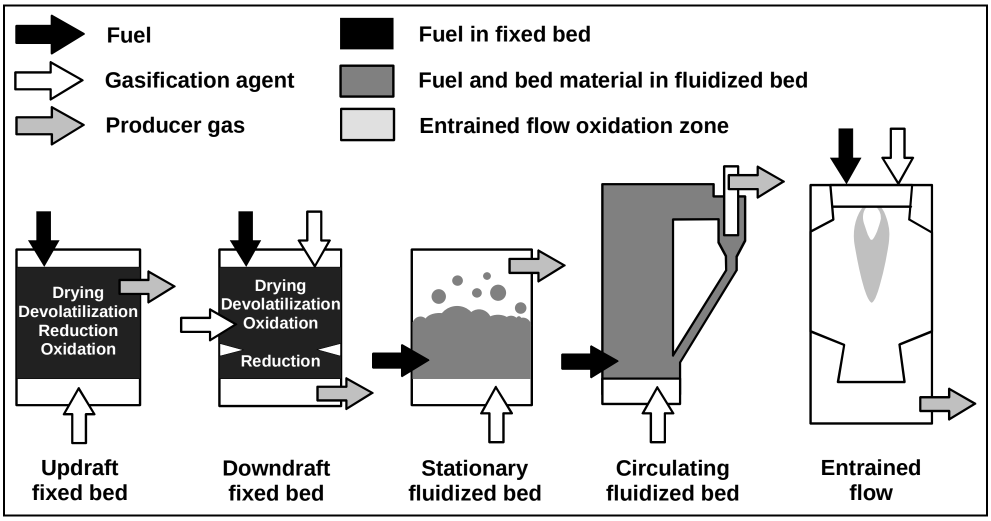
Fuel
Gasification agent
Producer gas
Fuel in fixed bed
Fuel and bed material in fluidized bed
Entrained flow oxidation zone
Drying
Devolatilization
Reduction
Oxidation
Drying
Devolatilization
Oxidation
Reduction
Updraft fixed bed
Downdraft fixed bed
Stationary fluidized bed
Circulating fluidized bed
Entrained flow

Figure 2-8: Gasification reactors with gas/solid flow patterns, adapted from [20]

Updraft wood gasifiers are fixed bed reactors. The wood is introduced at the top of the gasifier while the gasification agent, typically air, is introduced at the bottom through a grate. The producer gas is extracted at the top of the gasifier after passing through the wood material present in the gasifier. In contrast to the gasification agent and the producer gas, the wood particles move downwards in the gasifier, running through the sub-processes of gasification in the order "drying", "devolatilization", "reduction" and finally "oxidation". Char is partially combusted in the oxidation zone at temperatures between 1600 and 1000 °C. After the oxidant is spent, the hot exhaust gas reacts with char in the reduction zone at temperatures between 1000 and 600 °C. Further up in the gasifier, the temperature of the producer gas becomes to low for reducing reactions. The thermal decomposition of the wood takes place in the subsequent devolatilization zone at temperatures between 600 and 200 °C. Before exiting the gasifier, the producer gas dries the fresh wood at temperatures below 200 °C in the drying zone.

Updraft gasification producer gases are relatively cold with outlet temperatures typically between 200 and 300 °C. In [28], producer gas temperatures of 75 °C are reported. The cold gas efficiency including all combustible species in the producer gas can reach values in excess of 90 % as a consequence of the low sensible heat content of the producer gas, [4]. Due to the use of air as gasification agent, the heating value of updraft gasification producer gases is low in the range of 5 MJ/m_n^3 on a dry and tar free basis (dtf), [20]. Since the tars formed in the devolatilization zone only pass the colder drying zone before exiting the updraft gasifier, cracking is not likely to occur resulting in very high tar loads with values up to 150 g per m_n^3 (dtf), [4]. The tar mix mainly consists of oxygenated species such as phenols and acids as well as light aromatics, [29]. Heavier aromatic species might be present in the condensed phase. The particle load is usually low due to the filtration effect of the wood material bed which the producer gas passes on its way to the gasifier exit at its top, [4]. Alkali metals can be assumed to stay almost completely in the solid phase. For the same reason as for the high tar load, the presence of a notable amount of organic sulfur species is likely.

The updraft gasification process is very robust towards the size of the wood particles and their humidity. The large internal drying zone allows the conversion of wood with up to 50 % humidity. Updraft gasification reactors are well scalable to a size of 20 MW thermal input, [28], and the costs are relatively low due to the simple reactor concept.

Downdraft wood gasifiers are the second common type of fixed bed reactors. The wood is introduced at the top of the gasifier, while the gasification air is either introduced there as well or right above the hearth zone in the lower part of the reactor. The producer gas exits the gasifier at the bottom. Hence, wood particles and gasification air move both downwards in the gasifier running through the sub-processes of gasification in the order "drying", "devolatilization", "oxidation" and finally "reduction". In the upper part of downdraft gasification reactors, the wood is dried and decomposed at temperatures up to 600 °C. In contrast to the updraft gasification, the required heat does not directly come from the producer gas but is introduced to these zones via gasification air pre-heating and/or heating of the reactor walls, [19]. The char and the tars produced in the devolatilization zone are partially combusted in the oxidation zone at temperatures up to 1600 °C. The oxidation zone is situated directly above the so called throat which is characteristic for downdraft gasification reactors. This reduced cross-sectional area assures a homogenous layer of hot char and is the location of the reduction zone. Tars originating from the devolatilization zone that were not cracked in the oxidation zone are further degraded at temperatures around 1000 to 600 °C.

Downdraft gasification producer gases typically have temperatures between 500 and 900 °C, [25], and according cold gas efficiency values of 70 to 80 %, [4]. Similar to the updraft gasification, the heating value of downdraft producer gases is low in the range of 5 MJ/m_n^3 (dtf), [20]. Due to the reactor internal tar cracking, tar loads are low with maximum values of 6 g per m_n^3 (dtf), [4]. However, the tar species in the tar mix are mainly aromatic and hence more stable than those found in updraft gasification producer gases, [30]. The particle load is higher than that of updraft gasification producer gases. Due to the high producer gas temperatures, alkali metals may be present in the liquid phase. Similar to most of the tar species, organic sulfur species should be degraded in the oxidation and reduction zones. Sulfur is therefore most likely to be present in form of hydrogen sulfide and carbonyl sulfide.

The downdraft gasification process is sensible towards the size and geometry of the wood particles because it strongly influences the homogeneous distribution of the air in the oxidation zone and the controlled bridge building in the throat area, [19]. The poor heat exchange of the oxidation zone with the drying and devolatilization zones limits the wood humidity to values below 20 %, [30]. The maximum size of downdraft gasification reactors is around 2 MW thermal as the homogeneous gasification agent distribution in the hearth zone becomes increasingly difficult with larger diameters of the throat, [19].

Figure 2-9 shows the technical outlines of a commercial updraft and a commercial downdraft gasification reactor. The updraft reactor (left) has a rated thermal capacity of 4.8 MW and was built during 1993 in Harboore, Denmark, by the Babcock & Wilcox Volund A/S. The producer gas has a temperature of 75 °C and an average tar load of 70 g/m$_n^3$ (dtf). The gas is cleaned by means of a gas scrubber and electrostatic precipitator. With two gas engines producing 1536 kW electrical power, the overall power efficiency departing from wood chips with approx. 50 % humidity is in excess of 30 %, [29]. 3.2 MW of heat at 90 °C are delivered to a district heating grid. Since commissioning, the updraft gasification reactor has been operated several ten thousand hours with 8000 hours per year in average. The gas engines were commissioned in 2003 and operated until 2005 for over ten thousand hours, [25].

The downdraft reactor (right) has a rated thermal input of 0.8 MW. It was built during 2001 in Spiez, Switzerland, by Pyroforce AG. The almost tar free producer gas exits the gasifier at approx. 650 °C. Gas cleaning involves the addition of an adsorbent to the producer gas and its subsequent removal together with all other particles in a particle filter. A single gas engine is installed producing a maximum of 200 kW of power and 270 kW of heat. Since commissioning, the gasification reactor has been operated for 25000 hours and the gas engine for 15000 hours, [31].

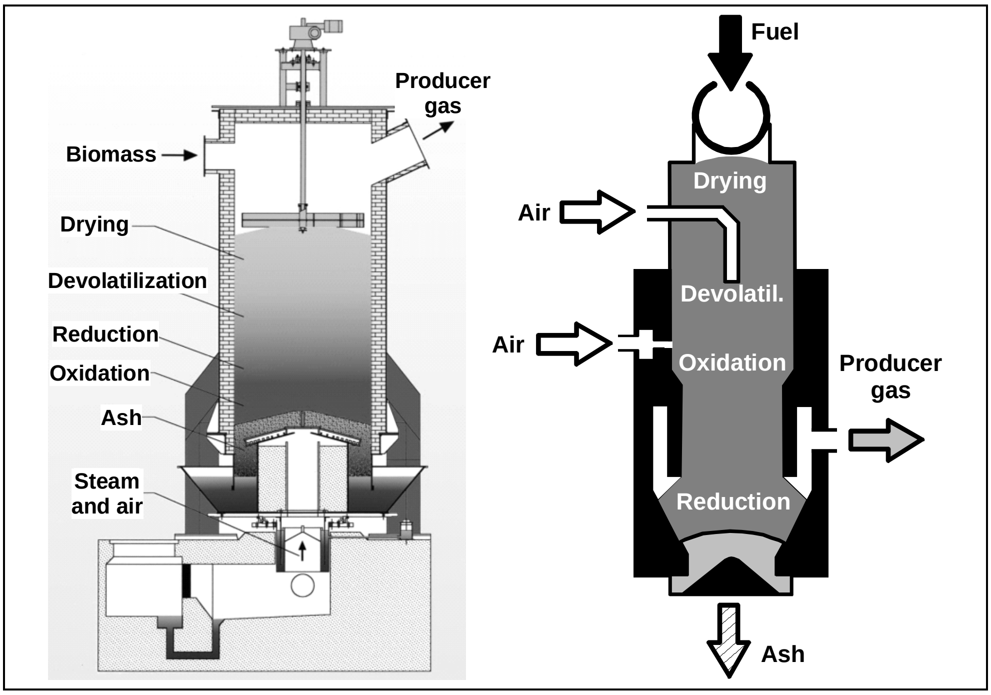

Figure 2-9: Technical outlines of the updraft gasification reactor in Harboore/DK (left), [28], and the Pyroforce downdraft gasification reactor in Spiez/CH (right), [32]

Fluidized bed gasifiers are categorized via their fluid dynamics and heat transfer into stationary and circulating fluidized bed gasifier types. Generally, the wood is introduced near the bottom of the gasifier where it is immediately mixed with a bed material such as sand. The portion of bed material in the reactor volume is typically over 90 %, [25]. The gasification agent is usually introduced through a nozzle floor or a frit. Due to the mixing of the wood with the bed material, the sub-processes of gasification do not take place in a defined zone of the reactor but throughout the whole reactor volume which yields almost isothermal conditions. The temperature in the gasification reactors is usually kept below 950 °C to prevent slagging of the bed material, [25]. The producer gas is extracted via a cyclone at the top of the gasifier.

In **stationary fluidized bed gasifiers**, the flow velocity of the gasification agent is adjusted so that only few bed particles are transported out of the bed region. Thus, mainly ash particles are blown out of the fluidized bed. The heat required for the gasification reactions is usually produced via partial combustion of the feed. Thus, air is commonly used as gasification agent. However, there are also reactors employing mixtures of air and steam or oxygen and steam. A recently developed approach is the use of high temperature heat pipes as means of heat input to the gasification reactor, [33].

The producer gas has temperatures around 800 to 950 °C, [25], which allows cold gas efficiency values around 70 to 85 %, [4]. Where air is used as gasification agent, the heating value of the produced gas is in the range of 3.6 to 5.9 MJ/m_n^3 (dtf), [4]. Similar to downdraft gasification, the high temperature prevalent in fluidized bed reactors yields a tar mix mainly consisting of aromatic species. The tar load is however considerably higher than that of downdraft gasifiers with 2 to 50 g/m_n^3 (dtf), [25]. This is because the formed aromatic tar species do not experience temperatures as high as prevalent in the oxidation zone of downdraft gasifiers and are hence degraded to a much lesser extent inside the gasification reactor. As a matter of principle, the particle load is high. Alkali metals are mainly in the liquid phase due to the high producer gas temperature, [34], which also accounts for the predominant presence of hydrogen sulfide and carbonyl sulfide as sulfur species. However, a notable amount of organic sulfur species may also be present.

The stationary fluidized bed gasification process is sensible towards the size and geometry of the wood particles as these properties determine the fluid dynamic behavior of the feed. To maintain the comparably high temperatures in the gasification bed, the feed humidity usually has to be lower than 15 %. This is particularly important for fluidized bed reactor concepts where the required heat is not produced via partial combustion of the feed but introduced by other means such as heat pipes, [33]. Stationary fluidized bed gasification is very well scalable for plant sizes between 1 to 50 MW thermal input, [4].

Circulating fluidized bed gasifiers feature almost the same properties as their stationary counterparts, except that the flow velocities are considerably higher. Consequently the mixing of bed material and wood particles is better which yields fully isothermal conditions. Moreover, bed material and unreacted char are continuously discharged from the gasification zone. In standard circulating fluidized bed reactors, the discharged bed material and char are reintroduced to the gasification zone where the required heat for the gasification reactions is produced via direct partial combustion of the feed. Two-zone circulating fluidized bed reactors however use the discharge mechanism for the spatial separation of gasification and combustion reactions. This way, air can be used as oxidant in the combustion zone and steam as gasification agent in the gasification zone yielding a non-diluted product gas. The heat for the gasification reactions is transported from the combustion zone to the gasification zone via the circulating bed material.

The producer gas from circulating fluidized bed reactors has basically the same properties as that of stationary fluidized bed reactors. Exceptions are the higher heating values of two-zone concepts around 14.2 to 18.1 MJ/m_n^3 (dtf), [4], and the typically lower tar load in the order of 1 to 20 g/m_n^3 (dtf), [25]. This can be assigned to the frequently used reactive bed materials such as olivine, [35]. Reasonable reactor sizes are between 20 to 200 MW thermal input, [4].

Figure 2-10 shows two fluidized bed gasification reactors employing steam as gasification agent and air for the combustion of unreacted char to produce the required heat for the gasification reactions. The stationary fluidized bed reactor (left) uses sodium heat pipes for the heat exchange between the combustion and the gasification chamber. The "Biomass heat pipe reformer" (BHPR) was developed and patented by the Technische Universität München. The first prototype reactor with a thermal capacity of 150 kW was commissioned in 2002 and operated for 72 hours non-stop. The producer gas had a temperature around 800 °C and was directly flared. In future, the product gas shall be produced with a cold gas efficiency around 70 % , [33], and converted to electricity via micro gas turbines and high-temperature fuel cells.

Figure 2-10: Technical outlines of the Biomass heat pipe reformer from TU Munich/D (left), [36], and the Fast internally circulating fluidized bed reactor in Güssing/AT (right), [37]

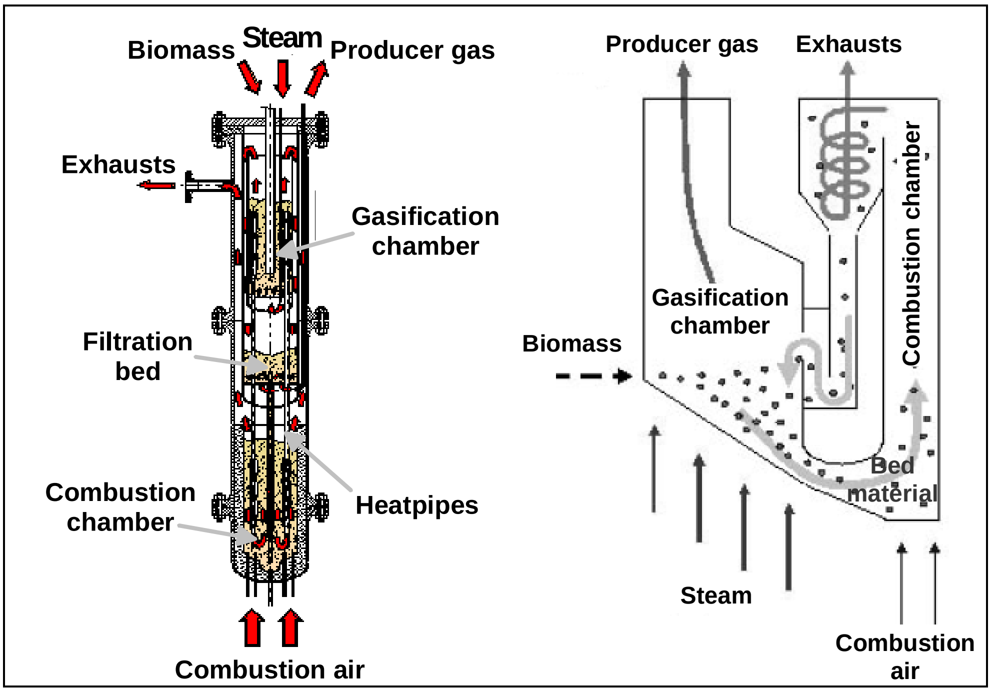
Biomass
Steam
Producer gas
Exhausts
Gasification chamber
Filtration bed
Combustion chamber
Heatpipes
Combustion air
Producer gas
Exhausts
Combustion chamber
Gasification chamber
Biomass
Bed material
Steam
Combustion air

The "Fast internally circulating fluidized bed" (FICFB) reactor depicted on the right of Figure 2-10 employs the bed material for the heat exchange between the combustion and the gasification chamber. The reactor was built in Güssing/Austria by the Repotec Umwelttechnik GmbH. Commissioning was completed in 2002 with a rated thermal capacity of 8 MW. The product gas exits the gasifier at approx. 850 °C with several g/m_n^3 (dtf) of tar load. The gas cleaning comprises a hot gas filtration and a gas scrubber. One single gas engines produces 2 MW of electrical power, which translates in an overall power efficiency of 25 %, and 4.5 MW of heat at 120 °C. With over 25000 operating hours of the gasification reactor and the gas engine, the FICFB plant in Güssing is one of the most successful biomass gasification power plants in existence.

Entrained flow gasifiers were initially developed for the gasification of coal which is fed to the reactors as either dry powder or water slurry. Oxygen is commonly employed as gasification agent yielding very high reactor temperatures between 1250 to 2000 °C. The conversion of wood to powder or slurry requires more effort than the simple grinding of coal. Entrained flow wood gasifiers are therefore usually combined with a pyrolysis reactor in which the sub-processes "drying" and "devolatilization" take place at temperatures around 600 °C. The heat required for the pyrolysis process may either come from exhaust gases or be produced via partial combustion of the feed. The pyrolysis reactor is then in fact a pre-gasification reactor. The sub-processes "oxidation" and "reduction" occur in the actual entrained flow gasification reactor. As the pyrolysis yields a mixture of gaseous, liquid and solid products the composition of which can be controlled via the pyrolysis process conditions, the form of the feed depends on the entrained flow gasifier design and can be either a gas/solid or a liquid/solid mixture.

Entrained flow gasification producer gases have temperatures between 800 and 1200 °C, [38, 39]. The cold gas efficiency of this process is in the range of 50 to 70 % depending on the reactor temperature. Despite the use of oxygen as gasification agent which inhibits nitrogen dilution, the heating value of entrained flow gasification syngases is only in the range of 8.8 to 9.3 MJ/m_n^3 (dtf). This is because the gases are almost free of hydrocarbon species with high heating values. The syngases are generally tar and particle free. Alkali salts may be present in the liquid and even gaseous phase. Sulfur is present in form of hydrogen sulfide and carbonyl sulfide only.

Entrained flow gasifiers are at the most sensible towards the ash melting point and content of the feed. The humidity of the gasified feed usually plays a less important role for the gasification itself but may be limited by the upstream pyrolysis. Due to the complexity of the involved reactors, entrained flow gasification is a large scale technology aiming at thermal inputs up to several hundred MW.

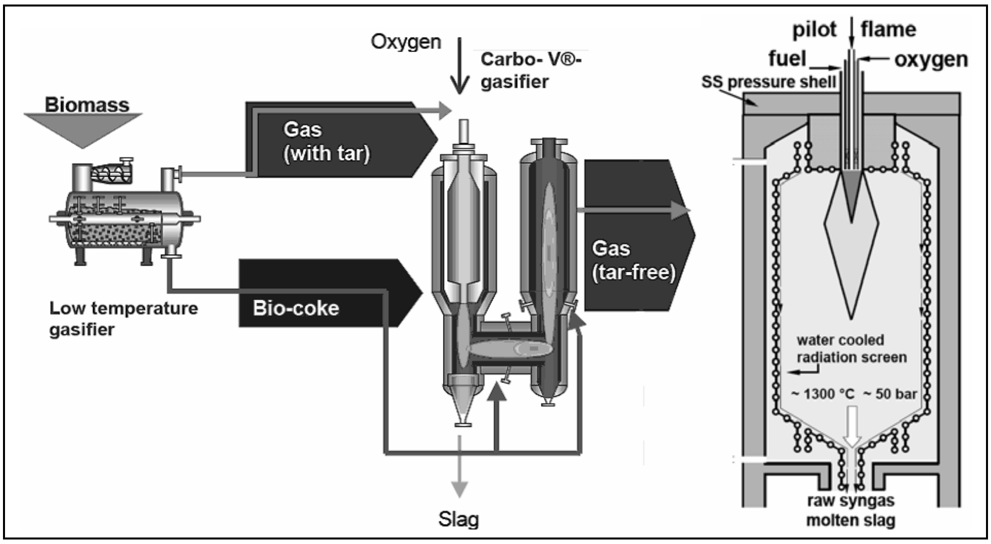

Figure 2-11: Technical outlines of the Carbo-V gasifier developed by CHOREN/D (left), [39], and the GSP gasifier developed by the Deutsches Brennstoffinstitut/DDR, [38]

Figure 2-11 shows the technical outlines of two entrained flow biomass gasifiers. CHOREN Industries GmbH has developed the Carbo-V® gasifier (left) and is currently building a Biomass-to-liquids (BtL) plant in Freiberg, Germany, based on this gasification technology. The biomass is first gasified with very little air, producing a highly tar laden gas and char. The gas is partially oxidized with oxygen in the entrained flow gasifier. The hot gases are cooled down to approx. 800 °C in the reduction section of the gasifier by means of quenching with grinded char from the low temperature gasification. The char is simultaneously gasified, [39].

The GSP gasifier (Gaskombinat Schwarze Pumpe, right) was developed for the gasification of salt-containing brown coal and therefore suits the gasification of biomass with high ash content well. In fact, the ash acts as protective layer for the reactor walls and is therefore required. As the gasifier requires a liquid feed, the Forschungszentrum Karlsruhe has developed a pyrolysis process that is suited for the production of slurry from various types of biomass. With 1200 °C, [38], the producer gas is hotter than that of the CHOREN gasifier as no reactor internal quenching is conducted. Table 2-4 summarizes the above paragraphs.

Table 2-4: Comparison of biomass gasification technologies based on [4, 19, 25, 30, 40]

	Unit	Updraft	Down-draft	Fluid. Bed	Circul. FB	Entrain. flow
Gasification agent	[-]	Air	Air	Air/O_2/ H_2O	H_2O	O_2
H_2	[mol-%]	10-14	15-21	15-22	17-36	29-40
CO		15-20	10-22	13-15	36-51	39-45
CO_2		8-10	11-13	13-15	7-15	18-20
CH_4		2-3	1-5	2-4	0.1-0.6	0.05-0.1
C_2		-	0.5-2	-	1.4-7.5	-
N_2		53-65	37-63	44-57	0-39	0.1-9
LHV	[MJ/m_n^3 (dtf)]	3.7-5.1	4.0-5.6	3.6-5.9	14.2-18.1	8.8-9.3
Gas temperature	[°C]	75-300	500-900	800-950	800-950	800-1000
Cold gas efficiency	[%]	$>90_{incl.tar}$	65-75	70-85	60-70	50-70
Particle load	[g/m_n^3 (dtf)]	0.1-3	0.02-8	20-100	8-100	-
Tar load		10-150	0.01-6	2-50	1-20	0
Tar signature	[-]	mostly oxygenated	aromatic	oxygenated and aromatic	oxygenated and aromatic	none
Alkali phase		solid	liquid	liquid	liquid	liquid/ gaseous
Sulfur signature		partially organic	mainly inorganic	partially organic	partially organic	inorganic
Feed size & geometry		non-sensitive	homogeneous	homogeneous	homogeneous	Suspension
Feed humidity		<50 %	<20 %	<15 %	<15 %	-
Process robustness		stable	sensitive, bridge building	stable	stable	sensitive, slagging
Reactor size	[MW_{th}]	0.1-20	0.1-2	1-50	20-200	30-600

2.3 Gas processing

The properties of the raw producer gas and the requirements of the employed fuel cell determine the design and the components of the gas processing in B-IGFC systems, Figure 2-1. The term "Gas processing" stands for the combination of gas cleaning and conditioning. Gas cleaning summarizes all required steps for the removal of impurities, while gas conditioning subsumes all processes involved in the conversion of the producer gas to a fuel gas suitable for the fuel cell in question.

2.3.1 Gas cleaning

Gas cleaning systems for producer gases usually comprise several unit operations in series of which each serves to the removal of at least one impurity type or specie. Currently a variety of technologies and apparatuses can be employed for the removal of impurities from gas streams. The state-of-the-art technologies and recent research results are outlined below focusing on the removal of the impurities discussed in section 2.2.3. The given information is partially based on [25, 34].

2.3.1.1 Particles

Particles in producer gases can cause erosion and blocking in the equipment downstream of the gasifier. Further, particles are subject to emission limits. For these reasons, the removal of particles is an integral part of every gas cleaning system for producer gases from biomass gasification. Ordered by their maximum operational temperature, the following particle removal technologies can be distinguished:

- Wet scrubbers
- Electrostatic precipitators
- Cyclones
- Barrier filters

Wet scrubbers employ a liquid, often water, for the removal of particles from gas streams. Their maximum operational temperature is usually below 100 °C which requires a cool down of the producer gas. The particles are captured in wash fluid droplets which are then removed from the gas stream in a demister. The most common wet scrubber type is the venturi scrubber. It allows removing particles below 1 μm diameter and achieving particle loads around 10 to 20 mg/m_n^3 (dtf). However, venturi scrubbers cause a pressure loss between 30 and 200 mbar.

Electrostatic precipitators consist of two zones. In the first zone, the product gas with the particles flows past high voltage electrodes that transfer a charge to the particles but do not interfere with the product gas. In the second zone, the product gas with the charged particles passes collector plates with the opposite polarity of the high voltage electrodes in the first zone. The charged particles consequently precipitate towards the collector plates where they deposit. Depending on the method of particle removal from the collector plates, electrostatic precipitators can be classified in wet and dry. Dry precipitators use mechanical means, while wet employ a liquid, usually water, to flush the deposited particles from the collector plates. Therefore, the maximum operational temperature of wet precipitators is limited to 65 °C, in contrast to their dry counterparts which may be operated at temperatures up to 500 °C. Wet and dry electrostatic precipitators achieve particle loads below 25 mg/m_n^3 (dtf), [29], and cause negligible pressure losses.

Cyclones are predestined for the removal of large quantities of large particles. For this reason they are an integral part of most fluidized bed gasification reactors. The particles are separated from the producer gas using the centrifugal force resulting from constraining the gas flow to a circular path, Figure 2-12 (left).

Figure 2-12: Working principle of cyclones and rigid barrier filters, [41]

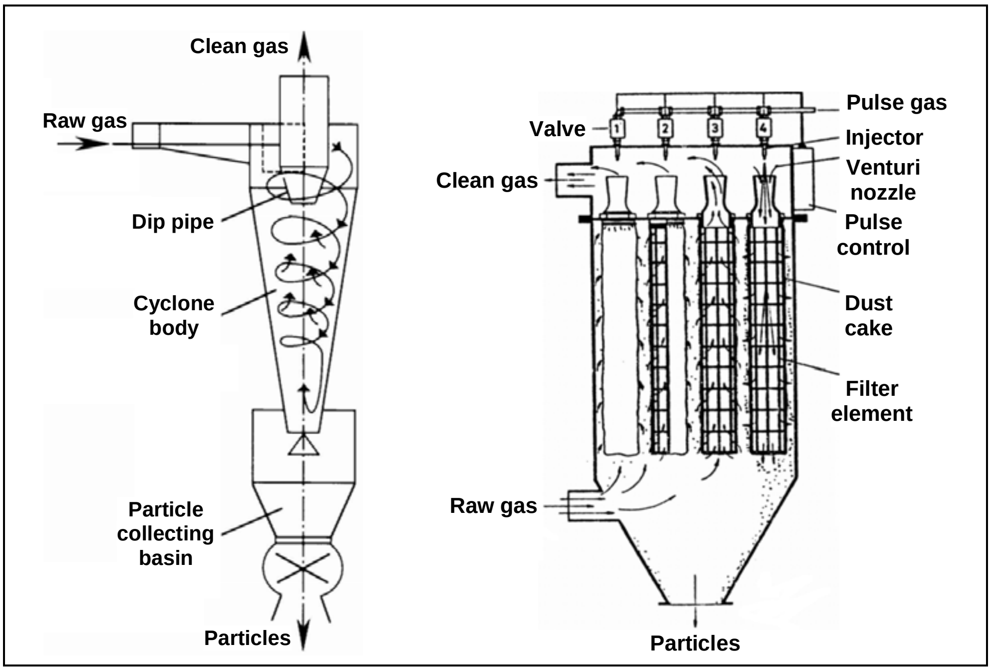
Clean gas
Raw gas
Dip pipe
Cyclone body
Particle collecting basin
Particles
Pulse gas
Valve
Injector
Venturi nozzle
Clean gas
Pulse control
Dust cake
Filter element
Raw gas
1
2
3
4
Particles

As a matter of principle, cyclones are relatively simple, robust and cheap devices. Their maximum operational temperature is solely limited by the material of construction. Especially for the application of high temperature fuel cells and gas turbines, this is a considerable advantage as no cool down of the producer gas is required and consequently no sensible heat of the gas is lost. Most commonly, several cyclones are connected in series thereby improving the collection efficiency. These multiclones reliably remove up to 90 % of the particles with a maximum diameter of 5 μm causing less than 10 mbar pressure loss. The collection efficiency of smaller particles is unsatisfactory even for high performance cyclones. This is particularly problematic as the char particles in producer gases from biomass gasification are predominantly of this smaller size fraction. Consequently particle loads of producer gases de-dusted by cyclones may still contain particle loads up to 30 g/m_n^3 (dtf).

Barrier filters use porous filter elements through which gases can penetrate but inhibit the passage of particles, Figure 2-12 (right). The collection efficiency increases with the thickness of the deposited dust cake. The filter elements may consist of rigid metallic or ceramic material or flexible woven material. Besides, barrier filters may consist of packed beds of ceramic spheres, sand etc. The removal of the deposited particles is usually carried out by periodically passing a clean gas flow through the filter elements in reverse direction of the normal gas flow. For reasons of costs reduction, barrier filters are usually employed in combination with cyclones to minimize the amount of cleaning pulses.

Bag filters mainly use the filtration effect of the deposited dust cake. Besides the reverse flushing of the filter elements, the dust cake can be removed by shaking. The maximum operational temperature is below 250 °C, which is acceptable in systems where the producer gas has to be cooled down for the end use device such as gas engines. The tars typically present in producer gases start condensing at the temperatures below 400 °C and may cause serious jamming problems. For this reason, bag filters are uncommon for the filtration of producer gases. However, precoat materials were recently demonstrated to prevent jamming, thus enabling the application of bag filters for producer gas filtration.

Packed bed filters can be operated in a wide range of temperatures. The greatest advantage of packed bed filters is that the bed materials can be easily exchanged once blocked by. e.g. tars. Therefore packed bed filters are often used for combined dust and tar removal.

Rigid barrier filters feature the possibility to retain the sensible heat of producer gases due to maximum operation temperatures up to 900 °C.

Hence they are predestined to the combination of biomass gasification with gas turbines and high-temperature fuel cells. Ceramic filter elements are however fragile and may break due to thermal stress induced by thermal cycling. Further, the ceramic materials are prone to react with alkali vapors leading to decomposition and plugging. Metallic filter elements have been reported to be prone to jamming especially with the high tar loads present in producer gases, see section 3.4.2. Further, partial producer gas cooling might be necessary to prevent metal sintering. Depending on the pore diameter of the used porous material, barrier filters can almost completely remove particulates down to 0.5 μm diameter. However, the according pressure loss is considerable.

2.3.1.2 Alkali metals

Alkali salts evaporate at temperatures above 800 °C. This volatilization is further facilitated by the chlorine present in biomass, [42, 43], see Table 2-2. Vaporized alkali salts cause damage to ceramic filter materials and corrosion of e.g. gas turbine blades.

State-of-the-art alkali removal from producer gases comprises the cooling of the gas below 600 °C, where alkali salts condense forming particles with diameters less than 5 μm. The particles are subsequently removed by means of particle filtration, [26]. After filtration with rigid filter elements at temperatures around 400 to 500 °C the alkali concentration in the filtered gas is typically in the order of 0.1 ppmw which translates in a removal efficiency above 99 %, [44]. The main drawback of this removal method is the inherent loss of sensible heat.

Recent research has shown that activated bauxite as alkali adsorbent achieves removal efficiencies for sodium and potassium between 95 and 99 % at temperatures between 650 and 750 °C, [45]. Reliable alkali removal systems based on these findings are however not available yet.

2.3.1.3 Tars

Producer gases can contain considerable amounts of tars. At temperatures below their dew point and/or at elevated pressures, tars condense causing operational problems due to the formation of droplets which accumulate to sticky films on cold surfaces of e.g. pipes and other equipment. Besides the condensation related issues, tars may cause carbon deposition problems at very elevated temperatures. Systems employing gas engines and gas turbines as end use devices require almost complete tar removal to avoid condensation problems, while systems using high-temperature fuel cells may cope with moderate tar loads. Besides the primary tar reduction via optimized gasification processes, see section 2.2.3, tars may be removed by physical means or decomposed by thermal and catalytic means.

Physical tar removal is the most frequently employed technology, involving the controlled condensation of tars and the subsequent removal of the tar droplets in wet scrubbers or electrostatic precipitators following the same principles as for the removal of particles. The maximum operational temperature is limited to values below 65 °C for wet scrubbers. Electrostatic precipitators may be operated at temperatures up to 150 °C if the collected tars exhibit low viscosity and thus do not need to be actively flushed from the collector plates with water, but drip down on their own. In the cleaned producer gas, tar loads between 20 and 40 mg/m_n^3 (dtf) can be achieved with water based wet scrubbers. Oil based wet scrubbers may achieve tar loads below 10 mg/m_n^3 (dtf) due to the additional solution of tars in the oil. The heat loss resulting from the required gas cool down is the main disadvantage of this technology. The main advantage is that physical tar removal and particle removal may be carried out in one single apparatus reducing the equipment cost.

Thermal tar decomposition requires high temperatures, ranging from 900 °C for oxygenated tar species originating from updraft gasification to 1200 °C and more for the refractory tar species formed during e.g. downdraft gasification, [34]. Electrically heated surfaces are one possibility to generate the required temperatures for thermal tar decomposition. The major drawbacks of this technology are incomplete tar decomposition and poor energy efficiency. Another possibility is the partial oxidation of the producer gas. Using oxygen, temperatures over 1200 °C can be achieved at low air-to-fuel ratios where only little of the producer gas energy content is converted to heat. However, oxygen is expensive. In contrast, air is abundant but the heating of the nitrogen introduced to the producer gas consumes a considerable amount of energy. For both oxidants the energy content of the tars is preserved in the producer gas either in form of sensible heat or heating value of the tar decomposition products. This is the main advantage of thermal tar decomposition technologies compared to physical tar removal technologies.

Catalytic tar decomposition aims at the conversion of tars at temperatures between 800 and 900 °C. The catalyst materials may be placed in the gasification reactor (in situ tar decomposition) or in an external reactor. The potential advantage of in situ tar decomposition is that the tars may be decomposed at the same time that they are formed. However, experiments showed that in fixed bed gasification reactors the contact time between catalyst and tars is insufficient for complete tar decomposition and that in fluidized bed reactors the attrition of the catalyst particles causes a fast deactivation. Further, the means of temperature control for in situ tar decomposition are limited. The latter is the main advantage of external tar decomposition reactors, which however involve additional costs. State-of-the-art non-metallic catalyst materials for tar decomposition are dolomites, zeolites and calcites. These materials are cheap, insensitive towards most impurities present in producer gases and allow tar decomposition rates of up to 99 %. Metallic tar decomposition catalysts employ a wide range of materials such as Ni, Mo, Co, Pt and Ru in pure form or as mixtures supported on silica alumina, zeolites etc. The main advantages of metallic catalysts are that they allow almost complete tar decomposition and simultaneous decomposition of ammonia. However, the long-term application in biomass gasification systems has not been demonstrated yet and the costs are higher than for non-metallic catalysts. Sections 2.3.2.1 and 2.3.2.2 give additional information for the catalytic decomposition of hydrocarbons and tars.

2.3.1.4 Halides

The average chlorine content of untreated wood is low, which yields low concentrations of hydrochloric acid in producer gases. If required, hydrochloric acid can be removed from producer gases using wet scrubbers which are well tested and commercially available. To avoid heat losses, high temperature capable adsorbent materials can be used such as e.g. lime, Eq. 17.

$$CaO + 2HCl \rightarrow CaCl_2 + H_2O \qquad \text{Eq. 17}$$

Lime can be used up to temperatures slightly below the melting temperature of the formed calcium chloride being 770 °C. Hydrochloric acid adsorption is a well tested technology.

2.3.1.5 Nitrogenous species

Ammonia (NH_3) is the most important nitrogen-containing impurity in producer gases. During combustion at high temperatures in gas engines and gas turbines, ammonia is likely to be converted to nitrogen oxides (NO_X), which are subject to strict legal limits and difficult to remove from the exhaust gases. Therefore, ammonia is commonly removed from the producer gas prior to its combustion in gas engines and gas turbines. In contrast, recent research has shown that ammonia is very well converted in high-temperature fuel cells with very little formation of NO_x, [46, 47]. This strongly indicates that ammonia removal might not be necessary when using high-temperature fuel cells for the conversion of producer gases. Nevertheless, a short summary of the available ammonia removal technologies is given below.

Ammonia can be removed from producer gases either by catalytic decomposition or by wet scrubbing. The latter technology, using the good solubility of ammonia in water, is well known and reliable. The catalytic decomposition of ammonia is usually carried out with catalysts similar to those used for the tar decomposition. Dolomites, nickel- and iron-based catalysts have been shown to achieve ammonia conversion rates in excess of 99 % at temperatures higher than 900 °C. However, thus far this technology has not been applied in commercial systems. Further, the employed catalysts are prone to deactivation by sulfur and halide compounds.

2.3.1.6 Sulfurous species

The average sulfur content of untreated wood is 600 mg/kg dry and ash free (daf), [48]. During combustion of the producer gas, the sulfurous species are converted to sulfur oxides (SO_x) which can be reliably removed from the exhaust gases to meet legal emission limits. The removal of sulfur species from the producer gas prior to the combustion in gas engines and gas turbines is therefore uncommon. In contrast, the nickel-based catalysts frequently used in high-temperature fuel cells are prone to sulfur poisoning, which reduces the power output noticeably and may also cause permanent damage. To prevent this and to minimize sulfur-induced power losses, the sulfur concentration in the producer gas has to be well below 10 ppmV, see section 3.4.5. The typically targeted sulfur concentration of below 1 ppmV can be reached by either absorptive or adsorptive methods.

Alkaline wet scrubbers have long been used for the removal of sulfur species from natural gas and syngases from coal gasification. The most important commercially available processes are the Rectisol process developed by the Linde AG and the Purisol process from the Lurgi GmbH. These processes employ different solvents which can be regenerated under separation of hydrogen sulfide containing gases that are usually converted to elemental sulfur via the Claus process. These processes are however complex and, from the economical point of view, hardly applicable to biomass gasification systems. Besides, the wet scrubbing processes require a gas cool down which is particularly unfavorable when employing high-temperature fuel cells as these require high producer gas temperatures.

The most common adsorptive sulfur removal process is based on the adsorption of hydrogen sulfide onto zinc oxide, Eq. 18. Despite that zinc oxide and zinc sulfide are non-volatile up to 1700 °C, in reducing atmospheres zinc oxide is likely to be reduced to pure zinc which has a considerably lower melting temperature. The maximum operation temperature of zinc oxide adsorbents is therefore limited to 350 to 450 °C.

$$ZnO + H_2S \rightarrow ZnS + H_2O \qquad \text{Eq. 18}$$

Depending on the operational temperature and the steam content of the producer gas, sulfur concentrations in the ppb range can be reached without the need of a heavy cool down of the producer gas. The sensible heat of the producer gas can thus largely be preserved. However, the formed zinc sulfide has to be recycled, which involves costs. Further, hydrochloric acid removal is mandatory before the producer gas gets in contact with the zinc oxide adsorbent. This is because hydrochloric acid may react with the zinc oxide forming zinc chloride which is volatile at temperatures above its melting point at 275 °C, Eq. 19. The removal of hydrochloric acid was discussed in section 2.3.1.4.

$$ZnO + 2HCl \rightarrow ZnCl_2 + H_2O \qquad \text{Eq. 19}$$

Recently, the adsorption of sulfur on metal-oxides such as titanium, iron, magnesium and aluminum oxides at temperatures around 500 °C has engendered some interest. In contrast to zinc sulfide, the formed metal sulfides can be regenerated with steam producing hydrogen sulfide containing exhaust gases. However, these materials are still under investigation and not yet commercially available. The same applies to the adsorption of sulfur onto dolomite and lime particles which are introduced in the product gas stream and removed by means of particle removal. Adsorption capacities in excess of 85 % were reported under lab conditions. Activated carbon may also be used for the sulfur removal from producer gases at temperatures up to 550 °C, [49]. However, the typically high steam content of producer gases might cause difficulties and has not yet been investigated.

The most important drawback of all discussed adsorption methods is that organic sulfur compounds are not directly adsorbed. Hence a conversion of these species to hydrogen sulfide is required. The state-of-the-art in the petrochemical industry is the conversion via hydrogenation over Ni/Mo or Cr/Mo catalysts with excess hydrogen. As the hydrogen content of producer gases is usually moderate, hydrogenation is most probably not feasible in biomass gasification systems. However, due to the tar-like nature of organic sulfur species, tar removal or decomposition technologies can be used for the conversion to hydrogen sulfide or the direct removal from producer gases.

2.3.2 Gas conditioning

Hydrogen is the most easily convertible fuel for fuel cells. However, it is difficult to store and prone to explosion, [50]. Further, it is not readily available as a fuel but needs to be produced from e.g. natural gas or biomass or by electrolysis. In addition, there is no area-wide hydrogen distribution infrastructure available currently. Therefore, research activities focus on the system-integrated generation of hydrogen-rich gases from hydrocarbons. Besides hydrocarbons, producer gases can contain oxygenated organic compounds. The amount of oxygenates depends on the biomass conversion process and can reach important levels.

State-of-the-art gas conditioning processes are steam reforming (STR), autothermal reforming (ATR) and catalytic (CPO) or non-catalytic partial oxidation (PO). These processes may take place in external reactors or directly in the fuel cell.

2.3.2.1 Steam reforming

The STR reaction was discovered in the early 19th century. Since then, the STR process using methane as educt has been developed by several groups and companies and is now one of the cheapest, [51], and most energy efficient, [15], processes for syngas production. Syngas is a mixture of hydrogen and carbon monoxide. The endothermic STR reaction of hydrocarbons and methane in particular are stated below.

$$C_nH_m + n \cdot H_2O \rightarrow n \cdot CO + \left(n + \frac{m}{2}\right) \cdot H_2 \ with \ (-\Delta H < 0) \qquad \text{Eq. 20}$$

$$CH_4 + H_2O \rightarrow CO + 3 \cdot H_2 \ with \ \left(-\Delta H_R^0 = -206 \frac{kJ}{mol}\right) \qquad \text{Eq. 21}$$

Eq. 21 shows the high heat requirement of the STR and explains why reactor designs are typically limited by heat transfer rather than the reaction kinetics. STR of most hydrocarbons takes place only over suitable catalysts and at high temperatures typically over 800 °C. Group VIII metals are employed as STR catalysts, [52], of which Ni is the mostly used material due to cost considerations. SOFCs offer all factors for an integrated STR process, see also section 2.4.3. The conversion can be performed cell internally or externally using the SOFC waste heat.

The main problem of the STR process is carbon deposition. High steam partial pressures help to prevent carbon deposition on the catalyst material. Typically, steam-to-carbon ratios (SC) of two and higher, [53], are required to prevent carbon deposition. The tendency towards carbon deposition increases with rising molecular weight of the hydrocarbon species in the educt gas, especially for polycyclic molecules, [54].

Poisoning of the STR catalyst is another issue. Hydrocarbon fuels are usually contaminated with small amounts of sulfur, which is likely to chemisorb on any metallic surface. Hence, a desulphurization step has to be carried out prior to the reformer, see section 2.3.1.6.

Oxygenated organic compounds can be steam reformed using Ni-based catalysts, [55, 56]. The corresponding reaction can be stated as:

$$C_nH_mO_k + (n-k)\cdot H_2O \rightarrow n\cdot CO + \left(n + \frac{m}{2} - k\right)\cdot H_2 \; with \; (-\Delta H < 0) \qquad \text{Eq. 22}$$

Although Eq. 22 appears similar to Eq. 20, there are significant differences between the reaction mechanisms of pure hydrocarbons and oxygenates. According to [55], the oxygenated organic compounds found in biomass-derived gases are thermally unstable and decompose without forming significant amounts of coke at the operating conditions of STR processes. The formed intermediates are instantly converted to hydrogen and carbon monoxide. Experiments showed that oxygenate STR allows lower reforming temperatures and higher space velocities than the comparable hydrocarbon STR process, [57]. The following sections provide an overview of state-of-the-art hydrocarbon STR reactors and integration possibilities of the STR process into SOFC designs.

2.3.2.1.1 External steam reforming

The heat integration of external STR reactors in SOFC systems is undertaken with heat exchangers. Heat on a high temperature level is recovered from the flue gas of the SOFC and transferred to the external

STR reactor. The advantage of this system design is that relatively cheap standard STR reactors can be used, [51], see Figure 2-13. However, the inherent heat transfer limitations usually lower the system efficiency. In addition, the STR process requires steam at an appropriate temperature. This steam is usually generated using de-ionized water and heat from the flue gas of the SOFC, while the steam content the SOFC flue gas remains unused.

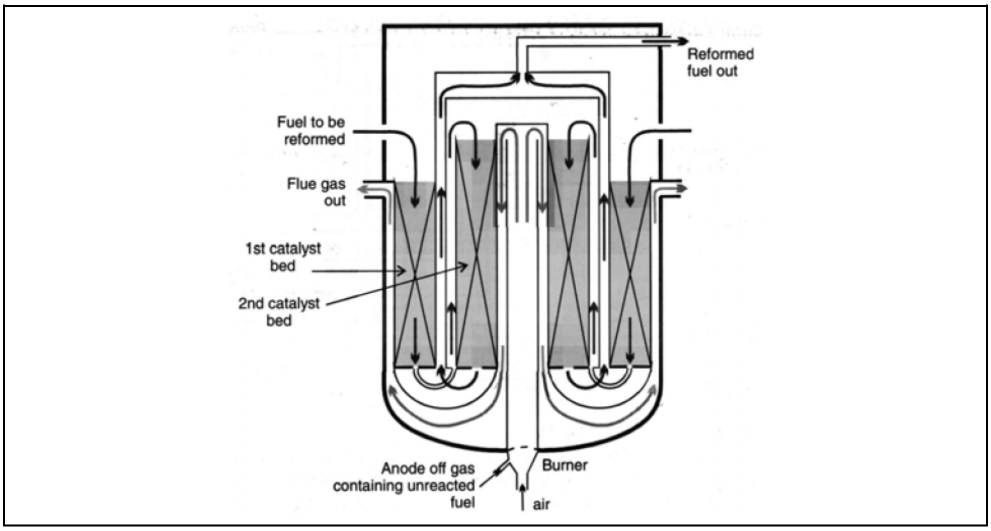
Reformed fuel out
Fuel to be reformed
Flue gas out
1st catalyst bed
2nd catalyst bed
Anode off gas containing unreacted fuel
Burner
air

Figure 2-13: External reforming reactor with integrated heat exchanger designed by Haldor Topsoe, [58]

2.3.2.1.2 Indirect internal steam reforming

Indirect internal reforming uses the operation temperature of the SOFC and the steam content of the flue gas via a recycle, [51], see Figure 2-14.

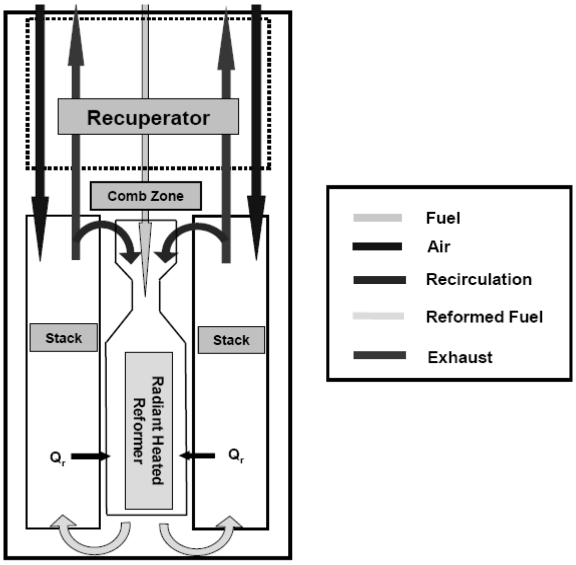
Recuperator
Comb Zone
Stack
Stack
Radiant Heated Reformer
Qr
Qr
Fuel
Air
Recirculation
Reformed Fuel
Exhaust

Figure 2-14: Indirect internal reforming concept by the Siemens AG, [59]

This integration strategy allows simplified system designs and generates additional cooling means for the SOFC stack via direct radiative heat exchange between the stack and the reforming reactor. The latter is also employed to reduce the required cooling air mass flow. Nevertheless, the integration of a separate STR reactor imposes important constraints for the stack design and is not necessarily possible for all cell designs.

2.3.2.1.3 Direct internal steam reforming

State-of-the-art SOFCs have nickel cermet anodes which provide sufficient STR activity at the typical operation temperatures, see section also 2.4.6.1. Therefore, the STR reactions may directly occur on the anode. The endothermic character of the STR can be used to chemically cool the cells, reducing the electricity need of the cooling air blower and hence increasing the net electrical efficiency of SOFC systems. The required steam and heat are continuously produced in exothermic electrochemical hydrogen oxidation and consumed in STR reactions. Well balanced, a more uniform temperature distribution over the cells can result, see also section 2.4.3. The overall system design is further simplified as no separate STR reactor is needed, [51].

2.3.2.2 Partial oxidation and autothermal reforming

The partial oxidation (PO) of hydrocarbons is an alternative to the STR process. Hydrocarbons are degraded to a mixture of hydrogen and carbon monoxide in a strongly exothermic reaction which can be written as:

$$C_nH_m + \frac{n}{2} \cdot O_2 \rightarrow n \cdot CO + \frac{m}{2} \cdot H_2 \; with \; (-\Delta H > 0) \qquad \text{Eq. 23}$$

The hydrocarbons react with oxygen at temperatures between 850 and 1700 °C whereas the provided amount of oxygen is insufficient for the complete combustion, [60]. PO reactors are largely used to process liquid fuels as evaporation and conversion can take place in one step. PO is also used to process gaseous fuels for mobile or small stationary applications due to the compact reactor design. No flue gas recycles or deionized water is needed to run a PO reactor, making the process simple. The main drawback of the PO process is that fuel is burned to produce the required high temperatures resulting in moderate efficiency, [61].

Recently, catalysts have been developed to lower the process temperature and increase the energy efficiency. This process, which has been termed catalytic partial oxidation (CPO), takes place at temperatures below 800 °C, [62]. In-situ temperature profile measurements of CPO monoliths have shown that two different reaction zones establish during operation. In the hotspot zone, oxygen is consumed in oxidation reactions producing temperatures around 1000 °C. The remaining hydrocarbons then take part in reforming reactions which are sustained by the heat and the steam generated in the hotspot zone. For more information, see [63].

The combination of STR and CPO is referred to as autothermal reforming (ATR). In contrast to the PO and the CPO, where only molecular oxygen is used as oxygen source, the ATR uses molecular oxygen and steam as oxygen sources. The reaction can be written as follows:

$$C_nH_m + \frac{n}{4}\cdot O_2 + \frac{n}{2}\cdot H_2O \rightarrow n\cdot CO + \left(\frac{n}{2}+\frac{m}{2}\right)\cdot H_2 \; with \; (-\Delta H \geq 0) \qquad \text{Eq. 24}$$

The ATR process requires less steam than the STR process. The required heat is generated via partial oxidation of the fuel, avoiding the need for a complex heat management, [58]. Both processes are well suitable for the conversion of biomass-derived fuel gases. For oxygenated organic compounds, Eq. 25 and Eq. 26 are reformulated as follows:

$$C_nH_mO_k + \frac{n-k}{2}\cdot O_2 \rightarrow n\cdot CO + \frac{m}{2}\cdot H_2 \; with \; (-\Delta H > 0) \qquad \text{Eq. 25}$$

$$C_nH_mO_k + \frac{n-k}{4}\cdot O_2 + \frac{n-k}{2}\cdot H_2O \rightarrow n\cdot CO + \left(\frac{n-k}{2}+\frac{m}{2}\right)\cdot H_2 \qquad \text{Eq. 26}$$
$$with \; (-\Delta H \geq 0)$$

CPO and ATR of oxygenated organic compounds have been shown using pyrolysis gas from cedar wood powder, [64]. It was found, that the tar content of the pyrolysis gas was almost completely converted to hydrogen and carbon monoxide.

2.4 Solid oxide fuel cell

2.4.1 Fuel cells in general

Fuel cells are energy converters which directly convert the chemical energy of a fuel into electricity and heat via electrochemical reactions. Fuel cells produce electricity as long as fuel is supplied. The principle was discovered in 1838 by the two scientists Christian Friedrich Schönbein and Sir William Grove, [65]. However, the fuel cell technology did not gain significance until the 1960s, where alkaline fuel cells were first employed in the NASA space program to produce electricity and drinking water in space crafts, [58]. Since then, fuel cells have been developed to cover applications such as combined heat and power generation, vehicle propulsion and replacement for batteries.

Fuel cells could play an important role in future energy conversion due to their high efficiencies, modular design, low noise and environmental impact. Although significant progress has been made in recent years, there are still many technical and economical problems, e.g. insufficient durability and the need for expensive catalyst materials. These problems have to be resolved to allow for a strong market penetration of fuel cell technologies.

Figure 2-15 gives a comparison of different fuel cell types. Currently the most important fuel cell (FC) types are the polymer electrolyte membrane FC (PEMFC), the molten carbonate FC (MCFC) and the solid oxide FC (SOFC). The direct methanol FC (DMFC) is derived from the PEMFC. Besides, there are the alkaline FC (AFC) and the phosphoric acid FC (PAFC), which are however no longer in fashion.

The different FC types are distinguished by the electrolyte used and their operating temperature. The MCFC and the SOFC are high-temperature, the PAFC mid-temperature and the rest low-temperature FCs. The last-mentioned (PEMFC, AFC) are aiming at mobile and portable applications, while SOFCs, MCFCs and PAFCs aim at stationary heat and power generation.

Fuel cells can operate on a variety of fuels ranging from pure hydrogen to gasified solid fuels, such as biomass or coal. Presently, hydrogen is the only fuel which can be oxidized electrochemically in PEMFC, AFC and PAFC. In addition, SOFCs and MCFCs can also electrochemically convert carbon monoxide and hydrocarbons. Fuel gases from renewable sources such as producer gas from biomass gasification are of special importance for the future. In this respect, MCFCs and SOFCs have the greatest potential as their actual development is focused on pre-reformed natural gas as fuel which exhibits similar properties as producer gases.

Figure 2-15: Comparison of fuel cell technologies

Pictures: [66]

FC Type	Low temperature FC		Mid temperature FC	High temperature FC	
	PEMFC	AFC	PAFC	MCFC	SOFC
Electrolyte	Solid organic polmer polyperfluorosulfonic acid	Aqueous solution of potassium hydroxide soaked in a matrix	Liquid phosphoric acid soaked in a matrix	Liquid solution of lithium, sodium and/or potassium catbonates soaked in a matrix	Solid yttrium stabilzed zirconium oxide
Oxidant - Cathode Gas	Oxygen or Air	Pure Oxygen	Air	Air	Air
Cathode Reaction	$2\,H^+ + 2\,e^- + 0.5\,O_2 \rightarrow H_2O$	$O_2 + 2\,H_2O + 4\,e^- \rightarrow 4\,OH^-$	$2\,H^+ + 2\,e^- + 0.5\,O_2 \rightarrow H_2O$	$0.5\,O_2 + CO_2 + 2\,e^- \rightarrow CO_3^{2-}$	$0.5\,O_2 + 2\,e^- \rightarrow O^{2-}$
Fuel - Anode Gas	Hydrogen	Pure Hydrogen	Hydrogen	Hydrogen, Carbon monoxide Methane	Hydrogen, Carbon monoxide Methane
Anode Reaction	$H_2 \rightarrow 2\,H^+ + 2\,e^-$	$2\,H_2 + 4\,OH^- \rightarrow 4\,H_2O + 4\,e^-$	$H_2 \rightarrow 2\,H^+ + 2\,e^-$	$H_2 + CO_3^{2-} \rightarrow H_2O + CO_2 + 2\,e^-$ $CO + CO_3^{2-} \rightarrow 2\,CO_2 + 2\,e^-$ $CH_4 + 4CO_3^{2-} \rightarrow 5CO_2 + 2H_2O + 8e^-$	$H_2 + O^{2-} \rightarrow H_2O + 2\,e^-$ $CO + O^{2-} \rightarrow CO_2 + 2\,e^-$ $CH_4 + 4O^{2-} \rightarrow CO_2 + 2H_2O + 8e^-$
Overall Reaction	$H_2 + 0.5\,O_2 \rightarrow H_2O$	$2\,H_2 + O_2 \rightarrow 2\,H_2O$	$H_2 + 0.5\,O_2 \rightarrow H_2O$	$H_2 + 0.5\,O_2 \rightarrow H_2O$ $CO + 0.5\,O_2 \rightarrow CO_2$ $CH_4 + 2\,O_2 \rightarrow CO_2 + 2\,H_2O$	$H_2 + 0.5\,O_2 \rightarrow H_2O$ $CO + 0.5\,O_2 \rightarrow CO_2$ $CH_4 + 2\,O_2 \rightarrow CO_2 + 2\,H_2O$
Fuel requirements	CO < 10 - 100 ppmV	Pure Hydrogen needed	CO < 1 vol.-% N_2 < 4 vol.-%	-	-
Operating Temperature	50 - 90°C	50 - 90°C	160 - 220 °C	600 - 660°C	700 - 1000°C
Electrical Efficiency	35 - 60%	50 - 70%	35 - 50%	40 - 55%	45 - 60%
Applications	Mobile Stationary power generation	Military Space	CHP-generation	CHP-generation	CHP-generation Additional Power Units
Advantages	- Quick start-up due to low temperature - Favorable power-to-weight ratio - Low sensitivity to orientation	- High Performance due to fast cathode reaction - Variety of non-precious catalysts - High efficiencies	- Most mature cell type - CHP-generation possible - Less fuel impurity sensitive	- High efficiency - CHP-generation possible - Fuel flexibility due to int. reforming - Non-precious metal catalysts	- Plate- and tube-like configurations - High efficiency and fuel flexibility - Non-precious metal catalysts - Most sulfur-resistant FC
Disadvantages	- Expensive catalysts required - Prone to carbon monoxide poisoning - Hydrogen storage or onboard fuel processor necessary	- Pure fuel and oxidant required - Prone to carbon dioxide poisoning	- Low efficiency compared to other FCs - Requires Pt-catalyst - Large size and weight	- Corrosive electrolyte - Accelerated breakdown of cell components due to high temperature	- Slow start-up - Necessity of thermal shielding - Accelerated breakdown of cell components due to high temperature
Functional Outline	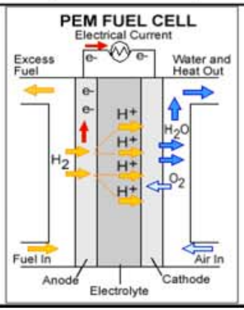 PEM FUEL CELL Electrical Current Excess Fuel Water and Heat Out e- H+ H_2 H_2O O_2 Fuel In Air In Anode Electrolyte Cathode	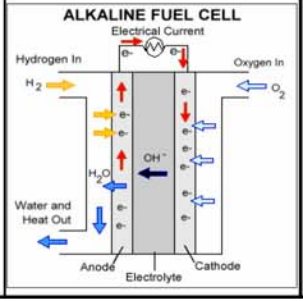 ALKALINE FUEL CELL Electrical Current Hydrogen In Oxygen In H_2 O_2 e- OH^- H_2O Water and Heat Out Anode Electrolyte Cathode	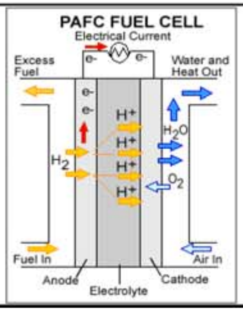 PAFC FUEL CELL Electrical Current Excess Fuel Water and Heat Out e- H+ H_2 H_2O O_2 Fuel In Air In Anode Electrolyte Cathode	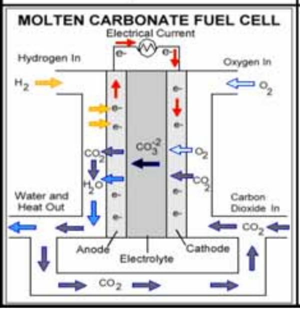 MOLTEN CARBONATE FUEL CELL Electrical Current Hydrogen In Oxygen In H_2 O_2 e- CO_3^{2-} CO_2 H_2O Water and Heat Out Carbon Dioxide In Anode Electrolyte Cathode	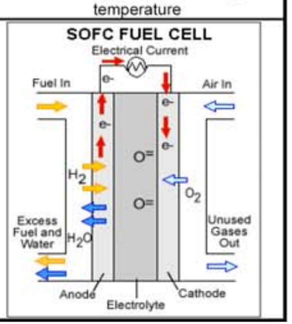 SOFC FUEL CELL Electrical Current Fuel In Air In e- O= H_2 O_2 H_2O Excess Fuel and Water Unused Gases Out Anode Electrolyte Cathode

2.4.2 Technology features

Compared to other fuel cell types, SOFCs feature:

- The highest fuel to electricity efficiency, [67]. Fuel cells in general are not limited by the Carnot efficiency.
- A wide operation temperature range (500 up to 1000 °C), [68].
- Great potential for hybridization due to the typically high operation temperature and incomplete fuel utilization, [67]. The generated surplus of high quality heat enables new power plant designs with Carnot heat engines and/or steam turbines as bottoming cycles. Thermodynamic systems analyses revealed that most hybrid systems proposed in the literature have the potential for highly efficient heat and power generation, especially when the systems are operated under elevated pressure. The NO_x emissions of such hybrid systems are expected to be low due to mostly electrochemical oxidation of the fuel, which takes place at comparably low temperatures.
- The application of low-cost catalyst materials due to the high operation temperatures. Typically, nickel is employed as anode catalyst in SOFCs while platinum is employed in PEMFCs, [68].
- High fuel flexibility. SOFCs can directly convert hydrogen, carbon monoxide and hydrocarbons, [68]. Furthermore, the employed catalysts and the high operation temperature allow for internal reforming of hydrocarbons and shifting of carbon monoxide. Hence, no complex gas processing aiming at the production of pure hydrogen is needed for the use of natural gas, syngas or producer gases.
- Good scalability from watts to multi- megawatts, [67].
- Almost noiseless operation. SOFCs for the application as replacement for batteries in cars, so called auxiliary power units (APUs), are developed by several groups, [67].

However, the SOFC technology is not mature yet. The actual status of development ranges from fundamental research mainly in the field of material science to pre-commercial system operations and development of market penetration strategies. The most important challenges which have to be addressed prior to a successful market penetration are:

- The manufacturing processes of the ceramic raw materials and cell components as well as the cell- and stack assembly processes are not yet optimized. Consequently, the stray area of cell performance and lifetime is usually wide and the number of deficient cells is high.

Simplifying the production processes should allow for significant cost reductions. To achieve this, every step in the stack production process has to be well understood, [68].

- The elevated operation temperatures induce high requirements for the employed sealing and interconnect materials. Currently these requirements can only be met, if at all, by expensive materials, [68].
- Start-up and shut-down usually take long and the tolerance of SOFCs towards temperature cycles is low.

In the emerging distributed power and heat generation market, SOFCs will face competition not only from established less efficient, but, less expensive, technologies such as gas engines, but also from micro turbines and not least MCFCs assuming comparable reliability and costs.

2.4.3 Working principle

Walter Hermann Nernst’s discovery in 1899 that zirconia (ZrO_2) is conductive for oxygen ions at elevated temperatures was the starting point for the SOFC technology, [58]. SOFCs, as all other fuel cells too, consist of two porous electrodes which are separated by an ion-conducting electrolyte. Figure 2-16 depicts the working principle of an internally reforming, anode-supported planar SOFC.

Figure 2-16: Working principle of an internally reforming anode-supported SOFC, [69]

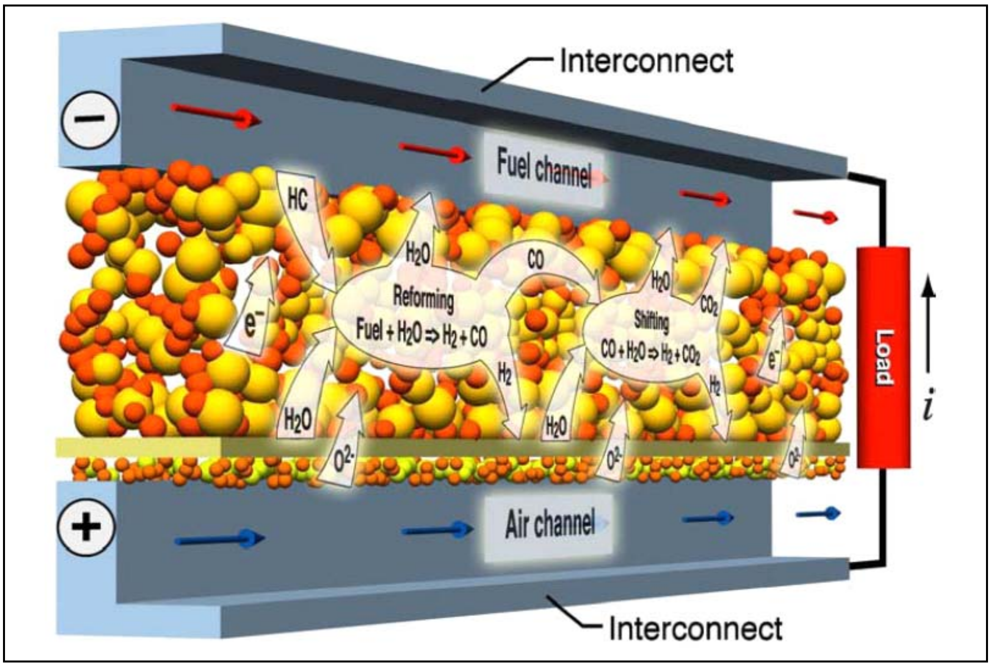
Interconnect
−
Fuel channel
HC
H_2O
CO
Reforming
Fuel + $H_2O \Rightarrow H_2 + CO$
H_2O
CO_2
Shifting
$CO + H_2O \Rightarrow H_2 + CO_2$
e^-
H_2
H_2O
O^{2-}
H_2O
O^{2-}
H_2
e^-
O^{2-}
Load
i
+
Air channel
Interconnect

Hydrocarbon containing fuels are most challenging for SOFCs as a variety of reactions take place in the cell simultaneously. The fuel gas diffuses through the anode and participates in STR, see section 2.3.2.1, and shifting reactions (SR), Eq. 14.

The required steam for both reactions is generated in the electrochemical oxidation of hydrogen at the anode triple phase boundary (TPB) where the fuel gas meets electrode and electrolyte material simultaneously. The hydrogen produced in the reforming reactions further diffuses to the anode TPB, while the major part of the formed carbon monoxide is converted to hydrogen and carbon dioxide via exothermal shifting reactions. Some of the carbon monoxide may be directly converted to carbon dioxide at the anode TPB. The heat of the shifting and of electrochemical reactions is partially consumed by the reforming reactions. At the TPB of the anode, hydrogen and carbon monoxide are oxidized by oxygen ions, at the same time releasing electrons:

$$H_2 + O^{2-} \rightarrow H_2O + 2e^- \qquad \text{Eq. 27}$$

$$CO + O^{2-} \rightarrow CO_2 + 2e^- \qquad \text{Eq. 28}$$

The free electrons flow through an external circuit to the cathode where oxygen is converted to oxygen ions at the TPB of the cathode consuming the free electrons:

$$\frac{1}{2}O_2 + 2e^- \rightarrow O^{2-} \qquad \text{Eq. 29}$$

The oxygen ions pass the electrolyte via vacancies in the crystal structure, hence closing the electrical circuit. In sum, the electrochemical reactions can be written as:

$$H_2 + \frac{1}{2}O_2 \rightarrow H_2O \qquad \text{Eq. 30}$$

$$CO + \frac{1}{2}O_2 \rightarrow CO_2 \qquad \text{Eq. 31}$$

The amount of generated electrical power depends on the current of free electrons and the voltage of the cell. Figure 2-17 shows a schematic voltage-current curve and the voltage loss shares. The Nernst potential (reversible potential) is the maximum possible voltage at non-standard conditions. The obtained voltage is lower than the Nernst voltage when a current flows. The Nernst voltage is therefore commonly referred to as “open circuit voltage” (OCV). The relation between voltage losses, operation temperature, current density and species concentrations constitutes the fuel cell characteristics.

Figure 2-17: Qualitative dependency of voltage losses and current

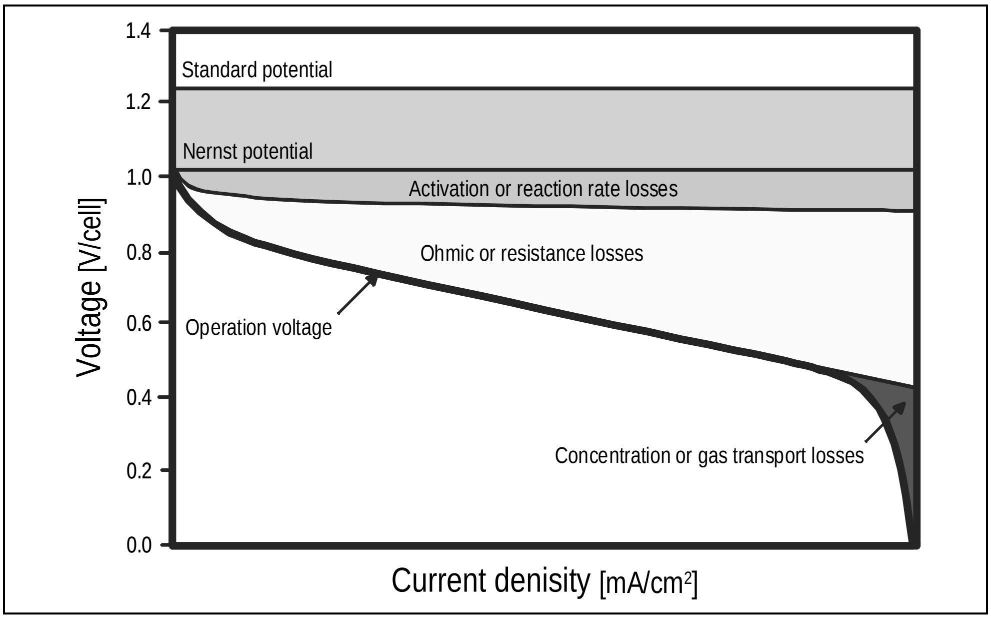

The voltage losses can be assigned to three mechanisms, Figure 2-17:

- Ohmic losses

  Electronic (electrodes and interconnect) and ionic (electrolyte) currents are accompanied by voltage losses. Ohmic losses are proportional to, [70]:

  - Temperature
  - Geometry of the current paths
  - Current density

  The magnitude of the ohmic losses depends on the resistivity of the employed materials and the interfacial resistances between electrolyte, electrodes and interconnects. In SOFCs, the ionic resistivity of the electrolyte is up to 500000 times higher than the electronic resistivity of the electrodes, [70]. This is why electrode supported cells are favored by most SOFC developers, see also section 2.4.5.

- Activation losses

  The electrochemical reactions (Eq. 27, Eq. 28, Eq. 29) are always taking place at the electrodes. At zero current, the reactions occur at equal rates in both directions. The exchange current represents the current flowing in one of the two directions. When a current flows, the voltage losses are usually higher than the ohmic losses alone. The additional losses are referred to as activation polarization. The activation polarization depends on, [70]:

    - Temperature
    - Current density and hence the electron concentration in the electrodes as well as the oxygen ion mobility in the electrolyte
    - Product (H_2O, CO_2) and educt (H_2, CO) partial pressures
    - Size of the TPB

  Figure 2-17 shows that the activation polarization increases fast with rising small current density values and then stabilizes on a certain level.

- Concentration losses

  The electrochemical reactions (Eq. 27, Eq. 28, Eq. 29) take place at the TPB. Due to slow diffusion processes, the product partial pressures are higher and the reactant partial pressures are lower at the TPB compared to the gas flow channels. Consequently, using the TPB instead of the gas flow channel partial pressures yields a lower Nernst voltage. The difference between the TPB and the gas flow channel Nernst voltage is referred to as concentration loss. Concentration losses become important at high current densities, where they increase against an asymptotic maximum current, see Figure 2-17. A further increase of the current is impossible because at this point the concentrations of the reactants at the TPB are equal to zero due to instant consumption.

2.4.4 Cell designs

Different cell designs have been developed over the years. Currently two base designs and combinations thereof can be differentiated, the first being the tubular and the second being the planar cell design. Each has different characteristics.

The tubular cell design, developed by the Siemens AG, features the largest presently achievable active cell area. This is due to the applied extrusion production process, which allows the production of long cell tubes. The cell components are deposited as thin layers on a ceramic cathode tube which is closed at one end, see Figure 2-18. Therefore, no sealing is needed to separate the fuel and the oxidant flow paths in contrast to planar cell designs, [51]. The oxidant (air or oxygen) is introduced via a coaxial ceramic air delivery tube (ADT) near the closed cathode tube end. It then flows through the space between the ADT and the cathode tube. The fuel flows at the outside of the cell. The depleted air exits the cell at the open end, where it is combusted with the partially depleted fuel, 50 to 90 % respectively.

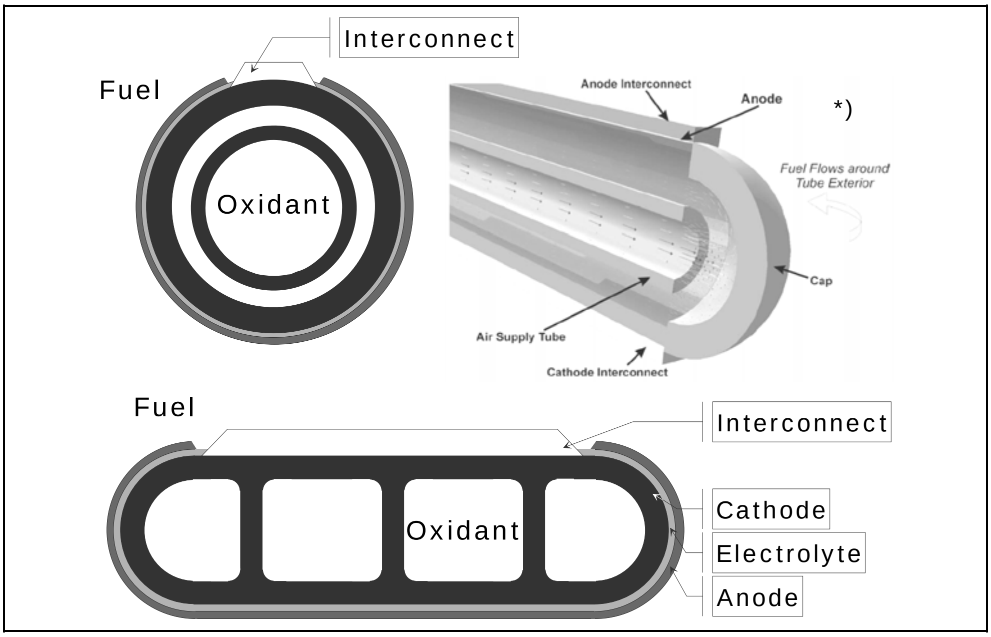
Interconnect
Fuel
Oxidant
Anode Interconnect
Anode
*)
Fuel Flows around Tube Exterior
Cap
Air Supply Tube
Cathode Interconnect
Fuel
Interconnect
Oxidant
Cathode
Electrolyte
Anode

Figure 2-18: Technical outline of the SOFC tubular and flattened tubular design

*) [71]

The tubular cell design is at present the most reliable and robust design, [72]. However, the tubular cell design features only low power density, [73]. This is due to high ohmic in-plane resistance resulting from long current paths, [51], and high concentration polarization losses resulting from long diffusion paths for the oxygen from the bulk gas phase to the cathode TPB. The employed coating techniques, e.g. electrochemical vapor deposition (EVD), carry a high cost, [51], leading to high overall cell costs. Finally, thermal stress can be a concern, [73].

The flattened tubular cell design, commonly referred to as HPD design (high power density), was also developed by the Siemens AG, see Figure 2-18. It allows for about 30 to 40 % higher volumetric power densities compared to standard tubular cells, [74], due to better stacking possibilities, [59]. The seal-less design, similar to the standard tubular design, avoids gas cross-over problems, [74]. Internal ribs were introduced to reduce the high ohmic resistance of the standard tubular design by shortening the current paths, [75].

The main difference between planar and tubular cells is that their flow channels are usually defined by the geometry of the interconnector plates. Three flow configurations can be distinguished, namely co-flow, cross-flow and counter-flow, see Figure 2-19.

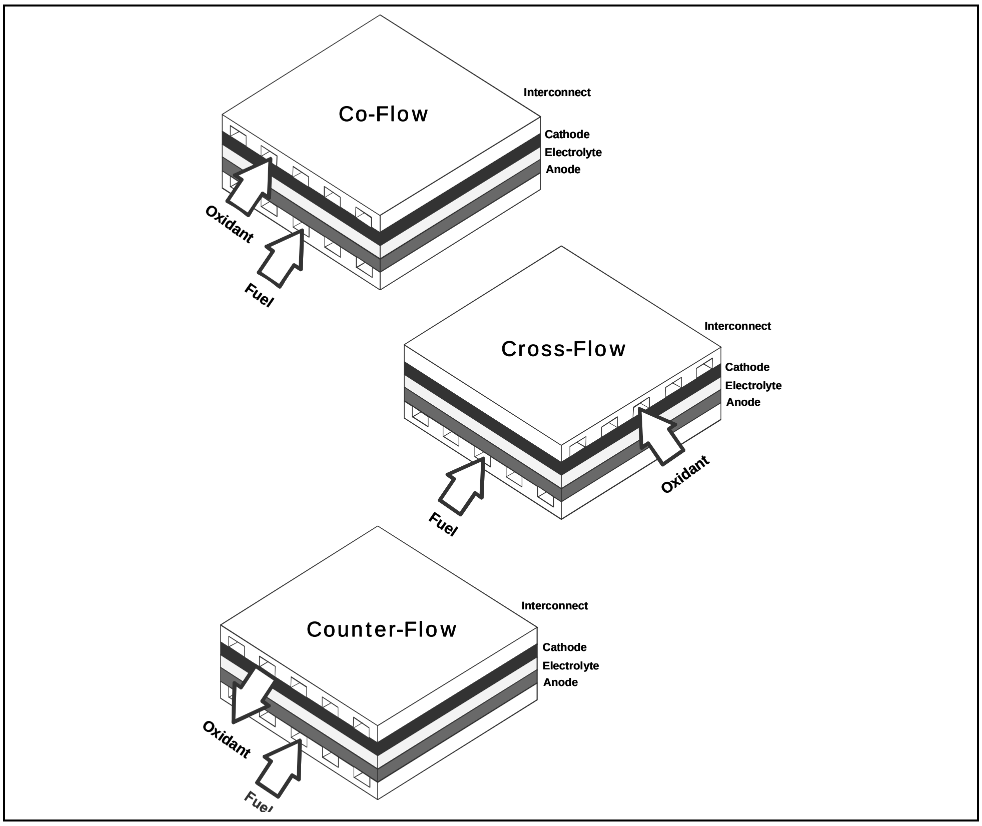
Co-Flow
Interconnect
Cathode
Electrolyte
Anode
Oxidant
Fuel
Cross-Flow
Interconnect
Cathode
Electrolyte
Anode
Oxidant
Fuel
Counter-Flow
Interconnect
Cathode
Electrolyte
Anode
Oxidant
Fuel

Figure 2-19:
Flow configurations of planar SOFCs

The planar cell design features higher area and especially volume specific power densities than standard tubular designs due to more efficient current collection, [73], and simple in-series connection of the single cells to stacks, [68]. The interconnectors may consist of ceramic or metallic materials. There exists a high cost reduction potential of the planar design as cost efficient production processes for high volume manufacturing of the flat cell components are available, [51]. The drawback of these cost efficient manufacturing techniques is that the maximum cell size is limited, [51]. The most important issue of the planar design is that sealings are necessary in order to avoid gas cross-over of oxidant and fuel gases.

Thermal stress is an important problem for planar cells, which are usually less robust than tubular cells. Thermal stress can result from multiple sources such as material property mismatches, poorly balanced endothermic and exothermic reactions and transients of operational parameters, [51].

2.4.5 Support designs

The support is the principal structural component of the anode-electrolyte-cathode assembly. It has to cover conflicting requirements like mechanical strength, in order to withstand thermal and mechanical stresses, and e.g. gaseous permeability, [76], or low ohmic resistance. Figure 2-20 depicts an overview of the four most common support designs, which are drawn to scale to give a better impression of the differences.

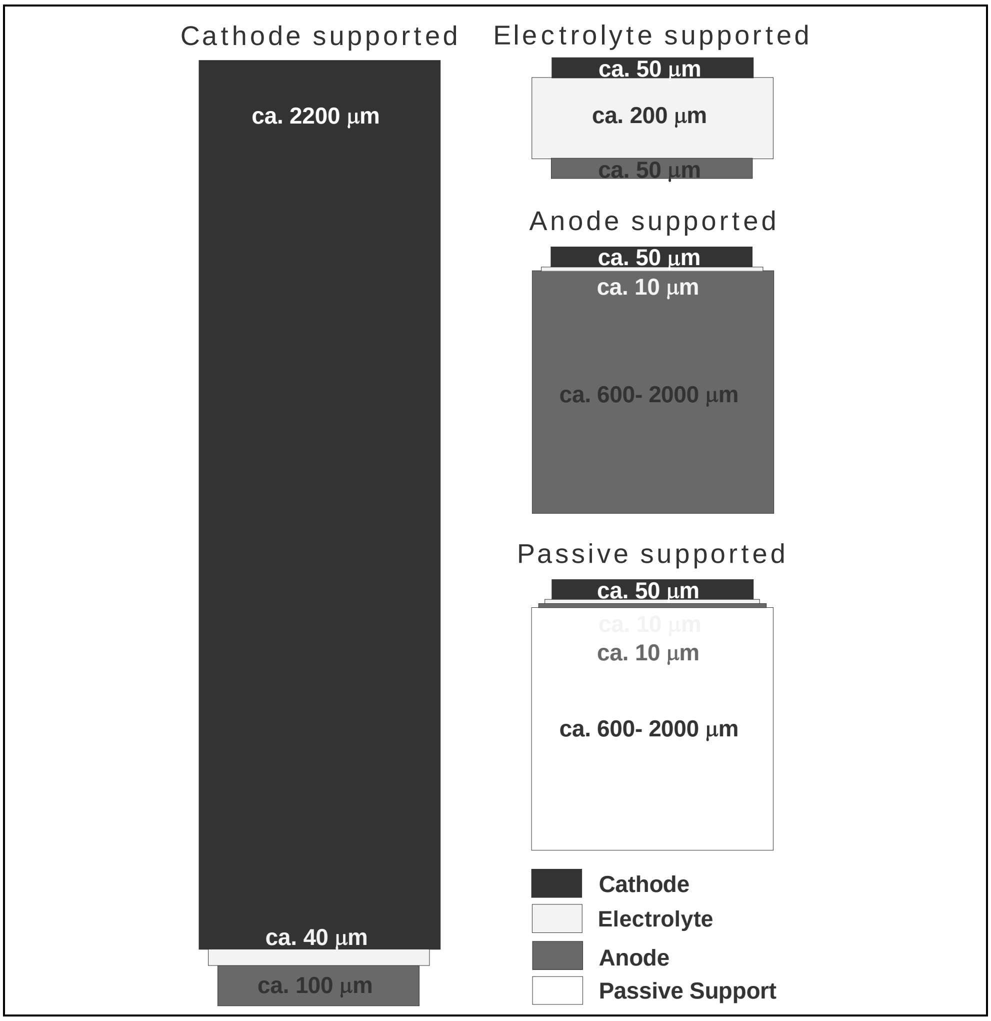
Cathode supported
Electrolyte supported
ca. 50 µm
ca. 2200 µm
ca. 200 µm
ca. 50 µm
Anode supported
ca. 50 µm
ca. 10 µm
ca. 600- 2000 µm
Passive supported
ca. 50 µm
ca. 10 µm
ca. 10 µm
ca. 600- 2000 µm
Cathode
Electrolyte
ca. 40 µm
Anode
ca. 100 µm
Passive Support

Figure 2-20:
Support designs, drawn to scale

The cathode-support design is widely used for tubular cells. It features high mechanical strength and has cost advantages as the cathode tubes are manufactured via relatively cheap extrusion processes. However, the gaseous permeability is an issue regarding the thick cathode leading to high cathode polarization losses.

The electrolyte-support design is state-of-the-art for planar cells. It is robust, [73], but suffers from high ohmic resistance, [75]. To counterbalance this disadvantage, electrolyte-supported cells are typically operated at high temperatures around 1000 °C.

The anode-support design has gained a lot of interest recently. The major advantage is that the thickness of the electrolyte can be heavily reduced as the mechanical strength of the cell is provided by the anode. Consequently, the ohmic losses caused by the electrolyte are heavily reduced, [77]. The good electrical conductivity of the supporting anode material allows for low operation temperatures around 700 to 800 °C, [75]. This, and the matching thermal expansion rate of the usually employed Ni-based anode materials makes the application of ferritic chromium interconnects possible, again lowering the internal resistance of the cells, [75]. Finally, the thick porous anode features a large specific surface and void volume which improves the conditions for Ni-catalyzed reactions, such as steam reforming of hydrocarbons and water gas shift. Although the anode-support design has significant advantages, it bears a relatively low mechanical strength compared to other support designs. Consequently, thermal stress and vibrations are the most important issues, [76].

The passive-support design allows very thin anode, electrolyte and cathode layers. These functional layers can be deposited via coating techniques onto either metallic or ceramic support structures.

Metallic support structures offer high mechanical strength, Redox stability, [75], and the potential for operation temperatures below 600 °C. The start-up times can therefore be reduced to values suitable for auxiliary power units (APUs), [76]. Other advantages of metallic support structures are the reduced need for expensive ceramic materials, [78], and the applicability of conventional joining techniques, [76]. The high thermal conductivity of metallic materials reduces spatial thermal gradients. Ceramic support structures provide reasonable mechanical strength at relatively low costs but struggle with low gas permeability and high concentration polarization losses.

2.4.6 Materials

Material and fabrication process improvements play an important role in reducing the stack costs. For instance, sulfur tolerant anode materials are presently an important research field because these materials would largely simplify the required gas cleaning and hence lower the costs of SOFC systems. Another important research area is in lowering the operation temperatures, enabling the use of cheaper materials for all cell elements. The working principle of the SOFC leads to the conductivity requirements shown in Table 2-5, [68].

Table 2-5: Conductivity requirements of the different cell components

Type of Conductivty Cell component	Electronic (via electron-gas-cloud)	Ionic (via atom vacancies in crystal structure)
Electrode	High	Desirable
Electrolyte	Very low or none	High
Interconnector	High	Very low or none

Other important requirements for SOFC materials are, [68]:

- Mechanical and chemical stability at high temperatures in reducing and oxidizing atmospheres
- Low formation risk of highly resistive phases
- Similar thermo-mechanical properties
- Low costs and ease of manufacture

Compared to the state-of-the-art materials mix, every new material represents an entirely new matrix of possible material interactions. Research activities focus on the thermal expansion compatibility and possible reactions at the material interfaces, such as phase decomposition via diffusion. This makes the search for and investigation of new materials more complex than the pure optimization of specific material properties such as e.g. the ionic conductivity of electrolyte materials. The subsequent sections provide an overview of state-of-the-art materials and a brief insight into the research work aiming at the identification and characterization of new promising materials for cell components.

2.4.6.1 Anode

Apart from the properties mentioned above, SOFC anode materials should feature, [68]:

- High surface to volume ratios. The porosity, tortuosity and average pore radius play an important role for the size of the TPB and the gas diffusion. These parameters are to a certain extent determined by the production processes.
- High catalytic activity towards electrochemical fuel oxidation, hydrocarbon reforming and water gas shift reactions.
- Chemical compatibility with electrolyte and interconnect materials.
- Mechanical strength in case that the cell is anode supported.
- Tolerance towards fuel contaminants.

State-of-the-art anodes are made of a ceramic metallic composite (cermet), typically containing 50 mass-% nickel oxide (NiO) and 50 mass-% yttria stabilized zirconia (YSZ). The NiO particles dispersed in the porous YSZ are reduced in-situ to metallic nickel. The porosity is typically 25 to 40 vol.-%, [79]. The TBP area, which determines the catalytic activity towards electrochemical reactions, is controlled by the YSZ powder size, the Ni to YSZ-ratio and the fabrication technique of the cell. Figure 2-21 shows the contact area between a state-of-the-art porous anode and the gastight electrolyte.

Figure 2-21:
SEM picture of the contact area between anode and electrolyte, [80]

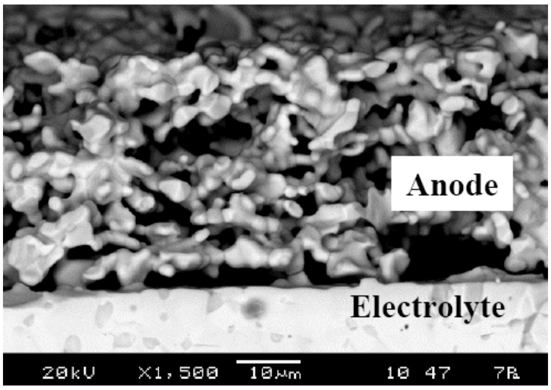

The advantages of Ni-YSZ anodes are:

- Nickel acts as electronic conductor and as STR catalyst, [73].
- The YSZ matrix assures a more or less equal thermal expansion coefficient of the anode and the usually employed YSZ electrolyte, [81].
- Nickel is a very good inexpensive electronic conductor showing an excellent oxidation activity for pre-reformed fuels, [81].
- The mixed cermet guarantees a large triple phased boundary (TPB).

However, the disadvantages of Ni-YSZ anodes are:

- Nickel is easily poisoned by sulfur, commonly used as odorant in natural gas, [81].
- The very high activity of nickel towards STR can lead to cold spots on the cell resulting in high spatial thermal gradients eventually leading to cell failures due to cracking of the AEC assembly, [68].

Although Ni-YSZ anodes show a satisfactory performance, there is still room for improvement. The research community investigates a variety of new materials. Nickel gadolinium doped cerium oxide (Ni-CGO) anodes feature:

- Low sintering temperatures around 1000 °C, allowing for cheap production processes, [76].
- Improved resistance against Ni-NiO cycling, [73].
- Strongly improved electrochemical oxidation activity as CGO is a mixed ionic and electronic conductor (MIEC). MIECs enable the oxidation of the fuel gas in the entire catalyst volume, [68].

However, Ni-CGO anodes have the following disadvantages:

- The low sintering temperature limits the operating temperature and hence the applicability of Ni-CGO to the anode-support design, [82].
- If other dopants than nickel are used, e.g. Cu, Au, etc., the STR activity is comparably low, [68].

Lanthanum strontium chromium perovskite (LSCr) anodes offer good Redox and sulfur tolerance. However, the electrochemical performance is lower than that of nickel-based anodes, [73].

Titanate anodes have drawn a lot of interest recently but their properties are hardly known yet. The material is stable in the reducing atmosphere and resistant against coking and sulfur poisoning. However, titanate anodes show only poor electronic conductivity, thus requiring highly conductive current collectors to keep the ohmic losses small, [82].

2.4.6.2 Electrolyte

Electrolyte materials should satisfy the following requirements besides those mentioned in section 2.4.6:

- Chemical compatibility with the electrode materials.
- Mechanical strength in case that the cell is electrolyte-supported.
- Gas tightness to prevent gas cross-over phenomena causing a strong decrease of the cell voltage and power output, [68].

State-of-the-art SOFCs employ yttria stabilized zirconia (YSZ) as electrolyte material. YSZ typically contains 8 mol-% of yttria. The advantages of YSZ electrolytes are, [82]:

- Acceptable ionic conductivity between 800 and 1000 °C.
- Excellent chemical stability in reducing and oxidizing atmospheres.
- Almost no electronic conductivity, [68].

YSZ shows only low ionic conductivity below 800 °C and is therefore not well suitable for low temperature SOFCs. Being a very refractory material, YSZ requires higher sintering temperatures than the other cell component materials. Co-sintering is hardly possible, increasing the production costs, [82].

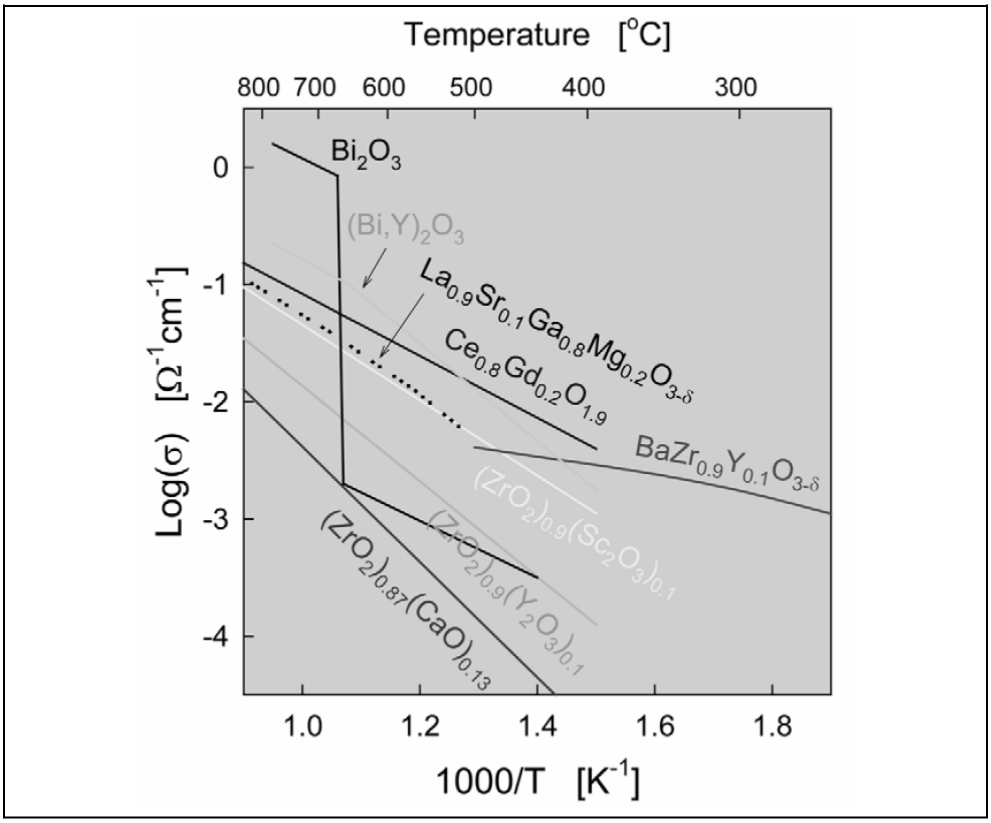

Figure 2-22: Ionic conductivities of selected high temperature conductors, [79]

The most important property of electrolyte materials is the ionic conductivity. A broad range of materials are summarized in Figure 2-22.

Of all zirconium solid solutions, scandia stabilized zirconia (ScSZ) has the highest ionic conductivity at temperatures above 750 °C, [68]. It is mechanically strong and allows operation temperatures below 800 °C, [73]. However, scandia is a very expensive material (4000$/kg) and ScSZ tends to be unstable at temperatures below 600 °C, [68].

LSGM (Lanthanum Strontium Magnesium Gallate) exhibits high ionic conductivity and is compatible with perovskite cathodes, [68]. LSGM is however difficult to process to a single phase and features only fair chemical stability in the operating conditions of SOFCs, [68], as the gallate is likely to evaporate, causing problems in other parts of the SOFC system, [73]. The material is less mechanically stable and may react with nickel, hence a barrier layer of e.g. doped ceria may be required, [82]. Further, gallium oxide is an expensive material (approx. 1000 $/kg).

2.4.6.3 Cathode

Apart from the properties mentioned in section 2.4.6, SOFC cathode materials should feature, [68]:

- High porosity to allow unrestricted gas diffusion to the cathode TPB.
- Catalytic activity towards electrochemical oxygen ionization.
- Chemical stability in oxidizing atmospheres.

State-of-the-art SOFCs use $La_{1-x}Sr_xMnO_{3-\delta}$, (lanthanum strontium manganite or LSM) as cathode material, where x is typically 0.15 to 0.25. Porosities are in the range of 25 to 40 %. Composite cathodes with YSZ to LSM ratios of 1:1 recently appeared and may be widely used in the near future, [79].

The advantages of LSM cathodes are, [82]:

- Good phase stability.
- Good thermal conductivity match with YSZ electrolytes.
- Well characterized in SOFC systems.

However, LSM is an almost pure electronic conductor with low conductivity. The electrochemically actives sites are therefore limited to the TPB, leading to a moderate catalytic activity.

Recently investigated mixed ionic-electronic conductors (MIEC) allow the ionization of oxygen in a larger active volume compared to standard LSM cathodes, where they are limited to the TPB area. This strongly reduces the cathode polarization losses, [82].

Most of the recently investigated cathode materials are mixtures of lanthanum and strontium with iron and/or cobalt (LSCF, LSF and LSC). The main concerns with these materials are low phase stability, yet unknown interface reactions and poor mechanical properties due to a strong mismatch of their thermal expansion coefficient with most electrolyte materials, [73]. For example, LSC cathodes were found to form resistive layers when combined with YSZ electrolytes. Hence, protective layers or other electrolyte materials have to be employed with LSC cathodes, [68].

Samarium-based perovskite cobaltites (e.g. $Sm_5Sr_5CoO_{3-x}$) are extensively investigated in Japan as they are amongst the best MIE conductors and feature smaller thermal expansion coefficients than LSCF, thus fixing the compatibility issue with standard electrolyte materials, [82].

2.4.6.4 Interconnect

Interconnects, also named bipolar plates in planar stack systems, establish the mechanical and electrical connection between the anode of one cell and the cathode of the next cell in SOFC stacks. There are different interconnect concepts under development which are suitable for different stack designs. Metallic, conducting ceramic and non-conducting ceramic interconnects with conducting vias can be distinguished.

Metallic interconnects usually consist of ferritic chromium. The chromium (up to 17 %, [76]) is used to improve the high-temperature oxidation resistance and to realize a sufficient electronic conductivity, [73]. Metallic interconnects feature:

- High electronic conductivity at low temperatures, [75].
- Production wise almost unlimited size, [75].
- Good thermal conductivity, thus reducing temperature gradients, [75].
- High mechanical integrity, [83].
- Lower production cost than ceramic interconnects, [83].

However, metallic interconnect exhibit a strong mismatch of the thermal expansion coefficient with all other cell components, [75]. The chromium can cause evaporation and deposition induced issues leading to severe cell degradation, [73]. Protective coatings are therefore mandatory, [84].

Conductive ceramic interconnects are usually made of doped lanthanum chromite perovskites. The specific dopant (typically, Sr, Ca or Mg) and concentration allow matching the thermal expansion coefficients of the cathode material and the other materials used for the remaining fuel cell components. Conducting ceramic interconnects feature negligible corrosion and low degradation. However, there are negative aspects to ceramic interconnects, [75]:

- The size is limited by available manufacturing processes.
- High sintering temperatures are needed.
- The thermal expansion coefficient is different in oxidizing and reducing atmospheres, which may cause thermal stress issues.
- The electrical and thermal conductivity is poor inducing thermal stress.
- The ceramic materials are difficult to process because chromium evaporation at high temperatures can lead to poor densification, [79].

A less common approach is the use of non-conducting ceramic interconnects with e.g. silver vias, [85]. This approach is well established in the microelectronics packing industry and combines the advantages of ceramic and metallic interconnects. However, the co-sintering of the vias and e.g. YSZ is an elaborate manufacturing process and a good match of the thermal expansion coefficients of the ceramic and the vias materials is difficult to achieve.

2.4.6.5 Sealant

In addition to anode, electrolyte, cathode and interconnects, SOFCs require sealant materials to isolate anode and cathode chambers from each other in planar configurations. Sealants are typically made of glasses or glass-ceramics, [79].

2.4.7 Cell failure and performance degradation

Long life time with low cell degradation and reliable operation are the most important prerequisites for a successful market introduction of the SOFC technology. Cell degradation manifests itself as a constant or sometimes sudden increase of the cell resistance resulting in a lower operational voltage or current depending on the operational mode of the cell. The cell degradation rate is expressed as the percentage of voltage lost during a certain period of time, where a constant current was drawn from the cell.

Most cell degradation is caused by the high operational temperature of SOFCs. It may also be induced by the composition of the fuel or oxidant gases. The detailed understanding of degradation mechanisms and the origin of their driving forces is the starting point for technology improvements. The comprehension of cell degradation is therefore currently the main scientific challenge in the SOFC materials and production processes research communities. Operational strategies to compensate for losses due to cell degradation on a short term basis have been identified already, [73]. For instance, an increase of the operational temperature by 15 K is sufficient to balance a performance degradation of 0.25 %. Further, cell degradation induced performance losses may be compensated by reducing the fuel utilization. The following paragraphs give an overview of the most important cell degradation mechanisms.

2.4.7.1 State-of-the-art

Cell degradation may vary by cell and stack size, fuel composition, fuel utilization and current load. A standardized degradation test procedure is yet to be defined by the research community. Consequently, a comparison of the degradation behavior of different SOFC types is difficult. However, general trends concerning the impact of the test conditions and test sample types can be observed. Button cell degradation tests do not reflect the impact of aging phenomena of sealants and spatial temperature gradients. The resulting degradation rates are usually lower than for the according SOFC cells or stacks. Tests conducted with gases containing hydrocarbons usually yield higher degradation rates due to higher thermal gradients stressing the cells.

Presently, the average cell or stack degradation determined with mostly pre-reformed natural gas is around 1 % per 1000 hours (%/1000h) with minimum values of 0.1 %/1000h and maximum values of 3.2 %/1000h, [59, 75, 86-95]. At the moment, the most reliable SOFC type is the tubular seal-less cell produced by the Siemens AG.

2.4.7.2 Changes in the structure of cell components

The performance of SOFCs strongly depends on the micro- and nanostructure of the cell components. Changes of properties on these scales may occur over long periods of time or be induced by specific events. The most important structural change mechanisms leading to cell degradation are:

- Nickel particle sintering at the anode

  State-of-the-art Ni-YSZ anodes, see section 2.4.6.1, predominantly degrade due to the agglomeration and coarsening of the nickel particles which are dissolved in an YSZ matrix, Figure 2-23.

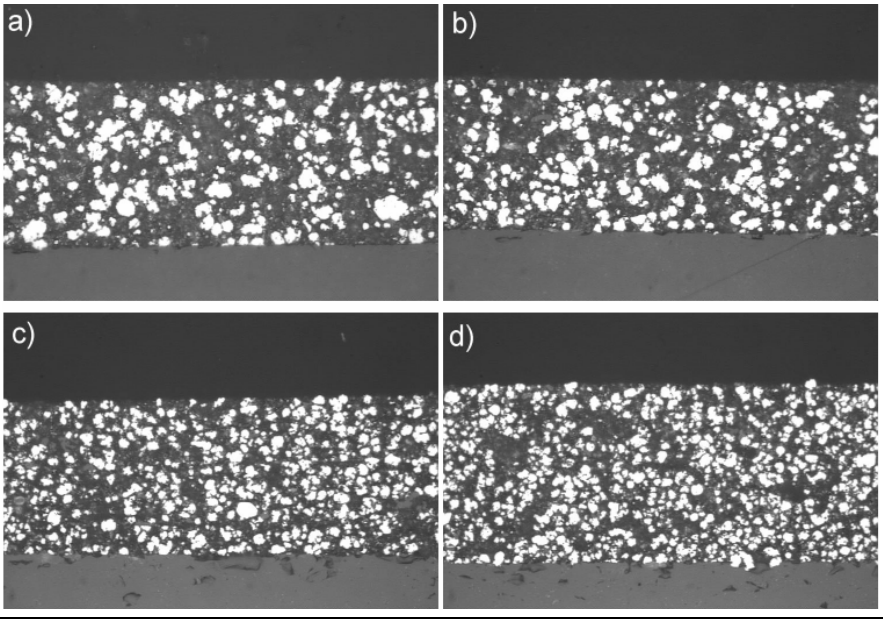

Figure 2-23: SEM pictures of a Ni-YSZ anode after 1500 h of operation (a, b) and after 8 h of operation (c, d); Width of pictures equals 100 µm, [96]

The thermodynamic driving force for nickel particle sintering is the poor wettability between metallic Ni and YSZ, [97]. In the reducing atmosphere of SOFC anode channels where steam is also present, nickel sintering takes place particularly fast, [98]. The formation of isolated large nickel islands in the YSZ matrix has two effects. First, the reduction of the specific nickel surface and of the attributed size of the triple phase boundary leads to an increase of the activation polarization, [99]. And second, the smaller amount of nickel particles and therewith of direct Ni-Ni contacts results in a lower electrical conductivity of the anode and increased ohmic polarization, [100].

- Nickel depletion of the anode

  The high operational temperatures call for nickel depletion of Ni-YSZ anodes which leads to increasing activation and ohmic polarization, see above. The nickel is discharged in form of either elemental nickel in the gas phase or gaseous nickel hydroxide ($Ni(OH)_2$) depending on the steam content of the anode gas, [96]. $Ni(OH)_2$ is the predominant volatile species at steam contents higher than 50 vol.-%.

- Delamination of the anode from the electrolyte

  During regular operation, the nickel particles are dissolved in the YSZ matrix in reduced form. If oxygen is introduced into the anode channel by e.g. diffusion processes through sealings or if steam partial pressures are very high due to insufficient fuel supply during load changes, the reduced nickel particles may be oxidized to nickel oxide. The associated large volume change may cause the disintegration of the cermet structure, [97]. The resulting delamination on the anode and the electrolyte reduces the size of the triple phase boundary and causes severe permanent cell degradation, [76].

- Demixing of electrolyte phases

  State-of-the-art electrolytes consist of yttria-stabilized zirconia. Zirconia (ZrO_2) is a polymorphic material, Figure 2-24. During cool down of zirconia oxide from the molten state, cubic crystals are formed at temperatures lower than 2680 °C. Below 2370 °C, the cubic crystals change to the tetragonal form. Further cool down below 1170 °C yields a third change of the lattice structure to the monoclinic form. The latter structural change involves a volume expansion of 3 to 5 % which entails that components made of pure zirconia are prone to dismember during cool down, [101].

Figure 2-24: Lattice structures of zirconia, [101]

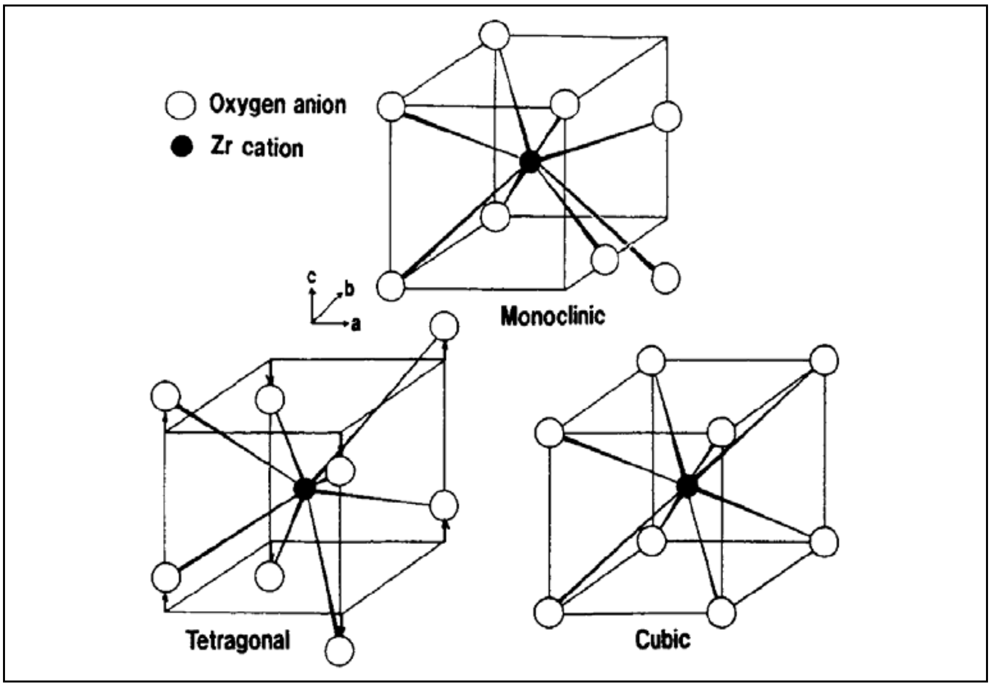

The addition of yttrium oxide (Y_2O_3) avoids the transformation of the crystals to the monoclinic form and hence stabilizes the zirconia. With yttria concentrations higher than 8 mol-%, the cubic form of zirconia is stable at room temperature. The exchange of tetravalent zirconium with trivalent yttrium yields oxygen vacancies in the lattice structure. These vacancies permit the passage of oxygen ions and constitute the ionic conductivity of YSZ, [101]. The number of vacancies is half that of the yttrium ions present in the electrolyte.

Typical SOFC electrolytes contain between 3 to 8 mol-% of yttria and therefore consist of a cubic zirconia crystal matrix with tetragonal embeddings which can stress-induced transform into the monoclinic form. The monoclinic form offers good mechanical properties and is therefore desired in electrolyte-supported cells. Degradation of YSZ electrolytes results from the demixing of the YSZ matrix into an yttria-rich cubic phase and an yttria-poor tetragonal phase, [102]. The tetragonal phase hinders the passage of oxygen ions and hence decreases the ionic conductivity of the electrolyte leading to increased ohmic losses.

- Ordering of vacancies in the electrolyte structure

  As discussed above, a uniform distribution of oxygen vacancies throughout the whole electrolyte is a prerequisite for high ionic conductivity. Long-term ordering processes of vacancies result in irreversible degradation of the electrolyte, [102, 103].

- Formation of low conductive layers between the cathode and the electrolyte

  The most commonly employed cathode material is lanthanum strontium manganite (LSM), see section 2.4.6.3. LSM cathodes tend to form resistive products with zirconia such as e.g. $La_2Zr_2O_7$ which entail severe irreversible cell degradation, [68]. Further, gaseous chromium in the oxidant gas originating from metallic interconnects or upstream equipment may lead to the formation of a spinel phase near the cathode triple phase boundary which deteriorates the electrochemical properties of LSM, [104].

- Pores between the cathode and the electrolyte

  Under load conditions, an oxygen potential difference may be created across the cathode which leads to a redistribution of the cathode materials. Pore formation and movement may result, leading to a decrease of the active triple phase boundary length at the electrolyte-cathode interface and consequently to higher cathode activation polarization. For a more detailed discussion of this complex and not yet fully understood degradation mechanism please see [105].

2.4.7.3 Carbon deposition

Carbon deposition is a concern in all catalytic conversion processes of hydrocarbons, including internally reforming SOFCs. Catalyst deactivation due to carbon deposition may result from encapsulation of nickel particles by polymeric carbon, blocking of catalyst pores and deterioration of the catalyst surface by carbon whiskers, [106], Figure 2-25.

Figure 2-25: Forms of permanent deactivation of nickel catalysts by deposited carbon, [40]

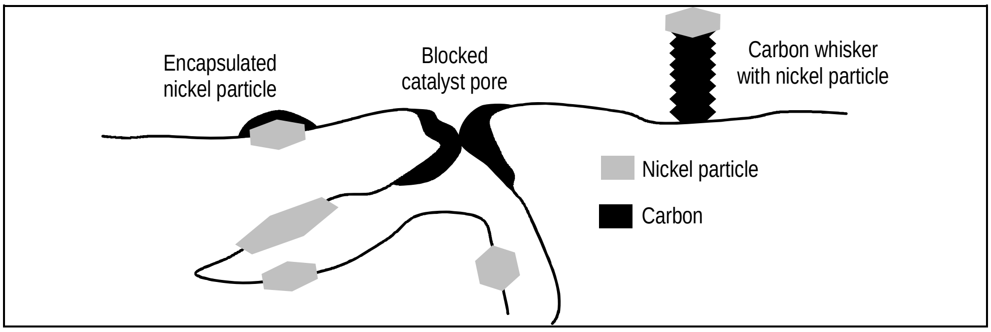
Encapsulated nickel particle
Blocked catalyst pore
Carbon whisker with nickel particle
Nickel particle
Carbon

Depending on their origin, carbon deposits are differentiated in carbon and coke. Carbon is the product of CO decomposition via the reverse carbon steam reaction, Eq. 12, and the reverse Boudouard reaction, Eq. 13. Carbon originating from the decomposition of hydrocarbons is summarized under the term coke. Methane may contribute to coke deposition via the reverse hydrogasification reaction, Eq. 15. The decomposition pathway of higher hydrocarbons is however more complex than that of carbon monoxide and methane. Hydrocarbons adsorb on the catalytic surface and split off hydrogen. The remaining carbon structures polymerize to form coke, [107]. The coking potential of higher hydrocarbons increases from paraffins via olefins to acetylenes, [108]. Aromats are also known for their potential towards coke formation, which is several times higher than that of carbon monoxide and increases with increasing molecular weight of the aromatic specie, [54]. More detailed information about carbon and coke formation can be found in [106, 109, 110].

Once deposited, carbon is difficult to remove at temperatures below 800 °C without the presence of a catalyst due to the slow carbon gasification reactions. Depending on the SOFC type, the temperatures may be significantly higher, which results in reduced carbon deposition risk. However, buildup of carbon deposits was observed in internally reforming SOFCs, [82], causing reduced STR activity and increased anode activation losses. The latter is due to shortened active length of the TPB. A material-based solution for the coking issues is copper doping of the anode material, [81, 111].

2.4.7.4 Structural stress

The anode-electrolyte-cathode assembly (AEC) of SOFCs consists of three thin ceramic material layers which are jointed via sintering processes. Additionally, planar SOFCs have glassy sealants which separate the anode and cathode gas channels at the gas in- and outlets. Cell failure and irreversible performance degradation due to gas cross-over is the result, if these fragile ceramic and glassy structures break or disassemble. Structural stress is the most important reason for such malfunctions, whereas its order of magnitude depends on the properties of the employed material, the operating conditions as well as the design and stacking concept, [112]. Structural stress may arise from:

- Different thermal expansion coefficients of the used materials

  Anodes, electrolytes, cathodes and sealings are made of different materials with different thermal expansion coefficients. Mismatches result in residual stress during operation as the operational temperatures of SOFCs are lower than the temperatures during manufacturing. These stresses can lead to micro crack formation and delamination of the ceramic and glassy structures, [113]. Residual stress is therefore one of the most important limiting factors for the scaling up of planar cells over 100 cm^2 active area, [114].

- Spatial and temporal thermal gradients

  Residual stresses are aggravated by spatial and temporal thermal gradients. Important spatial thermal gradients result from poorly balanced exothermic water gas shift and electrochemical reactions with endothermic steam reforming reactions of methane, higher hydrocarbons and tars, [51]. Cracking of the AEC and attributed cell failure was frequently reported as consequence of high spatial thermal gradients, [53, 113, 115]. Spatial thermal gradients may be reduced by metallic interconnects with high thermal conductivity, appropriate flow configurations, increased fuel utilization and operational voltages, [113], as well as higher degree of pre-reforming of the fuel gas in question. Temporal thermal gradients are most important during heat-up and start-up phases. The effects of temporal thermal gradients are similar to those of spatial thermal gradients.

- External mechanical loading

  SOFC stacks are usually charged with weights to assure correct orientation and good contact between the single cells. The induced mechanical stresses may cause stability issues within the AEC, [113].

2.4.7.5 Catalyst poisoning

The activity of the employed catalysts at the anode and cathode may be reduced or even eliminated by contaminants in the fuel or oxidant gas.

Alkali metals may cause deactivation of the STR activity of nickel and thus reduce the ability of SOFCs to convert hydrocarbon containing fuels. This effect is most pronounced for potassium and less for lithium and sodium, [13]. The impact of alkali metals towards the electrochemical activity of nickel has however not yet been studied.

Halides may also reduce the activity of nickel. In [95] however, no impact on cell performance was found for 1 ppmV of HCl in the fuel gas.

Sulfur is a well known poison for STR nickel catalysts, [107]. The type of sulfur species is usually not important for the poisoning, [116]. Sulfur chemisorbs on nickel, thus blocking active sites. In SOFCs this leads to reduced STR activity and shortening of the active length of the TPB. Hence, activation polarization losses increase very fast when sulfur is introduced to SOFCs. Figure 2-26 shows exemplarily that 1 ppmV of H_2S may result into a very fast 15 % performance drop, [117]. Sulfur poisoning is often reported to be reversible and less pronounced at higher temperatures, [10, 118-120]. However, irreversible degradation may also be caused by sulfur as it easily reacts with nickel, forming e.g. nickel sulfide (Ni_2S_3), [96]. Ni_2S_3 melts at 806 °C compared to 1455 °C of pure nickel. This may lead to enhanced nickel particle sintering and therefore irreversible degradation of Ni-YSZ anodes, see section 2.4.7.2, [96].

Chromium is known to be a poison for the state-of-the-art LSM cathodes. It may evaporate from metallic interconnects or up-stream equipment and subsequently condensate at the cathode TPB, [104, 121]. The condensed chromium inhibits the oxygen reduction and leads to increased cathode polarization losses.

Figure 2-26: Synergetic degradation effects of phosphorous, arsenic and sulfur, [117]

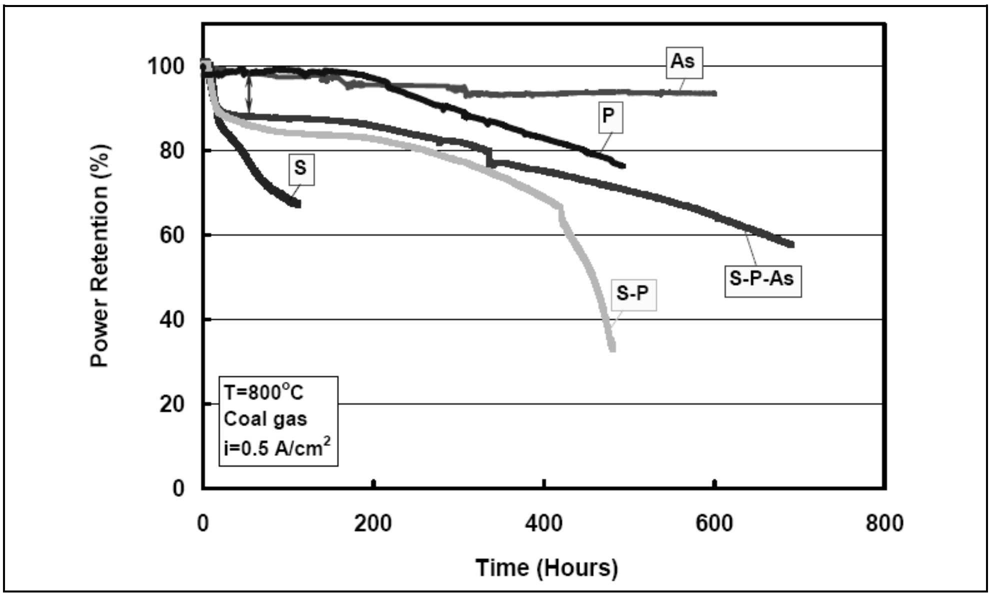

Arsenic reacts with standard Ni-YSZ anodes and yields Ni_5As_2, [117]. However, Figure 2-26 shows that the exposure of Ni-YSZ anodes to 1 ppmV AsH_3 for a period of 700 h at 800 °C resulted in minor cell degradation. According to [117], this can be explained with strong nickel arsenic interaction at the surface of the Ni-YSZ anode. Therefore the arsenic did not penetrate into the anode and did not provoke a change of the triple phase boundary structure.

Phosphorous in form of PH_3 was shown in [117] to react with nickel, forming Ni_3P which extensively agglomerates inside the anode layer. Figure 2-26 shows that the operation over 700 hours at 800 °C with 2 ppm of PH_3 resulted in considerable degradation. At room temperature, PH_3 can be removed with copper doped zeolites, [122].

3 Experiments

The experimental research agenda with respect to the development of a robust B-IGFC system design at Paul Scherrer Institut (PSI) began in 2000. Initial tests showed that aromatic tars such as benzene, toluene etc. rather than being mere impurities in the fuel gas can be considered as possible fuel for solid oxide fuel cells (SOFCs). Encouraged by these findings, system analysis calculations were carried out in 2002 and 2003, revealing that the link-up of an updraft gasifier with a SOFC via hot gas processing would be a promising B-IGFC concept, [123, 124]. In 2004, the proof-of-feasibility of wood gas operated SOFCs was achieved on lab scale. Further testing showed that tars are not inert but degraded in SOFCs to hydrogen and carbon monoxide, thus contributing to the electrochemical reactions and power generation. The characterization of all important unit operations was completed by mid 2007. For the final proof-of-concept, an experimental setup based on the PSI B-IGFC concept was put in place, [125]. In late 2007, the setup covering the complete chain from wood to electricity was operated several times up to 28 h non-stop and 65 h in total. The following section outlines the most important experiments conducted, supervised or analyzed by the author.

3.1 The PSI B-IGFC system

3.1.1 System description

The PSI B-IGFC concept is shown in Figure 3-1. In a first step, the wood is converted to a highly tar-laden producer gas in an updraft wood gasifier. The cold gas efficiency of this gasification process is above 90 % due to the relatively low temperature of the raw producer gas of around 75 to 250 °C. At these temperatures, inorganic impurities such as e.g. alkali metals are in the solid phase condensed on particles. Together with the particles, the condensed impurities are removed from the producer gas via a hot gas cyclone and a particle filter employing filter candles. The particle free producer gas is then fed to a catalytic partial oxidation where the tar and hydrocarbon content is decreased to levels suitable for SOFCs. After the catalytic partial oxidation, the producer gas is cooled down from approx. 750 to 400 °C in order to allow for the removal of chlorine and sulfur compounds in sorbent trap beds. This temperature is the maximum possible temperature to avoid volatilization of the employed sorbent materials, namely sodium carbonate and zinc oxide.

Figure 3-1: PSI B-IGFC system outline

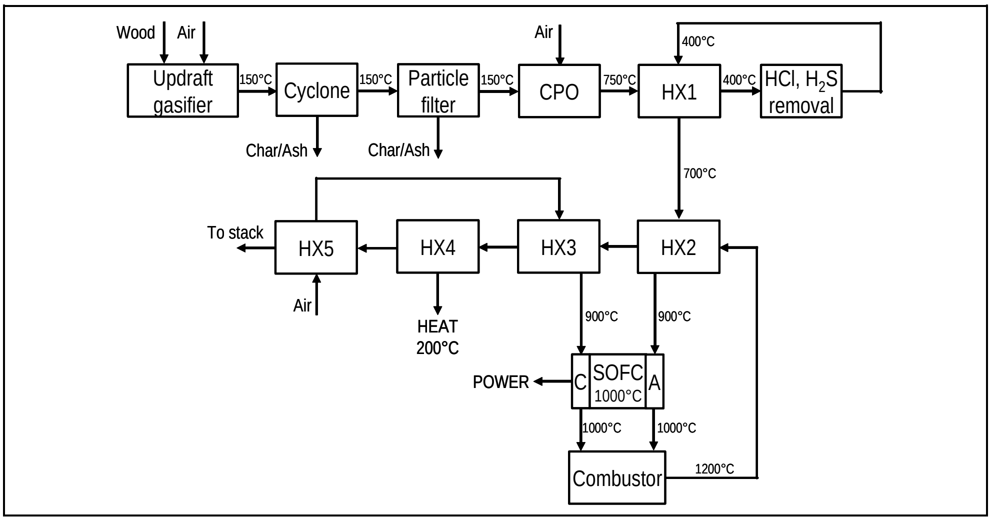
Wood
Air
Updraft gasifier
150°C
Cyclone
150°C
Particle filter
150°C
Air
CPO
750°C
HX1
400°C
400°C
HCl, H_2S removal
Char/Ash
Char/Ash
700°C
To stack
HX5
HX4
HX3
HX2
Air
HEAT 200°C
900°C
900°C
POWER
C
SOFC 1000°C
A
1000°C
1000°C
Combustor
1200°C

The producer gas is then heated up again to approx. 700 °C in the gas-to-gas heat exchanger HX1 and superheated to 900 °C in HX2 before entering the anode channels of the SOFC. The depleted producer gas is mixed with the depleted cooling air of the SOFC and completely burned in a catalytic combustor. The hot flue gas is used to superheat the producer gas in HX2 and the cooling air of the SOFC in HX3. Heat at a temperature level of 200 °C is recuperated in HX4. The remainder of the flue gas heat is used to pre-heat the SOFC cooling air in HX5 before it is sent to the stack. The SOFC produces direct current at a given cell voltage which is converted to AC power in an inverter.

3.1.2 Discussion of the chosen approach

The starting point for the development of the PSI B-IGFC system was an analysis of potential threats for SOFCs arising from the composition and the impurity load of biomass gasification derived fuel gases. The considered threats were carbon deposition, temperature gradients and sulfur poisoning.

Evaluation of biomass gasification processes

Nickel is usually employed as catalyst material in SOFC anodes. At the typical SOFC operating temperatures of around 600 to 1000 °C, nickel catalysts are prone to coking and therewith induced deactivation. The mechanisms of carbon deposition on and removal from nickel catalysts is the subject of several other investigations, [106, 109, 110, 126]. Carbon deposition can either result from CO dissociation following the exothermic Boudouard reaction or from the dehydrogenation of hydrocarbons and of aromatics in particular, [127].

The probability of carbon deposition can be roughly estimated with equilibrium calculations assuming carbon depositions as graphite. This approach was chosen by several other research teams for similar investigations, [128-131]. Figure 3-2 shows the ternary diagram of the carbon-hydrogen-oxygen system. The inscribed isotherms divide the diagram into a region where graphite formation can be expected and one in which it is unlikely to take place. It can be seen that the probability of graphite formation decreases with increasing temperatures. Air or oxygen gasification of dry wood shifts the point representing the corresponding producer gas towards the oxygen corner. Increasing wood humidity and steam gasification shifts it towards the H_2O point in the diagram.

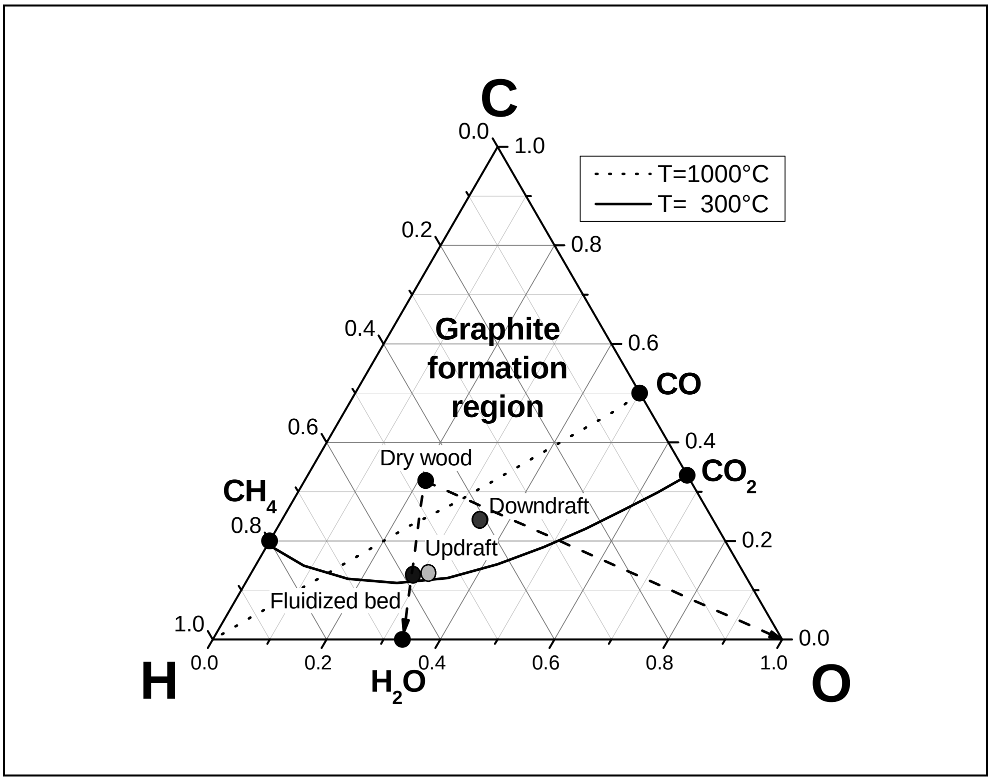

Figure 3-2:
C-H-O ternary diagram for the thermodynamic graphite formation at equilibrium conditions with inscribed fuel gases as received from different biomass gasifier types

For fixed bed downdraft gasification, the humidity of the wood is limited to less than 12 %. The cold gas efficiency of this process is typically around 80 to 85 %. The corresponding producer gas is close to the connection line between the dry wood point and the oxygen corner of the diagram as air is employed as gasification agent.

The updraft gasification process also employs air as gasification agent, but allows for the conversion of wood with humidity up to 50 %. Consequently, the corresponding point in the diagram is close to the connection line between the dry wood point and the water point. The cold gas efficiency of this process can be up to 95 %.

For the fluidized bed steam gasification process, the feed humidity should be kept below 10 % in order to reach satisfying conversion efficiencies in the range of 70 %, [33]. Using steam as gasification agent, the corresponding producer gas point lies directly on the connection line between the dry wood point and the water point of the diagram.

Figure 3-2 shows that all raw fuel gases are in the graphite formation free region at 1000 °C. However at 300 °C, which is considered the lowest temperature at which carbon formation can occur at a considerable rate, only the updraft and the fluidized bed producer gases are close to the graphite formation free zone. The required water addition to prevent carbon deposition, the low content of hydrocarbons and the conversion efficiency of 80 % were clear factors against the application of the downdraft gasification in the PSI B-IGFC system.

The tar species found in producer gases from updraft wood gasifiers are mainly oxygenates, [29], which decompose in the gas phase at temperatures of 500 °C or higher without forming significant amounts of coke, [55]. In contrast, the tar load of producer gases originating from fluidized bed steam gasification typically consists to a major extent of aromatic species which are prone to coking as discussed above. For this reason and due to the higher conversion efficiency, the updraft gasification process was identified as best choice for the application in the PSI B-IGFC system.

Evaluation of gas processing options

In a next step, the required gas processing was defined based on the fuel gas requirements imposed by SOFCs and the producer gas properties of the chosen updraft fixed bed gasification process. Fuel gases for SOFCs have to be particle free in order to avoid physical blocking of the gas channels. Another issue are impurities such as e.g. alkali salts. Due to migration processes of these impurities into the electrode materials, they can cause serious damage to fuel cells via micro structural changes of the electrode structure, [13]. The particle load of producer gases from updraft gasification is usually low and at the typical producer gas temperatures of updraft gasifiers around 75 to 200 °C, alkali salts can be assumed to be condensed on particles to a major extent. Therefore it was concluded, that the particle removal via a cyclone and a particle filter should resolve both issues.

State-of-the-art gas processing is focused on the application of internal combustion engines which require fuel gas temperatures below the dew point of tars. In order to prevent blocking of valves etc. tars are almost completely removed. SOFCs, in contrast to internal combustion engines, require high fuel gas temperatures and can, to some extent, use tars as fuel. The reforming of oxygenated tars, which are mainly present in the producer gas from the updraft gasification process, was demonstrated in e.g. [55]. Applying cold gas processing for the complete removal of tars in a B-IGFC system therefore entails a loss of both fuel and sensible heat, which ultimately results in lower system efficiencies, [132]. Consequently, hot gas processing at temperatures above the dew point of tars was considered for the PSI B-IGFC system. This consideration took place despite the handling of tars being more delicate than their removal, as especially the heat-up of tar-laden gases can cause serious coking problems, [133].

Cell internal reforming of hydrocarbons and tars is a possibility for the chemical cooling of SOFCs, which reduces the cooling air mass flow required to maintain the operational temperature. Further, internal reforming increases the electrical efficiency of SOFCs as the heat of the electrochemical reactions is used cell internally to increase the heating value of the fuel gas. However, hydrocarbon and tar reforming reactions are relatively fast in the presence of nickel at the typical operating temperatures of SOFCs. High hydrocarbon and tar contents can therefore lead to thermal stress due to cooling of the cell inlet region as a consequence of the endothermic character of reforming reactions. It was therefore concluded that the gas processing must allow for a precise partial conversion of hydrocarbons and tars to yield the best compromise between thermal stress problems and efficiency benefits.

A further issue which has to be addressed by the gas processing is sulfur. Sulfur is known for its tendency to form strong bonds with nickel, [134-136], and thereby blocking active sites making these unavailable for reactant molecules. For the poisoning, the type of the sulfur species is largely irrelevant, [116, 118]. However for the removal of sulfur, the type of species is of major importance and must be considered in the definition of the gas processing.

Catalytic partial oxidation (CPO) was identified to possibly cover all the above requirements. CPO catalysts are usually ceramic monoliths coated with noble metals, [63]. The average temperature of the process is below 800 °C, [62]. A characteristic feature of the CPO is that two different reaction zones can be distinguished within the monolith during operation. Near the monolith inlet, a hotspot with temperatures of approx. 1000 °C indicates that the supplied oxygen is consumed by the partial combustion of the fuel. In the downstream parts of the monolith, the heat and the steam originating for the combustion reactions are consumed by steam reforming reactions. CPO catalysts may be to a large extent sulfur tolerant. Furthermore, the high hotspot temperatures are beneficial for an almost complete conversion of organic sulfur compounds to hydrogen sulfide. The hydrogen sulfide can then be removed in high temperature zinc oxide trap beds. The rate of conversion of hydrocarbons and tars may be controlled through the geometry and the operating conditions of the CPO monoliths.

3.2 Gas analysis

In all experiments, Varian micro gas chromatographs (μ-GCs) were employed to monitor the dry and clean composition of gas mixtures online.

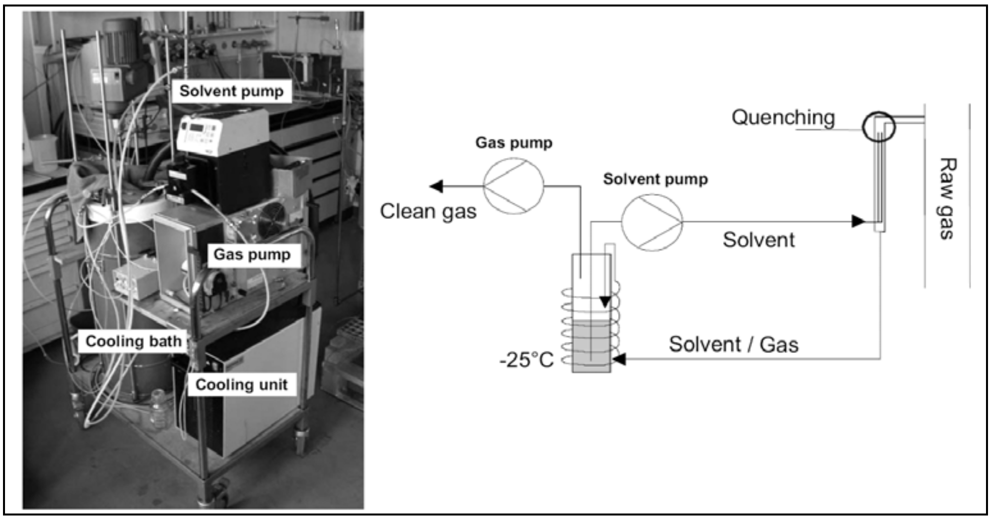

Figure 3-3: Outline of used gas sampling system

The columns employed for the separation of different gaseous species allow the measurement of the following permanent gas species: hydrogen, helium, carbon monoxide, carbon dioxide, methane, ethene, propane, nitrogen and oxygen. All other species have to be removed from the analyzed gas prior to the injection to the μ-GC. The employed gas sampling system is based on the design proposed in [137] and has been further developed at PSI, Figure 3-3.

In a first step, the raw gas is quenched with a solvent. Condensable species, such as tars, water and other impurities, are thus dissolved. The solution is cooled to -25 °C to assure that only traces of condensable species remain gaseous. After a gas-liquid separation, the dry and clean gas is pumped to the μ-GC while the used solvent is either reused for another quench cycle, as depicted in Figure 3-3, or bottled for later analysis. 1-methoxy-2-propanol is used as solvent due to its good solubility for both organic carboneous species and water.

At times the employed solvent was analyzed in order to determine the amount and nature of impurities in the raw gas and its water load. The employed methods were:

- *Gas chromatography coupled with mass spectrometry* (GC/MS) for the identification of aromatic species such as benzene, toluene etc. and quantification of their concentration in the raw gas.
- *Gravimetric method* for the determination of the concentration of hydrocarbons with dew point above approx. 140 °C in the raw gas.

  Following the gravimetric method, a given amount of used solvent is placed in a vacuum oven at 40 °C and 30 mbara until the weight loss of the specimen due to evaporation of volatile compounds subsides. Based on the remaining mass of the sample, which is attributed to the mass of higher hydrocarbons, the corresponding concentration in the raw gas is computed.
- *Karl-Fischer titration method* for the analysis of the water concentration in the raw gas.

Given that offline analysis is time-consuming, mass balance calculations were performed to estimate the tar and water concentrations of the raw gas based on the measured dry and clean gas compositions. The general assumptions were:

- Carbon (C), hydrogen (H), oxygen (O) and nitrogen (N) are the only considered elements.
- There are no uncontrolled leakages in the balanced system.
- Nitrogen appears as molecular nitrogen only.

Most of the experiments presented in the subsequent sections involved a lab scale wood gasifier as gas source. Following assumptions were made to account for the heterogeneous character of wood and the complexity of the gasification process:

- Dry wood contains 50 mass-% C, 44 mass-% O and 6 mass-% H.

  An elemental analysis of the used wood pellets was commissioned to two independent laboratories. The analyzed samples consisted of 49.85 to 50.09 mass-% carbon, 43.41 to 43.65 mass-% oxygen, 5.93 to 6.03 mass-% hydrogen and 0.15 to 0.2 mass-% nitrogen. The sulfur mass fraction was found to be about 0.01 to 0.03 mass-%.
- The average humidity of the gasified wood is 6 %.
- Air consists of 79 vol.-% nitrogen and 21 vol.-% oxygen.
- All carbon introduced to the gasifier is converted to gaseous or liquid species. The formation of char or soot is neglected.
- All nitrogen in the producer gas comes from the gasification agent.

  Consequently, the total molar flow of the dry and clean producer gas equals the gasification air molar flow times the quotient of the nitrogen fraction of air and raw gas. The molar flows of atomic carbon, oxygen and hydrogen bound in permanent gases are computed using the measured molar fractions and according stoiciometric coefficients.
- All carbon, which is not bound in permanent gases, is bound in "tars".
- "Tar" is approximated by the empirical formula $CH_{1.34}O_{0.81}$.

  The investigated lab scale gasifier is based on the countercurrent fixed bed process. In this process, the "tars" mainly originate from pyrolysis sub-processes, which take place close to the gas outlet and occur in reducing atmospheres. According to [57], the composition of "tars" originating from fast pyrolysis processes can be approximated as mixture of 67 % acetic acid, 16.5 % m-cresol, 16.5 % syringol which translates in the above empirical formula.
- All hydrogen and oxygen, which is neither bound in the measured dry and clean gas species nor bound in "tars", is assumed to be bound in water molecules.
- Where the water load is measured via the Karl-Fischer coulombmetry method, the empirical formula for "tars" was determined to satisfy the mass balance. The resulting empirical formula can be used as indicator for the tar signature of the investigated producer gas.

All incoming gaseous mass streams where directly monitored using mass flow controllers, rotameters or gas meters. Liquid and solid mass flows where indirectly determined by time averaging the measured absolute mass difference for a given time interval.

3.3 Proof-of-feasibility tests

3.3.1 Lab scale tests under load conditions

The feasibility of the PSI B-IGFC concept was shown by linking-up a laboratory scale SOFC with an updraft gasifier in 2004, Figure 3-4.

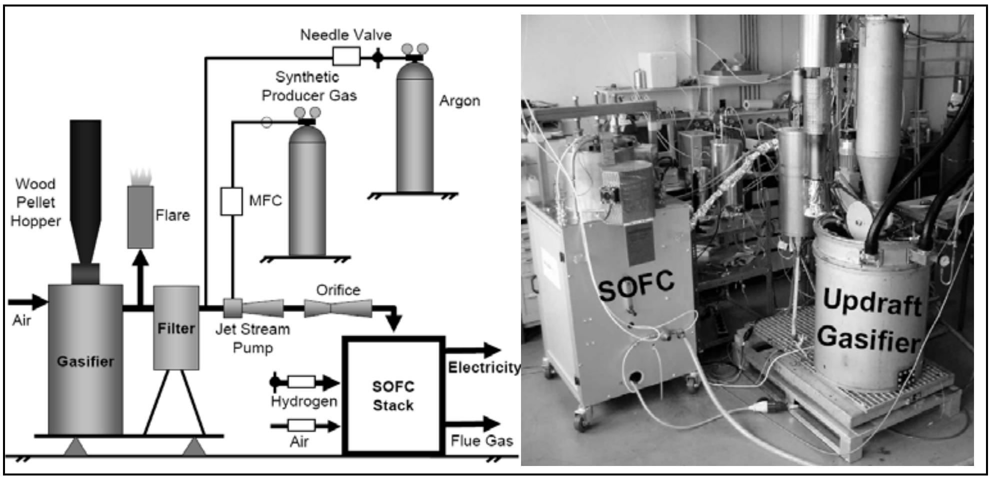
Needle Valve
Synthetic Producer Gas
Argon
Wood Pellet Hopper
Flare
MFC
Orifice
Air
Gasifier
Filter
Jet Stream Pump
Electricity
Hydrogen
SOFC Stack
Air
Flue Gas
SOFC
Updraft Gasifier

Figure 3-4: Technical outline and photograph of the experimental setup used for proof-of-feasibility tests in 2004

The gasifier had a maximum feed of 2.7 kg/h of wood pellets. For the experiments, the mass flow was reduced to 1.3 kg/h or 6 kW of thermal input, respectively. The non-stop operation period was limited to 16 hours. Typical gasifier air-to-fuel ratios were between 0.2 and 0.4. A planar lab scale stack provided by the Hexis AG (formerly Sulzer Hexis) was used for the experiments. The SOFC stack consisted of five single cells with an active area per cell of 60 cm^2. The stack was designed for a nominal electric power output of 60 W when operated with reformate gas originating from the catalytic partial oxidation of natural gas from the Swiss grid. The stack was placed in an oven which kept the operational temperature of the stack at approx. 950 °C.

Due to the stack and system design aiming at natural gas applications, means of heating had to be introduced to the normally non-heated feed gas inlet area. This area as well as the pipe system connecting the gasifier and the SOFC system were heated to 400 °C in order to prevent condensation of tars and thereby blocking. Further, a particle filter was employed to remove particles which could also cause blocking. No other gas processing steps were undertaken.

The particle free, humid and tar laden producer gas was fed to the fuel cell through a jet pump, the reason being that the gasifier had a producer gas output of approx. 5 kW (based on the lower heating value - LHV) and only a few percent of the producer gas flow rate were required for the operation of the 60W-SOFC. The specifically developed jet pump delivered approx. four standard liters of fuel gas per minute with the required overpressure of 20 mbar to the stack. The propellant gas composition was adjusted to match the main components of the tar-free producer gas. The mixing ratio was on average one part of producer gas per part of propellant gas. Due to the particle filter, the feeding system could be operated for several hours at a time. The fuel gas volume flow was monitored with a heated orifice. For more information see [125].

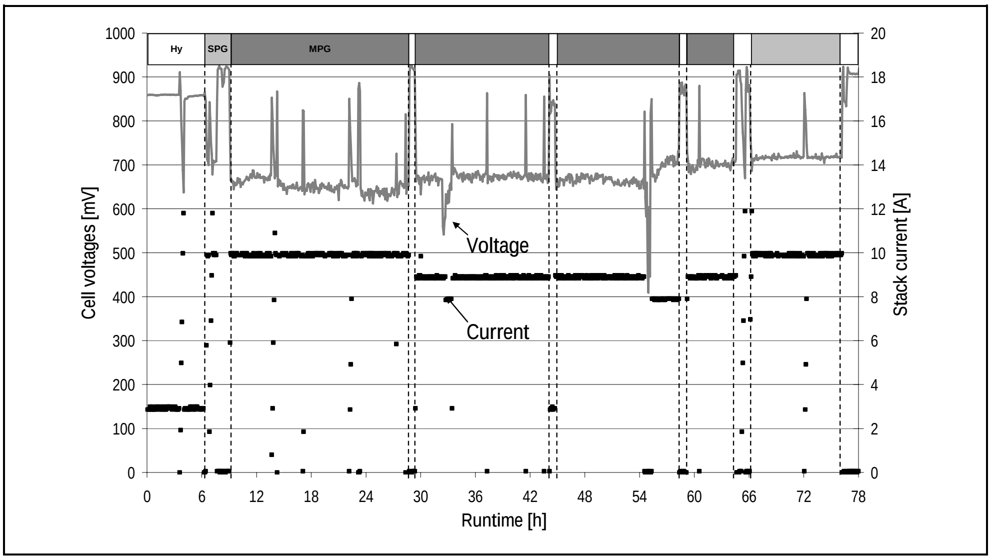

Figure 3-5:
55 h operation of the 5-cell SOFC stack with wood gas under isothermal conditions in an oven

"Hy": Hydrogen
"SPG": Synthetic gas
"MPG": Mixed synthetic and real producer gas

The voltage progression of the longest experimental run, shown in Figure 3-5, was obtained from the cell in the middle of the stack. In total, the SOFC stack was operated for over 100 h with diluted producer gas corresponding to an equivalent pure producer gas volume of 15 standard cubic meters on dry and tar free basis (dtf). The average tar load was 85 g/m_n^3 (dtf). Nonstop experiments of up to 16 h were performed. The producer gas operation of the fuel cell caused a continuous increase of the pressure loss of the fuel cell. Variations of the electrochemical performance parameters of the fuel cell showed no effect on the pressure loss. However by switching to hydrogen as fuel gas for short periods of time, the pressure loss could be reset to normal levels. The voltage-current-curve remained almost constant during operation with real producer gas as well as with synthetic producer gas. The observed minor cell deactivation after the experiments was on normal levels compared to that of natural gas operation of the same duration. The tar species typically present in updraft gasification producer gases, such as e.g. phenol and acetic acid, were not found to have a negative impact on the performance of SOFCs. Unlike most relevant literature, this result once more supported the hypothesis that SOFCs are, to some degree, tolerant towards tars.

3.3.2 Lab scale tests under open circuit conditions

The fate of tar species in SOFCs was investigated with the experimental setup shown in Figure 3-6.

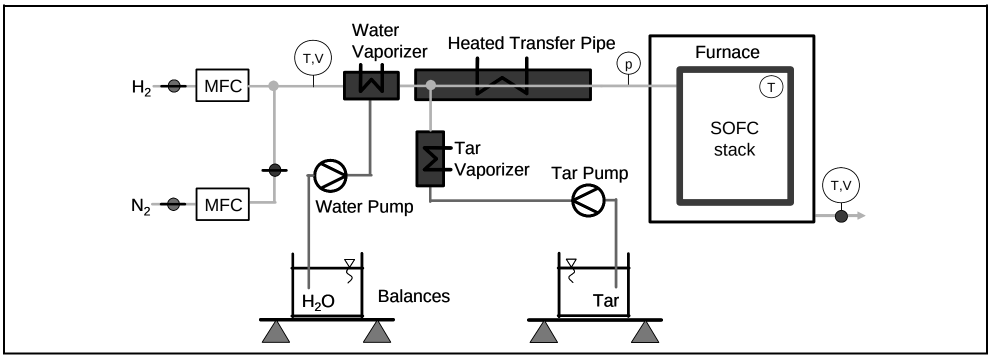

Figure 3-6: Technical outline of the experimental setup used for stack tests in 2004

Humidified hydrogen with a tar load of approx. 240 g/m_n^3 (dtf) was fed via a heated transfer pipe to a SOFC lab scale stack. The stack was not electrically connected to a power unit. This was done in order to reduce the costs of the experiment in case the stack might get destroyed due to the high tar load. The stack was mounted in a tinder resistant INCONEL housing placed in an oven heated to 900 °C. The hydrogen mass flow was controlled via a mass flow controller (MFC). Further, a nitrogen line was installed for inertization purposes in emergency cases and for the conservation of deposits in the SOFC for post-test analysis. The hydrogen volume flow was monitored manually using a gas meter prior to entering the water vaporizer. The added steam mass flow was set via the flow rate of the water pump and monitored manually by means of a balance. A similar approach was used to add a mixture of tar species representing the typical composition of tars found in producer gases from fluidized bed gasifiers, [138]. This mixture was chosen as it was considered more difficult to degrade than the mixture of oxygenated tars typically found in updraft producer gases. The mixture consisted of benzene (63.0 mass-%), toluene (9.5 mass-%) and naphthalene (27.5 mass-%). The composition of the gas after passing the SOFC was measured through gas chromatography using the above described sampling system. The gas volume was monitored with a gas meter.

After the experiments, mass balance calculations were conducted yielding tar conversions between 92 and almost 99 % for different steam-to-carbon ratios, see Table 3-1. In comparison, the tar conversion found for the empty INCONEL housing was in the order of 10 %. Therefore, the observed tar conversions were attributed to a major extent to the catalytic activity of the investigated nickel anode catalyst.

Table 3-1: Tar conversion observed on Nickel-cermet

Exp.	C	H	O	C	H	O	H_2	CO	CO_2	CH_4	Tar conversion
	Input [mol/h]			Output [mol/h]			Output [mol-%]				[% input]
1	0.94	12.59	3.33	0.89	8.07	1.14	81.87	12.75	5.27	0.11	94.5
2	0.88	12.41	3.23	0.81	7.56	1.04	82.22	12.67	4.97	0.14	93.1
3	0.97	9.06	1.59	0.96	7.78	1.06	80.13	17.44	2.29	0.14	98.9
4	0.95	7.64	0.86	0.88	7.25	0.86	80.14	18.91	0.19	0.76	92.5

Figure 3-7 compares the measured gas composition at the stack outlet and the equilibrium composition calculated with ASPEN PLUS.

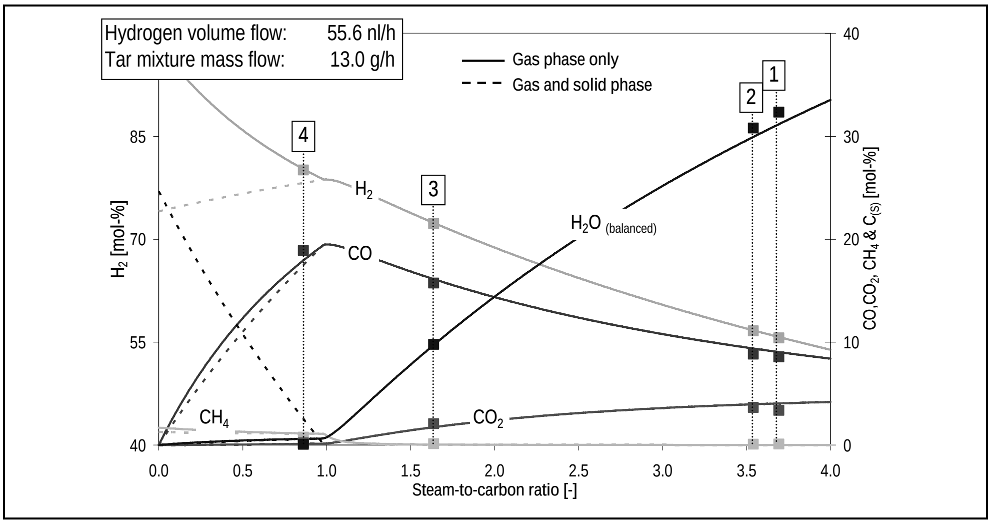

Figure 3-7: Measured anode off-gas composition vs. equilibrium calculation

The equilibrium calculations were conducted for the set oven temperature and the input gas composition considering H_2, CO, CO_2, CH_4, C_2H_2,

C_2H_4, C_2H_6, C_3H_6, C_6H_6, C_7H_8, $C_{10}H_8$, O_2, water and graphite as possible products. The full lines in Figure 3-7 represent the equilibrium molar fractions of the most important species in the gas phase for varying steam-to-carbon ratios. The dotted lines stand for the equilibrium molar fractions considering solid graphite, which is formed for steam-to-carbon ratios below one at 900 °C. It can be seen that the tars in the input gas were degraded to hydrogen and carbon monoxide and that the reformate gas almost reached equilibrium. The assumption for SOFC models that the water gas shift, [139-141], and the steam reforming reaction, [142-144], are at equilibrium was therewith confirmed.

In order to provoke carbon depositions the steam-to-carbon ratio of the last experimental point was chosen below one. In fact, the deposits caused an increasing pressure loss. For a closer analysis, the deposits were conserved by flushing the stack with nitrogen during cool down. This allowed not only the verification of the formation of carbon depositions but also their location was determined. Figure 3-8 shows the top view (A) of an interconnector plate with carbon deposition at the gas inlet. View (B) shows that the carbon depositions grew from the interconnector plate in the central gas channel, see view (C). This indicates that carbon depositions are self-catalyzing. An explanation for the location of the carbon depositions at the cell inlet is the local temperature, which must have been considerably lower than the average cell temperature due to endothermal steam reforming reactions.

Figure 3-8:
Carbon depositions in anode channel inlet region and central fuel gas channel

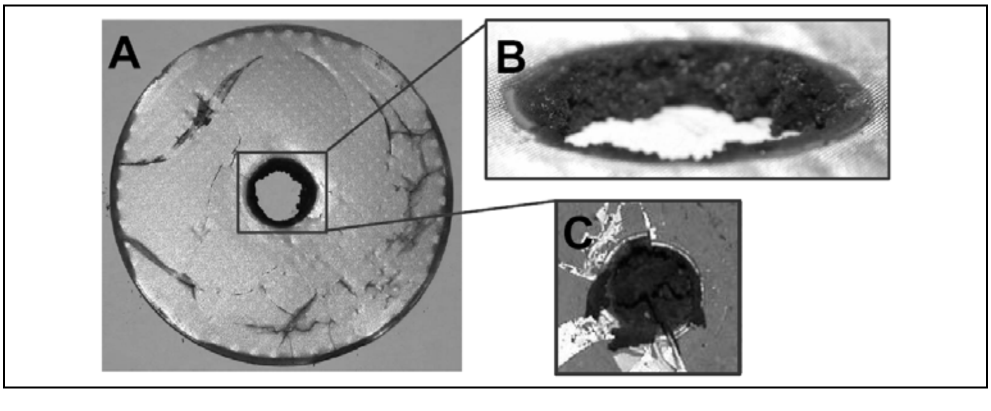

Overall 0.5 g of deposits were found. Assuming the deposits to be 100 % carbon, this amount corresponds to a deposition rate of 0.07 mol/h, Table 3-1. The formation rate of graphite at equilibrium for the given feed gas composition was calculated to 0.16 mol/h. It was therefore concluded that the carbon deposit formation is kinetically controlled.

In summary, the experiments have shown that the anode catalyst of the investigated SOFC catalyses the degradation of aromatic tars to hydrogen and carbon monoxide. Oxygenated tars should be degraded even more easily. Water gas shift and steam reforming reactions were found to be very close to equilibrium while the formation of carbon deposits was found to be locally limited to the cell inlet and kinetically controlled.

3.4 Characterization of important unit operations

The proof-of-feasibility tests confirmed the main assumptions forming the basis for the PSI B-IGFC concept. It was shown, that

- producer gas originating from the updraft gasification of wood can be electrochemically converted in a SOFC.
- tars are degraded to hydrogen and carbon monoxide and contribute to the electrochemical reactions and power generation in SOFCs.

The construction of a lab-scale demonstration unit and the achievement of the proof of concept were defined as next steps. Prior to the assembly of the PSI B-IGFC system demonstration unit, each of the important unit operations was characterized experimentally in stand-alone operations. This way, the optimal operating conditions of the single unit operations and possible interactions in the overall system were identified.

3.4.1 Updraft gasification reactor

During the proof-of-feasibility tests over 100 hours of SOFC wood gas operation were accumulated, see section 3.3.1. The non-stop duration of the experiments was limited to around 16 h due to gasifier problems such as strong increase of pressure or over-temperatures. The gasifier had to be regenerated via burnout cycles, thus removing deposits in the reactor and the piping downstream. During these regeneration cycles, the SOFC was fed with humidified hydrogen. As it could not be excluded that the SOFC regenerated as well while being fed with humidified hydrogen, drawing conclusions for long-term deactivation processes due to producer gas operation was not possible. Therefore, the following requirements were defined for the gasifier of the demonstration unit:

- Stable non-stop operation for 200 h or more.
- Adjustable tar load of the raw gas between 150 g/m_n^3 (dtf) and approx. 80 g/m_n^3 (dtf) via gasifier-internal degradation of tars.

- Thermal input up to 25 kW in order to allow for the operation of 10 kW SOFC stacks.

Based on the design of the gasifier used in the first proof-of-feasibility tests, a new gasifier capable of pressurized operation was built. The gasifier is fed from a fully automated wood pellet hopper, which can be operated at pressures up to 3 bara. The hopper has a capacity of 60 kg of commercial wood pellets. The maximum feed to the gasification reactor is approx. 5 kg of pellets per hour which satisfies the requirement of 25 kW thermal input. The pellets are introduced at the top of the gasifier while air as gasification agent is introduced at the bottom through a grate. The grate area is 100 cm^2 which corresponds to a maximum of 250 W per cm^2 thermal area loading. The firebed is separated from the grate by alumina balls. Besides the protective function, the alumina balls promote a homogeneous distribution of the gasification air throughout the grate area, [145]. The producer gas is taken out near the top of the gasifier.

An initial commissioning run of the gasifier is shown in Figure 3-9. It can be seen that the temperature in the middle of the gasification reactor, the producer gas temperature and the gasifier pressure fluctuated, ultimately leading to a shutdown of the gasifier due to over-pressure and over-temperature alarm after roughly 24 h of operation. The mass flow of wood pellets was approx. 2.8 kg/h, which corresponds to 45 % of the rated capacity.

Figure 3-9:
24 h operation of the new updraft gasifier with fluctuating temperatures and pressures

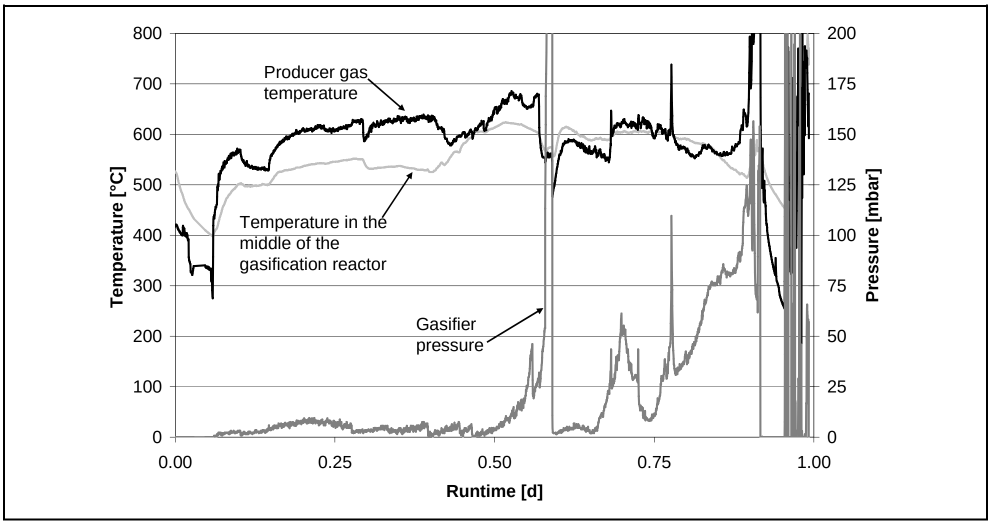

The gasifier produced about 2.2 m_n^3 of producer gas on a dry and tar free basis per hour at an air-to-fuel ratio in the range of 0.25 to 0.27. A mass balance was applied to the gasifier, taking into consideration the dry gas composition and measured water content. It was found that the sum of the tar species maintained a C-H-O ratio corresponding to the stoiciometric formula $CH_{1.2}O_{0.5}$. This implied abundance of oxygenated tar species in the producer gas as also reported in [28, 29] for a commercial updraft gasifier. The tar load was calculated to be as high as 160 g/m_n^3 (dtf). This is an elevated value even for an updraft gasifier, where most of the volatile tars escape during the pyrolysis occurring at the upper part of the reactor. Apart from being detrimental to a SOFC stack at such levels, the high tar load also rendered stable long-term operations of the gasifier. This called for further improvements.

Thermodynamic calculations indicated that with the injection of steam into the gasifier, keeping the reaction zone temperature above 650 °C, a considerable fraction of the tars could be reformed or formation could be inhibited. Consequently, a steam generator along with a super heater coil was integrated with the gasifier, capable of injecting up to 800 g/h of steam at 600 °C into the alumina ball bed.

Figure 3-10 shows 167 h of operation of the gasifier with constant steam injection at 600 g/h, which corresponds to 460 g per kg of dry wood pellets or a theoretical humidity of the wood pellets of approx. 30 %.

Figure 3-10:
167 h operation progression with stable temperatures and stable pressure build-up and decline cycles

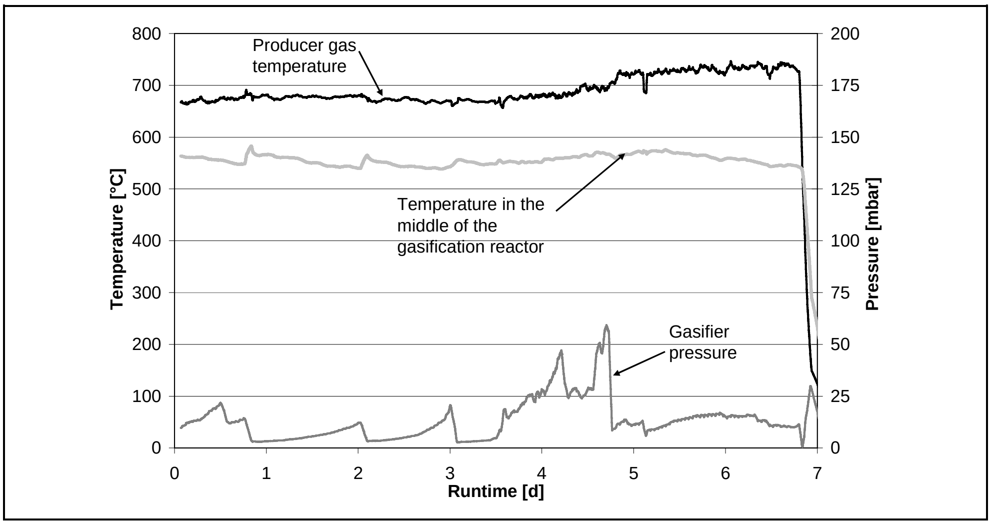

The temperature in the middle of the gasification reactor and the producer gas temperature did not fluctuate and the gasifier pressure showed no trend for blocking of the gasifier or the downstream piping. However, the gasifier pressure did not remain at a constant level. It increased up to a maximum of 60 mbar over-pressure, before the deposits causing this over pressure were removed by the producer gas flow. Besides allowing for a stable operation of the gasifier, the steam injection had the expected positive impact on the producer gas composition and tar load. Figure 3-11 shows the improvement of gas composition, starting from no steam injection mode, as the steam rate was gradually increased till 640 g/h. This corresponds to a theoretical wood pellet humidity of approx. 33 %. The air-to-fuel ratio was fixed at 0.26.

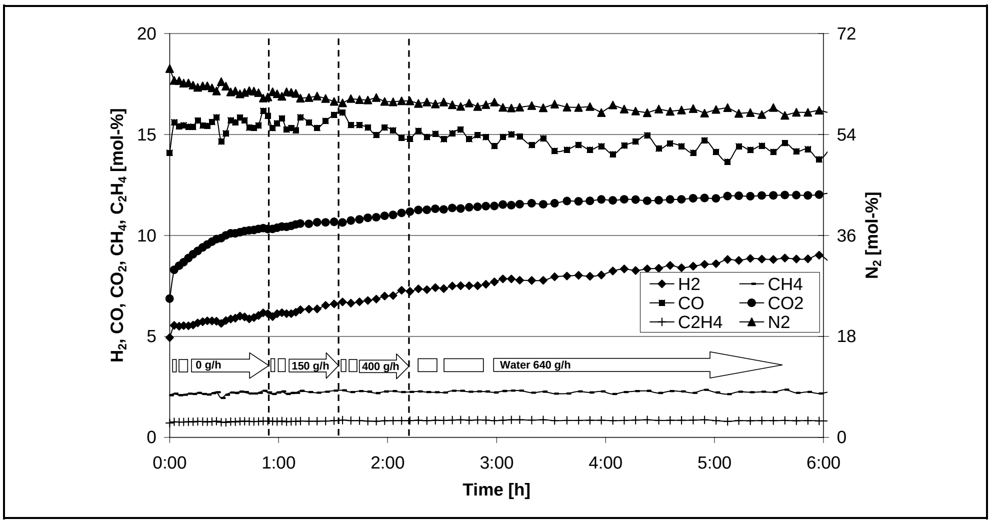

Figure 3-11: Effect of steam injection on the raw producer gas composition of the PSI updraft gasifier

It can be seen that the molar fraction of hydrogen almost doubled with increasing steam injection from approx. 5 to 9 %. The carbon dioxide molar fraction increased from approx. 8 to 12 %, while the carbon monoxide molar fraction decreased from 15 to 13 %. This indicates that water gas shift reactions were enhanced by the injected excess steam. The nitrogen fraction decreased from approx. 63 to 56 % with increasing steam injection. This corresponds to a gain of dry and tar free gas volume of roughly 13 %.

Mass balance calculations were performed to estimate the tar load of the producer gas with steam injection, Figure 3-12. It was found that the steam injection allowed an effective conversion of the tars into preferable permanent gas species, decreasing the tar load by about 50 %. This also explained the increased producer gas volume. The remaining tars are not expected to pose problems to a SOFC anode at an operating temperature around 900 °C due to their oxygenated, thus unstable nature.

In summary it can be said, that the gasifier built for the demonstration unit fulfills all the defined requirements, allowing for long-term tests.

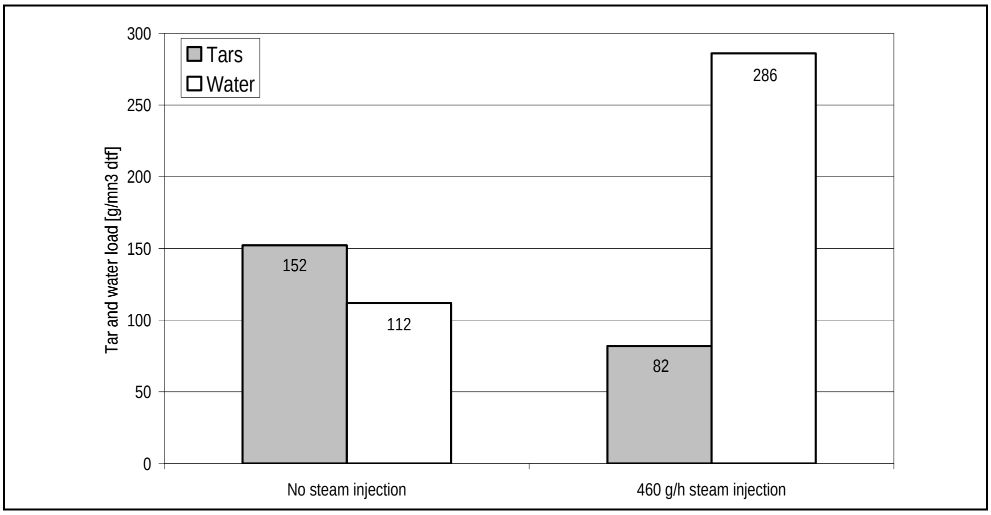

Figure 3-12: Comparison of tar and water load of the producer gas produced by the PSI updraft gasifier operated with and without steam injection

3.4.2 Hot gas particle removal

For the removal of particles from hot producer gases, a filter unit employing candle filter elements was built. Despite the current high standards of candle filtration systems, the design is still based on empirical findings and experiments. Compared to the typical flue gas filtration, the unsteady physical and chemical properties of the particles and the producer gas originating from the gasification process may cause problems, [41]. Especially the tar load of producer gases makes predictions about the technical behavior of hot producer gas filtration systems (HGF) difficult. Consequently, only little information about the operation of HGF systems with real producer gas is available. Further, the effect of HGF systems on the producer gas composition has hardly been investigated. Eventual positive effects regarding the conversion of tars may be possible. Therefore, the scope of the HGF characterization experiments was:

- To demonstrate a stable operation with real producer gas over a period of at least 24 h.
- To determine the impact of the HGF system employing different filter candle elements on the producer gas composition and the tar load.

Figure 3-13 shows the experimental setup employed for this investigation. The updraft wood gasifier used for the first proof-of-feasibility tests was coupled with a heated filter housing. The housing was designed to accommodate a single filter candle of either ceramic or metallic material. Further, the gas sampling points SP1 and SP2 were installed for the monitoring of the producer gas composition up- and downstream of the HGF unit. The raw gas was sucked through the HGF system by different gas pumps depending on the desired volume flow. The non-filtered gas was burned in a flare. The volume flow of the filtered producer gas was monitored with a heated orifice and subsequently sucked through a wet scrubber where condensable tar species were removed in order to prevent blocking of the employed pumps. After passing the pumps, the producer gas was forced through a gas meter and finally into the flare for combustion.

Figure 3-13: Updraft wood gasifier combined with a hot gas filtration system and an oil scrubber

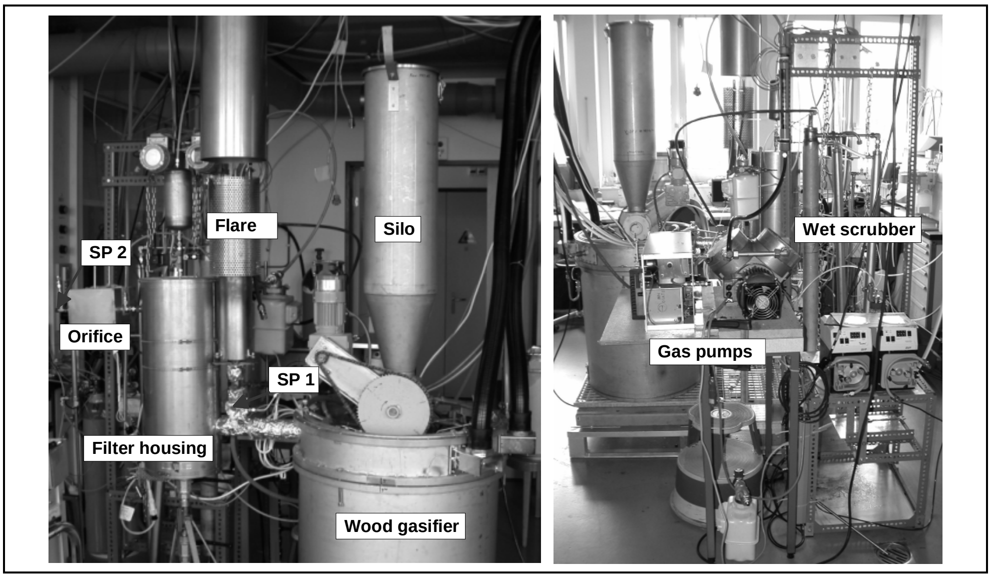

The time progression of the pressure loss over the investigated HGF system is a good indicator for its operational condition.

Figure 3-14: Typical pressure history of filtration systems with cleaning cycles, [41, 146]

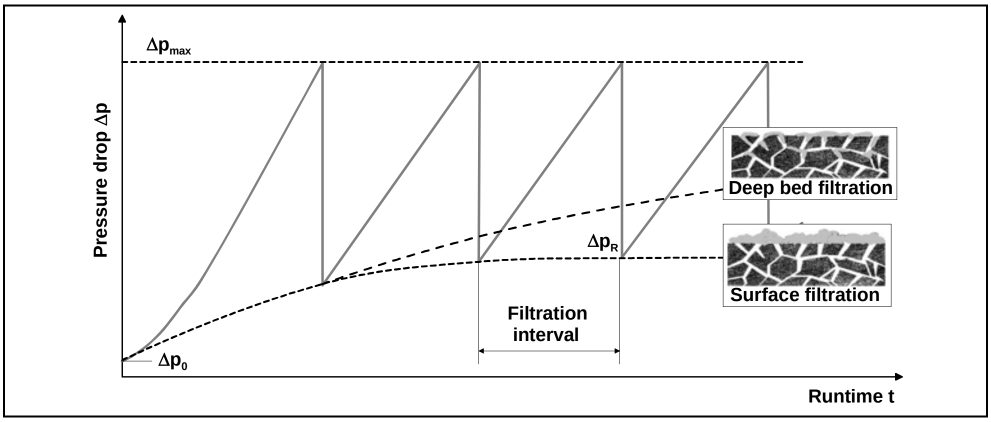

Figure 3-14 shows a typical pressure loss time progression of candle filter element based HGF systems. New filter elements pass through a commissioning phase prior to reaching stable operating conditions. At first, the pressure loss over the filter housing Δp_0 originates only from the filter element. Particles deposit in the filter element and induce an increase of the pressure loss over the filter element. The commissioning phase is completed after the saturation level of particles in the filter element is reached. The particles then deposit only on the surface of the filter element accumulating to a dense dust cake with lower porosity compared to the fresh filter element. The dust cake is allowed to build up until the pressure loss reaches the design level Δp_{max}. This initiates a regenerative cycle, where the dust cake and parts of the particles deposited in the filter element are removed by a reversed gas flow through the filter element. Due to the flammability of producer gases, pressurized argon was employed for the regeneration cycles. The filtration interval is defined as the time period between two consecutive regeneration cycles. The pressure loss after a regenerative cycle, Δp_R, draws near a given value for stable operation. If it steadily increases, particles penetrate deep into the filter element ultimately leading to operational failure.

Two types of filter elements were characterized, namely a non-ceramic fiber filter candle with a pore diameter less than 1 µm and a metallic filter candle with a pore diameter less than 5 µm. The gasifier was operated with a wood pellet mass flow of 1.3 kg/h and an air-to-fuel ratio of 0.36 which translates into a gasification air volume flow of 33 l_n/min. The filtration velocity is defined as the quotient of filtered producer gas volume flow and filtration area of the investigated filter element. For the demonstration of a stable operation, the filtration velocity was maintained at 1.6 cm/sec. The temperature of the HGF unit was held constant at 400 °C.

Figure 3-15:
27 h operation of hot and highly tar laden gas filtration employing ceramic filter candles

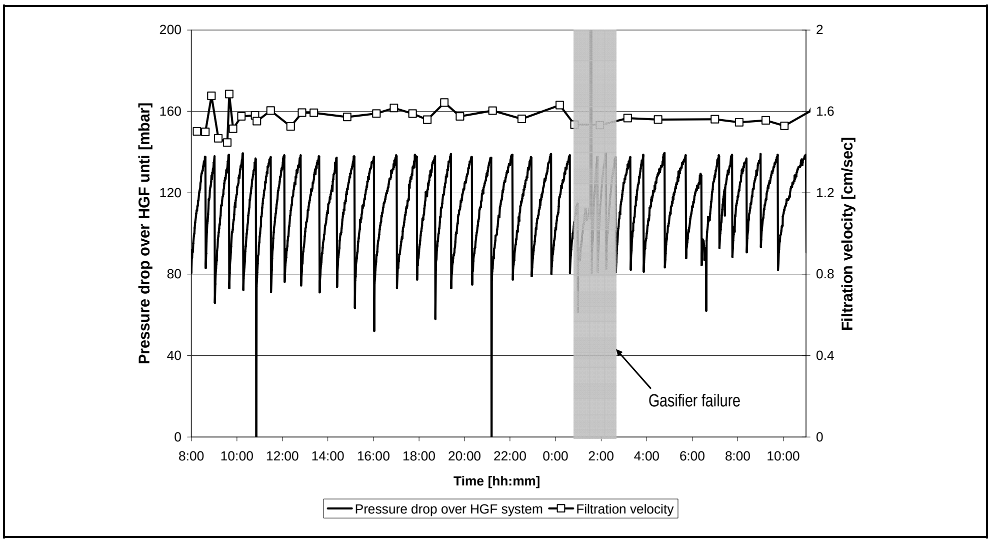

Figure 3-15 depicts 27 h of non-stop operation of the HGF unit employing the non-ceramic fiber candle. In total approx. 75 hours of stable operation were achieved with this filter element type. This corresponds to a total filtered gas volume of approx. 57 m_N^3, thereof approx 27 m_N^3 non-stop. The grey area indicates a gasifier failure which made a burnout cycle necessary. The HGF unit was operated throughout this burnout cycle, showing no signs of clogging due to the strongly increased particulate matter load of the gasifier flue gas. The pressure after cleaning pulses, Δp_R, leveled off at 80 mbar with Δp_{max} set to 140 mbar. The regeneration cycles occurred at regular 60 minutes intervals. No particles were found in the wet scrubber. It was concluded, that stable operation was reached with the investigated non-ceramic fiber filter element.

In contrast, the metallic filter candles were clogged almost instantly when operated at 400 °C. The temperature of the HGF unit was therefore increased to 500 °C, which allowed a continuous operation. However, large amounts of soot were found in the wet scrubber fluid. The soot was either produced in the metallic filter candle or consisted of char particles originating from the gasifier which passed the filter element. For both cases it was concluded, that metallic filter candles are highly problematic for the filtration of tar laden producer gases.

The impact of the HGF system was assessed via the measurement of the producer gas composition up- and downstream of the filtration unit. The tar and water load was estimated with mass balance calculations, see section 3.2. It was found that the HGF system employing the non-ceramic filter elements influenced the producer gas composition. Due to the inert character of the filter element material, it is most probable that the observed activity is due to the soot cake, which is continuously deposited on the candles. The molar fractions of H_2, CO, H_2O and CH_4 increased notably passing the HGF system, while the molar fractions of C_2H_2, CO_2 and tars decreased. This indicates that tar and ethylene decomposition processes and reverse water gas shift reactions took place in the HGF system, see Figure 3-16. It has to be pointed out that these values were calculated based on the measured species concentration and the balanced tar and water load. As it cannot be excluded, that the principal tar signature changed, the values should be understood as rough trend indicators. More detailed studies are required in order to determine the exact reaction scheme. The variation of the filtration velocity had no measurable impact on the discussed trends.

The metallic filter elements were two to three times more active than the non-ceramic fiber filter elements towards the decomposition of tars and ethylene. With ethylene being a well-known soot pre-cursor, this reinforced the conclusion that the soot found in the wet scrubber fluid was formed in the filter element.

Figure 3-16: Conversion of measured gas species and balanced tar and water load in the HGF system employing a non-ceramic fibre filter element

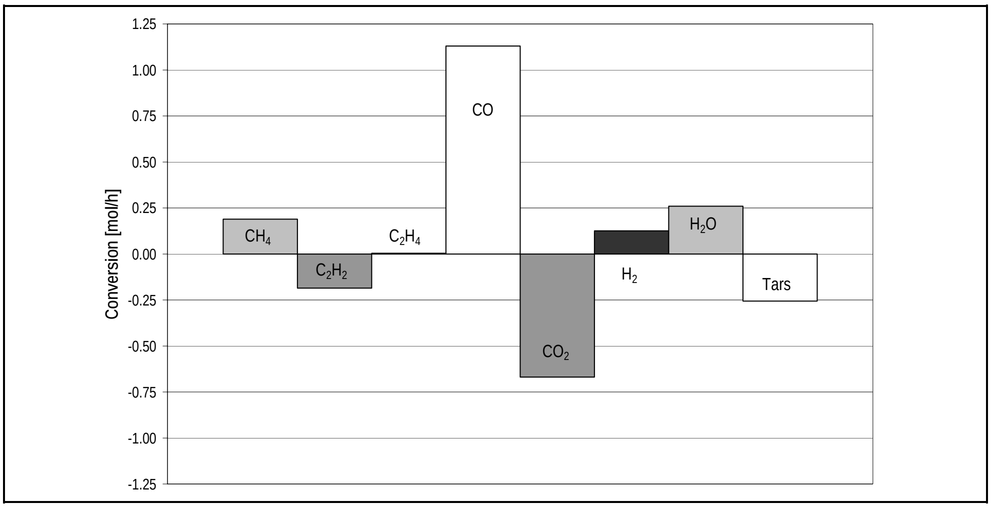

In summary, stable operation with tar-laden producer gas was shown with non-ceramic fiber filter elements. These inert filter elements in combination with the soot cake typical for this filtration technology had a positive impact on the producer gas via tar and ethylene decomposition. For filter elements made of metallic materials this impact was found to be noticeably stronger. The high activity of the metallic material leads to soot formation in the filter element, negating the filtration function. Therefore metallic filter elements should not be used for the filtration of tar-laden producer gases.

3.4.3 Catalytic partial oxidation

The catalytic partial oxidation (CPO) was identified as a possible converter of aromatic and oxygenated aromatic tars to hydrogen and carbon monoxide as well as organic sulfur species to hydrogen sulfide. Initial experiments with a CPO operated with real wood gas were conducted and proved the robustness of the catalyst. The results were reported in [147]. However, to prove that the employed commercial CPO catalyst actually does convert the typical tar species found in biomass producer gases, dedicated experiments were conducted. Three representative tar species were investigated, namely toluene, representing single ring aromatics, anisole, representing oxygenated aromatics and thiophene, representing aromatic organic sulfur compounds, see Figure 3-17. The experiments discussed in the following were part of a diploma thesis co-supervised by the author, [148].

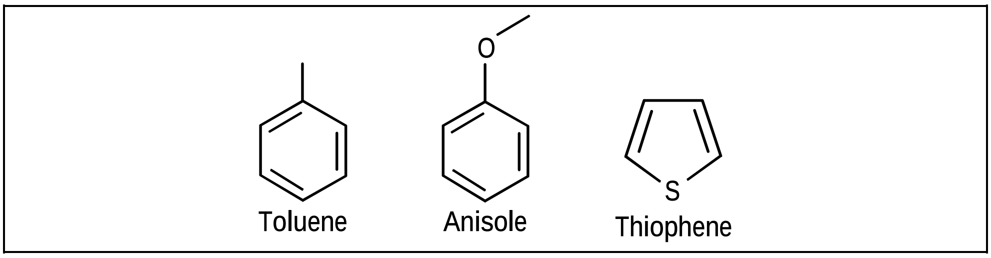
O
S
Toluene
Anisole
Thiophene

Figure 3-17: Representative tar species for CPO characterization experiments

With these representative tar species most of the structures of biomass gasification tars were covered, except primary tars such as e.g. acetic acid which should not be problematic for conversion due to their low stability. The tests with toluene provided an indication of the influence of the catalyst on stable aromats, while the tests with thiophene aimed at the conversion of organic sulfur species to H_2S and the proof of sulfur tolerance of the investigated CPO catalyst. Despite phenol being a more frequently encountered oxygenated tar specie in biomass producer gases, anisole was used for the experiments because it is less difficult to handle at room temperature and features almost the same properties with respect to its interaction with catalytic surfaces. The experimental setup used is outlined in Figure 3-18.

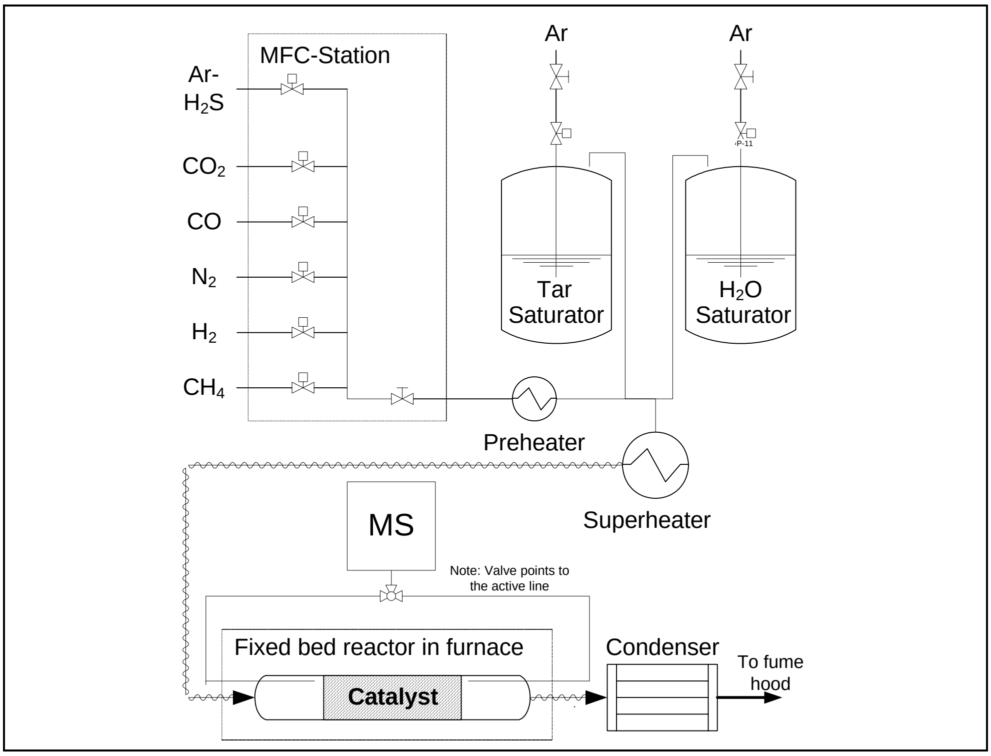
MFC-Station
Ar-H2S
CO2
CO
N2
H2
CH4
Ar
Ar
Tar Saturator
H2O Saturator
Preheater
Superheater
MS
Note: Valve points to the active line
Fixed bed reactor in furnace
Catalyst
Condenser
To fume hood

Figure 3-18: Experimental setup for catalyst characterization experiments

The setup was designed to allow for catalyst tests with tar-laden and humidified synthetic gas mixtures. Six mass flow controllers enabled the generation of a wide range of dry gas mixtures consisting of H_2, CO, CO_2, CH_4 and N_2. Hydrogen sulfide diluted in argon could be added as well. The dry gas mixture was then preheated to 180 °C and humidified with deionized water via a water saturator with argon as carrier gas. The water load was controlled via the saturator temperature which was set to 70 °C for the experiments. The addition of liquid tars followed the same scheme. The saturator temperatures were 30 °C for thiophene, 60 °C for toluene and 90 °C for anisole. The tar-laden and humidified gas mixture was then superheated and piped into a packed-bed reactor housing, which was placed in an electric furnace. The gas samples for the Thermo VG ProLab quadrupole mass spectrometer (MS) were sucked through fused silica capillaries which were placed before and after the catalyst. A condenser located at the reactor outlet was used for the recovery of non converted water or organic compounds.

As mentioned in section 3.1.2, CPO catalysts feature two reaction zones, the first being the oxidation and the second being the steam reforming zone. It was assumed, that while oxidation occurs fast, producing water, carbon dioxide and heat, the steam reforming is a slow process. Therefore, a diluted "post-oxidation" gas composition was defined as matrix for the tests, consisting of 9 mol-% H_2, 8 mol-% CO, 6 mol-% CO_2, 15 mol-% H_2O and 62 mol-% N_2. The temperature range chosen for the experiments was 700 to 800 °C. The weight hourly space velocity (WHSV) was varied between 2.75 and 7 $g_{tar}/(g_{catalyst}\ h)$.

For WHSVs between 2.75 and 5.5 $g_{toluene}/(g_{cat}h)$, toluene conversions between 38 and 59 % were observed using 119 mg of catalyst at a temperature of 700 °C, see Figure 3-19. At 800 °C the conversion was considerably higher with values between 72 and 90 %. While at 800 °C most of the toluene was reformed to hydrogen and carbon monoxide, Eq. 1, at 700 °C an important part of the toluene was degraded to benzene, Eq. 33.

$$C_7H_8 + 7H_2O \rightarrow 7CO + 11H_2 \qquad \text{Eq. 32}$$

$$2C_7H_8 + 2H_2O \rightarrow 2C_6H_6 + 2CO + 4H_2 \qquad \text{Eq. 33}$$

The produced benzene however should not be problematic in an SOFC due to the high reforming activity of the typically used anode catalysts, see section 3.3.2.

Figure 3-19: Toluene conversion over a CPO catalyst for different temperatures and WHSVs, [148]

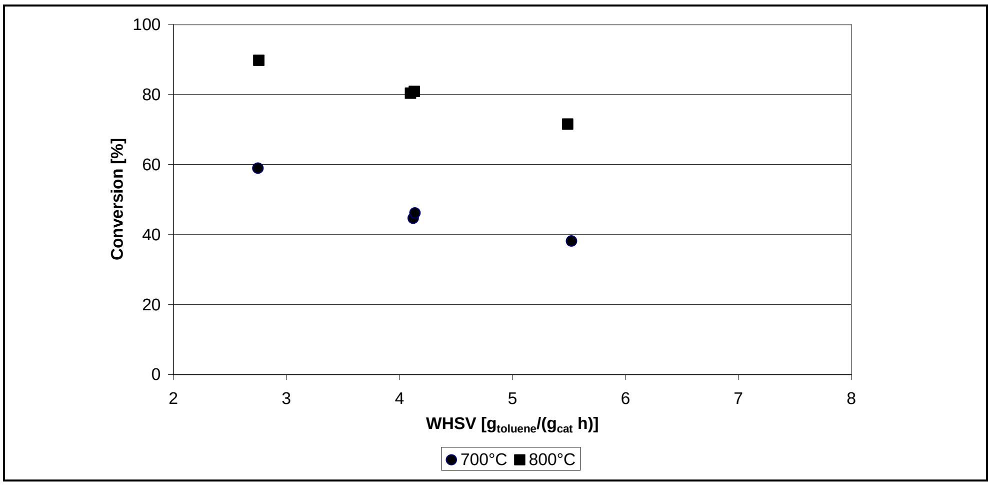

Figure 3-20 depicts the conversion of anisole over the investigated CPO catalyst. The observed conversions of anisole were between 61 and 83 % at 700 °C and between 78 and 87 % at 800 °C. In contrast to the conversion of toluene, no formation of benzene was observed during the reforming of anisole. The high conversions and the lack of benzene as side product support the assumption that oxygenated tars are easier to degrade than pure aromatic species.

Figure 3-20: Anisole conversion over a CPO catalyst for different temperatures and WHSVs, [148]

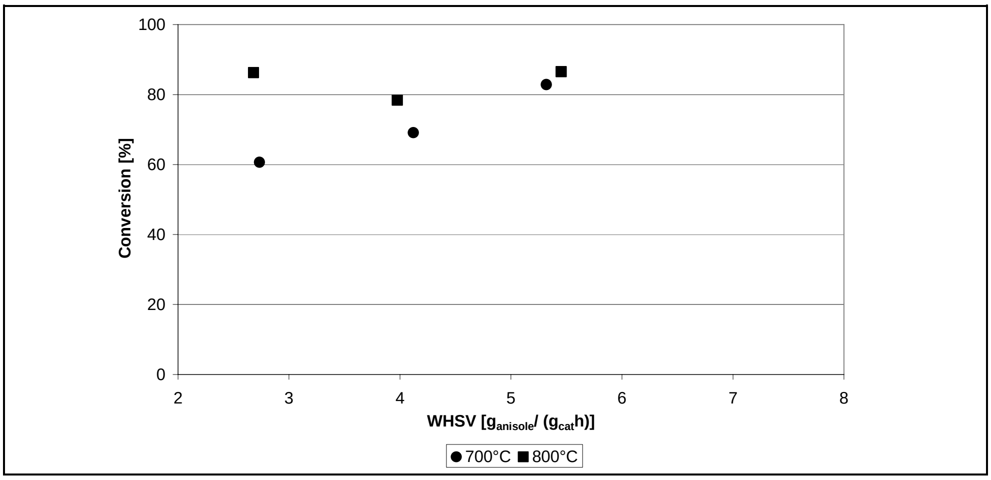

The observed conversions for thiophene were between 34 and 45 % at 700 °C and between 68 and 72 % at 800 °C, Figure 3-21. Keeping in mind that the oxidation zone of the CPO catalyst exhibits temperatures up to 1000 °C, a complete conversion of organic sulfur compounds is probable. This was also enforced by the finding that at higher temperatures, the produced amount of hydrogen sulfide increases, which suggests a cracking mechanism of the thiophene ring.

Figure 3-21: Thiophene conversion over a CPO catalyst for different temperatures and WHSV, [148]

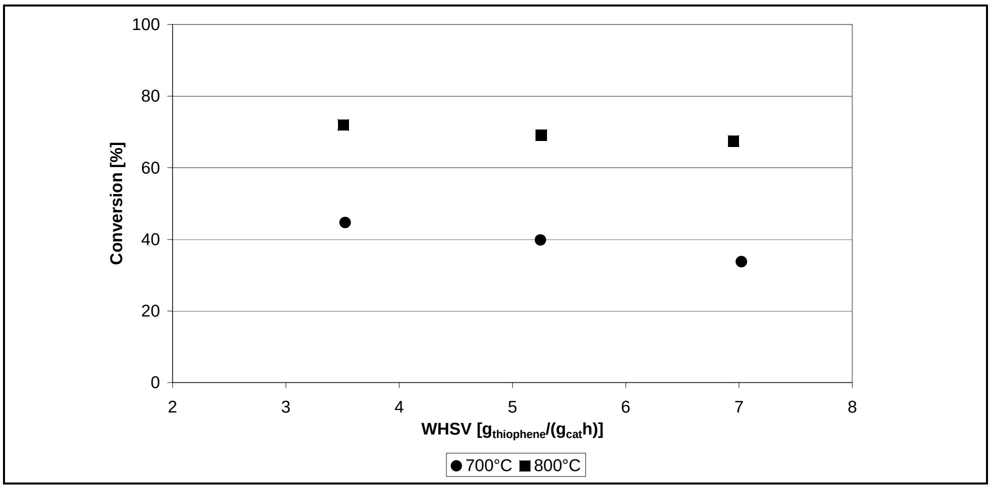

In summary the order of reactivity of the three model compounds of biomass gasification tars towards steam reforming was found to be anisole, thiophene and toluene. It was approved that oxygenated tars are easier to degrade than pure aromatics as also reported in [55]. Further, the investigated catalyst was found suitable for the decomposition of organic sulfur compounds.

3.4.4 Sulfur absorption by zinc oxide

The desulphurization of producer gases from biomass gasification was investigated in the framework of a diploma thesis co-supervised by the author, [149]. The experimental setup used for the investigation was already discussed, see Figure 3-18. Besides the mass spectrometer, a Sievers/Ionics SCD 355 sulfur chemiluminescence detector with a detection limit below 0.1 ppmV was used to determine the total sulfur concentration in the producer gas downstream of the adsorption bed. The sulfur species of interest were hydrogen sulfide and organic sulfur compounds represented by thiophene. Carbonyl sulfide was not considered assuming that it is converted to hydrogen sulfide via Eq. 34 at the investigated conditions.

$$COS + H_2O \leftrightarrow CO_2 + H_2S \qquad \text{Eq. 34}$$

The chemisorption of hydrogen sulfide by zinc oxide follows Eq. 35.

$$ZnO + H_2S \rightarrow ZnS + H_2O \qquad \text{Eq. 35}$$

The experiments with zinc oxide as state-of-the-art sulfur adsorbent were focused on the separation efficiency, the thermal stability in reducing atmospheres and the impact on the producer gas composition.

For hydrogen sulfide, the sulfur separation efficiency was close to 100 %, yielding sulfur concentrations at the adsorbent bed outlet below 1 ppmV. These values were also reached despite an increase of the water fraction in the producer gas matrix from 5 to 13 mol-%. Tests with thiophene confirmed, that organic sulfur species are not adsorbed by zinc oxide. With organic sulfur concentrations up to several ppmVs, this confirms that a conversion unit for organic sulfur species such as a CPO is most required in B-IGFC systems. Otherwise sulfur concentrations around 1 ppmV cannot be reached.

The thermal stability of the investigated zinc oxide adsorbent was assessed with thermo-gravimetric measurements. The maximum operation temperature was found around 450 °C, see Figure 3-22. Starting from 550 °C, zinc oxide is reduced to pure zinc and quickly begins evaporating. The measured curve compares well with the vapor pressure curve of pure zinc calculated with ASPEN PLUS.

Figure 3-22: Thermo gravimetric evaporation curve of zinc oxide sulfur adsorbent, [149]

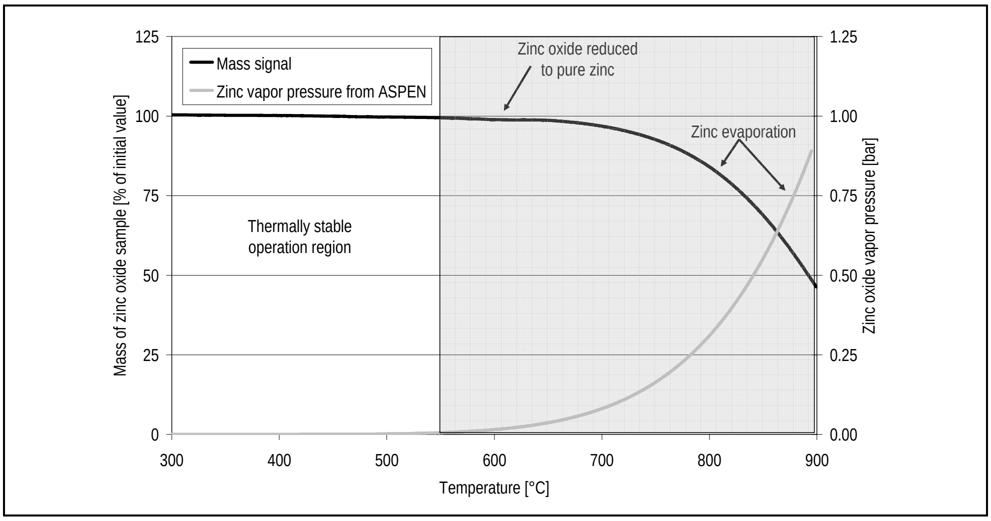

The composition of the producer gas matrix was not altered in the presence of zinc oxide. In summary, the experiments confirmed that the findings reported in [107] with respect to zinc oxide for the desulphurization of syngases originating from natural gas or coal gasification can be carried forward to biomass gasification applications.

3.4.5 Solid oxide fuel cell

The poisoning effect of sulfur on the electrochemical performance of SOFCs is the subject of numerous studies, [10, 118, 119]. The corresponding results are however strongly linked to the investigated SOFC and catalyst materials. The fuel requirements must therefore be determined for the SOFC in question. However, the primary targeted fuel provides an initial indication about the sulfur tolerance of a specific SOFC concept.

The primary targeted fuel of the Hexis SOFC is odorized natural gas. These cells exhibit therefore some tolerance towards sulfur. For this reason, and for its proven reliability in numerous long-term field tests with over 120 running systems, [75], the Hexis SOFC was found a promising candidate for the proof-of-concept tests. For a test duration of several days with a resulting permanent degradation on moderate level, the minimum required desulphurization level was determined experimentally using a full-scale Hexis SOFC system.

Figure 3-23:
The Hexis SOFC system, [150]

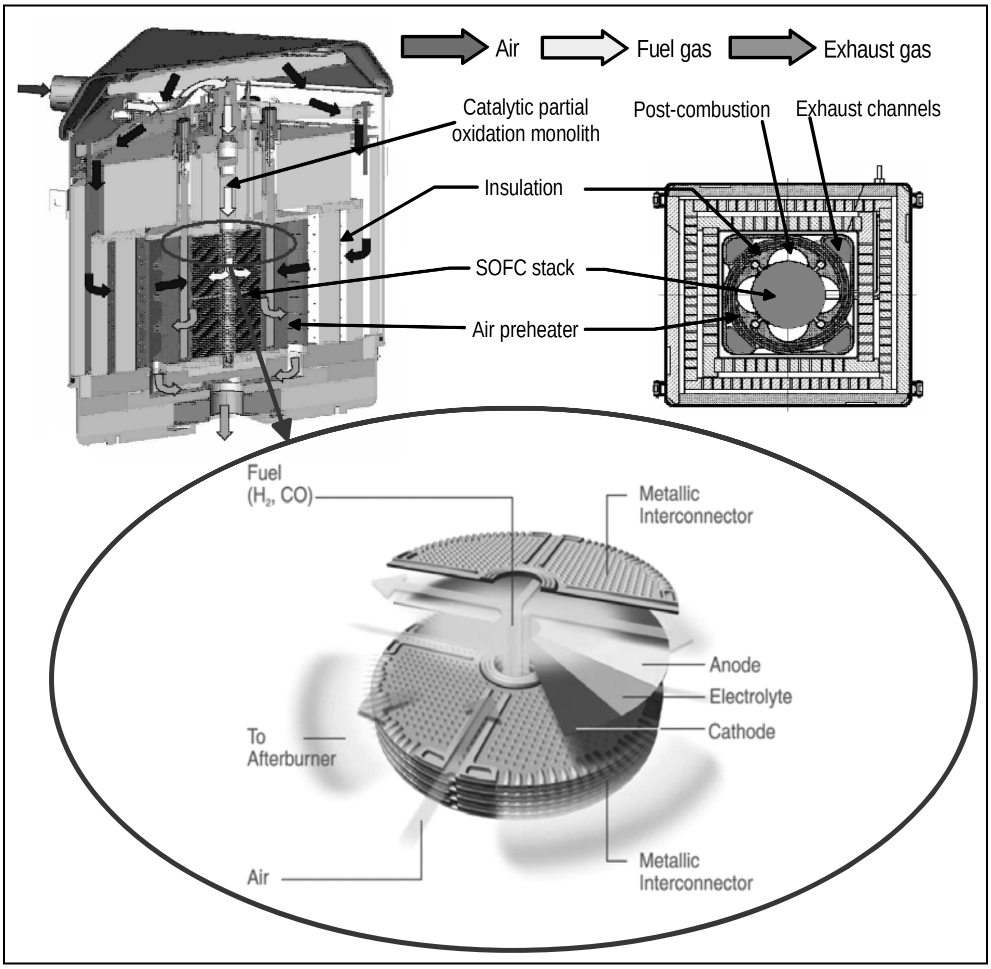
Air
Fuel gas
Exhaust gas
Catalytic partial oxidation monolith
Post-combustion
Exhaust channels
Insulation
SOFC stack
Air preheater
Fuel (H_2, CO)
Metallic Interconnector
Anode
Electrolyte
Cathode
To Afterburner
Air
Metallic Interconnector

Figure 3-23 shows the Hexis SOFC system. The Hexis cell design is planar circular, electrolyte-supported and optimized for co-flow operation. The stack consists of 63 metallic current collectors and electrode-electrolyte assemblies. The active area per cell is roughly 100 cm^2. The maximum electrical output of the stack is 1 kW.

Air is introduced to the SOFC stack via an air pre-heater. The pre-heated air enters the SOFC stack on the cathode side through four air channels which are formed by the metallic interconnector plates and the anode-electrolyte-cathode assemblies. After participating in electrochemical reactions, the air exits the stack radial and takes part in the post-combustion of the partially depleted fuel gas. The fuel gas entering the stack is reformed and heated to a temperature suitable for the SOFC stack using a catalytic partial oxidation monolith. The processed fuel gas is introduced to the SOFC stack on the anode side via a central fuel gas channel. After being partially electrochemically converted to water and carbon dioxide, the depleted fuel is mixed with the depleted air and combusted. The exhausts are used for the pre-heating of the fresh air.

Pure methane was used as model fuel for the experiments. A thiophene saturator, see sections 3.4.3 and 3.4.4, was installed in an ice bed. Argon was used as carrier gas. The thiophene concentration in the fuel gas was adjusted via the carrier gas flow. The employed mass flow controller allowed producing thiophene concentrations in the fuel gas up to 400 ppmV. This translates into approx. 80 ppmV at the cell inlet, due to the volume expansion of the fuel gas resulting from the CPO. To account for the adsorption of sulfur on the metallic surfaces, the voltage-current curves were only recorded after several hours of steady-state operation. Assuming that in steady-state the ad- and desorption of sulfur on the metallic surfaces of the feed line occur at equal rates, the sulfur concentration at the cell inlet should correspond to the set value.

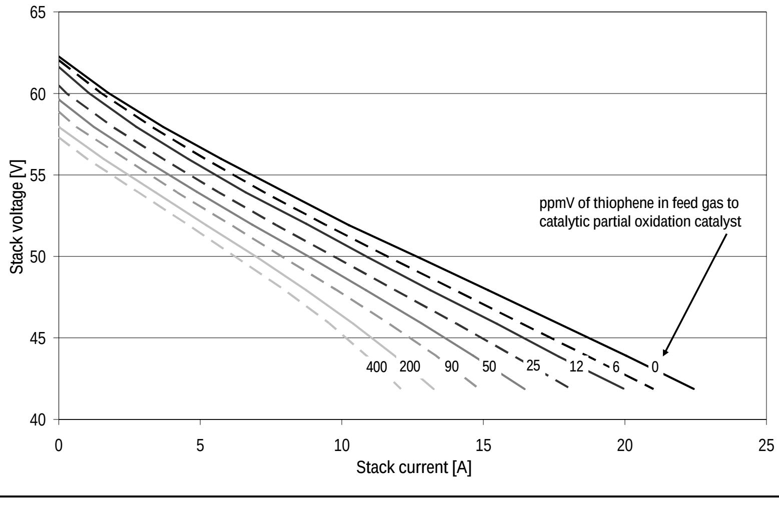

Figure 3-24: Voltage-current curves obtained from the investigated Hexis-stack for different sulfur concentrations

Figure 3-24 shows the measured voltage-current curves for varying thiophene concentrations. The Hexis SOFC proved to be very sulfur tolerant, allowing sound operation even at the highest tested sulfur concentrations. The power output declined considerably with increasing sulfur concentration due to decreasing open circuit voltages (OCV) and steeper slopes of the voltage-current curves.

The steeper slopes could be explained by limitations of the electrochemical reactions due to the blocking of active sites at the fuel electrode- electrolyte interface as reported in [118]. The decline of the OCV follows an s-shaped curve, Figure 3-25. This indicates that more than one mechanism must be active. The present work proposes a combination of three mechanisms.

Figure 3-25:
Open circuit voltage for different sulfur concentrations

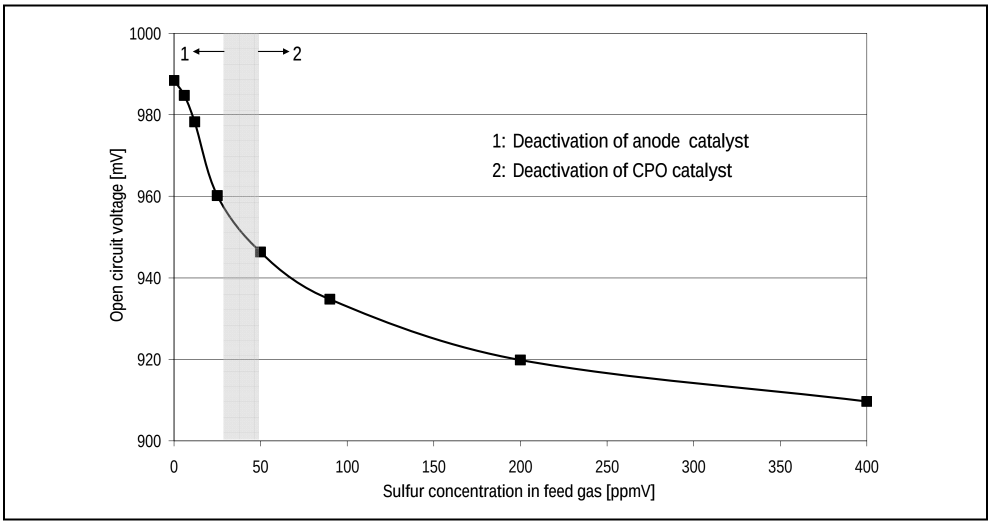

The OCV decrease between 0 and 30 ppmV could be a consequence of the deactivation of the nickel-based anode catalyst towards steam reforming reactions (STR). Slower STR cause flattened Nernst voltage distributions resulting in lower effective OCV values. Assuming the interconnector plates as equipotential, the effective OCV is the voltage at which the sum of in-plane currents is zero.

The impact of the reforming activity on the OCV was investigated with the SOFC model discussed in depth in chapter 5. The deactivation of the catalyst was modeled by reducing the STR reaction rate. Similar to the experiments, methane, after a catalytic partial oxidation with an air-to-fuel ratio of 0.27, was assumed as fuel gas for the model calculations and the overall air-to-fuel ratio was set to three. As in OCV operation the entire fuel is converted in the post-combustion zones, which directly heat the stack, isothermal conditions were assumed with a temperature of 950 °C. The precise geometry of the Hexis cell was not considered but a generalized geometry was assumed. Despite these simplifications, the modeling results provide an indication about the impact of the proposed OCV drop mechanism. Figure 3-26, shows the Nernst voltage distributions for a fully active anode catalyst and a catalyst with 60 % reduced activity. The effective OCV drops considerably with decreasing reforming activity.

Figure 3-26: Calculated Nernst voltage distributions and effective open circuit voltages for 100 % and 40 % reforming activity

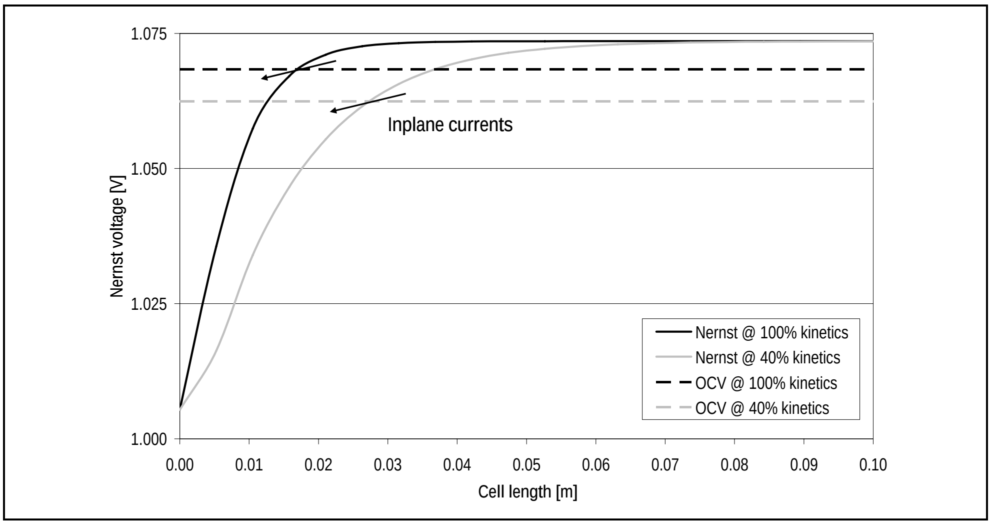

Figure 3-27 correlates the OCV drop with the reforming activity.

Figure 3-27: Calculated OCV drop for varying reforming activities

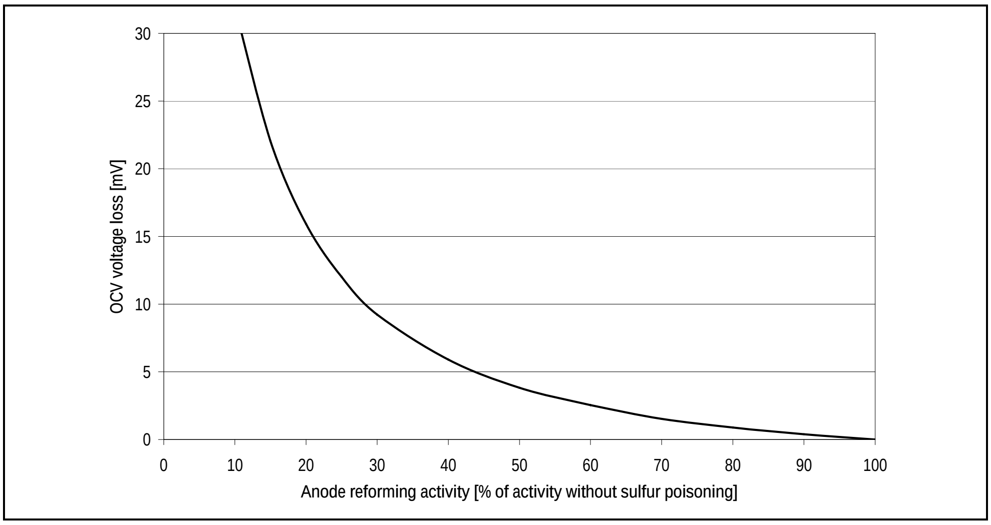

Assuming that the first 30 mV of OCV drop in Figure 3-25 result from reduced STR activity leads to approx. 90 % deactivation according to Figure 3-27. This magnitude of deactivation is reasonable for high-temperature steam reforming catalysts operated at 950 °C with sulfur concentrations of 10 ppmV, [107]. However, in the experiment the sulfur concentration at the cell inlet causing 30 mV OCV drop was about 5 ppmV. Considering that in the regions where STR takes place the temperatures can be up to 200 K lower than the average cell temperature leads to critical sulfur concentrations of 1 ppmV, [107]. Therefore, a 90 % deactivation with 5 ppmV of sulfur in the fuel gas might be possible.

The second mechanism which could play a role for the observed OCV drop is the deactivation of the CPO catalyst. Lower conversion rates of the CPO yield less hydrogen and more water due to reduced methane reforming. The lower hydrogen-to-water ratios yield directly lower OCV values. To account for a 50 mV of OCV drop, the deactivation of the CPO was calculated to approx. 30 %.

The double potential formation between hydrogen/water and hydrogen sulfide/sulfur dioxide could be another explanation for the observed OCV drop, [119]. However, this mechanism has thus far not been investigated in depth. Future experiments should focus on hydrogen as a model fuel, the Nernst voltage of which is independent of the STR activity, to prove or disprove the proposed hypotheses.

Figure 3-28: Comparison of voltage- current curves obtained before and after sulfur experiments

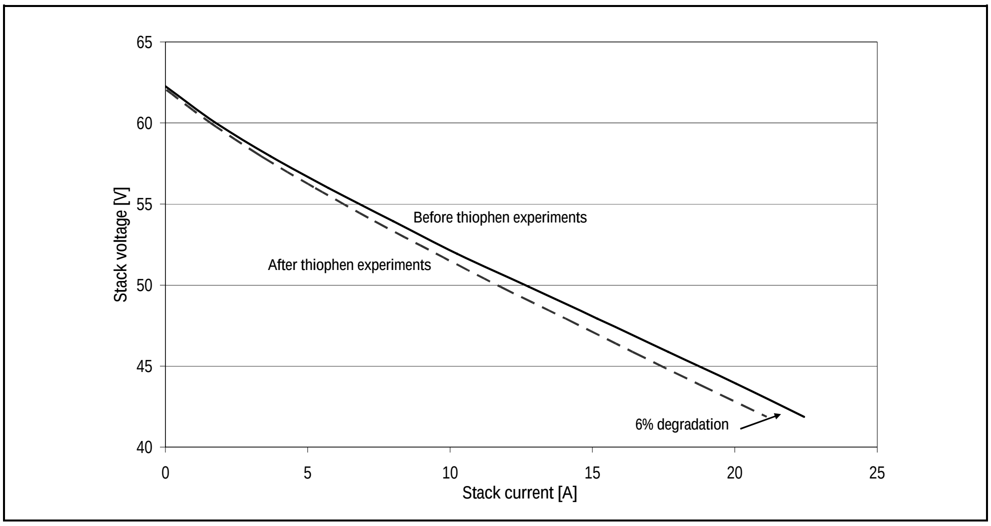

Figure 3-28 compares the voltage-current curves obtained before and after the sulfur experiments. It is well known, that nickel-based catalysts operated at high temperatures can be regenerated after sulfur poisoning by switching to a sulfur-free fuel, [70, 107]. However, excessive sulfur concentrations can cause permanent degradation via bulk sulfidation, [151]. This is probably the reason for the 6 % permanent degradation after the sulfur experiments. Given that such degradation values are normal after Redox and thermo cycle test programs, [84], the role of sulfur as a limiting factor to the proof-of-concept test can be put in perspective.

In summary, the desulphurization is the key to substantially minimize sulfur poisoning induced power losses. For the proof-of-concept tests, a desulphurization was found desirable but not necessary. Indeed sulfur reduces the power output of the Hexis SOFC but does not inhibit its stable operation. In addition, omitting the desulphurization neglects the need for a high temperature heat exchanger, simplifying the experimental setup for the proof-of-concept test considerably.

3.5 Proof-of-concept of the PSI B-IGFC system

The demonstration of a SOFC running with pure producer gas is an important milestone in the development process of the B-IGFC technology. A corresponding experiment was recently conducted in the framework of the BioCellus project and reported in [152]. In this experiment, the investigated single SOFC membrane was placed in a temperature-controlled oven and operated with producer gas from a two-stage downdraft gasifier. A slip stream of the particle-free producer gas with approx. 1 mg/m_n^3 (dtf) tar load was further cleaned in two activated carbon adsorber beds and then humidified in a water saturator before being introduced to the anode compartment of the SOFC test rig. The experiment lasted 150 h without operational problems or signs of cell degradation.

However, due to the extensive gas cleaning, it is difficult to draw conclusions concerning the tolerance of the tested SOFC towards typical producer gas impurities such as tars. Further, the differences regarding the operational characteristics between an externally heated SOFC membrane, [152], and a thermally self-sustaining SOFC system are large. For instance, planar SOFC stacks consist of numerous cells where the uniform fuel distribution is a major concern. Fluctuations of gas compositions may also become critical for the achievement of a suitable and stable operational temperature for a SOFC stack.

These questions can only be addressed experimentally under realistic conditions. Hence, once all important unit operations had been characterized, the next steps were to assemble, operate and gradually optimize a demonstration unit, which would realistically represent the complete process chain from wood to electricity.

3.5.1 First demonstration unit tests and derived modifications

In a first step, a Hexis SOFC system that had already completed several thousand operating hours on natural gas (BZM66) was linked to the PSI wood gasifier through a hot gas cyclone designed to remove particles with a minimum diameter of 15 μm. The BZM66 with internal CPO unit, see Figure 3-23, was operated under open circuit conditions to investigate the impact of the producer gas induced off-design gas flow conditions on the thermal management and the post-combustion. By operating BZM66 for 24 h, the proof was achieved that producer gas from air-blown updraft gasification is suitable for thermally self sustaining operation of the Hexis SOFC system. Nevertheless, the temperatures of the SOFC stack did fluctuate in the range of 100 K around the design value. The variations were mainly induced by producer gas flow discontinuities. The over pressure at the SOFC system inlet was stable at approx. 100 mbar. For more information see [147]. Based on these results, BZM66 was replaced with a new Hexis SOFC system (BZM79) for tests under load conditions. To reduce the system inlet pressure, the ceramic heat shield, which was placed above the internal CPO unit, was removed. For commissioning, BZM79 was operated soundly for 350 h with methane processed via the internal CPO unit.

During the **first producer gas experiment** with BZM79, the entire producer gas was fed to an external CPO unit for pre-conditioning. Gas flow discontinuities were reduced via adaptation of the operational parameters of the gasifier. A slipstream of the producer gas, approx. one third, was supplied to the SOFC stack through the internal CPO unit where tars should be further degraded. Within the 10 h duration of the experiment, the produced current decreased from initially 13 A to zero. Furthermore, a constant decline of the stack top temperature was observed while the pressure at the SOFC system inlet was stable at around 15 mbar. The strong reduction of the system inlet pressure confirmed the positive impact of removing the heat shield. The declining stack top temperature and current were allocated to a blockage of the valve used to control the producer gas slip stream to the SOFC system. It was concluded that, with increasing blockage, the producer gas flow to the SOFC was reduced, yielding a higher than wanted air-to-fuel ratio in the internal CPO unit. This in turn reduced the open circuit voltage of the producer gas below the operational voltage, thus leading to zero current production. The reduced fuel gas heating value and volume flow most probably resulted in disturbance of the post-combustion zone, which would account for the changes in the temperature distribution of the stack. Currently no apparent reason for why these phenomena did fail to occur with BZM66 has been found.

To avoid blockage of the slipstream valve, it was decided to manually open and close it regularly during the next test, in an effort to thereby loosen and discharge possible particle agglomerations in the valve.

The **second producer gas experiment** with BZM79 lasted 19 h and was terminated due to a gasifier failure. On average, the stack produced 6 A of current, corresponding to 280W, with maximum values of 11 A and minimum values around 5 A. More information can be found in [153]. The regular open-close cycles of the slipstream valve allowed maintaining a relatively constant producer gas volume flow throughout the experiment duration. The pressure at the cell inlet was observed to be lower after each open-close cycle. A possible explanation for this being that during the short periods of time where the valve was closed, approx. one minute, the air initially fed to the internal CPO unit reached the central fuel gas channel of the stack and removed particle agglomerations in this area. Keeping in mind the limited efficiency of the used cyclone with respect to the removal of particles with diameters below 15 μm, such agglomerations may have formed. After the experiment, the stack rendered approx. 6 % less power in methane operation. This indicated that the Redox cycles triggered by the open-close cycles of the slipstream valve were detrimental to the stack.

In subsequent tests, the strategy of operating the SOFC with a producer gas slip stream was abandoned. Instead, the SOFC would be operated with the complete producer gas volume. To achieve this, the wood mass flow to the gasifier had to be reduced by two thirds. First tests showed that the firebed with the reduced wood mass flow was too loose and led to an unstable gasifier operation. Stable operation was reached again by reducing the grate area of the gasifier with a liner. Additionally the internal CPO unit was recognized to be an uncertainty factor in the demonstration unit as it inhibited the measurement of the exact producer gas composition at the stack inlet. Consequently, the internal CPO unit was taken out of BZM79 and replaced by a second external CPO unit for methane operation. A new cyclone was also designed and built for the removal of particles with a minimum diameter of approx. 5 μm and suitable for the reduced producer gas volume flow.

3.5.2 Present demonstration unit configuration

Figure 3-29 outlines the present demonstration unit configuration.

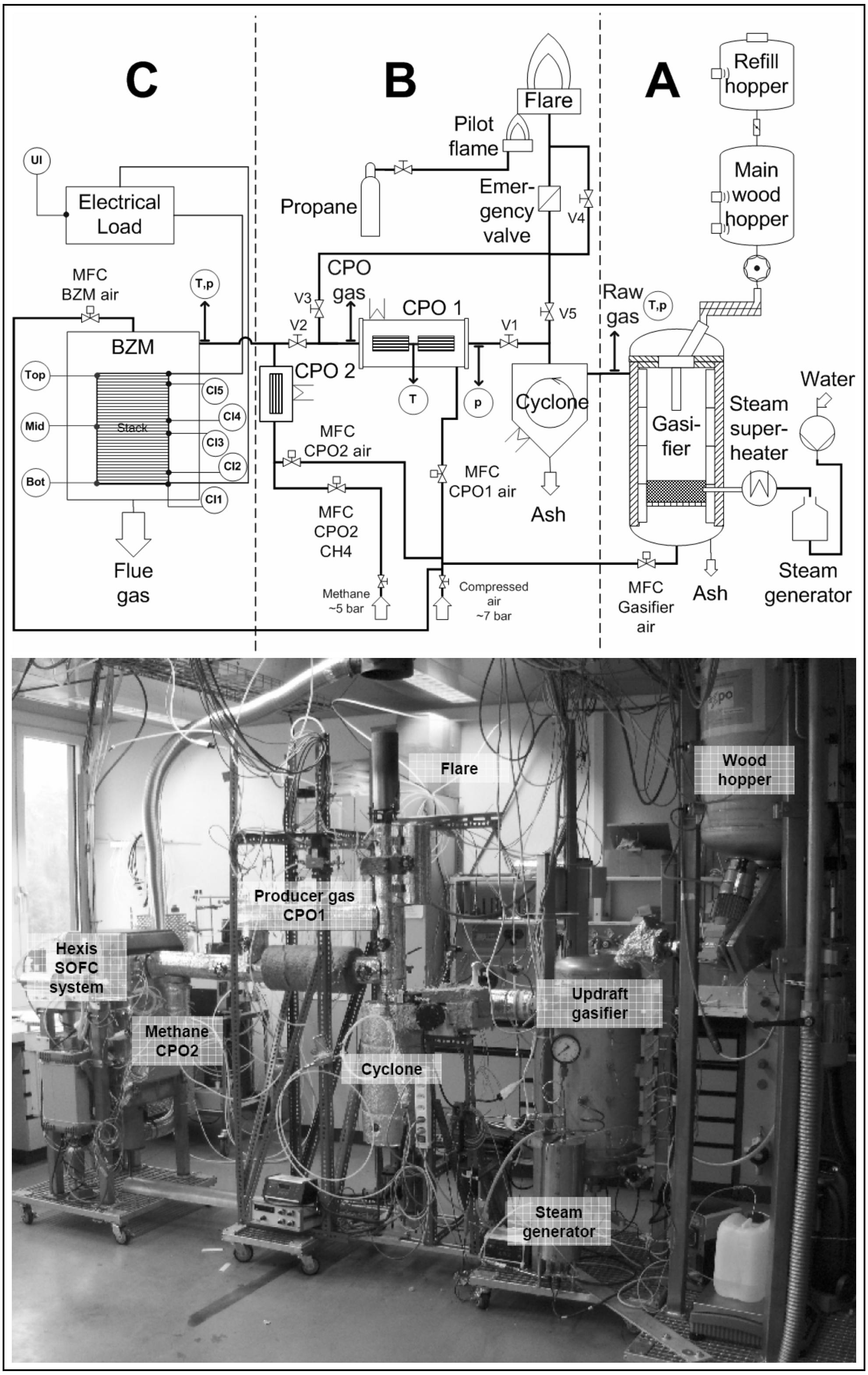
C
B
A
Flare
Refill hopper
Pilot flame
UI
Electrical Load
Propane
Emer-gency valve
V4
Main wood hopper
CPO gas
MFC BZM air
T,p
V3
CPO 1
V5
Raw gas
T,p
V2
V1
BZM
CPO 2
Top
CI5
T
p
Cyclone
Water
CI4
Mid
Stack
CI3
Gasi-fier
Steam super-heater
MFC CPO2 air
CI2
Bot
MFC CPO1 air
CI1
Ash
MFC CPO2 CH4
Flue gas
Steam generator
Methane ~5 bar
Compressed air ~7 bar
MFC Gasifier air
Ash
Flare
Wood hopper
Producer gas CPO1
Hexis SOFC system
Updraft gasifier
Methane CPO2
Cyclone
Steam generator

Figure 3-29: Technical outline and photograph of the present demonstration unit configuration

In **section (A)**, a scheme of the PSI wood gasifier is shown. The technical details were discussed in section 3.4.1. The gasification air is controlled by means of a mass flow controller (MFC). The temperature and composition of the raw producer gas as well as the pressure loss over the gasifier are measured approx. 10 cm downstream the gasifier outlet. **Section (B)** shows the current configuration of the gas processing setup. Particles larger than approx. 5 μm are removed in a cyclone and discharged with a screw conveyor. To prevent tar condensation during the start-up phase of the gasifier, the cyclone and all producer gas flowed through pipes are electrically heated to 400 °C. The tar load of the producer gas is reduced in the first external catalytic partial oxidation unit (CPO1). The minimum ignition temperature of the CPO catalyst is approx. 450 °C. CPO1 can hence be electrically heated to over 600 °C. The air volume fed to CPO1 is set using a MFC. The pressure upstream and the temperature in the middle of CPO1 are monitored. The composition of the catalytic partially oxidized producer gas is measured directly at the reactor outlet. The second catalytic partial oxidation unit (CPO2) is placed downstream valve V2. The methane and air volumes are both controlled by means of MFCs. In **section (C)**, the SOFC system is outlined. The temperature and pressure of either the catalytic partially oxidized methane or the producer gas are measured at the SOFC system inlet. The cooling air flow for the system is adjusted using a MFC. The actual condition of the SOFC stack is monitored via thermocouples in the top, middle and bottom cells. The electrochemical performance is determined by measuring the voltages of 5 cell clusters, Cl1 to 5. The net stack voltage is maintained constant using an electrical load generator which automatically adjusts the stack current.

Table 3-2: Valve status for the four operational modes of the demonstration unit

Operational mode	Description	Valve 1	2	3	4	5
1	Burning of the unprocessed producer gas	closed	closed	closed	open	open
2	Burning of the catalytic partially oxidized gas	open	closed	open	open	closed
3	SOFC system operation with catalytic partially oxidized gas	open	open	open	closed	closed
4	SOFC system operation with unprocessed producer gas	closed	open	open	closed	open

Table 3-2 summarizes the four operational modes of the demonstration unit and the corresponding valve status, see Figure 3-29. During the start-up of the gasifier, the producer gas is entirely flared by default (mode 1). A propane pilot flame ensures the reliable combustion of the producer gas in the flare. Once the gasifier has reached stable operation, normally approx. 2 h after ignition, CPO1 can be put on stream (mode 2) or the producer gas may be directly fed to the SOFC system (mode 4). In mode 4, valve 4 and the emergency valve are normally closed. However, in case the control unit registers any malfunction of the SOFC system, the emergency valve and the SOFC system nitrogen purge valve open automatically. Thus, the producer gas is flared and back diffusion into the SOFC system is prevented. The same procedure applies in mode 3 when the producer gas is processed via CPO1 before being fed to the SOFC system. During the switching phase from mode 1 to mode 4 or mode 2 to 3, respectively, the methane and air volume guided through CPO2 and into the SOFC system are gradually decreased with increasing producer gas quantities.

3.5.3 Long-term test results

The demonstration unit in the above discussed configuration was operated non-stop for over 30 h with the SOFC system on-stream for 28 h. Figure 3-30 shows that the gasifier outlet temperature hardly fluctuated and was on average 690 °C with a slight increasing trend. The gasifier was operated with 25 l_n/min of air and 1.12 kg/h of wood pellets, yielding an effective air-to-fuel ratio of approx. 0.32. The average humidity of the wood pellets was 6 %. 600 g/h of steam at 550 °C were additionally injected into the gasifier, simulating a wood humidity of approx. 39 %. The CPO1 temperature was stable around 790 °C. The air volume to CPO1 was 865 l_n/h, which translates into an air-to-fuel ratio of 0.26. Both, gasifier and CPO1 air volume flows were not changed during the experiment, Figure 3-31. The temperature at the SOFC inlet was on average 550 °C. The 140 K temperature difference between the SOFC inlet and the CPO1 temperature was a consequence of a secondary air injection through CPO2 to avoid coke depositions in the non-heated area where the internal CPO monolith was initially placed, see Figure 3-32: Point 5, 300 °C isotherm. With 56 l_n/h, the injected air volume yielded an oxygen concentration in the producer gas at the SOFC system inlet of approx. 0.25 mol-%. An anode reoxidation should not have occurred as the small oxygen amount should have either reacted with coke depositions, if any, or with hydrogen or carbon monoxide in the central fuel gas channel before reaching the anode compartments.

Figure 3-30:
Time plots of gasifier outlet, CPO1 mid and SOFC system inlet temperatures as well as measured raw and CPO gas compositions plus derived volume flows, heating values, steam-to-carbon ratios, tar and water loads

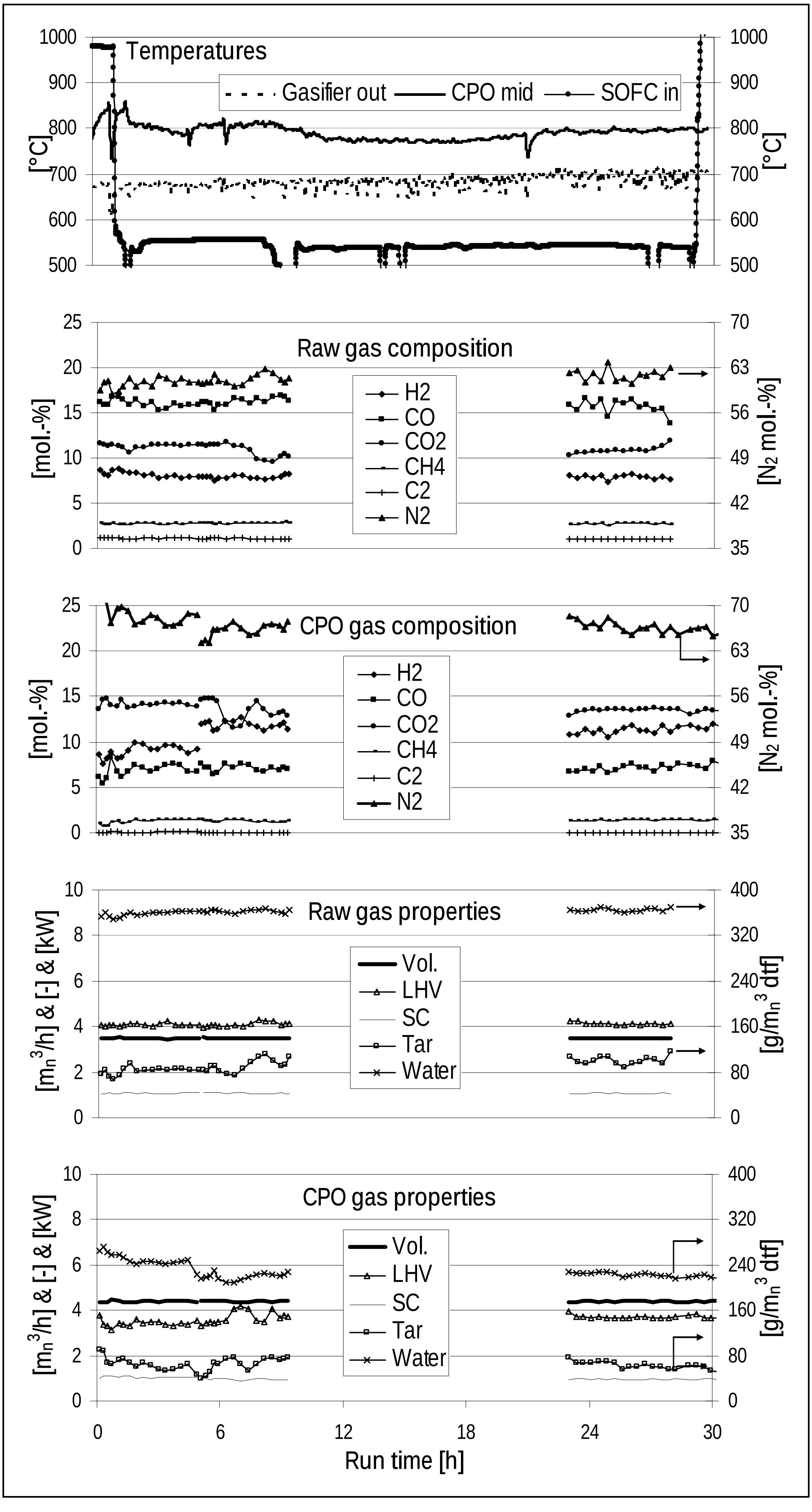

Figure 3-30 shows the raw and CPO gas composition measured during the first 9 h and the last 7 h of the experiment. Note that the discontinuity in the CPO gas progressions in the 5th hour of the experiment is a result of a change of the sampling point from the middle to the outlet of the CPO1 reactor. The characteristic properties of the gases, the tar and water load, volume flow, LHV power and steam-to-carbon ratio (SC), were calculated based on the measured dry gas compositions. The SC was defined as the ratio of the total carbon content of the gases to their steam content. It can be seen, that the gasifier and the CPO1 operated steady state. Especially the smooth gas volume and steam-to-carbon ratio progressions are of interest. Table 3-3 summarizes the average and the standard deviation values of the gas compositions and their characteristic properties.

Table 3-3:
Raw and CPO gas composition with characteristic properties

Parameter	Unit	Raw gas		CPO gas	
		Average	Standard deviation	Average	Standard deviation
H_2	[mol-% (dtf)]	8.01	0.56	11.60	1.05
CO		16.02	1.18	7.20	0.98
CO_2		11.00	0.62	13.49	0.81
CH_4		2.75	0.20	1.36	0.17
C_2		1.08	0.08	0.03	0.01
N_2		61.15	2.03	66.31	2.14
Tar load	[g/m_n^3 (dtf)]	90.27	28.07	61.98	20.57
Water load		361.69	11.95	221.04	12.88
Volume flow	[m_n^3/h]	3.50	0.02	4.40	0.03
LHV power	[kW]	4.11	0.10	3.69	0.18
SC	[-]	1.07	0.01	0.95	0.03

From Table 3-3 it can be seen that the CPO1 predominantly promoted the water gas shift reaction. In terms of hydrocarbons, it converted almost all C_2 species and on average about 40 % of the methane in the raw gas. The tar conversion was on average around 15 %. The low tar conversion might be a consequence of diffusion limitations in the wide channels of the employed CPO monolith with 100 channels per square inch. A finer meshed monolith could not be used due to blocking issues caused by the moderate particle removal efficiency of the cyclone. The LHV loss resulting from the partial combustion of the raw producer gas was approx. 10 %.

Figure 3-31:
Time plots of stack current and voltage, cluster specific average single cell voltages, stack temperatures, pressure differences and air volume flows of the main components of the demonstration unit

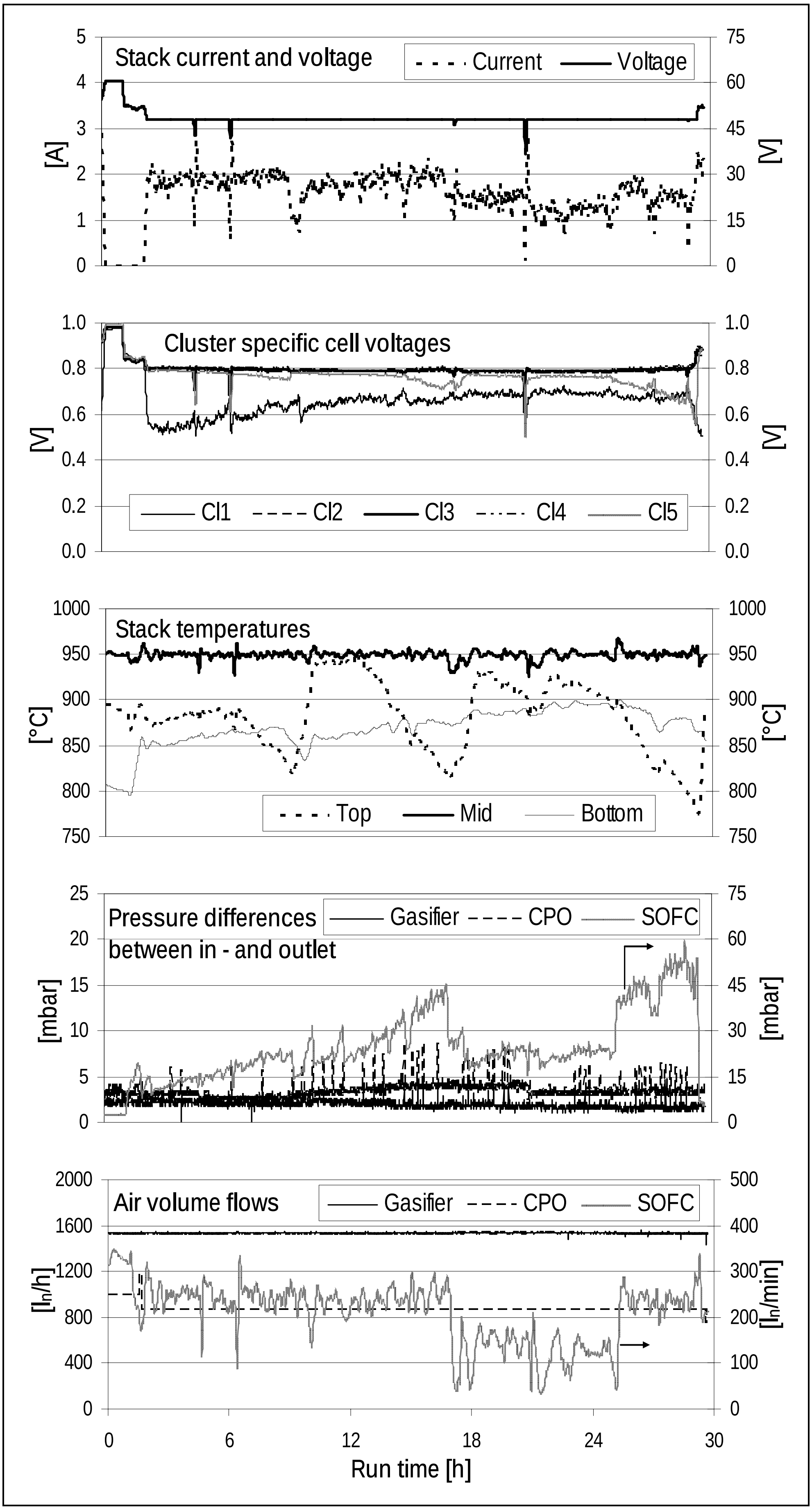

The SOFC stack produced approx. 3.3 A in methane operation prior to switching to producer gas. This more than halved current output compared to after the commissioning phase was a consequence of the harsh test conditions during the experiments reported in section 3.5.1. The reason for the low current output was that the top cluster did not reach the average cell voltage of the four other cell clusters. Due to the in-series connection of the five clusters, the maximum current is limited by the lowest single cell voltage, which should not under-run 0.6 V. Hence, the low performance of the top cluster considerably limited the stack current. The present discussion focuses therefore on the operational behavior of the SOFC rather than the absolute produced current.

Figure 3-31 depicts the stack current and voltage progression obtained from the highly tar laden producer gas. The current produced for a stack voltage of 48 V was around 2 A during the first 15 h, then declined to around 1.5 A for 7 h and finally swung around 1.75 A for the remaining 6 h of the experiment. This correlates well with the cooling air flow which averaged 250 l_n/min during the first 15 h of the experiment, then dropped to an average value of 100 l_n/min for the following 7 h and than increased again to 250 l_n/min for the remaining 6 h of the experiment. Numerous possible reasons for this correlation are conceivable. One reason could be that the higher oxygen partial pressure at the cathode resulting from the increased cooling air flow yields reduced cathode polarization losses. Another reason could be, that the increased air flow reduced fuel gas diffusion into the cathode compartment, which otherwise strongly reduced the open circuit voltage and hence the current for a given operational voltage.

The stack middle and bottom temperatures were quite stable. This is due to the cooling air flow being controlled to maintain a temperature of 950 °C in the middle of the stack. The fluctuations of the stack top temperature indicate that in this part of the stack, either the fuel gas distribution or the post-combustion of the depleted fuel gas was disturbed. Despite that thermodynamic carbon deposition should not occur under the given operating conditions, Figure 3-32, it was assumed during the experiment that coke agglomerations could be present in the central fuel gas channel. To remove these possible agglomerations, the secondary air injection volume flow was increased from 56 to 600 l_n/h for short periods of time. This corresponds to an air-to-fuel ratio of 0.23 and an oxygen fraction in the gas of 2.2 mol-%. The response of the system to the increase of the secondary air injection (SAI) was however contradictory.

Figure 3-32:
C-H-O ternary diagram for the thermodynamic graphite formation with inscribed C-H-O molar fractions of dry and wet wood and producer gas after the different process steps

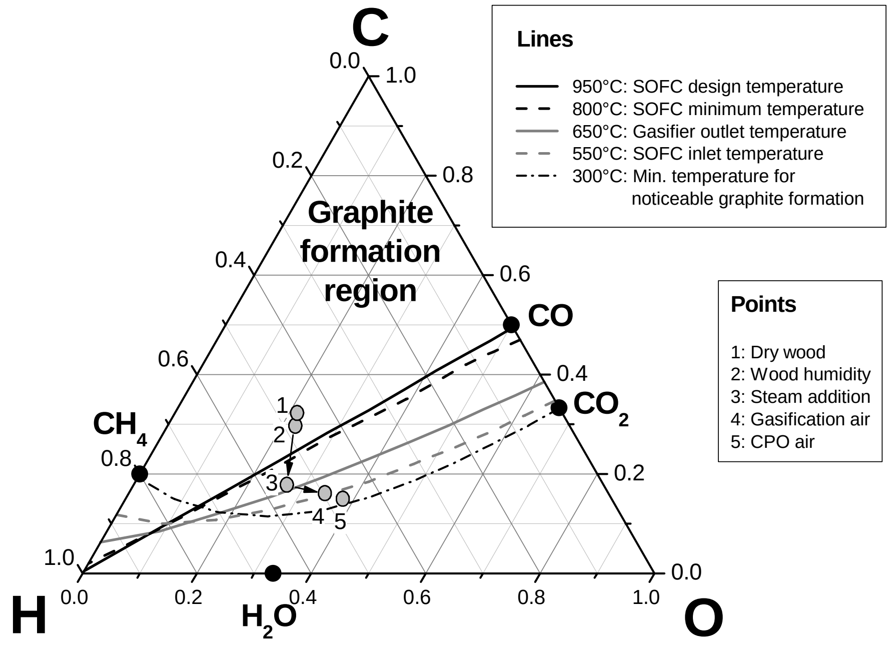

The first SAI at around 9.5 h experimental run time resulted in an instant stack top temperature increase and system pressure decrease indicating a successful discharge of deposits from the SOFC system. The following SAI at 12.5 h and at 27 h experimental run time had no impact on the stack top temperature. The system pressure was lowered during the SAIs due to an automatic decrease of the cooling air flow resulting from the cooling effect of the increased gas flow at the anode. However after the SAIs, the system pressure went back to the initial value as the cooling air flow returned to normal. Post-test examination of the central fuel gas channel showed that it was clear throughout the experiment. The assumption of coke deposition was hence shown wrong and the operational conditions were confirmed as safe in this respect. In contrast, evidence was found for ash deposits in cold regions of the system.

Figure 3-33:
Ash deposits on the mounting of the thermocouple at the SOFC system inlet

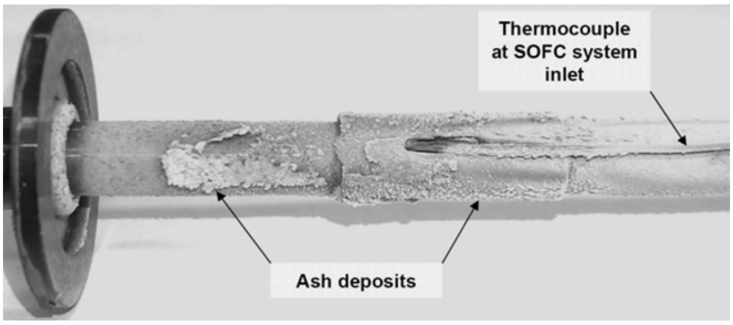

Figure 3-33 shows ash deposits on the mounting of the thermocouple at the SOFC system inlet. At this point the temperature was around 550 °C, which is below the melting point of biomass ash. Besides the SOFC system inlet, the spiral cooling air pre-heater is the only part in the whole demonstration unit where the temperatures are generally below the melting point of biomass ash. Fouling in heat exchangers for the recovery of heat from flue gases is a common issue. The average ash content of the gasified wood pellets is approx. 1 mass-%. With a wood pellet mass flow on dry basis of 1.05 kg/h and an on-stream time of the SOFC system of approx. 28 h, 294 g of ash could have condensed in the cooling air pre-heater. It is assumed that this amount is sufficient to noticeably disturb the post-combustion of the depleted fuel gas resulting in the observed fluctuations of the stack top temperature. A continuous ash deposition also explains the relatively steady system pressure increase at reasonably constant cooling air and fuel gas flows.

In summary, the gasifier and the catalytic partial oxidation were operated without problems, delivering a fuel gas to the SOFC system with relatively constant composition and properties. The tar conversion in the CPO1 was found to be limited, most probably by the mass transport through the wide channels of the coarse CPO monolith. Compared to methane operation, the SOFC system delivered approx. 40 % less current. With the chosen operating conditions, carbon deposition was effectively prevented. Ash deposits were however identified as a major obstacle to a smooth SOFC system operation.

4 Modeling work literature review

Modeling power cycles based on the SOFC technology has gained much interest in recent years. Especially the natural gas fed SOFC-gas turbine (GT) cycle has been investigated by several groups with different approaches regarding the size and design of the cycles, the fuel cell concept and the model type. Consequently, the estimated cycle efficiencies vary in the range of 55 % for small scale systems to 77 % for power plant configurations, [154]. In contrast, system analysis studies of SOFC based cycles fed with biomass derived gases are scarce. The following sections give a brief review of commonly used model types with typical assumptions and field of application, as well as recent works in the field of B-IGFC systems analysis. The discussion regarding the different model types focuses on their application for B-IGFC systems analysis.

4.1 Modeling approaches for steady-state investigations

Modeling fuel cells is a challenging task. A number of coupled phenomena have to be considered e.g. heat transfer via convection, solid and gaseous conduction and radiation, chemical reaction kinetics for e.g. the steam reforming reaction, voltage losses due to the irreversibility of the electrochemical reactions, electric and ionic conduction. Therefore, fuel cell models are generally tailored to the investigation in question. SOFC model types in the literature vary from lumped models, which are often used to study power plant cycles, to detailed computational fluid dynamics models (CFD) for cell design optimization where e.g. flow phenomena in the SOFC gas channels are optimized. The permissibility of every model assumption has to be scrutinized with respect to the impact of the generated information. The assumptions and the spatial resolution are the main criteria for the classification of different model types. The following levels of modeling can be distinguished with respect to the latter criterion, [112]:

- Molecular level (nm-scale)
- Electrode level (μm-scale)
- Cell level (mm-scale)
- Stack level (cm-scale)
- Plant level (m-scale)

4.1.1 Molecular level models

Molecular level models typically deal with reaction kinetics. The aim of such models is e.g. to find rate limiting reaction steps.

An extrapolation of the results of such models to the plant level for systems analysis is not feasible as no information about the performance of the SOFC in question is generated.

4.1.2 Electrode level models

Electrode level models aim at the investigation of charge and mass transfer phenomena within the anode-electrolyte-cathode (AEC) structure and interconnect. A typical result of such a model is the share of different voltage loss mechanisms and the total voltage loss for a given current density, temperature and set of geometrical and structural details of the modeled SOFC.

The extrapolation of electrode level model results to the plant level for systems analysis is the most commonly used approach within the B-IGFC research community. This is mainly due to rapid calculation times in the order of seconds and the ease of model development. All extrapolated electrode level models (lumped models) in the literature dealing with B-IGFC systems analysis have the following assumptions in common:

- The SOFC is considered as a continuous stirred tank reactor (CSTR).
- All chemical and electrochemical reactions occurring in the SOFC reach equilibrium.
- The mean current density and fuel utilization are model input values. Faraday's law directly relates the fuel input mol flow to the current generated by the fuel cell and the fuel utilization at the specific operational point. The required oxygen ion flow from the cathode to the anode is given by the stoichiometry of the combustion reaction. Hence, the overall mass balance of the fuel cell is defined by the model input.

Lumped models can be easily calibrated to fit measured data for a specific cell type, feed gas and operating conditions set. However, investigations of conditions strongly differing from the calibration case have to be seen as approximation. As a consequence of the CSTR assumption, lumped models do not allow for the investigation of the local conditions in the SOFC. Hence, the generated results have to be examined with respect to the operational feasibility of the investigated SOFC, [155].

The main differentiating factor of the plethora of lumped models in the literature is how the effective operational voltage, the fuel and air input mol flows are calculated. Three common approaches can be identified:

I. *Models with fixed operational voltage*

   The power output of the SOFC is a function of the current and the operational voltage. By specifying an operational voltage, usually between 0.6 and 0.8 V, the output power and therefore the efficiency of the investigated SOFC is defined. Furthermore, the temperatures of the output fuel and air streams are functions of the power in- and output of the SOFC. Thus, these model types are not predictive as the model output is defined via the model input. This type of model has been used in [132, 143, 156, 157]. These investigations aimed at the impact of different gas cleaning strategies and bottoming cycles downstream of the SOFC.

II. *Models with measured voltage-current curves*

   The operational voltage and the input fuel flow are calculated based on measured voltage-current curves (UI) to reach a targeted power output. The oxygen ion mol flow is not fixed, but defined by the measured UI curve. The impact of fuel gas compositions differing from the reference composition is usually considered through empirical correction correlations. Within the scope of these correlations, results can be regarded as realistic and quantitative statements with respect to different overall system designs are valid. [142, 144, 158-160] are examples of such investigations, mainly focusing on natural gas fed SOFCs. However, the scope of the empirical correction correlations is narrow. Hence, one should not act based on the assumption of a real fuel flexibility of these models, which is however mandatory for B-IGFC systems analysis due to the varying gas compositions resulting from different gasification processes.

III. *Models with detailed electrochemistry*

   The calculation of the operational voltage is based on correlations describing the ideal reversible voltage (Nernst voltage) and the voltage loss mechanisms. These mechanisms are the activation, the ohmic and the diffusion voltage losses which depend on the operational temperature, the species partial pressures, the current density and the geometrical as well as structural details of the modeled SOFC. Fuel and air flows are calculated analogously to the above outlined model type with measured voltage-current curves. This type of lumped model possesses some flexibility towards cell design details and fuel gas compositions. Calculation times are still in the range of seconds.

The main problem with this type of lumped model is the gas composition, which is used in the calculations of the operational voltage for a given current density. In reality, the gas composition changes along the fuel channel and therewith the Nernst voltage as well as the voltage losses and the local current density. If the inlet gas composition is used for the lumped model calculations, the voltage and power output is systematically overestimated, while it is systematically underestimated if the outlet gas composition is used, [161]. To yield realistic results, most lumped models use a theoretic gas composition, which is calculated as arithmetic average of the inlet and the outlet gas composition. The oxygen ion flow, which is transferred to the anode from the cathode side, is determined from the predefined fuel utilization. The outlet gas composition is calculated based on the inlet gas composition and the oxygen ion mol flow assuming chemical equilibrium at the predefined operational temperature.

This lumped model type is the most accurate of the three lumped model types. However, it lacks information about the local conditions in the SOFC. Critical conditions such as excessive temperature gradients cannot be identified. [161-168] are examples for investigations conducted with this model type.

4.1.3 Cell level models

Cell level models are also referred to as repeat element models. They include voltage, mass and energy balances in one or two dimensions. These models are generally used for cell design optimization as they allow for the prediction of local cell operating conditions, e.g. temperature, current density and species partial pressure distribution. Typically design parameter such as cell length, channel width as well as the flow design, are investigated with these models. The voltage balance is calculated via an electrode level sub-model. The impact of structural details of the AEC is therefore also considered. Cell level models differ in the considered dimensions and the numerical solution approach:

- One dimensional models (1D)

  Tubular cells are usually modeled 1D assuming heat and mass transfer only in axial direction. Planar co-flow and counter-flow cells can also be modeled 1D by neglecting boundary effects perpendicular to the gas flow direction, Figure 2-19. According to [169], the error due to this assumption is negligible when the feed properties are equal for all gas channels. In consequence, all other properties along the gas channels should be equal and so should the local temperature be. Hence, no perpendicular heat transfer should occur. 1D cell level models feature short calculation times in the order of minutes and are therefore suitable for system analysis calculations.

- Two dimensional models (2D)

  Planar cross-flow cells, Figure 2-19, have to be modeled 2D due to the perpendicular gas flow channels. The sizeable additional effort is why this type of flow design remains largely neglected in system analysis calculations. However, such a model was used in [154] for the investigation of an SOFC/gas turbine (GT) cycle.

For cell level models the following discretization methods can be distinguished:

- Finite element method (FEM)

  The idea of this method is to discretize the investigated object, e.g. flow channel, but also solid structure, and to allocate transfer functions to all considered physical properties, which can change within a discrete element. The solution is found, when the difference of the boundary values of all directly adjacent elements is within the tolerance. FEM based fuel cell models are usually employed for detailed investigations of flow phenomena in the gas ducts and channels. The calculation times are rather long. As a result this approach is seldom employed for systems analysis calculations.

- Numerical volume averaging method (NVAM)

  The NVA method is extensively discussed in [170]. The major difference to the FE method is, that transfer functions are not only defined for physical properties, but also for properties such as pressure, flow velocity etc. which are changing due to the internal structure of the discretized element. The corresponding transfer functions are computed via detailed FEM models of the discretized elements. The overall solution is found analogously to the FE method. NVAM models feature shorter calculation times than FEM models.

- Finite volume method (FVM)

  The FV method is often used for one and two dimensional SOFC models. The discrete elements are assumed as continuously stirred tanks reactors (CSTR). The change of any considered property in a specific CSTR element is calculated with the output value of the antecedent element. The calculated value is assumed to be valid for the entire element. Due to this simplification, FVM models feature shorter calculation times than FEM and NVAM models and are therefore preeminently suitable for systems analysis calculations. This is most probably the reason for their popularity.

The information regarding local conditions in the SOFC allows conclusions about potential failure sources, such as carbon deposition and thermal stress caused by steep temperature gradients. The spectrum of published studies conducted with cell level models is discussed below.

The model of a tubular SOFC in [171] was developed by assuming isothermal conditions throughout the cell. Although this assumption is a strong simplification, the authors show that the accuracy of the predicted power output values is greatly improved by solving the mass balance and calculating the power output with the local species partial pressures as compared to lumped models. This approach was also considered in [141] for a planar cross-flow cell with the same conclusion for the predicted power output. However, the temperature of the output gas streams, which needs to be known for investigations of combined cycles, cannot be predicted. Further, the temperature distribution cannot be forecasted and thus no information is generated about critical conditions in the cell. Models including the full energy balance are reported by the following authors:

The risk of carbon deposition is usually approximated via the computation of the probability of graphite formation. Therefore, the chemical equilibrium is calculated for the given local species partial pressures and temperatures, [129-131, 172]. Fuel starvation effects in a stack of cells, which are connected in series, are discussed in [173, 174].

The impact of different fuel gas compositions on the fuel cell efficiency and the risk of carbon deposition is explored in [175-177] with FVM models. All three studies are in agreement, that the fuel gas composition has an important impact on the temperature distribution. Hence, it can be stated that the implementation of the full energy balance generates valuable information for the prediction of critical operational conditions in the cells.

More detailed CFD based models are reported in the following studies: The study in [178] aimed at the investigation of radial temperature distribution induced thermal stress. The implemented 3D CFD cell level model requires approximately 40 minutes of calculation time and is therefore not suitable for systems analysis calculations. The model employed in the studies [179-181] is also based on the FE method. The model was used to investigate different cell designs aiming at the reduction of e.g. the anode re-oxidation risk by optimizing the flow field geometry. Analogously to [178], calculation times are rather long.

The extrapolation of cell level model results to the plant level is based on the assumption, that all cells in the stack or fuel cell system are operated under the same conditions, e.g. fuel gas input, gas temperatures, heat losses. The error resulting from this assumption is rather small and the predicted power output and temperature values are close to reality, [169]. However, boundary effects, such as increased heat losses of the cells at the outer ends of the stack, or effects resulting from different stacking or ducting designs can not be studied.

4.1.4 Stack level models

Stack level models are used to investigate the impact of realistic boundary conditions of the repeat cell elements in a stack, e.g. the impact of different gas duct designs on the fuel gas distribution and therewith on the temperature and current density distribution in the stack. In consequence, stack level models are mostly three dimensional (3D).

The model types can be differentiated from the point of view of a numerical discretization approach just as the cell level models. The stack is discretized and the mass and energy balances are solved for all the discrete elements. Contrary to cell level models, heat conduction has to be considered in all three dimensions in order to allow for the prediction of the impact of realistic boundary conditions such as increased heat losses at the outer stack surfaces to the surroundings.

The study in [141] addresses the cooling effect of the outer stack surface of a seven cell cross-flow stack. The authors show, that the radiative heat losses of the end cell results in a cold spot temperature of approx. 80K less than the cell in the middle of the stack, which can be considered almost adiabatic. Further studies conducted with stack level models are reported in [139, 182].

The surplus of possibilities offered by stack level models compared to cell level models is associated with a strongly increased modeling effort and long calculation times of up to several hours. System analysis calculations conducted with stack level models have hence not been reported as yet.

4.1.5 Plant level models

Plant level models consider the interaction between the fuel cell stack and the balance of plant components such as pumps, turbines, compressors and heat exchangers. Investigations focus on the optimization of the overall plant efficiency through a high degree of heat integration. The specific system components are generally modeled as lumped models with measured characteristic performance curves, e.g. voltage-current curves of the fuel cell stack in question. The scope of the specific models is typically narrow. Hence, results for strongly differing input values to that of the performance curves have to be cross-referenced with corresponding measurements or detailed models. In the long run, it would be desirable to incorporate all model levels into one model to asses all possible interactions between the phenomena occurring on the different length scales.

4.2 Recent studies of biomass fed SOFC cycles

A plethora of system studies dealing with natural gas fed SOFC cycles can be found in the literature. Most of the studies consider the tubular Siemens AG design. Model types vary from lumped models to detailed FEM models validated with voltage-current curves. A detailed discussion of these studies is not given in this work but can be found in e.g. [140, 141, 154, 155].

In contrast to natural gas fed SOFC cycles, only few studies about biomass producer gas fed SOFC cycles were thus far published. The most important contributions are briefly summarized in the following. The focus is on the approach chosen for the investigations as benchmark for the approach taken in the present work.

The study of Singh, [129], from the University of North Dakota/USA addresses the carbon deposition risk under typical SOFC operating conditions resulting from the operation with a tar-laden producer gas. The employed lumped model is based on Faraday's law. Carbon is assumed to be represented by graphite. The carbon deposition risk is calculated under the assumption of chemical equilibrium at the characteristic SOFC operation temperatures. The oxygen partial pressures required for the equilibrium calculations are determined based on averaged current density values. The main finding is that by increasing the current, the carbon deposition risk decreases. This phenomenon is associated with the increasing oxygen partial pressure at the anode with increasing current. Furthermore, the threshold current density value, at which no graphite formation occurs, is found to increase with higher tar loads.

Kivisaari, [156], from the Royal Institute of Sweden explores the relations between a MCFC and the balance of plant (BoP) components in B-IGFC systems. The employed model is of the lumped type based on Faraday's law with pre-defined voltage. The main finding is that increasing fuel utilization results in reduced cooling requirements of the MCFC.

Omosum, [132], from the Imperial College/United Kingdom has performed a cost and efficiency analysis of two B-IGFC systems with hot and cold gas processing system. The employed model is of the same type as Kivisaari's. Omosum concludes that the hot gas processing has advantages on the overall efficiency side due to improved heat integration possibilities. Furthermore, process waste heat can be sold leading to increased revenues. These two aspects are assumed sufficient to cover the higher investment costs of the hot gas processing. Omosum also states that an increased rate of internal reforming leads to lower cooling requirements of the SOFC and hence reduced BoP costs.

Van Herle, [160], from the Swiss Federal Institute of Technology in Lausanne/Switzerland uses a lumped model to study the impact of sewage gas on the operational behavior of a SOFC operated at full and partial load. The model includes empirical correlations for activation, ohmic and diffusion losses. The carbon deposition risk is also considered through equilibrium calculations for graphite formation. The system analysis reveals an electrical system efficiency of 48.5 % by employing a pre-reformer as compared to 43 % by employing a catalytic partial oxidation, which also causes higher cooling requirements of the stack.

Proell, [163], from the Technical University of Vienna/Austria analyses different options of heat integration, bottoming cycles and system pressures focused on a B-IGFC system based on the FICFB gasifier in Güssing/ Austria. The applied lumped model includes detailed electrochemical calculations. The operational voltage is calculated based on the average gas composition between the cell in- and output gas composition. The output gas composition is calculated assuming chemical equilibrium. The overall electrical system efficiency is calculated to be 40 %. The largest losses are found in the gasification section.

Panopoulos, [168], from the National Technical University of Athens/Greece uses the same lumped model type as Proell. The investigations, in the framework of the European project "BioCellus", focus on the coupling between a novel biomass gasification reactor and SOFCs. The idea is to transfer heat from the SOFC to an allothermal gasification reactor via high-temperature heat pipes. The overall electrical efficiency is calculated to be approx. 36 %. The variation of the fuel gas water content showed that the efficiency of sulfur removal decreases with increasing water load. Sulfur was assumed as H_2S and its adsorption on ZnO was assumed at equilibrium.

Cordiner, [183], from the University of Rome/Italy employs a cell level model to investigate the coupling of a biomass gasifier with an SOFC. The SOFC model is based on the FE method and is implemented in the CFD software "Fluent". The producer gas composition delivered by the biomass gasifier is calculated by assuming chemical equilibrium. At set conditions the investigated dry producer gas consists of 56 vol.-% hydrogen, 39 vol.-% carbon monoxide and the remainder being carbon dioxide. Cordiner calculates an electrical overall system efficiency of 46 % with a fuel utilization of 57 %. The unburned fuel is required to cover the heat needs of the gasification section.

Hernández-Pacheco, [175], from the University of North Dakota/USA explores the impact of biomass derived producer gases with low CH_4 content and different H_2/H_2O- and CO/CO_2-ratios on the electrical efficiency of anode and electrolyte supported SOFCs. The used 1D cell level SOFC model is based on the FV method and allows for the prediction of the local conditions in the SOFC. This study concludes that high H_2 concentrations in the fuel gas yield the highest efficiencies. However, the study does not account for the gasification efficiency and the impact of methane, which is often present in producer gases.

Sucipta, [184], from the Shibaura Institute of Technology/Japan uses a 1D cell level model for his investigation of a SOFC–GT hybrid system fuelled with producer gases from air-, oxygen- and steam-blown biomass gasification. The origin of the investigated producer gas compositions is not further detailed. The main finding of the study is that the SOFC-GT system efficiency is lower when operated with producer gases instead of methane. Amongst the producer gases, the one originating from steam-blown gasification is found to yield the highest electrical efficiency, while that from air-blown gasification yields the lowest electrical efficiency. However, this investigation does not account for the efficiency of the gasification processes, which may considerably alter the reported coherences. Besides, the targeted mean current density is comparably high leading to operational voltages below 0.5 V. Consequently the proposed operational conditions are neither sustainable for SOFCs nor are the reported efficiency values from gas to electricity of around 38 % competitive with modern gas engines.

Regarding published B-IGFC systems analysis, the latter three studies use the most detailed SOFC model types. However, the authors do not focus on the impact of real producer gas compositions, but consider instead idealized fuel gases with very low hydrocarbon contents even though the hydrocarbon content of real producer gases can be as high as 20 vol.-%. Furthermore the gasification efficiency is not considered in the latter two studies. This is a serious drawback as the gasification efficiency may vary between 50 to over 95 % depending on the gasification process, [25]. Finally, the impact of impurities on the system design and performance is not considered in any of these studies. For instance, the removal of organic sulfur species, which may be present in producer gases in considerable concentrations, has a strong impact on the overall system design which in return affects the overall system efficiency.

5 Modeling

5.1 Overall modeling approach

The modeling approach developed in this work aiming at thermo-economic evaluations of B-IGFC systems is outlined in Figure 5-1.

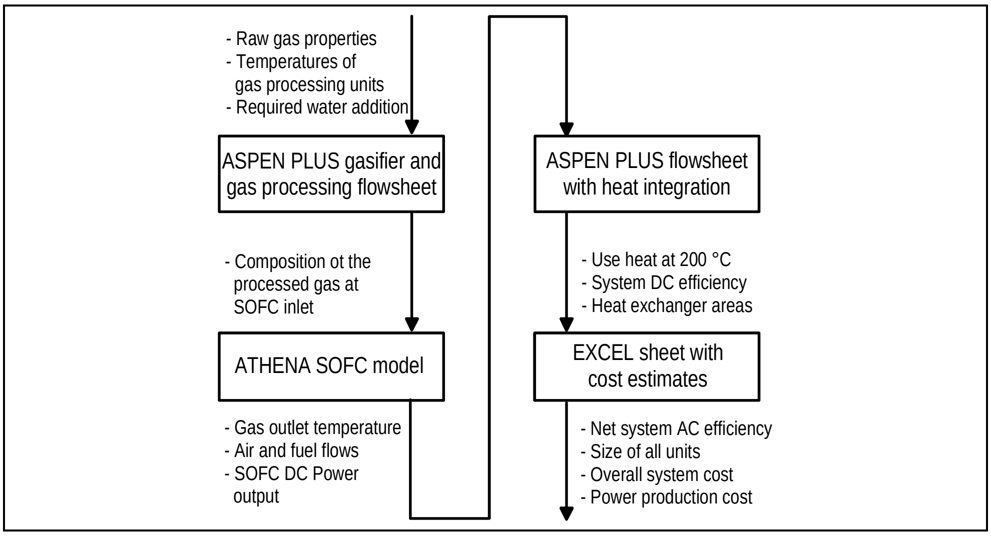
- Raw gas properties
- Temperatures of gas processing units
- Required water addition
ASPEN PLUS gasifier and gas processing flowsheet
- Composition ot the processed gas at SOFC inlet
ATHENA SOFC model
- Gas outlet temperature
- Air and fuel flows
- SOFC DC Power output
ASPEN PLUS flowsheet with heat integration
- Use heat at 200 °C
- System DC efficiency
- Heat exchanger areas
EXCEL sheet with cost estimates
- Net system AC efficiency
- Size of all units
- Overall system cost
- Power production cost

Figure 5-1: Overall modeling approach

In a first step, the producer gas composition at the SOFC inlet is determined using the commercial flowsheeting software ASPEN PLUS (version 12.1). ASPEN PLUS was developed for the simulation of chemical process applications and solves heat and mass balances in complex systems. The input data for this first calculation involves the raw gas composition, temperature and yield, the gas processing unit operations and their operational temperatures as well as the eventually required additional amount of water or steam to prevent graphite formation.

The predicted gas composition at the SOFC inlet is transferred to a SOFC model code implemented in the ATHENA equation solver language, [185]. The SOFC model yields the gas outlet temperatures, the required air volume flow to maintain the design temperature of the SOFC, the fuel volume flow required for a certain operational voltage at a given fuel utilization and the direct current (DC) power output. The SOFC model is discussed in section 5.3.

The results of the SOFC model are used as input for a second flowsheeting simulation. Figure 5-2 exemplarily shows the ASPEN PLUS flowsheet of the B-IGFC system 1, see section 6.2.2.

Figure 5-2: Flowsheet of "System 1"

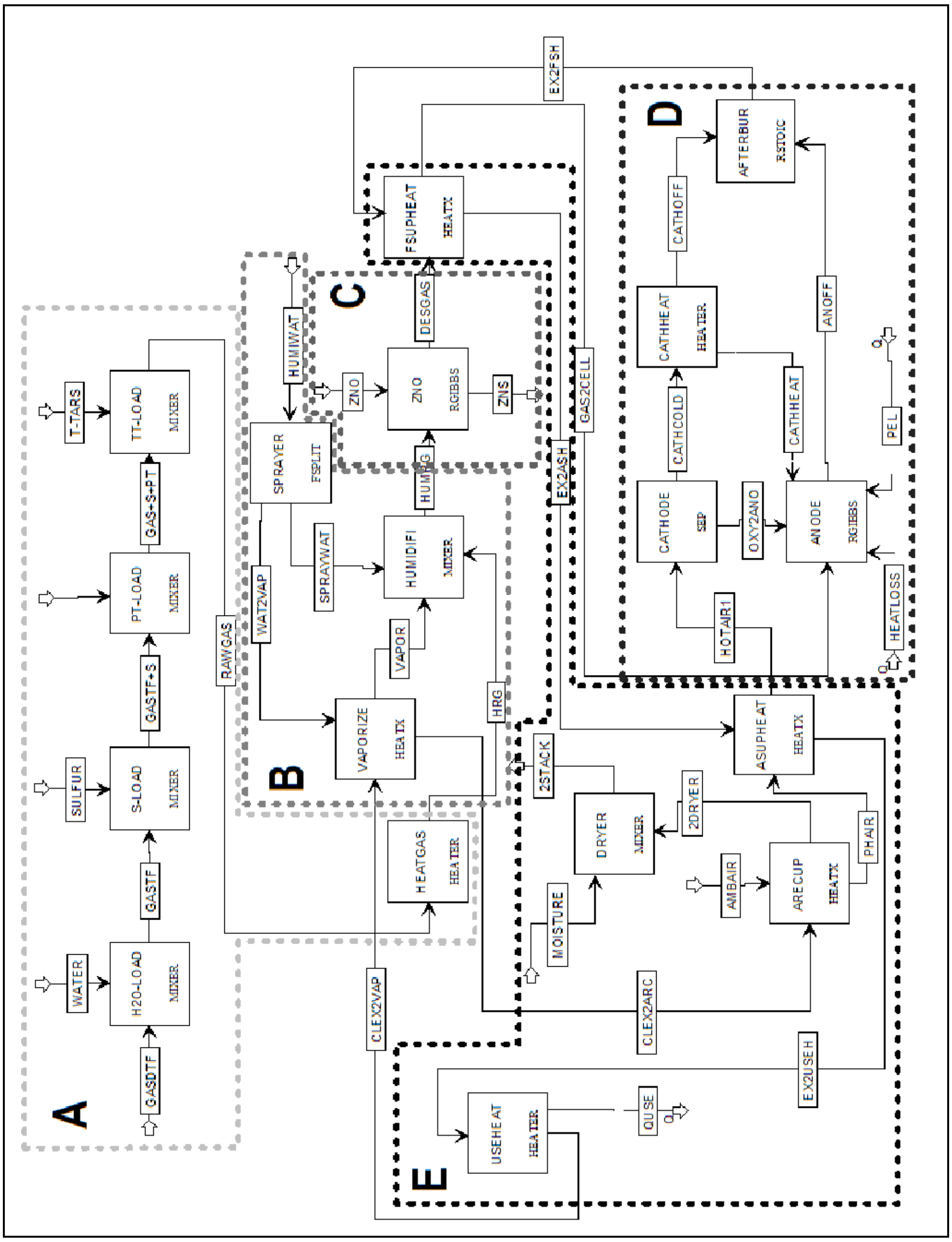
A
B
C
D
E
T-TARS
TT-LOAD
MIXER
GAS+S+PT
PT-LOAD
GASTF+S
SULFUR
S-LOAD
GASTF
WATER
H2O-LOAD
GASDTF
RAWGAS
WAT2VAP
SPRAYER
FSPLIT
HUMIWAT
SPRAYWAT
HUMIDIFI
HUMIG
VAPOR
VAPORIZE
HEATX
HRG
HEATGAS
HEATER
ZNO
RGIBBS
ZNS
DESGAS
FSUPHEAT
EX2FSH
GAS2CELL
EX2ASH
2STACK
DRYER
MOISTURE
2DRYER
ASUPHEAT
AMBAIR
ARECUP
PHAIR
CLEX2ARC
CLEX2VAP
EX2USEH
USEHEAT
QUSE
Q
CATHODE
SEP
OXY2ANO
ANODE
HOTAIR1
HEATLOSS
CATHCOLD
CATHHEAT
CATHOFF
AFTERBUR
RSTOIC
ANOFF
PEL

Section (A) represents the gasification process model which composes the raw gas based on measured input data, see section 5.2.1.

Section (B) is the raw gas humidification unit, see section 5.2.2.

Section (C) comprises gas cleaning and conditioning steps depending on the investigated system design, see sections 5.2.4 to 5.2.6.

Section (D) reproduces the energy and mass balance of the SOFC using the results of the detailed model calculations, see section 5.2.7.

Section (E) is the generalized heat integration network. The heat of the post-combusted SOFC flue gas is used to heat up the anode and cathode gas prior to the SOFC inlet. After this, use heat at 200 °C is extracted from the flue gas. The remaining heat is used for steam generation, air pre-heating and biomass drying, see section 5.2.3.

The second flowsheeting simulation yields the overall process DC power efficiency, the amount of use heat at 200 °C for which all other heat requirements are still satisfied, the areas of all heat exchangers in the heat integration network and other data relevant to component sizing such as sulfur adsorbent mass, steam reforming reactor heat duties etc.

The results of the second flowsheeting simulation are passed to an EXCEL spread sheet where the net AC power efficiency, the equipment sizes, the overall system costs and the power production costs are determined, see section 5.4.

5.2 Flowsheeting models

ASPEN PLUS features a graphical interface, an extensive library of physical property data and equations of state as well as a number of pre-defined unit operation models. Flowsheeting models consist of a number of combined unit operation models. The most important flowsheeting models implemented in this work are discussed below. For more detailed information about ASPEN PLUS models see [17].

5.2.1 Biomass gasifier

A flowsheet model was implemented to reproduce measured producer gas compositions. The corresponding data was either gathered through own measurements or taken from the literature.

Tar is defined as organic matter that can condense under the operating conditions of process units subsequent to the thermochemical conversion process, [186]. For modeling purpose, the variety of potentially present tar species in producer gases was reduced to three representative species:

- **Acetic acid** represents tar species originating from the thermal decomposition of cellulose and hemicellulose.
- **Anisole** represents tar species originating from the thermal decomposition of lignin such as e.g. m-cresol and syringol, [57].
- **Toluene** represents tar species formed in secondary tar reactions such as e.g. xylene, naphthalene.

Data concerning the sulfur load and signature of producer gases is scarce. The sulfur load and the signature were therefore estimated, assuming that all sulfur present in the gasified wood are bound in either **hydrogen sulfide** or **thiophene**. The latter was chosen as representative of organic sulfur species. The ratio between organic and inorganic sulfur species was assumed similar to that of carbon bound in tars to carbon bound in permanent gas species. These are carbon monoxide, carbon dioxide, methane and ethene, respectively.

Figure 5-2 (A) shows that the dry raw gas composition "GASDTF" is first humidified in the unit operation block MIXER "H2O-LOAD". The sulfur species are added to the raw gas in the MIXER "S-LOAD". Acetic acid and anisole as primary tar species are introduced to the raw gas via the MIXER "PT-LOAD". And finally the raw gas is loaded with toluene as tertiary tar species in the MIXER "TT-LOAD". The HEATER "HEATGAS" is used to adjust the raw gas temperature to the measured value.

5.2.2 Gas humidifier

A humidification of the producer gas may be required to prevent carbon deposition problems. In this work, the additional water amount was determined in separate graphite formation equilibrium calculations. As the probability of graphite formation increases with decreasing temperature, the calculations were performed at the lowest system temperature. This way carbon deposition should not occur in the hotter sections of the considered system, especially the SOFC. For e.g. updraft gasifier based systems, where the minimum temperature is almost on ambient level, 300 °C was used for the equilibrium calculations assuming that carbon formation does not occur below this temperature due to kinetic limitations. Figure 5-2 (B) shows that the additional water is added to the raw gas in the MIXER "HUMIDIFI". Depending on the gas temperature requirements of the downstream equipment, the water is added in form of either vapor or wet steam or liquid water. Vapor addition results in a slight gas cool down while liquid water addition may be used for heavy gas cool down. The steam is produced in the evaporator HEATX "VAPORIZE" using flue gas heat, while liquid water is injected via a spray chamber modeled with the block FSPLIT "SPRAYER".

5.2.3 Heat integration network

To recover heat from the post-combusted SOFC flue gas, a generalized however not optimized heat integration network was defined, Figure 5-2 (E). In a first step, the readily processed fuel gas is heated or cooled to the fuel inlet temperature of the SOFC in the heat exchanger block

HEATX "FSUPHEAT" or HEATX "FCOOL", respectively. The flue gas is then guided through the superheater HEATX "ASUPHEAT", where the temperature of the pre-heated cooling air is adjusted to the required SOFC air inlet temperature. After these two high temperature heat exchangers, the flue gas is cooled down to 200 °C in the block HEATER "USEHEAT" to determine the available use heat amount for sales or for the operation of a bottoming cycle. The 200 °C hot flue gas is then introduced to the evaporator block HEATX "VAPORIZE" of the gas humidifier unit to deliver the required heat of evaporation in case steam may be added to the raw producer gas. The remaining heat of the flue gas is used to pre-heat the cooling air in the block HEATX "ARECUP" and to dry the wet biomass in the block MIXER "DRYER" if external drying is required by the gasification process. Successful drying is assumed if the liquid fraction in the flue gas to stack is zero. This indicates that the temperature of the flue gas is high enough to hold the additionally introduced humidity of the biomass.

For all the heat exchangers with two in- and output streams, the ASPEN PLUS unit operation model HEATX was employed. HEATX can be used for the simulation of various shell and tube heat exchangers in co- and counter-current configuration. However, in the present work the shortcut mode was used. The flow configuration was counter-current by default. Based on a user-specified heat duty or cold/hot side outlet temperature ("FSUPHEAT", "FCOOL", "ASUPHEAT") or temperature approach ("ARECUP") or vapor fraction in one of the two outlet streams ("VAPORIZE"), the short cut mode yields a first estimate for the heat exchange area. A differentiation concerning the phase of the heat exchanging streams is done through phase specific heat exchange coefficients. 40 W/m^2 K were assumed for hot vapor-cold liquid and 31.25 W/m^2 K for vapor-boiling heat exchange ("VAPORIZE"), [187]. For vapor-vapor heat exchange, 22.5 W/m^2 K were assumed, [187].

5.2.4 Steam reforming and methanation reactors

Steam reforming (STR) of methane is currently the most readily applied process for syngas production, see section 2.3.2. In this work, a highly active STR catalyst and a relatively homogenous temperature distribution in STR reactors were assumed, [142, 144, 155, 160, 188, 189]. Further, the STR temperature was assumed 100 K below the SOFC design temperature and the minimum steam-to-carbon ratio was set to two by default, [53]. Based on these assumptions, STR reactors were modeled as isothermal equilibrium using the ASPEN PLUS unit operation model RGIBBS by specifying the reactor temperature and pressure. The heat to maintain the STR temperature was subtracted from the SOFC flue gas. RGIBBS computes chemical equilibria as well as simultaneous phase and chemical equilibria by minimizing the Gibbs free energy under atom balance constraints. For this reason no reaction stoichiometry is required for the simulation.

The **Methanation** of producer gases is currently being investigated by the PSI TPE research group, [40]. The adiabatic and thus partial methanation of producer gases has been identified as promising gas processing step in B-IGFC systems. Similar to the STR, highly active catalysts and homogeneous reactor temperatures were assumed. Instead of a reactor temperature, zero heat duty was specified for the RGIBBS simulation of the heat constrained equilibria.

5.2.5 Catalytic partial oxidation reactors

The catalytic partial oxidation (CPO) is an alternative process to the STR. Instead of steam, air or oxygen is used as oxidant gas, see section 2.3.2. The scheme of the CPO process flowsheeting model is shown in Figure 5-3.

Figure 5-3: ASPEN PLUS model of catalytic partial oxidation

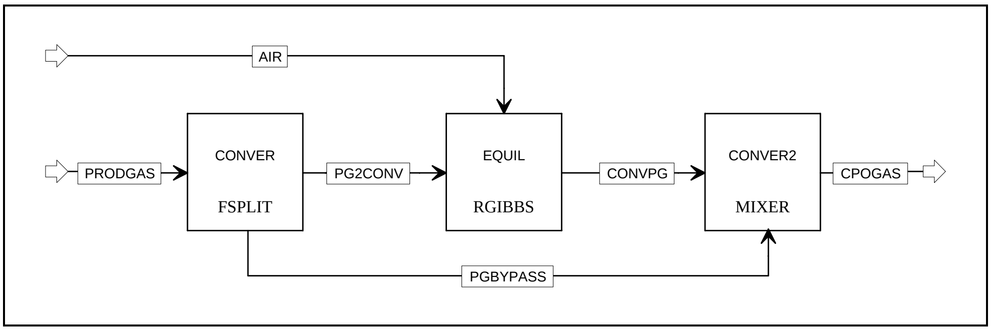

Based on the experimental results reported in [148], see section 3.4.3, the CPO process was modeled as adiabatic equilibrium with incomplete conversion. The block FSPLIT "CONVER" diverts 10 % of the incoming producer gas to a bypass stream. The remainder of the producer gas together with a set amount of air is introduced to the equilibrium block RGIBBS "EQUIL" where the adiabatic equilibrium is calculated. The amount of air depends on the desired air-to-fuel ratio. In the MIXER "CONVER2", the producer gas at equilibrium and the diverted raw producer gas are mixed again.

5.2.6 Sulfur adsorbent beds

Based on the experimental results reported in [149], the hydrogen sulfide adsorption on zinc oxide was modeled as isothermal chemical equilibrium using the ASPEN PLUS model RGIBBS. The block temperature was set to 400 °C by default to ensure safe operation, see section 3.4.4.

Except for H_2S, all gaseous species in the producer gas were marked as inert. The allowed products for the equilibrium calculations were H_2S, H_2O, ZnO, ZnS and metallic Zn. To reproduce the conditions in adsorption reactors, where excess adsorbent is present compared to hydrogen sulfide, the zinc oxide adsorbent mol flow was set to 1 mol/sec. A similar approach was chosen in [168]. Control calculations revealed that the predicted H_2S outlet concentration is independent on the adsorbent mol flow as long as it is higher than the stoiciometric required.

5.2.7 SOFC

The flowsheeting model shown in Figure 5-2 (D) was implemented to enable the application of the results of the ATHENA SOFC model, see section 5.3, to the overall system simulations. The flowsheeting model reproduces the mass and energy balance results of the more intricate ATHENA model. The fuel gas mol flow required to achieve a predefined fuel utilization at a given operational voltage is calculated by the ATHENA model. In the overall system model, this mol flow is used to compute the required dry raw gas mol flow "GASDTF" and thus the mass flow of wood chips. The oxygen ion transfer through the electrolyte is modeled with the separator block SEP "CATHODE". SEP blocks are used to divert single species streams to a certain output stream while the rest of the input stream is guided to given output stream. The oxygen ion mol flow is computed based on the fuel gas mole flow and the fuel utilization predefined for the ATHENA model calculations. The anode is modeled as equilibrium block RGIBBS "ANODE" with a given heat duty. The heat duty depends on the heat required to reproduce the cathode outlet temperature and the power output determined by the ATHENA model. The depleted anode and cathode off gases are post-combusted in a catalytic burner for heat recovery reasons. This burner is modeled with the block RSTOIC "AFTERBUR" as adiabatic combustion. RSTOIC is used when the reaction stoichiometry and degree of conversion is known and the reaction kinetics are either unknown or irrelevant. Combustion reactions are predefined in RSTOIC.

5.3 ATHENA SOFC model

5.3.1 Model description

The envisaged degree of detail in the development of any numerical model largely depends on the desired level of information to be conveyed. In the present work, the development of the numerical SOFC model was focused on investigating the impact of different fuel compositions on state-of-the-art cell designs for power plant applications. Of particular interest were the expected power output for a given combination of fuel composition and cell design and the identification of critical operating conditions such as

- local excess of maximum allowed material temperatures
- and unacceptable temperature gradients.

Against this background, all phenomena and mechanisms which are influenced by the fuel composition and the cell design had to be modeled as detailed as possible or valid assumptions had to be formulated.

5.3.1.1 Assumptions, definitions and model structure

Developing a detailed SOFC model to investigate the impact of different fuel compositions on alternative cell designs involves the formulation of assumptions in order to keep calculation time within reasonable limits allowing for overall system calculations. However, assumptions should not lower the degree of detail of the model such that the desired information is a result of the assumptions.

The main assumptions of the developed SOFC model are:

- Steady-state conditions are assumed.
- Gases are assumed as ideal with temperature-dependent heat capacity, viscosity and thermal conductivity.
- The considered SOFC designs can be divided into a number of repeating structures, termed control volumes (CV).
- Each CV is assumed as continuously stirred tank reactor (CSTR).
- Pressure losses in the gas channels are not considered.
- Due to their high electrical conductivity, the interconnector or bipolar plates of planar cell designs are considered equipotential, [141].
- The flow regime in the gas channels is assumed as plug flow, [190]. Turbulent flow is not considered, despite its possible occurrence in

the oxidant gas channels due to excessive cooling air flows, [191]. Mass transport in normal direction to the flow direction arises via diffusion only.

- A constant Nusselt number with the value 4 is assumed for the calculation of the convective heat transfer coefficients, [190].
- Radiative heat transport between solid structure and gas streams is ignored as the patch length of the radiation is too short for a significant amount of absorbed heat by the gas streams, [191].
- Heat is transferred within the solid structure via heat conduction.
- All heterogeneous reforming reactions are considered so fast, that no diffusion into the porous anode takes place.
- The heats of reaction of all heterogeneous reactions can be attributed to the solid structure of the fuel cell.
- The geometry- and fuel composition-dependent diffusion of the reactants of the reforming reactions through the gas channel to the catalytic surface is considered.
- The water-gas-shift reaction is regarded as non-diffusion limited homogenous reaction which is always at equilibrium.
- The electrochemical oxidation of hydrogen and carbon monoxide are considered to occur in parallel. Direct electrochemical conversion of hydrocarbons is disregarded. Instead, hydrocarbons are oxidized through reforming reactions and subsequent electrochemical conversion of the produced hydrogen and carbon monoxide.

Besides local values such as solid temperature and current density, the developed model calculates integral values which characterize the operational conditions and the performance of the investigated cell design and fuel composition. The definitions of the integral values are given in the following:

- The average solid temperature represents the operational temperature of the cell and is calculate as the arithmetic average of all local temperatures. It is assumed, that the operation of SOFCs is optimized according to the average solid temperature.
- The maximum temperature gradient is the maximum value of the quotient of the temperature difference between adjacent CVs and their length. The calculation is performed for all CVs in order to find the maximum value. In reality this value can hardly be measured.

- The fuel utilization is defined as the ratio of the hydrogen equivalent mol flows at the cell inlet and outlet.

$$UF = 1 - \frac{Eq_{H_2,out}}{Eq_{H_2,in}}$$
$$with\ \ Eq_{H_2} = y_{H_2} + y_{CO} + 4 \cdot y_{CH_4} + 6 \cdot y_{C_2H_4} + 18 \cdot y_{C_7H_8} + 4 \cdot y_{C_2H_4O_2} + 17 \cdot y_{C_7H_8O} \qquad \text{Eq. 36}$$

  - The hydrogen equivalent mol flow, Eq_{H2}, is calculated for the inlet and outlet fuel composition assuming that all hydrocarbons are completely reformed to hydrogen and carbon monoxide and that all carbon monoxide is shifted to hydrogen.
- The air utilization is defined as the ratio of the oxygen mol flows at the cell inlet and outlet. It is equal to the quotient of the fuel utilization and the air-to-fuel ratio.
- The air-to-fuel ratio is defined as the ratio between the effective and the stoichiometry oxygen mol flow for total combustion.
- The average current density is calculated as the quotient of the current produced by the cell or the considered part of the cell and the overall area of the cell or the considered part of the cell. This definition accounts for the fact, that in some cases not the entire cell area participates in the electrochemical reactions e.g. areas which are covered by the interconnector plates, see section 5.3.1.3. The average current density is computed for the total current and for the currents originating from hydrogen or carbon monoxide conversion separately.
- The direct current (DC) power produced is calculated as the product of total produced current and the according operational voltage.
- The electrochemical efficiency is defined as the ratio between produced DC power and the change of enthalpy of the fuel gas.
- The fuel cell efficiency is defined as the ratio between DC power and LHV input to the cell or considered part of the cell, Eq. 182.

The developed model consists of three coupled sub-models, namely the electrochemical performance model, the mass balance model and the energy balance model. The chosen modular structure of the developed model is highly flexible with respect to the integration of further reactions and species.

Figure 5-4 depicts the model structure and the corresponding iterative solution algorithm. The three sub-models are coupled via the fuel composition and the temperatures of the gases and the solid structure yielding a highly non-linear equation system. The solution can therefore only be found iteratively.

Figure 5-4: Model structure and iterative solution algorithm

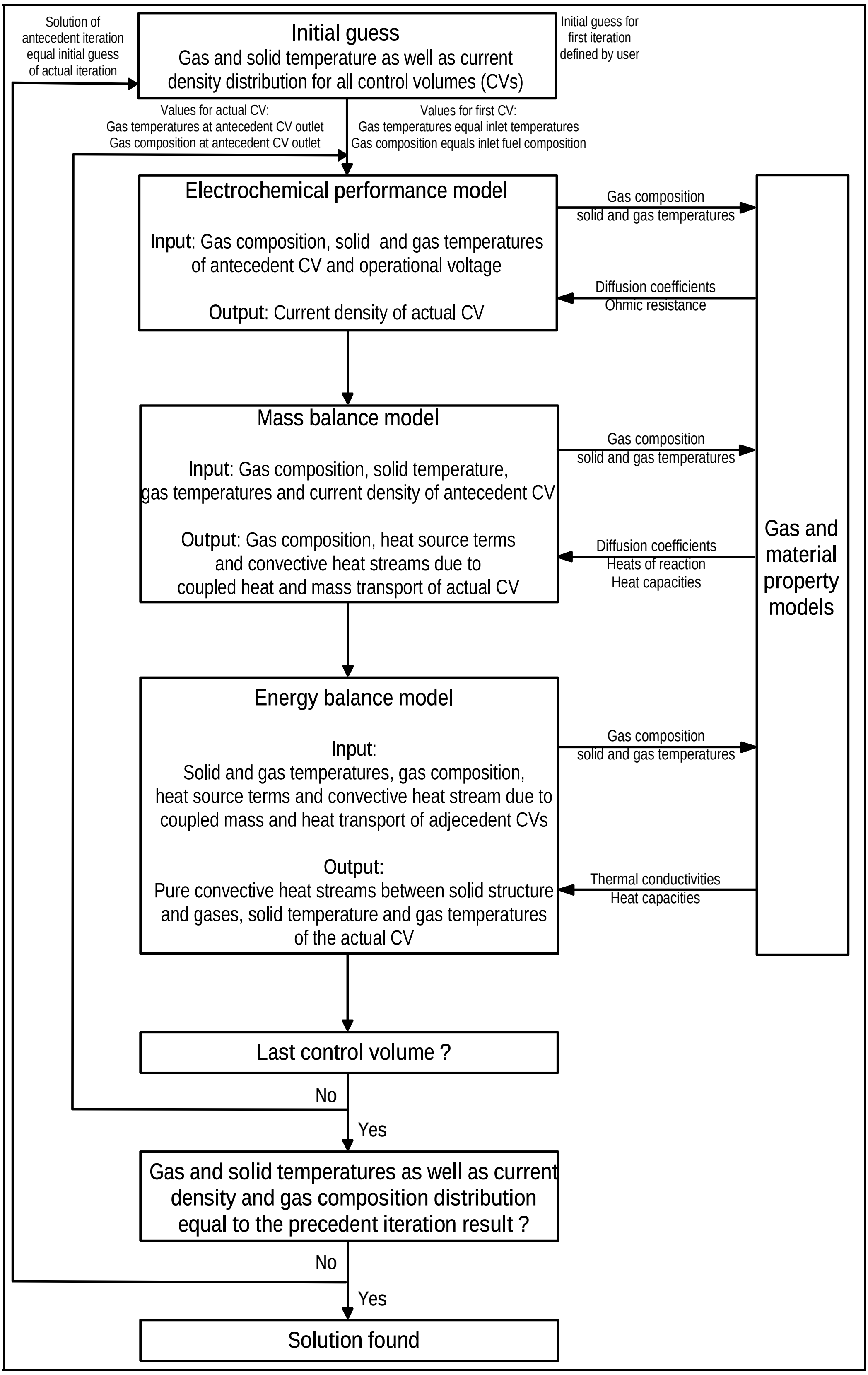
Solution of antecedent iteration equal initial guess of actual iteration
Initial guess
Gas and solid temperature as well as current density distribution for all control volumes (CVs)
Initial guess for first iteration defined by user
Values for actual CV:
Gas temperatures at antecedent CV outlet
Gas composition at antecedent CV outlet
Values for first CV:
Gas temperatures equal inlet temperatures
Gas composition equals inlet fuel composition
Electrochemical performance model
Input: Gas composition, solid and gas temperatures of antecedent CV and operational voltage
Output: Current density of actual CV
Gas composition
solid and gas temperatures
Diffusion coefficients
Ohmic resistance
Mass balance model
Input: Gas composition, solid temperature, gas temperatures and current density of antecedent CV
Output: Gas composition, heat source terms and convective heat streams due to coupled heat and mass transport of actual CV
Gas composition
solid and gas temperatures
Diffusion coefficients
Heats of reaction
Heat capacities
Gas and material property models
Energy balance model
Input:
Solid and gas temperatures, gas composition, heat source terms and convective heat stream due to coupled mass and heat transport of adjecedent CVs
Output:
Pure convective heat streams between solid structure and gases, solid temperature and gas temperatures of the actual CV
Gas composition
solid and gas temperatures
Thermal conductivities
Heat capacities
Last control volume ?
No
Yes
Gas and solid temperatures as well as current density and gas composition distribution equal to the precedent iteration result ?
No
Yes
Solution found

In this work, the modeling package "ATHENA Visual Studio 11.0" was used to implement the numerical code in the FORTRAN language. ATHENA includes strong numerical solver algorithms specifically developed for this kind of numerical problem. Furthermore, ATHENA models can be easily linked with state-of-the-art flow sheeting software packages such as e.g. ASPEN PLUS. A more detailed discussion of the used modeling package can be found elsewhere, [185].

The electrochemical performance model calculates the current density for a given fuel composition and operational voltage in a control volume. The core of the model is the voltage balance according to which the Nernst voltage minus the current density-dependent voltage losses has to equal the operational voltage.

The mass balance model requires the current density as input for the calculation of the conversion rates of the electrochemically active species. According to the afore mentioned assumptions, these are hydrogen, water, carbon monoxide and carbon dioxide. Furthermore, the mass balance model includes the calculation of reaction rates for all considered homogenous and heterogeneous reactions based on applied kinetic models. Besides the calculation of the conversion rates, the mass balance model also calculates the related heat source terms and the convective heat transport terms, which are coupled to the mass transport to and from the catalytic surface.

The energy balance model serves for the calculation of the effective temperatures in the solid structure and the gas channels based on the heat source terms and the convective heat transport terms stemming from the mass balance model. Furthermore, the energy balance model includes the calculation of the purely convective heat transfer between the gases and the solid structure as well as the conductive heat transport within the solid structure.

5.3.1.2 Gas and solid material properties

5.3.1.2.1 Thermodynamic properties of gases

The employed thermodynamic property values are the basis of any numerical model of a technical process or apparatus. Much reliable research has been conducted in this area leading to consistent correlations. The final choice of correlation depends on the process temperature and the temperature variation, which occurs during the process. For processes that are operated in a narrow temperature band it is valid to assume temperature independent material properties, hence applying fixed values. However this approach is not applicable to the present model due to the operational temperatures, which vary from 650 to 1000 °C depending on the cell designs which had to be covered by the model.

For the estimation of the thermodynamic properties of the pure gas species, correlations according to the DIPPR 801 standard (Design Institute for Physical Property Data) were implemented as subroutines, [192].

The DIPPR standard includes the Aly-Lee heat capacity correlation, [193], Eq. 37, where T denotes the corresponding gas temperature.

$$c_{p,x} = B_x + C_x \left(\frac{\frac{D_x}{T}}{\sinh\left(\frac{D_x}{T}\right)} \right)^2 + E_x \left(\frac{\frac{F_x}{T}}{\cosh\left(\frac{F_x}{T}\right)} \right)^2 \qquad \text{Eq. 37}$$

The coefficients (B,C,D,E and F) for the considered pure specie (subscript x) in the model were taken from the flow sheeting package ASPEN PLUS, Table 5-1. Gas mixture heat capacities are calculated through molar fraction weighting.

Table 5-1: Coefficients used in the DIPPR correlation for the estimation of gas heat capacities

Specie	B	C	D	E	F
Hydrogen	27.617	9.56	2466.0	3.76	567.6
Carbon monoxide	29.108	8.773	3085.1	8.4553	1538.2
Carbon dioxide	29.37	34.54	1428.0	26.4	588.0
Water	33.363	26.79	2610.5	8.896	1169.0
Methane	33.298	79.933	2086.9	41.602	991.96
Ethene	33.38	94.79	1596.0	55.1	740.8
Nitrogen	29.1050	8.6149	1701.6	0.1035	909.79
Toluene	58.14	286.3	1440.6	189.8	-650.43
Acetic acid	40.2	136.75	1262.0	70.03	569.7
Anisole	76.37	293.77	1605.1	217.0	751.2
Oxygen	29.103	10.04	2526.5	9.3560	1153.8

The viscosity and thermal conductivity of the pure gas species considered in the model are also computed according to DIPPR correlations, Eq. 38 and Eq. 39, respectively.

$$\eta_x^v = \frac{K_x \cdot T^{L_x}}{1 + \frac{M_x}{T} + \frac{N_x}{T^2}} \qquad \text{Eq. 38}$$

$$\lambda_x^v = \frac{G_x \cdot T^{H_x}}{1+\frac{I_x}{T}+\frac{J_x}{T^2}} \qquad \text{Eq. 39}$$

The coefficients were taken from ASPEN PLUS and are summarized in Table 5-2 and Table 5-3.

Table 5-2: Coefficients used in the DIPPR correlation for the estimation of gas thermal conductivity

Specie	G	H	I	J
Hydrogen	0.002653	0.7452	12.0	0.0
Carbon monoxide	0.00059882	0.6863	57.13	501.92
Carbon dioxide	3.69	-0.3838	964.0	1860000.0
Water	0.0021606	0.76839	3940.5	-445340.0
Methane	6325.2	0.43041	770400000.0	-3.84e+10
Ethene	0.00001744	1.368	439.3	-38700.0
Nitrogen	0.00033143	0.7722	16.323	373.72
Toluene	0.00002392	1.2694	537.0	0.0
Acetic acid	1.691e-6	1.6692	658.0	-95400.0
Anisole	0.00059858	0.7527	354.04	241830.0
Oxygen	0.00044994	0.7456	56.699	0.0

Table 5-3: Coefficients used in the DIPPR correlation for the estimation of gas viscosity

Specie	K	L	M	N
Hydrogen	1.7970e-7	0.685	-0.59	140.0
Carbon monoxide	1.1127e-6	0.5338	94.7	0.0
Carbon dioxide	2.148e-6	0.46	290.0	0.0
Water	6.1839e-7	0.67779	847.23	-73930.0
Methane	5.2546e-7	0.59006	105.67	0.0
Ethene	2.0789e-6	0.4163	352.7	0.0
Nitrogen	6.5592e-7	0.6081	54.714	0.0
Toluene	8.7268e-7	0.49397	323.79	0.0
Acetic acid	2.7449e-8	1.0123	7.4948	0.0
Anisole	1.7531e-7	0.72	176.17	0.0
Oxygen	1.1010e-6	0.5634	96.3	0.0

The calculation of the viscosity of mixtures is undertaken according to the Wilke approximation of the Chapman-Enskog equation, Eq. 40, [194].

$$\eta_{mix}^v = \sum_i \frac{y_i \cdot \eta_i^v}{\sum_j y_j \cdot \phi_{ij}} \quad with \quad \phi_{ij} = \frac{\left(1+\left(\frac{\eta_i^v}{\eta_j^v}\right)^{0.5}\left(\frac{M_j}{M_i}\right)^{0.25}\right)^2}{\left(8\cdot\left(1+\frac{M_i}{M_j}\right)\right)^{0.5}} \qquad \text{Eq. 40}$$

Eq. 40 involves the molar fractions of the mixture, y, the pure specie viscosity, η^v, and the interaction parameter ϕ_{ij} which further involves the molar weight of the pure species, M.

The calculation of the thermal conductivity of mixtures is done using the Wassiljewa-Mason-Saxena mixing rule, Eq. 41, [194].

$$\lambda^v_{mix} = \sum_i \frac{y_i \cdot \lambda^v_i}{\sum_j y_j \cdot A_{ij}} \quad with \quad A_{ij} = \frac{\left(1 + \left(\frac{\eta^v_i}{\eta^v_j}\right)^{0.5} \left(\frac{M_j}{M_i}\right)^{0.25}\right)^{0.5}}{\left(8 \cdot \left(1 + \frac{M_i}{M_j}\right)\right)^{0.5}} \qquad \text{Eq. 41}$$

Besides the already mentioned variables, Eq. 41 involves the interaction parameter A_{ij}. The implemented subroutines were checked against ASPEN PLUS results and proved correct.

In order to enable the prediction of diffusion limited phenomena, the developed model includes a subroutine for the calculation of effective diffusion coefficients. Two diffusion mechanisms were considered to describe the diffusion of gases through porous media such as the electrodes of fuel cells. The first mechanism is the Knudsen diffusion, which is of importance when the mean free path length of the gas molecules is large, compared to the pore diameter. In this case, the molecules collide more often with the pore walls then with each other. The corresponding Knudsen diffusion coefficient is calculated according to Eq. 42, where r_{pore} denotes the average pore radius of the porous media and $v_{av,x}$ denotes the average molecular speed of the species x. The calculation of $v_{av,x}$ involves the ideal gas constant R, temperature T and molecular weight, M_i.

$$D_{K,x} = \frac{2}{3} \cdot r_{pore} \cdot v_{av,x} \quad with \quad v_{av,x} = \left(\frac{8 \cdot R \cdot T}{\pi \cdot M_i}\right)^{0.5} \qquad \text{Eq. 42}$$

The second diffusion mechanism is the molecular diffusion, where the mean free path length of the molecules is small compared to the pore diameter. In this case, the gas molecules collide more frequently with each other than with the pore walls.

For the calculation of the molecular diffusion coefficients two methods were implemented in the subroutine. The first method according to the kinetic gas theory features an average variance of 8 % and can be applied to a wide range of pure species including e.g. acetic acid. Detailed information about the method based on the kinetic gas theory can be found in [194]. The second method is the empirical Fuller method derived from an extensive experimental data base and featuring an average variance of 4 %. The Fuller equation, Eq. 43, comprises the temperature, T, the pressure, p, the molecular weight relation between the diffusing specie (subscript x) and the matrix specie (subscript z), M_{zx}, and the atomic diffusion volumes, V_z *and* V_x. The atomic diffusion volumes have to be determined experimentally, which is the major drawback of the Fuller method.

$$D_{m,zx} = \frac{0.00143 \cdot T^{1.75}}{p \cdot M_{zx}^{0.5} \cdot \left(V_z^{0.33} + V_x^{0.33}\right)^2} \quad with \quad M_{zx} = 2 \cdot \left(\frac{1}{M_z} + \frac{1}{M_x}\right)^{-1} \qquad \text{Eq. 43}$$

Based on the atomic diffusion volumes, which are only available for very common species such as e.g. hydrogen, carbon monoxide, water etc., the Fuller method is less flexible than the kinetic gas theory method. Approximation correlations are available for the atomic diffusion volume of more exotic species, [194], but the impact on the accuracy of the results is unknown. Nevertheless, the Fuller method was chosen as standard method, the reason being that the partial pressures of the exotic species considered in the developed model are expected to be small compared to the common species. The employed atomic diffusion volumes are given in Table 5-4.

Table 5-4:
Fuller atomic diffusion volumes and molecular weight of considered species

*Value approximated

Specie	Fuller atomic diffusion volume [m³/mol]	Molecular weight [g/mol]
Hydrogen	6.12	2.01588
Carbon monoxide	18.0	28.0104
Carbon dioxide	26.9	44.0098
Water	13.1	18.01528
Methane	25.14 *	16.04276
Ethene	41.04 *	28.05376
Nitrogen	18.5	28.01348
Toluene	111.48 *	92.14052
Acetic acid	53.26 *	60.05256
Anisole	117.59 *	108.13992
Oxygen	16.3	31.9988

Eq. 43 only allows for the calculation of binary diffusion coefficients. In order to estimate the molecular diffusion coefficient of a specific specie in gas mixtures, the following mixing rule was implemented, Eq. 44, [194].

$$D_{m,mix,x} = \frac{1-y_x}{\sum_i \frac{y_i}{D_{m,i,x}}} \qquad \text{Eq. 44}$$

Eq. 44 comprises the molar fraction of the diffusing specie, y_x, the molar fractions of the all species in the gas mixture, y_i, and the binary molecular diffusion coefficients of the diffusing specie with all other species in the gas mixture, $D_{m,i,x}$.

5.3.1.2.2 Temperature-dependent solid material properties

The materials used in solid oxide fuel cells have to fulfill different tasks hence influencing the behavior of the cell. The most important properties in this respect are the electrical and the ionic conductivity, which directly impact the power output of the cell. As a general rule, the ceramic materials employed in solid oxide fuel cells feature only poor electrical and ionic conductivities at room temperatures. At elevated temperatures however the conductivity improves. The relation between specific conductivity and temperature was mathematically formulated in [191] for state-of-the-art materials. Equations Eq. 45 to Eq. 48 give the specific conductivities as functions of the temperature for the anode (ρ_{an}), electrolyte (ρ_{el}), cathode (ρ_{ca}) and interconnect (ρ_{ic}) materials, respectively.

$$\rho_{an} = \frac{95.0 \cdot 10^6}{TsK} \cdot \exp\left(\frac{-1150.0}{TsK}\right) \qquad \text{Eq. 45}$$

$$\rho_{el} = 3.34 \cdot 10^4 \cdot \exp\left(\frac{10300.0}{TsK}\right) \qquad \text{Eq. 46}$$

$$\rho_{ca} = \frac{42.0 \cdot 10^6}{TsK} \cdot \exp\left(\frac{-1200.0}{TsK}\right) \qquad \text{Eq. 47}$$

$$\rho_{ic} = \frac{9.3 \cdot 10^6}{TsK} \cdot \exp\left(\frac{-1100.0}{TsK}\right) \qquad \text{Eq. 48}$$

The variable TsK denotes the solid material temperature. The corresponding curves are depicted in Figure 5-5.

It can be seen, that even at very elevated temperatures the electric conductivity of the employed materials for the anode and cathode electrodes as well as for the current collectors (also called interconnectors, IC) are three orders of magnitude higher than the ionic conductivity of the electrolyte. Further it can be observed, that small temperature variations from e.g. 1100 K to 1300 K result in an increase of the ionic conductivity by a factor of five.

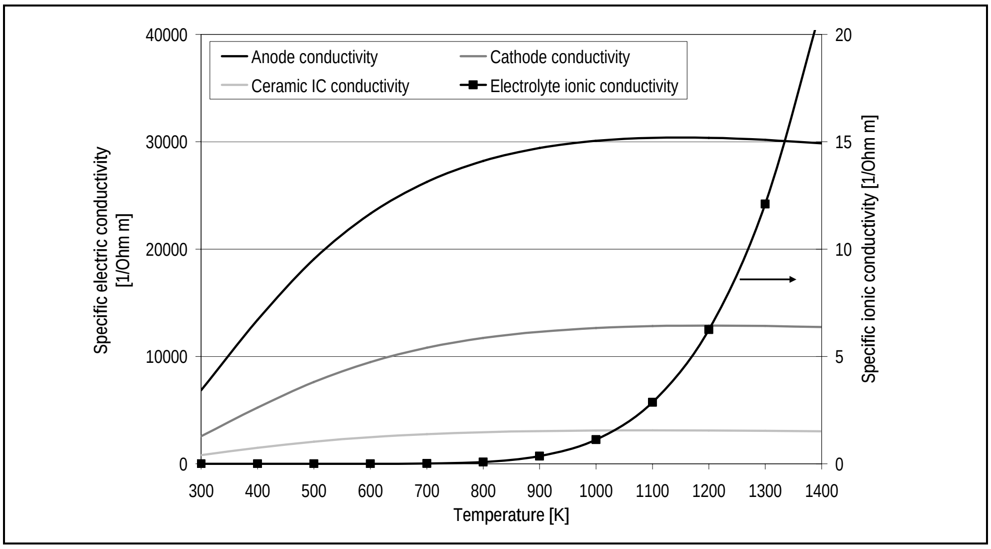

Figure 5-5: Specific electric conductivity of anode, cathode and ceramic interconnect material (left scale) and ionic conductivity of electrolyte (right scale)

5.3.1.3 Geometries and discretization

The range of fuel cell designs under development mainly differs in two aspects, which are the geometry and the materials employed in the fuel cell components. Concerning the term geometry, it is useful to distinguish between the macro and the micro geometry of fuel cells. The micro geometry describes the construction of the anode-electrolyte-cathode (AEC) assembly, while the macro geometry describes the construction of the cell itself.

The micro geometry has a strong influence on the electrochemical performance of the fuel cell through ohmic losses and transport limitations due to the diffusion of the reacting species through the electrodes to the electrolyte where the electrochemical reactions take place.

The macro geometry of a given fuel cell design has an impact on the electrochemical performance through ohmic losses occurring in the current conducting components of the fuel cell, the heat balance through convective and conductive heat exchange processes and the mass balance through the catalytically active surfaces areas.

Hence, micro and macro geometry have a strong bearing on the overall behavior of the fuel cell. Accounting for this was one of the most important requirements regarding the developed model. The model had to be capable of representing fuel cells with different macro geometries, such as tubular and planar fuel cells, and different micro geometries, such as electrolyte-supported and anode-supported planar fuel cells. The chosen approach for the geometry description is based on characteristic lengths and areas. The according definitions of characteristic lengths and areas for the considered geometries are presented in the following.

5.3.1.3.1 Planar geometry

Figure 5-6 depicts the considered planar geometry. The planar cell stack consists of bipolar plates, which also form the rectangular gas channels. The bipolar plates are separated by AEC assemblies. The surface of the AEC assemblies is consequently partially covered by the ribs of the bipolar plates. As assumed above, the cell is divided into repeating structures according to the number of gas channels.

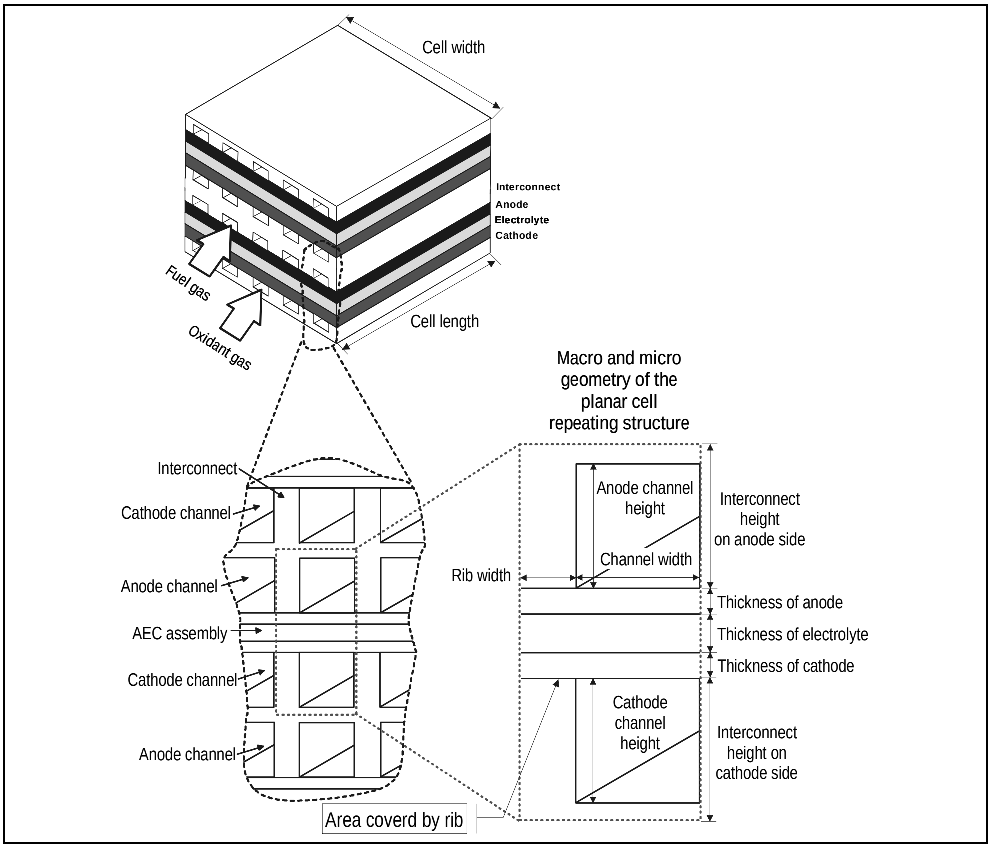
Cell width
Interconnect
Anode
Electrolyte
Cathode
Fuel gas
Oxidant gas
Cell length
Macro and micro geometry of the planar cell repeating structure
Interconnect
Cathode channel
Anode channel
AEC assembly
Cathode channel
Anode channel
Area coverd by rib
Rib width
Anode channel height
Channel width
Interconnect height on anode side
Thickness of anode
Thickness of electrolyte
Thickness of cathode
Cathode channel height
Interconnect height on cathode side

Figure 5-6: Generalized planar cell geometry and repeating structure description

The micro geometry of the planar cell design is entirely expressed by the thicknesses of the anode, $\delta_{p,an}$, electrolyte, $\delta_{p,el}$, and cathode, $\delta_{p,ca}$. The complete description of the macro geometry includes the number of gas channels, n_{ch}, the cell length, l_c, and width, w_{ce}, the anode and cathode gas channel heights, $h_{p,an}$, $h_{p,ca}$, and width, w_c, and the interconnect or bipolar plate height on the anode and cathode side, $h_{ic,an}$, $h_{ic,ca}$. Based on these geometrical values, the following characteristic lengths and areas were defined for the repeating structure of the planar geometry:

- Total active area, $A_{p,act}$

$$A_{p,act} = \left(w_{ce} / n_{ch}\right) \cdot l_c \qquad \text{Eq. 49}$$

- Electrochemically active length, $l_{p,elact}$, where $x_{p,elact}$ denotes the fraction of the area covered by a rib participating in electrochemical reactions

$$l_{p,elact} = w_c + \left(\left(w_{ce}/n_{ch}\right) - w_c\right) \cdot x_{p,elact} \qquad \text{Eq. 50}$$

- Chemically active length, $l_{p,chact}$, where $x_{p,chact}$ denotes the fraction of the area covered by a rib contributing to chemical reactions

$$l_{p,chact} = w_c + \left(\left(w_{ce}/n_{ch}\right) - w_c\right) \cdot x_{p,chact} \qquad \text{Eq. 51}$$

- Hydraulic diameter of anode gas channel, $d_{p,hyd,an}$

$$d_{p,hyd,an} = (2 \cdot w_c \cdot h_{p,an})/(w_c + h_{p,an}) \qquad \text{Eq. 52}$$

- Hydraulic diameter of cathode gas channel, $d_{p,hyd,ca}$

$$d_{p,hyd,ca} = (2 \cdot w_c \cdot h_{p,ca})/(w_c + h_{p,ca}) \qquad \text{Eq. 53}$$

- Circumferential length of anode gas channel perpendicular to gas flow direction, $l_{p,circ,an}$

$$l_{p,circ,an} = 2 \cdot (w_c + h_{p,an}) \qquad \text{Eq. 54}$$

- Circumferential length of cathode gas channel perpendicular to gas flow direction, $l_{p,circ,ca}$

$$l_{p,circ,ca} = 2 \cdot (w_c + h_{p,ca}) \qquad \text{Eq. 55}$$

- Cross-sectional area of solid structure perpendicular to gas flow direction, $A_{p,cross}$

$$A_{p,cross} = \left(w_{ce}/n_{ch}\right) \cdot \left(h_{ic,an} + \delta_{p,an} + \delta_{p,el} + \delta_{p,ca} + h_{ic,ca}\right) - w_c \cdot \left(h_{p,an} + h_{p,ca}\right) \qquad \text{Eq. 56}$$

5.3.1.3.2 Tubular geometry

Figure 5-7 depicts the tubular geometry based on the cell design promoted by the Siemens AG. The standard tubular cell consists of a fuel cell tube with one closed end and a concentrical air delivery tube (ADT). The annular gap between the outer surface of the ADT and inner surface of the fuel cell tube forms the cathode gas channel. The anode gas flows around the outer surface of the fuel cell tube. The geometry of the anode gas channel is not defined by the cell design itself but rather by the arrangement of the single fuel cell tube in the whole stack. For modeling purpose however, an annular gap shaped anode gas channel was assumed. In the case of the tubular geometry, the fuel cell tube itself was considered as a repeating structure in the complete fuel cell stack.

Similar to the planar cell geometry, the micro geometry of the tubular cell design is entirely described by the thicknesses of the anode, $\delta_{t,an}$, the electrolyte, $\delta_{t,el}$, and the cathode, $\delta_{t,ca}$. The complete description of the tubular cell design macro geometry encompasses the active tube length, l_t, the inner, $r_{i,ADT}$, and outer radius, $r_{o,ADT}$, of the air delivery tube, the inner radius of the fuel cell tube, $r_{i,FC}$, and the height of the virtual anode channel, $h_{t,an}$.

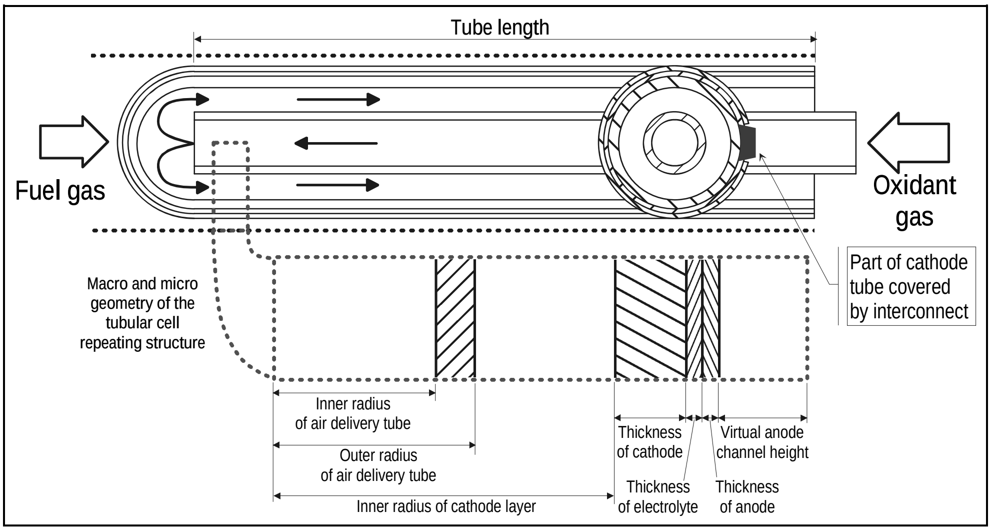
Tube length
Fuel gas
Oxidant gas
Part of cathode tube covered by interconnect
Macro and micro geometry of the tubular cell repeating structure
Inner radius of air delivery tube
Outer radius of air delivery tube
Inner radius of cathode layer
Thickness of cathode
Virtual anode channel height
Thickness of electrolyte
Thickness of anode

Figure 5-7: Standard tubular cell geometry

Similar to the planar geometry, the following characteristic lengths and areas were defined for the repeating structure of the tubular geometry:

- Middle radius of the AEC assembly, $r_{m,AEC}$

$$r_{m,AEC} = r_{i,FC} + (\delta_{t,ca} + \delta_{t,el} + \delta_{t,an}) / 2 \qquad \text{Eq. 57}$$

- Outer radius of the cell tube, $r_{o,FC}$

$$r_{o,FC} = r_{i,FC} + \delta_{t,ca} + \delta_{t,el} + \delta_{t,an} \qquad \text{Eq. 58}$$

- Total active area, $A_{t,act}$

$$A_{t,act} = 2\pi \cdot r_{m,AEC} \cdot l_t \qquad \text{Eq. 59}$$

- Electrochemically active circumferential length, $l_{t,elact}$, where $x_{t,ic}$ denotes the fraction of the cell tube surface covered by the interconnect

$$l_{t,elact} = 2\pi \cdot r_{m,AEC} \cdot (1 - x_{t,ic}) \qquad \text{Eq. 60}$$

- Chemically active circumferential length, $l_{t,chact}$, where $x_{t,ic}$ denotes the fraction of the cell tube surface covered by the interconnect

$$l_{t,chact} = 2\pi \cdot r_{o,FC} \cdot (1 - x_{t,ic}) \quad \text{Eq. 61}$$

- Hydraulic diameter of air delivery tube, $d_{t,hyd,ADT}$

$$d_{t,hyd,ADT} = 2 \cdot r_{i,ADT} \quad \text{Eq. 62}$$

- Hydraulic diameter of virtual anode gas channel, $d_{t,hyd,an}$

$$d_{t,hyd,an} = 2 \cdot h_{t,an} \quad \text{Eq. 63}$$

- Hydraulic diameter of cathode gas channel, $d_{t,hyd,ca}$

$$d_{t,hyd,ca} = 2 \cdot (r_{i,FC} - r_{o,ADT}) \quad \text{Eq. 64}$$

- Circumferential length of air delivery tube perpendicular to gas flow direction, $l_{t,circ,ADT}$

$$l_{t,circ,ADT} = \pi \cdot (r_{o,ADT} + r_{i,ADT}) \quad \text{Eq. 65}$$

- Circumferential length of virtual anode gas channel perpendicular to gas flow direction, $l_{t,circ,an}$

$$l_{t,circ,an} = 2\pi \cdot r_{o,FC} \cdot (1 - x_{t,ic}) \quad \text{Eq. 66}$$

- Circumferential length of cathode gas channel perpendicular to gas flow direction, $l_{t,circ,ca}$

$$l_{t,circ,ca} = 2\pi \cdot r_{i,FC} \quad \text{Eq. 67}$$

- Cross-sectional area of solid structure perpendicular to gas flow direction, $A_{t,cross}$

$$A_{t,cross} = (\pi \cdot r_{o,FC}^2) - (\pi \cdot r_{i,FC}^2) \quad \text{Eq. 68}$$

5.3.1.3.3 Triangular geometry

Figure 5-8 depicts the triangular geometry based on the latest Siemens AG cell design referred to as Delta8 design (D8). Similar to the standard tubular cell design, the D8 employs centered air delivery tubes (ADT) for the injection of the cathode air. The D8 cell is composed of eight connected triangular-shaped fuel cell tubes with closed ends, Figure 5-8a. The spaces between the ADTs and inner surface of a triangular fuel cell tubes form the cathode gas channels, Figure 5-8d.

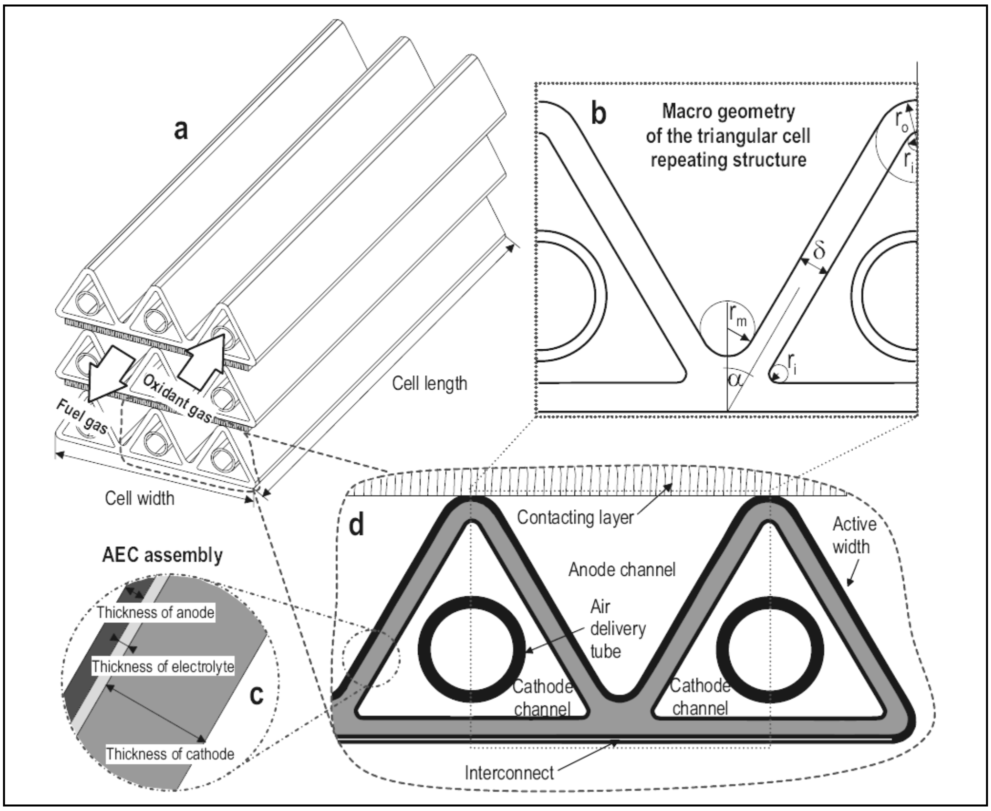
a
Cell length
Fuel gas
Oxidant gas
Cell width
AEC assembly
Thickness of anode
Thickness of electrolyte
Thickness of cathode
c
b
Macro geometry
of the triangular cell
repeating structure
r_o
r_i
δ
r_m
α
r_i
d
Contacting layer
Active width
Anode channel
Air delivery tube
Cathode channel
Cathode channel
Interconnect

Figure 5-8: Triangular cell geometry

The outer upper surface of the D8 cell and the outer lower surface of the next D8 cell form the anode gas channels, Figure 5-8d. Note that the D8 cells are stacked like planar cells, Figure 5-8a. For better contacting and current distribution, a porous contact layer is placed between the individual cells. Due to its high electrical conductivity and porosity, the contact layer was not considered in the developed model. The D8 repeating structure was defined as one triangular-shaped fuel cell tube.

Similar to the above discussed geometries, the micro geometry of the triangular cell design is entirely described by the thicknesses of the anode, $\delta_{D8,an}$, the electrolyte, $\delta_{D8,el}$, and the cathode, $\delta_{D8,ca}$, Figure 5-8c.

The description of the triangular cell design macro geometry is more complex than that of the standard tubular and planar cell design. However, the complexity can be reduced by introducing geometrical dependencies for the curvature radii. For the model, it was assumed, that the upper outer curvature radius r_o equals 1.5 times the D8 cell tube wall thickness δ. The lower outer curvature radius r_m was assumed equal to the cell tube wall thickness and the inner curvature radius r_i equal to half the cell tube wall thickness, Figure 5-8b.

Based on the above assumptions and the overall cell width, w_{D8}, the cell length, l_{D8}, the upper triangle half-angle, α, and the number of triangular-shaped fuel cell tubes forming the D8 cell, n_{tri}, the following characteristic lengths and areas were derived for the triangular geometry:

- Electrochemically and chemically active width, $l_{D8,elact}$

$$l_{D8,elact} = l_{D8,chact} = \frac{2\delta}{n_{tri}\cdot\cos\alpha} + \frac{90-\alpha}{n_{tri}\cdot 90}\cdot\pi\cdot\delta + 2\cdot X$$
$$with\ X = \frac{w_{D8}}{n_{tri}} - \frac{5}{2}\cdot\frac{\delta}{\tan\alpha} + \frac{90-\alpha}{72}\cdot\pi\cdot\delta \qquad \text{Eq. 69}$$

The active width of one control volume is the arithmetic middle of the overall active width of the D8 cell and the number of triangular cell tubes. Note that the additional electrochemically active areas of the lower curvature of the two outer triangular cells were also considered, Figure 5-8d.

- Total active area, $A_{D8,act}$

$$A_{D8,act} = l_{D8,elact}\cdot l_{D8} \qquad \text{Eq. 70}$$

- Circumferential length of ADT perpendicular to gas flow, $l_{D8,circ,ADT}$

$$l_{D8,circ,ADT} = \pi\cdot\left(r_{D8,o,ADT} + r_{D8,i,ADT}\right) \qquad \text{Eq. 71}$$

- Circumferential length of anode channel perpendicular to gas flow, $l_{D8,circ,an}$

$$l_{D8,circ,an} = l_{D8,elact} + \frac{w_{D8}}{n_{tri}} \qquad \text{Eq. 72}$$

- Circumferential length of cathode channel perpendicular to gas flow, $l_{D8,circ,ca}$

$$l_{D8,circ,ca} = \frac{\sin\alpha+1}{\sin\alpha}\cdot\left(\frac{w_{D8}}{n_{tri}} - \frac{\delta+2\cdot\sin\alpha}{\cos\alpha}\right) + \frac{90+\alpha}{120}\cdot\pi\cdot\delta - \frac{3\cdot\delta}{\tan(45-\alpha/2)} \qquad \text{Eq. 73}$$

- Cross-sectional area of cathode channel, $A_{D8,cross,ca}$

$$A_{D8,cross,ca} = \frac{X^2}{4\cdot\tan\alpha} + \frac{3}{4}\cdot\delta^2\cdot\left(\frac{90+\alpha}{360}\cdot\pi - \cot\left(45-\frac{\alpha}{2}\right)\right) - \pi\cdot r_{D8,o,ADT}^2$$
$$with\ \ X = \left(\frac{w_{D8}}{n_{tri}} - \frac{\delta+2\cdot\sin\alpha}{\cos\alpha}\right) \qquad \text{Eq. 74}$$

- Cross-sectional area of anode channel, $A_{D8,cross,an}$

$$\begin{aligned}
&A_{D8,cross,an} = X^2 \cdot \tan\alpha + Y \cdot \frac{9}{4} \cdot \delta^2 - \frac{5}{4} \cdot \pi \cdot \delta^2 \cdot \frac{90-\alpha}{180} - \frac{\delta^2}{\tan\alpha} \\
&with \;\; X = \frac{w_{D8} \cdot \cos\alpha + n_{tri} \cdot \delta \cdot (\sin\alpha - 2)}{2 \cdot n_{tri} \cdot \sin\alpha} \\
&and \;\; Y = \frac{2 \cdot \sin\alpha + \cos\alpha - 1 - \sin^2\alpha}{\sin\alpha \cdot \cos\alpha}
\end{aligned} \qquad \text{Eq. 75}$$

- Cross-sectional area of solid structure, $A_{D8,cross}$

$$\begin{aligned}
&A_{D8,cross} = \frac{w_{D8}}{n_{tri}} \cdot X - A_{D8,cross,ca} - A_{D8,cross,an} - \pi \cdot r_{D8,o,ADT}^2 \\
&with \;\; X = \left(\frac{w_{D8} \cdot \cos\alpha}{2 \cdot n_{tri} \cdot \sin\alpha} - \frac{\delta}{\sin\alpha} + \frac{3}{2} \cdot \delta \right)
\end{aligned} \qquad \text{Eq. 76}$$

- Hydraulic diameter of ADT, $d_{D8,hyd,ADT}$

$$d_{D8,hyd,ADT} = 2 \cdot r_{D8,i,ADT} \qquad \text{Eq. 77}$$

- Hydraulic diameter of anode gas channel, $d_{D8,hyd,an}$

$$d_{D8,hyd,an} = \frac{4 \cdot A_{D8,cross,an}}{l_{D8,circ,an}} \qquad \text{Eq. 78}$$

- Hydraulic diameter of cathode gas channel, $d_{D8,hyd,ca}$

$$d_{D8,hyd,ca} = \frac{4 \cdot A_{D8,cross,ca}}{l_{D8,circ,an} + 2 \cdot \pi \cdot r_{D8,i,ADT}} \qquad \text{Eq. 79}$$

5.3.1.4 Electrochemical performance model

The electrochemical performance model calculates the current density for a given fuel composition and operational voltage.

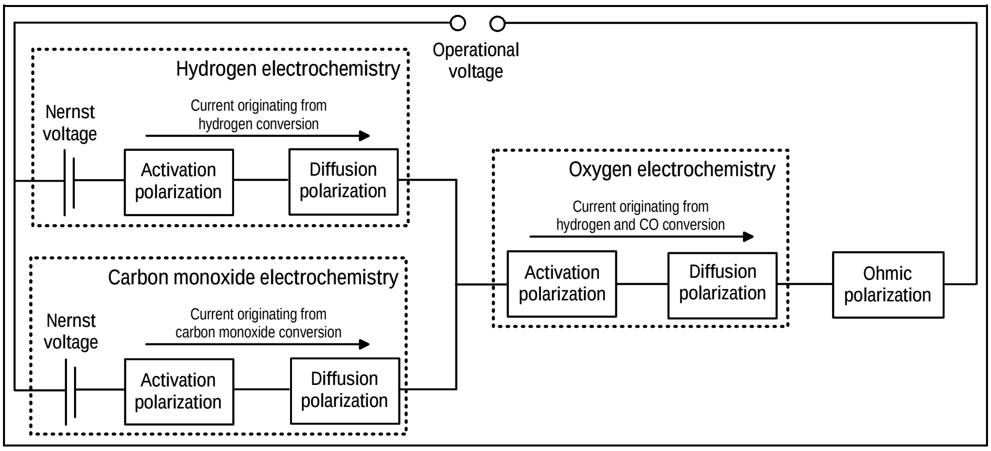
Operational voltage
Hydrogen electrochemistry
Nernst voltage
Current originating from hydrogen conversion
Activation polarization
Diffusion polarization
Carbon monoxide electrochemistry
Nernst voltage
Current originating from carbon monoxide conversion
Activation polarization
Diffusion polarization
Oxygen electrochemistry
Current originating from hydrogen and CO conversion
Activation polarization
Diffusion polarization
Ohmic polarization

Figure 5-9: Equivalent circuit of the electrochemical performance model

To meet the requirement of high fuel flexibility, the electrochemical conversion of hydrogen and carbon monoxide was considered to occur in parallel. Furthermore, activation, ohmic and diffusion losses were considered.

Figure 5-9 shows the equivalent circuit of the electrochemical performance model, assuming that the voltage losses can be treated as electrical resistors. The corresponding equation system is highly non-linear and a solution for the current density can only be found numerically.

The starting point for the calculation of the current density is the reversible potential of the given fuel gas composition, commonly referred to as the Nernst voltage. The Nernst voltage of the hydrogen oxidation, $E_{Nernst,H2}$, is calculated according to Eq. 80 and for the carbon monoxide oxidation, $E_{Nernst,CO}$, following Eq. 81.

$$E_{Nernst,H_2} = \left(\frac{R \cdot TsK}{n \cdot F}\right) \cdot \left(\ln Kp_{H_2 oxi} + \ln\left(\frac{p_{H_2} \cdot p_{O_2}{}^{0.5}}{p_{H_2O}}\right)\right) \qquad \text{Eq. 80}$$

$$E_{Nernst,CO} = \left(\frac{R \cdot TsK}{n \cdot F}\right) \cdot \left(\ln Kp_{CO oxi} + \ln\left(\frac{p_{CO} \cdot p_{O_2}{}^{0.5}}{p_{CO_2}}\right)\right) \qquad \text{Eq. 81}$$

In Eq. 80 and Eq. 81, R denotes the ideal gas constant, TsK stands for the solid structure temperature, n represents the number of transferred electrons (in both cases 2), F is the Faraday constant, Kp is the equilibrium constant and the factors p_i represent the partial pressures of the products and educts of the oxidation reactions in the bulk gas phase.

In this work, the equilibrium constant values for the hydrogen and carbon monoxide oxidation reaction were taken from [195]. The tabulated values were compiled to yield two fit correlations, which both take the form of Eq. 82.

$$X = y_0 + A_1 \exp\left(\frac{-TsK}{t_1}\right) + A_2 \exp\left(\frac{-TsK}{t_2}\right) + A_3 \exp\left(\frac{-TsK}{t_3}\right) \qquad \text{Eq. 82}$$

X denotes either the equilibrium constant of the hydrogen oxidation or of the carbon monoxide oxidation, depending on the employed set of fit correlation coefficients, Table 5-5.

Figure 5-9 shows that the Nernst voltages of the hydrogen and carbon monoxide oxidation minus the according current density-dependent voltage losses have to equal the operational voltage of the fuel cell (E_{op}), Eq. 83 and Eq. 84.

Table 5-5: Coefficients of the equilibrium constant fit correlation for hydrogen and carbon monoxide oxidation

Coefficient	Hydrogen oxidation	Carbon monoxide oxidation
y_0	-1.093	-3.020
A_1	42.296	376.372
t_1	1297.858	94.704
A_2	106.613	143.468
t_2	319.283	284.902
A_3	284.347	51.766
t_3	107.556	1179.242

$$E_{op} = E_{Nernst,H_2} - \eta_{act,H_2} - \eta_{diff,H_2} - \eta_{act,O_2} - \eta_{diff,O_2} - \eta_{ohm} \quad \text{Eq. 83}$$

$$E_{op} = E_{Nernst,CO} - \eta_{act,CO} - \eta_{diff,CO} - \eta_{act,O_2} - \eta_{diff,O_2} - \eta_{ohm} \quad \text{Eq. 84}$$

Consequently the developed model must distinguish between currents originating from either the oxidation of hydrogen, I_{H2}, or of carbon monoxide, I_{CO}, which sum up to the total produced current, I_{tot}, Eq. 85.

$$I_{tot} = I_{H_2} + I_{CO} \quad \text{Eq. 85}$$

From Eq. 83 and Eq. 84 or Figure 5-9 it can be seen, that a current originating from carbon monoxide oxidation can only be produced, when the corresponding Nernst voltage minus the voltage losses of the oxygen electrochemistry and the ohmic losses, due to an already flowing current originating from hydrogen oxidation, still yields a positive value. The same applies vice versa.

5.3.1.4.1 Activation polarization

Even though no current is drawn from the fuel cell, the electrochemical reactions, Eq. 86, Eq. 87 (anode) and Eq. 88 (cathode), are taking place.

$$H_2 + O^{2-} \leftrightarrow H_2O + 2e^- \quad \text{Eq. 86}$$

$$CO + O^{2-} \leftrightarrow CO_2 + 2e^- \quad \text{Eq. 87}$$

$$O_2 + 4e^- \leftrightarrow 2O^{2-} \quad \text{Eq. 88}$$

Without electrical load however, the reactions occur at equal rates in both directions. This exchange current represents the current flowing in one of the two directions at equilibrium conditions. In order to generate a current into one direction a certain potential is required. This potential is commonly referred to as activation polarization, n_{act}, and mathematically best described by the Butler-Volmer equation, Eq. 89, where I denotes the prevalent current density, [196]:

$$I = I_0 \left[\exp\left(\beta \cdot \frac{n \cdot F \cdot \eta_{act}}{R \cdot TsK} \right) - \exp\left(-(1-\beta) \cdot \frac{n \cdot F \cdot \eta_{act}}{R \cdot TsK} \right) \right] \qquad \text{Eq. 89}$$

Other correlations such as the Tafel equation, Eq. 90, the linear current-potential equation, Eq. 91, and more empirical relations can also be found in the literature and are mostly derivates of the Butler-Volmer equation. A detailed discussion of the application of these simplified equations is given in [141].

$$\eta_{act} = \frac{R \cdot TsK}{n \cdot F \cdot \beta} \cdot \ln\left(\frac{I}{I_0} \right) \qquad \text{Eq. 90}$$

$$\eta_{act} = \frac{R \cdot TsK}{n \cdot F} \cdot \frac{I}{I_0} \qquad \text{Eq. 91}$$

The Butler-Volmer equation, Eq. 89, which was implemented in the developed model, comprises two important model parameters. The first parameter is the transfer coefficient β, which represents the part of the change in polarization leading to a change in the reaction rate constant. For fuel cell applications and in the developed model, the value is usually assumed to be 0.5, [182, 196].

The second parameter is the exchange current density I_0, which represents the forward and reverse electrode reaction rate at the equilibrium potential. High exchange current density values denote a high electrochemical reaction rate and hence low activation losses. More detailed information can be found in [197].

The literature discusses a vast number of models used to calculate the exchange current density at the anode and cathode. A detailed discussion of these models is given in [182]. In the present work, the anode exchange current density is calculated according to Eq. 92 for the hydrogen electrochemistry and Eq. 93 for the carbon monoxide electrochemistry. The exponent near to the stoichiometry of the anodic electrochemical reactions results in a direct proportional dependence of the anode exchange current density to the educt and an inversely proportional dependence to the product partial pressures. With the inverse dependency of the activation losses to the exchange current density, the exponents yield lower activation losses with increased educt or decreased product partial pressures and vice versa, [182]. The cathode exchange current density is given by Eq. 94. The positive exponent yields lower cathode activation losses with rising oxygen partial pressures.

$$I_{0,an,H_2} = \gamma_{an,H_2}\left(\frac{p_{H_2}}{p}\right)\left(\frac{p_{H_2O}}{p}\right)^{-0.5}\cdot\exp\left(\frac{-E_{act,an,H_2}}{R\cdot TsK}\right) \quad \text{Eq. 92}$$

$$I_{0,an,CO} = \gamma_{an,CO}\left(\frac{p_{CO}}{p}\right)\left(\frac{p_{CO_2}}{p}\right)^{-0.5}\cdot\exp\left(\frac{-E_{act,an,CO}}{R\cdot TsK}\right) \quad \text{Eq. 93}$$

$$I_{0,ca} = \gamma_{ca}\left(\frac{p_{O_2}}{p}\right)^{0.25}\cdot\exp\left(\frac{-E_{act,ca}}{R\cdot TsK}\right) \quad \text{Eq. 94}$$

The material-dependent parameters, activation energies, $E_{act,an,H2}$, $E_{act,an,CO}$, $E_{act,ca}$, and pre-exponential factors of anode, $\gamma_{an,H2}$, $\gamma_{an,CO}$, and cathode, γ_{ca}, were taken from [182] for the planar geometry and [155] for the tubular geometry. In [155, 182], the parameters were estimated based on experimental data.

As only the conversion of hydrogen was considered in [182], no parameters for the carbon monoxide conversion were specified. However, in [190] it is stated that the activation potential loss of the electrochemical conversion of carbon monoxide is approx. 1.4 times higher than that for the electrochemical hydrogen conversion. Based on this, the pre-exponential factor for the calculation of the carbon monoxide conversion exchange current density was determined.

It has to be emphasized, that due to the implicit character of the Butler-Volmer equation its solution can only be determined numerically. This effort is however justified by higher accuracy, [164], as the straightforward calculation of the activation polarization is only possible using simplified equations such as Eq. 90 and Eq. 91.

5.3.1.4.2 Ohmic polarization

Electronic currents through the electrodes and interconnects as well as ionic currents through the electrolyte induce voltage losses in all fuel cells. For a given resistance and current density, the calculation of the ohmic voltage loss (η_{ohm}) simply follows Ohm's law, Eq. 95.

$$\eta_{ohm} = R_{equiv}\cdot I_{tot} \quad \text{Eq. 95}$$

The area specific equivalent resistance (R_{equiv}) of SOFCs depends on the geometry and the conductivity of the current conducting components. The temperature-dependent conductivity of the ceramic materials employed in SOFCs is calculated according to Eq. 45 to Eq. 48.

Based on the conductivity values, the area specific equivalent resistance of the considered cell designs is approximated in the present model using the transmission line model instead of calculating it through the numerical solution of the Laplace equation. The methodology was developed by Nisancioglu, [198], and others, e.g. [199], and features a high flexibility towards different fuel cell designs.

The general idea of the transmission line model is that complex SOFC geometries can be described by a set of five standard cell sub-units. Each of these cell sub-units has a characteristic current path pattern and corresponding analytical formula for the equivalent resistance calculation, see Table 5-6. In these formulas, L denotes the length of the cell sub-unit, δ stands for the thickness of the cell sub-unit or parts of it and ρ represents the conductivity of the corresponding material. The subscripts *an*, *el* and *ca* stand for anode, electrolyte and cathode.

Table 5-6: Equivalent resistance formulas for five cell sub-units with the arrowed lines indicating the current flow path from cathode to anode, [198]

Cell sub-unit	Geometry factor J [-]	Resistance R [Ω m]
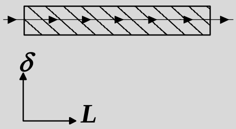 1	-	$\frac{\rho L}{\delta}$
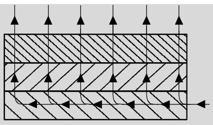 2	$L\sqrt{\frac{\rho_{ca}/\delta_{ca}}{\rho_{el}\delta_{el}}}$	$\frac{\sqrt{\rho_{el}\delta_{el}\left(\frac{\rho_{ca}}{\delta_{ca}}\right)}}{\tanh J}$
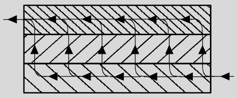 3	$L\sqrt{\frac{1}{\rho_{el}\delta_{el}}\left(\frac{\rho_{an}}{\delta_{an}}+\frac{\rho_{ca}}{\delta_{ca}}\right)}$	$\frac{\left(\left(\frac{\rho_{an}}{\delta_{an}}\right)^2+\left(\frac{\rho_{ca}}{\delta_{ca}}\right)^2\right)\cdot\cosh J+\left(\frac{\rho_{an}\rho_{ca}}{\delta_{an}\delta_{ca}}\right)\cdot(2+J\cdot\sinh J)}{\sqrt{\frac{1}{\rho_{el}\delta_{el}}}\cdot\sqrt[3]{\frac{\rho_{an}}{\delta_{an}}+\frac{\rho_{ca}}{\delta_{ca}}}\cdot\sinh J}$
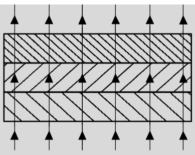 4	-	$\frac{\rho_{an}\delta_{an}+\rho_{el}\delta_{el}+\rho_{ca}\delta_{ca}}{L}$
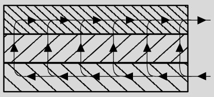 5	$L\sqrt{\frac{1}{\rho_{el}\delta_{el}}\left(\frac{\rho_{an}}{\delta_{an}}+\frac{\rho_{ca}}{\delta_{ca}}\right)}$	$\frac{\sqrt{\rho_{el}\delta_{el}\left(\frac{\rho_{an}}{\delta_{an}}+\frac{\rho_{ca}}{\delta_{ca}}\right)}}{\tanh J}$

Application to the tubular geometry

Figure 5-10 shows the cross section with current paths of the tubular geometry considered in the developed model (a). The transmission line model approximation (b) consists of two type 3 cell sub-units connected in parallel, representing the two halves of the cell tube, and one type 2 cell sub-unit, representing the interconnect area, connected in series.

Figure 5-10: Cross section of the standard tubular Siemens AG design (a) and transmission line model (b)

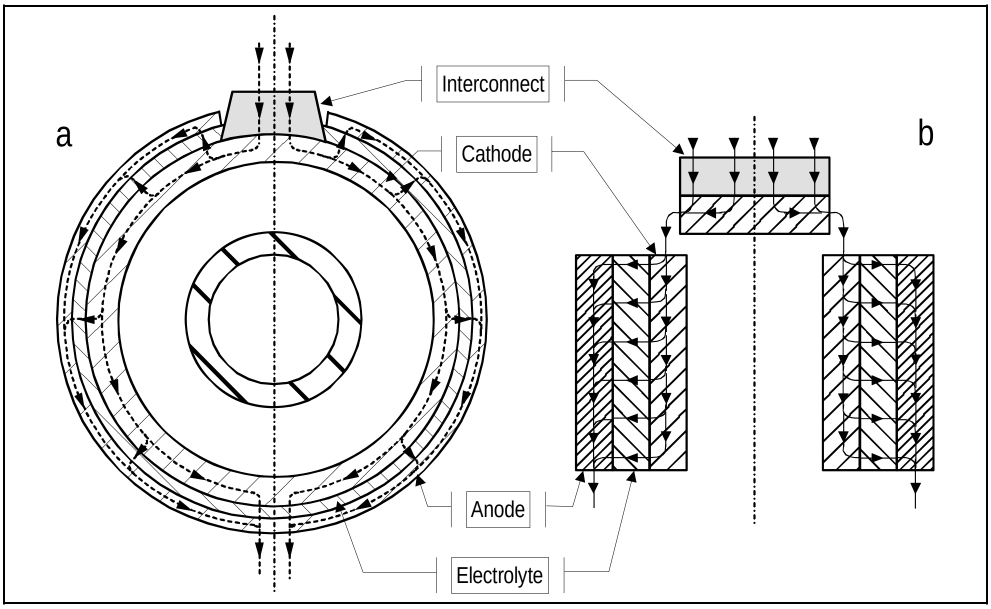

Due to the perfect symmetry of the tubular geometry, the equivalent resistance is only calculated for one half-cell and then divided by 2. The length of the type 3 cell sub-unit (L_e) for one half-cell is calculated according to Eq. 96 and for cell sub-unit type 2 (L_{ic}) according to Eq. 97.

$$L_e = \pi \cdot r_{m,AEC} \cdot (1 - x_{t,ic}) \qquad \text{Eq. 96}$$

$$L_{ic} = \pi \cdot r_{m,AEC} \cdot x_{t,ic} \qquad \text{Eq. 97}$$

The resistance of one half of the cell tube (R_e) is given by Eq. 98.

$$R_e = \frac{\left(\left(\frac{\rho_{an}}{\delta_{an}}\right)^2 + \left(\frac{\rho_{ca}}{\delta_{ca}}\right)^2\right) \cdot \cosh J_e + \left(\frac{\rho_{an}\rho_{ca}}{\delta_{an}\delta_{ca}}\right) \cdot \left(2 + J_e \cdot \sinh J_e\right)}{\sqrt{\frac{1}{\rho_{el}\delta_{el}}} \cdot \sqrt[3]{\frac{\rho_{an}}{\delta_{an}} + \frac{\rho_{ca}}{\delta_{ca}}} \cdot \sinh J_e} \qquad \text{Eq. 98}$$

$$with \quad J_e = L_e \sqrt{\frac{1}{\rho_{el}\delta_{el}} \left(\frac{\rho_{an}}{\delta_{an}} + \frac{\rho_{ca}}{\delta_{ca}}\right)}$$

The resistance of the interconnect (R_{ic}) is calculated according to Eq. 99.

$$R_{ic} = \frac{\sqrt{\rho_{ic}\delta_{ic}\left(\frac{\rho_{ca}}{\delta_{ca}}\right)}}{\tanh J_{ic}} \; with \; J_{ic} = L_{ic}\sqrt{\frac{1}{\rho_{el}\delta_{el}} \cdot \frac{\rho_{ca}}{\delta_{ca}}} \qquad \text{Eq. 99}$$

The equivalent resistance is calculated following Kirchhoff's law for in-series connection. In order to obtain the area specific resistance value for the calculation of the ohmic voltage loss using a current density instead of an absolute current, the equivalent resistance is multiplied with the electrochemically active circumferential length of the cell tube.

$$R_{t,equiv} = l_{t,elact} \cdot (R_e + R_{ic}) \qquad \text{Eq. 100}$$

Application to the triangular geometry

The triangular geometry exhibits current paths, which can be described using the same approach as for the standard tubular cell, Figure 5-11.

Figure 5-11: Cross section of the triangular Siemens AG design (a) and transmission line model (b)

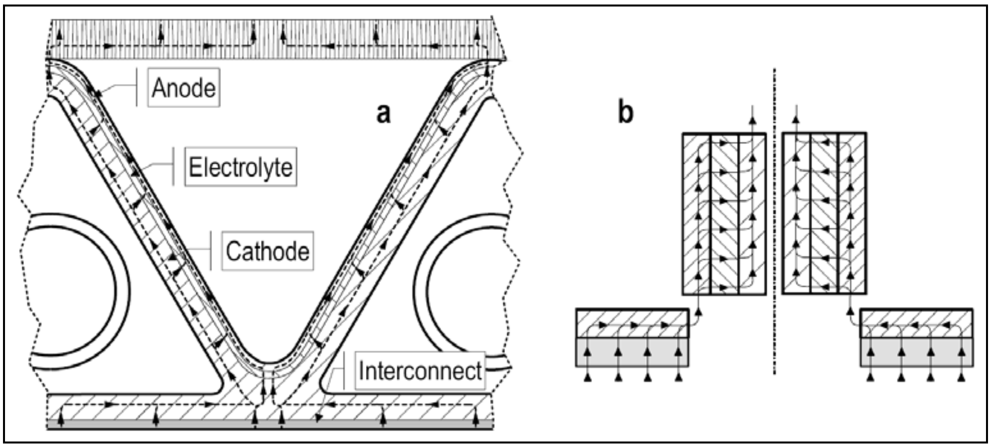

The cell sub-unit lengths, L_e and L_{ic}, are given by Eq. 101 and Eq. 102.

$$L_{D8,e} = 0.5 \cdot l_{D8,elact} \qquad \text{Eq. 101}$$

$$L_{D8,ic} = \frac{w_{D8}}{2 \cdot n_{tri}} \qquad \text{Eq. 102}$$

As only one half of the current path is considered, the area specific resistance is obtained by multiplying the equivalent resistance with half of the electrochemically active width of the repeat element, Eq. 103.

$$R_{D8,equiv} = 0.5 \cdot l_{D8,elact} \cdot (R_e + R_{ic}) \qquad \text{Eq. 103}$$

Application to the tubular geometry

The calculation of the area specific equivalent resistance for the considered planar geometry is done in the same manner as for the tubular geometry. Figure 5-12 shows a cutout of the considered planar stack and the cross-section of a repeating structure with the corresponding current paths (a) and transmission line model approximation (b).

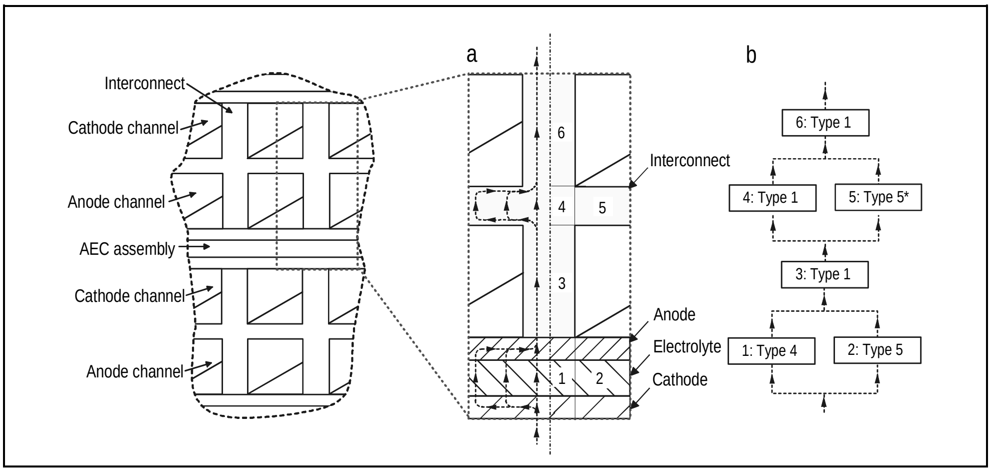
a
b
Interconnect
Cathode channel
Anode channel
AEC assembly
Cathode channel
Anode channel
6
4
5
3
1
2
Interconnect
Anode
Electrolyte
Cathode
6: Type 1
4: Type 1
5: Type 5*
3: Type 1
1: Type 4
2: Type 5

Figure 5-12: Cross section of the considered planar cell design (a) and transmission line model (b)

The equivalent resistance of the repeat element includes 6 cell sub-units. In the developed model, the current flow through the AEC assembly is divided into a sub-unit type 4 (R_1) and type 5 (R_2), Eq. 104 and Eq. 105.

$$R_1 = \frac{2\cdot(\rho_{ca}\delta_{ca}+\rho_{el}\delta_{el}+\rho_{an}\delta_{an})}{w_c/n_{ch}-w_{ch}} \qquad \text{Eq. 104}$$

$$R_2 = \frac{\sqrt{\rho_{el}\delta_{el}\left(\frac{\rho_{an}}{\delta_{an}}+\frac{\rho_{ca}}{\delta_{ca}}\right)}}{\tanh J_2} \; with \; J_2 = \frac{w_{ch}}{2}\sqrt{\frac{1}{\rho_{el}\delta_{el}}\left(\frac{\rho_{an}}{\delta_{an}}+\frac{\rho_{ca}}{\delta_{ca}}\right)} \qquad \text{Eq. 105}$$

The two cell sub-units are connected in parallel. The interconnect contacts anode and cathode of two superposed AEC assemblies. The resistances of the interconnect ribs on the anode (R_3) and cathode (R_6) side are calculated using type 1 cell sub-units, Eq. 106 and Eq. 107.

$$R_3 = \frac{2\cdot\rho_{ic}h_{p,an}}{w_c/n_{ch}-w_{ch}} \qquad \text{Eq. 106}$$

$$R_6 = \frac{2\cdot\rho_{ic}h_{p,ca}}{w_c/n_{ch}-w_{ch}} \qquad \text{Eq. 107}$$

The resistance of the bar between adjoining ribs is calculate by assuming a parallel connection of a type 1 cell sub-unit (R_4) and a modified type 5* (R_5), [200].

$$R_4 = \frac{2\cdot\rho_{ic}\cdot((h_{ic,an}+h_{ic,ca})-(h_{p,an}+h_{p,ca}))}{w_c/n_{ch}-w_{ch}} \qquad \text{Eq. 108}$$

$$R_5 = \frac{\rho_{ic}}{0.41 \cdot \left(1 - \exp\left(-0.6 \cdot \left(\frac{w_{ch}}{(h_{ic,an} + h_{ic,ca}) - (h_{p,an} + h_{p,ca})}\right)\right)\right)} \qquad \text{Eq. 109}$$

Finally, the equivalent circuit depicted in Figure 5-12 yields Eq. 110. Similar to the tubular geometry, the area specific resistance is multiplied with the electrochemically active length of the repeat structure.

$$R_{p,equiv} = \left(\frac{w_{ce}}{n_{ch}}\right) \cdot \left(\left(\frac{1}{R_1} + \frac{1}{R_2}\right)^{-1} + R_3 + \left(\frac{1}{R_4} + \frac{1}{R_5}\right)^{-1} + R_6\right) \qquad \text{Eq. 110}$$

5.3.1.4.3 Diffusion polarization

The diffusion polarization losses account for the difference of the Nernst voltage considering the reactant partial pressures in the bulk gas phase and at the reaction sites located at the triple phase boundary (TPB) where electrolyte and electrode material as well as reactant gases meet. The partial pressures of the educts are generally lower, while those of the products are generally higher at the TPB then in the bulk gas phase. The exact partial pressure values depend on the prevalent current density and the material parameters of the porous electrodes through which the educts and products have to diffuse in order to reach the TPB. The prevalent current density determines the concentration gradient between the TPB and the bulk gas phase. The material parameters of the porous electrodes include tortuosity, porosity and pore radius. These three material parameters together with the fuel composition determine the effective diffusion coefficient required in order to calculate the partial pressures at the TPB through the application of e.g. Fick's law of diffusion. Concentration losses become important for highly diluted fuel gases and at high current densities, where they increase against an asymptotic maximum. At this specific point a further increase of the current is impossible since the reactant partial pressures at the TPB equal zero due to instant conversion.

The developed model considers diffusion limitation in the anode and the cathode electrode. At the anode, the educts and the products of the electrochemical reactions diffuse with equal rates to the TPB and back into the gas flow channel. This equimolar counter-flow diffusion yields a zero net diffusion flux. Applying Fick's law of diffusion by assuming, that the electrochemical reaction rate equals the mass flux via diffusion, the partial pressures of educts and products at the TPB can be calculated based on the partial pressures in the bulk gas phase according to Eq. 111.

$$\begin{aligned} & p_i^{TPB} = p_i \mp \left(\frac{R \cdot TaK \cdot I_{H_2} \cdot \delta_{an} \cdot \tau_{an}}{n \cdot F \cdot D_{eff,H_2} \cdot \varepsilon_{an}} \right) \\ & with - for\, i = H_2, CO \\ & and + for\, i = H_2O, CO_2 \end{aligned} \qquad \text{Eq. 111}$$

In these equations, TaK denotes the temperature of the anode gas flow, I_{H2} and I_{CO} represent the currents originating from the hydrogen and carbon monoxide conversion, δ_{an} stands for the thickness of the anode electrode, τ_{an} gives the tortuosity and ε_{an} the porosity of the anode electrode material and $D_{eff,H2}$ and $D_{eff,CO}$ denote the effective diffusion coefficients of hydrogen and carbon monoxide of the anode gas mixture. The effective diffusion coefficients are calculated based on binary molecular diffusion coefficients of hydrogen and carbon monoxide with all other considered species in the gas mixture and the Knudsen diffusion coefficient. The calculation of binary molecular and Knudsen diffusion coefficients is discussed in section 5.3.1.2.1. The binary molecular diffusion coefficients are summed up to yield the effective molecular diffusion coefficient according to Eq. 44. For the calculation of the effective diffusion coefficient it is assumed, that Knudsen and molecular diffusion occur simultaneously. Therefore, the Bosanquet formula was implemented in this model, Eq. 112, where x denotes either hydrogen or carbon monoxide.

$$D_{eff,x} = \frac{D_{m,x-mix} \cdot D_{K,x}}{D_{m,x-mix} + D_{K,x}} \qquad \text{Eq. 112}$$

For known partial pressures of the educts and products in the bulk gas phase and at the TPB, the diffusion voltage losses are computed according to Eq. 113. The temperature used in the calculation is the temperature of the solid structure of the fuel cell and not that of the gas mixture.

$$\eta_{diff,i} = \left(\frac{R \cdot TsK}{n \cdot F} \right) \cdot \ln \left(\frac{p_i \cdot p_j^{TPB}}{p_j \cdot p_i^{TPB}} \right) with\, i = H_2, CO\, and\ j = H_2O, CO_2 \qquad \text{Eq. 113}$$

At the cathode, only oxygen takes part in the electrochemical reactions, where it is consumed without forming products that return to the bulk gas phase.

$$
\begin{aligned}
&A\cdot\frac{p_{O_2}^{TPB}-p}{D_{K,O_2}\cdot\left(\alpha\cdot p_{O_2}^{TPB}-p\right)-D_{m,O_2-N_2}}=\exp\left(I_{tot}\cdot TcK\cdot B\right)\\
&with\quad A=\frac{D_{K,O_2}\cdot\left(\alpha\cdot p_{O_2}-p\right)-D_{m,O_2-N_2}}{p_{O_2}-p}\\
&and\quad B=\frac{\tau_{ca}\cdot R\cdot\delta_{ca}\cdot\left(D_{m,O_2-N_2}-D_{K,O_2}\cdot(\alpha-1)\right)}{\varepsilon_{ca}\cdot 2\cdot n\cdot F\cdot D_{m,O_2-N_2}\cdot D_{K,O_2}\cdot p}\\
&and\quad \alpha=1-\left(\frac{M_{O_2}}{M_{N_2}}\right)
\end{aligned}
\qquad \text{Eq. 114}
$$

Eq. 114 was implemented in this model for the implicit calculation of the partial pressure of oxygen at the cathode TPB, [155]. In contrast to the diffusion at the anode, the effective diffusion coefficient is calculated for the non-dilute two-component gas mixture at the cathode according to [201], which includes the relation between the molecular masses, α, of the components nitrogen and oxygen. Further, Eq. 114 comprises the porosity and tortuosity of the cathode electrode, τ_{ca} and ε_{ca}, the cathode electrode thickness, δ_{ca}, the Knudsen diffusion coefficient of oxygen, $D_{K,O2}$, the binary molecular diffusion coefficient of the oxygen-nitrogen system, $D_{m,O2\text{-}N2}$, the prevalent total current density, I_{tot}, and the temperature of the cathode gas, TcK. The diffusion voltage loss at the cathode is calculated analogously to the anode, Eq. 115.

$$
\eta_{diff,O_2}=\left(\frac{R\cdot TsK}{2\cdot n\cdot F}\right)\cdot\ln\left(\frac{p_{O_2}}{p_{O_2}^{TPB}}\right)\qquad \text{Eq. 115}
$$

5.3.1.5 Mass balance model

The current density values computed by the electrochemical performance model are related to the reactions Eq. 86 to Eq. 88 via the Faraday law yielding the area specific reaction rates of the electrochemical reactions and the number of consumed moles of hydrogen, carbon monoxide and oxygen per area, respectively. In the present model, the axial length of the gas flow channels was defined as the integration variable. In order to account for the 2-dimensional distribution of the electrochemical reactions, the area specific reaction rate has to be multiplied with the electrochemically active length of the considered fuel cell design, $l_{t,elact}$ or $l_{p,elact}$, in order to be converted into the integration length specific reaction rate. Accordingly, Eq. 116 to Eq. 118 were applied in this model.

$$r_{H_2\,oxi} = l_{t/p,elact} \cdot \left(\frac{I_{H_2}}{2 \cdot F} \right) \qquad \text{Eq. 116}$$

$$r_{CO\,oxi} = l_{t/p,elact} \cdot \left(\frac{I_{CO}}{2 \cdot F} \right) \qquad \text{Eq. 117}$$

$$r_{O_2\,ion} = l_{t/p,elact} \cdot \left(\frac{I_{tot}}{4 \cdot F} \right) \qquad \text{Eq. 118}$$

Besides the mentioned electrochemical reactions, this model considers water-gas-shift, Eq. 119 and Eq. 120, and steam reforming reactions, Eq. 121 to Eq. 125, of methane, ethene, toluene and anisole as well as the thermal decomposition of acetic acid through applied kinetic models.

$$CO + H_2O \leftrightarrow CO_2 + H_2 \qquad \text{Eq. 119}$$

$$CO_2 + H_2 \leftrightarrow CO + H_2O \qquad \text{Eq. 120}$$

$$CH_4 + H_2O \leftrightarrow CO + 3H_2 \qquad \text{Eq. 121}$$

$$C_2H_4 + 2H_2O \rightarrow 2CO + 4H_2 \qquad \text{Eq. 122}$$

$$C_7H_8 + 7H_2O \rightarrow 7CO + 11H_2 \qquad \text{Eq. 123}$$

$$C_2H_4O_2 \rightarrow 2CO + 2H_2 \qquad \text{Eq. 124}$$

$$C_7H_8O + 6H_2O \rightarrow 7CO + 10H_2 \qquad \text{Eq. 125}$$

To facilitate the extension of the present model with respect to the considered chemical reactions and applied kinetic models, a generalized kinetic approach was developed, Eq. 126.

$$\begin{aligned}
& r_{reac} = f_{act} \cdot \frac{A \cdot B \cdot C \cdot D}{E \cdot F} \\
& with \quad A = k_0 \cdot \exp\left(\frac{-E_a}{R \cdot T} \right) \\
& and \quad B = p_{e1}^{ro_{e1}} \cdot p_{e2}^{ro_{e2}} \\
& and \quad C = p_{p1}^{ro_{p1}} \cdot p_{p2}^{ro_{p2}} \\
& and \quad D = 1 - \frac{p_{p1}^{\nu_{p1}} \cdot p_{p2}^{\nu_{p2}}}{K_{eq} \cdot \left(p_{e1}^{\nu_{e1}} \cdot p_{e2}^{\nu_{e2}} \right)} \\
& and \quad E = K_{eq} \\
& and \quad F = (1 + G + H + I)^{ro_{ads}} \\
& with \quad G = K_{ads1}^{0} \cdot \exp\left(\frac{\Delta H_{ads1}}{R \cdot T} \right) \cdot p_{ads11}^{ro_{ads11}} \cdot p_{ads12}^{ro_{ads12}} \\
& with \quad H = K_{ads2}^{0} \cdot \exp\left(\frac{\Delta H_{ads2}}{R \cdot T} \right) \cdot p_{ads21}^{ro_{ads21}} \cdot p_{ads22}^{ro_{ads22}} \\
& with \quad I = K_{ads3}^{0} \cdot \exp\left(\frac{\Delta H_{ads3}}{R \cdot T} \right) \cdot p_{ads31}^{ro_{ads31}} \cdot p_{ads32}^{ro_{ads32}}
\end{aligned} \qquad \text{Eq. 126}$$

This approach enables the reproduction of equilibrium, power law and Langmuir-Hinshelwood kinetic models with up to three adsorption terms for reactions with a maximum of two educt and product species. Eq. 126 involves the following terms:

- A: Reaction constant term

  The reaction constant term comprises the pre-exponential factor, k_0, and the activation energy of the reaction, E_a. In this model, the temperature T is assumed to equal the temperature of the solid structure of the fuel cell.

- B: Educt partial pressure term

  The educt partial pressure term is the product of the partial pressures of the two educts, p_{e1} and p_{e2}, to the power of their corresponding reaction orders, ro_{e1} and ro_{e2}.

- C: Product partial pressure term

  The product partial pressure term is the product of the partial pressures of the two products, p_{p1} and p_{p2}, to the power of their corresponding reaction orders, ro_{p1} and ro_{p2}.

- D: Equilibrium limitation term in the numerator

  In the equilibrium term, K_{eq} denotes the equilibrium constant of the considered reaction and ν_{p1}, ν_{p2}, ν_{e1}, and ν_{e2} the stoiciometric coefficients of the reaction products and educts.

- E: Equilibrium limitation term in denominator

- F: Overall adsorption term

  The overall adsorption term includes a maximum of three adsorption terms to the power of the according reaction order of the adsorption reactions, ro_{ads}.

- G, H, I: Adsorption terms

  Each of the three adsorption terms includes an adsorption constant, K^0_{ads1}, K^0_{ads2} and K^0_{ads3}, a corresponding heat of adsorption ΔH_{ads1}, ΔH_{ads2} and ΔH_{ads3} and a maximum of two adsorption specie partial pressures to the power of their corresponding reaction order.

Each of the discussed terms can be enabled or disabled in order to reproduce the envisaged applied kinetic model. Note that Eq. 126 includes the factor f_{act}. For reactions where an applied kinetic model was specifically developed, f_{act} is set to unity. However, where no specific kinetic model is available f_{act} can be set to values other than unity in order to adapt an available applied kinetic model for another reaction to the reaction in question. The value of f_{act} has to be determined by comparison of the reaction in question with the reaction for which the applied kinetic model has been developed. Although this approach lacks a solid data base, it is nevertheless valuable as it hints towards possible impacts of hitherto uninvestigated reactions in fuel cells such as e.g. the steam reforming of tars.

The water-gas-shift reaction (WGS), Eq. 119, and the reverse water-gas-shift reaction (REV-WGS), Eq. 120, were assumed to be at equilibrium. This assumption is found frequently in the literature, e.g. [141, 202, 203], and was confirmed in experiments conducted by the author, see section 3.3.2. Besides, the WGS and REV-WGS were considered to be non-diffusion limited homogenous reactions. The reaction rates were calculated according to Eq. 127 and Eq. 128.

$$r_{WGS} = 10000.0 \frac{mol}{m \cdot \sec \cdot bara^2} \cdot p_{CO} \cdot p_{H_2O} \qquad \text{Eq. 127}$$

$$r_{REV-WGS} = 10000.0 \frac{mol}{m \cdot \sec \cdot bara^2} \cdot p_{CO_2} \cdot p_{H_2} \cdot \left(1 - \frac{p_{CO} \cdot p_{H_2O}}{K_{eq,WGS} \cdot p_{CO_2} \cdot p_{H_2}} \right) \qquad \text{Eq. 128}$$

Table 5-7 lists the coefficients for the equilibrium constant fit correlation, Eq. 82, of the WGS and the methane steam reforming reaction (CH_4 STR). The equilibrium constant values were taken from [195].

Table 5-7: Coefficients of the equilibrium constant fit correlation for water-gas-shift and methane steam reforming reactions

Coefficient	Water-gas-shift reaction	Methane steam reforming reaction
y_0	-2.08873	20.45485
A_1	9.5544	-294.50512
t_1	354.50643	69.62891
A_2	6.81354	-144.02845
t_2	758.72139	182.27607
A_3	45.01004	-70.17964
t_3	134.0971	693.27912

In contrast to the WGS, the STR is considered a heterogeneous reaction. A literature review revealed contradictory results with respect to applied kinetic models for the STR over nickel-cermet materials. The highest discrepancies were found in the reaction order of water. Achenbach found a reaction order of zero, [204], Ahmed and Foger as well as Lee found negative reaction orders, [205, 206], and Leinfelder found a positive reaction order, [53]. Drescher has shown, that all these findings are correct and a result of the chosen operating conditions of the experiments, more precisely of the chosen steam-to-carbon ratio (SC), [207]. Small SC yield positive reaction orders, SC in the order of 2 yield reaction orders of zero while high SC lead to negative reaction orders of water. Drescher developed a Langmuir-Hinshelwood kinetics model for temperatures around 650 °C.

To allow for an analysis of the impact of the kinetic models on the model results, Eq. 129 to Eq. 133 and the equilibrium approach were implemented. The equilibrium constant for the CH_4 STR is calculated using the fit correlation coefficients given in Table 5-7. Note that Dreschers kinetic model, Eq. 133, was initially related to the mass of catalyst in the fuel cell. Consequently the pre-exponential factor had to be recalculated to an area specific value to allow for the application in the presented model. The author assumed that only the upper 25 microns of the nickel-cermet participate in the steam reforming reactions. All other data for the recalculation were taken from [207] in order to keep the kinetic model concise.

$$r_{CH_4\,STR,eq} = 10000.0\frac{mol}{m\cdot\sec\cdot bara^2}\cdot p_{CH_4}\cdot p_{H_2O}\cdot\left(1-\frac{p_{CO}\cdot p_{H_2}^3}{K_{eq,STR}\cdot p_{CH_4}\cdot p_{H_2O}}\right)$$ Eq. 129

$$r_{CH_4\,STR,Ach} = 4274.0\frac{mol}{m^2\cdot\sec\cdot bara}\cdot p_{CH_4}\cdot\exp\left(\frac{-82000\frac{J}{mol}}{R\cdot TsK}\right)$$ Eq. 130 [204]

$$r_{CH_4\,STR,Ahm} = 8542.0\frac{mol}{m^2\cdot\sec\cdot bara^2}\cdot p_{CH_4}^{0.85}\cdot p_{H_2O}^{-0.35}\cdot\exp\left(\frac{-95000\frac{J}{mol}}{R\cdot TsK}\right)$$ Eq. 131 [205]

$$r_{CH_4\,STR,Lei} = 30.8e+10\frac{mol}{m^2\cdot\sec\cdot bara^2}\cdot p_{CH_4}\cdot p_{H_2O}\cdot\exp\left(\frac{-205000\frac{J}{mol}}{R\cdot TsK}\right)$$ Eq. 132 [53]

$$r_{CH_4\,STR,Dre} = \frac{288.52\frac{mol}{m^2\cdot\sec\cdot bara^2}\cdot p_{CH_4}\cdot p_{H_2O}\cdot\exp\left(\frac{-11000\frac{J}{mol}}{R\cdot TsK}\right)}{\left(1+16.0\frac{1}{bara}\cdot p_{CH_4}+0.143\frac{1}{bara}\cdot p_{H_2O}\cdot\exp\left(\frac{39000\frac{J}{mol}}{R\cdot TsK}\right)\right)}$$ Eq. 133 [207]

For the reactions Eq. 122 to Eq. 125, no valid kinetic models regarding the application in a solid oxide fuel cell model were found in the literature. Therefore, it was assumed, that the STR of higher hydrocarbons follows the kinetic model of Achenbach, [204]. Further it was assumed that the reactions occur faster than the CH_4 STR due to the higher reactivity of the considered hydrocarboneous species. Following this assumption, the activity factor, f_{act}, was set to 2.5, 1.5, 2.0 and 1.75 for the reactions Eq. 122, Eq. 123, Eq. 124 and Eq. 125, respectively. The subsequent expressions for the reaction rates of the STR of ethene, toluene and anisole and the thermal decomposition of acetic acid were formulated as:

$$r_{C_2H_4\,STR,Ach} = 10685.0\frac{mol}{m^2\cdot\sec\cdot bara}\cdot p_{C_2H_4}\cdot\exp\left(\frac{-82000\frac{J}{mol}}{R\cdot TsK}\right) \qquad \text{Eq. 134}$$

$$r_{C_7H_8\,STR,Ach} = 6411.0\frac{mol}{m^2\cdot\sec\cdot bara}\cdot p_{C_7H_8}\cdot\exp\left(\frac{-82000\frac{J}{mol}}{R\cdot TsK}\right) \qquad \text{Eq. 135}$$

$$r_{C_7H_8O\,STR,Ach} = 7479.5\frac{mol}{m^2\cdot\sec\cdot bara}\cdot p_{C_7H_8O}\cdot\exp\left(\frac{-82000\frac{J}{mol}}{R\cdot TsK}\right) \qquad \text{Eq. 136}$$

$$r_{C_2H_4O_2\,Dec,Ach} = 8548.0\frac{mol}{m^2\cdot\sec\cdot bara}\cdot p_{C_2H_4O_2}\cdot\exp\left(\frac{-82000\frac{J}{mol}}{R\cdot TsK}\right) \qquad \text{Eq. 137}$$

Depending on the geometry of the anode gas flow channel, heterogeneous reactions can be diffusion limited. That is, the diffusion of the reacting species from the bulk gas phase to the catalyst surface is slower than the actual chemical reaction. Therefore, the partial pressures of the reactants at the catalyst surface can differ significantly from the bulk gas phase. The calculation of the precise reactant partial pressures at the catalyst surface requires the solution of the complete concentration field perpendicular to the gas flow direction. In order to avoid solving the corresponding partial differential equations, a mass transfer analogy was used in this model to compute the reactant partial pressure at the catalyst surface, Eq. 138, [190]. In this equation, $\beta_{x,diff}$ denotes the mass transfer coefficient of the diffusion limited considered reactant specie x, TaK stands for the temperature of the anode gas flow and p_x and p_x^{cs} represent the reactant specie partial pressure in the bulk gas phase and at the catalyst surface, respectively.

$$r_{x,diff} = \frac{\beta_{x,diff}}{R \cdot TaK} \cdot \left(p_x - p_x^{cs}\right) \qquad \text{Eq. 138}$$

The mass transfer coefficient $\beta_{x,diff}$ is calculated by considering the analogy of heat and mass transfer according to Eq. 139, including the Nusselt number Nu, the molecular diffusion coefficient of the diffusion limited considered reactant specie x in the gas mixture, $D_{m,mix,x}$, and the hydraulic diameter of the anode gas channel of the according fuel cell design, $d_{t/p,hyd,an}$.

$$\beta_{x,diff} = \frac{D_{m,mix,x}}{d_{t/p,hyd,an}} \cdot Nu \cdot \left(\frac{p}{p - p_x}\right) \qquad \text{Eq. 139}$$

The calculation of the reactant partial pressure at the catalyst surface can be avoided, by considering the diffusion process and the chemical reaction as two mechanisms connected in parallel. Mathematically this requires the introduction of a reaction conversion coefficient for the considered chemical reaction, $\beta_{x,reac}$, which is based on the reaction rate, r_{reac}, calculated with the bulk gas phase partial pressures, Eq. 140. Note that the reaction rate is divided by the partial pressure of the diffusion-limited specie, p_x, to the power of its reaction order, ro_x.

$$\beta_{x,reac} = r_{reac} \cdot \frac{R \cdot TsK}{p_x^{ro_x}} \qquad \text{Eq. 140}$$

The diffusion limited and integration length specific reaction rate, $r_{dl\text{-}reac}$, is obtained from Eq. 141.

$$r_{dl-reac} = l_{t/p,chact} \cdot \beta_{x,diff-reac} \cdot \frac{p_x^{ro_x}}{R \cdot TsK} \;\; with \;\; \beta_{x,diff-reac} = \frac{\beta_{x,diff} \cdot \beta_{x,reac}}{\beta_{x,diff} + \beta_{x,reac}} \qquad \text{Eq. 141}$$

In this equation, $l_{t/p,chact}$ denotes the chemically active length of the considered fuel cell design and $\beta_{x,diff\text{-}reac}$ represents the diffusion limited reaction conversion coefficient. The partial pressure of the diffusion-limited specie, p_x, to the power of its reaction order, ro_x, is thus reintroduced.

Knowing the reaction rate of all reactions and neglecting axial diffusion mass transport, the spatial distribution of the species along the anode channel can be computed according to following differential equations:

$$\frac{d\dot{n}_{H_2}}{dx} = R_{H_2}$$
$$\text{with } R_{H_2} = -r_{H_2\,oxi} + 3 \cdot r_{dl-CH_4\,STR} + r_{WGS} - r_{REV-WGS} + 4 \cdot r_{dl-C_2H_4\,STR} + 11 \cdot r_{dl-C_7H_8\,STR} + 2 \cdot r_{dl-C_2H_4O_2\,Dec} + 10 \cdot r_{dl-C_7H_8O\,STR} \qquad \text{Eq. 142}$$

$$\frac{d\dot{n}_{CO}}{dx} = R_{CO}$$
$$\text{with } R_{CO} = -r_{CO\,oxi} + r_{dl-CH_4\,STR} - r_{WGS} + r_{REV-WGS} + 2 \cdot r_{dl-C_2H_4\,STR} + 7 \cdot r_{dl-C_7H_8\,STR} + 2 \cdot r_{dl-C_2H_4O_2\,Dec} + 7 \cdot r_{dl-C_7H_8O\,STR} \qquad \text{Eq. 143}$$

$$\frac{d\dot{n}_{CO_2}}{dx} = R_{CO_2} \ \text{ with } R_{CO_2} = r_{CO\,oxi} + r_{WGS} - r_{REV-WGS} \qquad \text{Eq. 144}$$

$$\frac{d\dot{n}_{H_2O}}{dx} = R_{H_2O}$$
$$\text{with } R_{H_2O} = r_{H_2\,oxi} - + r_{dl-CH_4\,STR} - r_{WGS} + r_{REV-WGS} - 2 \cdot r_{dl-C_2H_4\,STR} - 7 \cdot r_{dl-C_7H_8\,STR} - 6 \cdot r_{dl-C_7H_8O\,STR} \qquad \text{Eq. 145}$$

$$\frac{d\dot{n}_{CH_4}}{dx} = R_{CH_4} \ \text{ with } R_{CH_4} = -r_{dl-CH_4\,STR} \qquad \text{Eq. 146}$$

$$\frac{d\dot{n}_{C_2H_4}}{dx} = R_{C_2H_4} \ \text{ with } R_{C_2H_4} = -r_{dl-C_2H_4\,STR} \qquad \text{Eq. 147}$$

$$\frac{d\dot{n}_{N_2,an}}{dx} = 0.0 \qquad \text{Eq. 148}$$

$$\frac{d\dot{n}_{C_7H_8}}{dx} = R_{C_7H_8} \ \text{ with } R_{C_7H_8} = -r_{dl-C_7H_8\,STR} \qquad \text{Eq. 149}$$

$$\frac{d\dot{n}_{C_2H_4O_2}}{dx} = R_{C_2H_4O_2} \ \text{ with } R_{C_2H_4O_2} = -r_{dl-C_2H_4O_2\,Dec} \qquad \text{Eq. 150}$$

$$\frac{d\dot{n}_{C_7H_8O}}{dx} = R_{C_7H_8O} \ \text{ with } R_{C_7H_8O} = -r_{dl-C_7H_8O\,STR} \qquad \text{Eq. 151}$$

The spatial distribution of oxygen and nitrogen in the cathode channel is computed analogously. Note that the subscripts ca and an in the equations Eq. 148 and Eq. 152, denote the nitrogen flow in the cathode or the anode gas channel, respectively. Furthermore the mass balance equation for oxygen is different for the two modeled flow patterns in the planar cell design, namely co- and counter flow. In the co-flow case the oxygen content decreases with the axial coordinate when a current is produced. For the counter-flow case, the opposite applies. The different boundary conditions for the considered flow patterns will be addressed in subsequent sections.

$$\frac{d\dot{n}_{N_2,ca}}{dx} = 0.0 \qquad \text{Eq. 152}$$

$$\frac{d\dot{n}_{O_2}}{dx} = R_{O_2} \;\; with \;\; R_{O_2} = -r_{O_2\,ion}\,(co-flow) \;\; or \;\; R_{O_2} = r_{O_2\,ion}\,(counter-flow) \qquad \text{Eq. 153}$$

The total molar flow in the anode and the cathode channel are calculated according to Eq. 154 and Eq. 155.

$$\begin{aligned}\dot{n}_{an} = \dot{n}_{H_2} + \dot{n}_{CO} + \dot{n}_{CO_2} + \dot{n}_{H_2O} + \dot{n}_{CH_4} + \dot{n}_{C_2H_4} \\ + \dot{n}_{N_2,an} + \dot{n}_{C_7H_8} + \dot{n}_{C_2H_4O_2} + \dot{n}_{C_7H_8O}\end{aligned} \qquad \text{Eq. 154}$$

$$\dot{n}_{ca} = \dot{n}_{N_2,ca} + \dot{n}_{O_2} \qquad \text{Eq. 155}$$

Based on the calculated reaction rates, the mass balance model also computes the related heat source term according to Eq. 156.

$$\begin{aligned}\Delta H_r = {} & r_{H_2\,oxi} \cdot \Delta H_{R,H_2\,oxi} + r_{CO\,oxi} \cdot \Delta H_{R,CO\,oxi} + r_{dl-CH_4\,STR} \cdot \Delta H_{R,CH_4\,STR} \\ & + r_{WGS} \cdot \Delta H_{R,WGS} + r_{REV-WGS} \cdot \Delta H_{R,REV-WGS} + r_{dl-C_2H_4\,STR} \cdot \Delta H_{R,C_2H_4\,STR} \\ & + r_{dl-C_7H_8\,STR} \cdot \Delta H_{R,C_7H_8\,STR} + r_{dl-C_2H_4O_2\,Dec} \cdot \Delta H_{R,C_2H_4O_2\,Dec} \\ & + r_{dl-C_7H_8O\,STR} \cdot \Delta H_{R,C_7H_8O\,STR}\end{aligned} \qquad \text{Eq. 156}$$

The heats of reaction, $\Delta H_{R,reaction}$, are calculated via Eq. 157, where i denotes each considered specie, ν_i gives the stoiciometric coefficient of the specie in the considered reaction, $\Delta H^0_{f,i}$ stands for the ideal gas enthalpy of formation and T_0 is the temperature at standard conditions.

$$\begin{aligned}& \Delta H_{R,reaction} = \Delta H^0_{R,reaction} + \sum_i \nu_i \cdot \int_{T_0}^{TsK} c_{p,i}\, dT \\ & with\;\; \Delta H^0_{R,reaction} = \sum_i \nu_i \cdot \Delta H^o_{f,i} \\ & and\;\; \int_{T_0}^{TsK} c_{p,i}\, dT = B \cdot TsK + C \cdot D \cdot \coth\left(\frac{D}{TsK}\right) - E \cdot F \cdot \tanh\left(\frac{F}{TsK}\right) - O\end{aligned} \qquad \text{Eq. 157}$$

The coefficient O and the applied ideal gas enthalpy of formation value for the considered species are given in Table 5-8, whereas the coefficients B, C, D, E and F can be found in Table 5-1. All values were taken from ASPEN PLUS.

By definition, the heats of reaction of all heterogeneous reactions are attributed to the solid structure of the fuel cell. The differing heat capacities of educt and product species as well as the different temperature of the gas phase and the solid structure result in an enthalpy flux coupled to the mass flow from the solid structure to the gas phase and vice versa.

Table 5-8: Ideal gas enthalpy of formation and DIPPR correlation coefficient O for the calculation of the heats of reaction

Specie	Ideal gas enthalpy of formation [J/mol]	O [J/mol]
Hydrogen	0.0	29767.51
Carbon monoxide	-110530.0	22739.05
Carbon dioxide	-393510.0	43153.18
Water	-241814.0	69491.22
Methane	-74520.0	135578.96
Ethene	52510.0	120989.08
Nitrogen	0.0	23243.35
Toluene	50170.0	309484.72
Acetic acid	-432800.0	146450.25
Anisole	-67900.0	333408.36
Oxygen	0.0	23257.56

This mass transport coupled enthalpy flux was considered in this model. Eq. 158 to Eq. 160 give the mass transfer coupled enthalpy flux of the educts, $\dot{Q}_{SH,ed,an}$, and products, $\dot{Q}_{SH,prod,an}$, at the anode and the enthalpy flux at the cathode, $\dot{Q}_{SH,ed,ca}$.

$$\dot{Q}_{SH,ed,an} = \sum_j r_j \cdot TaK \cdot \sum_i \nu_{i,ed} \cdot c_{p,i,TaK} \qquad \text{Eq. 158}$$

$$\dot{Q}_{SH,prod,an} = \sum_j r_j \cdot TsK \cdot \sum_i \nu_{i,prod} \cdot c_{p,i,TsK} \qquad \text{Eq. 159}$$

$$\dot{Q}_{SH,ed,ca} = r_{O_2\,ion} \cdot TcK \cdot c_{p,O_2,TcK} \qquad \text{Eq. 160}$$

In these equations, r_j stands for the reaction rate of the considered heterogeneous reactions, including the electrochemical reactions, occurring at the anode, Eq. 121 to Eq. 125 as well as Eq. 86 and Eq. 87, and $r_{O2\,ion}$ represents the reaction rate of reaction Eq. 88. TaK, TcK and TsK denote the anode and cathode gas and the solid structure temperature, respectively. Further, ν_i represents the stoiciometric coefficient of educt (subscript ed) and product (subscript $prod$) species of the according reaction. Finally, the heat capacity of the educts and products is calculated at the gas or the solid structure temperature (subscripts TaK, TcK and TsK).

5.3.1.6 Energy balance model

Considering the strong heat exchange mechanisms between the solid cell components, namely heat conduction and radiation, and taking into account the compactness of the considered fuel cell designs, the assumption of only one effective solid structure temperature for all solid cell components is reasonable, [190]. However, this assumption does not necessarily include the gas phase temperatures due to the weak heat exchange via convection and the negligible radiative heat exchange between solid structure and gas phase.

In order to account for these conclusions, the energy balance model determines the axial temperature profile of the solid structure, of the anode gas and cathode gas as well as the air in the air delivery tube in case of a tubular design. The calculations are based on the results of the electrochemical performance model and of the mass balance model.

Figure 5-13 depicts the outline of the energy balance model for an infinitesimal control volume with the three balance cases of the planar design, namely the anode and cathode gas channel as well as the solid structure, and the additional fourth balance case of the tubular cell design, namely the air delivery tube.

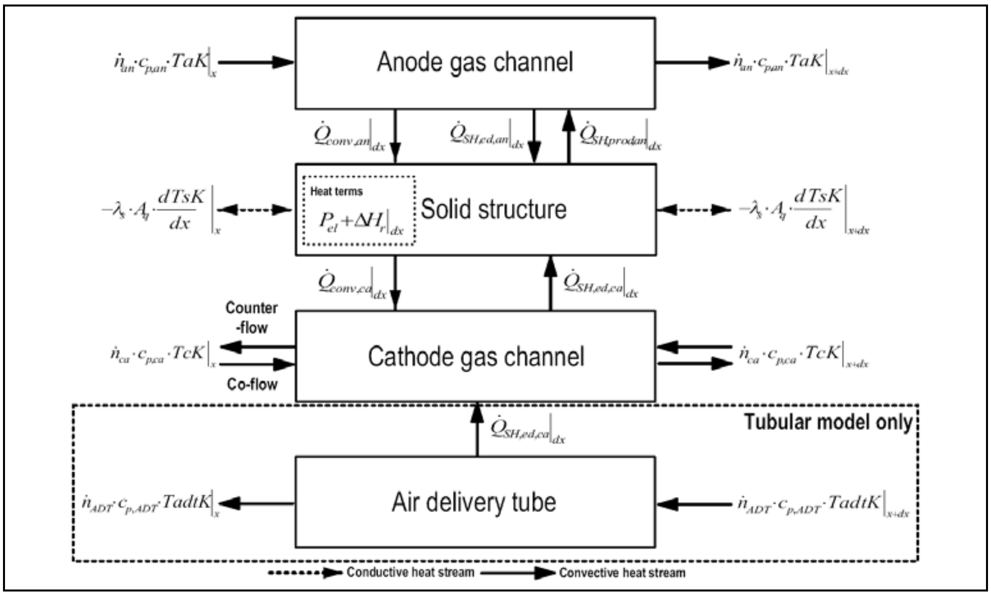
Anode gas channel
$\dot{n}_{an} \cdot c_{p,an} \cdot TaK|_x$
$\dot{n}_{an} \cdot c_{p,an} \cdot TaK|_{x+dx}$
$\dot{Q}_{conv,an}|_{dx}$
$\dot{Q}_{SH,ed,an}|_{dx}$
$\dot{Q}_{SH,prod,an}|_{dx}$
Heat terms
$P_{el} + \Delta H_r|_{dx}$
Solid structure
$-\lambda_s \cdot A_q \cdot \frac{dTsK}{dx}|_x$
$-\lambda_s \cdot A_q \cdot \frac{dTsK}{dx}|_{x+dx}$
$\dot{Q}_{conv,ca}|_{dx}$
$\dot{Q}_{SH,ed,ca}|_{dx}$
Counter -flow
Co-flow
Cathode gas channel
$\dot{n}_{ca} \cdot c_{p,ca} \cdot TcK|_x$
$\dot{n}_{ca} \cdot c_{p,ca} \cdot TcK|_{x+dx}$
Tubular model only
$\dot{Q}_{SH,ed,ca}|_{dx}$
Air delivery tube
$\dot{n}_{ADT} \cdot c_{p,ADT} \cdot TadtK|_x$
$\dot{n}_{ADT} \cdot c_{p,ADT} \cdot TadtK|_{x+dx}$
Conductive heat stream
Convective heat stream

Figure 5-13: Outline of the energy balance model

The energy balance of the anode gas channel includes the sensible heat stream, $\dot{n}_{an} \cdot c_{p,an} \cdot TaK$, entering the control volume at the coordinate x and leaving it at $x+dx$. Furthermore, the enthalpy fluxes due to the different heat capacity of the educt, $\dot{Q}_{SH,ed,an}$, and product species, $\dot{Q}_{SH,prod,an}$, reacting at the anode are accounted for. The value of the enthalpy fluxes is calculated according to Eq. 158 and Eq. 159, respectively. Finally the conductive heat stream between solid structure and anode gas channel is considered, Eq. 161. α_{an} denotes the heat transfer coefficient, TaK stands for the anode gas temperature and TsK

represents the solid structure temperature. The heat transfer coefficient α_{an} is calculated using the Nusselt number Nu, the thermal conductivity of the anode gas, λ_{an}, which is considered temperature and composition dependent, see Eq. 39 and Eq. 41, and the hydraulic diameter of the anode gas channel, $d_{t/p,hyd,an}$.

$$\dot{Q}_{conv,an} = \alpha_{an} \cdot l_{t/p,circ,an} \cdot \left(TaK - TsK\right) \;\; with \;\; \alpha_{an} = \frac{Nu \cdot \lambda_{an}}{d_{t/p,hyd,an}} \qquad \text{Eq. 161}$$

The differential equation describing the axial temperature distribution along the anode gas channel can thus be formulated as follows:

$$\frac{d\left(\dot{n}_{an} \cdot c_{p,an} \cdot TaK\right)}{dx} = \dot{Q}_{SH,prod,an} - \dot{Q}_{SH,ed,an} - \dot{Q}_{conv,an} \qquad \text{Eq. 162}$$

It should be noted, that this model considers the change of the total molar flow, n_{an}, and the change of the heat capacity, $c_{p,an}$, due to the change of the gas composition over the control volume. In some models found in the literature, only the temperature change is accounted for by assuming the heat capacity and sometimes also the molar flows are fixed at the inlet conditions of the corresponding control volume, [140, 182, 208]. For coarse discretization aiming at short calculation times, this can cause problems with the gas channel energy balance closure.

The energy balance of the solid structure involves the overall heat of reaction, Eq. 156, and the mass transfer coupled enthalpy fluxes at the anode and cathode electrode, Eq. 158 to Eq. 160. Besides this, the convective heat streams between the solid structure and anode, $\dot{Q}_{conv,an}$, as well as cathode gas channel, $\dot{Q}_{conv,ca}$, have to be taken into account. In the present model, the produced electrical power, P_{el}, is regarded as a source term for the solid structure and is computed according to Eq. 163. Note that the total current density I_{tot} results from the electrochemical performance model and E_{op} is the user-defined operational voltage of the fuel cell. In order to transform this area specific power density into an integration length specific value, it has to be multiplied with the electrochemically active length of the fuel cell design in question, $l_{t/p,elact}$.

$$P_{el} = -l_{t/p,elact} \cdot I_{tot} \cdot E_{op} \qquad \text{Eq. 163}$$

The convective heat stream between the cathode gas channel and the solid structure is determined according to Eq. 164 considering the temperature difference between cathode gas, TcK, and solid structure, TsK, the effective heat transfer coefficient, α_{ca}, and the circumferential length of the cathode gas channel, $l_{t/p,circ,ca}$. Analogously to Eq. 161, the heat transfer coefficient of the cathode gas channel is calculated with the temperature and gas composition dependent thermal conductivity of the cathode gas, λ_{ca}, and the hydraulic diameter of the cathode gas channel, $d_{t/p,hyd,ca}$, of the investigated fuel cell design. The Nusselt number, Nu, is assumed to equal that of the anode gas channel, as in both cases laminar flow is assumed. It is important to emphasize that the convective heat stream of the cathode gas channel is considered positive, when heat is transferred from the solid structure to the cathode gas. This is due to the cooling task of the air flow in the cathode channel.

$$\dot{Q}_{conv,ca} = \alpha_{ca} \cdot l_{t/p,circ,ca} \cdot (TsK - TcK) \;\; with \;\; \alpha_{ca} = \frac{Nu \cdot \lambda_{ca}}{d_{t/p,hyd,ca}} \qquad \text{Eq. 164}$$

Finally in this model, the energy balance of the solid structure includes solid heat conduction. This yields the second order derivate differential equation, Eq. 165, for the solid structure temperature, TsK, where λ_s symbolizes the average solid heat conduction coefficient of the solid structure and $A_{t/p,cross}$ stands for the cross-sectional area which is perpendicular to the gas flow channels.

$$\lambda_s \cdot A_{t/p,cross} \cdot \frac{d^2TsK}{dx^2} = \dot{Q}_{conv,ca} - \dot{Q}_{conv,an} - \dot{Q}_{SH,ed,an} - \dot{Q}_{SH,ed,ca} + \dot{Q}_{SH,prod,an} + \Delta H_r + P_{el} \qquad \text{Eq. 165}$$

All terms required to compute the cathode gas temperature of the planar cell design have been previously mentioned and yield Eq. 166.

$$\begin{aligned} \frac{d(\dot{n}_{ca} \cdot c_{p,ca} \cdot TcK)}{dx} &= \dot{Q}_{conv,ca} - \dot{Q}_{SH,ed,an} + \dot{Q}_{conv,ADT} \quad (co-flow) \\ &= \dot{Q}_{SH,ed,an} - \dot{Q}_{conv,ca} \quad (counter-flow) \end{aligned} \qquad \text{Eq. 166}$$

Analogously to the differential equation of the anode gas channel, the change of the molar flow and of the heat capacity is considered.

In the presented model, the two considered flow patterns of the planar cell designs where modeled through the cathode gas balances, see also the mass balance, e.g. Eq. 153. In principle, the tubular cell design has a co-flow pattern. However, the design typical air delivery tube, adds one more term to the cathode gas energy balance, namely the convective heat stream from the air delivery tube to the cathode gas, $\dot{Q}_{conv,ADT}$.

$\dot{Q}_{conv,ADT}$ aggregates the convective heat transport from the cathode air, with the temperature TcK, to the air delivery tube and from the air delivery tube (ADT) to the cold air flowing inside the ADT, with the temperature $TadtK$, Eq. 167. In this model, the two processes are accounted for through an effective heat exchange coefficient, $\alpha_{ADT,eff}$, which was proposed in [209]. The calculation of $\alpha_{ADT,eff}$ includes the inner, $r_{i,ADT}$, and outer radius, $r_{o,ADT}$, of the ADT, the heat exchange coefficients of the cathode gas, α_{ca}, and inside the ADT, α_{ADT}. Also included is the solid heat conduction coefficient of the ADT material, $\lambda_{s,ADT}$, which leads to either enhanced or reduced convective heat exchange in cold or hot regions of the ADT, respectively. α_{ADT} is computed analogously to the other heat exchange coefficients.

$$\begin{aligned}
&\dot{Q}_{conv,ADT} = \alpha_{ADT,eff} \cdot l_{t,circ,ADT} \cdot (TadtK - TcK) \\
&with\ \ \alpha_{ADT,eff} = \frac{1}{r_{i,ADT}} \cdot \left(\frac{1}{r_{i,ADT} \cdot \alpha_{ADT}} + \frac{1}{4 \cdot \lambda_{s,ADT}} \cdot \ln\left(\frac{r_{o,ADT}}{r_{i,ADT}}\right) + \frac{1}{r_{o,ADT} \cdot \alpha_{ca}} \right) \\
&and\ \ \alpha_{ADT} = \frac{Nu \cdot \lambda_{ADT}}{d_{t,hyd,ADT}}
\end{aligned} \qquad \text{Eq. 167}$$

The energy balance of the air flow inside the ADT can then be formulated as Eq. 168. Since the air flow inside the ADT is not partaking in any chemical or electrochemical reactions, the molar flow is constant. Accordingly the differential equation for the ADT energy balance was simplified in the present model.

$$\dot{n}_{ADT} \cdot \frac{d(c_{p,ADT} \cdot TadtK)}{dx} = \dot{Q}_{conv,ADT} \qquad \text{Eq. 168}$$

5.3.1.7 Boundary conditions

The energy balance model alongside the mass balance and the electrochemical performance model constitute a highly coupled and strongly non-linear differential equation system. In this model, the cells are divided into n control volumes (CV). An inclusive solution is found once the governing equations are solved for each CV. Boundary conditions need to be defined for the CVs at the outer ends of the cells. The mass balance boundary condition values are calculated based on the user-defined operating conditions. The fuel inlet composition is therefore specified in molar fractions of the considered species, y_i. The total molar flow of the fuel gas at the cell inlet, $n_{an,0}$, is either calculated based on a targeted overall current density, $I_{tot,av}$, and related fuel utilization, UF, Eq. 169, or by specifying a lower heating value (LHV) based input power, P_{in}, Eq. 170.

$$\begin{aligned}\dot{n}_{an,0} &= \frac{I_{tot,av}\cdot A_{p/t,act}}{2\cdot F\cdot UF\cdot Eq_{H_2}}\\ with\ \ Eq_{H_2} &= y_{H_2}+y_{CO}+4\cdot y_{CH_4}+6\cdot y_{C_2H_4}\\ &\quad +18\cdot y_{C_7H_8}+4\cdot y_{C_2H_4O_2}+17\cdot y_{C_7H_8O}\end{aligned} \qquad \text{Eq. 169}$$

In Eq. 169, $A_{p/t,act}$ denotes the electrochemically active area of the considered fuel cell design and Eq_{H2} represents the hydrogen equivalent of the prescribed input gas composition.

$$\dot{n}_{an,0} = \frac{P_{in}}{LHV_{in}\cdot n_{RE}} \quad with\ \ n_{RE} = n_{ch}\cdot n_{cells}\ \ or\ \ n_{RE} = n_{tubes} \qquad \text{Eq. 170}$$

n_{RE} in Eq. 170 stands for the number of repeating elements in the stack. For the tubular design, the repeating element is a whole cell tube, whereas for the planar design only one fuel and air channel is considered. Hence, for the planar design the number of repeating elements is the product of the number of cells in the stack, n_{cells}, and the number of channels per cell, n_{ch}. Furthermore, LHV_{in} stands for the lower heating value of the prescribed fuel gas composition.

In this model, the standard cathode gas input composition is equal to that of air or more precisely 79 mol-% nitrogen and 21 mol-% oxygen. However, other compositions such as e.g. pure oxygen can also be defined. The inlet molar flow of the cathode gas, $n_{ca,0}$, is either assigned directly or by specifying an air-to-fuel ratio, λ.

$$\begin{aligned}\dot{n}_{ca,0} &= \frac{\dot{n}_{O_2,stoic}\cdot\lambda}{y_{O_2}}\\ with\ \ \dot{n}_{O_2,stoic} &= \dot{n}_{an,0}\cdot(0.5\cdot y_{H_2}+0.5\cdot y_{CO}+2\cdot y_{CH_4}\\ &\quad +3\cdot y_{C_2H_4}+9\cdot y_{C_7H_8}+2\cdot y_{C_2H_4O_2}+8.5\cdot y_{C_7H_8O})\end{aligned} \qquad \text{Eq. 171}$$

In the latter case Eq. 171 applies, where $n_{O2,stoic}$ gives the oxygen molar flow required for the stoiciometric combustion of the fuel gas. Depending on the investigated fuel cell design and the considered flow pattern, the mass balance boundary values were assigned to different CVs, see Table 5-9 where *(0)* denotes the first and *(n)* the last CV.

Table 5-9: Mass balance boundary conditions

Mass balance	Planar Co-flow	Planar Counter-flow	Tubular
Anode gas	$\dot{n}_{an(0)} = \dot{n}_{an,0}$	$\dot{n}_{an(0)} = \dot{n}_{an,0}$	$\dot{n}_{an(0)} = \dot{n}_{an,0}$
Cathode gas	$\dot{n}_{ca(0)} = \dot{n}_{ca,0}$	$\dot{n}_{ca(n)} = \dot{n}_{ca,0}$	$\dot{n}_{ca(0)} = \dot{n}_{ca,0}$
Air delivery tube	-	-	$\dot{n}_{ADT(n)} = \dot{n}_{ca,0}$

The total molar flow values n_{an}, n_{ca} and n_{ADT} are related to the molar flows of the single species via the user-defined molar fractions.

Besides the inlet molar flow, the present model requires the definition of the gas temperatures at the inlet in order to solve the energy balance equation of the gas channels. The inlet gas temperature of the anode gas channel, $T_{an,in}$, the cathode gas channel, $T_{ca,in}$ and eventually of the air deliver tube, $T_{ADT,in}$, are user-defined values and assigned as shown in Table 5-10.

Table 5-10:
Gas phase energy balance boundary conditions

Energy balance	Planar Co-flow	Planar Counter-flow	Tubular
Anode gas	$TaK_{(0)} = T_{an,in}$	$TaK_{(0)} = T_{an,in}$	$TaK_{(0)} = T_{an,in}$
Cathode gas	$TcK_{(0)} = T_{ca,in}$	$TcK_{(n)} = T_{ca,in}$	$TcK_{(0)} = TadtK_{(0)}$
Air delivery tube	-	-	$TadtK_{(n)} = T_{ADT,in}$

In case of the tubular cell design, the boundary conditions of the cathode gas channel ensure the continuity between the temperature and the molar flow of the air flow exiting the air delivery tube and entering the cathode gas channel.

Owing to the considered solid heat conduction, the energy balance of the solid structure includes a second derivate term. Hence, the solution of each CV depends on the solutions of the neighboring CVs. Consequently, boundary conditions have to be defined at both ends of the integration region.

The differential equation applying at the left boundary (first control volume of the integration region) is given by Eq. 172.

$$\lambda_s \cdot A_{t/p,cross} \cdot \frac{dTsK}{dx} = \dot{Q}_{hloss} \qquad \text{Eq. 172}$$

$\dot{Q}_{hloss}$ represents the heat loss stream to the surroundings. At the right boundary, the source terms of the last CV of the integration region have to be taken into account, Eq. 173.

$$\begin{gathered} \lambda_s \cdot A_{t/p,cross} \cdot \frac{dTsK}{dx} = \\ \left(\dot{Q}_{conv,ca} - \dot{Q}_{conv,an} - \dot{Q}_{SH,ed,an} - \dot{Q}_{SH,ed,ca} + \dot{Q}_{SH,prod,an} + \Delta H_r + P_{el}\right) \cdot dx - \dot{Q}_{hloss} \end{gathered} \qquad \text{Eq. 173}$$

For the tubular design the cell ends are generally assumed adiabatic. In contrast, the developed model features the possibility to assume adiabatic cell ends, radiative or conductive heat losses at the cell ends of planar cells. Where adiabatic cell ends are assumed for the simulation of a perfect insulation, $\dot{Q}_{hloss}$ is set to zero. The value of the radiative heat loss streams is calculated according to Eq. 174, [190], where α_{rad} denotes the radiative heat exchange coefficient, σ stands for the Stefan-Boltzmann constant and $Tsur$ represents the Temperature of the surroundings.

$$\dot{Q}_{hloss} = \alpha_{rad} \cdot A_{t/p,cross} \cdot (TsK - Tsur) \;\; with \;\; \alpha_{rad} = 4 \cdot \sigma \cdot \left(\frac{Tsur + TsK}{2} \right)^3 \qquad \text{Eq. 174}$$

Assuming conductive heat losses through an insulation, Eq. 175, [190], applies, where α_{insul} stands for the heat transfer coefficient through the insulation and $Tamb$ represents the ambient temperature.

$$\dot{Q}_{hloss} = \alpha_{insul} \cdot A_{t/p,cross} \cdot (TsK - Tamb) \qquad \text{Eq. 175}$$

5.3.1.8 Solution strategies

The strongly coupled and highly non-linear nature of the model equation system inhibits an algebraic solution. Instead, it requires a numerical solution starting with an initial conjecture. Convergence is fastly reached, when the initial conjecture approximates the true solution. If the initial conjecture is far off the mark, convergence might not be reached.

In the present model, the standard initial conjecture is that the inlet values apply to all CVs. With this linear initial guess, the developed model reliably reaches convergence with respect to fuel gases with a hydrocarbon content of up to 5 vol.-%. Fuel gases with higher hydrocarbon contents lead to strongly non-linear spatial species distributions, which are difficult to solve numerically. One way to overcome these convergence problems is to compute interim solutions which are used as initial conjectures for the next iteration process until the final solution is found. ATHENA allows the computation of a new solution beginning with a "saved" solution instead of using the linear initial conjecture. The boxes "*save the final solution*" and "*start with the saved solution*" in the solver panel under the tab "*solution history*", need to be activated.

Experience has shown that it is advantageous to begin the solution iteration from a gas composition containing hydrogen and carbon monoxide at equal rates. In this case the solver needs not to overcome an activation barrier to compute carbon monoxide originating currents for a hydrocarbon containing fuel gas. Usually, three to five interim solutions are sufficient to find the desired final solution. Following this strategy allows this model to handle fuel gases with almost unlimited hydrocarbon content. The investigation of different operating conditions implies fewer convergence difficulties. Guidelines that might promote a faster outcome can also be formulated. Changes of the model input that strongly influence the anode gas mass balance, e.g. increase of the fuel mass flow or change of the fuel composition, have to be undertaken in small incremental steps. On the other hand changes of e.g. the voltage can be performed in comparably large increments. This is due to the absolute mass flow values remaining virtually constant. Changes of input gas temperatures have a strong impact on the energy balance and therefore also require an iterative approach in small steps.

If the employed numerical solver is unable to find a solution, the values of the state variables of the last solution need to be examined. If the values of any of the state variables have reached numbers very close to zero or are disproportionately high the envisaged operational point could be physically unfeasible. This physical unfeasibility might be the reason for the perceived non-convergence. If on the other hand physical infeasibility was ruled out the solver could be blocked in a semi-stable solution point. In this case the only operational strategy is to return to a stable and physically adequate solution and change the input for the next interim solution so that the semi-stable point is avoided.

5.3.2 Planar model verification

A quantitative validation of the planar model is almost infeasible as only few complete data sets of real planar SOFC stacks have been published thus far. Furthermore, the ohmic losses of a cell depend largely on the geometry of the bipolar plates, also called interconnector plates (IC). This model considers a generalized geometry of the bipolar plates for which data is not available at all.

Nevertheless, a verification of the developed model is carried out by comparing the results to a benchmark test (BMT) to ensure that the developed numerical code has reached the BMT quality standard. The BMT was defined in an International Energy Agency (IEA) program for the numerical simulation of SOFCs with planar geometry, [112]. In total, nine academic and industrial institutions participated in the BMT. The independently developed numerical SOFC models showed good agreement regarding the predicted physical behavior for two fuel gas compositions, which were humidified hydrogen and 30 % pre-reformed methane, Table 5-11.

Table 5-11:
Fuel and cathode gas compositions of the BMT

Specie	Unit	Fuel gas IEA 1	Fuel gas IEA 2	Cathode gas	Source
Hydrogen	vol.-%	90.00	26.26	-	[112]
Carbon monoxide		-	2.94	-	
Carbon dioxide		-	4.36	-	
Water		10.00	49.34	-	
Methane		-	17.10	-	
Nitrogen		-	-	79.00	
Oxygen		-	-	21.00	

Table 5-12 gives the BMT geometry data of the planar SOFC stack.

Table 5-12:
Geometrical input data of BMT

Model input data	Unit	Value	Source
Macro geometry of planar cell			
Flow design	-	Co- and counter-flow	[112]
Number of cells in stack	-	1	
Number of gas channels per cell	-	18	
Cell width	m	0.1	
Cell length	m	0.1	
Gas channel width	m	0.003	
Anode and cathode channel height	m	0.001	
Height of IC on anode/ cathode side	m	0.00125	
Area covered by IC participating in electrochemistry	%	100.0	
Chemically act. area covered by IC	%	0.0	
Micro geometry of planar cell			
Support design	-	Electrolyte	[112]
Anode thickness	μm	50.0	
Electrolyte thickness	μm	150.0	
Cathode thickness	μm	50.0	

Table 5-13 shows the operational conditions defined for the BMT.

Table 5-13:
Operational conditions of BMT

Model input data	Unit	Value	Source
Operational conditions			
Targeted mean current density	A/m^2	3000.0	[112]
Targeted fuel utilization	%	85.0	
Air-to-fuel ratio	-	7.0	
Fuel gas inlet temperature	K	1173.15	
Cathode gas inlet temperature	K	1173.15	
Ambient temperature	K	293.15	
System pressure	bara	1.01325	

The BMT participants agreed to consider only ohmic losses for a better comparability of the model results. The specific ohmic resistances of the ceramic components were calculated according to the equations Eq. 45 to Eq. 48. For the planar SOFC, ceramic bipolar plates were assumed. Further, the applied kinetics data for the steam reforming reaction (STR) were prescribed, Eq. 130. Table 5-14 gives the BMT parameter used for the energy balance calculations.

Table 5-14: Energy balance input data of BMT

Model input data	Unit	Value	Source
Solid heat conduction			
Heat conductivity of anode	W/ m K	2.0	[112]
Heat conductivity of electrolyte		2.0	
Heat conductivity of cathode		2.0	
Heat conductivity of interconnect		2.0	
Convective heat transfer			
Nusselt number	-	4.0	[112]

Besides the described model input data, several assumptions were defined for the BMT, Table 5-15.

Table 5-15: Model settings of BMT

Model settings	Description
Electrochemical loss model settings	
Considered electrochemical active species	Hydrogen
Activation polarization equation	Equal to ohmic loss of electrolyte
Energy balance settings	
Solid heat transfer mechanism	Non-isothermal with solid heat conduction
Coupled heat and mass transport	Considered
Heat loss mechanism at outer surface	Conduction through insulating plates
Heat capacity and heat of reaction correlation	published in [190]
Definition of sensible heat gradient	$\dot{n} \cdot c_p\big|_x \cdot \frac{dT}{dx}$

The most important assumptions were that the activation polarization losses are equal to the ohmic loss of the electrolyte and that the diffusion losses are negligible. For this reason, a validation of activation and diffusion loss model parameters is not indicated using the BMT results. Furthermore, the change of the molar flow and the heat capacity of the gas mixture was neglected in the calculation of the gas phase energy balance. Instead the calculations were performed with a simplified definition of the sensible heat gradient by holding the molar flow and heat capacity constant at the value of the antecedent control volume for the respective control volume. Further information can be found in [112].

Figure 5-14 shows the comparison of results of the developed model for the co-flow pattern considering both IEA fuel gases, Table 5-11.

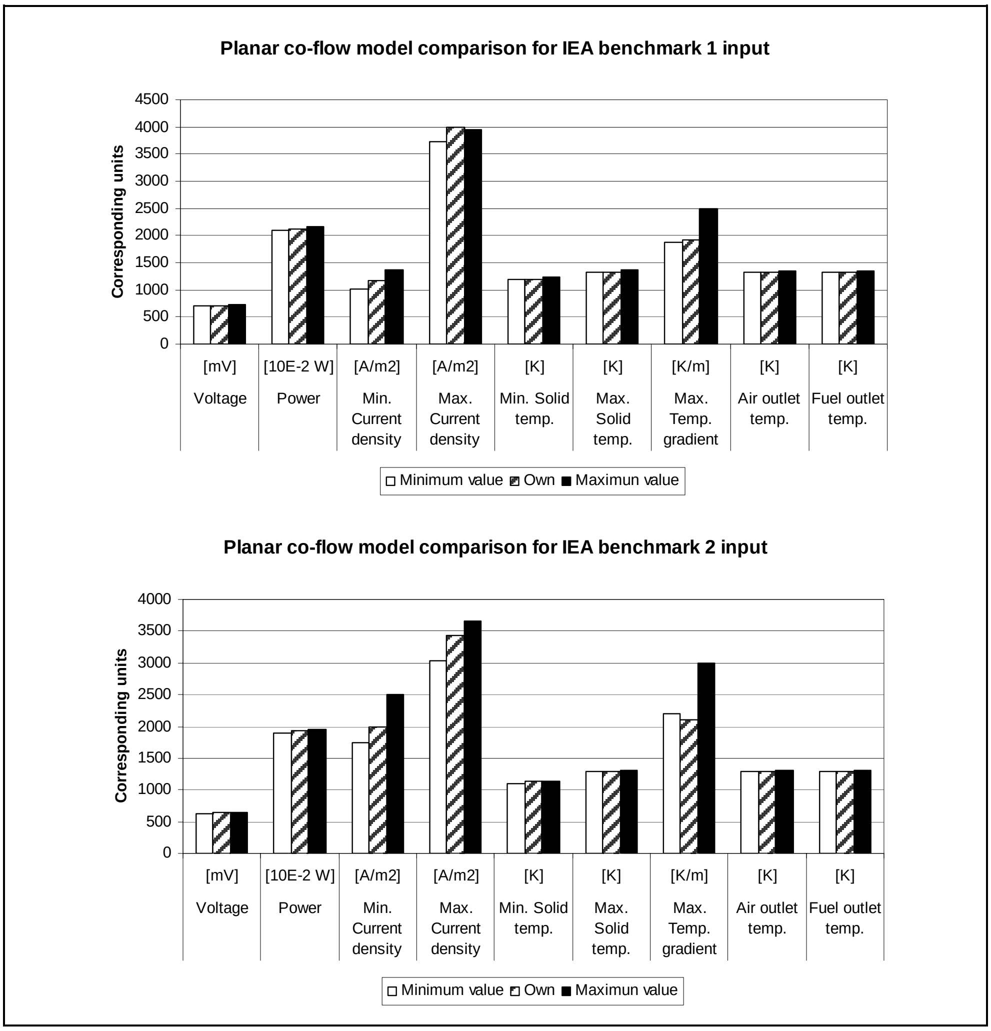

Figure 5-14: Comparison of co-flow model results with BMT results for fuel compositions IEA 1 and IEA 2

The terms "Minimum value" and "Maximum value" refer to the minimum and maximum values among all the BMT participants, whereas "Own" refers to the results obtained from the author's model.

Figure 5-15 shows the comparison of results for the counter-flow pattern. It can be seen, that the results of the developed model lie mostly between the minimum and maximum values of the BMT. Exceptions are found for the maximum current density (Figure 5-14, fuel gas IEA 1) and the maximum solid temperature gradient (Figure 5-14 and Figure 5-15, fuel gas IEA 2).

Figure 5-15: Comparison of counter-flow model results with BMT results for fuel compositions IEA 1 and IEA 2

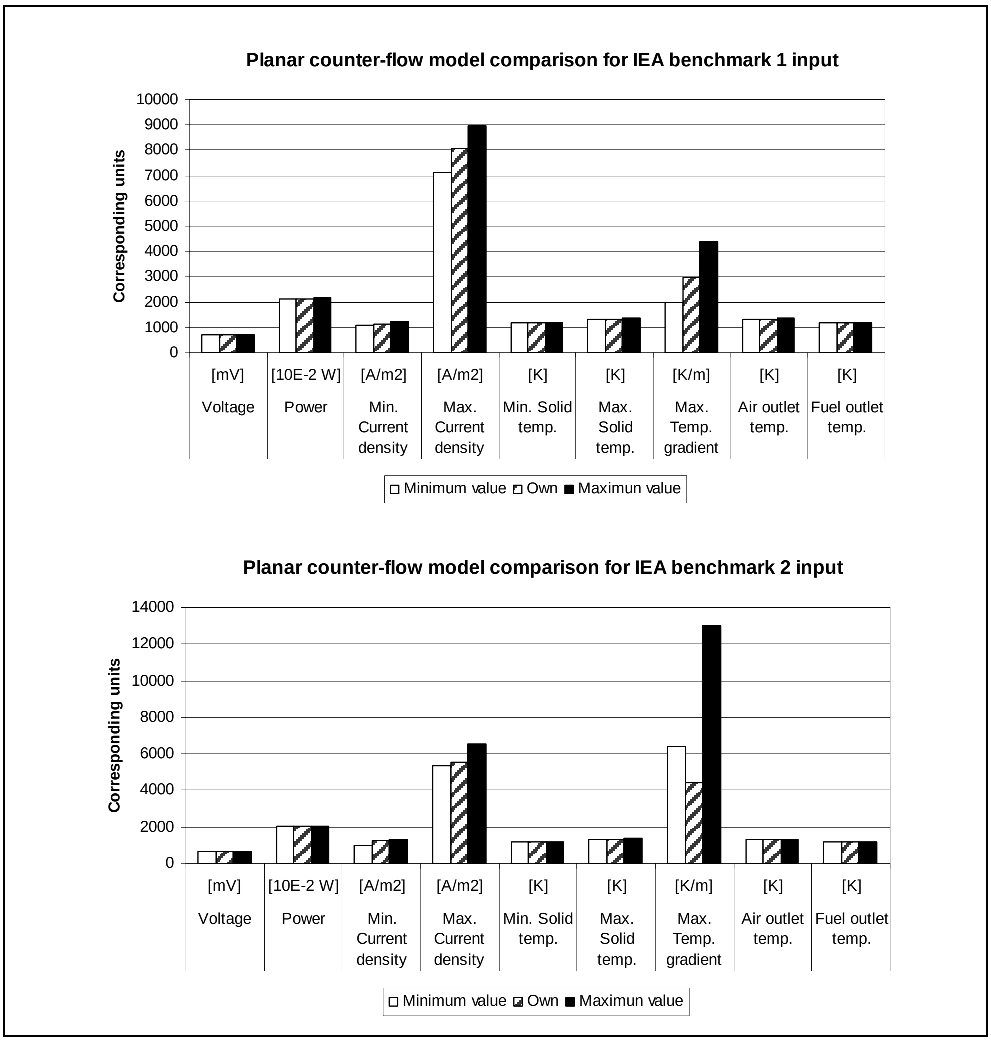

The local temperature curves obtained from the author's model were compared with those of the BMT activity leader, Achenbach, [112], to find explanations for the discrepancies, Figure 5-16.

Figure 5-16: Comparison of temperature profiles for the IEA 1 fuel composition and counter-flow pattern computed by the Achenbach model, [112], and the developed model with 20 and 100 discretization points

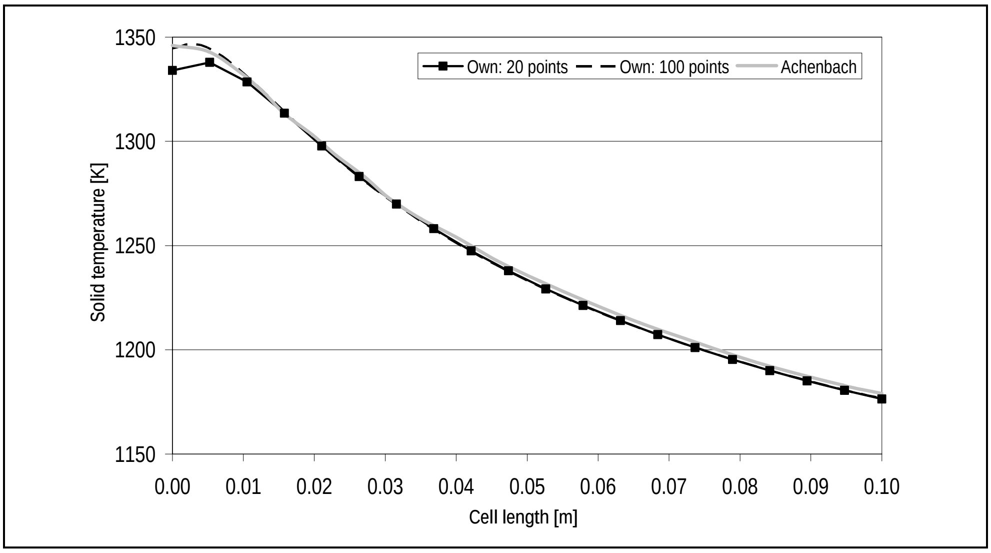

It was found that different numbers of control volumes were used for the discretization of the considered planar cell. Figure 5-16 shows the impact of the number of discretization points on the computed temperature profile. The temperature gradients at the channel ends are determined by the considered heat losses. Coarse discretization leads to an overestimated impact of the cell end heat losses on the temperature profile.

However, the general trends were not affected by the coarse discretization which has the advantage of short calculation times around 30 seconds run on a conventional personal computer. In summary it can be stated that the author's model behaves physically correct and that there is no systematic discrepancy with the results of other participants in the BMT. In all the simulations, the error in the mass balance was below 0.5 % and in the energy balance below 2 %. Compared to the state-of-the-art with 1 % error in the mass balance and up to 6 % error in the energy balance, [114], the author's model is considered a reliable tool for the simulation of planar SOFCs.

5.3.3 Tubular model validation

In contrast to the planar geometry, suitable experimental data can be found in the literature for a quantitative validation of the tubular geometry. Moreover, the modeled tubular geometry is not generalized, but based on the cell design promoted by the Siemens AG. The geometrical data for the description of the standard tubular Siemens AG cell is given in Table 5-16.

Table 5-16: Geometrical input data for tubular Siemens AG cell model

Model input data	Unit	Value	Source
Macro geometry of tubular cell			
Flow design	-	Co-flow with air delivery tube	[140, 155]
Cell tube length	m	1.5	
Inner radius of air delivery tube	m	0.0025	
Outer radius of air delivery tube	m	0.004	
Inner radius of cell tube	m	0.00866	
Thickness of virtual fuel channel (depends on stacking of cell tubes)	m	0.0023	
Percentage of circumferential length of cell tube covered by IC	%	10.0	
Micro geometry of planar cell			
Support design	-	Cathode	[140, 155]
Anode thickness	μm	100.0	
Electrolyte thickness	μm	40.0	
Cathode thickness	μm	2200.0	

The aim of validating the developed model considering the tubular cell geometry is to ensure that the generalized approach, which is based on characteristic lengths and areas, has been properly adapted to the tubular cell design. Although the most important parts of the model code were already confirmed using the BMT for the planar geometry, there is still a need to also verify the equations involved in the calculation of the activation and diffusion losses given these were excluded from the BMT.

The experimental voltage-current curves used for the validation are published in [70]. The characterized standard tubular Siemens AG cell was operated with a fuel gas mixture consisting of 89 vol.-% H_2 and 11 vol.-% H_2O at three different cell temperatures, 900 °C, 940 °C and 1000 °C. The latter feature predestines this data set for model validation, as it allows the model to be checked regarding the correct prediction of temperature effects. Model results obtained for other temperatures can be assumed valid, in case the model reliably predicts the temperature induced effects of the validation case. When model validation is carried out with data sets measured at a single temperature, the results are only valid for this temperature. Hence extrapolated results have to be considered less reliable.

The voltage-current curves were experimentally determined with constant fuel utilization of 85 % and an air-to-fuel ratio of 4. For the simulation, the model further requires as operational input data the gas inlet temperatures, system pressure and temperature of the surroundings. The gas inlet temperatures were assumed 100 K lower than the respective mean cell temperature, [155]. As the author of [70] stated that the measurements were carried out using a prototypic cell, it was assumed that the cell was operated in an oven exhibiting a constant wall temperature. The surroundings temperature required for the radiational heat transfer calculation was assumed equal to the mean cell temperature, [155]. The heat transfer calculation input data is given in Table 5-17.

Table 5-17: Energy balance input data for tubular Siemens AG cell model validation

Model input data	Unit	Value	Source
Solid heat conduction			
Heat conductivity of anode	W/ m K	6.23	[140]
Heat conductivity of electrolyte		2.7	
Heat conductivity of cathode		9.6	
Heat conductivity of air delivery tube		11.8	
Nusselt number	-	4.0	

The electrochemical loss model parameters are given in Table 5-18.

Table 5-18: Electrochemical loss model input data for tubular Siemens AG cell model

Model input data	Unit	Value	Source
Activation polarization			
H_2 oxidation activation energy	J/mol	110000.0	[202]
H_2 oxidation pre-exponential factor	A/m^2	7000000000.0	
CO oxidation activation energy	J/mol	110000.0	[190, 202]
CO oxidation pre-exponential factor	A/m^2	5000000000.0	
O_2 reduction activation energy	J/mol	149500.0	[155]
O_2 reduction pre-exponential factor	A/m^2	10260000000.0	
Ohmic polarization			
Electric conductivity of anode	1/Ohm m	T-dependent, Eq. 45	[191]
Ionic conductivity of electrolyte	1/Ohm m	T-dependent, Eq. 46	
Electric conductivity of cathode	1/Ohm m	T-dependent, Eq. 47	
Electric conductivity of interconnect	Ohm m	2.0E-7	[155]
Diffusion polarization			
Porosity of anode	-	0.4	[140]
Tortuosity of anode	-	3.0	
Pore diameter of anode and cathode	m	1.0E-6	
Porosity of cathode	-	0.5	
Tortuosity of cathode	-	1.8	-

The conductivity of the anode, electrolyte and cathode were calculated using the same correlations as in the BMT. The diffusion polarization loss parameters were taken from Stiller, [140]. However, the cathode electrode tortuosity was slightly increased from 1.5 to 1.8 in order to closer reproduce the diffusion limitation at high current densities. The activation polarization parameters for the hydrogen oxidation and for the oxygen ionization were taken from Campanari, [202], and Thorud, [155], respectively. Both authors determined the values by means of parameter estimation. A drawback of this approach is, that all uncertainties of the remaining model input parameters and of the measurement to which the model is fitted are summed up in the activation loss parameters. Nevertheless, the lack of complete experimental data sets from which these parameters could be derived justifies this approach. The activation loss parameters for the carbon monoxide oxidation were calculated based on those of the hydrogen oxidation and the relation proposed in [190].

Figure 5-17: Comparison of simulated and measured voltage-current curve of a standard tubular Siemens AG cell measured at a mean cell temperature of 900 °C

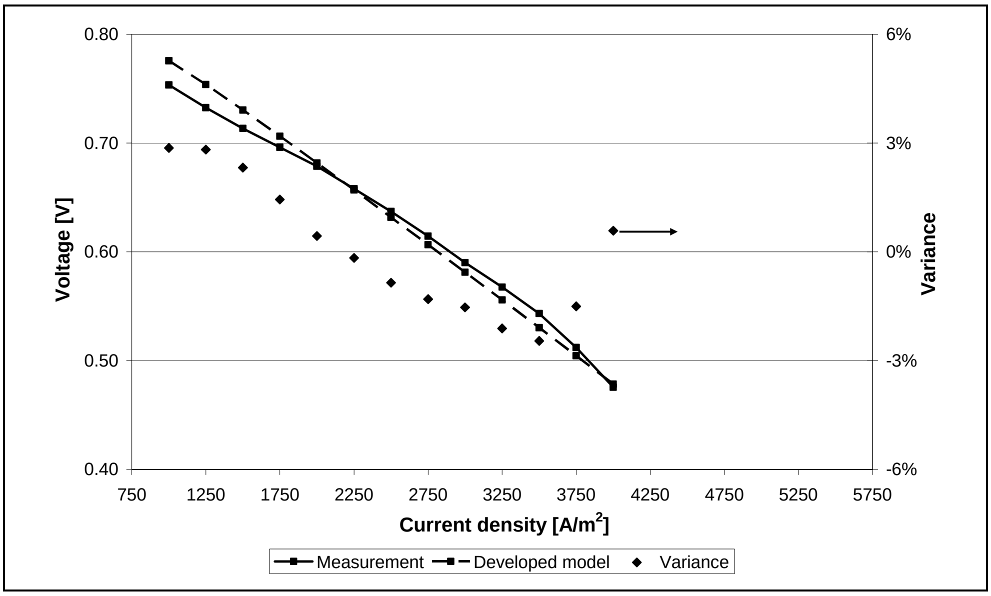

Figure 5-17 shows the comparison of simulated (dashed line) and measured (full line) voltage-current density (UI) characteristics of the tubular cell operated at 900 °C. The slightly higher slope of the simulated UI curve indicates an overestimation of the ohmic resistance and an underestimation of the activation polarization at low current density values. The mean variance of the predicted voltage for 900 °C operational mean cell temperature compared to the measured values is 1.6 % and the maximum variance is below +/-3 % (right axis of graph).

Figure 5-18 shows, the simulated and measured U-I curve for 940 °C mean cell temperature.

Figure 5-18: Comparison of simulated and measured voltage-current curve of a standard tubular Siemens AG cell measured at a mean cell temperature of 940 °C

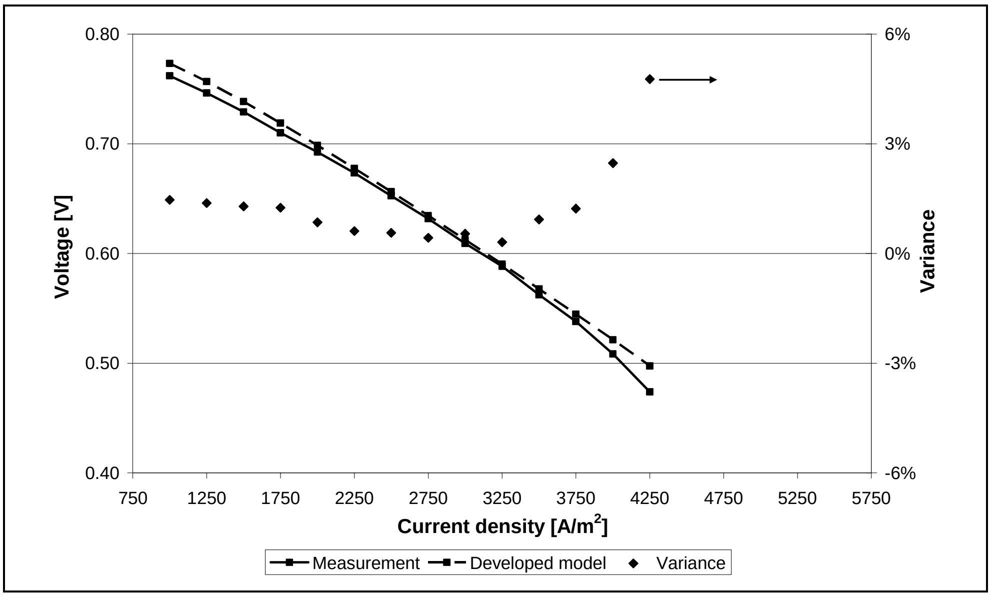

It can be seen, that the predicted voltage values diverge by less than 1 % for small and medium current density values. At higher current density values the variance increases up to 5 %, indicating an underestimation of the diffusion polarization losses. However, the activation and ohmic losses are predicted well resulting in a good match of the UI curve slope of the simulated and measured curve. The mean variance between predicted and measured voltage values for 940 °C mean cell temperature is 1.3 % and the maximum variance is below +5 %.Figure 5-19 depicts the comparison of simulated and measured voltage-current curve measured at a mean cell temperature of 1000 °C.

Figure 5-19: Comparison of simulated and measured voltage-current curve of a standard tubular Siemens AG cell measured at a mean cell temperature of 1000 °C

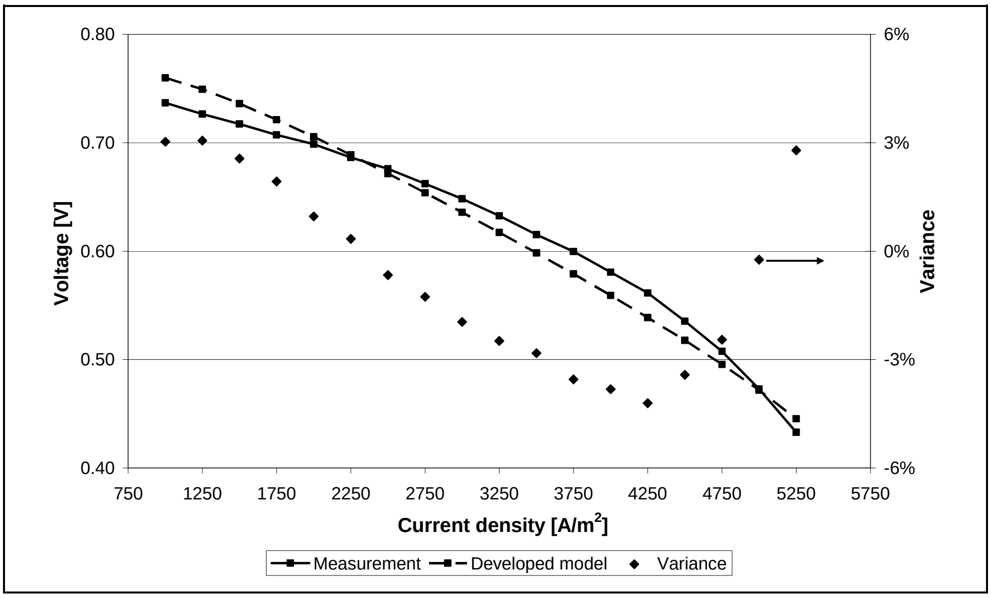

Similar to the predicted UI curve for 900 °C, the model underestimates the activation losses at low current densities for 1000 °C mean cell temperature. Further, the slope of the predicted curve is again steeper than of the measured UI curve indicating a slight overestimation of the ohmic losses. At high current density values, the model predicts a slight bend of the UI curve due to increasing diffusion losses. This phenomenon can be observed more pronounced for the measurement. Nevertheless, the prediction of this phenomenon clearly shows that the developed tubular cell model behaves physically correct. The mean variance between predicted and measured voltage values for 1000 °C mean cell temperature is 2.3 % and the maximum variance is below +/-4 %.

In summary, the mean variance of the model results from the measurement results was found to be below 2.5 % for all the three considered mean cell temperatures. The developed tubular cell model behaves physically correct and there is no systematic discrepancy to the measurement results. In conclusion it can be stated that the developed generalized model was properly adapted to the tubular cell geometry promoted by the Siemens AG. Furthermore, the activation and diffusion loss model equations and related model parameters proved to yield accurate results. Keeping in mind that the model parameters were collected from various sources, the validation was considered successful.

5.3.4 Triangular model validation

The data regarding DELTA8 cells (D8) is scarce as this type of cells has only recently been developed by the Siemens AG. Nevertheless, Table 5-19 gives the currently available D8 cell geometrical data.

Table 5-19: Geometrical input data for triangular D8 cell model

Model input data	Unit	Value	Source
Macro geometry of tubular cell			
Flow design	-	Co-flow with air delivery tube	-
Cell length	m	1.0	[210]
Cell width	m	0.15	
Triangle half angle	°	30.0	
Number of triangular tubes per cell	-	8	
Inner radius of air delivery tube	m	0.002	-
Outer radius of air delivery tube	m	0.003	-
Micro geometry of planar cell			
Support design	-	Cathode	[211]
Anode thickness	μm	100.0	
Electrolyte thickness	μm	60.0	
Cathode thickness	μm	1500.0	
Interconnect thickness	μm	100.0	

It is important to point out, that the geometry of the air delivery tube was not taken from a publication but was assumed to yield an adequate cathode gas channel cross-sectional area. This assumption directly impacts the convective heat transfer between the cathode gas and the air delivery tube. The convective heat transfer between the cathode gas and the solid structure however dominates in any case, such that the overall impact of this assumption is considered less significant.

The experimental voltage-current curve used for the validation of the triangular cell model was measured at the Siemens AG using a D8 cell segment, [210]. The 1 cm long D8 cell segment was operated under isothermal conditions in an oven at temperatures between 950 and 965 °C with fuel and air excess. The fuel mixture consisted of 50 vol.-% H_2 and 50 vol.-% H_2O, being the expected average gas composition of a full-scale cell operated at 85 % fuel utilization with 89 vol.-% H_2 and 11 vol.-% H_2O. Due to the isothermal conditions and the virtually constant reactant partial pressures along the D8 cell segment, the voltage-current curve was simulated by using the electrochemical performance model without consideration to the energy and heat balance. With respect to the model parameters, it was assumed that the anode and cathode materials used for the D8 cells resemble those used for the standard tubular cells. Accordingly, the model parameters given in Table 5-18 were used for the simulation. Exceptions were the electric conductivity of the interconnect material, which was calculated according to Eq. 48, and the ionic conductivity of the electrolyte, as D8 cells employ scandia-stabilized zirconia (ScSZ) instead of the state-of-the-art yttrium-stabilized zirconia (YSZ) as electrolyte material, [210]. At temperatures above 900 °C, ScSZ features ionic conductivities about three times higher than YSZ, [79]. Hence, the conductivity values computed via Eq. 46 were multiplied by three for the D8 cell segment simulation.

Figure 5-20: Comparison of simulated and measured voltage-current curve of a D8 cell segment measured at a temperature between 950 and 965 °C

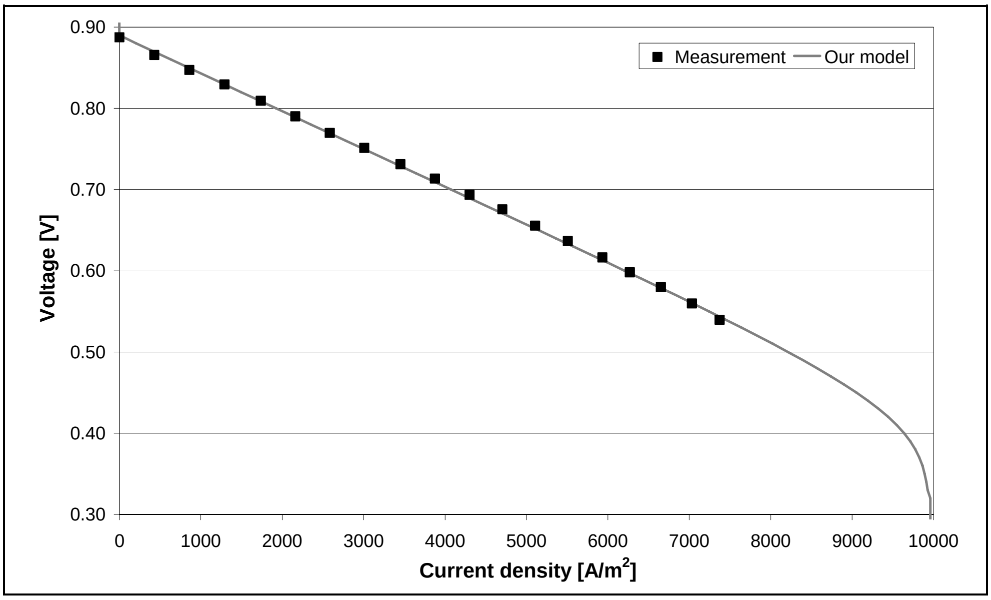

Figure 5-20 depicts the comparison of the measured and the simulated voltage-current curve of the D8 cell segment.

The simulation result for 957 °C fits the measured data well. It is concluded, that the author's model was successfully applied to the triangular geometry thereby validating the discussed assumptions.

5.3.5 Sensitivity analysis

The complex mechanisms of SOFC electrochemistry are still not fully understood and are therefore mostly modeled using semi-empirical correlations. This introduces several constants to the model equation system, which have to be determined experimentally in order to allow for a reliable performance prediction of the SOFC in question. The relative importance of model parameters was assessed with the following sensitivity analysis aiming at the impact on the current density distribution and local temperatures resulting in the predicted power output.

The applied methodology is that a single model parameter or a set of interdependent parameters is varied at once while all other parameters are held constant at the reference value. Unless otherwise stated, the varied model parameter is increased or decreased by 25 and 50 % based on the corresponding reference value.

The operational voltage is the only actual control variable of SOFCs as the fuel input flow is a design value defined by the targeted fuel utilization and the active cell area. Further, the input air flow follows from the targeted mean cell temperature and the maximum allowed solid temperatures. In order to conform to this, the fuel utilization is being held constant by adjusting the operational voltage throughout the whole sensitivity analysis. This allows to better isolate the impact of the varied model parameter from side effects that are an indirect consequence of the parameter variation. For instance, increasing the ohmic resistance with constant operational voltage yields lower fuel utilization. As a consequence of the reduced amount of electrochemical reactions, the mean cell temperature drops, causing higher ohmic losses and so on. This self-energizing effect leads to an overestimation of the impact of the increased ohmic loss. Unfortunately, it is not always obvious what side effects might distort the impact of a model parameter.

5.3.5.1 Reference case

The values of the varied model parameters are given in Table 5-20 for the reference case. It should be noted that the exchange current density for the activation polarization loss calculation were computed using the equations Eq. 92 to Eq. 94, [182].

The sensitivity analysis was carried out for the two BMT fuel gases, Table 5-11. The IEA 1 gas allows for the explicit investigation of the model constant variation impact on the electrochemistry. The IEA 2 gas was investigated to determine the coherences when also internal reforming reactions take place. The STR reaction rates were computed via Eq. 130.

Table 5-20: Electrochemical loss model input data of reference case

Model input data	Unit	Value	Source
Activation polarization			
H_2 oxidation activation energy	J/mol	120000.0	[182]
H_2 oxidation pre-exponential factor	A/m^2	290000000.0	
CO oxidation activation energy	J/mol	120000.0	[190]
CO oxidation pre-exponential factor	A/m^2	207000000.0	
O_2 reduction activation energy	J/mol	120000.0	[182]
O_2 reduction pre-exponential factor	A/m^2	700000000.0	
Ohmic polarization			
Electric conductivity of anode	1/Ohm m	T-dependent, Eq. 45	[191]
Ionic conductivity of electrolyte	1/Ohm m	T-dependent, Eq. 46	
Electric conductivity of cathode	1/Ohm m	T-dependent, Eq. 47	
Electric conductivity of ceramic IC	1/Ohm m	T-dependent, Eq. 48	
Diffusion polarization			
Porosity of anode	-	0.5	[141]
Tortuosity of anode	-	3.0	
Average pore diameter of anode	m	1.0E-6	
Porosity of cathode	-	0.5	
Tortuosity of cathode	-	3.0	
Average pore diameter of cathode	m	1.0E-6	

The cell geometry is planar and equal to that of the IEA BMT, Table 5-12. The considered flow configuration is co-flow. Operational conditions for the sensitivity analysis are given in Table 5-13. The material property parameters used in the energy balance calculations are given in Table 5-14. Table 5-21 summarizes the integral model response values for the reference case and both considered fuel gases.

Table 5-21: Model response values for the reference case for IEA 1 and IEA 2 gas

Response value	Unit	Fuel gas IEA 1	Fuel gas IEA 2
Maximum solid temperature gradient	K/mm	2.2	2.0
Maximum solid temperature	K	1327.9	1286.9
Minimum solid temperature		1212.0	1146.3
Mean solid temperature		1282.7	1221.9
Operational voltage for 85 % fuel utilization	V	0.683	0.624

Figure 5-21 depicts the predicted temperature profiles of the solid structure for the reference case and both considered fuel gases.

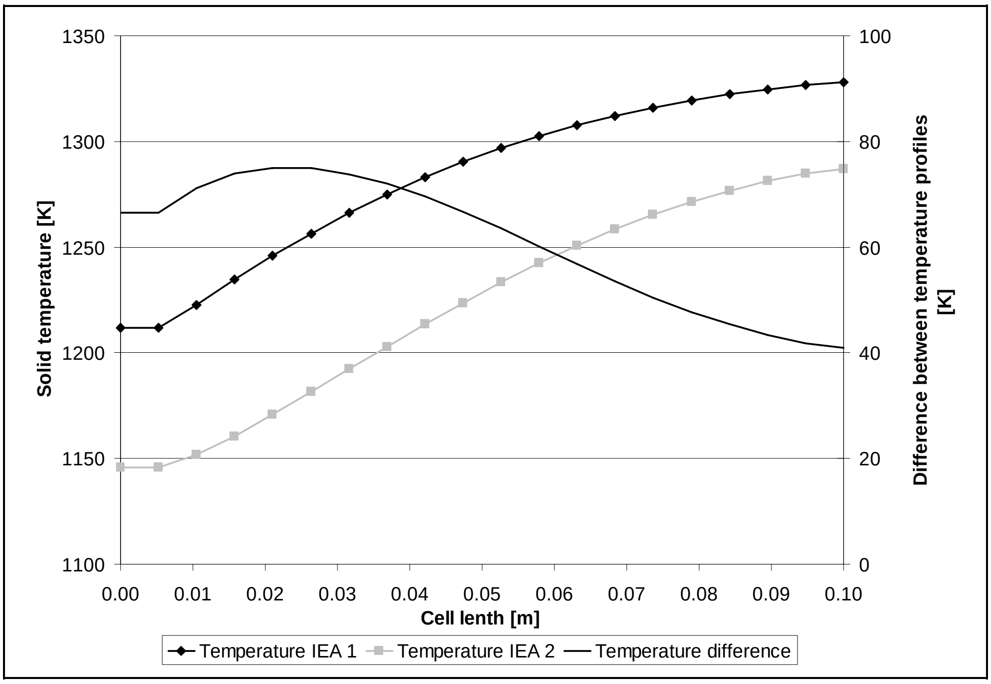

Figure 5-21:
Solid temperature distributions and difference for the reference case for IEA 1 and IEA 2 gas

It can be seen, that at the cell inlet (x-axis: cell length equals zero) the temperature predicted for the fuel gas IEA 1 is approx. 65 K higher than for the fuel gas IEA 2. That can be explained with the endothermal steam reforming reactions taking place due to the methane containing fuel gas IEA 2. At the cell outlet (x-axis: cell length equals 0.1 m), the difference between the two temperature distributions is decreased to approx. 40 K. The difference between the temperature profiles of the two fuel gases is represented by the curve named "Temperature difference". This curve is considered an indicator for the thermal prediction behavior of the model towards changes of the fuel composition.

5.3.5.2 Variation of activation polarization parameters

In the author's model, the electrochemical conversion of hydrogen and carbon monoxide were assumed to occur in parallel. Each of the conversion processes is described with an activation energy value and a pre-exponential factor. These model parameters are interdependent as e.g. increasing only the activation energy of the hydrogen conversion leads to a compensating carbon monoxide current and vice versa. To avoid this, the activation energy values of both conversion processes are varied at once. The same applies for the pre-exponential factors.

5.3.5.2.1 Activation energy

Figure 5-22 depicts the sensitivity of the current density distribution towards the anode activation energy.

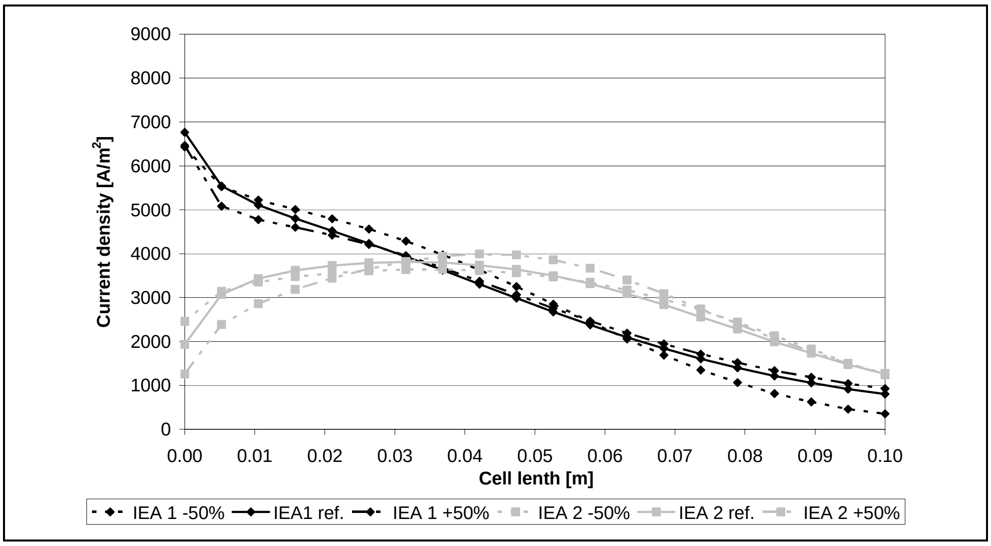

Figure 5-22: Sensitivity of current density distribution towards anode activation energy for IEA 1 and IEA 2 gas

For the IEA 1 gas, the maximum current is produced at the cell inlet. This is due to the high hydrogen partial pressure of the IEA 1 gas. From thereon the current density constantly decreases along the cell length because of the ongoing fuel conversion and accordingly decreased educt partial pressures. In contrast, the IEA 2 gas yields the maximum educt partial pressures in the region where the methane steam reforming reactions are complete. Consequently, the current density is not constantly decreasing along the cell length, but is somewhat evenly distributed with a wide and flat peak.

Decreasing the anode activation energy means to increase the activity towards electrochemical reactions yielding higher current density values in the cell inlet region for both gases. The increased fuel consumption in the cell inlet region causes a considerable current density decrease at the cell outlet for the IEA 1 gas. However, for the IEA 2 gas the current density at the cell outlet remains constant, as the fuel consumption in the cell inlet region is dominated by the hydrogen production through steam reforming reactions. This leaves more hydrogen over for the latter part of the cell. In short, the less hydrogen is produced cell internally through steam reforming, the more does a decrease of the activation energy yield an increased current density at the cell inlet which accompanies a current density decrease at the outlet.

Table 5-22 shows that for both fuel gases, the increase of the anode activation energy yields an increase of the temperature extremes, the maximum temperature gradient and the mean cell temperature.

Table 5-22: Model response values for different anode activation energy values for IEA 1 and IEA 2 gas

Parameter value	Max. dT [K/mm]	Cell outlet temperature [K]	Cell inlet temperature [K]	Mean cell temperature [K]	Operational Voltage [V]
IEA 1 gas					
-50 %	2.1	1311.6	1208.1	1274.2	0.750
-25 %	2.1	1312.6	1208.4	1274.5	0.746
Reference	2.2	1327.9	1212.0	1282.7	0.683
+25 %	3.0	1384.7	1223.9	1320.3	0.446
+50 %	3.9	1449.5	1237.3	1364.5	0.175
IEA 2 gas					
-50 %	1.7	1264.2	1142.9	1207.1	0.717
-25 %	1.7	1265.8	1143.2	1208.4	0.710
Reference	2.0	1286.9	1146.3	1221.9	0.624
+25 %	2.8	1345.4	1150.0	1255.2	0.376
+50 %	3.7	1408.4	1153.9	1290.6	0.107

This is the result of the constant fuel utilization, which requires higher temperatures due to the lower activity towards electrochemical reactions when the activation energy value is increased.

The operational voltage to meet the defined fuel utilization is strongly decreased for higher activation energies while it is only little increased for lower values, Figure 5-23.

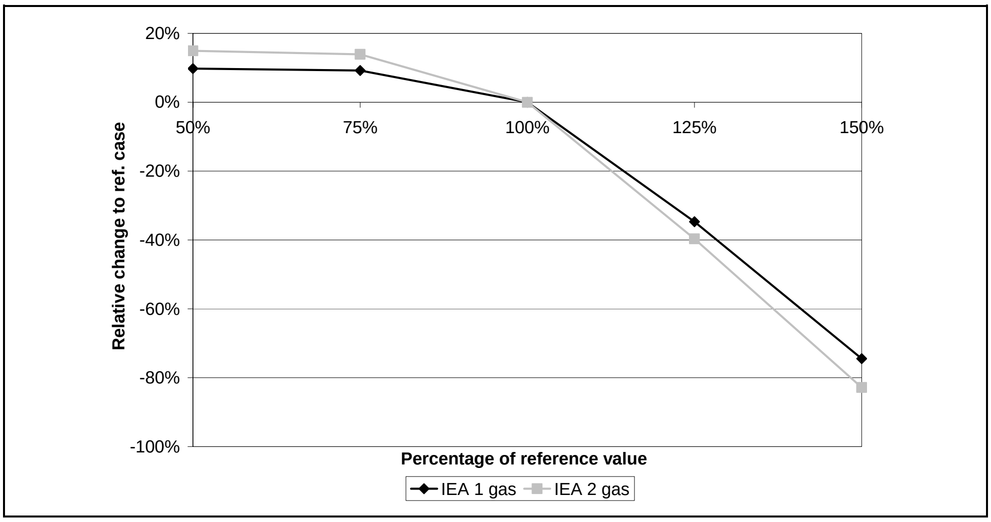

Figure 5-23: Difference between the predicted power output for varying anode activation energy values obtained for IEA 1 and IEA 2 gas

It is important to point out that SOFCs are usually not operated at voltages below 0.5 V. The predicted voltage values for increased activation energies indicate that in reality a fuel cell employing such an anode catalyst can not reach 85 % fuel utilization. For the lower activation energy values, the power output increases by a maximum of 15 % and decreases by 80 % for the higher values.

Figure 5-24: Temperature difference between the predicted temperature distributions for varying anode activation energy values obtained for IEA 1 and IEA 2 gas

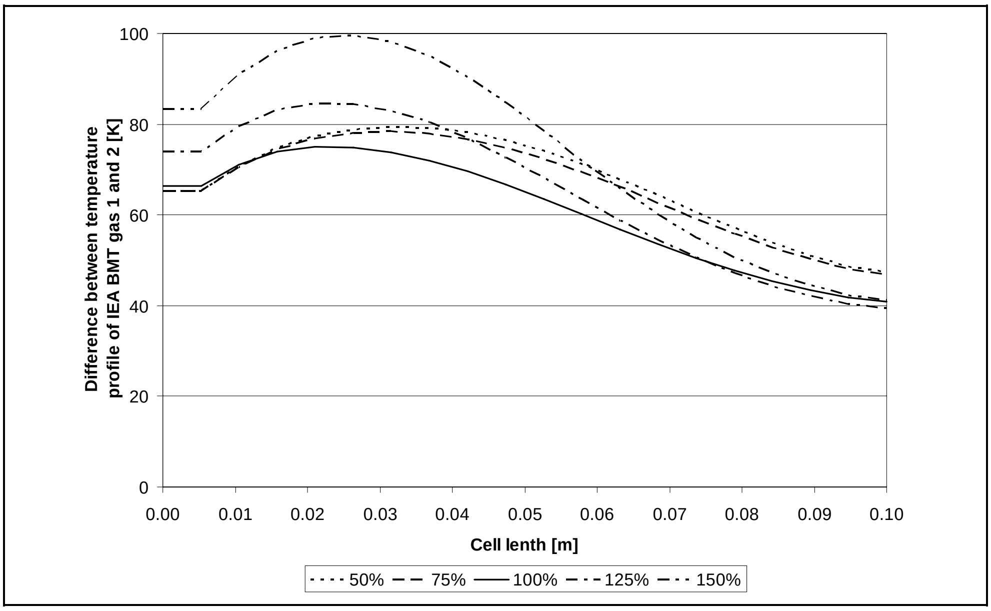

Figure 5-24 depicts the sensitivity of the difference between the temperature profiles of the two fuel gases towards the anode activation energy. The local temperatures are strongly influenced by the locally produced power, which depends on the prevalent current density and the operational voltage, see also Table 5-22. For a fixed operational voltage, high current densities usually lead to high temperatures. However, endothermal reactions such as steam reforming counteract this, provided that the reaction rate is considerable.

It can be seen, that higher values of the activation energy yield an increase of the difference between the predicted temperatures near the cell inlet and a higher reforming peak. This can be traced back to the fact that the temperature at the cell inlet for the fuel gas IEA 2 is dominated by the steam reforming reaction and does not change significantly by varying the activation energy. In contrast, the temperature at the cell inlet increases significantly with increasing activation energy for the IEA 1 gas. The reason for this is that the operational voltage was strongly reduced in order to meet the required overall fuel utilization. As a consequence, the amount of produced power is low even though the current density is only slightly decreased with increasing activation energy. As less electrical power is produced from a still considerable amount of converted fuel, more sensible heat is released from the electrochemical reactions resulting in higher local temperatures.

Lowering the anode activation energy causes an increase of the temperature difference towards the cell end. Similar to the above discussed increase of the activation energy, the cell inlet temperature of the IEA 2 gas remains almost equal to the reference case. However with low activation energy values, the high amount of produced power plus the heat consumed by the endothermal steam reforming leads to a lower temperature for the IEA 2 gas at the cell outlet compared to the reference case. For the IEA 1 gas the missing steam reforming cooling is compensated to a smaller extent by low current densities at the cell outlet due to fuel depletion. Hence, the temperature difference between the two gases is increased at the cell end.

Figure 5-25 depicts the sensitivity of the current density distribution towards the cathode activation energy. Note that the cathode activation energy was not decreased by more than 20 % as the associated high electrochemical activity at the cell inlet for both fuel gases caused substantial fuel depletion effects at the cell outlet, which resulted in numerical instability of the employed solver.

Figure 5-25: Sensitivity of current density distribution towards cathode activation energy for IEA 1 and IEA 2 gas

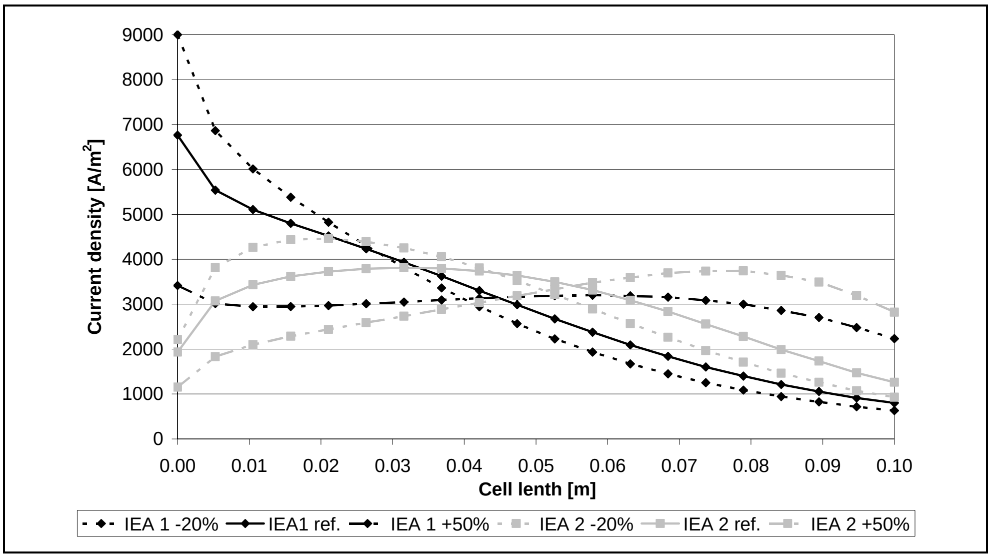

For the reference case the anode activation losses are slightly higher than the cathode activation losses. By decreasing the cathode activation energy the anode activation polarization becomes dominant. As a consequence of the dependency of the anode activation polarization on the educt partial pressures, the current density increases near the cell inlet or the end of the reforming region due to the high educt partial pressures and decreases at the cell outlet due to the upstream fuel consumption. This can be observed for both investigated fuel gases.

In contrast, an increase of the cathode activation energy yields a shift from anode to cathode activation polarization as dominant activation loss mechanism. The current density then depends on the oxygen partial pressure rather than on the educt partial pressures at the anode. The oxygen partial pressure does not change significantly along the cell length due to the considerably smaller air utilization as compared to the fuel utilization. For the IEA gas 1, the high current density values at the cell inlet are inhibited by the high cathode polarization and less hydrogen is consumed. Consequently, more hydrogen is left over for conversion in the latter parts of the cell. This results in a very even current density distribution for high cathode activation energy values.

For the IEA 2 gas an increase of the cathode activation energy strongly reduces the already small current density at the cell inlet. Similar to the IEA 1 gas, more educts are left for conversion in the latter part of the cell. However, in contrast to the IEA 1 gas, a current density peak can be observed at the cell outlet as additional hydrogen is produced via steam reforming reactions and a considerable oxygen partial pressure remains present in this region. In other words, increasing the cathode activation energy yields a considerable shift of the typical steam reforming induced current density peak for hydrocarbon containing fuel gases towards the cell end. The less hydrocarbons are present in the fuel gas, the more even the current density distribution becomes.

Table 5-23 shows that for both fuel gases, the increase of the cathode activation energy yields an increase of the cell outlet temperature whereas the cell inlet temperature remains almost constant. This results in higher temperature gradients. The cell inlet temperature stays constant because the smaller amount of fuel conversion at the cell inlet is compensated by more released sensible heat. This is because less electrical power is produced due to the lower operational voltage.

Table 5-23: Model response values for different cathode activation energy values for IEA 1 and IEA 2 gas

Parameter value	Max. dT [K/mm]	Cell outlet temperature [K]	Cell inlet temperature [K]	Mean cell temperature [K]	Operational Voltage [V]
IEA 1 gas					
-20 %	2.3	1322.4	1218.8	1284.7	0.705
-10 %	2.3	1323.9	1216.8	1284.2	0.699
Reference	2.2	1327.9	1212.0	1282.7	0.683
+25 %	2.1	1368.1	1205.1	1290.3	0.520
+50 %	2.6	1431.6	1209.1	1319.5	0.258
IEA 2 gas					
-20 %	2.2	1280.2	1149.6	1225.6	0.656
-10 %	2.2	1281.7	1148.3	1224.3	0.648
Reference	2.0	1286.9	1146.3	1221.9	0.624
+25 %	2.4	1334.9	1143.8	1234.0	0.424
+50 %	3.3	1397.3	1145.4	1258.6	0.162

The impact of the cathode activation energy on the required operational voltage to maintain the defined fuel utilization is depicted in Figure 5-26.

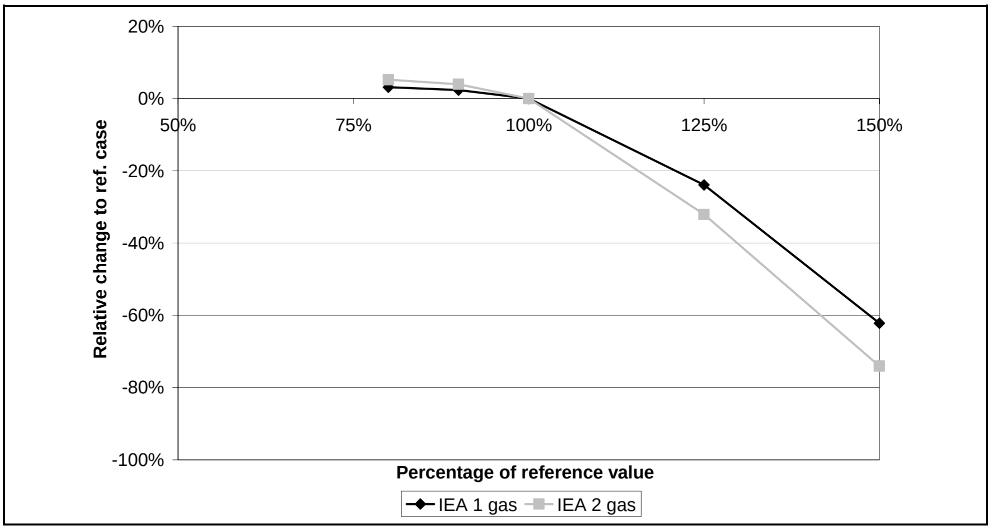

Figure 5-26: Difference between the predicted power output for varying cathode activation energy values obtained for IEA 1 and IEA 2 gas

Similar to the analysis of the anode activation energy, it is emphasized that operational voltages below 0.5 V are usually not applied.

With a maximum of approx. 5 % power output increase, the decrease of the cathode activation energy has a smaller impact as compared to the decrease of the anode activation energy. This can be traced back to the dominating role of the anode activation polarization which was calculated based on the reference parameters and hence inhibits a strong power output increase.

Increasing the cathode activation energy yields a maximum power output decrease of approx. 75 %. In this case, the reason for the smaller impact is that the cathode activation polarization dominates the process thereby weakening the impact of fuel depletion towards the cell end. Thus, the power loss, due to higher cathode activation losses, is counteracted by lower anode activation losses towards the cell end.

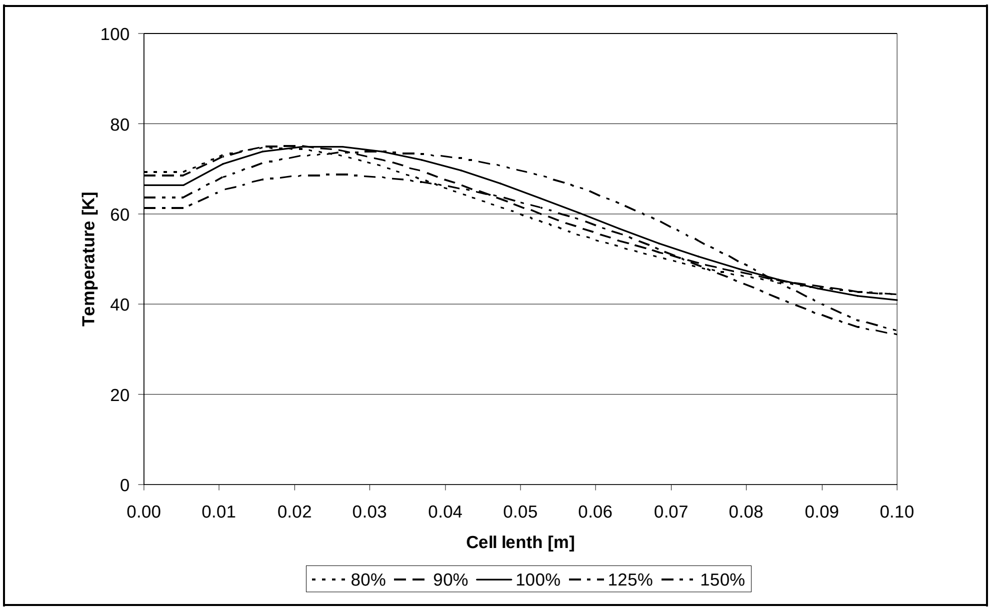

Figure 5-27: Temperature difference between the predicted temperature distributions for varying cathode activation energy values for IEA 1 and IEA 2 gas

Figure 5-27 shows the sensitivity of the difference between the temperature profiles of the two fuel gases towards the cathode activation energy. Comparing Figure 5-27 and Figure 5-24 one could pre-maturely conclude that the cathode activation energy has a weaker impact than the anode activation energy values on thermal behavior of the fuel cell for the two investigated fuel gases. However, the current density distributions for different cathode activation energy values reveal a different picture.

The strong reforming peak, which was discussed for higher anode activation energies, cannot be observed for the increased cathode activation energy values. Similar to the anode activation energy variation, the temperature at the cell inlet considering the IEA 2 gas is dominated by the occurring steam reforming reactions and does barely change with varying cathode activation values.

Considering the IEA 1 gas with higher cathode activation energy, the temperature at the cell inlet is slightly lower then in the reference case. The reason for that is that the produced current in this region is strongly reduced compared to the reference case due to the low oxygen partial pressure at the cathode compared to the initial hydrogen partial pressure of the IEA 1 gas. However, a strong temperature decline is inhibited by the low operational voltage, which results in a tangible amount of released sensible heat sufficient to maintain the inlet temperature on a level close to the reference case. Hence, the temperature difference found at the cell inlet for increased cathode activation energy values is slightly lower than for the reference case, which in turn explains the missing steam reforming peak.

Towards the cell end, the increased cathode activation causes higher current density values due to less fuel depletion in the front parts of the cell. This can be observed for both fuel gases. However, the temperature increase towards the cell end for the IEA 2 gas is stronger due to the previously discussed current density peak near the cell end. This explains the slightly lower temperature difference between the two investigated fuel gases at the cell end for higher cathode activation energy values as compared to the reference case.

As discussed for the current density distribution, decreasing the cathode activation energy puts the anode polarization into a dominant position. As the anode polarization losses are computed using the reference values, the temperature difference progression remains almost unchanged by the lowered cathode activation energy.

In conclusion it can be said, that the cathode and anode activation polarization energy values are model parameters which have to be handled carefully. The thermal prediction behavior, the predicted current density distribution and power output are all strongly influenced by these model parameters. In particular, the impact of the anode and cathode activation energy values has in each case a different nature. Thus, it is important to know if anode or cathode activation polarization is dominant. Dominating anode activation emphasizes the impact of the educt partial pressure distribution leading to high fuel conversion where educt partial pressures are high and vice versa. In contrast, high cathode activation losses yield a relatively even fuel consumption along the cell due to the almost constant oxygen partial pressures at the cathode resulting from the usually low air utilization. Regarding the local temperatures, large activation losses yield a higher amount of released sensible heat partially compensating the lower amount of converted fuel and vice versa. Unfortunately, these general rules are distorted in case internal reforming reactions take place. These reactions dominate the local temperature in the region where they occur.

5.3.5.2.2 Pre-exponential factor

Within the scope of variation, the impact of the anode activation pre-exponential factor on the predicted current density distribution is small compared to the above discussed activation energy. Increased fuel consumption at the cell inlet takes place for higher pre-exponential factor values. Analogously to decreased activation energy values, the higher fuel conversion at the cell inlet yields fuel depletion induced lower current densities at the cell outlet. However, the magnitude of changes is almost negligible. The sensitivity of the predicted power for constant fuel utilization towards the anode pre-exponential factor is shown in Figure 5-28. In contrast to the activation energy, a decrease of the pre-exponential factor leads to a decrease of power. This is because, in Eq. 92 to Eq. 94, the exchange current density depends linearly on the pre-exponential factor, whereas it depends on the multiplicative inverse of the activation energy.

Figure 5-28: Difference between the predicted power output for varying anode pre-exponential factor values for IEA 1 and IEA 2 gas

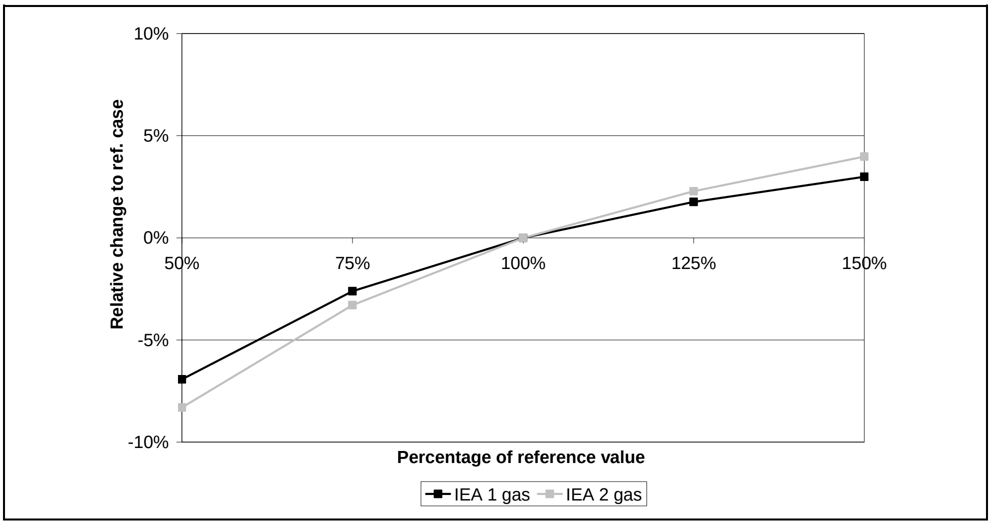

For lower anode pre-exponential factor values, the power output decreases by a maximum of 8 %, while it increases by a maximum of 4 % for higher anode pre-exponential factor values. Similar to the variation of the activation energy values, the IEA 2 gas shows a more pronounced response. The reasons for which were discussed above.

The minor changes of the current density distribution appear for both gases to almost equal rates. Further, as shown in Figure 5-28, the anode pre-exponential factor has a comparably small impact on the operational voltage or predicted power, respectively, for both gases. Together this yields almost negligible changes of the temperature difference. The reason for that is that the exchange current density linearly depends on the pre-exponential factor in contrast to the exponential dependency on the activation energy value. Similar results were found in [202]. Figure 5-29 depicts the sensitivity of the temperature distribution trend towards the anode pre-exponential factor.

Figure 5-29: Temperature difference between the predicted temperature distributions for varying anode activation pre-exponential factor values for IEA 1 and IEA 2 gas

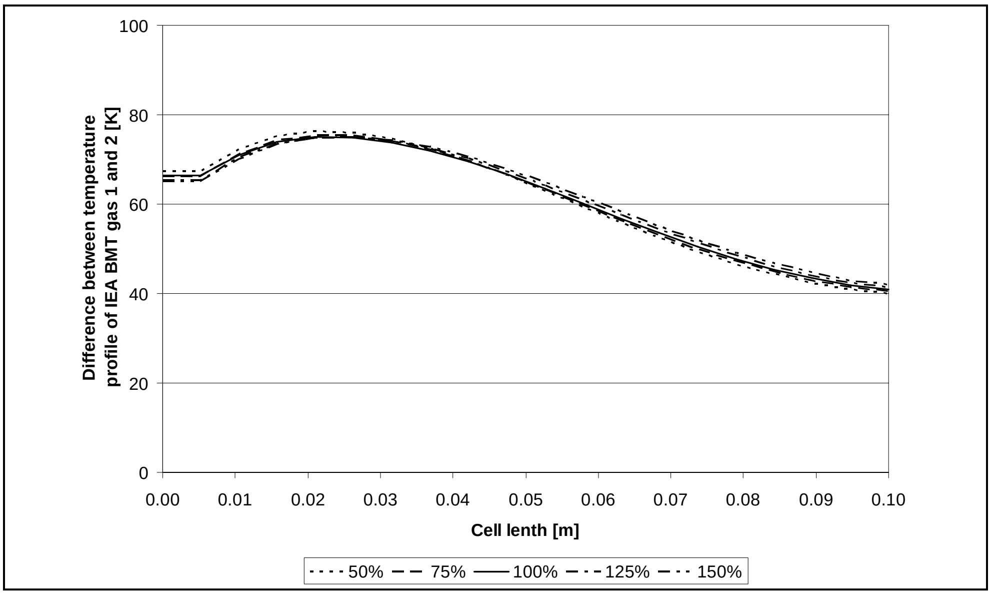

The impact of the cathode activation pre-exponential factor on the predicted current density distribution is slightly more pronounced than for the anode activation pre-exponential factor.

Figure 5-30: Difference between the predicted power output for varying cathode pre-exponential factor values for IEA 1 and IEA 2 gas

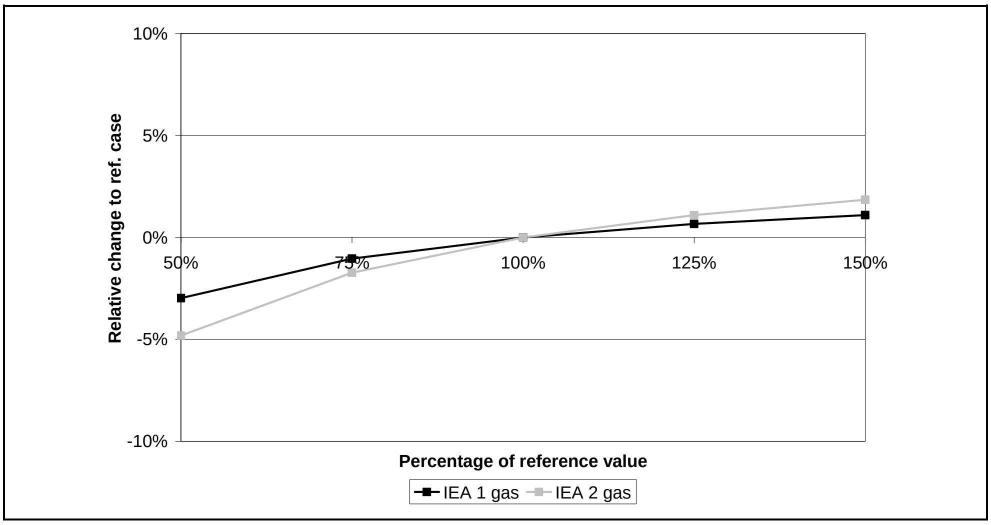

In contrast, the opposite is the case for the impact on the predicted power, Figure 5-30. For lower cathode pre-exponential factor values, the power output decreases by a maximum of 5 %, while it increases by a maximum of 2 % for higher cathode pre-exponential factor values. The reasons for that are the same as already discussed for the cathode activation energy variation. Higher cathode activation pre-exponential factors put the anode activation into the dominant role, while lower values lead to a more homogeneous current density distribution, which equalizes fuel depletion losses at the cell ends.

Figure 5-31 depicts the low sensitivity of the temperature distribution trend towards the cathode pre-exponential factor.

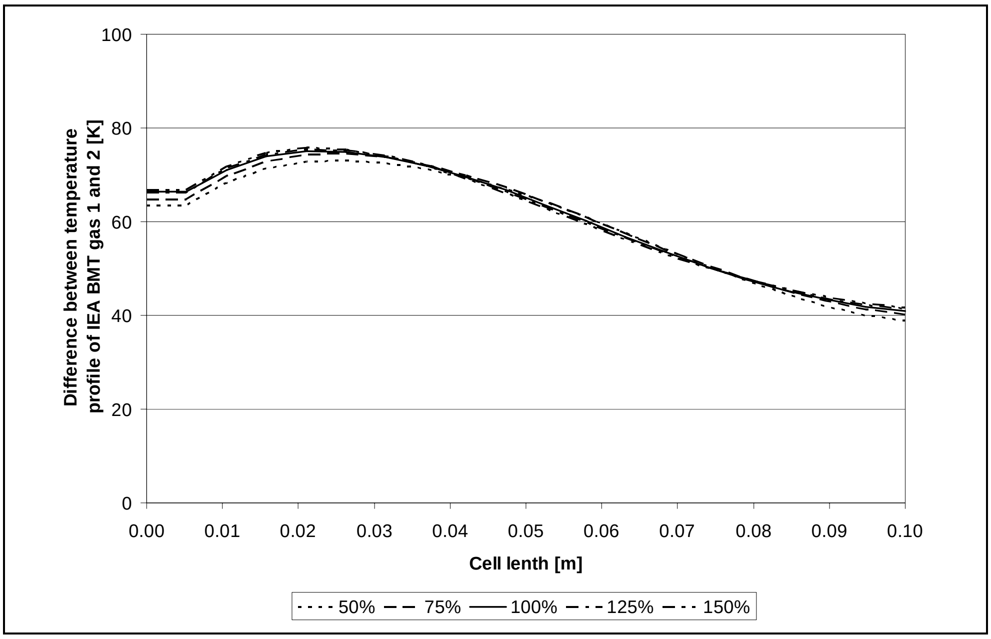

Figure 5-31: Temperature difference between the predicted temperature distributions for varying cathode activation pre-exponential factor values for IEA 1 and IEA 2 gas

In summary it can be said, that the cathode and anode pre-exponential factor values are model parameters featuring only a minor impact on the thermal prediction behavior, the predicted current density distribution and the predicted power output.

5.3.5.3 Variation of diffusion polarization parameters

In order to calculate the diffusion losses both the composition of the gas mixture and the properties of the porous media through which the specie of interest diffuses are required. The porous media properties include the pore diameter, which is important for Knudsen diffusion, and the porosity as well as the tortuosity, see section 5.3.1.4.3. Besides the gas composition and the properties of the porous media, diffusion losses further depend on the prevalent temperature, the diffusion path length and prevalent current density. The latter is causing the concentration gradient between the triple phase boundary (TPB) where the electrochemical reactions take place and the bulk gas phase. The diffusion path length has a direct impact on the concentration at the end of the diffusion path. In particular, the educt partial pressure at the TPB decreases with increasing diffusion path length. Hence, with respect to diffusion losses, the investigated type of support design is of major importance. Cathode supported cells, such as are the tubular cells of the Siemens AG, feature a stronger cathodic diffusion limitation then e.g. electrolyte supported cells, because of their approx. 20 times longer diffusion path through the cathode. At low and intermediate current densities, diffusion losses however are usually small or even negligible. Nevertheless, this sensitivity study was carried out considering an electrolyte-supported planar cell in order to investigate whether the according material properties could lead to a change of these coherences.

The variation of the pore diameter was omitted as it merely re-enforces the impact of Knudsen for smaller pore diameter values or weakens it for larger pore diameters. Instead, the material parameters influencing both diffusion mechanisms, namely the porosity and tortuosity, were varied. For the reference case the quotient of the interdependent porosity and tortuosity has the value 0.166 assuming a tortuosity of 3 and a porosity of 0.5. It was decreased by 70 % to 0.05, which corresponds to a porosity of 0.25 and a tortuosity of 5 (typical values of "dense membranes"), and increased by 110 % to 0.35, which corresponds to a porosity of 0.7 and a tortuosity of 2, in order to cover the entire range of technically possible values.

The current density distribution for varied anode material parameters remained unchanged. Therefore, no discussion on this aspect is undertaken. In contrast, Figure 5-32 depicts the sensitivity of the current density distribution towards the cathode material parameters. Increasing the parameter quotient does not produce any effect. This can be explained by the magnitude of the diffusion losses for the investigated operational conditions, which is about two orders of magnitude lower than ohmic and activation losses. However, the current density progression computed with the dense membrane values shows a considerable decrease of the current density at the cell inlet for the IEA 1 gas. This indicates that in this region, the reached current density is close to the diffusion limited current density of the cathode electrode. In the latter cell parts higher current density is a result of the higher educt partial pressures discussed above. For the IEA 2 gas, the same phenomenon can be observed, however to a lesser impact.

Figure 5-32: Sensitivity of current density distribution towards cathode diffusion material parameters for IEA 1 and IEA 2 gas

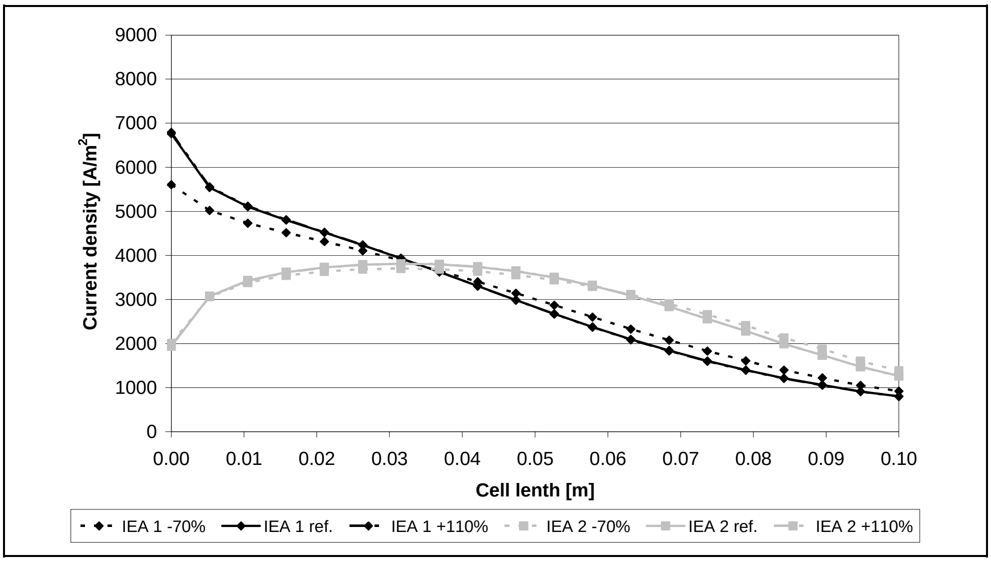

For the increased porosity and decreased tortuosity, the power output remains constant. In contrast, assuming dense membrane properties for the anode yields a decreased power output of 0.5 %. Decreasing the cathode material properties quotient results in a 2.5 % decreased power output. A cause for this somewhat stronger response can be found in the smaller effective diffusion coefficient of oxygen as compared to hydrogen.

Figure 5-33: Temperature difference between the predicted temperature distributions for varying cathode diffusion material parameter for IEA 1 and IEA 2 gas

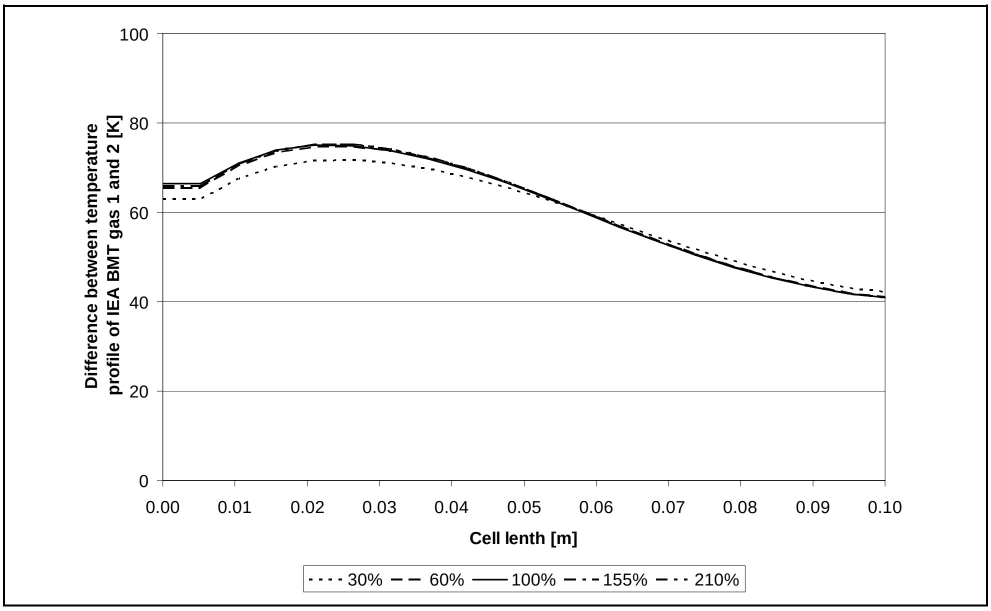

Figure 5-33 shows the sensitivity of the temperature difference towards the cathode diffusion material parameter. The dense membrane like parameter set leads to a slightly decreased cell inlet temperature for the IEA 1 gas as less fuel is electrochemically converted than for the reference case. For the IEA 2 gas the temperature remains on the reference level due to only minor changes of the prevalent current density and the dominating steam reforming reactions. Overall the temperature difference decreases at the cell inlet for the dense membrane parameter set.

In summary it can be stated that for the investigated electrolyte supported cell the anode diffusion material parameters have almost no impact on the model results. In contrast, the cathode diffusion material parameters can be set such that diffusion limitations become relevant to some extent. It is important to point out, that this is especially the case when other support designs with long current path, such as cathode and anode, are investigated. Nevertheless, for the investigated support design and operating conditions the impact on the predicted power output and the thermal behavior can be considered as negligible.

5.3.5.4 Variation of heat exchange parameters

The author's model considers convective heat transport between the gases in the gas channels and the solid structure as well as conductive heat transport within the solid structure. As can be seen in Eq. 161 and Eq. 164, the convective heat streams depend on the corresponding heat transfer coefficient, the heat exchange surface area and the temperature difference between the gases and the solid structure. The heat transfer coefficient is a function of the Nusselt number (Nu), the thermal conductivity of the considered gas mixture and the hydraulic diameter of the corresponding gas channel. In the presented model, Nu is assumed to be constant at a value of 4. This value lies between the two special cases of heat transfer with constant heat flux, Nu equal to 4.36, and with constant surface temperature, Nu equal to 3.66, and is therefore deemed a valid assumption, [190]. The sensitivity analysis, considering both mentioned values, was carried out in order to asses the impact of the presented assumption. An investigation of Nu values higher than 4.36 and lower than 3.66 was not carried out. This is because lower Nu values are unlikely in typical operating conditions of SOFCs. Higher Nu values can be found for turbulent flow conditions. However, this case was excluded from the current model.

The current density distributions of both investigated gases are not changed by varying the Nu values. Consequently, the change of predicted power output is in the magnitude of 0.1 %, hence insignificant. Figure 5-34 depicts the sensitivity of the temperature difference towards Nu. The lower Nu value does not have a noticeable impact on the predicted temperature distribution difference for the two investigated fuel compositions. However, the increased Nu value yields slightly lower temperatures at the cell inlet for the IEA 1 gas and higher temperatures for the IEA 2 gas overall resulting in a smaller temperature difference at the cell inlet.

Figure 5-34: Temperature difference between the predicted temperature distributions for different Nusselt numbers for IEA 1 and IEA 2 gas

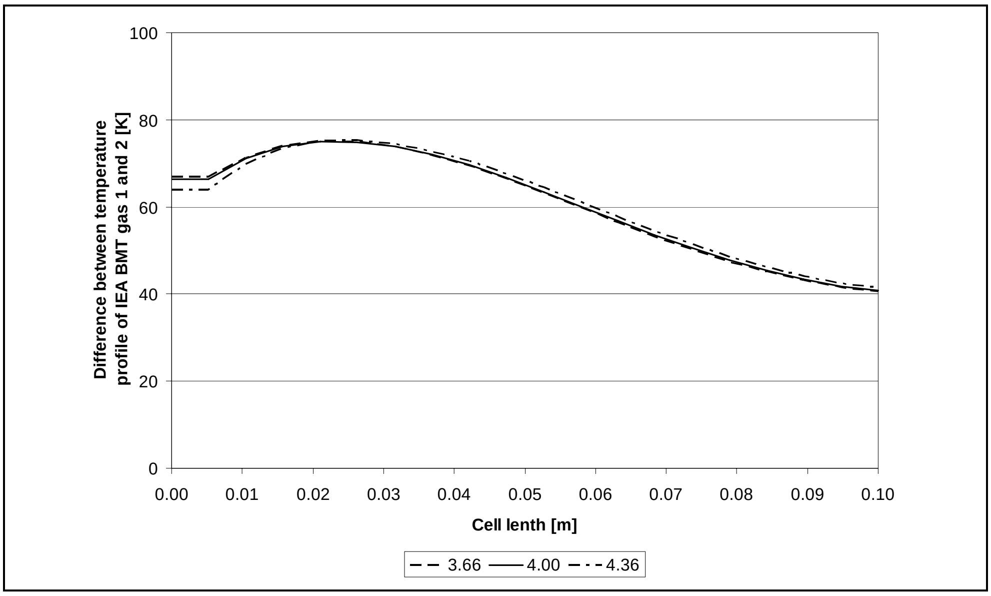

The observed opposite trends of both gases can be explained through the driving temperature difference between the solid structure and the inlet gas temperature. For the IEA 1 gas, the solid temperature is approx. 27 K higher than the inlet gas temperature. The inlet gases are hence being heated by the solid structure, which in turn is being cooled down in the process. Increased heat transfer therefore results into increased cooling of the cell inlet region. In contrast, the strongly endothermal steam reforming reactions occurring for the IEA 2 gas at the cell inlet generate solid structure temperatures approx. 30 K below the inlet gas temperature. Therefore, the solid structure is heated up by the inflowing gases. Consequently, increased heat transfer leads to increasing solid structure temperatures explaining the observed trends.

The energy balance of the solid structure is given by Eq. 165. From this equation it can be derived, that the solid structure temperature depends on the source terms originating from chemical and electrochemical reactions, the convective heat transport between gases and solid structure and the conductive heat transport. The conductive heat transport is a function of the cross-sectional area of the solid structure through which heat is transported, the temperature difference within the solid structure and finally the effective solid heat conductivity represented by a material parameter. For the reference case, the solid heat conductivity coefficient (λ_s) was set to 2 W/m K, which is a typical value for the ceramic components employed in SOFCs. The effect of the solid heat conductivity was investigated by increasing λ_s to 20 W/ m K, representing the value found in high-temperature stainless steel materials which are used in some state-of-the-art SOFCs, and decreasing λ_s to 0.2 W/m K, which covers the case of an almost non heat conducting material.

Figure 5-35 presents the predicted current density distribution for the investigated solid heat conductivity coefficients for IEA 1 and IEA 2 gas.

Figure 5-35: Sensitivity of current density distribution towards the solid heat conductivity coefficient for IEA 1 and IEA 2 gas

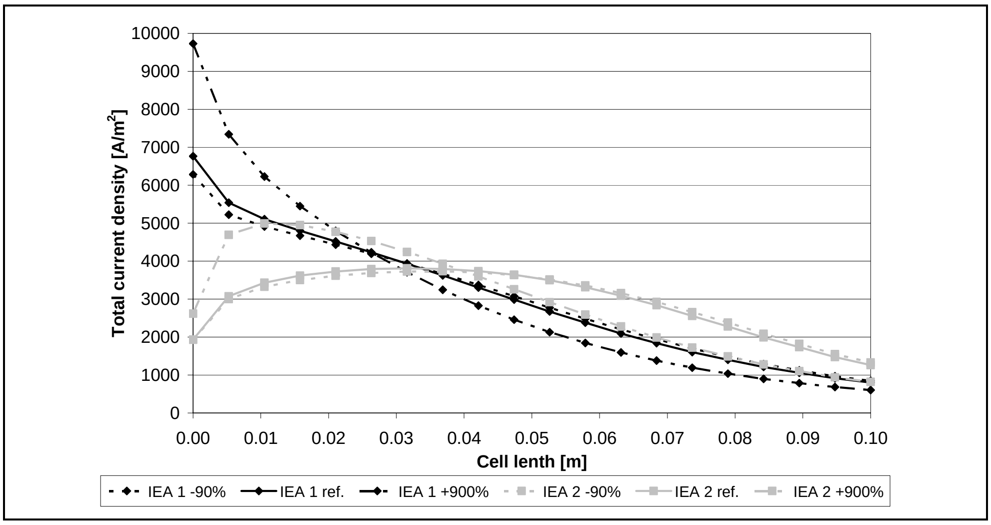

Higher λ_s values yield a strong increase of the current density at the cell inlet and corresponding decrease at the cell outlet. In contrast, lower λ_s values show a minor impact on the predicted current density distribution, the power output and the thermal prediction behavior of the model considering different fuel gases. These results are sensible, given that the reference case value of λ_s is already small. Lowering this value further reduces the already humble conductive heat transfer to values close to zero. The remainder of this discussion hence focuses on the impact of increased λ_s values, which induce stronger changes to the energy balance of the cell.

Table 5-24: Model response values for different solid heat conductivity coefficients for IEA 1 and IEA 2 gas

Parameter value	Max. dT [K/mm]	Cell outlet temperature [K]	Cell inlet temperature [K]	Mean cell temperature [K]	Operational Voltage [V]
IEA 1 gas					
-90 %	2.4	1324.9	1198.7	1274.6	0.679
-45 %	2.3	1326.5	1205.8	1278.9	0.681
Reference	2.2	1327.9	1212.0	1282.7	0.683
+450 %	1.8	1338.5	1257.3	1309.2	0.696
+900 %	1.4	1345.2	1284.2	1324.1	0.702
IEA 2 gas					
-90 %	2.0	1286.5	1141.5	1216.6	0.618
-45 %	2.0	1286.5	1143.6	1219.1	0.621
Reference	2.0	1286.9	1146.3	1221.9	0.624
+450 %	2.0	1296.3	1186.3	1252.7	0.647
+900 %	1.7	1307.4	1223.5	1276.7	0.659

Table 5-24 gives the cell temperatures and operational voltage values for varying λ_S values. Comparing the cell inlet temperature of both fuel gases for the reference case and the increased solid heat conductivity it was found that the IEA 2 gas features a stronger increase by approx. 5 K. In detail, the cell inlet temperature for the IEA 1 gas increased by 72 K versus 77 K for the IEA 2 gas, Figure 5-36.

Figure 5-36: Sensitivity of temperature profile towards the solid heat conductivity coefficient for IEA 1 and IEA 2 gas

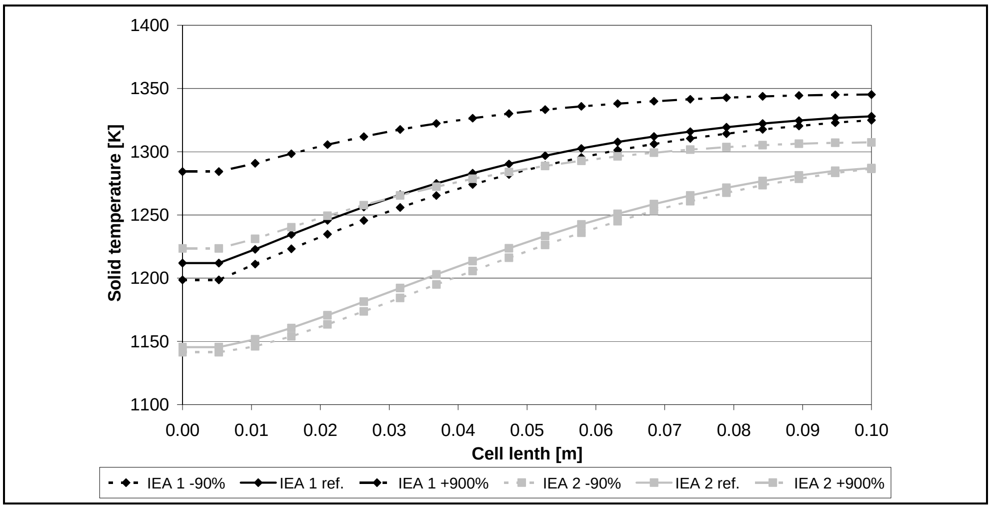

Similar effects were observable for the cell outlet temperatures which increased by 18 K for the IEA 1 gas and 20 K for the IEA 2 gas. Summed up these temperature differences result in an increased mean cell temperatures by 13 K for the IEA 2 gas (54 K increase) as compared to the IEA 1 gas (41 K increase). The differently strong pronounced temperature increase of the two investigated gases is attributed to the endothermal steam reforming reactions occurring at the cell inlet for the IEA 2 gas, which represent a considerable heat sink and additional driving force for solid heat conduction. Increased λ_s values allow more heat to be transferred from the latter parts of the cell to the cell inlet, resulting into considerably higher temperature as compared to the reference case for the IEA 2 gas.

In contrast, for the IEA 1 gas no endothermal reactions take place at the cell inlet. The heat transfer from the cell outlet to the cell inlet region is thus only driven by temperature equalization. The more pronounced mean temperature increase due to the less distinct sub cooling region for the IEA 2 gas in turn reveals the stronger impact of the solid heat conductivity coefficient on the predicted power output which is depicted in Figure 5-37.

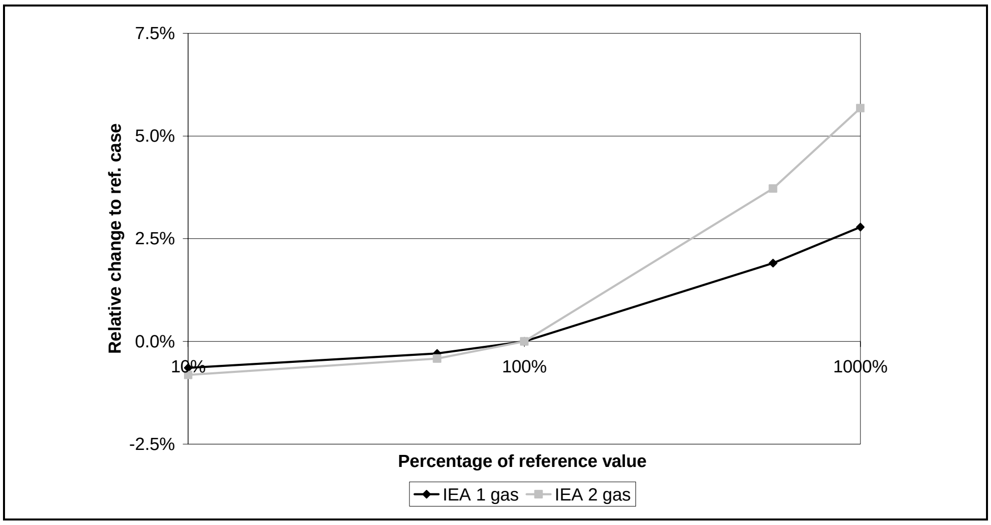

Figure 5-37: Difference between the predicted power output for varying solid heat conductivity coefficients obtained for IEA 1 and IEA 2 gas

The lower λ_s values lead to approx. 1 % power output decrease while it increases by a maximum of 5.5 % for higher λ_s values.

In this respect, it is important to emphasize that all the model parameters used for the calculation of voltage losses were held constant. Keeping this in mind, the revealed power output dependency on the solid heat conduction coefficient is considerable. This also provides an additional justification for the efforts undertaken by the SOFC community to use metallic materials for the interconnector plates in planar cells.

Despite the inhomogeneous current density distribution shown in Figure 5-35, higher λ_s values lead to a more homogeneous local temperature distribution as shown in Figure 5-36. The dominating role of the steam reforming reactions considering the cell inlet temperatures is weakened as the corresponding heat requirements are covered by the enhanced solid heat conduction. The consequences of that are that the predicted temperature profiles for different fuel gases converge, resulting in a flattened temperature distribution trend progression without considerable steam reforming peak as for the reference case, Figure 5-38.

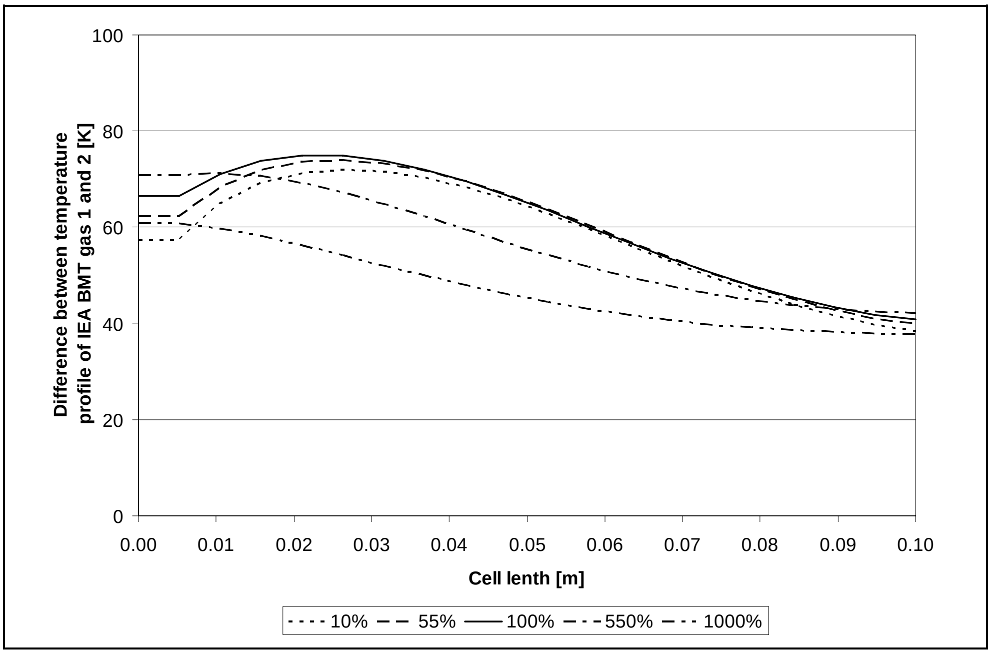

Figure 5-38: Temperature difference between the predicted temperature distributions for varying solid heat conductivity values obtained for IEA 1 and IEA 2 gas

Therefore it can be said that the Nusselt number has almost no impact on the model results which justifies the according assumption. The heat conductivity coefficient strongly affects the predicted current density distribution and local temperature distribution. The current density tends to be less uniform for higher heat conductivity values whereas the opposite is the case for the temperature distribution. Further for high solid heat conduction coefficients, the dominating role of the steam reforming reactions occurring at the cell inlet is weakened. Hence, the differences for the local temperatures between hydrocarbon containing gases and pure syngases are reduced. A considerable impact on the predicted power output was found despite the fact that the model parameters used for the electrochemical performance prediction were held constant at their reference value. However, the solid heat conduction is a material parameter which can be reliably determined. Therefore is it not likely to introduce an uncontrolled uncertainty to the model results.

5.3.5.5 Investigation of different applied kinetics models

In SOFCs, hydrocarbons can be converted to hydrogen and carbon monoxide through steam reforming reactions (STR) due to the usually employed nickel based anode material. The STR reaction rate affects the hydrogen and carbon monoxide as well as the related Nernst voltage distribution and the temperatures where the STR reactions take place. The STR thereby indirectly affects the electrochemical reactions occurring in SOFCs. To asses this impact, five different STR kinetics models were investigated, see section 5.3.1.5: Eq. 129 to Eq. 133.

The reaction order of steam is controversially discussed in the literature related to STR kinetic models. The reference case of the sensitivity analysis employs the STR applied kinetics power law model (PL) proposed by Achenbach, [204]. Achenbach found a reaction order equal to zero for steam. Ahmed also formulated a PL kinetics model for the STR, [205]. In contrast to Achenbach, Ahmed found a negative reaction order for steam. Another PL model was developed by Leinfelder, who derived a first-order dependency of the STR on the steam partial pressure from his experimental data, [53]. Drescher chose a Langmuir-Hinshelwood approach (LH) to describe the STR of methane over nickel cermet electrodes of SOFCs, [207]. LH approaches feature variable effective reaction orders depending on the prevalent partial pressures and temperatures of the corresponding species. The last investigated approach is based on the equilibrium constant of the methane STR.

Figure 5-39 shows the axial distribution of methane, hydrogen and carbon monoxide for the different STR kinetic models. The Achenbach model predicts the end of the STR region at around a quarter of the total cell length. The model proposed by Ahmed predicts slightly higher reaction rates, hence completing the STR reactions after a fifth of the cell length. Dreschers LH model yields reaction rates, which are about half of those obtained from the Achenbach model. The Leinfelder model results are almost congruent with the equilibrium approach, indicating that the nickel-cermet investigated by Leinfelder was highly active. Note that the considered diffusion limitation inhibits the completion of the STR reactions within the first control volume even though equilibrium is assumed. The faster the STR occurs, the higher is the corresponding hydrogen and carbon monoxide peak as the electrochemical consumption is slower than the production through the STR reactions.

Figure 5-39: Sensitivity of methane, hydrogen and carbon monoxide distribution towards STR kinetics

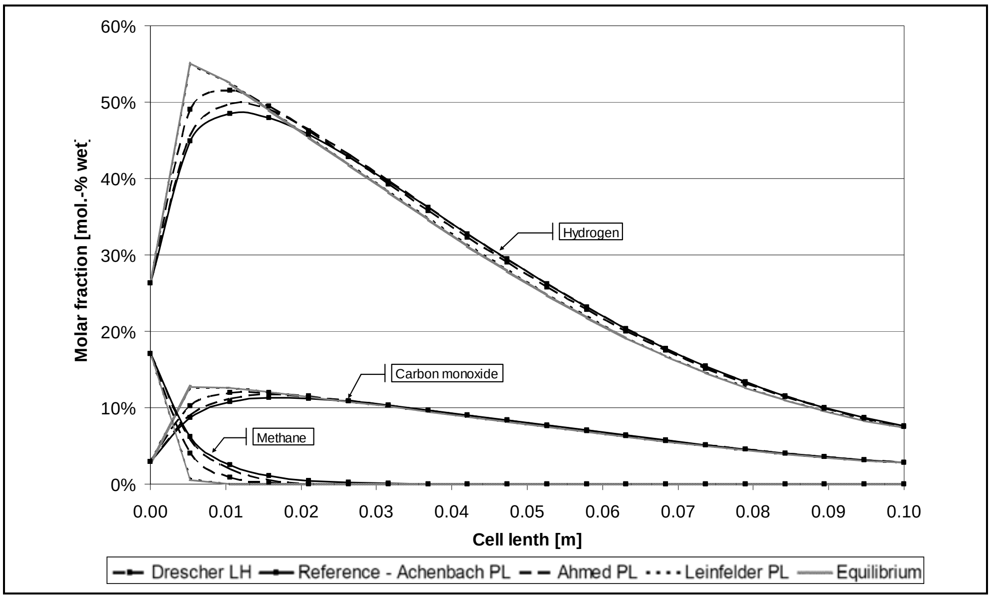

Figure 5-40 shows the predicted current density and Nernst voltage distribution for the different STR kinetics models. For faster STR kinetics, the current density at the cell inlet increases yielding slightly decreased current density values at the cell outlet due to fuel depletion effects.

Figure 5-40: Sensitivity of current density and Nernst voltage distribution towards STR kinetics

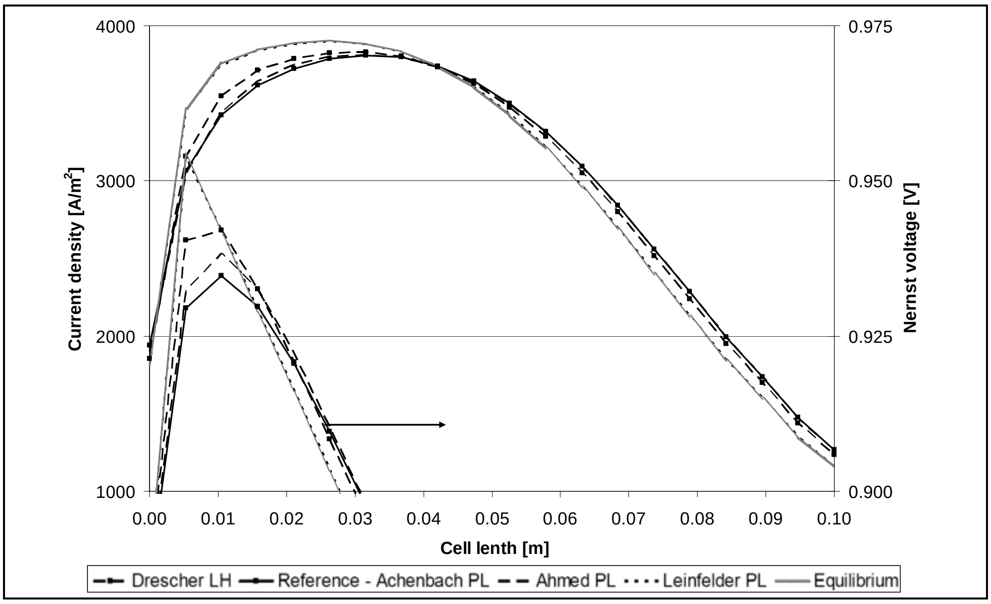

The reason for the higher current density values at the cell inlet observed for faster STR kinetics can be found in the predicted Nernst voltage within the STR region. From Eq. 80 and Eq. 81 it can be derived that higher hydrogen and carbon monoxide partial pressures yield higher Nernst voltages. Further, the Nernst voltage increases with decreasing temperatures due to the endothermal STR reactions.

Figure 5-41 and Table 5-25 show that the cooling effect in the STR region is more pronounced for faster STR kinetics as the locally higher heat requirements cannot be fully covered via heat conduction and convection. However, towards the cell outlet, fast STR kinetics yield higher temperatures than the slow kinetics. Overall, faster STR kinetics yield higher average cell temperatures.

Figure 5-41: Sensitivity of the temperature distribution for the IEA 2 gas towards STR kinetics

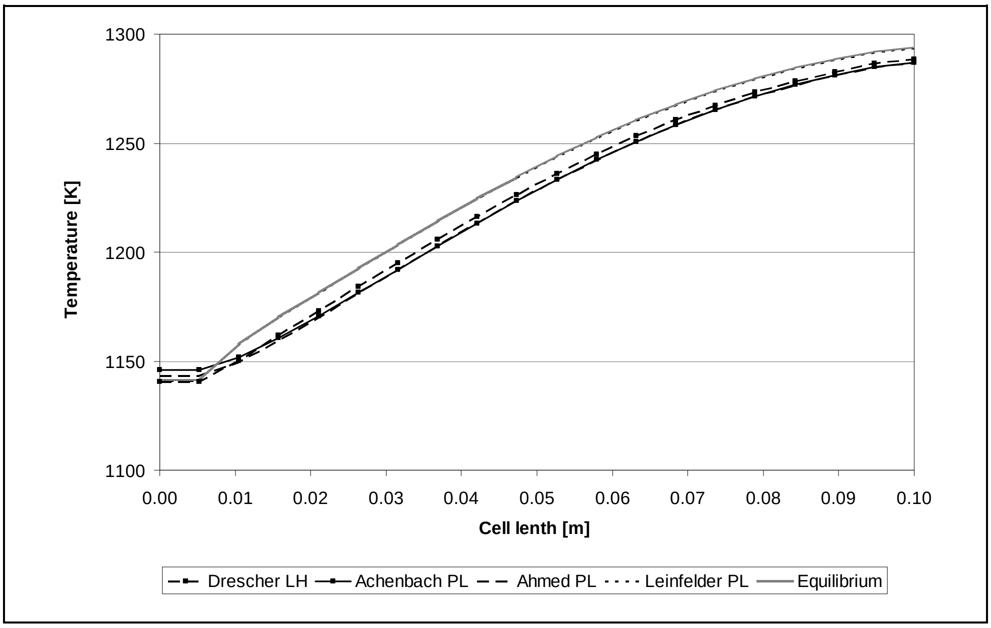

Table 5-25 gives the predicted maximum temperature gradients and operational voltages to maintain 85 % fuel utilization.

Table 5-25: Model response values for different methane steam reforming applied kinetics for IEA 2 gas

Parameter value	Max. dT [K/mm]	Cell outlet temperature [K]	Cell inlet temperature [K]	Mean cell temperature [K]	Operational Voltage [V]
IEA 2 gas					
Reference	2.0	1286.9	1146.3	1221.9	0.624
Drescher LH	2.2	1288.4	1140.7	1223.2	0.626
Ahmed PL	2.1	1286.8	1143.2	1221.4	0.624
Leinfelder PL	3.1	1293.5	1141.0	1229.6	0.630
Equilibrium	3.2	1293.7	1141.2	1230.0	0.631

As a consequence of the more pronounced cooling effect and the resulting higher cell temperatures towards the cell outlet, the maximum temperature gradients increase with faster STR kinetics. The increased mean cell temperatures allow for higher operational voltage values due to less activation and ohmic voltage losses. However, the gained power output increase is in the order of 1 % for the equilibrium model as compared to the reference case considering the Achenbach model.

Figure 5-42 depicts the temperature difference obtained for the different STR kinetics models. The faster the STR reactions occur, the flatter and the nearer to the cell inlet is the STR peak.

Figure 5-42: Temperature difference between the predicted temperature distributions for different STR kinetic models obtained for IEA 1 and IEA 2 gas

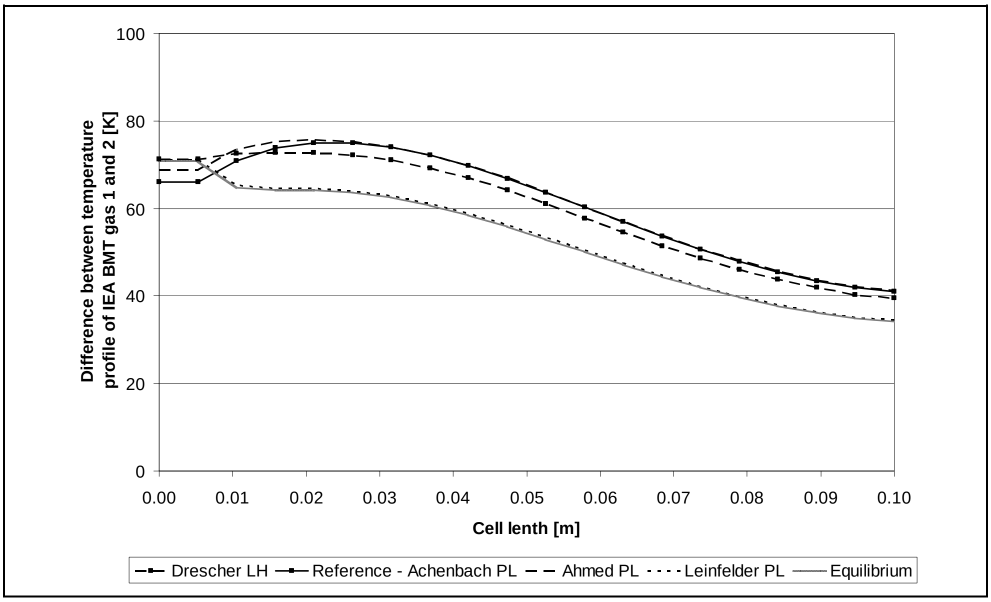

In conclusion it can be stated that the predicted temperature distribution is considerably affected by the employed STR kinetics model. Faster STR kinetics yield a stronger pronounced cooling effect of the STR reactions which is counteracted by higher temperatures in the latter parts of the cell resulting from higher current density values at the cell inlet. Regarding the predicted temperature differences for different gases, the STR kinetics model also has a considerable impact. Especially the reforming peak observed in the reference case almost disappears for faster STR kinetics. In contrast, the power output is only slightly changed. The equilibrium approach, which yields almost instant methane conversion, shows power output values increased by approx. 1 %.

5.3.5.6 Conclusions from the sensitivity analysis

It is concluded that the predicted trends regarding the difference between the temperature distributions predicted for different fuel gases are not changed but are at the most emphasized or understated by the investigated model parameters. Especially the activation polarization energy values, the solid heat conduction coefficient and the applied kinetics of the steam reforming showed a considerable impact. However, the impact of all variations in model parameters on the predicted temperature distribution trends remained always smaller than the impact of the different fuel gases themselves. In this respect, the author's model has shown a fair robustness. The predicted trends for the power output based on different fuel gases were also hardly affected by the variations in model parameters. With respect to the absolute value of the power output, only the activation polarization activation energy values were found to have a strong impact. All other investigated model parameters, including the applied kinetics of the steam reforming reactions, had less then 10 % variance to the reference case within the variation bandwidth.

5.4 Economic model

For the design of power generation systems, low capital cost and high electrical efficiencies are generally conflicting requirements. The final decision to implement a chosen system design is thus based on its profitability. To determine the profitability for different B-IGFC system designs, an economic model was developed. The results of the thermodynamical system simulations conducted with the models discussed in sections 5.1 to 5.3 provided the input data for the economic model. The economic model calculates the size and cost estimates for the most important equipment pieces, the direct and indirect plant costs, the operational and capital cost as well as the net AC system efficiency. These values are then translated into the average power production cost, which allows a terminal comparison of different system designs.

Figure 5-43 shows that the accuracy of cost estimations strongly depends on the invested effort, which in turn determines its cost. Similar to other important works in the field of thermo-economic fuel cell systems analysis, [188, 189, 212], the author's economic model belongs to the study estimate category. This type of estimate is based on a list of the major equipment pieces required in the investigated system, including pumps, blowers, reactors, heat exchangers, furnaces etc. Applying rough sizing procedures to each piece of equipment, a first cost estimate can be determined. The total equipment cost is further factored to yield an estimate for the total direct and indirect plant cost. The accuracy of study estimates is expected to be in the range of +/- 20 to 30 %.

Figure 5-43: Accuracy and cost of different cost estimation classes, derived from [213]

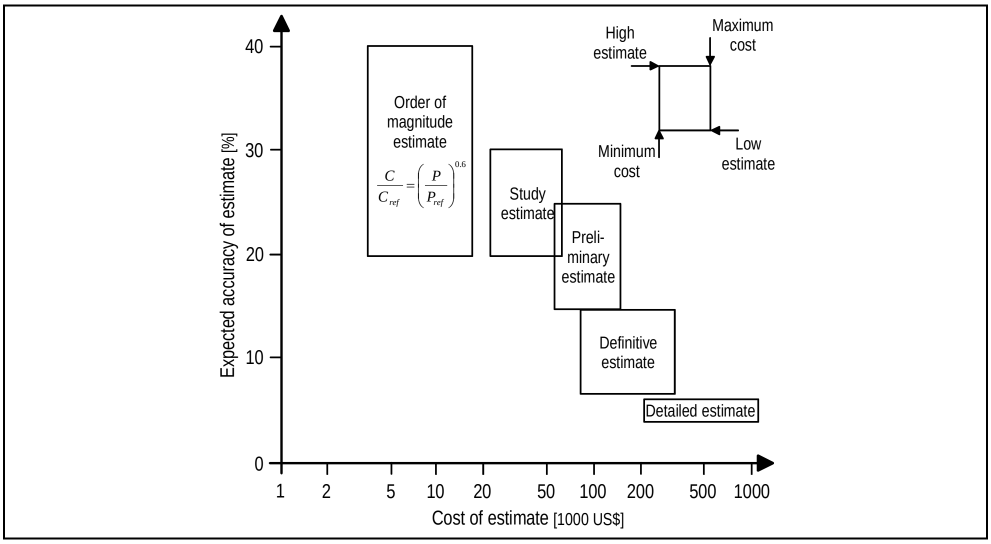

5.4.1 Equipment purchase cost estimate functions

Many cost functions have been published over the years, all with the aim to enable engineers to perform quick and inexpensive equipment cost estimations. The major drawback of these functions is their relatively low accuracy which mainly depends on how current the underlying data is and on the methodology of data collection. Even with recent data, the estimated cost of a single equipment piece can vary between -50 % and +100 % based on current price quotations of vendors due to widely differing quality, designs and specifications, [214]. This illustrates that determining a cost function yielding a good estimate of equipment costs over a wide range of equipment sizes is a challenging task.

Figure 5-44 shows a comparison of the cost functions for spiral, double pipe, air cooled as well as shell and tube heat exchangers proposed by Garrett, [214], and Turton, [213].

Figure 5-44: Comparison of equipment cost estimates for different heat exchanger types using cost functions of Garrett (lines without symbols) and Turton (lines with symbols)

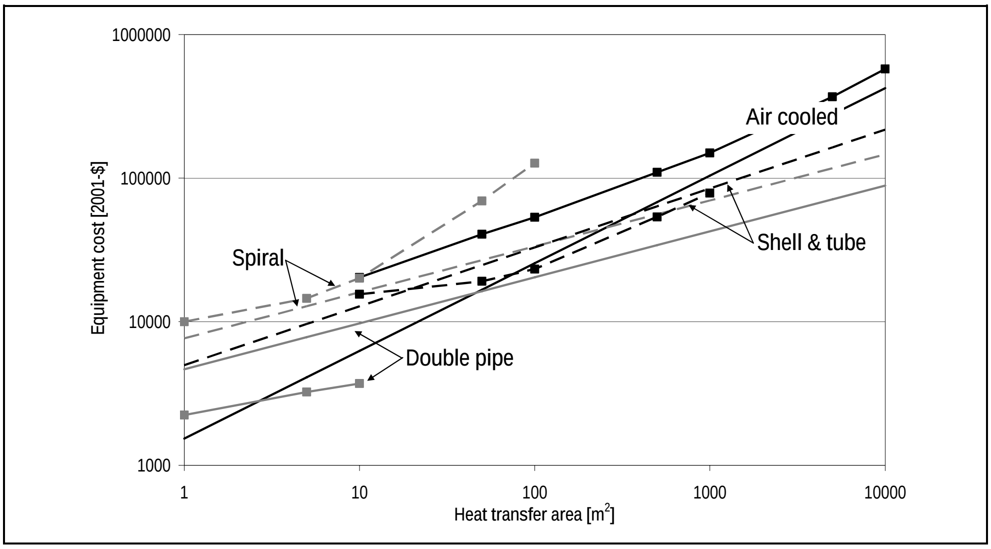

The Turton functions yield cost estimates with values on average twice as high as the Garrett functions. Employing Eq. 176, the renown "*Chemical Engineering magazine Plant Cost Index*", CEPCI, was adopted to adjust the Garrett cost estimates based on data from 1987 to 2001, the year in which the data for the Turton functions was collected.

$$C_{present} = \frac{CEPCI_{present}}{CEPCI_{reference}} \cdot C_{reference} \qquad \text{Eq. 176}$$

The CEPCI is a lumped inflation cost indicator, which represents the average price inflation of all major equipment pieces used in the chemical industry. Figure 5-45 shows a plot of the CEPCI from 1950 through 2007.

Figure 5-45: Chemical Engineering Plant Cost Index from 1950 to 2007

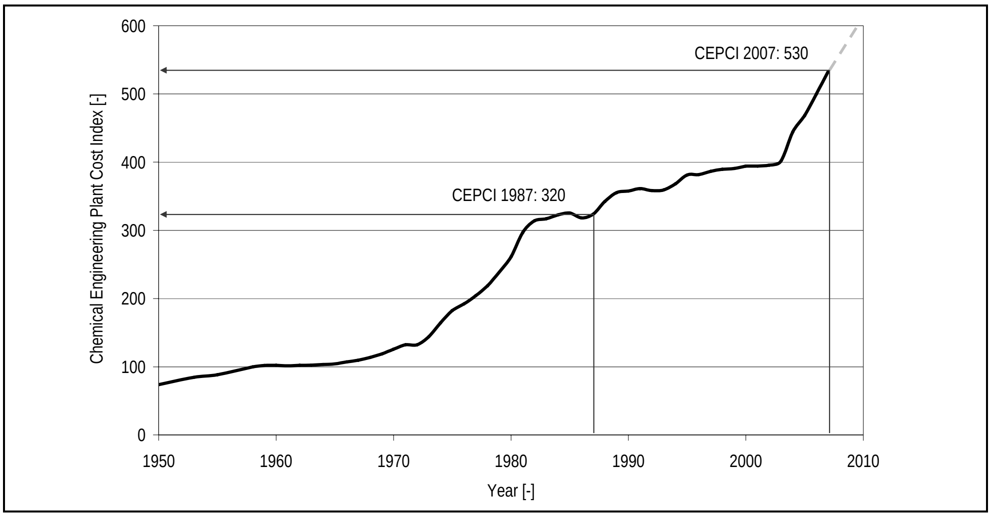

It is likely that technology changes and unequal price inflations for different equipment pieces lead to considerable differences between the estimated costs obtained from functions developed at various times. However, keeping the general stray area of cost estimates compared to vendor quotations in mind, the functions of both authors appear to apply well to the comparisons of different system designs with respect to their economical performance. The choice of function is thus a matter of taste rather than of accuracy. The Turton functions were used in e.g. [212], while Garretts functions were employed in e.g. [215].

As Garrett offers more specified cost functions than Turton, the cost functions formulated by Garrett were applied in this work. Being formulated in 1987, the reference CEPCI is 320. The cost estimates were updated to the year 2007 with a CEPCI of 530. Further, the estimated equipment prizes were converted from US$ to €, assuming a currency rate of 1.4 US$ per € of the year 2007.

5.4.2 Equipment sizing and purchase cost estimation

The investigated system designs are broken down into six operational modules comprising typical equipment pieces. The size of the different equipment pieces was either determined based on a general plant layout assuming a 50 m x 100 m plant footprint, which is the case for equipment required for wood transportation, exhaust stacks and control buildings or alternatively based on the temperatures, mass and energy flows computed with the flowsheeting model and the ATHENA SOFC model. Following modules were differentiated:

- Wood handling module
- Gasification module
- Gas processing module
- Fuel cell balance of plant module
- Fuel cell module
- Auxiliary equipment module

The cost of the equipment pieces discussed below was estimated using cost functions named similar in [214], if not stated otherwise. The cost of high temperature equipment was adjusted through material factors for stainless steel or other appropriate materials given in [214].

The **wood handling module** comprises all required steps to deliver wood chips of a specific moisture and geometry to the gasification reactor in question. This includes conveyor belts for transportation of the wood, shredders to conform the wood as delivered to wood chips of certain geometry, storage facilities and wood drying installations.

For the transportation of the wood pieces from the truck dump to the shredder, 25 m long 16" belt conveyors were assumed adequate. The capacity of the shredder was assumed three times the daily wood consumption of the investigated B-IGFC system, thus allowing complete processing of the raw wood within a regular working shift.

9" screw conveyors were chosen for the transportation of the wood chips. Wood chips are first conveyed from the shredder to a chip pile, stocking wood for approx. 2 weeks of autonomous operation. This amount was considered sufficient to bridge considerable wood supply gaps. For fire protection reasons, a clearance distance of the chip pile from the other plant equipment of 50 m was assumed. The return conveyor is also 50 m long and delivers the wood chips from the chip pile to either a drying installation or a hopper.

As a matter of simplification a convective wood chips dryer was chosen in this analysis. This dryer type consists of a belt conveyor on which wet wood chips are transported through a dryer housing streamed-through by flue gas. The belt conveyor length and the dryer housing size are roughly sized, assuming constant temperature and flow of the flue gas. As mentioned in section 5.2.3, the drying is performed using the sensible heat of the flue gas after all heat requirements have been covered. In a first step, the residence time in the dryer required to reach a predefined humidity of the wet wood chips is calculated according to [216]. The calculation involves the wood chips mass flow, geometry, density, temperature and humidity at the dryer inlet and outlet. Further, the temperature of the gas flow used for the drying at the dryer inlet is required. Based on the roughly estimated residence time, and assuming a conveyor belt width of 7.5 m, the dryer length is determined. The footprint of the dryer housing equals the belt conveyor length plus 2 m clearance times its width and an additional meter of clearance. The cost of the dryer housing is estimated using the "*Warehouse*" cost function, [214].

Another 9" screw conveyor of 15 m length is used to transport the dried wood chips to a hopper. The hopper volume is sized such that it stocks enough wood for five consecutive days of operation. The hopper cost is estimated employing the "*Warehouse*" cost function, [214]. From the hopper to the gasifier, two more 15 m 9" screw conveyors are used.

The **gasification module** includes the gasification reactor and all additional equipment required for its operation. The up- and downdraft gasification processes considered in this work, see section 2.2.3, require one single reactor whose cost is estimated using the "*Cylindrical type furnace*" cost function, [214]. To account for the lower complexity of updraft compared to downdraft gasification reactors, the standard material factor for furnaces was used for the updraft gasifier. The LHV input of wood to those reactors is known from the flowsheet simulations and sufficient for a rough sizing. Both processes use air as gasification agent. The air flow rate is determined through a molar nitrogen balance, Eq. 177. The cost for the corresponding air blower is assessed via the "*Rotary, centrifugal, turbo 10 psi*" cost function, [214].

$$\dot{V}_{air,gasi} = \frac{y_{N_2,PG}}{y_{N_2,Air}} \cdot \dot{V}_{PG} \qquad \text{Eq. 177}$$

The investigated fluidized bed gasifier, see section 2.2.3, consists of a gasification chamber, a combustion chamber, sodium heat pipes for the heat exchange between the gasification and the combustion chamber, a combustion air pre-heater, a steam generator and the associated water pump. Similar to the fixed bed gasification reactors, the cost of the gasification and the combustion chamber are estimated using the "*Cylindrical type furnace*" cost function, [214]. For the gasification chamber, the entire LHV input of wood is considered, while for the combustion chamber the LHV input results from the assumption that 17 mass-% of the dry wood input in form of char is being combusted, [33]. The same assumption applies to the quantification of the air flow required for the char combustion with an air-to-fuel ratio of 1.3, [33]. For efficiency reasons, the combustion air is pre-heated. The size of the required heat exchanger is computed via the mean logarithmic temperature difference, which results from the heating of air from ambient temperature to 400 °C while the combustion flue gas is cooled from 900 to 584 °C. Similar to all other heat exchanger sizing calculations, 22.5 W/m^2 K was assumed as heat exchange coefficient. For this high-temperature heat exchanger the "*Plate and frame*" cost function is used, [214]. The water mass flow required for the steam gasification reactions taking place in the gasification chamber at an equivalence ratio of 1.8 is used to size the corresponding pump. The size and cost of the required evaporator is determined similar to the combustion air pre-heater using the 584 °C hot combustion flue gas after the air pre-heating. The heat transfer coefficients are considered phase dependent with the same value as mentioned in section 5.2.3. The sodium heat pipes are important cost factors of the investigated fluidized bed reactor. According to [168], a single heat pipe can transport approx. 2.6 kW of heat into the gasification chamber. For highest efficiencies, approx. 20 % of the LHV input of wood to the gasification chamber has to be provided by the heat pipes, [33]. Thus, the number and cost of heat pipes can be straightforwardly estimated, assuming a unit price of 1000 € in 2007 (2007-€).

The **gas processing module** covers the equipment required for the gas cleaning and conditioning. Cyclones and ceramic particle filters are used for particle removal. Their cost is estimated based on the wet and tar-laden producer gas flow rate at the gasifier outlet temperature. The "*Electrostatic*" cost function was chosen as conservative estimate for ceramic particle filters, [214].

The humidification of the producer gas includes a water pump, a spray chamber in case liquid water shall be injected aiming at a cooling of the producer gas and a steam generator operated with flue gas heat. The water pump is pricewise rated as conventional pump based on its power computed according to Eq. 178. $\dot{V}_{air,sys}$ stands for the total displacement volume, Δp_{sys} is the counter pressure which the pump has to handle and η_{blow} represents the pump efficiency.

$$P_{Aux} = \frac{\dot{V}_{air,sys} \cdot \Delta p_{sys}}{\eta_{blow}} \qquad \text{Eq. 178}$$

The cost of the spray chamber is determined by its water flow rate, see section 5.2.2. As the steam generator is an integral part of the heat integration network discussed in section 5.2.3, its area is known from the flowsheeting simulation.

State-of-the-art producer gas cleaning systems operate at low temperatures and usually consist of a particle removal unit and a wet scrubber. The wash liquid, mostly water, has to be treated after its use. The "*Spray chamber*" function was used for the prize estimation of wet scrubbers. The considerably higher cost estimates account for the wash liquid treatment. The wet scrubbers are sized according to [28], where it is reported that approx. 2 l of water are spent to clean 1 m^3_n of wet and tar-laden producer gas.

For the removal of hydrogen sulfide from producer gases, solely zinc oxide adsorbers were considered using the "*Activated carbon adsorber*" cost function, [214]. It was assumed that the adsorber should allow for one month non-stop operation. The molar amount of hydrogen sulfide which is adsorbed during this period is known from the flowsheeting simulations, see section 5.2.6. Assuming a maximum sulfur capacity of zinc oxide of 10 %, [149], the adsorbent mass and the cost is computed.

The adiabatic methanation of producer gas, see section 5.2.4, is carried out in a fluidized bed reactor. The cost function "*Fluid bed*" is based on the reactor volume, [214], which is sized to yield similar operating conditions as applied in [40].

The catalytic partial oxidation of producer gas is conducted using coated monoliths. Based on the experiments reported in section 3.5, a tolerable catalyst load of 2.5 kW LHV producer gas power per monolith with 1" diameter, 3" length and 400 cpsi was assumed to estimate the required number of monoliths and the CPO reactor volume. The CPO reactor is pricewise rated employing the "*Jacketed reactor*" cost function, [214]. Eq. 178 is used for the power requirement calculation of the CPO air blower. The air flow rate is determined for an air-to-fuel ratio of 0.12.

The **fuel cell balance of plant module** contains all the heat exchangers required to adjust the producer gas and the cooling air temperature to the predefined SOFC inlet temperatures, the cooling air blower, the DC/AC power converter and the SOFC off-gas combustor. The heat exchange areas of the air pre- and super heater, the producer gas cooler (if required) and super heater are known from the flowsheeting simulation, see section 5.2.3. The costs of all heat exchangers are determined using the "*Plate and frame*" cost function, except for the air pre-heater the cost of which is estimated based on the "*Shell and tube*" function, [214], see Figure 5-44.

Similar to all other air blowers, Eq. 178 is used for the power requirement calculation of the fuel cell cooling air blower. The air flow rate is determined by the ATHENA SOFC model.

In 2003, the American Department of Energy together with the Department of Defense has launched a design competition for DC/AC power converters tailored to the application with SOFCs. The cost target of less than 40 $ per kW_{el}, [217], was adopted in this work.

The oxidation of the depleted SOFC fuel gas is performed in a catalytic combustor to ensure complete conversion. Its heat duty is known from the flowsheeting calculations, see section 5.2.7, and used for the cost estimation based on the "*Catalytic incinerator*" cost function, [214].

The **fuel cell module** comprises the SOFC stack and all catalyst, which have to be exchanged in regular intervals. For 2012, the American Solid State Energy Conversion Alliance (SECA) has defined a cost target for SOFC systems of 400 2002-$ per kW_{el} output using natural gas as fuel, [59]. Despite this objective was formulated for SOFC systems, it was assumed for the stack cost to be more conservative in this work. In systems using an adiabatic methanation, the catalyst cost are estimated based on a price of 50000 2007-€ per ton corresponding to the average nickel price in 2007. The catalyst mass is determined to yield operating conditions as applied in [40]. For systems using a CPO, 100 € was assumed as piece prize for a 1" CPO catalyst.

The **auxiliary equipment module** summarizes all equipment units which are not directly related with the electricity generation. These are the stack, the emergency flare and the heat exchanger employed to extract useful heat from the SOFC flue gas.

The stack is assumed by default 20 m height and pricewise rated using the "*Short chimney*" cost function, [214].

In case of an emergency, the producer gas may have to be flared to prevent serious damage of the equipment downstream of the gasifier. An elevated emergency flare was therefore considered necessary. The flare cost is evaluated based on the full producer gas mass flow rate. The size of the heat exchanger employed to extract useful heat from the SOFC flue gas is known from the flowsheeting simulation and the cost is determined similar to all other high-temperature heat exchangers.

5.4.3 Total investment, direct and indirect plant costs

The total investment, TI, for technical installations is the sum of direct and indirect plant cost plus contingencies and contractor fees. The direct plant cost, DPC, includes not only the purchase cost of the equipment but also the cost for shipment, installation and commissioning of each equipment piece. These additional costs are determined by multiplying the single equipment cost estimates with a module factor. For the equipment pieces, which are pricewise rated according to [214], the denoted average module factors have been used. For non-standard equipment such as the SOFC stack, a module factor of 1.5 was generally assumed. Although this approach is rather general and does not ameliorate the accuracy of the cost estimation, the estimated direct plant costs were expected to be in the right general cost range for preliminary estimates, [214].

The indirect plant costs, IPC, comprise the project development and financial cost as well as the interest, engineering and administration cost during the construction period. All costs attributed to the IPC arising from borrowing of funds depend on the length of the construction period, CP, the prevailing interest rate, IR, and the credit given by the debt portion, DP, and the TI. The factors and the equation used to determine the IPC, the contingencies and the contractor fees are summarized in Table 5-26. These values are in good agreement with e.g. [215].

Table 5-26: Factors and equation used for the calculation of the indirect plant cost

Cost component	Factor assumed [%] or equation used	Basis
Project development cost	8.75	DPC
Financial cost	2.0	DP*TI
Interest during construction	$(1+IR)^{CP}-1$	DP*TI
Engineering and administration during construction	5.0	DPC
Contingencies	10.0	DPC+IPC
Contractor fees	5.0	DPC+IPC

For B-IGFC systems, a CP of 1 year, an IR of 8 % and a DP of 75 % were assumed.

5.4.4 Net AC power efficiency

The performance of power generation systems is rated based on their ability to convert the energy of a feedstock into electrical AC grid power. The ATHENA SOFC model computes the DC power efficiency of the SOFC. Based on this, the ASPEN PLUS flowsheet model yields the DC power efficiency of the investigated B-IGFC system. The net AC power efficiency, $\eta_{net,AC}$, is defined according to Eq. 179.

$$\eta_{net,AC} = \eta_{CG} \cdot \eta_{GP} \cdot \eta_{SOFC,DC} \cdot x_{S,loss} \cdot \left(1 - \frac{P_{Aux}}{x_{S,loss} \cdot P_{SOFC,DC}}\right) \cdot \eta_{Inv} \qquad \text{Eq. 179}$$

The **cold gas efficiency**, η_{CG}, is given by the ratio between the chemical energy content of the producer gas (PG) exiting the gasifier to that of the converted wood, Eq. 180.

$$\eta_{CG} = \frac{\dot{V}_{PG} \cdot LHV_{PG}}{\dot{m}_{feed} \cdot LHV_{feed}} \qquad \text{Eq. 180}$$

The **gas processing efficiency**, η_{GP}, relates the chemical energy content of the processed gas at the SOFC inlet (CG) to that of the raw producer gas (PG), Eq. 181. It thus describes chemical energy losses occurring in the gas processing system.

$$\eta_{GP} = \frac{\dot{V}_{CG} \cdot LHV_{CG}}{\dot{V}_{PG} \cdot LHV_{PG}} \qquad \text{Eq. 181}$$

The **SOFC DC efficiency**, $\eta_{SOFC,DC}$, includes the fuel utilization and the electrochemical conversion efficiency of the SOFC. It is defined as the ratio between the produced DC power and the chemical energy content of the processed gas at the SOFC inlet (CG), Eq. 182

$$\eta_{SOFC,DC} = \frac{P_{SOFC,DC}}{\dot{V}_{CG} \cdot LHV_{CG}} \qquad \text{Eq. 182}$$

Sulfur induced power losses were considered in this economic model through a correlation derived from sulfur experiments with the Hexis SOFC, see section 3.4.5. The fair sulfur tolerance of the Hexis SOFC was assumed for all SOFCs despite the employed anode catalysts strongly varying for different SOFCs. Eq. 183 yields the expected percentage of power output, $x_{S,loss}$, of the Hexis SOFC operated with sulfur containing fuel gas.

$$x_{S,loss} = 0.52695 + 0.20716 \cdot \exp\left(-\frac{y_S}{3.7608}\right) + 0.26521 \cdot \exp\left(-\frac{y_S}{27.0748}\right) \qquad \text{Eq. 183}$$

y_S represents the molar fraction of the total sulfur content in the fuel gas in parts per millions. Note that the loss of electrical power due to sulfur is added to the heat output of the SOFC.

The **auxiliary power requirements**, P_{Aux}, originating from air blowers for e.g. the SOFC cooling and pumps for e.g. producer gas humidification, were calculated according to Eq. 178. As no momentum balance was performed in the thermodynamical simulations, a counter pressure, Δp_{sys}, of 375 mbar and a blower or pump efficiency, η_{blow}, of 75 % was generally assumed for the auxiliary power requirement estimation.

The **inverter efficiency**, η_{Inv}, for the conversion of the DC produced by the SOFC to AC deliverable to the grid was assumed to be 92.5 %.

5.4.5 Power production costs

The calculation of the power production cost is based on the average yearly power output and cost during a given planning horizon, PH, discounted to the year of start of production, SoP, Figure 5-46. A PH of 20 years was considered and SoP in 2008 was generally assumed. All input data required for the power production cost is summarized in Table 5-27 at the end of this paragraph.

Figure 5-46: Structure of the power production cost calculation, derived from [218]

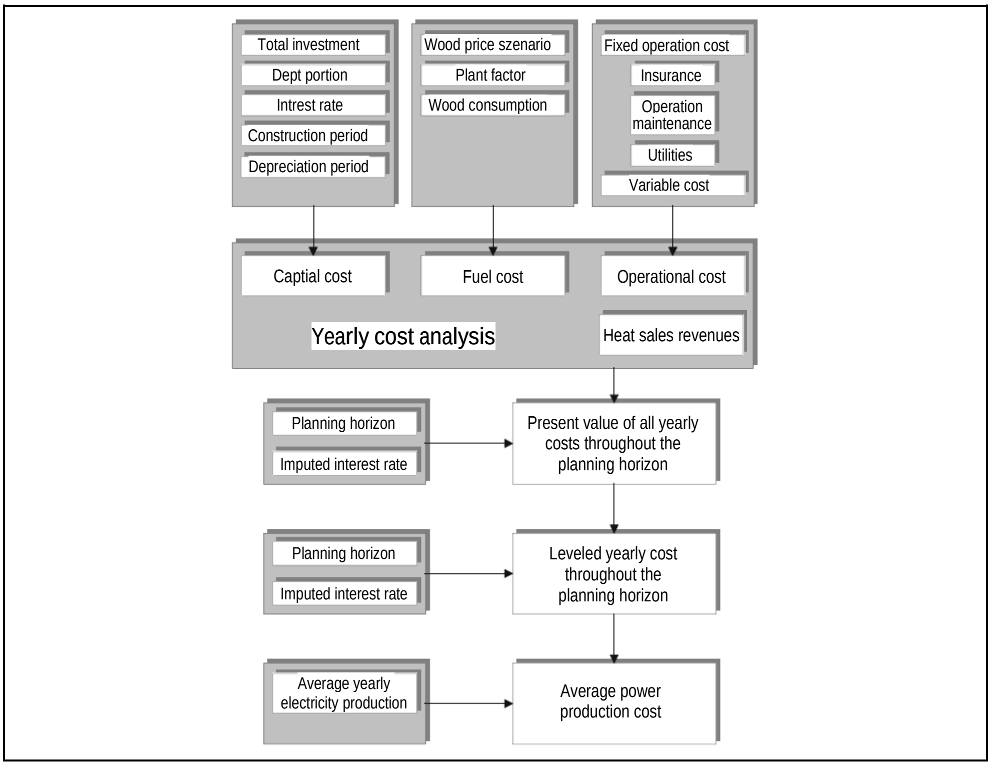
Total investment
Dept portion
Intrest rate
Construction period
Depreciation period
Wood price szenario
Plant factor
Wood consumption
Fixed operation cost
Insurance
Operation maintenance
Utilities
Variable cost
Captial cost
Fuel cost
Operational cost
Yearly cost analysis
Heat sales revenues
Planning horizon
Imputed interest rate
Present value of all yearly costs throughout the planning horizon
Planning horizon
Imputed interest rate
Leveled yearly cost throughout the planning horizon
Average yearly electricity production
Average power production cost

The starting point for the calculation is a detailed cost analysis on either a yearly or monthly basis. Most of the regular and customary recurring costs are assumed subject to 2 % inflation, IF. This includes costs for operation and maintenance, feedstock, utilities and replacement of worn-out equipment. Following cost factors were considered:

- Fuel cost

  The fuel cost for the operation year i, $C_{fuel,i}$, is computed via Eq. 184.

  $$C_{fuel,i} = \dot{m}_{wood} \cdot 8760 \cdot PF \cdot C_{wood} \cdot (1 + IF + WI)^{(i+SoP-2007)} \qquad \text{Eq. 184}$$

  The wood mass flow per hour, $\dot{m}_{wood}$, is known from the flowsheeting simulation. The plant factor, PF, describes the availability of the plant and is assumed to be 85 %. The wood price, C_{wood}, of 84 2007-€ per dry ton in the year 2007 is in accordance with the German Coordinating Office for Renewable Raw Materials, [219]. To account for the increasing future demand of wood, a market-driven wood price increase, WI, of 1 % per annum in addition to regular inflation, IF, was added.

- Insurance cost

  For the insurance costs, a fixed rate per annum of 1 % of the total investment was assumed over the entire planning horizon, Eq. 185.

  $$C_{Ins,i} = 0.01 \cdot TI \qquad \text{Eq. 185}$$

- Operation and maintenance cost

  The operation and maintenance costs (O+M) are subject to inflation and were assumed to be 4 % of the DPC per annum, which includes all expenses for labor and minor repairs, Eq. 186.

  $$C_{O+M,i} = (0.04 \cdot DPC) \cdot (1 + IF)^{i} \qquad \text{Eq. 186}$$

- Utility cost

  Water for the producer gas humidification was considered the only utility cost factor with a price of 0.94 2007-€ per m^3. The required water flow rate is known from the flow sheeting simulation.

  $$C_{utility,i} = \dot{V}_{water} \cdot 8760 \cdot PF \cdot C_{water} \cdot (1 + IF)^{i} \qquad \text{Eq. 187}$$

- Revenues from heat sales

  All the useful heat, an amount known from the flowsheeting simulation, is assumed to be sold for a price of 0.04 2008-€ per kWh_{th}. The corresponding yearly revenues, $R_{heat,i}$, are computed via Eq. 188.

$$R_{heat,i} = P_{th} \cdot 8760 \cdot PF \cdot p_{heat} \cdot (1 + IF)^{i} \qquad \text{Eq. 188}$$

P_{th} stands for the output of useful heat from the B-IGFC system in question. The heat output increases with proceeding degradation of the SOFC stack. However, it was assumed that only the heat amount produced by a new stack is sold.

- Depreciation

  Linear depreciation was generally assumed.

  - Standard equipment

    The yearly depreciation of the standard equipment, $C_{Dep,SE,i}$, is calculated according to Eq. 189. Standard equipment comprises all equipment pieces except the fuel cell stack and any employed catalysts, the initial cost of which, C_{FC_0} and C_{cat_0} , are subtracted from the DPC, see section 5.4.2. The depreciation period, DeP, was assumed to be 10 years.

$$\begin{aligned} &For\ \ i \le DeP: C_{Dep,SE,i} = \frac{DPC - C_{FC_0} - C_{cat_0}}{DeP} \\ &For\ \ i > DeP: C_{Dep,SE,i} = 0 \end{aligned} \qquad \text{Eq. 189}$$

  - Fuel cell stack

    Fuel cell stacks degrades with growing age. Within the planning horizon of 20 years, one or several stack exchanges are necessary. Each stack is depreciated during its operation period, DeP_{FC}, which depends on the threshold degradation value, TRD, the degradation rate, DR_{FC}, and the plant factor, PF. TRD represents the upper-limiting power degradation value at which a stack is exchanged. A TRD of 16.8 % and a DR_{FC} of 0.2 % per 1000 h were assumed in this work. The latter is the target for 2012 defined by the SECA for natural gas operated SOFCs, [220]. The yearly depreciation of the stacks, $C_{Dep,FC,i}$, is determined via Eq. 190. DeP_{FC} was considered on a monthly basis to allow stack exchange close to the point of time when the TRD is reached. C_{FC} gives the cost of the stack in operation. Stack costs were considered subject to inflation. The last stack within the planning horizon depreciates during the remaining time between its installation and the end of the planning horizon.

$$\begin{aligned} &C_{Dep,FC,i} = \sum_{m=1}^{12} \frac{C_{FC}}{DeP_{FC}} \\ &with\ \ DeP_{FC} = \frac{1000}{730} \cdot \frac{TRD}{DR_{FC} \cdot PF} \end{aligned} \qquad \text{Eq. 190}$$

- Catalysts

  Catalysts are subject to deactivation processes and have to be exchanged in due course. It was assumed that both the methanation and the CPO catalyst materials are operable for a maximum period of 24 months in which they are depreciated, DeP_{Cat}. The yearly depreciation of catalysts, $C_{Dep,cat,i}$, is computed according to Eq. 191. Similar to the fuel cell stack, catalyst costs were considered subject to inflation. Hence, C_{cat} denotes the costs of the catalyst in operation.

$$C_{Dep,cat,i} = \sum_{m=1}^{12} \frac{C_{cat}}{DeP_{cat}} \qquad \text{Eq. 191}$$

- Amortization of indirect plant cost, contingencies and contractor fees

  The amortization of indirect plant costs, contingencies and contractor fees was considered to take place within a period of 5 years, AmP. The corresponding yearly costs, $C_{Am,i}$, are determined via Eq. 192.

$$\begin{aligned} &For\ i \le AmP : C_{Am,i} = \frac{TI - DPC}{AmP} \\ &For\ i > AmP : C_{Am,i} = 0 \end{aligned} \qquad \text{Eq. 192}$$

- Interest expenses

  The yearly interest expenses, $C_{IE,i}$, are due to the debt owing on total investment, TI, plus the additional cost resulting from fuel cell stack, C_{FC}, and catalyst exchanges, C_{cat}. As interest payments in arrear were assumed, the first depreciation and amortization payments are effective only from the second year of operation onwards.

$$\begin{aligned} &C_{IE,i} = \left(TI + C_{FC} + C_{Cat} - \sum_{1}^{i} DA_{i-1} \right) \cdot NCIR \\ &with\ DA_i = C_{Dep,SE,i} + C_{Dep,FC,i} + C_{Dep,cat,i} + C_{Am,i} \end{aligned} \qquad \text{Eq. 193}$$

  To account for the mixed structure of the invested capital, a nominal capital interest rate, NCIR, is calculated according to WACC method (Weighted Average Cost of Capital), Eq. 194.

$$NCIR = RoE \cdot (1 - DP) + IR \cdot DP \qquad \text{Eq. 194}$$

  RoE denotes the return on equity demanded by the investor. In this work a moderate RoE of 12 % was assumed.

$$C_{Cap,i} = C_{Dep,SE,i} + C_{Dep,FC,i} + C_{Dep,Cat,i} + C_{Am,i} + C_{IE,i} \qquad \text{Eq. 195}$$

The total yearly capital costs are given by Eq. 195. The net value at SoP of the operational and capital costs accrued over the planning horizon,

$C_{Op,net}$, is determined by summing up the yearly cost less heat revenues discounted by the nominal capital interest rate, NCIR, Eq. 196.

$$C_{Op,net} = \sum_{i=1}^{PH} \frac{C_{fuel,i} + C_{Ins,i} + C_{O+M,i} + C_{utility,i} + C_{Cap,i} - R_{heat,i}}{(1 + NCIR)^i} \qquad \text{Eq. 196}$$

To evenly distribute the net value at SoP of all costs throughout the planning horizon, the annuity method is used. The annuity factor, AN, follows from Eq. 197.

$$AN = \frac{NCIR \cdot (1 + NCIR)^{PH}}{(1 + NCIR)^{PH} - 1} \qquad \text{Eq. 197}$$

Finally, the power production cost, PPC, is determined with the annuity factor, AN, the net value of all costs at SoP, $C_{Op,net}$, the plant factor, PF, and the average power output, $\overline{P}_{el}$, Eq. 198.

$$PPC = \frac{AN \cdot C_{Op,net}}{\overline{P}_{el} \cdot 8760 \cdot PF} \qquad \text{Eq. 198}$$

$\overline{P}_{el}$ depends on the TRD and the DR_{FC} and is determined through a yearly averaging of the produced electricity during the entire planning horizon.

Table 5-27: Input data for power production cost calculation

Variable	Description	Unit	Value
PH	Planning horizon	years	20
SoP	Start of production year	-	2008
IF	Inflation rate	%	2.0
PF	Plant factor	%	85.0
C_{wood}	Wood price	2007-€/dry ton	84.0
WI	Yearly wood price increase	%	1.0
C_{water}	Water price	SoP-€/m^3	0.94
p_{heat}	Heat price	2008-€/kWh$_{th}$	0.04
DeP	Depreciation period for standard equipment	years	10
TRD	Threshold degradation	%	16.8
DR_{FC}	Degradation rate	%/1000 h	0.2
DeP_{cat}	Depreciation period for catalysts	months	24
AmP	Amortization period	years	5
RoE	Return of equity	%	12.0
IR	Interest rate	%	8.0
DP	Dept portion	%	75.0

6 System analysis

The main objective of this system analysis was to assess the technical and economical feasibility of different B-IGFC systems with an electrical power output of around 1 MW_{el} based on already or soon available biomass gasification processes, gas processing technologies and SOFC designs for stationary power applications. Particular attention was given to the thermal gradients and temperature extremes caused by different producer gases during their electrochemical conversion in SOFCs. The interactions between different biomass gasification processes, gas processing technologies and SOFC concepts were also investigated and the overall system efficiencies and power output as well as the requirements for the balance of plant equipment resulting from the SOFC cooling were determined. By relating the system efficiency to system cost estimates, the power production costs were approximated and used as basis for the economic comparison of the various B-IGFC systems.

6.1 Analysis constraints

6.1.1 SOFC simulation assumptions

6.1.1.1 Cell designs

A number of SOFC concepts are currently under development. However, only few developers aim at stationary applications, Table 6-1.

Table 6-1:
SOFC designs for stationary power applications

Developer	Cell design	Support design	Flow design	Operational temperature
Delphi Corporation	Planar	Anode	Co-current	650 to 750 °C
Siemens AG	Tubular	Cathode	Co-current	800 to 1000 °C
Haldor Topsoe A/S	Planar	Anode	Co-, Counter-, Cross-current	700 to 850 °C
J-POWER Co. Ltd.	Tubular	Passive	Co-current	900 to 1000 °C
Mitsubishi Heavy Industries Ltd.	Planar	Electrolyte	Cross-current	900 to 1000 °C
Rolls-Royce International Ltd.	Tubular	Passive	Cross-current	850 to 950 °C
ZTEK Corporation, Inc.	Planar	Electrolyte	Co-current	900 to 1000 °C

To cover most of the SOFC designs summarized above, the SOFC cell designs listed below were investigated in the system analysis.

Cell design 1: Planar anode-supported counter-current cells with metallic bipolar plates and 760 °C operational temperature.

Cell design 2: Planar anode-supported co-current cells with metallic bipolar plates and 760 °C operational temperature.

Cell design 3: Planar electrolyte-supported co-current cells with ceramic bipolar plates and 950 °C operational temperature.

Cell design 4: Tubular cathode-supported co-current cells with air delivery tube, ceramic interconnects and 1000 °C operational temperature.

6.1.1.2 Operational parameters

The operational parameters of the SOFCs were defined based on the results reported in [188].

Fuel utilization: The fuel utilization was set at 85 %.

Operational voltage: To obtain a high power output, the operational voltage was fixed at 0.6 V. This voltage is comparably low but not endangering the safe operation of SOFCs. Higher voltages yield higher conversion efficiencies but less power output.

Current density: The current density, which together with the stack size determines the fuel flow rate, was adjusted to satisfy the pre-defined fuel utilization and operational voltage.

Gas temperature at cell inlet: The air and fuel gas temperature at the cell inlet were determined for the reference system discussed in section 6.2.1 and each of the investigated SOFC designs, see above. Therefore, an air-to-fuel ratio of 4.25 was assumed, which corresponds to an air utilization of 20 % at 85 % fuel utilization. The gas inlet temperatures were appraised to yield a mean cell temperature equal to the operational temperature of the respective SOFC design. The thus determined gas inlet temperatures were fixed for the simulation of the B-IGFC systems presented in sections 6.2.2.2 to 6.2.2.4.

Air-to-fuel ratio: The air-to-fuel ratio was adjusted for the different B-IGFC systems to yield a mean cell temperature equal to the operational temperature of the respective SOFC design with the corresponding cell inlet gas temperatures determined for the reference system. Fixing the mean cell temperature has the advantage that the electrochemical conversion of different fuel gases takes place on the same overall temperature level. This ensures the comparability of the performance achieved by different B-IGFC systems because power output increasing effects induced by higher cell temperatures are excluded. For instance, fuel gases containing considerable concentrations of hydrocarbons effectively cool SOFCs, which leads to lower temperatures and thus increased voltage losses and reduced power output. Without fixing the mean cell temperature, the power output obtained from these gases is systematically underestimated compared to fuel gases with lower hydrocarbon content. Nevertheless, high temperature gradients and local temperature extremes are possible despite a fixed mean cell temperature. This leaves the possibility of comparing different producer gases with respect to thermal stress and sintering issues in the SOFC open.

Steam-to-carbon ratio: The power output of SOFCs usually decreases with increasing water content of the fuel gas. Hence, the steam-to-carbon ratio (SC) should be as low as possible without risking carbon deposits. As the carbon deposition risk decreases with rising temperature, the SC was determined for the lowest temperature prevalent in the different investigated B-IGFC systems, please refer to section 6.3.1.

6.1.1.3 Model parameters and settings

The parameters and model setting used for the simulation of the four investigated cell designs, see section 6.1.1.1, with the ATHENA SOFC model are listed below. The macro cell geometry of the anode-supported planar cell designs is given in Table 5-12. The corresponding micro geometry is summarized in Table 6-2.

Table 6-2: Micro geometry of planar anode-supported cell design

Description	Unit	Value	Source
Anode thickness	μm	750.0	[75]
Electrolyte thickness	μm	10.0	
Cathode thickness	μm	50.0	

The heat conductivity coefficients of the ceramic materials used for the simulation of planar cell designs can be found in Table 5-14. For the heat conduction in the metallic bipolar plates, 18 W/m^2 K was assumed. Table 6-3 summarizes the parameters applied in the reproduction of the electrochemical behavior of anode-supported cells. The data used for the reproduction of planar electrolyte-supported cells is summarized in Table 5-12, Table 5-14 and Table 5-20. Table 5-16 to Table 5-18 give the geometry and model input data for the tubular cathode-supported cell design. The general model settings are compiled in Table 6-4.

Table 6-3: Electrochemical loss model input data for simulation of anode-supported cell designs

Description	Unit	Value	Source
Activation polarization			
H_2 oxidation activation energy	J/mol	100000.0	[174]
H_2 oxidation pre-exponential factor	A/m^2	550000000.0	
CO oxidation activation energy	J/mol	100000.0	[139]
CO oxidation pre-exponential factor	A/m^2	393000000.0	
O_2 reduction activation energy	J/mol	120000.0	[174]
O_2 reduction pre-exponential factor	A/m^2	700000000.0	
Ohmic polarization			
Electric conductivity of anode	1/Ohm m	T-dependent, Eq. 45	[191]
Ionic conductivity of electrolyte	1/Ohm m	T-dependent, Eq. 46	
Electric conductivity of cathode	1/Ohm m	T-dependent, Eq. 47	
Electric conductivity of metallic IC	1/Ohm m	T-independent	[190]
Diffusion polarization			
Porosity of electrodes	-	0.3	assumed
Tortuosity of electrodes	-	6.0	
Average pore diameter of electrodes	m	1.0E-6	

Table 6-4: ATHENA SOFC model settings for system analysis

Model settings	Description
Electrochemical loss model settings	
Considered electrochemical active species	Hydrogen and Carbon monoxide
Activation polarization	According to Eq. 89
Ohmic polarization	Contact resistance neglected
Diffusion polarization	According to Ficks law, Eq. 111 to Eq. 115
Chemistry model settings	
Methane steam reforming reaction	According to Eq. 133
Water gas shift reaction	At equilibrium
Ethane steam reforming reaction	According to Eq. 134
Toluene steam reforming reaction	According to Eq. 135
Thermal decomposition of acetic acid	According to Eq. 137
Anisole steam reforming reaction	According to Eq. 136
Film diffusion limitation for heterogeneous reactions	Considered
Energy balance settings	
Solid heat transfer mechanism	Non-isothermal with solid heat conduction
Coupled heat and mass transport	Considered
Heat loss mechanism at outer surface	Neglected
Definition of sensible heat gradient	$\frac{d(\dot{n} \cdot c_p \cdot T)}{dx}$
General model settings	
Number of discretization points	40
Tolerance of mass balance calculations	0.5 %
Tolerance of energy balance calculations	1.0 %

6.1.2 Overall system simulation assumptions

The aims of the overall system simulations were fourfold. Firstly to determine the overall system efficiency, secondly to identify heat pinch points, thirdly to determine the amount of useful heat at 200 °C which can be recovered from the flue gas after all heat requirements were covered and finally to estimate the size of the most important equipment pieces, especially of the heat exchangers. It needs to be noted that an optimization of the heat exchanger network was not part of the investigation. Instead, the generalized heat integration network (HIN) discussed in section 5.2.3 was defined. The assumptions made for the overall system simulations are summarized in Table 6-5.

Table 6-5: Overall system simulation assumptions

Parameter	Unit	Value
Ambient temperature	°C	25.0
System pressure	bara	1.01325
Wood humidity as delivered to plant	%	42.0
Gasifier heat losses	-	Included in raw producer gas temperature
Heat losses in other equipment	%	0.0
Desulfurization temperature, [149]	°C	400
Post-combustor efficiency	%	100.0
Useful heat temperature	°C	200.0
Temperature approach of flue gas and SOFC cooling air in recuperator	K	20.0
Pressure loss over system for blower power estimation	bara	0.375

By employing measured producer gases temperatures at the outlet of the corresponding gasification reactor, the resulting heat losses were included in the system analysis. Heat losses of other equipment pieces however were neglected. This assumption does not affect the electrical system efficiency but yields slightly overestimated amounts of useful heat. The useful heat temperature level was assumed at 200 °C to allow the application of e.g. an organic rankine bottoming cycle. Because pressure losses were neglected in the system simulations, an overall system pressure loss of 375 mbar was assumed for the estimation of the power requirement of blowers and pumps. The net AC power produced by the SOFC is calculated according to Eq. 199 based on the net AC efficiency, see section 5.4.4, the wood mass flow and its lower heating value. The thermal and the overall system efficiency are computed according to Eq. 200 and Eq. 201, where P_{th} represents the useful heat.

$$P_{net,AC} = \eta_{net,AC} \cdot \dot{m}_{feed} \cdot LHV_{feed}$$ Eq. 199

$$\eta_{th} = \frac{P_{th}}{\dot{m}_{feed} \cdot LHV_{feed}}$$ Eq. 200

$$\eta_{tot} = \frac{P_{net,AC} + P_{th}}{\dot{m}_{feed} \cdot LHV_{feed}}$$ Eq. 201

6.2 System definition

6.2.1 Natural gas reference system

The development of standardized SOFC units operated with natural gas is the primary goal of the American Solid State Energy Conversion Alliance (SECA), [221]. The “mass customization” approach pursued by the SECA should allow the linkage of these units to standardized and thus cost efficient power plant size SOFC systems. Accordingly, a natural gas fuelled SOFC stack with a size sufficient for a power output of 1 MW_{el} was assumed as standard for the application in B-IGFC systems. The natural gas reference system, shown in Figure 6-1, was defined to determine for the four different cell designs the number of cells forming the assumed standard stack and the gas inlet temperatures.

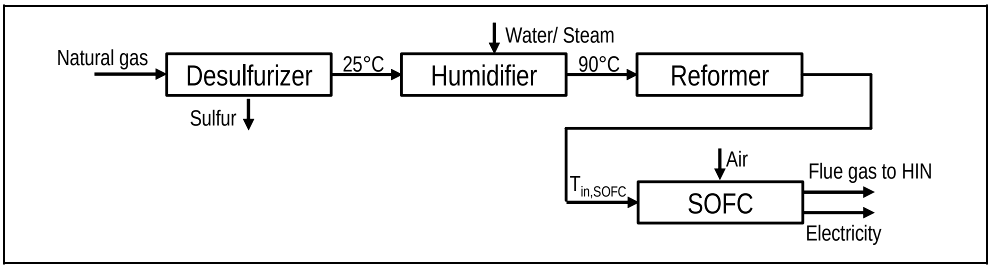

Figure 6-1: Outline of the natural gas reference system

In a first step, the odorant of the natural gas, assumed as pure methane, is removed. The gas is then humidified to yield a steam-to-carbon ratio of 2, which was found sufficient to prevent carbon deposition in corresponding equilibrium calculations, see section 6.3.1. The humidified natural gas is introduced to an isothermal convective pre-reformer where, depending on the reformer temperature, 25 to 30 % of the methane is converted to hydrogen and carbon monoxide, see Table 6-6. The heat required for both, the steam generation and the endothermic reforming reactions, is taken from the hot flue gas. The temperature of the pre-reformer was assumed 100 K below the operational temperature of the various cell designs to ensure that enough heat at the required temperature level is available. After being heated to the cell design specific temperature, the pre-reformed gas is fed to the SOFC, where its chemical energy content is partially converted to electricity. For heat recovery, the depleted anode off gases are post-combusted and then conducted through the heat integration network (HIN) discussed in section 5.2.3. The electrical efficiency achieved with a fuel utilization of 85 % at a voltage of 0.6 V was 45 to 46 % depending on the pre-reforming degree achieved at the cell design specific reformer temperature.

Table 6-6:
Gas compositions of pre-reformed natural gas at the cell inlet of the four considered cell designs

Species	Unit	Cell design		
		1 and 2	3	4
H_2	mol-%	23.49	26.38	26.25
CO		4.15	6.66	6.83
CO_2		2.76	1.60	1.44
H_2O		48.02	46.02	46.15
CH_4		21.58	19.34	19.32

For the four investigated cell designs, Table 6-7 lists the number of cells required to produce 1 MW_{el} DC power and the gas inlet temperatures needed for the accordance of the mean cell temperature and the operational temperature at an air-to-fuel ratio of 4.25. The established maximum temperature gradients and solid temperatures were adopted as upper limit values for the safe operation of the various cell designs.

Table 6-7:
Stack sizes and gas inlet temperatures as well as permitted maximum temperature gradients and solid temperatures for the four cell designs determined with the reference natural gas system

Description	Unit	Cell design			
		1	2	3	4
Number of cells	-	55164	51553	48057	6914
Anode gas temperature	°C	605.5	641.0	891.0	900.0
Cathode gas temperature		605.5	641.0	891.0	850.0
Mean current density	A/m^2	3037.1	3232.9	3468.1	2891.1
Max. temperature gradient	K/mm	2.61	2.62	3.34	1.29
Max. solid temperature	K	1094	1110	1341	1356

6.2.2 B-IGFC systems

6.2.2.1 Gasification processes

A fixed bed updraft and a fixed bed downdraft air gasification process as well as a fluidized bed steam gasification process were investigated. The composition of the producer gases and the main features of the gasification processes are compiled in Table 6-8. The functional principles of the investigated processes were outlined in the section 2.2.3.

Table 6-8: Producer gas compositions and properties of the gasification processes considered in the system analysis

Description	Unit	Updraft gasification	Downdraft gasification	Fluidized bed gasification
General information				
Manufacturer	-	Babcock& Wilcox Vølund A/S	Pyroforce AG	HPR Technologies GmbH
Data sources		[28], [29]	Own measurement	[33], own measurement
Gasification agent		Air	Air	Steam
Humidity of feed at gasifier inlet	%	42.0	8.0	7.4
Gas temperature at gasifier outlet	°C	75.0	650.0	756.0
Gas yield	m_n^3 (dtf)/ $kg_{dryfeed}$	2.054	2.902	1.073
LHV	MJ/ m_n^3	5.193	4.797	7.288
Hydrogen equivalent	mol H_2/ m_n^3	22.30	18.96	31.17
Dry and tar free gas composition				
H_2	mol-% (dtf)	19.23	17.67	34.93
CO		20.53	19.41	28.08
CO_2		13.52	10.32	19.18
CH_4		5.51	1.63	9.59
C_2H_4		0.00	0.10	2.74
N_2		41.21	50.87	5.48
Water load				
H_2O	g/ m_n^3 (dtf)	493.0	43.3	626.7
Tar load				
C_7H_8 (Toluene)	mg/ m_n^3 (dtf)	35330	1366	15430
$C_2H_4O_2$ (Acetic acid)		13608	0	98
C_7H_8O (Anisole)		5832	0	42
Sulfur load				
C_4H_4S (Thiophene)	mg/ m_n^3 (dtf)	83	3	40
H_2S		173	145	380

The water load of the producer gas originating from the updraft gasification process was calculated to satisfy saturation at 75 °C, [28]. The gas yield, which represents the producer gas volume on dry and tar free basis (dtf) per kg of dry wood, was computed to yield a cold gas efficiency of 95 % including the heating value of tars, [4]. The producer gas composition as well as the tar load and its composition were reported in [28] and [29].

For the downdraft gasification process, the water load of the producer gas was determined by means of mass balance, assuming a char flow rate in form of carbon of 4 g/m_n^3 (dtf), [4]. The gas yield was calculated to achieve a cold gas efficiency including tars of 80 %, [4]. The producer gas composition was measured in the framework of a measuring campaign conducted by fellow researchers of the author in 2003.

The water load of the fluidized bed steam gasification producer gas was evaluated by application of mass balance calculations for a steam-to-fuel ratio of 2.16, [33]. As no tar load and composition data could be found for the investigated fluidized bed gasification process, values obtained during a measuring campaign at a similar steam gasification plant were employed. The gas yield was computed with a predefined cold gas efficiency of 76 %, which corresponds to the development target of the investigated fluidized bed gasification process, [33], increased by 10 %.

Measured data regarding the sulfur load and composition was not available for the three gasification processes. Hence, a rough estimation was performed by hypothesizing that the sulfur present in the gasified wood is entirely converted to either H_2S or thiophene. This assumption yields a conservative estimate due to the neglect of the amount of sulfur usually bound in particles, [222]. According to the DIN Plus norm, a sulfur content of wood of 400 mg/kg on dry basis was assumed. The fractions of thiophene and hydrogen sulfide were appraised via an analogy. It was assumed that the ratio between organically bound sulfur and sulfur bound in hydrogen sulfide equals the ratio between carbon bound in tars and carbon bound in permanent gas species (CO, CO_2, CH_4, C_2H_4).

6.2.2.2 Downdraft gasification based B-IGFC systems

The producer gas obtained from the examined downdraft gasification process has a temperature of 650 °C at the gasifier outlet, which forces on the application of high temperature gas processing.

Due to the hydrocarbon content below 2 mol-%, the potential of the producer gas for the chemical cell cooling via reforming reactions is low. In this respect, a methanation unit in the gas processing could be favorable.

With roughly 1.4 g/m_n^3 (dtf), the tar load of the producer gas is very low. Thus, the heating of the producer gas in heat exchangers should be unproblematic regarding coking issues.

According to the assumption in section 6.2.2.1, sulfur is present in the producer gas to over 99 % in form of hydrogen sulfide, which can be removed by employing zinc oxide adsorbents (ZnO). The sulfur bound in organic species is unlikely to be an issue for stable SOFC operation.

Figure 6-2: Outline of the downdraft gasification based "System 1"

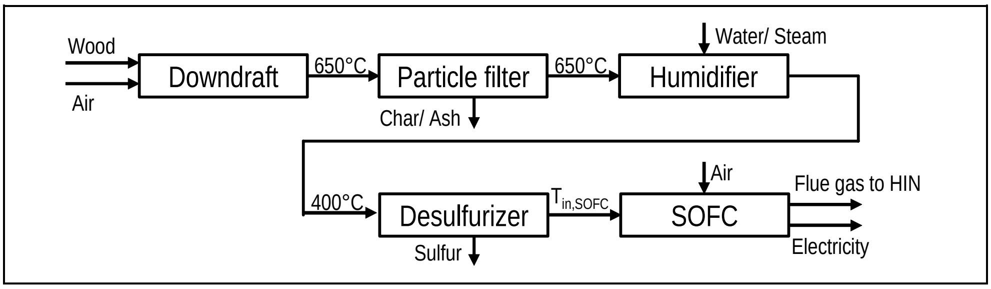

Figure 6-2 shows the outline of the first downdraft gasification based B-IGFC system configured for this analysis, named "System 1". In System 1, the humidity of the wood is decreased from 42 to 8 % in a convective exhaust gas dryer. The dried wood is injected to the downdraft gasifier where it is gasified with air. The gasification air is forced into the gasifier by an electric air blower. The hot producer gas is de-dusted in a ceramic particle filter operated at 650 °C and then humidified with wet steam. This results in a cool down of the producer gas to 400 °C, which corresponds to the operating temperature of the zinc oxide adsorbent bed employed for the removal of hydrogen sulfide. Besides yielding the desired gas cool down, the humidification is necessary to prevent carbon deposition at the temperature of the zinc oxide adsorbent bed temperature. The de-dusted and desulphurized gas is heated to the cell design specific gas inlet temperature, see Table 6-7, and subsequently fed to the SOFC, where the chemical energy of the producer gas is partially converted to electricity and heat. The cooling air for the SOFC is provided by an electric air blower. The depleted electrode off-gases are then guided through the heat integration network, explained in section 5.2.3, to cover the heat requirements resulting from the air and fuel heating, steam generation and wood drying. Note that in System 1, organic sulfur species are not removed from the producer gas.

Figure 6-3 depicts the second downdraft gasification based B-IGFC system configured for this analysis, named "System 2". In addition to System 1, an adiabatic methanation unit is placed downstream the ZnO desulfurizer in System 2. The aim of the methanation step is to increase the methane content of the producer gas, which should allow for more SOFC internal reforming reactions and thus lower the required cooling air flow rate.

Figure 6-3: Outline of the downdraft gasification based "System 2"

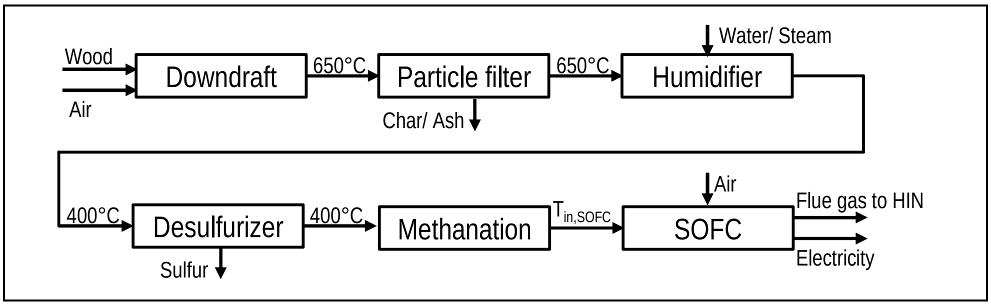
Wood
Air
Downdraft
650°C
Particle filter
Char/ Ash
650°C
Water/ Steam
Humidifier
400°C
Desulfurizer
Sulfur
400°C
Methanation
$T_{in,SOFC}$
Air
SOFC
Flue gas to HIN
Electricity

6.2.2.3 Updraft gasification based B-IGFC systems

The investigated updraft gasifier yields a producer gas at 75 °C temperature. Hence, both cold and hot gas processing may be applied.

With a hydrocarbon content over 5 mol-%, the potential for chemical cell cooling through reforming reactions is indeed three times higher than that of the downdraft gasification producer gas but still lower than that of the pre-reformed natural gas assumed as reference fuel for SOFCs.

With almost 55 g/m_n^3 (dtf), the updraft gasification producer gas is highly tar laden. Coking issues during heating and tar condensation problems in pipes are therefore most probable. To prevent these issues, the tar load should be reduced to moderate values as near as possible to the gasifier outlet either by tar removal or by tar conversion to permanent gas species.

Following the assumption in section 6.2.2.1, the sulfur signature of the updraft producer gas strongly differs from that of the downdraft producer gas. With almost 17 % of the sulfur present in the gasified wood being bound in organic sulfur species, measures to degrade these species to hydrogen sulfide for subsequent adsorption are inevitable to allow for the effective operation of SOFCs.

Figure 6-4: Outline of the updraft gasification based "System 3"

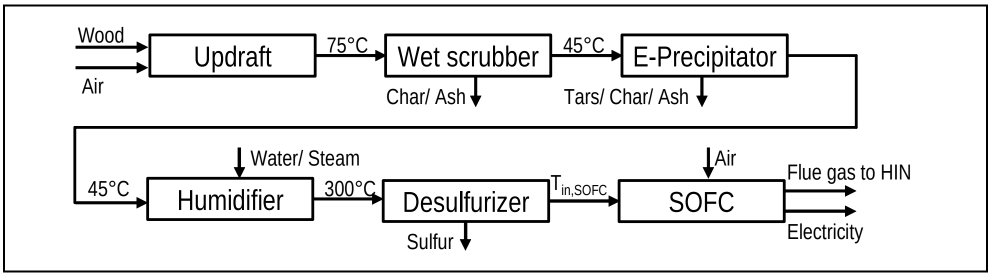
Wood
Air
Updraft
75°C
Wet scrubber
Char/ Ash
45°C
E-Precipitator
Tars/ Char/ Ash
45°C
Water/ Steam
Humidifier
300°C
Desulfurizer
Sulfur
$T_{in,SOFC}$
Air
SOFC
Flue gas to HIN
Electricity

The scheme of the first updraft gasification based B-IGFC system defined for this analysis is named "System 3" and depicted in Figure 6-4. System 3 uses cold gas processing technology, thus representing state-of-the-art. The wood with a humidity of 42 % is directly introduced to the updraft gasifier, where it is dried and converted to producer gas using air as gasification agent. The gasification air is again forced through the gasifier using an electric air blower. The comparably cold and water saturated producer gas is coarsely de-dusted in a wet scrubber of which the gas exits water saturated at a temperature of 45 °C. The remaining particles together with the tars and organic sulfur species are removed from the producer gas in an electrostatic precipitator. To prevent carbon deposition in the zinc oxide adsorbent bed and the subsequent gas heating to the cell inlet temperature, vapor is injected in a humidifier. Hydrogen sulfide is adsorbed in a ZnO trap bed at a temperature of 300 °C yielding concentrations around 0.1 ppmV. The de-dusted and almost tar and sulfur free producer gas is super heated to the cell inlet temperature and then fed to the SOFC. The heat recovery is conducted in the same manner as in System 1 and 2.

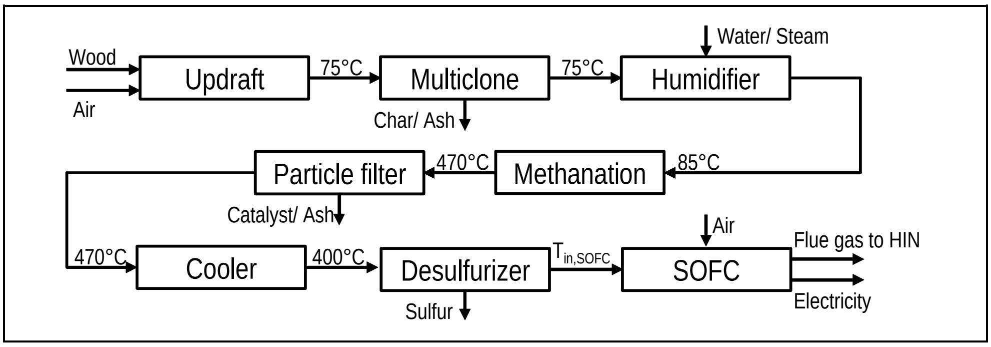

Figure 6-5: Outline of the updraft gasification based "System 4"

The second investigated updraft gasification based B-IGFC system is named "System 4" and presented in Figure 6-5. Similar to System 3, the wet wood is directly put into the updraft gasifier without external drying. The producer gas is de-dusted in a multiclone and then humidified. In an adiabatic fluidized bed methanation reactor, tars and organic sulfur species are degraded to permanent gas species and hydrogen sulfide, respectively. The methanation of tar laden producer gases using the fluidized bed reactor concept was shown in [223]. It was found to be fairly tolerant towards carbon depositions usually caused by higher hydrocarbons due to reactor internal carbon exchange processes, [224]. The methane content of the producer gas is considerably increased, which should be beneficial with respect to the cooling requirements of the employed SOFC. Simultaneously, the heat of the methanation reactions yields an increase of the producer gas temperature from approx. 85 °C at the reactor inlet to roughly 470 °C at the outlet. Ash and catalyst particles are removed from the hot producer gas in a ceramic particle filter. After a slight cool down, the hydrogen sulfide content is removed from the producer gas in a ZnO trap bed at 400 °C. The subsequent heating of the gas, conversion in the SOFC and heat recovery is carried out as already mentioned above for the other investigated systems.

Figure 6-6 shows the third updraft gasification based B-IGFC system, named "System 5". The producer gas originating from the air gasification of the un-dried wood is again de-dusted in a multiclone.

Figure 6-6: Outline of the updraft gasification based "System 5"

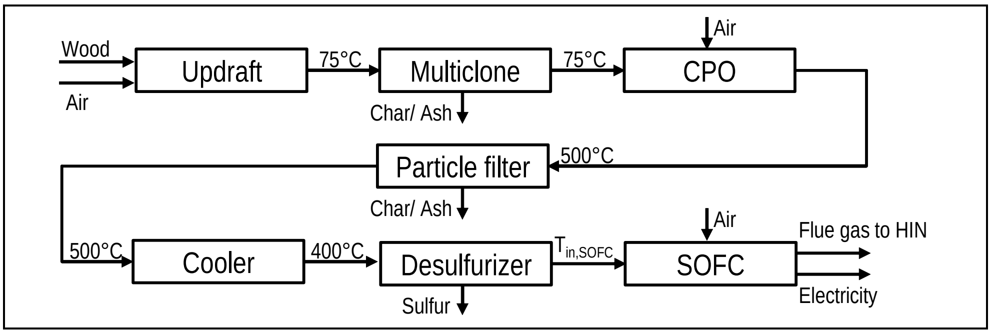

Tars and organic sulfur species are degraded in a catalytic partial oxidation reactor (CPO) through combustion and reforming reactions. Thus, a part of the chemical energy of the producer gas is converted to heat which results in a considerable increase of the producer gas temperature. To minimize the loss of chemical energy, the air-to-fuel ratio is kept as low as possible without risking carbon deposition in the equipment downstream of the CPO. The catalytic partial oxidation of tar-laden producer gases was shown and reported in [153]. The CPO air flow rate is provided by an electric blower. Ash particles are removed from the partially oxidized producer gas in a ceramic particle filter before it is cooled to 400 °C for subsequent hydrogen sulfide removal in a ZnO trap bed. The conversion of the gas to electricity and useful heat through the SOFC and heat integration network is conducted as discussed above.

6.2.2.4 Fluidized bed steam gasification based B-IGFC systems

The producer gas originating from the investigated fluidized bed steam gasification process has a temperature of 750 °C. Thus, high temperature gas processing is strongly recommended.

The potential of the steam gasification producer gas for chemical cell cooling is higher than that of both other gases. Therefore, measures to further increase the methane content were not investigated.

Despite the elevated tar load around 16 g/m_n^3 (dtf), the gas handling should be rather unproblematic. At the high temperature of the steam gasification producer gas, all tar species are in the gas phase. In contrast, coking problems usually arise during the evaporation of condensed tars, [133]. Hence regarding coking issues, it should suffice to ensure the gas phase state of the tars by restraining a minimum system temperature of 400 °C, which is well above the dew point of most tars.

According to the assumption in section 6.2.2.1, the sulfur load consists of hydrogen sulfide to more than 96 %. Hence, it is possible that a removal of organic sulfur species is not necessary.

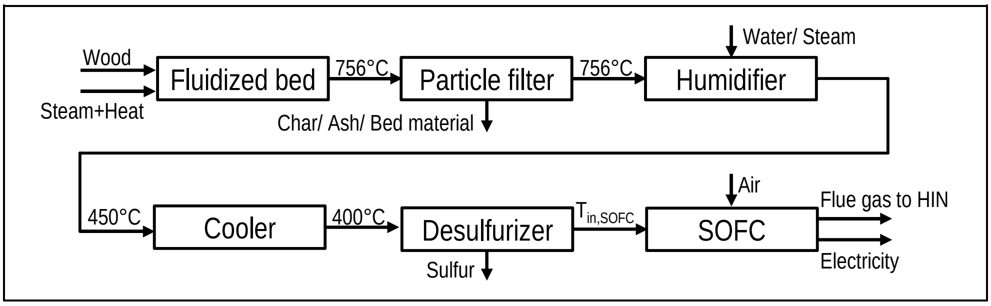

Figure 6-7: Outline of the fluidized bed gasification based "System 6"

The first investigated fluidized bed steam gasification based B-IGFC system is named "System 6" and depicted in Figure 6-7. For efficiency reasons, the wood humidity is decreased from 42 to 7.4 % before the wood is fed to the steam gasification reactor. The steam is produced using flue gas heat. The heat for the gasification reactions is generated via combustion of unreacted char and transported into the gasification reactor using heat pipes. For more information please see [168]. The quasi nitrogen free producer gas has a temperature of 756 °C at which it is de-dusted using a ceramic particle filter. To allow for the desulfurization of the producer gas with ZnO, it is cooled and humidified by liquid water injection thus also preventing carbon deposition. The temperature after the water injection is approx. 450 °C thereby requiring further cool down in a gas cooler. The heat is used for the pre-heating of the SOFC cooling air. At 400 °C, H_2S is removed from the gas, while organic sulfur species remain. The de-dusted and partially desulphurized producer gas is than heated to the cell inlet temperature and converted to heat and electricity in the SOFC. The depleted off-gases are guided through the heat integration network to cover all heat requirements of the system.

Figure 6-8 shows the second fluidized bed steam gasification based B-IGFC system investigated in this work, which is named "System 7".

Figure 6-8: Outline of the fluidized bed gasification based "System 7"

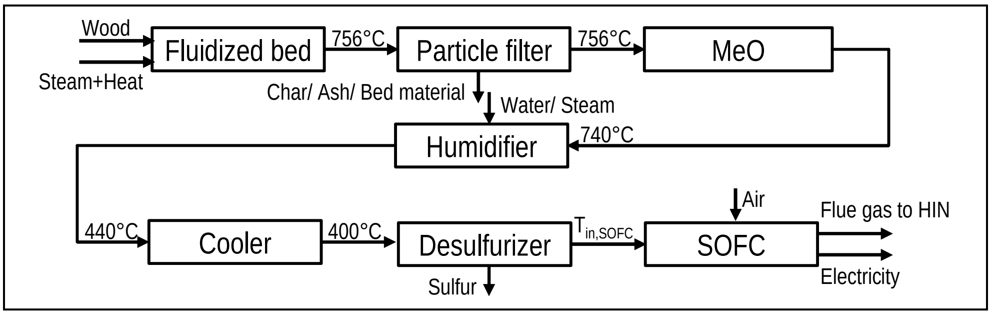

The only difference between System 7 and System 6 is that a sulfur adsorbent bed containing a metal oxide is placed downstream the particle filter for coarse desulfurization and cracking of organic sulfur species. According to [149], the metal oxide material has the potential to degrade organic sulfur species. Accounting for the found influence of the metal oxide on the producer gas composition, it was assumed that 10 % of the producer gas reach equilibrium. The sulfur load in the raw producer gas can thus be almost completely removed in the subsequent zinc oxide trap bed, which should have a positive effect on the SOFC performance.

6.3 Technical evaluation

6.3.1 Simulation results of gas processing sections

Carbon deposition is an issue which is not limited to the SOFC but which also has to be considered as potential failure source of all equipment pieces in direct contact with producer gas at temperatures above 300 °C. Below 300 °C, carbon deposition can be assumed slow as long as no catalyst is present. Note that carbon deposition results from the decomposition of hydrocarbons or carbon monoxide, see section 2.4.7.3, and should not be confused with tar condensation. Generally, the probability of carbon deposition decreases with increasing temperature and atomic oxygen molar fraction of the producer gas. The latter may be increased by adding water or oxygen. In turn, water removal and gas cooling may cause carbon deposition issues.

The producer gases characterized in Table 6-8 exhibit water loads, which are high enough to prevent carbon deposition at the operational temperatures of the considered SOFC designs. However, this is not the case at temperatures around 300 to 400 °C, which form the operational temperature range of the ZnO adsorbents employed for H_2S removal. Except for System 5, where air is injected to the producer gas for its subsequent catalytic partial oxidation, the atomic oxygen fraction of the producer gases was increased simply through addition of water or steam in this analysis.

Table 6-9: Steam-to-carbon (SC) ratios of raw producer gases, minimum and safe SC values
*: Air-to-fuel ratio of CPO

Para-meter	Unit	System							
		NG	1	2	3	4	5	6	7
Min. T	°C	600	400	400	300	400	400	400	400
SC_{raw}	-	0.0	0.17	0.17	0.26	1.29	1.29	1.20	1.20
SC_{min}		1.5	1.25	1.25	1.48	1.4	0.09*	1.33	1.33
SC_{safe}		2.0	1.66	1.66	1.97	1.86	0.12*	1.78	1.78

Table 6-9 summarizes the steam-to-carbon ratios (SC) of the raw producer gases, the minimum SC at which graphite does not exist at equilibrium conditions and the SC used in this analysis, which is 33 % higher than the minimum SC. Note that Table 6-9 gives the minimum and the safe air-to-fuel ratio for the CPO performed in System 5.

Figure 6-9 shows the C-H-O ternary diagram with isotherm lines for 760 °C, 600 °C and 400 °C, which are the lowest operational temperature of the four investigated cell designs, the critical temperature for carbon deposition from methane and the operational temperature of the ZnO trap beds in Systems 4 and 5, respectively.

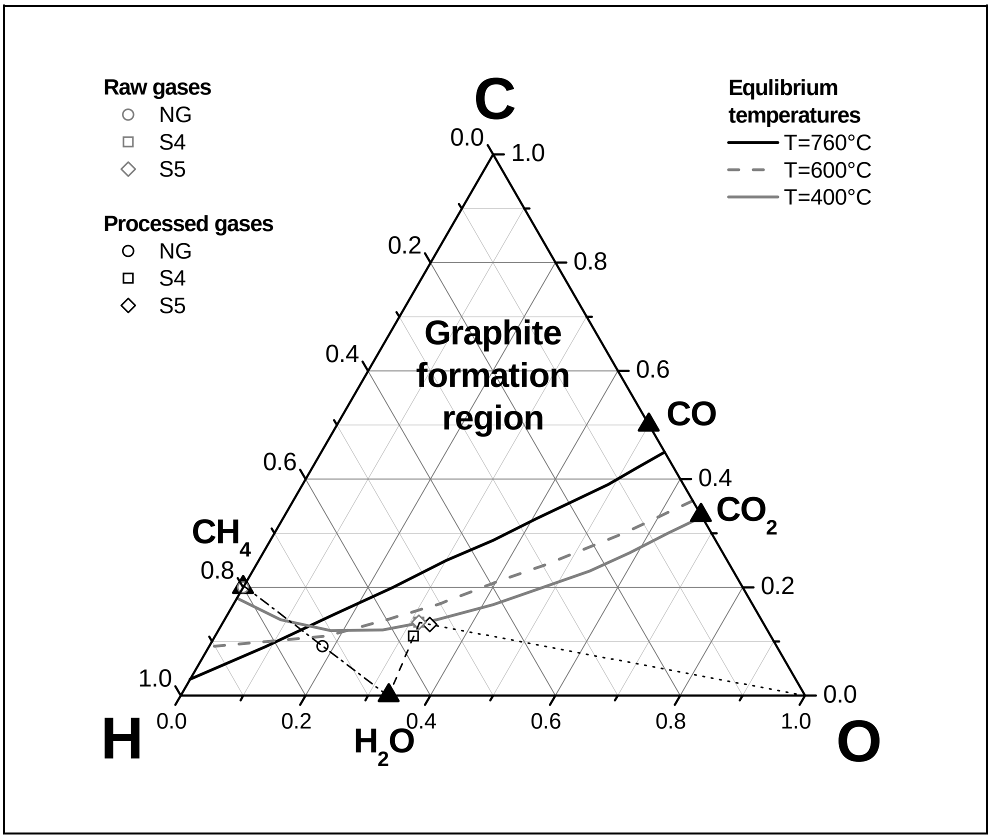

Figure 6-9: C-H-O molar fraction ternary diagram for graphite formation under equilibrium conditions.

The isotherm lines computed for different temperatures divide the diagram in a region where graphite is formed at equilibrium and a graphite free region. The inscribed points represent the raw fuel gases as received from the gasifier or the NG grid and the processed fuel gases. The points are only moved when additional carbon, hydrogen or oxygen is added to the gases. Thus, only the humidification and the air injection for the CPO result in a shift of the points representing the different fuel gases.

The raw updraft producer gas used in System 4 and 5 is slightly above the isotherm line of 400 °C, indicating that carbon deposition is likely to occur in the ZnO trap bed. The water addition in System 4 shifts the representing point out of the graphite formation region following the dashed line. The air addition for the CPO in System 5 shifts the point representing the raw updraft producer gas towards the oxygen corner of the diagram following the dotted line. Methane is clearly in the graphite formation region for all the displayed temperatures. In contrast to the updraft producer gas, the carbon deposition risk for methane is not highest at 400 °C but at 600 °C. This is because methane is stable at temperatures below 300 °C. The water addition to yield a SC of 2 follows the dashed-dotted line.

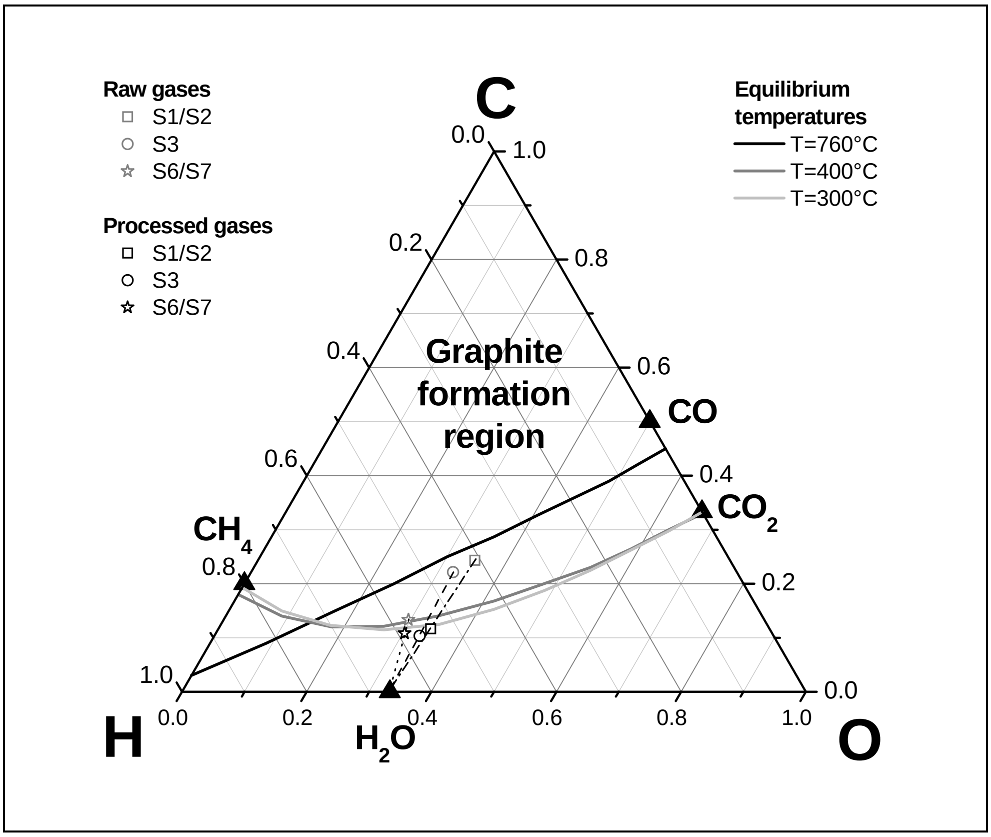

Figure 6-10:
C-H-O molar fraction ternary diagram for graphite formation under equilibrium conditions.

The isotherm lines computed for different temperatures divide the diagram in a region where graphite is formed at equilibrium and a graphite free region. The inscribed points represent the raw fuel gases as received from the gasifier and the processed fuel gases. The points are only moved when additional carbon, hydrogen or oxygen is added to the gases. Thus, only the humidification results in a shift of the points representing the different fuel gases.

Figure 6-10 shows the C-H-O ternary diagram with isotherm lines for 760 °C, 400 °C and 300 °C, where the latter is the operational temperature of the ZnO trap bed used in System 3. The lower ZnO temperature calls for more water addition in System 3 than in System 4. Together with the removal of almost 75 % of the water content occurring in the wet scrubber, the amount of additional water needed in System 3 is three times higher than in System 4, see dashed line in Figure 6-10.

The water load of the raw downdraft producer gas (S1/S2) is low, due to the limited wood humidity that can be sustained by the downdraft gasification process. For the desulfurization at 400 °C, the amount of additional water is comparable to that required in System 3, see dashed-dotted line in Figure 6-10.

The raw producer gas originating from the investigated fluidized bed steam gasification process (S6/S7) exhibits a comparably high water content despite the low humidity of the gasified wood. This is due to steam being used as gasification agent. Nevertheless, this producer gas does not allow for desulfurization at 400 °C without water addition, see dotted line in Figure 6-10.

The producer gas compositions at the cell inlet, including the above discussed additional water, obtained from the seven B-IGFC systems defined in section 6.2.2, are compiled in Table 6-10. The models used to simulate the methanation, catalytic partial oxidation and ZnO trap bed desulfurization units were explained in the sections 5.2.4 to 5.2.6.

Table 6-10: Producer gas compositions a cell inlet

Species	Unit	System						
		1	2	3	4	5	6	7
H_2	mol-%	11.56	19.26	10.81	7.87	17.15	16.17	17.93
CO		12.70	3.00	11.55	0.22	3.53	13.00	12.62
CO_2		6.75	16.19	7.60	16.98	17.28	8.88	9.59
H_2O		34.54	26.04	43.80	42.48	25.94	53.54	51.79
CH_4		1.07	1.85	3.10	9.37	4.14	4.44	4.26
C_2H_4		0.07	0.00	0.00	0.00	0.00	1.27	1.13
N_2		33.29	33.67	23.16	23.08	31.88	2.54	2.52
C_7H_8	ppmV	217.5	0.0	0.0	0.0	459.7	1700.0	1600.0
$C_2H_4O_2$		0.0	0.0	0.0	0.0	271.7	0.0	0.0
C_7H_8O		0.0	0.0	0.0	0.0	64.7	0.0	0.0
C_4H_4S		0.5	0.0	0.0	0.0	1.2	4.9	0.0
H_2S		1.8	2.4	0.0	2.2	1.4	2.8	2.7

In summary, the use of ZnO trap beds for desulfurization requires an increase of the water content of the producer gas to avoid carbon deposition in all investigated systems except System 5. One way to overcome this requirement could be the application of adsorbent materials with operational temperatures above 700 °C. However, presently such materials are not available. Regarding the system design, in Systems 1, 2 and 3 the extra water calls for additional equipment such as steam generators and spray chambers as a matter of principle. In System 4, the water content could be increased just by increasing the humidity of the gasified wood to values higher than the standard 42 %. In System 6 and 7, an increase of the steam-to-fuel ratio to values higher than the investigated 2.16 would render supplementary gas humidification equipment superfluous, however at the expense of the cold gas efficiency of the steam gasification process.

6.3.2 Simulation results of SOFC operation with producer gases

The fuel gas composition plays a crucial role in the mass, heat and charge transport processes taking place in SOFCs, section 5.3.5. The impact of the producer gases compiled in Table 6-10 is discussed below, focusing on not only the conversion efficiencies and expectable current densities but also the maximum solid temperatures and temperature gradients. The latter are critical for degradation processes, section 2.4.7.2, and structural stress induced cell failures, section 2.4.7.4.

6.3.2.1 Conversion efficiencies

Due to the predefined operational voltage and fuel utilization, the conversion efficiency is the same for all investigated cell designs and only depends on the fuel gas composition, Eq. 202, [70].

$$\eta_{SOFC,DC} = UF \cdot \frac{E_{op}}{E_0} \quad with \quad E_0 = -\frac{\Delta G}{2 \cdot F} \qquad \text{Eq. 202}$$

Figure 6-11 shows the accordingly computed conversion efficiencies, where System 4 yields the highest efficiency of all investigated gases.

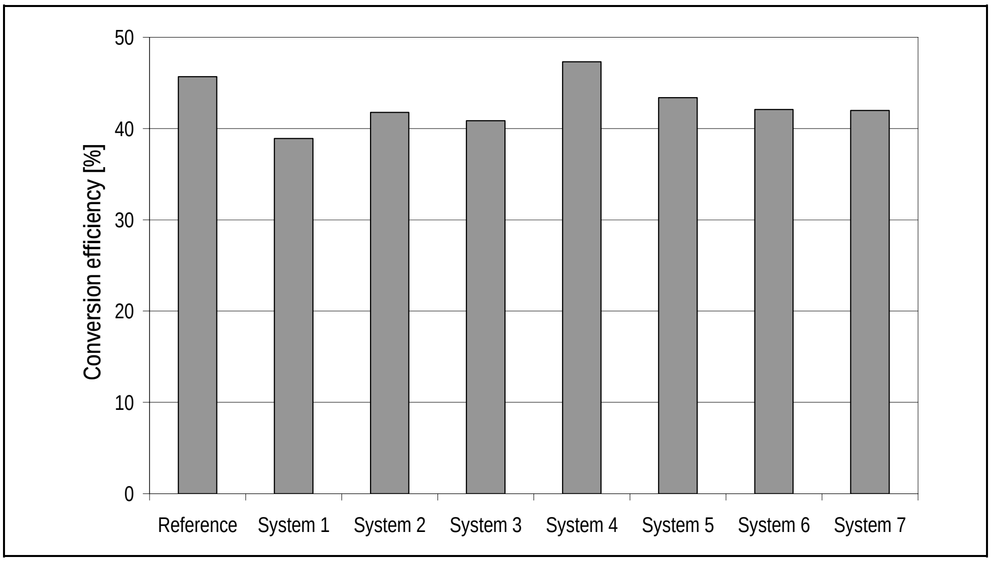

Figure 6-11: Conversion efficiencies of the different producer gases and the reference gas at 85 % fuel utilization and 0.6 V operational voltage

6.3.2.2 Current densities

Figure 6-12 compares the predicted average current density obtained from the different cell designs and producer gases with 85 % fuel utilization an operational voltage of 0.6 V.

Figure 6-12: Comparison of the predicted average current density obtained from the investigated cell designs and producer gases

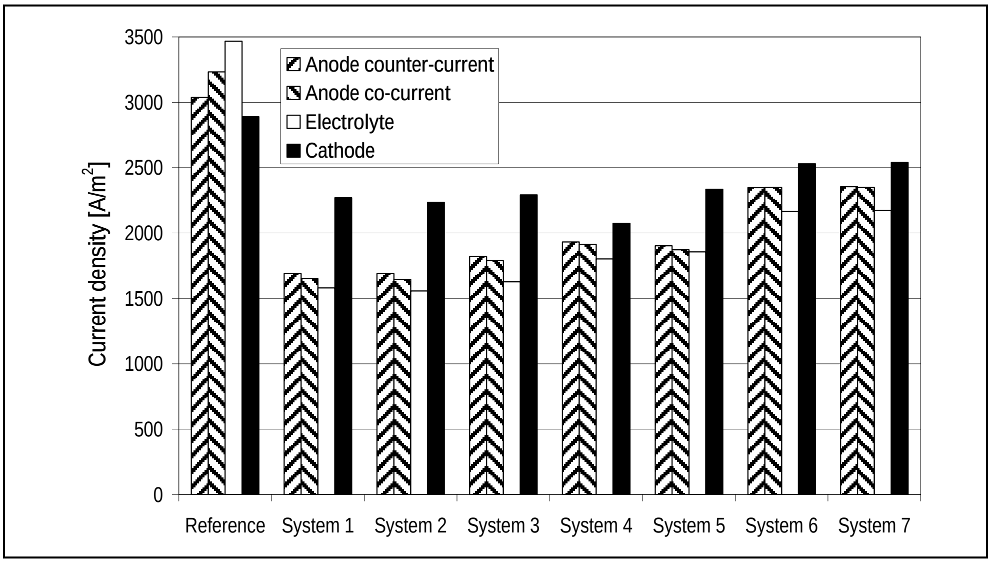

None of the investigated producer gases yields current densities as high as those obtained with the reference gas. The main reason for this is that the reference gas is not diluted with nitrogen, such as the producer gases in systems 1 to 5, which reduces activation losses, and is drier than the producer gases, which yields higher Nernst voltages. The trends regarding the current density values achieved with different producer gases are quite similar in all four investigated cell designs.

Figure 6-13: Voltage loss and current density distributions of the electrolyte-supported cell predicted for the reference gas

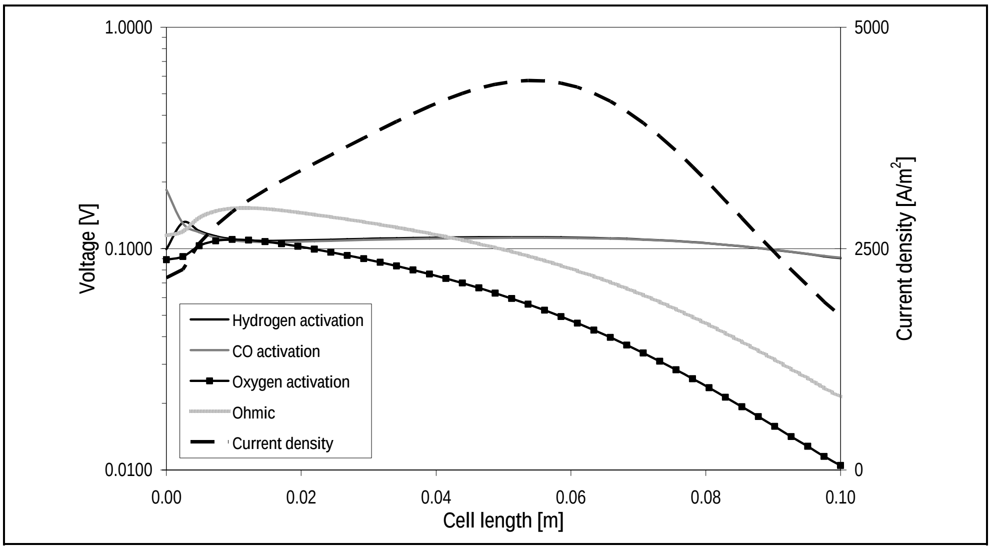

The electrolyte-supported cell produces the highest current density with the reference gas. In this case, the dominating voltage losses are anode activation and ohmic losses. The latter dominate at the cell inlet and decrease towards the cell end, Figure 6-13. With producer gas, the power output of the electrolyte-supported cell is decreased by 50 % in average.

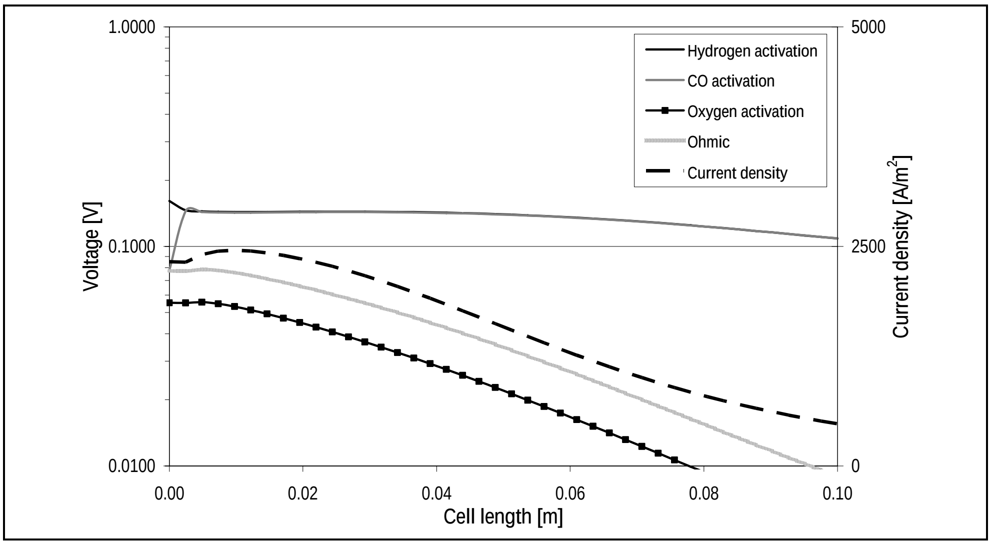

Figure 6-14: Voltage loss and current density distributions of the electrolyte-supported cell predicted for the producer gas of System 2

Figure 6-14 shows the voltage loss and current density distributions of the electrolyte-supported cell operated with the System 2 producer gas. In contrast to the reference gas, the anode activation losses dominate the ohmic losses along the entire cell length. Compared to the reference gas, the activation losses are increased by 50 to 100 %, indicating that the model parameters used for the electrolyte-supported cell describe an anode catalyst with low activity in dilute gases.

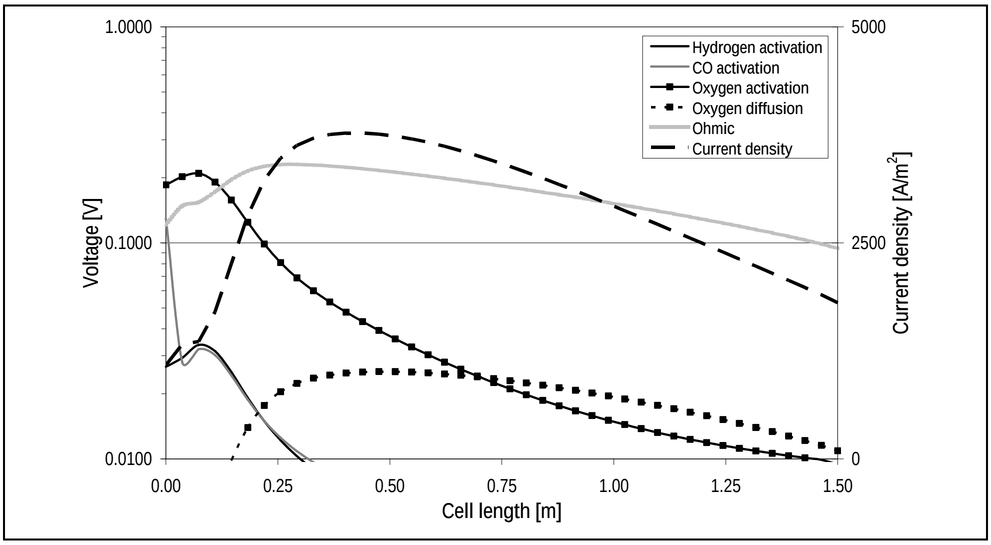

Figure 6-15: Voltage loss and current density distributions of the cathode-supported cell predicted for the reference gas

The power output of the tubular cell is limited by ohmic losses, which are at least one order of magnitude higher than the anode activation losses for all the investigated gases, Figure 6-15. This explains the moderate power output reduction of the tubular cell by 15 % in average when operated with producer gases and indicates a very active anode catalyst.

Figure 6-16: Voltage loss and current density distributions of the anode-supported co-current cell predicted for the reference gas

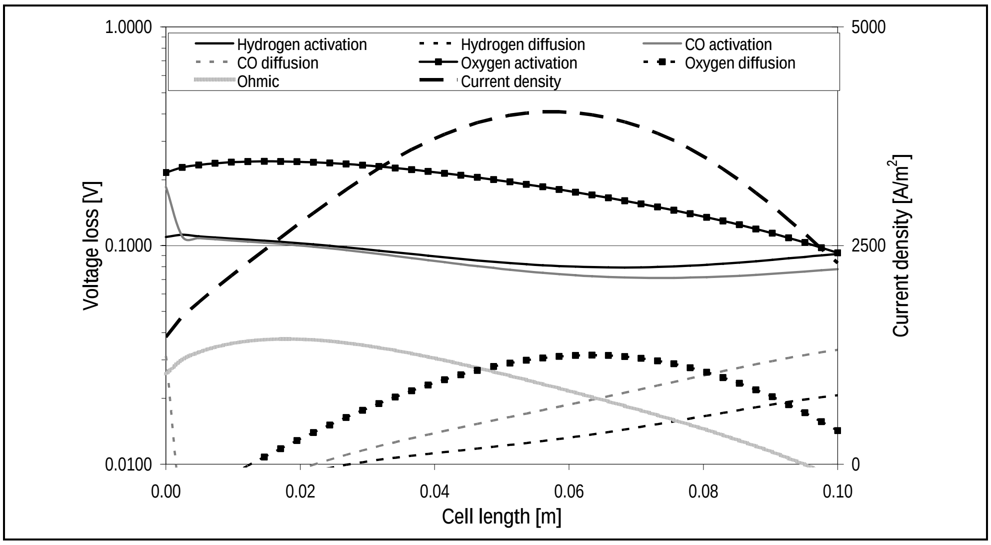

Figure 6-16 shows the voltage loss and current density distributions of the co-current anode-supported cell operated with the reference gas. The power output is limited by the oxygen activation and to a lesser extent by the anode activation. The oxygen activation losses are approx. twice as high as the anode activation losses. The anode diffusion losses gain significance towards the cell end, which can be attributed to fuel depletion and the long diffusion path through the thick anode.

Figure 6-17: Voltage loss and current density distributions of the anode-supported co-current cell predicted for the producer gas of System 2

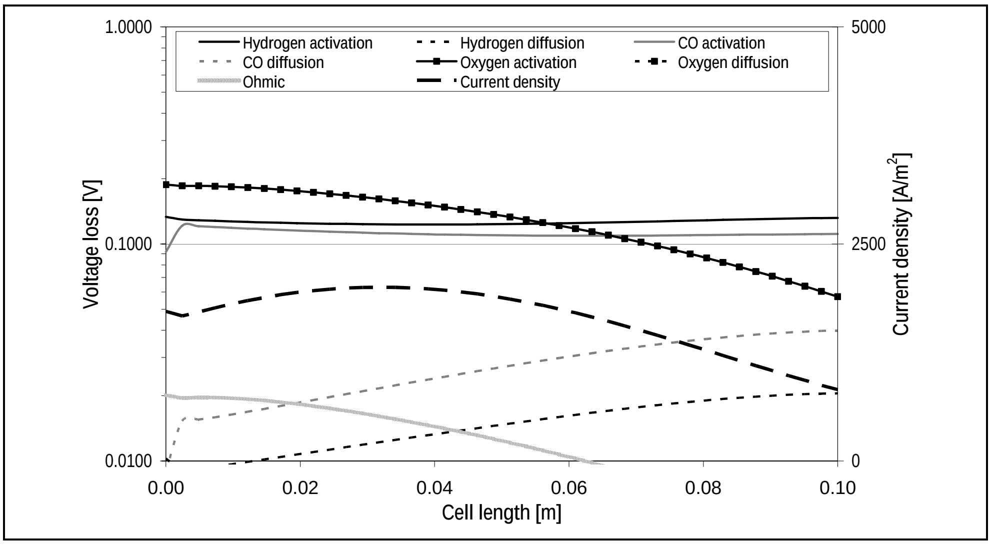

On average, the anode-supported cells yield 30 % less power output with producer gas. Figure 6-17 depicts the voltage loss and current density distributions predicted for the co-current anode-supported cell operated with System 2 producer gas. Compared to the reference gas, the anode activation losses increase by 50 to 100 % and reach values close to the oxygen activation losses at the cell inlet and even higher values at the cell outlet. Moreover, a considerable increase of the anode diffusion losses can be observed, which is attributed to the high nitrogen content of the System 2 producer gas. Given the almost 200 K lower operational temperature of the anode-supported cells compared to the electrolyte-supported cell, the anode catalyst described by the used model parameters appears quite active in dilute gases. This advantage is however cancelled by the lower operational temperature.

The power output differences between the anode-supported co- and counter-current cells are comparatively small. Nevertheless an interesting trend can be observed in Figure 6-12. With the reference gas, the co-current cell yields an almost 10 % higher current density than the counter-current cell. With the producer gases however, the co-current cell always yields slightly lower current densities than the counter-current cell. The reason for this can be found in temperature and current density distributions resulting for the different flow patterns.

Figure 6-18: Comparison of predicted solid temperature und current density distribution of anode-supported co- and counter-current cells for the reference gas

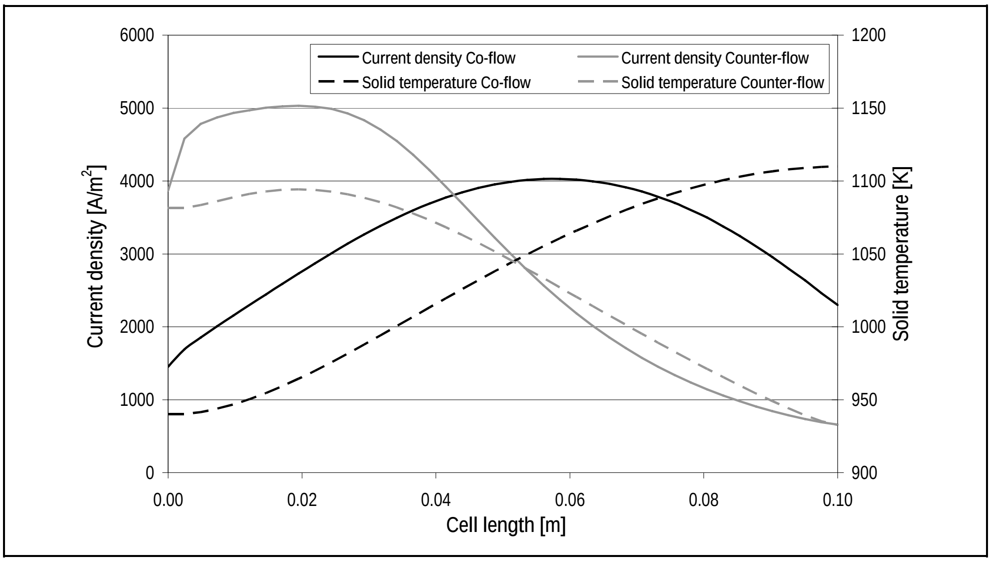

Figure 6-18 compares the temperature and current density distributions of the anode-supported co- and counter-current cells predicted for the reference gas. The co-current cell yields a current density distribution with a wide and flat peak in the middle part of the cell. This is the result of the low temperatures at the cell inlet, due to endothermic STR reactions, which yield only low fuel conversion in this cell region leaving over most of the fuel for the conversion in the latter parts of the cell. Throughout the entire co-current cell, the anode and oxygen activation are the dominant voltage losses.

In contrast, the counter-current cell features a plateau of very high current densities due to high temperatures at the fuel inlet, despite endothermic STR reactions taking place. The high temperatures are maintained by the cooling air, which is heated in the latter parts of the cell. The fuel conversion at the cell inlet is mainly limited by the oxygen activation and diffusion. Towards the fuel outlet, the current density is increasingly limited by anode activation losses, which result from the fast fuel depletion in the front parts of the cell. In sum, the counter-current cell yields a lower average current density with the reference gas than the co-current cell due to the diffusion limitations at the cell inlet.

Figure 6-19: Comparison of predicted solid temperature und current density distribution of anode-supported co- and counter-current cells for the producer gas of System 2

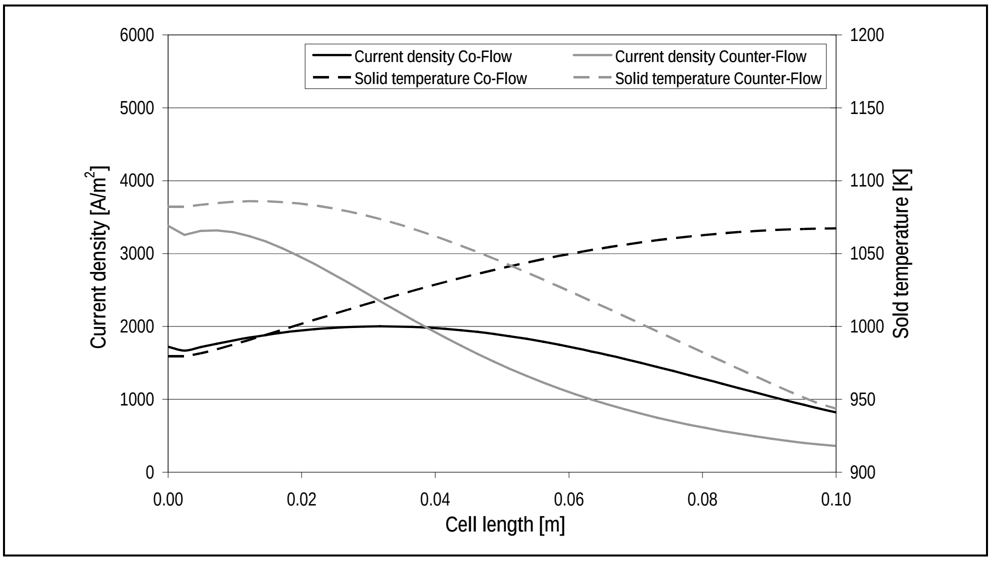

Figure 6-19 compares the temperature and current density distributions of the anode-supported cells predicted for the System 2 producer gas. The co-current cell yields a relatively even current density distribution with a slightly decreasing trend towards the cell end. The fuel conversion at the fuel inlet is fast due to the lack of STR reactions resulting in approx. 40 K higher solid temperatures compared to the reference gas. However, this is not beneficial to the total produced current as most of the fuel is converted at a comparably low solid temperature of 1020 K, where the activation losses are relatively high. For the reference gas, the maximum current density is reached in the second cell half at 1060 K. This is due to the low temperatures at the cell inlet resulting from the STR inhibiting a fast fuel conversion.

The counter-current cell yields considerably higher current densities at the fuel inlet than the co-current cell due to 50 K higher solid temperatures. In contrast to the reference gas, with producer gas the counter-current cell is not limited by oxygen diffusion but by the anode activation like the co-current cell. Thus, the fast fuel conversion at the cell inlet (and high temperatures) is beneficial to the current production of the counter-current cell. In consequence, the total amount of current produced by the counter-current cell is slightly higher than that produced by the co-current cell when operated with producer gases.

In summary it can be said that for a given operational voltage the anode catalyst activity is the dominating factor with respect to the mean current density obtained from different cell designs operated with producer gases. Due to their high degree of nitrogen or water dilution, producer gases require highly active anode catalysts to yield satisfying mean current densities. It appears that an initial estimation of the catalyst activity can be based on the cell design. Designs limited by ohmic losses, such as the tubular and the planar electrolyte-supported cells, will probably feature more active anode catalysts to compensate the ohmic losses. The reason why this does not apply to the electrolyte-supported cell investigated in this analysis is because it was primarily developed as a catalytic burner to provide heat to households. Thus, the anode catalyst is most likely not tuned for high activity with dilute gases. Regarding diffusion limitations resulting from the dilution quality of producer gases it can be said that only the anode-supported cells showed a slight and hence negligible response. Finally, it was found that cell designs with counter-current flow pattern allow for high temperatures at the fuel inlet and are thus beneficial to the conversion of producer gases.

6.3.2.3 Cooling requirements

The air-to-fuel ratio (AF) determines the power requirement of the cooling air blower and the size of the heat exchangers required for air preheating, hence making it significant in the overall system design. Figure 6-20 shows that the AF strongly varies for different cell designs and producer gases. Regarding the latter, the general trend is that fuel gases with high conversion efficiencies require lower AF due to the reduced amounts of waste heat. The differences between the AF required by the different cell designs arise from the geometry dependent heat exchange areas and cell internal heat transport mechanisms.

Figure 6-20: Comparison of the predicted air-to-fuel ratios required to achieve a mean cell temperature equal to the operational temperature of the investigated cell designs operated with the different producer gases

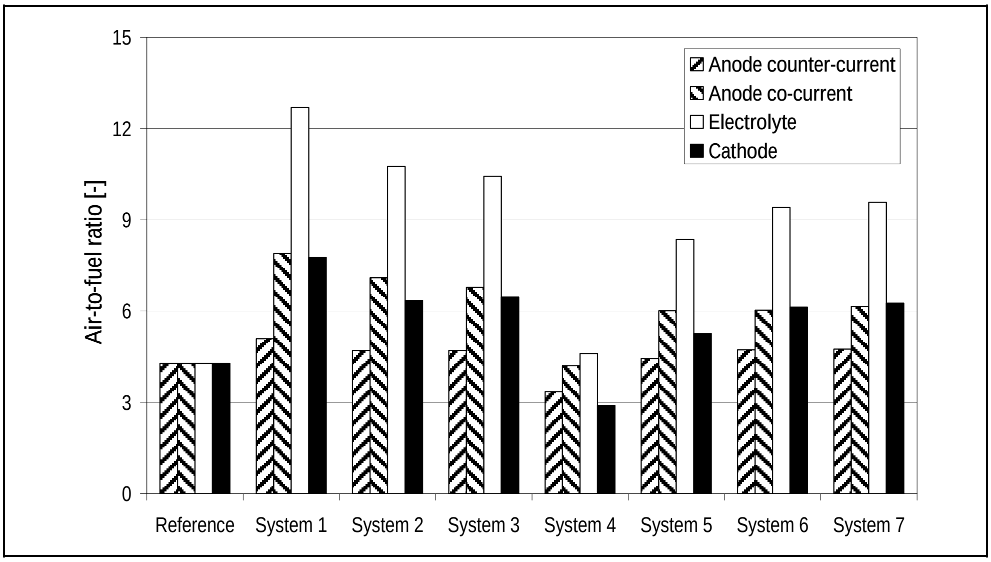

The electrolyte-supported cell requires the highest AF of all cell designs. A strong increase of the AF can be observed with decreasing internal reforming potential of the different producer gases, which is a function of the fraction of heating value provided by hydrocarbons.

Figure 6-21: Specie molar fractions and solid temperature distribution predicted for the electrolyte-supported cell operated with the reference gas and 1164 K cell inlet temperature

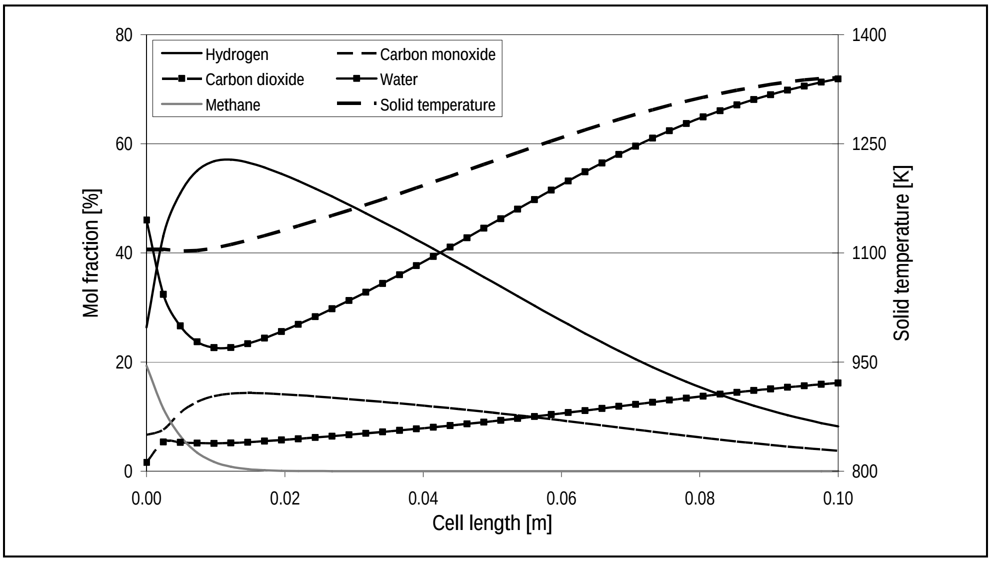

The reason for this can be found in the cell inlet temperatures. Figure 6-21 shows the species molar fractions and the solid temperature distributions predicted for the electrolyte-supported cell operated with the reference gas. The methane STR is fast at the temperatures prevalent in the electrolyte-supported cell. To prevent excessive cooling of the cell inlet region and to reach a mean cell temperature of 1223 K for the AF of the reference case, the cell inlet temperature of the fuel gas and the cooling air was set to comparably high 1164 K, which is only 59 K below the operational temperature. When operated with producer gases with lower internal reforming potential than the reference gas, the amount of heat that has to be removed from the cell increases. Consequently, to preserve a temperature gradient between the solid structure and the cooling air throughout the entire cell that is sufficient for the removal of the increased heat amount, the air flow rate and thus the AF have to be increased. Alternatively, the gas inlet temperatures can be reduced, yielding a reduction of the required AF. In this analysis the gas inlet temperatures were fixed.

The cathode-supported tubular cell features an air delivery tube in which the cooling air is heated before it flows through the cathode gas channel. In the reference case, the cooling due to the endothermic STR reactions at the fuel inlet results in considerably increased temperatures in the latter parts of the cell. The cooling air in the air delivery tube is thus effectively pre-heated and transports heat from the hot cell end region to the STR region, Figure 6-22.

Figure 6-22: Solid structure and gas temperature distributions predicted for the cathode-supported tubular cell with air delivery tube operated with the reference gas

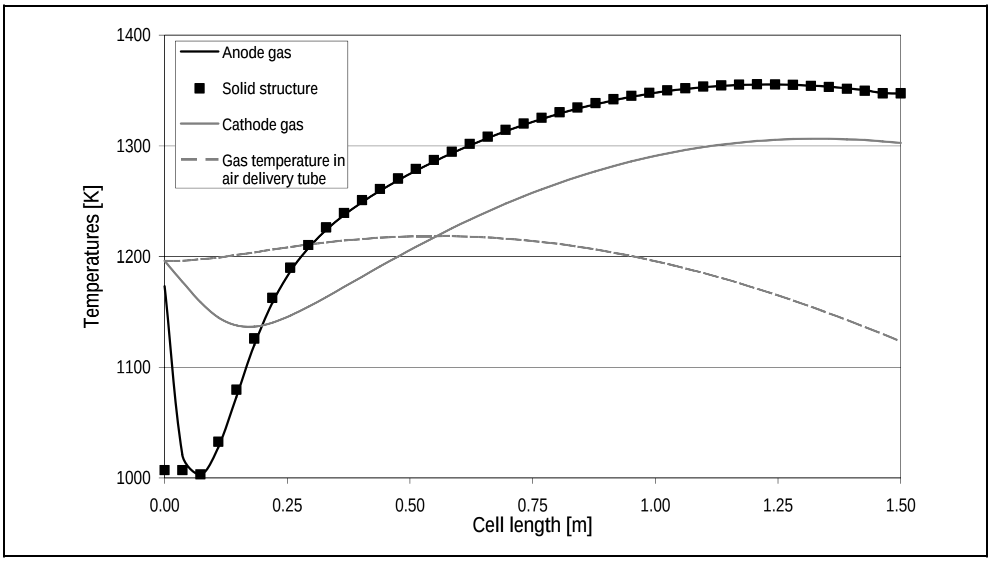

Once in the cathode gas channel, the temperature of the cooling air is lowered due to the STR reactions. This results in a considerable increase of the temperature gradient between the solid structure and the cooling air and accordingly allows a low AF.

When operated with producer gas with low internal reforming potential, the cell inlet region is not sub-cooled yielding lower temperatures in the latter parts of the cell. Figure 6-23 shows the temperature distribution predicted for the tubular cathode-supported cell operated with the producer gas of System 1, which has the lowest internal reforming potential of all investigated gases. Compared to the reference gas, the solid temperature in the later parts of the cell is approx. 50 K lower, while at the fuel inlet it is almost 200 K higher. The cooling air is gradually heated along the air delivery tube and the cathode channel and does not act as heat source for the fuel inlet region. Hence, the AF has to be increased to preserve a sufficiently high temperature gradient between the solid structure and the cooling air for the removal of the cell waste heat.

Figure 6-23: Solid structure and gas temperature distributions predicted for the cathode-supported tubular cell with air delivery tube operated with the producer gas of System 1

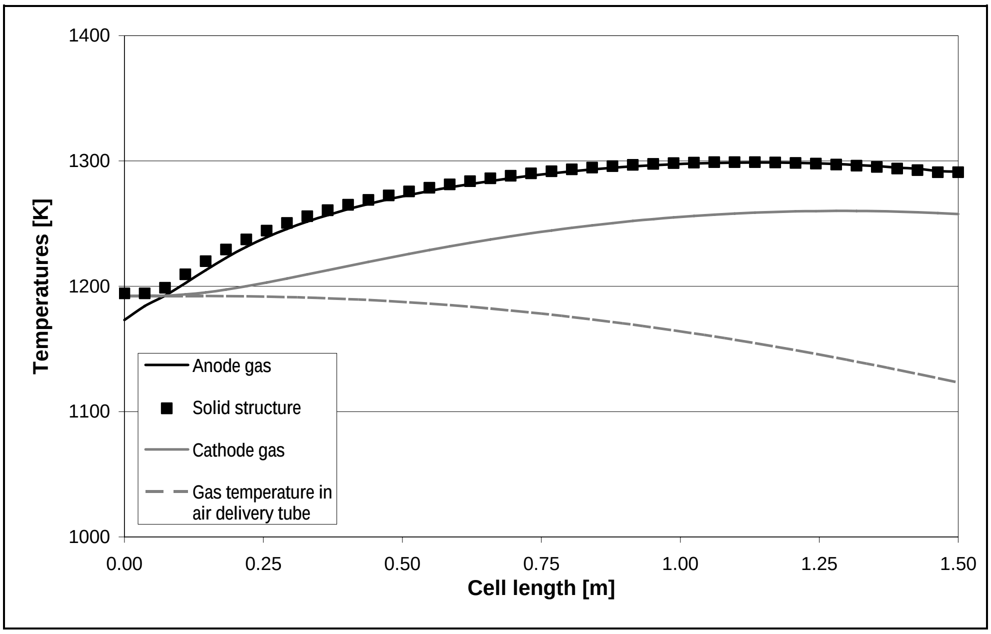

The anode-supported co-current cell is less sensitive than the electrolyte-supported cell towards the internal reforming potential of the fuel gas despite the similar geometry and flow pattern. This can be attributed to the cell inlet gas temperatures determined for the reference gas, which are 119 K lower than the mean cell temperature compared to the 59 K determined for the electrolyte-supported cell. The lower cell inlet temperatures are possible due to considerably slower STR reactions and the enhanced heat conduction through the metallic bipolar plates compared to the ceramic ones used in the electrolyte-supported cell.

Figure 6-24 shows that in the anode-supported co-current cell the STR reactions are distributed over a length roughly three times longer than in the electrolyte-supported cell, Figure 6-21. Thus, most of the heat required for the endothermic STR reactions is provided by electrochemical reactions and heat conduction through the metallic bipolar plates and needs not to be provided in form of sensible heat of the inflowing fuel gas and cooling air as is the case for the electrolyte-supported cell.

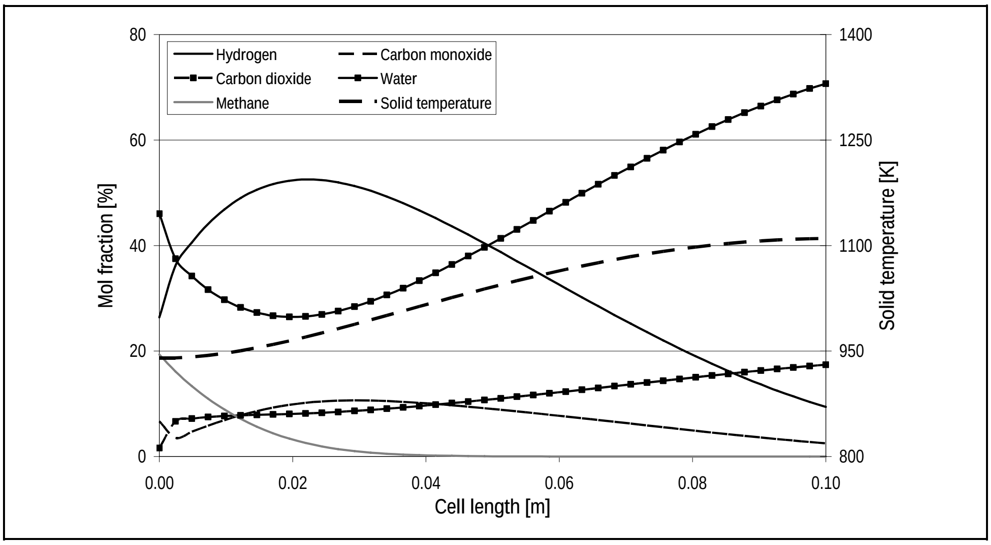

Figure 6-24: Specie molar fractions and solid temperature distribution predicted for the anode-supported co-current cell operated with the reference gas and 914 K cell inlet temperature

When operated with producer gas with lower internal reforming potential, the anode-supported co-current cell requires lower AF than the electrolyte-supported cell due to more effective cooling resulting from the lower cell inlet gas temperatures.

Among all investigated cell designs, the anode-supported counter-current cell shows the lowest sensitivity of the AF towards the internal reforming potential of the fuel gas. For gases with high internal reforming potential, the heat amount produced in electrochemical reactions at the cell inlet is high enough to cover the heat demand of the STR reactions taking place. Further, the cooling air transports heat from the latter parts of the cell to the cell inlet region where it is also consumed by the STR reactions. When operated with fuel gas featuring low internal reforming potential, the heat amount produced in the latter cell parts is reduced due to fuel depletion resulting from the fuel conversion at the cell inlet. The heat is then primarily transported from the fuel inlet region to the latter cell parts through solid heat conduction. Thus, the counter-current cell yields relatively constant AF for different fuel gases.

Overall it was found that the AF increases with decreasing internal reforming potential of the fuel gas. The sensitivity of the AF towards the internal reforming potential depends on the cell design. Co-current cells were found to be highly sensitive due to the constraint of the cell inlet gas temperatures to the values determined for the reference case. In contrast, the AF required by counter-current cells was established to be almost independent of the internal reforming potential of the fuel gas. This robustness makes this cell design appealing for the operation with producer gases, whose temperatures and compositions often fluctuate.

6.3.2.4 Maximum solid temperatures and temperature gradients

Sintering of the nickel particles that are dissolved in the YSZ matrix of Ni-YSZ anodes is one of the most important long-term degradation mechanisms of SOFCs, [96], see section 2.4.7.2. Sintering takes place at faster rates with rising temperature. This attributes special importance to the maximum solid temperature caused by different fuel gases.

Figure 6-25: Comparison of the maximum solid temperatures predicted for the investigated cell designs operated with the reference gas and different producer gases

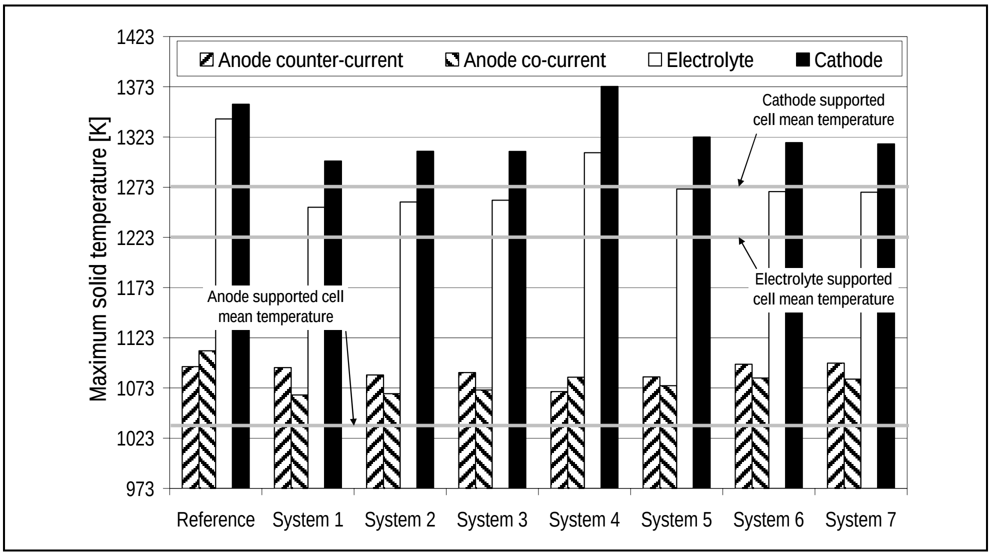

Figure 6-25 compares the maximum solid temperatures predicted for the investigated cell designs and producer gases. It can be seen that fuel gases with high internal reforming potential tend to yield high maximum solid temperatures, see "Reference" and "System 4". This can be attributed to the low solid temperatures resulting from endothermic STR reactions at the fuel inlet, which are compensated by increased solid temperatures in the latter cell parts to satisfy the accordance of the mean cell temperature with the operational temperature of the respective cell design.

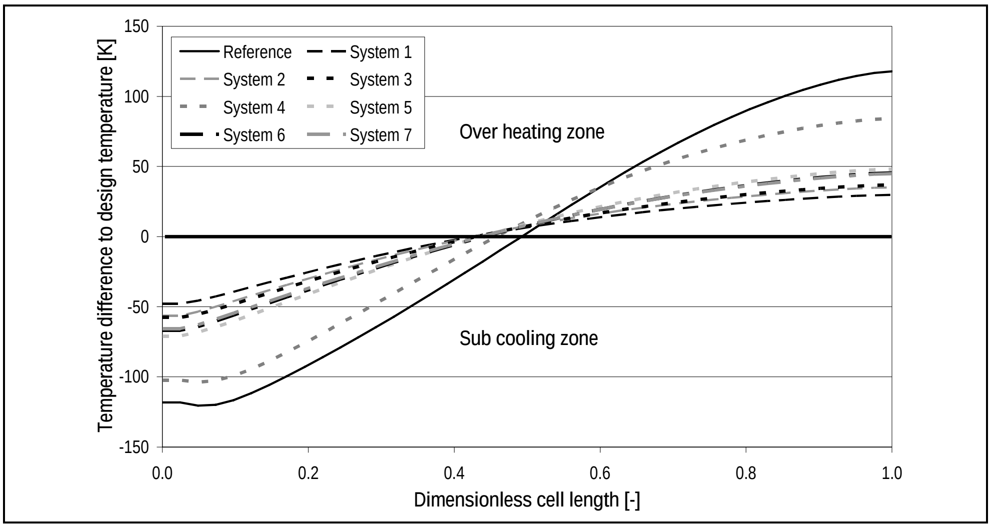

Figure 6-26: Comparison of the solid structure temperature distributions predicted for the electrolyte-supported cell operated with the reference gas and the different producer gases

Figure 6-26 gives the comparison of the solid structure temperature distributions predicted for the **electrolyte-supported** cell when operated with the reference gas and the different producer gases. Despite the producer gas of System 4 having the highest internal reforming potential of all investigated fuel gases, it does not yield the highest maximum solid temperature. The reason for this is that the fuel inlet region is less cooled compared to the reference case. For the System 4 producer gas, the anode activation losses are dominant. Consequently, the maximum current density is produced close to the fuel inlet where the reactant partial pressures are comparably high. The released heat of the electrochemical reactions is sufficient to hinder a strong cooling of the fuel inlet area. With the reference gas, the maximum current density is reached in the second half of the cell as a consequence of the dominating ohmic losses which only allow for high current densities at elevated temperatures. The cooling of the fuel inlet area is more pronounced because, compared to the heat required by the STR reactions, less heat is produced through electrochemical reactions. The more pronounced cooling results in higher maximum solid temperatures at the cell outlet.

For the **cathode-supported** cell, Figure 6-27 shows that the maximum solid temperatures are not reached at the fuel outlet but at around three quarters of the cell length. This is due to the cooling effect stemming from the fresh air flowing through the air delivery tube. The producer gas of System 4 does not yield lower solid temperatures at the fuel inlet than the reference gas despite its higher internal reforming potential. Nevertheless, the maximum solid temperature attained with the producer gas of System 4 is higher than that obtained with the reference gas. The reason for this is discussed based on Figure 6-28.

Figure 6-27: Comparison of the solid structure temperature distributions predicted for the cathode-supported cell operated with the reference gas and the different producer gases

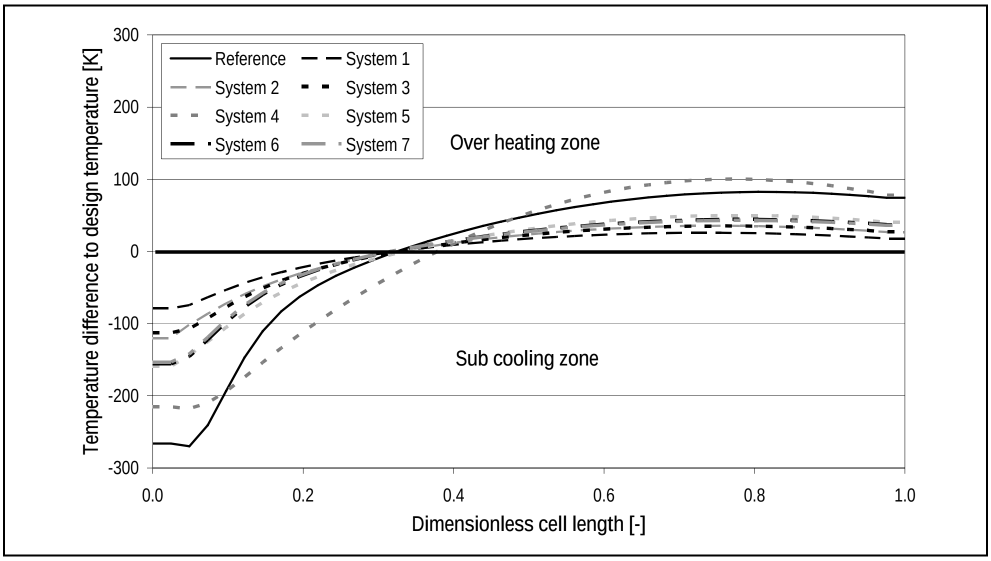

The STR reactions taking place in the fuel inlet region with the reference gas require considerably more heat than is provided by electrochemical reactions and the pre-heated cooling air. This results in reduced solid structure temperatures, which are again the reason for the ohmic limitations hindering more electrochemical reactions. The producer gas of System 4 yields current densities at the fuel inlet comparable to the reference gas, which in turn allow higher solid structure temperatures at the cell inlet. Additionally, compared to the reference gas more heat is provided to the fuel inlet by the pre-heated cooling air.

Figure 6-28: Solid structure temperature, gas temperature and current density distributions predicted for the cathode-supported tubular cell operated with the producer gas of System 4 and the reference gas

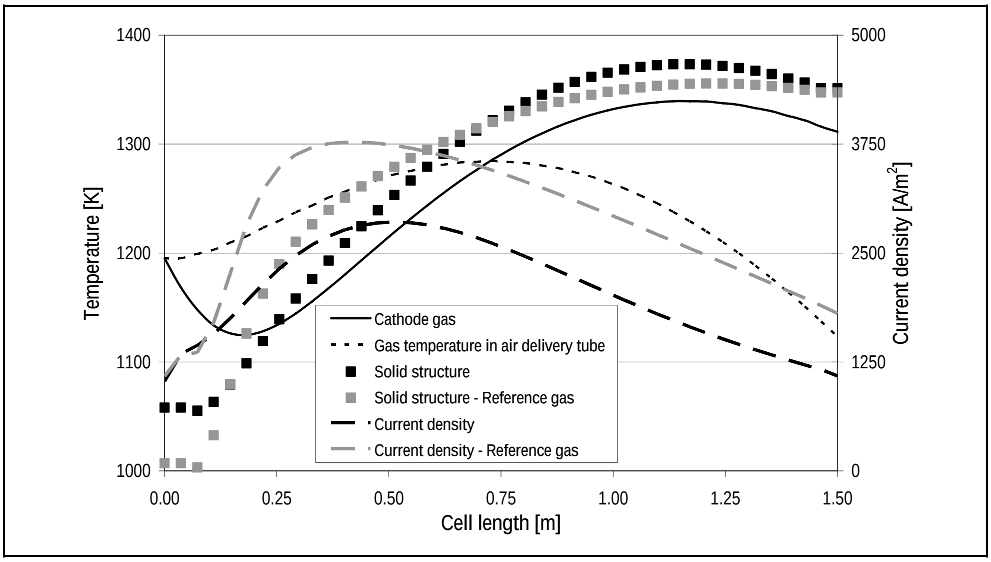

The STR reactions are complete after roughly one tenth of the cell length for both gases. For the reference gas, a very fast temperature increase occurs, caused by equally fast increasing current densities. However for the producer gas of System 4, the current densities and solid temperatures increase only slowly due to anode activation limitations resulting from the dilution of the producer gas. Compared to the reference gas, this shifts the maximum current density towards the cell end, and yields higher temperatures in the latter parts of the cell. These induce more effective cooling air pre-heating in the ADT, thus also increasing the amount of heat supplied to the fuel inlet region.

Figure 6-29: Comparison of the solid structure temperature distributions predicted for the anode-supported co-current cell operated with the reference gas and the different producer gases

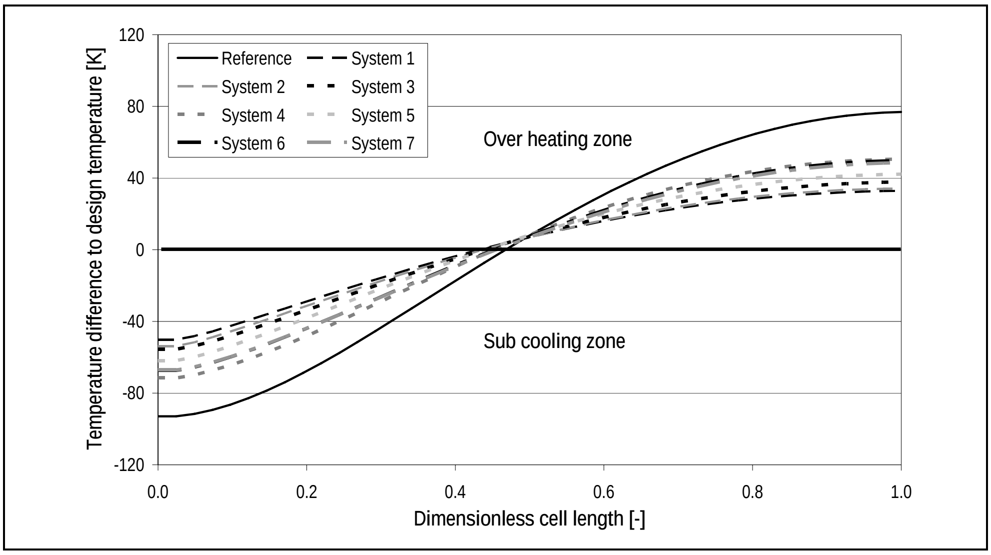

As with the electrolyte-supported cell, the maximum solid temperatures are achieved at the fuel outlet for the **anode-supported co-current** cell, Figure 6-29. The low operational temperature slows down the STR reactions considerably, which thus take place along almost half of the cell length, Figure 6-24. Consequently, the fuel inlet region is noticeably less cooled, which explains the maximum solid temperatures of 80 K over the mean cell temperature compared to 120 K found for the electrolyte-supported cell. In addition to the slower STR reactions, the temperatures in the fuel inlet region are kept high due to enhanced heat conduction through the metallic bipolar plates. Similar to the electrolyte-supported cell, the producer gas of System 4 does not yield the highest maximum solid temperature. The mechanism is the same as already discussed for the electrolyte-supported cell.

The **anode-supported counter-current** cell reaches the maximum solid temperature in the fuel inlet area, Figure 6-30. For decreasing internal reforming potential of the fuel gas, the maximum solid temperature moves towards the fuel inlet and vice versa. The magnitude of the maximum solid temperature depends on the ratio of the heat required by STR and the heat supplied by electrochemical reactions, heat conduction through the metallic bipolar plates and heat convection from the preheated cooling air which flows from the fuel outlet to the fuel inlet region.

Figure 6-30: Comparison of the solid structure temperature distributions predicted for the anode-supported counter-current cell operated with the reference gas and the different producer gases

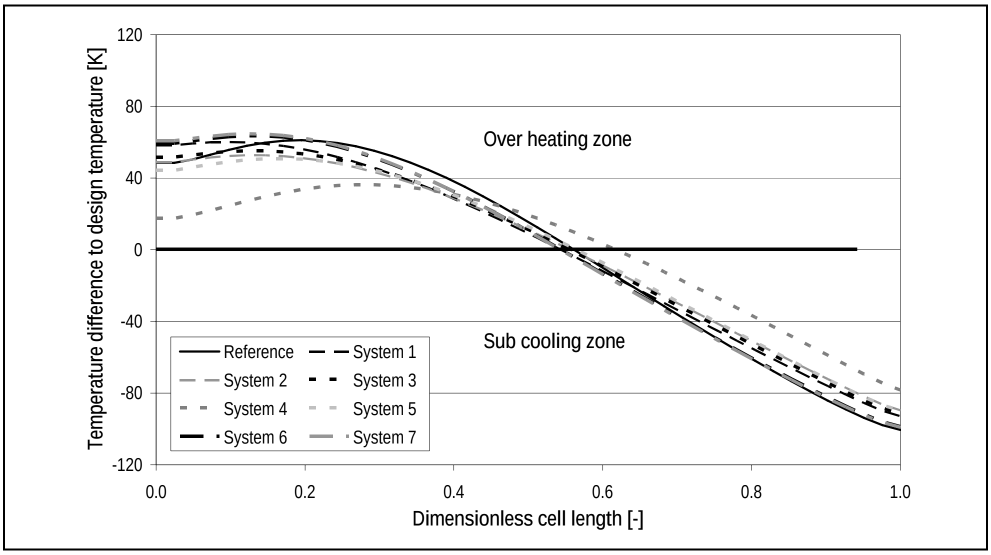

All investigated gases except the producer gas of System 4 yield maximum temperatures in the narrow range between 1084 and 1098 K. The undiluted gases of the Systems 6 and 7 and the reference gas achieve the highest maximum solid temperatures. This is because the current densities are considerably higher in the fuel inlet region compared to the other gases due to less activation polarization losses. Compared to the reference case, the current densities reached with the diluted producer gas of System 4 are considerably lower due to increased activation losses. The heat amount released in the electrochemical reactions is thus not sufficient to cover the heat demand of the STR reactions taking place close to the fuel inlet. Consequently, the predicted solid temperatures close to the fuel inlet for the System 4 producer gas are lower than those obtained with all other gases. To satisfy the accordance of the mean cell temperature and the design temperature, the lower solid temperatures at the fuel inlet are compensated with higher temperatures towards the fuel outlet region.

The role of tars in the cooling of the cell inlet area was investigated by comparing the solid temperature distribution predicted for the electrolyte-supported cell operated with the tar free producer gas of System 3 with that predicted for the raw updraft producer gas, Table 6-8. Figure 6-31 depicts that the added tar load does contribute to the cooling of the cell inlet area. With a 6 K lower solid temperature at the cell inlet, the impact of the tars is however small. Tar removal especially to prevent excessive maximum solid temperatures or thermal gradients is therefore not necessary.

Figure 6-31: Comparison of the solid structure temperature distributions predicted for the electrolyte-supported cell operated with the producer gas of System 3 and the producer gas as obtained from the updraft gasifier

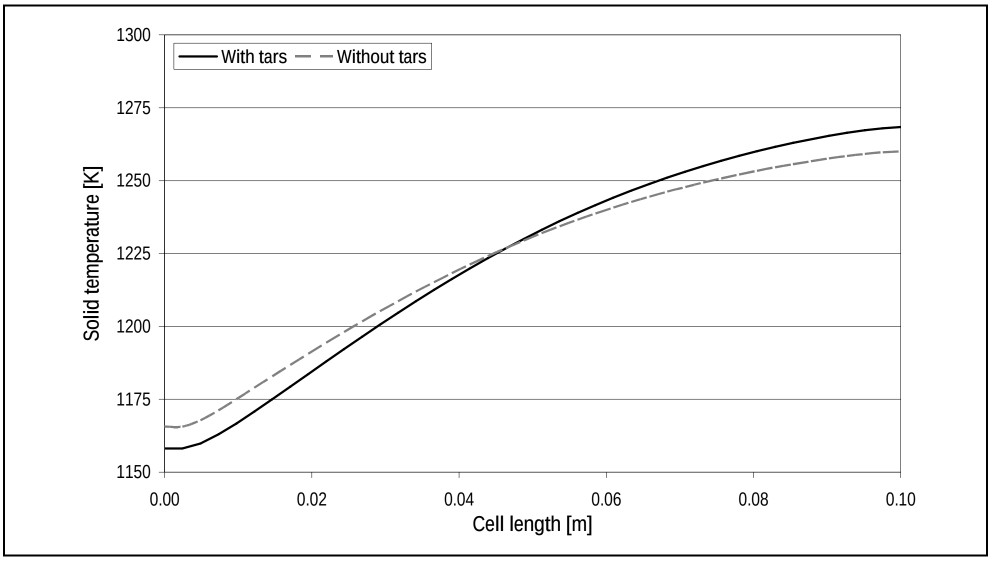

Besides the maximum solid temperatures, the maximum temperature gradients are important with respect to the safe operation of SOFCs. Figure 6-32 shows the maximum temperature gradients predicted for all investigated fuel gases and cell designs.

Figure 6-32: Comparison of the maximum temperatures gradients predicted for the four cell designs operated with the different investigated fuel gases

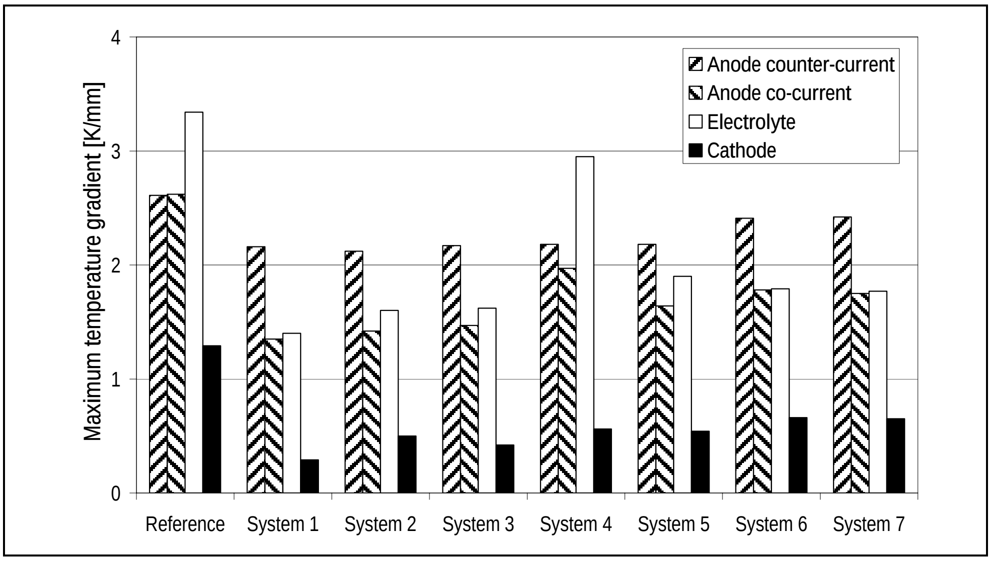

The reference gas yields the highest temperature gradients for all cell designs and gases. Similar to the maximum solid temperatures, the temperature gradients increase with increasing internal reforming potential for the co-current cell designs. The counter-current cell design yields quite similar temperature gradients for all investigated fuel gases. The reason for this is that the maximum temperature gradient is reached in the latter cell parts, where the cell is cooled by the inflowing cooling air. Thus it is almost independent of the fuel gas composition, which mainly determines the temperature level of the fuel inlet area.

In summary it can be stated that the conversion of the investigated producer gases in SOFCs should cause fewer temperature-induced degradation and failure issues than the conversion of pre-reformed natural gas. The maximum solid temperatures established for the different producer gases are considerably lower than those predicted for the reference gas. The only exception is the maximum solid temperature of the cathode-supported cell operated with the producer gas of System 4, which is 18 K higher than that of the reference case. Hence, it is possible that the cathode-supported cell degrades slightly faster when operated with System 4 producer gas compared to the reference gas. Regarding the maximum temperature gradients, all investigated gases were found less problematic than the reference gas. For co-current cells, the thermal stress usually increases with increasing internal reforming potential. Exceptions from this mostly originate from gas dilution or high water loads, which are both decisive for the importance of the anode activation losses compared to the other voltage losses and may lead to considerable changes in the current density distribution. This again affects the temperature distribution and thus the thermal stress. In contrast, counter-current cells are, as a matter of principle, comparably insensitive regarding the impact of different fuel gases on thermal stress.

6.3.3 System simulation results

As discussed above, considerable differences between the expectable mean current densities and air-to-fuel ratios were found for the investigated cell designs and producer gases. Due to the top-down approach chosen for this analysis, the mean current density of the SOFC determines the overall system size. The air-to-fuel ratio defines the size of the SOFC balance of plant equipment and the power requirements for the SOFC cooling. The latter is important for the overall net system efficiency. System simulations were performed to investigate the interactions between the different gasification processes, gas processing sections and SOFC designs.

6.3.3.1 Wood input

The stack sizes were determined for the different cell designs operated with the reference gas to yield 1 MW$_{el}$ DC output at 85 % fuel utilization and an operational voltage of 0.6 V, see Table 6-7. The basic idea behind this top-down approach is to base the analysis on a standardized SOFC stack of 1 MW$_{el}$ DC power output with methane as reference fuel. The producer gas flow rates at the cell inlet were calculated through Faraday's law, Eq. 203.

$$\dot{n}_{CG,in} = \frac{I_{tot} \cdot A_{act}}{2F \cdot UF \cdot Eq_{H_2,in}}$$

$$\begin{aligned} with\ \ Eq_{H_2,in} &= y_{H_2,in} + y_{CO,in} + 4 \cdot y_{CH_4,in} + 6 \cdot y_{C_2H_4,in} \\ &+ 18 \cdot y_{C_7H_8,in} + 4 \cdot y_{C_2H_4O_2,in} + 17 \cdot y_{C_7H_8O,in} \end{aligned} \qquad \text{Eq. 203}$$

In Eq. 203, I_{tot} stands for the mean current densities obtained for the various producer gases and cell designs, see Figure 5-1, A_{act} represents the active area of the corresponding stacks, F is the Faraday constant, UF defines the fuel utilization and $Eq_{H2,in}$ is the hydrogen equivalent coefficient of the respective producer gas.

The mass flow rates of wet wood were computed for all the investigated systems and cell designs based on the raw gas yields, see Table 6-8, to deliver the required producer gas flow rates at the cell inlet, Figure 6-33.

Figure 6-33: Mass flow of wet wood for the different B-IGFC systems and cell designs

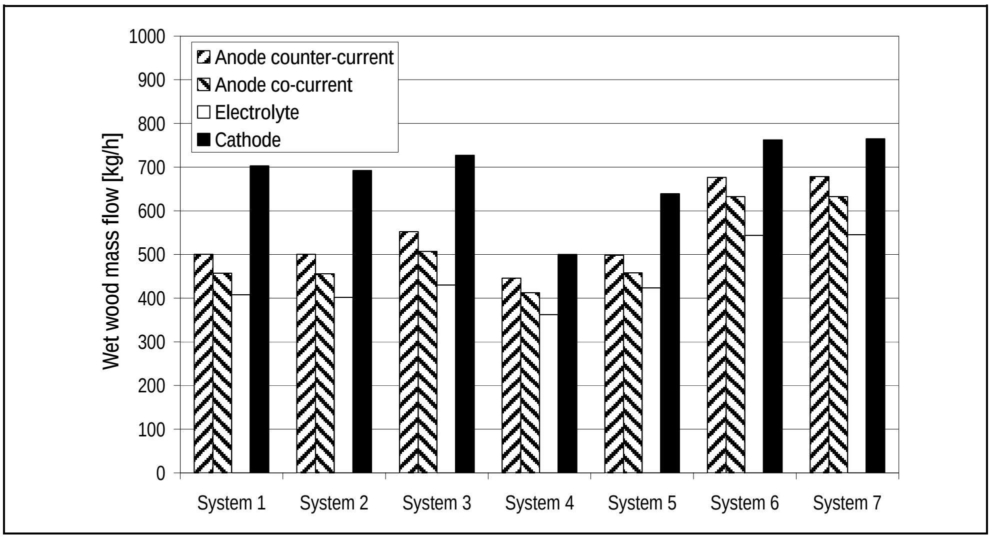

6.3.3.2 Heat integration network sizing

The system heat flux depends on the producer gas flow rate, the air-to-fuel ratio of the used SOFC and its respective cell inlet temperatures.

For all investigated systems and cell designs, no heat pinch points were found, indicating that the sensible heat of the post-combusted SOFC off-gases is sufficient to cover all heat requirements.

Based on the predefined heat exchange coefficients, see section 5.2.3, the required heat exchange areas were computed. Figure 6-34 shows that the heat exchange areas of the systems employing anode-supported cells are generally smaller than those of systems using electrolyte- or cathode-supported cells. This can be traced down to the considerably lower cell inlet temperatures of the anode-supported cells. Despite lower cell inlet temperatures, the electrolyte-supported cells require larger heat exchange areas than the cathode-supported cells. This is the consequence of the lower air-to-fuel ratios predicted for the cathode-supported cells due to the cell internal air pre-heating through the air delivery tube. Regarding the different flow patterns of the anode-supported cells, Figure 6-34 shows that the lower cell inlet temperatures and predicted air-to-fuel ratios of the counter-current cells result in considerably smaller heat exchange areas compared to co-current cells.

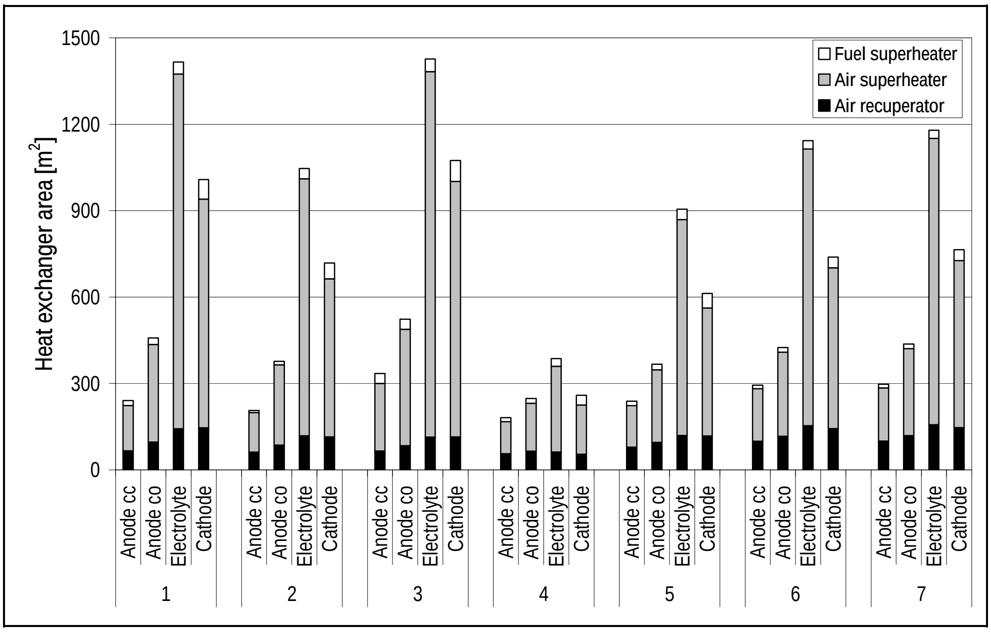

Figure 6-34: Heat exchanger areas for the different B-IGFC systems and cell designs

In conclusion it can be said that the heat exchange mechanisms in the SOFC and the cell inlet temperatures, which mainly depend on the operational temperature of the SOFC, are crucial for the required heat exchange areas. Especially the air pre-heating involves comparably large heat exchangers.

6.3.3.3 Efficiency losses

Figure 6-35 shows the efficiency loss fractions and the net AC electrical efficiencies of the investigated B-IGFC systems and cell designs based on their LHV input in form of wood.

Figure 6-35: Efficiency loss fractions and net AC electrical efficiencies for the different B-IGFC systems and cell designs

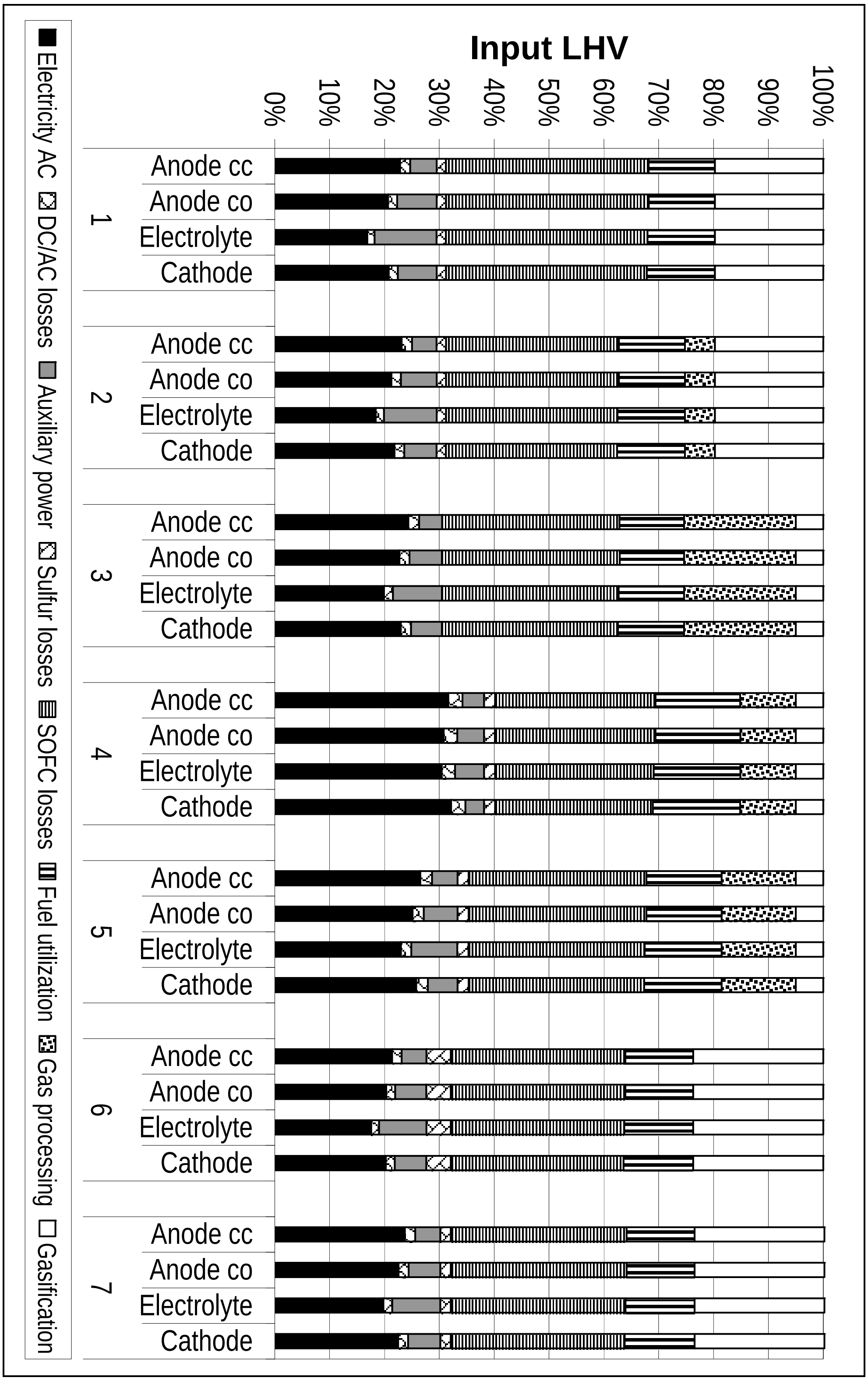

The losses attributed to the gasification processes, the fuel utilization, the electrochemical conversion and those originating from the sulfur content of the different producer gases vary for the seven investigated systems but are independent of the cell designs. The cell designs however differ in the auxiliary power requirements, which have to be covered by the power produced by the SOFC stacks. Thus, the net AC efficiencies vary for the different cell designs. Despite the fuel utilization being fixed at 85 %, the corresponding loss fractions vary for the different investigated systems. This is because the basis for the loss fractions was defined as the total thermal input to the systems, while the 85 % fuel utilization apply to the thermal input to the SOFCs. Thus, with increasing efficiency of the gasification and the gas processing, the fuel utilization losses increase in relative terms.

Downdraft gasification based B-IGFC systems: System 1 and 2

Both systems have a gross DC power efficiency of approx. 30 %. 20 % of the total thermal input is converted to heat in the downdraft gasifier.

The adiabatic methanation employed in System 2 converts approx. 5 % of the chemical energy of the producer gas into heat. This heat is however consumed again in the SOFC for the STR of the produced methane, allowing the reduction of the air-to-fuel ratio of the SOFC and lowering the auxiliary power requirements of System 2. For the co-current cell designs, the cooling effect resulting from the adiabatic methanation results in approx. 2 % lower auxiliary power requirements, thus increasing the net AC efficiency. For the counter-current anode-supported cell, which is comparably insensitive towards the producer gas composition regarding the air-to-fuel ratio, the adiabatic methanation yields only a negligible net AC efficiency increase.

The sulfur induced losses amount to approx. 2 % for both systems due to similar total sulfur concentrations in both producer gases. The adiabatic methanation of System 2 in fact converts the organic sulfur species to hydrogen sulfide but also increases the water content of the producer gas. Consequently, the hydrogen sulfide concentration leaving the zinc oxide trap bed in System 2 is almost equal to the total sulfur concentration in the producer gas of System 1, where the organic sulfur species were not removed.

The auxiliary power losses amount to a minimum of 5 % for the anode-supported counter-current cell and to a maximum of almost 12 % for the electrolyte-supported cell, the cathode-supported cell being in between.

The losses attributed to the conversion of the direct current obtained from the SOFCs to alternating current suitable for feed-in to the electrical grid account for 1.5 to 2 % of the thermal input, depending on the net DC electricity efficiency of the system.

The anode-supported counter-current cell achieves the highest net AC efficiencies with 22.8 % and 23.1 % for System 1 and 2, respectively.

Updraft gasification based B-IGFC systems: System 3, 4 and 5

In all three systems, the gasifier converts 95 % of the thermal input into the chemical energy of the producer gas and the remainder into low-temperature heat. By entirely removing the tar load in System 3, approx. 20 % of the thermal input is lost yielding an effective cold gas efficiency of approx. 75 %.

In System 4, 10 % of the LHV of the producer gas are converted to heat in the adiabatic methanation which is, similar to System 2, consumed again in the SOFC for the STR of the produced methane. Compared to System 2, the amount of methane produced in the adiabatic methanation is considerably higher due to the low temperature of the raw producer gas at the methanation reactor inlet. This results in a heavy reduction of the required air-to-fuel ratios due to intensive chemical cooling of the SOFCs. Further, instead of removing the tar load, their chemical energy is partially used for the fuel gas heat up in the adiabatic methanation and partially converted the chemical energy bound in methane. The steam reforming of the produced methane in the SOFC can thus be seen as relocation of the final gasification reactions into the SOFC, directly using the SOFC waste heat. Such methanation-steam reforming based processes to transport heat, referred to as "*Chemical heat pipes*", were intensively studied in the nineteen eighties, [225].

The catalytic partial oxidation (CPO) employed in System 5 converts approx. 45 % of the LHV of the tar load to high-temperature heat. This heat is used for the conversion of the remaining tar load to hydrogen, carbon monoxide but also methane due to comparably low process temperatures of around 500 °C. Especially for the co-current cell designs, the latter has a positive effect on the required air-to-fuel ratios.

For System 3, it was assumed that organic sulfur species are entirely removed from the producer gas in the employed cold gas cleaning system. The remaining H_2S is adsorbed in the ZnO trap bed to levels below 0.1 ppmV. Consequently, the sulfur-induced losses of System 3 are negligible. In contrast, the sulfur induced losses amount to approx. 2 %

for Systems 4 and 5. Similar to System 2, the water produced during the methanation in System 4 seriously obstructs the attainment of sulfur concentrations below 2 ppmV. In System 5, total sulfur concentrations around 2 ppmV are reached despite remaining parts of the organic sulfur species in the producer gas. The reason for this is the lower water content of the producer gas after the CPO which allows achieving H_2S concentrations in the zinc oxide trap bed that are low enough to compensate the organic sulfur species.

The auxiliary power losses resulting from the power consumption of fans and blowers in System 4 are around 4 to 5 % and therewith the lowest in this analysis. This is because the corresponding producer gas has the highest internal reforming potential of all investigated gases and therefore requires the lowest air-to-fuel ratios. Due to the comparably high net DC efficiencies, the DC/AC conversion losses are in the range of 2 to 3 % and thus are slightly higher than in the Systems 1, 2, 6 and 7.

Similar to systems 1 and 2, the anode-supported counter-current cell yields the highest net AC efficiencies in the Systems 3 and 5 with 24.3 % and 26.5 %, respectively. Regarding System 4, the cathode-supported cell designs benefits from the cooling air cool down at the fuel inlet which allows a lower air-to-fuel ratio than that of the anode-supported counter-current cell. The correspondingly lower auxiliary power losses lead to a net AC efficiency of 32.1 % compared to 31.7 % reached by the anode-supported counter-current cell. Overall it can be stated that System 4 outperforms all other investigated systems because the combination of updraft gasification and adiabatic methanation yields a producer gas with high internal reforming potential with a comparably high cold gas efficiency of approx. 85 %.

Fluidized bed steam gasification based systems: System 6 and 7

In the fluidized bed steam gasification process, 76 % of the chemical energy of the feedstock is converted to chemical energy of the producer gas and the remainder into high-temperature heat.

In System 7, the tar load and the hydrocarbon content are slightly decreased over the metal oxide bed used for the degradation of organic sulfur species. The loss of internal reforming potential is however compensated by a noticeable amount of carbon monoxide that is shifted to hydrogen and carbon dioxide. If this shift occurs cell internally, the released heat of reaction adds to the SOFC waste heat thus lowering the conversion efficiency.

The sulfur induced losses of System 6 are 4.5 % compared with 1.9 % of System 7. This shows that the neglect of the removal of almost 5 ppmV organic sulfur species in the system design may result in considerable overestimation of the system efficiency. Compared to the Systems 1 to 5, the excessive water content of the fluidized bed producer gases hinders the desulfurization in the zinc oxide trap beds more and yields approx. 0.5 ppmV higher sulfur concentrations in the producer gas at the cell inlet. A possibility to overcome this would be a reduction in the amount of added water and thus a decrease of the steam-to-carbon ratio. This however might cause carbon deposition problems.

The auxiliary power losses for the different cell types are almost similar for both systems in the range between 4.5 to almost 9 %. The DC/AC losses amount to roughly 2 %.

System 7 with the anode-supported counter-current cell reaches a net AC efficiency of 23.7 %, which is slightly higher than the efficiencies reached by the downdraft gasification based systems and close to the efficiency of System 3, where 20 % of the thermal input was removed from the producer gas in form of tars.

In sum it can be stated that the cold gas efficiency of the gasification process and the auxiliary power requirements of the SOFC resulting from the SOFC cooling are crucial for the overall system efficiency. In both cases, the downdraft gasification process is not favorable. The air-blown updraft gasification in contrast was found very promising for the application in B-IGFC systems due to the high cold gas efficiency and typically high hydrocarbon concentration in the producer gas. The latter allow for the relocation of the final gasification reactions into the SOFC using waste heat and thus lowering the cooling requirements and attributed auxiliary power requirements. The fluidized bed steam gasification yields producer gas with high hydrocarbon content too, however with lower cold gas efficiencies. The corresponding losses can barely be compensated by the subsequent producer gas conversion to electricity.

6.3.3.4 Power and useful heat output

The amount of heat that can be recovered from the system flue gases was determined through the generalized heat integration network discussed in section 5.2.3. Figure 6-36 shows that it strongly varies between the various cell designs. The electrolyte-supported cell generally yields the lowest amount of useful heat. This is because the sensible heat below 200 °C of the system flue gases is not used. The heat loss hence grows with increasing flue gas flow rate, which directly correlates with the air-to-fuel ratio. The air-to-fuel ratio thus not only considerably affects the net AC efficiency through the auxiliary power requirements but also the thermal efficiency.

System 3 yields the smallest amount of useful heat because it was assumed that the entire heating value of the tar load removed in the cold gas cleaning system is required for the treatment of the wash water.

Figure 6-36:
Net AC electrical efficiencies and thermal efficiencies for the different B-IGFC systems and cell designs

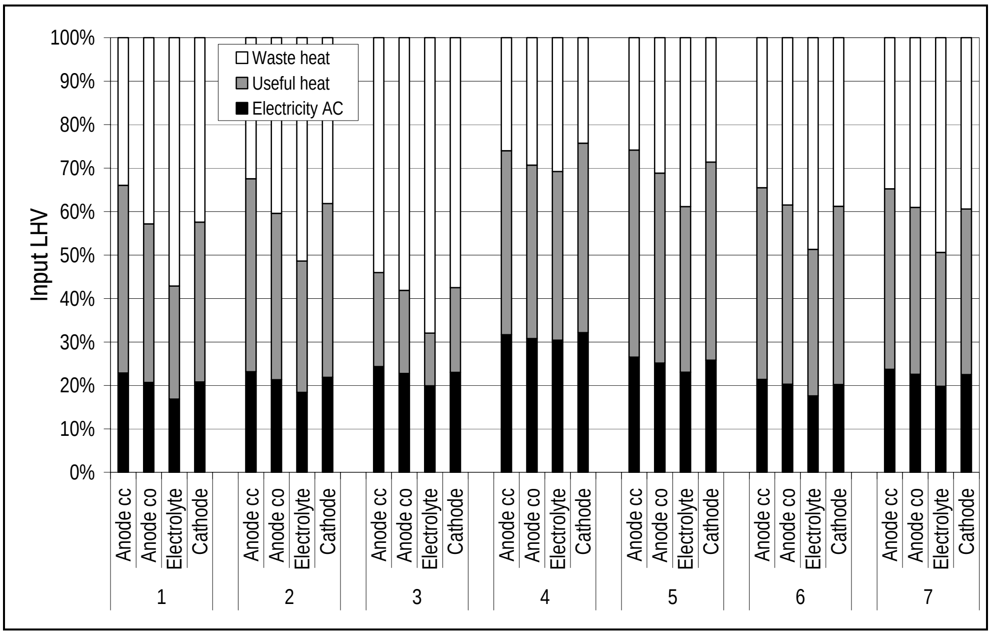

With 75.7 %, System 4 with the cathode-supported cell yields the highest total system efficiency in this analysis. The corresponding thermal efficiency is 43.6 %. The useful heat may be converted to additional electricity through a bottoming cycle, thus covering the auxiliary power requirements of the cooling air blower. Assuming a moderate electrical efficiency of 12 % for an organic rankine cycle operated at 200 °C, [163], the net AC system efficiency of System 4 could be increased to 37.3 %, while also increasing the system power output by 16 %. This is sufficient to be superior to state-of-the-art biomass gasification based gas engine power plants featuring electrical efficiencies around 25 %, [226, 227].

Figure 6-37 depicts the net AC electrical power output of the investigated B-IGFC systems and cell designs. The electrolyte-supported cell features the lowest power outputs in all investigated systems. This results from the obtained low current densities when operated with producer gas and the comparably small active area, which is a consequence of the reference gas based top-down approach chosen for this analysis. The auxiliary power requirements are high due to the repeatedly discussed high air-to-fuel ratios (AF). The cathode-supported cell in contrast yields the highest power outputs, due to the high mean current densities achieved with the producer gases and the moderate AF.

Figure 6-37:
Net AC electrical power output of the different B-IGFC systems and cell design

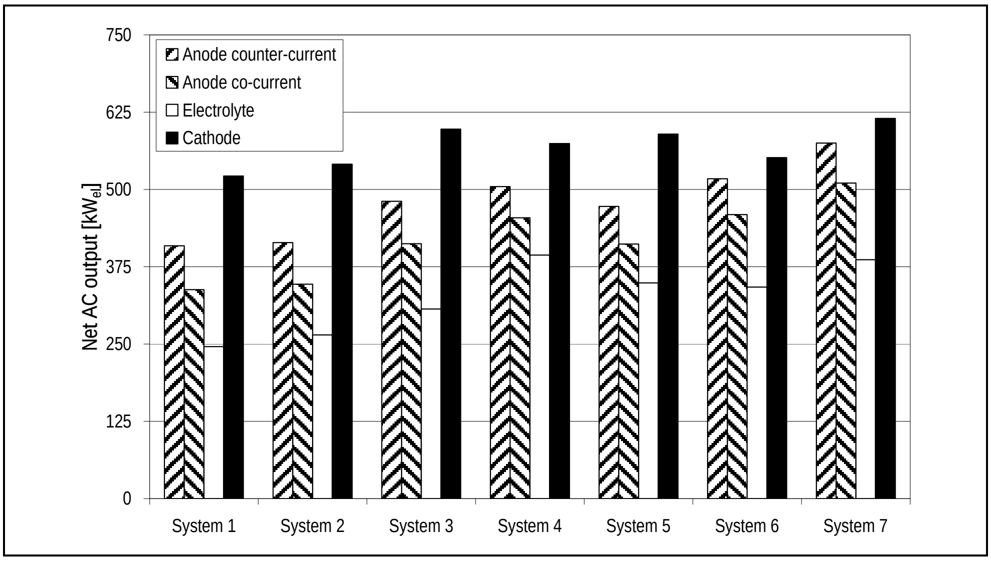

Compared to the power output of the NG reference system of 820 kW net AC, the operation with producer gases results in a power output decrease of a minimum 25 % for System 7 with the cathode-supported cell and a maximum 70 % for System 1 with the electrolyte-supported cell.

6.4 Economic evaluation

The system efficiencies are related to the total investments costs (TI) to asses the cost-effectiveness of the investigated B-IGFC systems, see section 5.4. The latter is represented by the power production costs. The TI linearly depend on the direct plant costs, which are estimated through rough sizing of all major equipment pieces according to the mass and energy fluxes determined in the system simulations. Note that the costs were estimated using the same cost functions for all systems, hence relative comparisons are considered valid. The absolute cost values however should be understood as order of magnitude estimates.

6.4.1 Direct plant cost estimates

Figure 6-38 shows the direct plant cost estimates structured according to the system modules discussed in section 5.4.2 for the different

B-IGFC systems and cell designs. The **wood handling module** is a considerable cost factor in downdraft and fluidized bed steam gasification based systems. This can largely be attributed to the wood drying, the costs of which strongly increase with decreasing air-to-fuel ratios and flue gas temperatures.

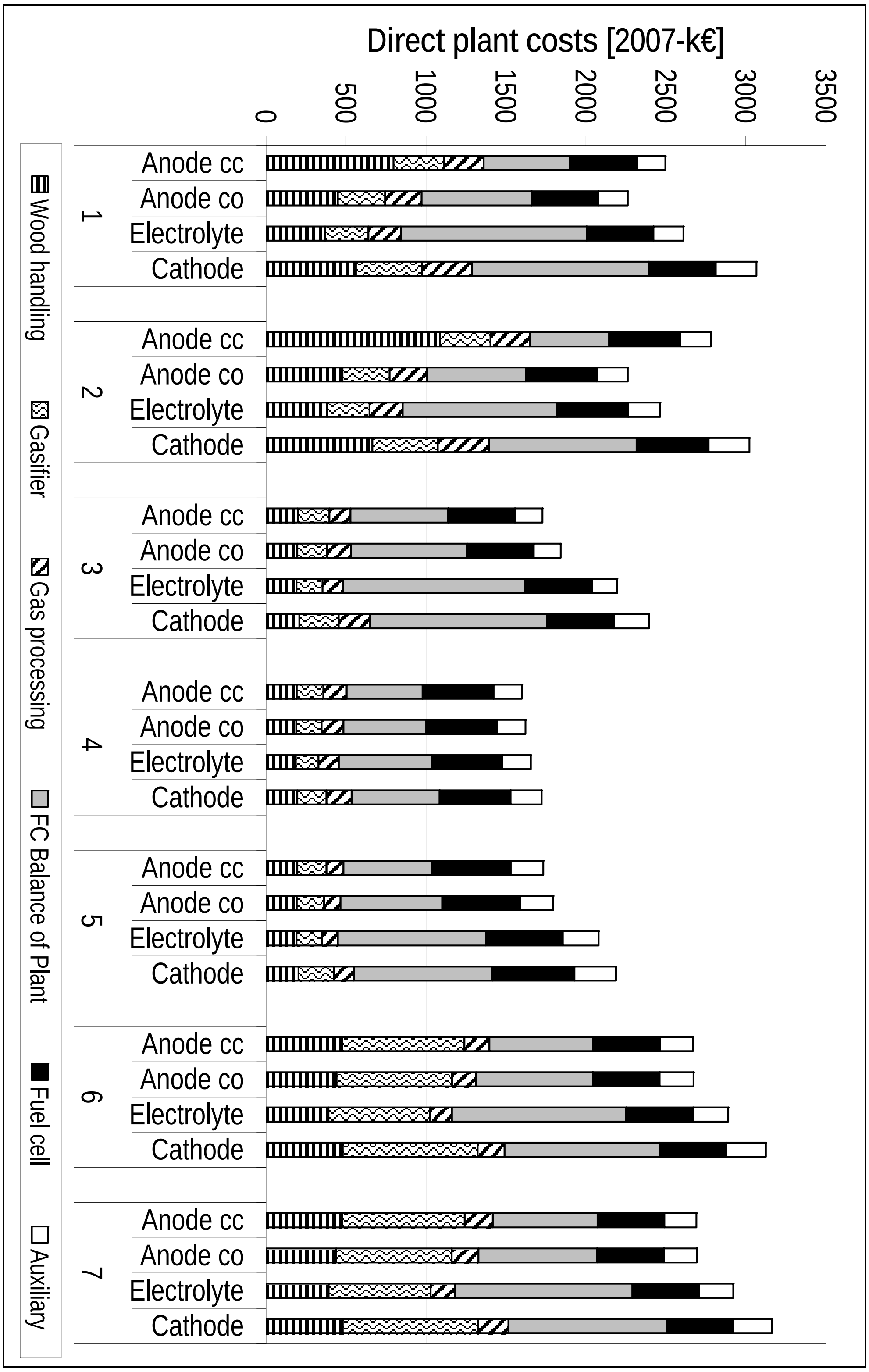

Figure 6-38: Direct plant cost estimates structured according to the system modules discussed in section 5.4.2 for the different B-IGFC systems and cell designs

Systems with anode-supported counter-current cells yield the highest costs for wood drying, responsible for around one third of the direct plant cost. Due to their high air-to-fuel ratios, electrolyte-supported cells have clear cost advantages with respect to wood drying. Reducing the costs for the wood drying is not possible in downdraft gasification based systems due to the stringent feed humidity requirements of the gasification process. In contrast, the fluidized bed steam gasification can operate on feedstock with higher humidity than that assumed in this analysis. Thus, the cost for wood drying in System 6 and 7 could be reduced. The updraft gasification does not require wood drying and has thus considerable cost advantages regarding the wood handling module.

The **gasification module** comprises the gasification reactor and all additional equipment required for its operation. In fixed bed gasification based systems, the costs for the gasification reactors are rather small, contributing around 10 % to the total system costs. Downdraft gasifiers are slightly more expensive than updraft gasifiers due to their more complex layout. It is difficult to further reduce the gasifier cost for the fixed bed gasification based systems. In fluidized bed steam gasification based systems, the gasification reactor costs amount to approx. one fourth of the total system cost. As discussed in section 5.4.2, the investigated reactor concept uses heat pipes for the heat transfer between a combustion chamber and a gasification chamber. The heat pipes and the combustion chamber each account for approx. 25 % of the reactor costs, the remainder is attributed to the reforming chamber and auxiliary equipment required for e.g. steam generation, combustion air preheating, etc. The costs incurred by the combustion chamber could be saved by extracting the required heat directly from the SOFCs, thereby also lowering the required air-to-fuel ratios and the cost attributed to the fuel cell balance of plant equipment, [228]. The cost reduction potential is considerable, however this option was not further investigated in this work as the required SOFCs are presently not available and the costs of these customized SOFCs are hence unknown.

The **gas processing module** includes all equipment pieces required for the gas cleaning and conditioning, constituting around 5 to 15 % of the total plant costs. In downdraft gasification based systems, the steam generator required for the gas humidification is the most important cost factor regarding the gas processing, accounting for approximately 50 % of this cost module. In System 3, where most of the water initially present in the producer gas originating from the updraft gasification process is removed in the employed cold gas cleaning system, the steam generator required for the re-humidification of the producer gas accounts for almost 80 % of the gas processing module costs. This is because no ceramic particle filter unit and zinc oxide trap bed are employed. The fluidized bed systems have the advantage that the producer gas can be humidified without the need for a steam generator by using the sensible heat of the producer gas for the evaporation of the additional water. Consequently, the gas processing module of these systems is comparatively inexpensive. The costs of the gas processing could be effectively reduced in fluidized bed and updraft systems by increasing the wood humidity at the gasifier inlet. This would not only reduce the cost incurred by the gas humidification but also the cost of wood drying as mentioned above.

The **fuel cell balance of plant module** (FC-BoP) includes the heat exchangers required to adjust the producer gas and the cooling air temperature to the predefined cell inlet values, the cooling air blower, the DC/AC power converter and the anode off-gas combustor. Except for the downdraft and fluidized bed steam gasification based systems employing anode-supported counter-current cells, the FC-BoP module is the dominant cost factor in all the investigated systems, accounting for 25 to 50 % of the total system costs. In the systems employing electrolyte- or cathode-supported cells, the FC-BoP costs are generally higher than in the corresponding systems based on anode-supported cells. This is due to the considerably lower cell inlet temperatures and air-to-fuel ratios required by the anode-supported cells.

The **fuel cell module** (FC) accounts for one eights to a quarter of the total system cost. The fuel cell costs are equal for all the systems due to the top-down approach chosen for this analysis, which considers the FC size as fixed. Note that the costs entailed by the catalysts employed in systems 2, 4 and 5 were allocated to the FC module. The absolute module cost in these systems can thus be increased by up to 25 % compared to systems 1, 3, 6 and 7.

The **auxiliary equipment module** accounts for 7 to 12 % of the total system costs. Half of these costs can be attributed to the heat exchanger required to recover useful heat from the system flue gases.

The direct plant costs are related to the net AC power output for a better comparability of the systems. Figure 6-39 shows the specific direct plant costs computed for the investigated B-IGFC systems and cell designs.

Figure 6-39: Specific direct plant costs for the different B-IGFC systems and cell designs

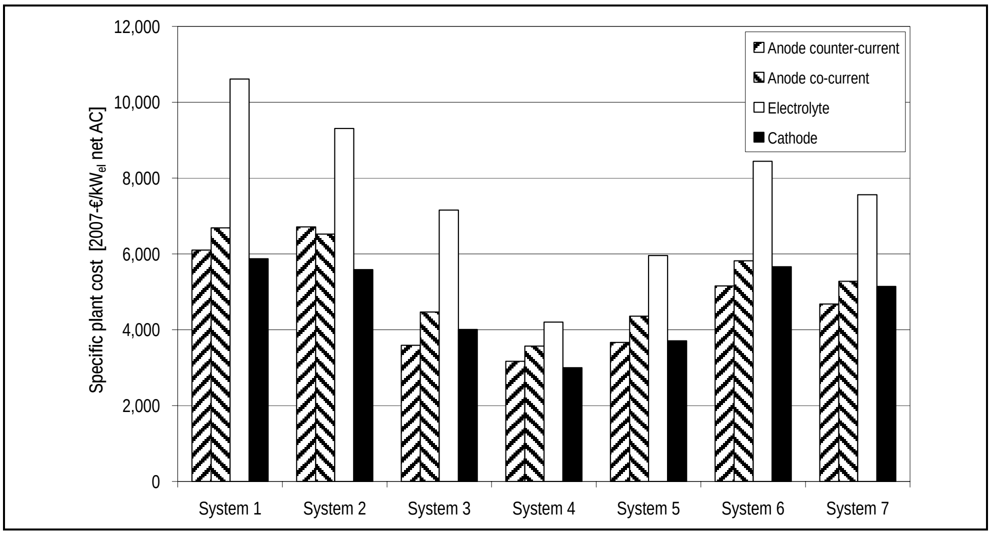

The downdraft gasification based systems yield comparably high specific costs in the range between 5587 and 10612 €/kW$_{el}$ net AC resulting from their low power output and high system costs. The updraft gasification based systems achieve the lowest specific plant costs, which are between 2999 and 7156 €/kW$_{el}$ net AC. This can be attributed to their satisfying power output and low system costs, which arise not only from the low feed humidity requirements of the updraft gasification process and the simple make of the corresponding reactors but also from the low producer gas humidification requirements. The fluidized bed systems are expensive but the undiluted producer gases allow relatively high power outputs, which in sum leads to specific plant cost between those of the downdraft gasification based systems and of the updraft gasification based systems in the range of 4679 to 8445 €/kW$_{el}$ net AC. With 2999 €/kW$_{el}$ net AC, System 4 with the cathode-supported cell yields the lowest specific plant costs of all the investigated systems.

6.4.2 Power production costs

The cost-effectiveness of the investigated B-IGFC systems is determined by relating the total investments for the investigated systems to their net AC system efficiencies and power outputs. As discussed in section 5.4.5, the time dependent worth of money is also taken into account by assuming a set planning horizon for which all expenses and revenues are entered in a corresponding balance sheet.

Figure 6-40 shows the power production cost (PPC) fractions arising from the depreciation of the different system modules, the feedstock purchasing, the amortization of the indirect plant costs and the operation and maintenance expenses. Further, the revenues from heat sales per sold kWh_{el} net AC are depicted assuming 100 % heat sales. It can be seen that for each of the systems and cell designs the sum of the PPCs resulting from the equipment depreciation (D-costs) equals the capital costs plus the costs for the operation and maintenance (C-costs).

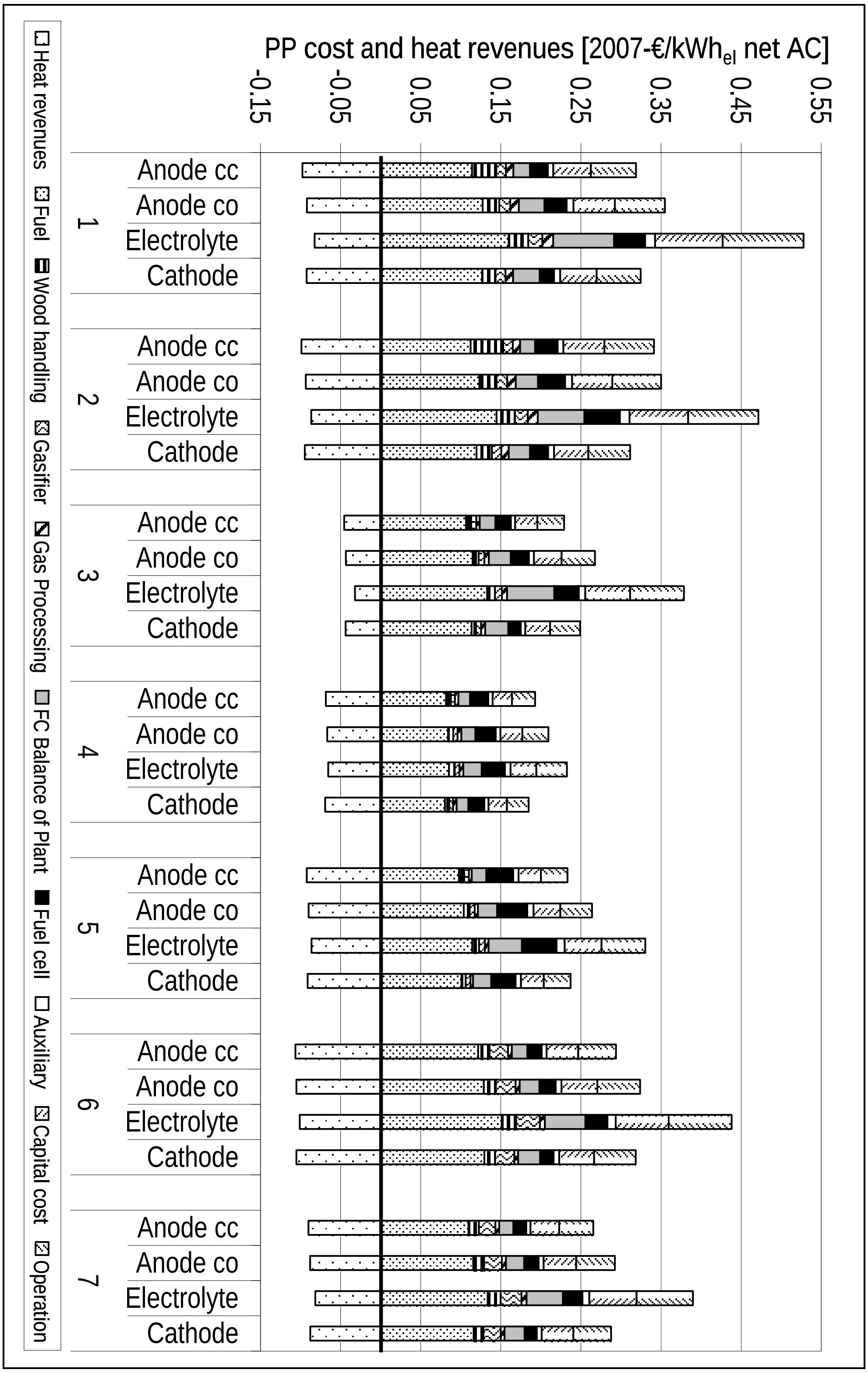

Figure 6-40: Power production costs structured according to the system modules discussed in section 5.4.2 including fuel, capital and operational costs as well as heat revenues for the different B-IGFC systems and cell designs

In Systems 1 and 2, the fuel costs (F-costs), the D-costs and the C-costs each contribute to approx. one third to the overall PPCs. In all other systems, the F-costs account for approx. 35 to 45 % of the PPCs. This is mainly due to the lower specific plant costs. Regarding the D-costs, the most important cost drivers are already discussed above. However, it is worthwhile noting that the fuel cell stack accounts for merely 5 to 15 % of the overall PPCs.

In the systems 1, 3, 5, 6 and 7, the anode-supported counter-current cell design yields the lowest PPCs compared to all other cell designs. System 1 is the only system, where the lowest PPCs are reached by a cell design that does not also yield the lowest specific plant costs. Compared to the cathode-supported cell design, the 8 % (relative) efficiency advantage of the anode-supported counter-current cell design is just sufficient to compensate 4 % higher specific plant costs. The counter example is System 2, where the cathode-supported cell design yields lower PPCs than the anode-supported counter-current cell design despite the latter featuring an almost 10 % (relative) higher net AC system efficiency. The reason for this can be found in the 20 % lower specific plant costs resulting from the higher current density produced by the cathode-supported cell due to high catalyst activity in dilute gases.

This clearly shows that the PPCs are more sensitive towards the specific plant costs than towards the system efficiency. The latter is effective only on the F-cost share, which accounts for moderate 30 to 45 % of the PPCs even though wood is an expensive feedstock. Hence, efficiency maximization is limited regarding the reduction of the PPCs. In contrast, power output increase and reduction of specific plant costs through optimization of the SOFC operational parameters is effective for 55 to 70 % of the PPCs. This emphasizes once more the importance of the power output of the cell, which mainly depends on the anode catalyst activity especially for the operation with dilute producer gases.

Figure 6-41 depicts the net power production costs assuming that the entire heat produced is sold. The heat revenues are sufficient to cover most of the F-costs and are therefore crucial for the market competitiveness of B-IGFC systems. Given the electricity price currently paid in Germany for electricity produced from biomass using highly advanced technologies (gray marked area), [229], the only competitive systems investigated in this analysis are the Systems 4 and 5. In System 4, the cathode-supported cell designs yields the lowest PPCs with 0.1154 €/kWh$_{el}$ net AC. In System 5, the anode-supported counter-current cell design is superior to the cathode-supported cell design with a PPC of 0.1409 €/kWh$_{el}$ net AC. Under subsidization, these systems may be already financially viable.

Figure 6-41: Effective power production costs assuming 100 % heat sales for the different B-IGFC systems and cell designs

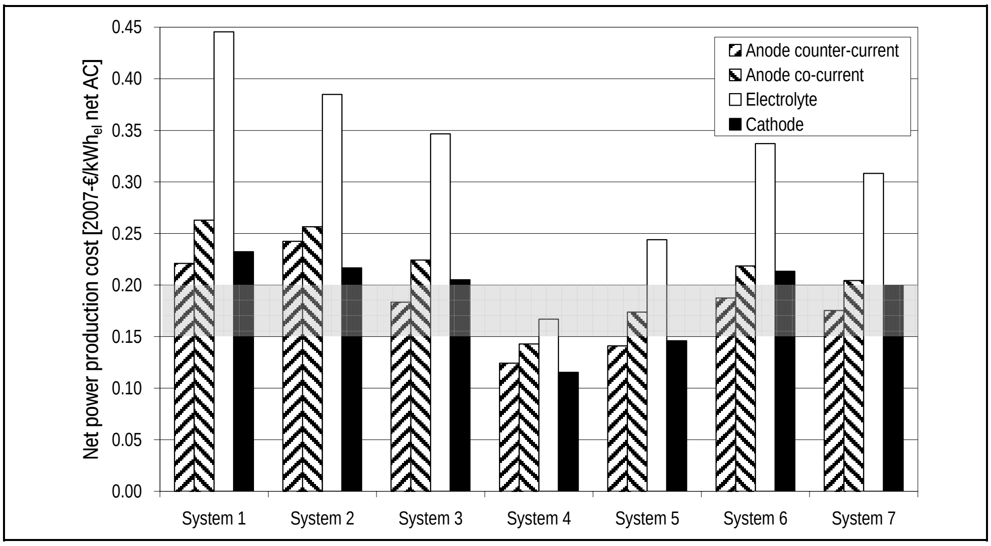

6.4.3 Sensitivity analysis

The impact of the most important assumptions in the economic analysis was assessed through the sensitivity analysis presented below. The base case for the sensitivity analysis is System 4 with the cathode-supported cell design.

6.4.3.1 Economic model factors

The economic model involves a variety of parameters whereby only a limited number can be actively influenced by engineers. These parameters include the plant availability and the lifetime of employed catalysts.

Figure 6-42: Sensitivity of the power production costs towards important parameters of the economic model

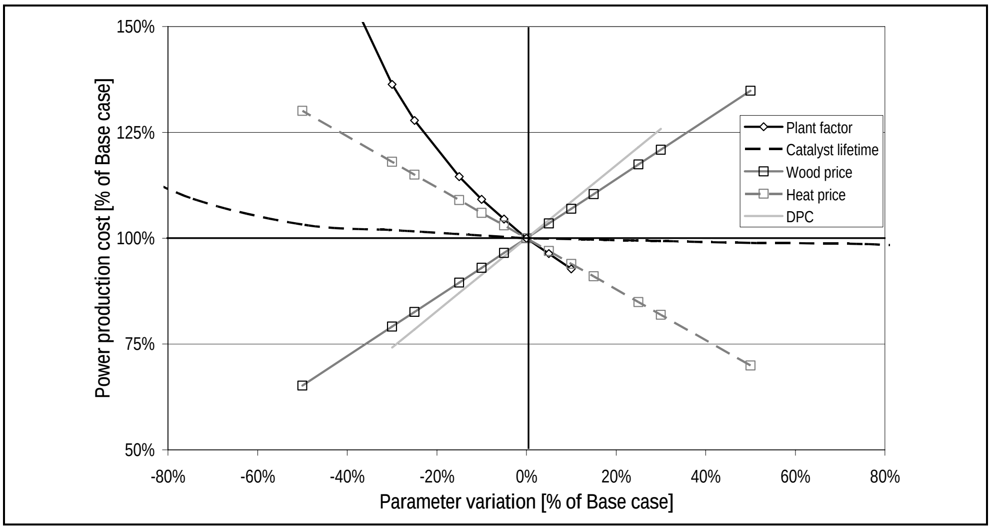

Figure 6-42 shows that the plant availability, represented by the plant factor (PF), has considerable PPC reduction potential. Increasing the PF by 10 % yields 7 % lower PPCs with values around 0.107 €/kWh$_{el}$ net AC. Reduced plant availability leads to fast increasing PPCs. With a PF of 63 %, which is 26 % (relative) lower than the base case value, the PPCs are already increased by 30 % and reach the lower limiting price of 0.15 €/kWh$_{el}$ net AC for biomass electricity from highly advanced technologies in Germany. A further reduction of the PF to approx. 45 %, which corresponds to 52 % (relative) of the base case, yields an increase of the PPCs by 73 % to 0.2 €/kWh$_{el}$ net AC, which is the upper limiting electricity price according to [229]. This shows that the plant availability plays a crucial role for the competitiveness of the B-IGFC technology due to the high involved capital costs.

Figure 6-42 further depicts that the PPCs increase fast with catalyst lifetimes below 50 % of the base case. This indicates that the catalyst development should focus on the achievement of catalyst lifetimes around one to two years. Further improvements regarding the lifetime of the catalysts employed in the adiabatic methanation and the catalytic partial oxidation reactors in the investigated systems 2, 4 and 5, have almost no impact on the PPCs.

The corresponding parameters in the economic model were varied to evaluate the general importance of the plant cost estimate accuracy, the wood price and the heat price or demand, respectively. The wood price and the heat price or demand, respectively, are equally sensitive and considerably affect the PPCs. However, the PPCs stay below the lower limiting electricity price of 0.15 €/kWh$_{el}$ net AC despite either a heat price or demand decrease or a wood price increase by 40 % compared to the base case. The latter shows that a wood price of 117 € per dry ton of wood would still allow profitable operation of System 4 with the cathode-supported cell design. The same applies, when assuming 30 % higher direct plant costs, which corresponds to the maximum error expected for the plant cost estimates.

6.4.3.2 SOFC degradation and operational voltage

The cell degradation causes a gradual reduction of the power output of the investigated B-IGFC systems and is thus a cost-effective factor. Figure 6-43 shows that several stack exchanges may be necessary during the planning horizon to reach the lowest possible PPCs. The number of required exchanges strongly depends on the degradation rate. With a degradation rate of 0.8 % per 1000 h, which corresponds to the fourfold of the SECA target, three stack exchanges are necessary to reach the lowest PPCs, which are increased by approx. 20 % compared to the base case where the stack has to be exchanged only once.

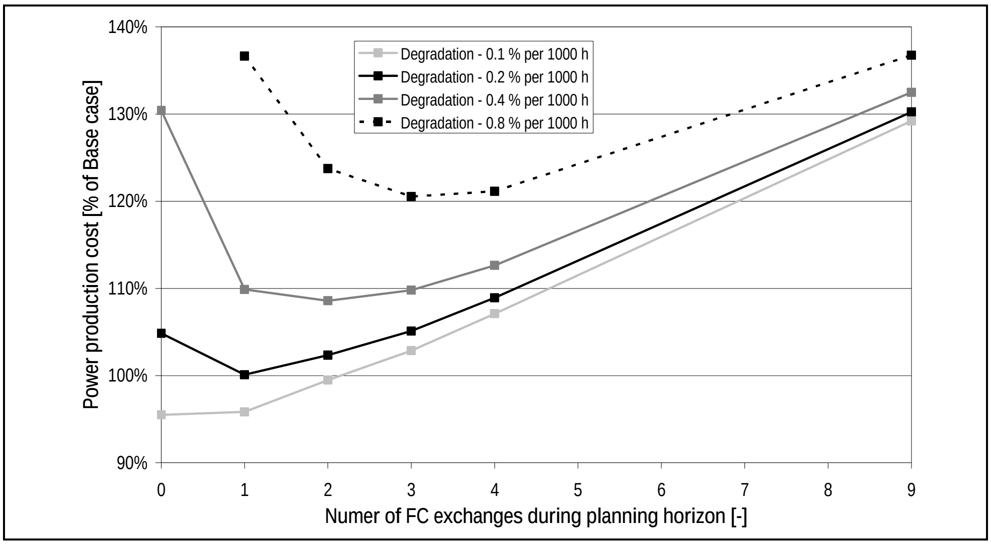

Figure 6-43: Sensitivity of the power production costs towards degradation and number of FC stack exchanges during the planning horizon

It may be that the cathode-supported cell in System 4 degrades faster than in other systems due to the maximum solid temperature which was found higher than the permitted temperature determined with the reference gas. Assuming the degradation rate increases by 100 %, the corresponding cathode-supported stack would need to be exchanged twice during the planning horizon to reach the lowest possible PPCs. Even though, the resulting PPCs are lower than those achieved by the second best cell design for System 4, namely the anode-supported counter-current cell. Note that this calculation does not consider possible revenues arising from the sale of used stacks.

The operational voltage was varied for the systems 2, 4 and 7 employing the cathode-supported cell design to investigate the corresponding impact on the PPCs, see Figure 6-44. The net AC system efficiency increases with the operational cell voltage which is mainly due to the increasing conversion efficiency of the SOFC following from Eq. 202. However, the efficiency increase is not linear with the operational voltages because of rising auxiliary power requirements. The latter result from the higher air-to-fuel ratios which are required to compensate the increasingly inhomogeneous current density and temperature distributions predicted for higher operational voltages, see Figure 6-46. At an operational voltage of 0.7 V, System 4 features a net AC system efficiency of 37.2 %. Despite this very high efficiency, the PPCs increase by almost 70 % compared to the base case yielding 0.1912 €/kWh$_{el}$ net AC, which renders profitable operation difficult.

Figure 6-44: Sensitivity of the net AC system efficiency and power production costs towards the operational cell voltage

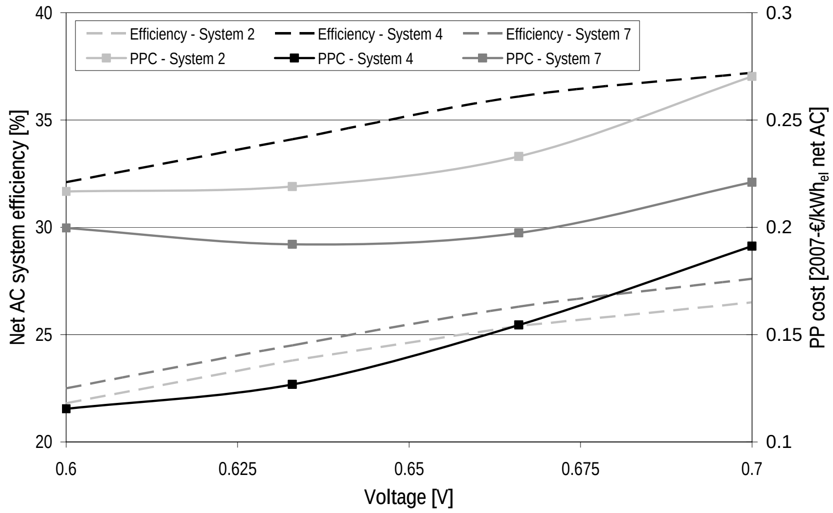

The same trend applies to System 2, which confirms the initial assumption that the operational voltage has to be as low as possible to yield reasonable power outputs and specific plant costs when SOFCs are operated with dilute fuel gases. For System 7, the PPCs initially decrease with increasing operational voltage. The minimum PPCs are reached at 0.63 V. Further increasing the operational voltage leads to increasing PPCs similar to Systems 2 and 4. The reason for the initial PPCs decrease is that the un-diluted producer gas of System 7 causes considerably less activation polarization losses. This reduces the power output decrease resulting from the higher operational voltages.

Figure 6-45: Sensitivity of the maximum temperature gradients towards the operational cell voltage

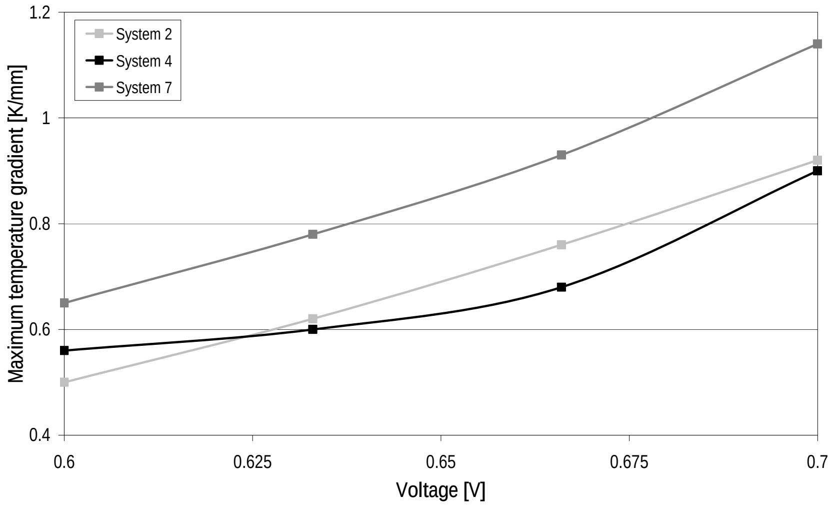

Thus up to a certain point, the efficiency surplus is sufficient to compensate the higher capital cost arising from the increased specific plant costs due to lower power output.

Figure 6-46: Sensitivity of the current density distribution predicted for the producer gas of System 7 towards the operational cell voltage

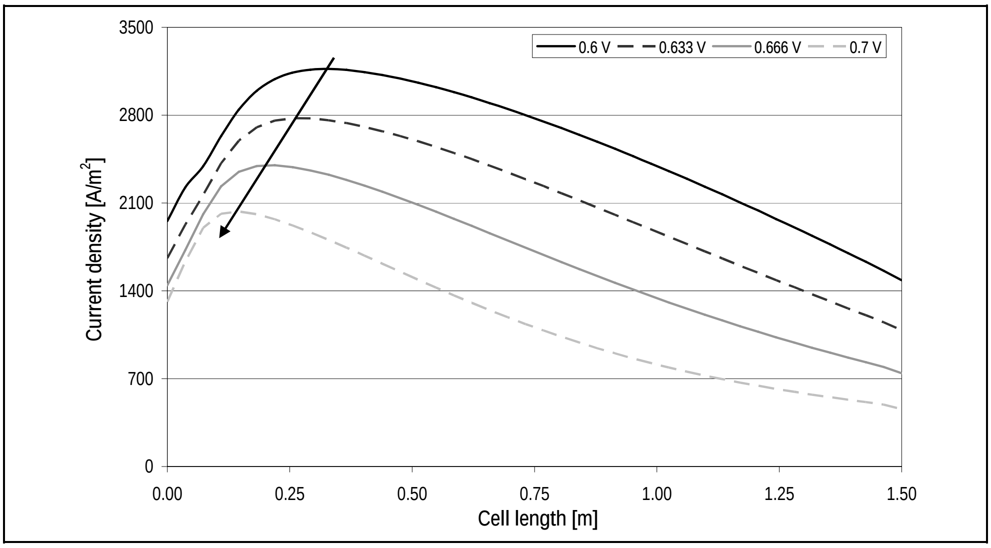

However, the thermal stress imposed on the SOFCs employed in the investigated systems increases with higher operational voltages. Figure 6-45 exemplifies that the maximum temperature gradients increase with increasing operational voltages. The reason for this lies in the current density distributions, which become increasingly inhomogeneous with rising operational voltages. Figure 6-46 shows for the producer gas of System 7 that despite in relative terms more producer gas is converted at the fuel inlet with higher operational voltages, the absolute amount decreases. This leads to a drop of the solid temperatures at the fuel inlet as the heat produced in the electrochemical reactions becomes insufficient to cover the heat demand of the STR reactions taking place. The lower solid temperatures at the cell inlet imply higher temperatures in the latter cell parts, which in turn lead to higher temperature gradients. Consequently, the PPCs benefit resulting from higher operational voltages for the producer gas of System 7 may be cancelled out by faster degradation due to higher thermal stress.

In conclusion it can be stated that none of the parameters of the economic models and important assumptions of the system analysis investigated in this sensitivity analysis change the relative differences between the considered B-IGFC systems. The absolute PPC estimates are however in parts considerably changed, which could lead to a better or worse competitiveness of the investigated systems.

7 Concluding remarks

Biomass has a large potential for electricity generation among the renewable energy sources. A promising approach to achieve high electrical efficiencies is the application of fuel cells for the conversion of producer gases originating from biomass gasification. This combination is referred to as "Biomass Integrated Gasification Fuel Cell System" (B-IGFC). The solid oxide fuel cell in particular has gained much interest due to its ability of converting hydrocarboneous fuel gases and its comparably low fuel gas requirements. This thesis aimed at the demonstration of the B-IGFC technology on kW-scale and at the identification of promising B-IGFC system concepts with power outputs around 1 MW_{el} by means of a systems analysis.

7.1 Conclusions

7.1.1 Experiments

The PSI B-IGFC system is based on the updraft gasification process. The resulting producer gas is de-dusted and its tar load is reduced through a catalytic partial oxidation (CPO) before being fed to the SOFC.

The starting point for the experimental part of the thesis was the achievement of stable long-term operation of the in-house developed lab-scale updraft gasifier. Diverse modifications of the gasifier and the addition of a steam generator made a stable operation over 165 h non-stop possible. Experiments with SOFC stacks showed that tar is to some extent a fuel for SOFCs and that sulfur reduces the power output but does not inhibit stable operation of SOFCs. Experiments with a commercial CPO catalyst revealed satisfying conversion performance for oxygenated tars and aromatics. The CPO catalyst was further found suitable for the decomposition of organic sulfur compounds.

The PSI B-IGFC concept was first time demonstrated on kW-scale. The SOFC delivered 40 % less current when operated with producer gas compared to partially oxidized methane. The gasifier and the CPO were operated without problems. Ash deposits in the SOFC system were found. Overall the first-time demonstration of the PSI B-IGFC concept was successful and possibilities for future improvements of the experimental setup were identified.

7.1.2 System analysis

While most published B-IGFC systems analyses employ lumped SOFC models and focus on idealized fuel gases, the system analysis in this thesis is based on a locally resolved SOFC model aiming at investigations of measured producer gases.

The finite volume method based SOFC model was developed with respect to fast applicability to various cell geometries, short calculation times and high fuel flexibility. To allow the identification of critical operating conditions in SOFCs, the model describes all relevant charge, mass and heat transport processes. Accounting for the hydrocarbon content of producer gases, a Langmuir-Hinshelwood type applied kinetic model for steam reforming reactions was included. The model was applied to the planar anode-supported co- and counter-current cell designs, the planar electrolyte-supported cell design and the tubular cathode-supported cell design with air delivery tube. The validation against experimental and benchmark test data proved that the model behaves physically correct with mass and energy balance errors considerably smaller than comparable state-of-the-art models. To assure the fuel flexibility of the model, an extensive sensitivity analysis was conducted. It was found that the impact of different fuel gases on the operational conditions of SOFCs generally dominates geometrical and material induced phenomena described by the corresponding model parameters.

The main objective of the conducted system analysis was to assess the technical and economical feasibility of various B-IGFC systems with a power output up to 1 MW_{el} based on already or soon available biomass gasification processes, gas processing technologies and SOFC designs for stationary power applications. The analysis assumes a standardized SOFC stack size. Based on the downdraft and updraft gasification processes as well as the fluidized bed steam gasification process, seven B-IGFC systems were defined, mainly differing in the way sulfur and tar removal or tar conversion are conducted. The producer gas compositions at the cell inlet were computed with ASPEN PLUS. In a first step, the power output, the thermal gradients and temperature extremes resulting from the various producer gas compositions were investigated.

With producer gases, the power output of the investigated SOFCs is decreased by minimum 25 % for the tubular cell and by maximum 70 % for the planar electrolyte-supported cell compared to pre-reformed natural gas. The activation losses are pronounced and eventually put into the dominant role due to the dilute character of producer gases. Thus, high anode catalyst activity is essential for high power outputs. According to the model parameters used in the analysis, the tubular cell features a highly active anode catalyst. The anode-supported counter-current cell partially balances out the lower catalyst activity with high temperatures at the cell inlet. Diffusion limitations do not gain importance for any of the investigated producer gases and cell designs.

The cooling requirements strongly depend on the SOFC flow pattern and the internal reforming potential of the producer gases. The required air-to-fuel ratios (AF) generally decrease with increasing internal reforming potential. The co-current cells are considerably more sensitive towards the internal reforming potential than the counter-current cell, which requires the lowest AFs of all cell designs. Compared to pre-reformed natural gas, all investigated producer gases cause lower temperature gradients and temperature extremes, which may reduce temperature induced cell degradation.

The interactions between the gasification processes, gas processing technologies and SOFC designs were investigated with respect to the net system efficiencies and balance of plant requirements resulting from the SOFC cooling. A generalized heat integration network was defined. The corresponding simulations were performed with ASPEN PLUS.

The water concentrations of the raw producer gases are insufficient to prevent carbon depositions at the operational temperature of the generally employed zinc oxide sulfur trap beds. In all investigated systems, except the one employing a CPO, considerable amounts of water have to be added to the producer gases.

The net system efficiency is preeminently determined by the cold gas efficiency of the biomass gasification process and the auxiliary power requirements. The latter directly correlate with the required air-to-fuel ratios, which in turn are a consequence of the internal reforming potential of the corresponding producer gases. The adiabatic methanation and the low-temperature CPO are effective means to increase the internal reforming potential of producer gases.

With 32.1 %, the highest system efficiency is reached by the combination of the updraft gasification with an adiabatic methanation and the tubular cell design. The high system efficiency results from the high cold gas efficiency of the updraft gasification process which already yields a producer gas with considerable internal reforming potential. The latter is further increased through the adiabatic methanation, which yields the fuel gas with the highest internal reforming potential in the entire analysis with an overall cold gas efficiency of 85 %. The formed methane is subsequently reformed in the SOFC directly using waste heat, which can be interpreted as the final gasification step, additionally lowering the cooling requirements and thus increasing the net system efficiency.

The fluidized bed steam gasification process also yields a producer gas with high internal reforming potential, however with low cold gas efficiency. The corresponding losses can not be compensated in the SOFC.

Downdraft gasification producer gases are almost fully reformed. Consequently, the amount of waste heat produced in the SOFC is increased leading to higher air-to-fuel ratios. Combined with the moderate cold gas efficiency of the downdraft gasification process, the corresponding B-IGFC systems feature the lowest system efficiencies in this analysis.

With respect to sulfur induced power losses, the neglect of organic sulfur compounds may lead to a considerable overestimation of the net system efficiencies. This applies especially to updraft and fluidized bed steam gasification based B-IGFC systems.

Based on the results of the system simulations, an economic model was developed to determine the profitability of the different B-IGFC systems. Major equipment pieces were sized and the direct plant costs were estimated using pertinent cost functions. The indirect plant costs were computed using factors relating the indirect to the direct plant costs.

For downdraft and fluidized bed steam gasification based systems, the wood drying is identified as considerable cost factor. The gas processing is a minor cost factor. Nevertheless, the producer gas humidification bears potential for cost reductions especially for updraft and fluidized bed steam gasification based systems, which allow an increase of the water content of the producer gases simply by adjusting the operational parameters of the gasification processes. The fuel cell balance of plant equipment is determined as dominant cost driver, amounting for up to 50 % of the direct plant costs, while the fuel cell itself accounts for up to 25 %. This emphasizes the importance of properly set cell inlet gas temperatures to yield low AFs and gas processing steps which increase the internal reforming potential of producer gases.

Relating the direct plant costs to the power output yields the specific plant costs. The downdraft gasification based systems feature the highest specific plant costs due to low power outputs, high wood drying and fuel cell balance of plant costs. For the fluidized bed steam gasification based systems, slightly lower specific plant costs are determined mainly because of the comparably high power outputs as result of the undiluted character of the corresponding producer gases. The lowest specific plant costs are established for the updraft gasification based systems. This is mainly because of the systems simplicity resulting in low direct plant costs and minor auxiliary power requirements.

The plant costs were related to the corresponding system efficiencies to yield power production cost (PPC) estimates. The basis for the calculation of the PPCs was a detailed cost analysis for a given planning horizon including costs not only for operation and maintenance, feedstock and utilities but also capital costs resulting from plant costs depreciation and interests. The net value of all costs was evenly distributed throughout the planning horizon using the annuity method.

The PPCs analysis revealed that the fuel costs amount to on average 40 % of the PPCs, the remainder being capital costs. Thus, specific plant cost reduction is considerably more effective on reducing the PPCs than increasing the system efficiency.

An increase of the operational voltage from 0.6 V to 0.7 V yields a significant increase of the SOFC conversion efficiency which in turn entails a gain of the net system efficiency from 32.1 to 37.1 % for the updraft gasification based system with adiabatic methanation. However, the PPCs increase from 0.1154 €/kWh$_{el}$ to 0.1912 €/kWh$_{el}$ too, mainly due to considerably reduced power output of the SOFC.

The reduction of auxiliary power requirements in contrast leads to an increase of the system efficiency and a decrease of the specific plant costs, thus considerably lowering the PPCs.

Finally, the revenues from heat sales are crucial for the economical viability of the investigated B-IGFC systems without bottoming cycles.

7.2 Recommendations for future work

7.2.1 Experiments

The following recommendations are made for future long-term test:

- Integration of a hot gas particle filtration unit

  The removal of particles must be optimized to prevent fouling in the cooling air pre-heater or other cold areas of the demonstration unit.

The currently installed cyclone is not sufficient and should be replaced by the hot gas particle filtration unit designed in the framework of a master thesis co-supervised by the author, Figure 7-1.

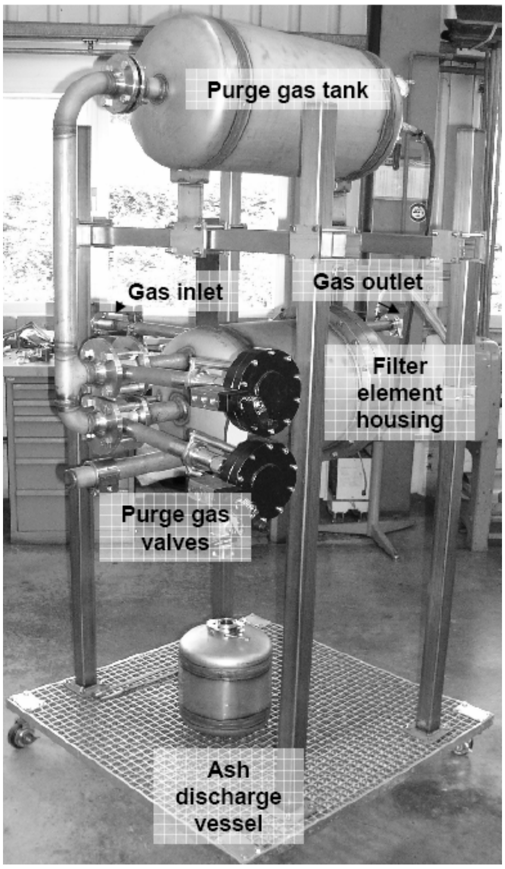

Figure 7-1:
Hot gas filtration system

To achieve a minimum fly ash load in the filtered producer gas, the filtration temperature must be kept below the ash melting point. Usually temperatures around 600 to 650 °C are chosen for this purpose. Means for active cooling may have to be added to the hot gas filtration unit.

- Application of fine meshed CPO monoliths

  Measurements of the producer gas composition downstream a CPO monoliths featuring 400 channels per square inch (cpsi) via a capillary showed that tar conversions over 90 % can be achieved. The application of such fine meshed monoliths in long-term tests was however not possible until now due to blocking issues resulting from the moderate particle removal efficiency of the used cyclone. After successful commissioning of the hot gas particle filtration unit, the currently used 100 cpsi CPO monolith should be replaced by a monolith with 400 cpsi.

- Integration of a sulfur adsorption unit

  The scope of future long-term tests should not merely be to demonstrate stable operation but also high current output of the SOFC system. Sulfur poisoning induced voltage losses should therefore be minimized by integrating a sulfur adsorption unit into the demonstration unit. As a consequence of the maximum operational temperature of 450 °C of state-of-the-art sulfur adsorbent materials, the integration of the sulfur adsorption unit includes a heat exchanger for gas cool down and/or a steam/water injection unit for additional humidification of the producer gas. The latter might be necessary to prevent carbon deposition problems at temperatures as low as 450 °C.

7.2.2 Modeling and system analysis

The following recommendations are made for future extensions of the SOFC model developed in this thesis:

- Embedding of the model into flowsheeting packages such as ASPEN PLUS, BELSIM or IPSEpro for simulation of B-IGFC systems with energy and mass flow recycles.
- Extension of the model to display the computed heats of reactions.
- Implementation of an initial conjecture estimation subroutine based on the database of already available solutions.
- Extension of the model to the second dimension to allow the simulation of SOFCs with cross-current flow patterns such as e.g. the Rolls Royce cells and the investigation of boundary effects.
- Implementation of a subroutine to compute the effective open circuit voltage resulting from hydrocarbon containing fuel gases.
- Implementation of steam reforming kinetics specifically determined for important tar species such as naphthalene etc.
- Implementation of Langmuir-Hinshelwood steam reforming kinetics including a sulfur adsorption term to determine the impact of sulfur poisoning on the mass and heat transfer processes taking place in SOFCs.
- Implementation of the Dusty-Gas diffusion model for higher accuracy of the diffusion loss estimation.
- Implementation of subroutine to compute chemical equilibria for the estimation of the formation risk of undesired solid species.
- Implementation of a subroutine for thermal stress approximations.

Following recommendations are made for future systems analysis:

- Systems analysis with minimum possible air-to-fuel ratio for all investigated producer gases

  In future system analyses, the cell inlet gas temperatures should be varied to yield the lowest possible air-to-fuel ratio for a given fuel gas composition and cell design dependent mean and maximum cell temperatures and temperature gradients. This accounts for the found major importance of the air-to-fuel ratio regarding the net system efficiency and the power production costs.

- Systems analysis including gas turbine and rankine bottoming cycles

  Bottoming cycles may be a good possibility to cover the auxiliary power requirements resulting from the SOFC cooling, simultaneously generating surplus electricity from the high-temperature heat produced in the SOFC. This way both cost-effective factors, net system efficiency and specific plant costs, could be lowered, provided that the power surplus generated by the bottoming cycle is sufficient to compensate the additional system costs.

Notation

Latin symbols

A	Area	[m^2]
AmP	Amortization period	[a]
AN	Annuity factor	[%]
c	Carbon mass fraction	[-]
C	Cost	[€]
c_p	Heat capacity	[J/(mol K)]
CP	Length of construction period	[a]
d	Diameter	[m]
D	Diffusion coefficient	[m^2/sec]
DA	Depreciation/Amortization costs	[€]
DeP	Depreciation period	[a]
D_K	Knudsen diffusion coefficient	[m^2/sec]
D_m	Molecular diffusion coefficient	[m^2/sec]
DP	Dept portion	[%]
DPC	Direct plant costs	[€]
DR	Degradation rate	[%/(1000 h)]
E	Voltage	[V]
E_{act}	Activation energy for exchange current density	[J/mol]
Eq_{H2}	Hydrogen equivalent molar flow	[mol/sec]
F	Faraday constant	[C/mol]
G	Gibbs enthalpy	[J/mol]
h	Height, Hydrogen mass fraction	[m], [-]
H	Enthalpy	[J/mol]
I	Current density	[A/m^2]
I_0	Exchange current density	[A/m^2]
IF	Inflation rate	[%]
IPC	Indirect plant costs	[€]
IR	Interest rate	[%]
Kp	Equilibrium constant	[-]
L	Length of cell-subunit	[m]

l	Length	[m]
l_c	Length of planar cell	[m]
l_{D8}	Length of Delta8 cell	[m]
LHV	Lower heating value	[J/mol]
l_t	Length of tubular cell	[m]
M	Molecular weight, Water load	[kg/mol], [%]
m	Mass	[kg]
n	Number of electrons, Nitrogen mass fraction	[-]
n_{ch}	Number of channels of planar cell	[-]
$NCIR$	Nominal capital interest rate	[%]
n_{dot}	Molar flow	[mol/sec]
n_{RE}	Number of repeating elements	[-]
n_{tri}	Number of triangular tubes in Delta8 cell	[-]
Nu	Nusselt number	[-]
o	Oxygen mass fraction	[-]
p	Total or partial pressure	[N/m^2]
P	Power	[W]
p	Price	[€]
P_{el}	Electrical Power (DC)	[W]
PF	Plant factor	[%]
PH	Planning horizon	[a]
PPC	Power production costs	[€/kWH$_{el}$]
Q_{dot}	Heat flux	[W/m]
R	Resistance or Ideal gas constant	[Ω], [J/(mol K)]
r	Radius	[m]
$r_{dl\text{-}reac}$	Diffusion limited, length specific reaction rate	[mol/(sec m)]
r_i	Inner radius	[m]
r_j	Reaction rate of reaction j	[mol/(sec m)]
r_m	Middle radius	[m]
r_o	Outer radius	[m]
ro	Reaction order	[-]
RoE	Return on equity	[%]
s	Sulfur mass fraction	[-]
SoP	Start of production	[-]
T	Temperature	[K]
$TadtK$	Gas temperature in air delivery tube	[K]

TaK	Anode gas temperature	[K]
$Tamb$	Ambient temperature	[K]
TI	Total investment costs	[€]
TRD	Threshold degradation	[%]
TsK	Solid structure temperature	[K]
UF	Fuel utilization	[-]
w	Humidity	[%]
w_c	Channel width of planar cell channels	[m]
w_{ce}	Width of planar cell	[m]
w_{D8}	Delta8 cell width	[m]
WI	Yearly wood price increase	%
X	Fraction	[%]
x_p	Active fraction of area covered by rib	[-]
x_t	Inactive fraction of tubular cell area	[-]
y	Molar fraction	[-]

Greek symbols

α	Upper triangular half angle	[°]
α	Convective heat exchange coefficient	[W/(m^2 K)]
α_{insul}	Heat transfer coefficient through insulation	[W/(m^2 K)]
β	Transfer coefficient	[-]
$\beta_{x,diff}$	Mass transfer coefficient of specie x	[m/sec]
$\beta_{x,diff\text{-}reac}$	Diffusion limited reaction conversion coefficient of specie x	
$\beta_{x,reac}$	Reaction conversion coefficient of specie x	
δ	Thickness of component	[m]
ΔH	Heat of reaction	[J/mol]
ε	Porosity of porous media	[-]
γ	Pre-exponential factor	[A/m^2]
η	Efficiency	[%]
η_{act}	Activation polarization voltage loss	[V]
η_{diff}	Diffusion polarization voltage loss	[V]
η_{ohm}	Ohmic voltage loss	[V]
λ	Air-to-fuel ratio	[-]
λ_{an}	Thermal conductivity of anode gas	[W/(m K)]
λ_{ca}	Thermal conductivity of cathode gas	[W/(m K)]

λ_s	Solid structure heat conductivity coefficient	[W/(m K)]
ν_{av}	Average molecular speed	[m/sec]
ν_{ij}	Stoiciometric coefficient	[-]
ρ	Specific conductivity	[1/(Ω m)]
τ	Tortuosity of porous media	[-]

Subscripts and superscripts

0,in	Inlet
act	Active, Activation, Actual
ADT	Air delivery tube
AEC	Anode-electrolyte-cathode assembly
Am	Amortization
an	Anode gas channel, Anode
Ash	Ash
Aux	Auxiliary
av	Average
blow	Blower, Fan, Pump
ca	Cathode gas channel, Cathode
Cap	Capital
cat	Catalyst
cat_0	First catalyst batch in planning horizon
CG	Clean gas, cold gas
chact	Chemically active
circ	Circumferential
conv	Convective
cross	Cross-sectional
cs	Catalyst surface
d	Dry
D8	Delta8
DC	Direct current
Dep	Depreciation
ed	Educts
eff	Effective
el	Electrolyte

elact	Electrochemically active
end	End
equiv	Equivalent
FC	Fixed carbon, Fuel cell
FC_0	First fuel cell in planning horizon
gasi	Gasification
GP	Gas processing
hloss	Heat loss
hyd	Hydraulic
ic	Interconnect
IE	Interest expense
Ins	Insurance
Inv	Inverter
mix	Gas mixture
net	Net
O+M	Operation and maintenance
op	Operational
oxi	Oxidation
p	Planar
PG	Producer gas
prod	Products
s	Start
S	Sulfur
SE	Standard equipment
SH	Sensible heat
SOFC	Solid oxide fuel cell
start	Start
stoic	Stoiciometric
STR	Steam reforming
sys	System
t	Tubular
th	Thermal
tot	Total
TPB	Triple phase boundary
VM	Volatile matter
WGS	Water gas shift

Abbreviations

AC	Alternating current
ADT	Air delivery tube
AEC	Anode-electrolyte-cathode assembly
AF	Air-to-fuel ratio
AFC	Alkaline fuel cell
APU	Auxiliary power unit
ATR	Autothermal reforming
BHPR	Biomass Heatpipe Reformer
B-IGFC	Biomass Integrated Gasification Fuel Cell System
BMT	Benchmark test
BoP	Balance of plant
BtL	Biomass to Liquids
CECPI	Chemical Engineering Magazine Plant Cost Index
CFD	Computational fluid dynamics
CGO	Gadolinium doped ceria
CHP	Combined heat and power
CPO	Catalytic partial oxidation
cpsi	Channels per square inch
CSTR	Continuous stirred tank reactor
CV	Caloric value, Control volume
D8	Delta8 cell design by the Siemens AG
daf	Dry and ash free
DC	Direct current
DMFC	Direct methanol fuel cell
dtf	Dry, tar and ash free
FC	Fuel cell
FEM	Finite element method
FICFB	Fast Internally Circulating Fluidized Bed
FVM	Finite volume method
GC	Gas chromatography
GT	Gas turbine
HDP	High power density
HGF	Hot gas filtration

HHV	Higher heating value
HIN	Heat integration network
IC	Interconnector, Bipolar plate
ICE	Internal combustion engine
IEA	International Energy Agency
LH	Langmuir-Hinshelwood kinetics
LHV	Lower heating value
LSCr	Lanthanum strontium chromium perovskite
LSGM	Lanthanum strontium magnesium gallate
LSM	Lanthanum strontium manganite
MCFC	Molten carbonate fuel cell
MFC	Mass flow controller
MIEC	Mixed ionic and electronic conductor
NVAM	Numerical volume averaging method
OCV	Open circuit voltage
PAFC	Phosphoric acid fuel cell
PEMFC	Polymer electrolyte membrane fuel cell
PG	Producer gas
PL	Power law kinetics
PO	Partial oxidation
PPC	Power production costs
PSI	Paul Scherrer Institute
REV-WGS	Reverse water gas shift
SAI	Secondary air injection
SC	Steam-to-carbon ratio
ScSZ	Scandia stabilized zirconia
SECA	Solid State Energy Conversion Alliance
SOFC	Solid oxide fuel cell
STR	Steam reforming
TPB	Triple phase boundary
UI	Voltage-current
WGS	Water gas shift
WHSV	Weight hourly space velocity
YSZ	Yttria stabilized zirconia

References

[1] Novatlantis, Smarter living - Generating a new understanding for natural resources as the key to sustainable development - the 2000-watt society, Dübendorf, Switzerland, 2005.

[2] A. Wokaun, Erneuerbare Energie, Teubner Verlag, Stuttgart, Leipzig, Germany, 1999.

[3] World Energy Outlook 2004, International Energy Agency, Paris, France, 2004.

[4] T. Nussbaumer, Technische Energienutzung von Biomasse, Swiss Federal Institute of Technology, Zurich, Switzerland, 2004.

[5] M. Gronli, A theoretical and experimental study of the thermal degradation of biomass, Norwegian University of Science and Technology, Trondheim, Norway, 1996.

[6] P. McKendry, Bioresour. Technol., 83 (2002) 37-46.

[7] G. W. Huber, S. Iborra, A. Corma, Chem. Rev., 106 (2006) 4044-4098.

[8] T. A. Hsu, M. R. Ladisch, G. T. Tsao, Chemtech, 10 (1980) 315-319.

[9] M. A. Serio, M. A. Wojtowicz, S. Charrenay, A. Bisio, S. Booty, Encyclopedia of Energy Technology and the Environmen, Wiley, New York, United States of America, 1995.

[10] N. Arnstein, Experimental investigation of Solid Oxide Fuel Cells using biomass gasification producer gases, Norwegian University of Science and Technology, Trondheim, Norway, 2005.

[11] B. M. Jenkins, L. L. Baxter, T. R. Miles, T. R. Miles, Fuel Process. Technol., 54 (1998) 17-46.

[12] L. L. Baxter, Biomass Bioenerg., 4 (1993) 85-102.

[13] J. R. Rostrupnielsen, L. J. Christiansen, Appl. Catal. A-Gen., 126 (1995) 381-390.

[14] K. Raveendran, A. Ganesh, K. C. Khilar, Fuel, 74 (1995) 1812-1822.

[15] K. Raveendran, A. Ganesh, K. C. Khilar, Fuel, 75 (1996) 987-998.

[16] H. Recknagel, E. Sprenger, W. Hönmann, Taschenbuch für Heizung und Klimatechnik, Universität Dortmund, Dortmund, Germany, 1994.

[17] User Documentation for Aspen Plus, Version 12.1, ASPEN Tech, Cambridge, United States of America, 2002.

[18] P. McKendry, Bioresour. Technol., 83 (2002) 47-54.

[19] A. Kaupp, J. Goss, Small scale gas producer-engine systems, German Appropriate Technology Exchange (GATE), Eschborn, Germany, 1984.

[20] P. Morf, Secondary Reactions of Tar during Thermochemical Biomass Conversion, Swiss Federal Institute of Technology, Zurich, Switzerland, 2001.

[21] J. Warnatz, U. Maas, R. W. Dibble, Verbrennung, Springer, Berlin, Germany, 1997.

[22] M. Bolhàr-Nordenkampf, H. Hofbauer, Biomass gasification combined cycle thermodynamic optimisation using integrated drying, in: Proceedings of the ASME Turbo Expo 2004: Power for Land, Sea and Air, 2004, 14th to 17th June.

[23] P. McKendry, Bioresour. Technol., 83 (2002) 55-63.

[24] J. C. Lee, R. A. Yetter, F. L. Dryer, Combust. Flame, 101 (1995) 387-398.

[25] A. Vogel, M. Bolhàr-Nordenkampf, M. Kaltschmitt, H. Hofbauer, R. Berger, A. Kather, M. Kübel, B. Staiger, L. Wiese, Analyse und Evaluierung der thermo-chemischen Vergasung von Biomasse, Landwirtschaftsverlag GmbH, Münster, Germany, 2006.

[26] K. R. Cummer, R. C. Brown, Biomass Bioenerg., 23 (2002) 113-128.

[27] P. Morf, P. Hasler, T. Nussbaumer, Fuel, 81 (2002) 843-853.

[28] B. Teislev, Wood-chips gasifier combined heat and power, Babcock & Wilcox Volund R&D Centre, Kolding, Denmark, 2001.

[29] B. Teislev, Harboore-woodchips gasifier and 1500 kW gas-engines operating at 32% power efficiency in CHP configuration, in: Proceedings of the 12th European Conference on Biomass, Amsterdan, 2002, 17th to 21st June.

[30] A. Beenackers, Renew. Energy, 16 (1999) 1180-1186.

[31] Website, http://www.pyroforce.ch, January 2008.

[32] Website, http://www.pyrocon.ch, January 2008.

[33] T. Metz, Allotherme Vergasung von Biomasse in indirekt beheizten Wirbelschichten, Technische Universität München, Munich, Germany, 2006.

[34] D. J. Stevens, Hot Gas Conditioning: Recent Progress with Larger-Scale Biomass Gasification Systems, National Renewable Energy Laboratory, Golden, United States of America, 2001.

[35] R. Rauch, C. Pfeifer, K. Bosch, H. Hofbauer, D. Swierczynski, C. Courson, A. Kiennemann, Comparison of different olivines for biomass steam gasification, in: Proceedings of the Science in Thermal and Chemical Biomass Conversion, Victoria, Canada, 2004, 30th August to 2nd September.

[36] Website, http://www.heatpipe-reformer.de, January 2008.

[37] R. Rauch, H. Hofbauer, Zweibett-Wirbelschichtvergasung in Güssing mit 2MWel/4,5MWth, in: Proceedings of the 7tes Holzenergiesymposion, Zurich, Switzerland, 2002, 18th October.

[38] E. Heinrich, The status of the FZK concept of biomass gasification, in: Proceedings of the 2nd European Summer School on Renewable Motor Fuels, Warsaw, Poland, 2007, 29th to 31st August.

[39] O. Schulze, Advanced gas cleaning for biomass gasification, in: Proceedings of the IEA Workshop 5, Dresden, Germany, 2006, 12th to 14th June.

[40] M. Seemann, Methanation of biosyngas in a fluidized bed reactor, Swiss Federal Institute of Technology, Zurich, Switzerland, 2007.

[41] B. Lohrengel, Abgasreinigung/Immisionsschutz, FH Heilbronn, Heilbronn, Germany, 2004.

[42] W. Mojtahedi, E. Kurkela, M. Nieminen, J. Inst. Energy, 63 (1990) 95-100.

[43] D. C. Dayton, B. M. Jenkins, S. Q. Turn, R. R. Bakker, R. B. Williams, D. Belle-Oudry, L. M. Hill, Energy Fuels, 13 (1999) 860-870.

[44] K. Salo, W. Mojtahedi, Biomass Bioenerg., 15 (1998) 263-267.

[45] S. Q. Turn, C. M. Kinoshita, D. M. Ishimura, T. T. Hiraki, J. Zhou, S. M. Masutani, Ind. Eng. Chem. Res., 40 (2001) 1960-1967.

[46] N. J. J. Dekker, G. Rietveld, J. Fuel Cell Sci. Technol., 3 (2006) 499-502.

[47] A. Wojcik, H. Middleton, I. Damopoulos, J. Van herle, J. Power Sources, 118 (2003) 342-348.

[48] Website, http://www.ecn.nl/phyllis, December 2007.

[49] M. P. Cal, B. W. Strickler, A. A. Lizzio, Carbon, 38 (2000) 1757-1765.

[50] K. Kendall, Nature, 404 (2000) 233-235.

[51] T. Sanderson, An updated assesment of the prospects for fuel cells in stationary power and CHP, DTI, Oxfordshire, England, 2005.

[52] L. Carrette, K. A. Friedrich, U. Stimming, Fuel Cells, 1 (2001) 5-39.

[53] R. Leinfelder, Reaktionskinetische Untersuchungen zur Methan-Dampf-Reformierung und Shift-Reaktion an Anoden oxidkeramischer Brennstoffzellen, Universität Erlangen-Nürnberg, Erlangen-Nürnberg, Germany, 2004.

[54] R. Coll, J. Salvado, X. Farriol, D. Montane, Fuel Process. Technol., 74 (2001) 19-31.

[55] D. Wang, D. Montane, E. Chornet, Appl. Catal. A-Gen., 143 (1996) 245-270.

[56] S. Czernik, A. V. Bridgwater, Energy Fuels, 18 (2004) 590-598.

[57] D. N. Wang, S. Czernik, E. Chornet, Energy Fuels, 12 (1998) 19-24.

[58] J. Larminie, A. Dicks, Fuel Cell Systems Explained, John Wiley & Sons, Ltd., Chicester, England, 2000.

[59] S. D. Vora, SECA Program at Siemens Westinghouse, in: Proceedings of the 6th Annual SECA Workshop, Pacific Grove, United States of America, 2005, 18th to 21st April.

[60] L. F. Brown, Int. J. Hydrog. Energy, 26 (2001) 381-397.

[61] S. Shaffer, Development Update on Delphi's Solid Oxide Fuel Cell System, in: Proceedings of the 6th Annual SECA Workshop, Pacific Grove, United States of America, 2005, 18th to 21st April.

[62] M. Klemm, Heissentteerung von Brenngas aus der Vergasung von Biomasse durch katalytische partielle Oxidation, Fortschritt-Berichte VDI Reihe 6 Nr. 525, Düsseldorf, Germany, 2005.

[63] U. Bartmann, Reaktionstechnische Untersuchungen zur katalytischen partiellen Oxidation von Methan mit Sauerstoff zu Synthesegas in Festbettreaktoren, Ruhr-Universität Bochum, Germany, Bochum, 1999.

[64] T. Miyazawa, T. Abe, K. Kunimori, K. Tomishige, J. Jpn. Pet. Inst, 48 (2005) 162-172.

[65] U. Bossel, The Birth of the Fuel Cell (1835-1845). Complete Correspondence between Christian Friedrich Schönbein and William Robert Grove, European Fuel Cell Forum, Lucern, Switzerland, 2000.

[66] Website, http://www.cogeneration.net/molten_carbonate_fuel_cells.htm, December 2006.

[67] R. Bosch, Perspectives on Fuel Cells vs. Incumbent Technologies, in: Proceedings of the 2005 Fuel Cell Seminar, Palm Springs, United States of America, 2005, 14th to 18th November.

[68] L. J. Gauckler, D. Beckel, B. E. Buergler, E. Jud, U. R. Muecke, M. Prestat, J. L. M. Rupp, J. Richter, Chimia, 58 (2004) 837-850.

[69] R. Kee, H. Zhu, D. Goodwin, Proceedings of the Combustion Institute, 30 (2005) 2379-2404.

[70] S. C. Singhal, K. Kendall, High-temperature Solid Oxide Fuel Cells: Fundamentals, Design and Applications, Elsevier, London, Great Britain, 2004.

[71] Fuel Cell Handbook (Sixth Edition), DOE/NETL, Morgantown, West Virginia, United States of America, 2002.

[72] Newsletter, FuelCell Japan, 1 (2004) 1-15.

[73] F. de Bruijn, Green Chem., 7 (2005) 132-150.

[74] A. Baker, Fuel Cell Today Market Survey: Large Stationary Applications, www.fuelcelltoday.com, 2005.

[75] L. Blum, W. A. Meulenberg, H. Nabielek, R. Steinberger-Wilckens, Int. J. Appl. Ceram. Technol., 2 (2005) 482-492.

[76] P. Bance, N. P. Brandon, B. Girvan, P. Holbeche, S. O'Dea, B. C. H. Steele, J. Power Sources, 131 (2004) 86-90.

[77] B. Morel, J. Laurencin, Y. Bultel, F. Lefebvre-Joud, J. Electrochem. Soc., 152 (2005) A1382-A1389.

[78] L. Ceres Power, DTI Project Summary No. PS210, (2005).

[79] S. M. Haile, Acta Mater., 51 (2003) 5981-6000.

[80] S. Elangovan, B. Heck, S. Balagopal, I. Bay, D. Larsen, Challenges in the Use of Lanthanum Gallate Electrolyte for Intermediate TemperatureSOFCs, in: Proceedings of the First International Conference on Fuel Cell Development and Deployment, Storrs, United States of America, 2004, 7th to 10th March.

[81] O. Marina, J. W. Stevenson, Development of Ceramic Composites as SOFC Anodes, in: Proceedings of the SECA Core Technology Program Review Meeting, Albany, United States of America, 2003, 30th September.

[82] M. Hill, Ceramic Energy: Material Trends in SOFC Systems, www.ceramicindustry.com, 2005.

[83] M. P. Brady, B. A. Pint, T. R. Armstrong, C. E. Milliken, E. D. Kreidler, Z. G. Lu, J. H. Zhu, Oxidation behaviour and in-cell performance of developmental SOFC interconnect

alloys, in: Proceedings of the 2002 ASM Fall Meeting, Columbus, United States of America, 2002, 7th to 10th October.

[84] C. Voisard, Das planare Sulzer Hexis SOFC Konzept, in: Proceedings of the DGM-Fortbildungsseminar Werkstofffragen der Hochtemperatur-Brennstoffzelle (SOFC), Jülich, Germany, 2005, 20th to 22nd April.

[85] T. A. Morris, E. A. Barringer, S. C. Kung, R. W. McKain, MRS Bull., 30 (2005) 596-600.

[86] L. Jones, Pressurisation of IP-SOFC technology for second generation hybrid application, DTI, Oxfordshire, England, 2005.

[87] Development of innovative metal-supported IT-SOFC technology, DTI, Oxfordshire, England, 2005.

[88] R. A. George, SECA Project at Siemens Westinghouse, in: Proceedings of the 3rd Annual Solid State Energy Conversion Alliance (SECA) Workshop, Washington D.C., United States of America, 2002, 21st to 22nd March.

[89] N. Bessette, Status of the Acumentrics SOFC Program, in: Proceedings of the 5th SECA Annual Workshop, Boston, United States of America, 2004, 11th to 13th May.

[90] P. Patel, Thermally Integrated High Power Density SOFC Generator, in: Proceedings of the 6th SECA Annual Workshop, Pacific Grove, United States of America, 2005, 18th to 21st April.

[91] R. Steinberger-Wilckens, Recent Results of SOFC Stack Development at Forschungszentrum Juelich, in: Proceedings of the 2004 Fuel Cell Seminar, San Antonio, United States of America, 2004, 2nd to 5th November.

[92] N. Christiansen, J. B. Hansen, S. Kristensen, H. Holm-Larsen, S. Linderoth, P. V. Hendriksen, P. H. Larsen, M. Mogensen, Status and Recent Progress in SOFC Development at Topsoe Fuel Cell /Risø National Laboratory, in: Proceedings of the 2005 Fuel Cell Seminar, Palm Springs, United States of America, 2005, 14th to 18th November.

[93] C. Wunderlich, M. Boltze, Auxiliary Power Unit Development - How the System Concept interacts with the Stack Concept, in: Proceedings of the 2005 Fuel Cell Seminar, Palm Springs, United States of America, 2005, 14th to 18th November.

[94] D. Norrick, Cummins Power Generation SECA Program Phase 1 Results and Experience, in: Proceedings of the 2005 Fuel Cell Seminar, Palm Springs, United States of America, 2005, 14th to 18th November.

[95] S. C. Singhal, Solid State Ion., 135 (2000) 305-313.

[96] R. Stübner, Untersuchungen zu den Eigenschaften der Anode der Festoxid-Brennstoffzelle (SOFC), Technische Universität Dresden, Dresen, Germany, 2002.

[97] S. P. Jiang, S. H. Chan, J. Mater. Sci., 39 (2004) 4405-4439.

[98] W. Z. Zhu, S. C. Deevi, Mater. Sci. Eng. A-Struct. Mater. Prop. Microstruct. Process., 362 (2003) 228-239.

[99] E. Ivers-Tiffee, A. Weber, D. Herbstritt, J. European Ceram. Soc., 21 (2001) 1805-1811.

[100] D. Simwonis, F. Tietz, D. Stover, Solid State Ion., 132 (2000) 241-251.

[101] J. Helbig, U. Schönholzer, Grundzüge der Keramik - Skript zur Vorlesung Ingenieurkeramik I, Swiss Federal Institute of Technology, Zürich, Switzerland, 2001.

[102] S. P. S. Badwal, Solid State Ion., 52 (1992) 23-32.

[103] S. Primdahl, M. Mogensen, J. Appl. Electrochem., 30 (2000) 247-257.

[104] E. Konysheva, J. Mertens, H. Penkalla, L. Singheiser, K. Hilpert, J. Electrochem. Soc., 154 (2007) B1252-B1264.

[105] M. J. Jorgensen, P. Holtappels, C. C. Appel, J. Appl. Electrochem., 30 (2000) 411-418.

[106] J. R. Rostrup-Nielsen, J. Sehested, Catalyst Deactivation 2001, Proceedings, 139 (2001) 1-12.

[107] M. V. Twigg, Catalyst Handbook, Wolfe Publishing Ltd., Frome, England, 1989.

[108] D. L. Trimm, Catal. Rev.-Sci. Eng., 16 (1977) 155-189.

[109] C. H. Bartholomew, Catal. Rev.-Sci. Eng., 24 (1982) 67-112.

[110] G. C. Bond, Appl. Catal. A-Gen., 149 (1997) 3-25.

[111] H. Kim, C. Lu, W. L. Worrell, J. M. Vohs, R. J. Gorte, J. Electrochem. Soc., 149 (2002) A247-A250.

[112] E. Achenbach, IEA Programm on R,D&D on advanced fuel cells: Final Report of Activity A2, (1996).

[113] A. Selimovic, M. Kemm, T. Torisson, M. Assadi, J. Power Sources, 145 (2005) 463-469.

[114] Structural limitations in the scale-up of anode supported SOFCs, Final report to DOE NETL, Cambridge, United States of America, 2002.

[115] A. L. Dicks, J. Power Sources, 71 (1998) 111-122.

[116] U. Hennings, M. Brune, R. Reimert, GWF Gas Erdas, 145 (2004) 92-97.

[117] O. Marina, L. R. Pederson, D. J. Edwards, C. W. Coyle, J. Templeton, M. Engelhard, Z. Zhu, SOFC Operation on Hydrogen and Coal Gas in the Presence of Phosphorus, Arsenic and Sulfur Impurities, in: Proceedings of the 8th Annual SECA Workshop, San Antonio, United States of America, 2007, 7th to 9th August.

[118] Y. Matsuzaki, Y. Isamu, Solid State Ion., 132 (2000) 261-269.

[119] L. Aguilar, S. Zha, Z. Cheng, J. Winnick, M. Liu, J. Power Sources, 135 (2004) 17-24.

[120] R. H. Cunningham, M. Fowles, R. M. Ormerod, J. Staniforth, Sulphur poisoning of the active materials used in SOFCs, DTI, Report F/01/00222/REP, 2004.

[121] H. Y. Tu, U. Stimming, J. Power Sources, 127 (2004) 284-293.

[122] W. C. Li, H. L. Bai, J. N. Hsu, S. N. Li, C. C. Chen, Ind. Eng. Chem. Res., 47 (2008) 1501-1505.

[123] R. Sime, S. Stucki, S. Biollaz, A. Wiasmitinow, Linking wood gasification with SOFC hybrid processes, in: Proceedings of the 5th European SOFC Forum, Lucerne, Switzerland, 2002, 2nd to 5th July.

[124] R. Sime, A. Wiasmitinow, S. Biollaz, S. Stucki, Evaluation of Biomass Fuelled Solid Oxide Fuel Cell - Gas Turbine Hybrid Process, in: Proceedings of the 2nd World Conference and Technological Exhibition on Biomass for Energy, Industry and Climate Protection, Rom, Italy, 2004, 10th to 14th May.

[125] F. P. Nagel, M. Künstle, S. Biollaz, Link-up of a SOFC to a Wood Gasifier, in: Proceedings of the 14th European Biomass Conference and Exhibition: Biomass for Energy, Industry and Climate Protection, Paris, France, 2005, 17th to 21st October.

[126] T. Borowiecki, Pol. J. Chem., 67 (1993) 1755-1766.

[127] B. Coughlan, M. A. Keane, J. Mol. Catal., 71 (1992) 93-109.

[128] K. Eguchi, H. Kojo, T. Takeguchi, R. Kikuchi, K. Sasaki, Solid State Ion., 152 (2002) 411-416.

[129] D. Singh, E. Hernandez-Pacheco, P. N. Hutton, N. Patel, M. D. Mann, J. Power Sources, 142 (2005) 194-199.

[130] K. Sasaki, Y. Teraoka, J. Electrochem. Soc., 150 (2003) A878-A884.

[131] K. Sasaki, Y. Teraoka, J. Electrochem. Soc., 150 (2003) A885-A888.

[132] A. O. Omosun, A. Bauen, N. P. Brandon, C. S. Adjiman, D. Hart, J. Power Sources, 121 (2004) 96-106.

[133] D. Wang, S. Czernik, D. Montane, M. Mann, E. Chornet, Ind. Eng. Chem. Res., 36 (1997) 1507-1518.

[134] C. H. Bartholomew, P. K. Agrawal, J. R. Katzer, Adv. Catal., 31 (1982) 135-242.

[135] C. H. Bartholomew, Appl. Catal. A-Gen., 212 (2001) 17-60.

[136] J. A. Rodriguez, J. Hrbek, Accounts Chem. Res., 32 (1999) 719-728.

[137] L. E. Amand, H. Kassman, M. Karlsson, B. Leckner, J. Inst. Energy, 70 (1997) 25-30.

[138] L. de Sousa, Gasification of wood, urban wastewood (Altholz) and other wastes in a fluidized bed reactor, Swiss Federal Institute of Technology, Zurich, Switzerland, 2001.

[139] E. Achenbach, J. Power Sources, 49 (1994) 333-348.

[140] C. Stiller, Design, Operation and Control Modelling of SOFC/GT Hybrid Systems, Norwegian University of Science and Technology, Trondheim, Norway, 2006.

[141] A. Selimovic, Modelling of Solid Oxide Fuel Cells Applied to the Analysis of Integrated Systems with Gas Turbines, Lund University, Lund, Sweden, 2002.

[142] W. Zhang, E. Croiset, P. L. Douglas, M. W. Fowler, E. Entchev, Energy Convers. Manage., 46 (2005) 181-196.

[143] T. Kivisaari, P. Björnbom, C. Sylwan, B. Jacquinot, D. Jansen, A. de Groot, Chem. Eng. J., 100 (2004) 167-180.

[144] S. Campanari, J. Power Sources, 92 (2001) 26-34.

[145] T. Reed, S. Gaur, A Survey of biomass gasification 2001 - Gasifier projects and manufacturers around the world, Solar Energy Research Institute, Golden, United States of America, 2001.

[146] F. Hebmüller, Einflussfaktoren auf die Kieselgurfiltration von Bier, TU Bergakademie Freiberg, Freiberg, Germany, 2003.

[147] F. P. Nagel, M. Jenne, S. Biollaz, S. Stucki, Link-up of a SOFC with an updraft-wood gasifier via hot gas processing, in: Proceedings of the 2006 Fuel Cell Seminar-30th Anniversary, Honolulu, USA, 2006, 13th to 17th November.

[148] C. Pitta, Investigation of tar reforming employing a catalytic partial oxidation catalyst, Swiss Federal Institute of Technology, Zurich, Switzerland, 2007.

[149] M. Damsohn, Heissgasentschwefelung im Biomass-Integrated-Gasification-Fuel-Cell-System, Technische Universität Clausthal, Clausthal, Germany, 2006.

[150] Website, www.hexis.com, January 2008.

[151] A. L. Dicks, J. Power Sources, 61 (1996) 113-124.

[152] P. Hofmann, A. Schweiger, L. Fryda, K. D. Panopoulos, U. Hohenwarter, J. D. Bentzen, J. P. Ouweltjes, J. Ahrenfeldte, U. Henriksen, E. Kakaras, J. Power Sources, 173 (2007) 357-366.

[153] F. P. Nagel, S. Biollaz, M. Jenne, S. Stucki, Link-up of a 1kW-SOFC with an updraft-wood gasifier via hot gas processing, in: Proceedings of the 15th European Biomass Conference 2007: From Research to Market Deployment, Berlin, Germany, 2007, 7th to 11th May.

[154] J. Palsson, Thermodynamic Modelling and Performance of Combined Solid Oxide Fuel Cell and Gas Turbine Systems, Lund University, Lund, Sweden, 2002.

[155] B. Thorud, Dynamic Modelling and Characterisation of a Solid Oxide Fuel Cell Integrated in a Gas Turbine Cycle, Norwegian University of Science and Technology, Trondheim, Norway, 2005.

[156] T. Kivisaari, P. Björnbom, C. Sylwan, J. Power Sources, 104 (2002) 115-124.

[157] E. Liese, R. S. Gemmen, J. Eng. Gas Turb. Power, 127 (2005) 86-90.

[158] S. Ghosh, S. De, Energy, 31 (2006) 345-363.

[159] Y. Yi, A. D. Rao, J. Brouwer, G. S. Samuelsen, J. Power Sources, 144 (2005) 67-76.

[160] J. Van herle, F. Maréchal, S. Leuenberger, Y. Membrez, O. Bucheli, D. Favrat, J. Power Sources, 131 (2004) 127-141.

[161] R. Bove, P. Lunghi, N. M. Sammes, Int. J. Hydrogen Energy, 30 (2005) 181-187.

[162] R. Suwanwarangkul, E. Croiset, M. W. Fowler, P. L. Douglas, E. Entchev, M. A. Douglas, J. Power Sources, 122 (2003) 9-18.

[163] T. Proell, R. Rauch, C. Aichering, H. Hofbauer, Coupling of biomass steam gasification and SOFC - gas turbine hybrid system for highly efficient electricity generation, in: Proceedings of the ASME Turbo Expo 2004: Power for Land, Sea and Air, Vienna, Austria, 2004, 14th to 17th June.

[164] E. Hernández-Pacheco, D. Singh, P. N. Hutton, N. Patel, M. D. Mann, J. Power Sources, 138 (2004) 174-186.

[165] P. Costamagna et al., J. Power Sources, 96 (2001) 352-368.

[166] S. H. Chan, K. A. Khor, Z. T. Xia, J. Power Sources, 93 (2001) 130-140.

[167] T. Aloui, K. Halouani, Appl. Therm. Eng., 27 (2007) 731-737.

[168] K. D. Panopoulos, L. E. Fryda, J. Karl, S. Poulou, E. Kakaras, J. Power Sources, 159 (2006) 570-585.

[169] D. Froning, U. Reimer, A. Gubner, Combined Treatment of the Stack and the Systems Level in SOFC - Modelling, in: Proceedings of the 3rd Fuel Cell Research Symposium - Modelling and Experimental Validation, Dübendorf, Switzerland, 2006, 16th to 17th March.

[170] M. Roos, E. Batawi, U. Harnisch, T. Hocker, J. Power Sources, 118 (2003) 86-95.

[171] R. Bove, P. Lunghi, N. M. Sammes, Int. J. Hydrogen Energy, 30 (2005) 189-200.

[172] C. Stiller, B. Thorud, S. Seljebø, Ø. Mathisen, H. Karoliussen, O. Bolland, J. Power Sources, 141 (2005) 227-240.

[173] T. Araki, T. Ohba, S. Takezawa, K. Onda, Y. Sakaki, J. Power Sources, 158 (2006) 52-59.

[174] P. Costamagna, A. Selimovic, M. Del Borghi, G. Agnew, Chem. Eng. J., 102 (2004) 61-69.

[175] E. Hernández-Pacheco, M. D. Mann, P. N. Hutton, D. Singh, M. K.E., Int. J. Hydrogen Energy, 30 (2005) 1221-1233.

[176] L. T. Lim, D. Chadwick, L. Kershenbaum, Ind. Eng. Chem. Res., 44 (2005) 9609-9618.

[177] H. Timmermann, H. U., W. A., E. Ivers-Tiffée, R. Reimert, Development of a Fuel-Flexible SOFC Stack Model, in: Proceedings of the 7th European SOFC Forum, Switzerland, Lucerne, 2006, 3rd to 7th July.

[178] R. Suwanwarangkul, E. Croiset, M. D. Pritzker, M. W. Fowler, P. L. Douglas, E. Entchev, J. Power Sources, 154 (2006) 74-85.

[179] D. Larrain, J. Van Herle, F. Maréchal, D. Favrat, J. Power Sources, 131 (2004) 304-312.

[180] N. Autissier, D. Larrain, J. Van Herle, D. Favrat, J. Power Sources, 131 (2004) 313-319.

[181] J. Van Herle, D. Larrain, N. Autissier, Z. Wuillemin, M. Molinelli, D. Favrat, J. European Ceram. Soc., 25 (2005) 2627-2632.

[182] P. Costamagna, K. Honegger, J. Electrochem. Soc., 145 (1998) 3995-4007.

[183] S. Cordiner, M. Feola, V. Mulone, F. Romanelli, Appl. Therm. Eng., 27 (2007) 738-747.

[184] M. Sucipta, S. Kimijima, K. Suzuki, J. Power Sources, 174 (2007) 124-135.

[185] Website, http://www.athenavisual.com, June 2007.

[186] T. A. Milne, R. J. Evans, N. Abatzoglou, Biomass Gasifier "Tars": Their Nature, Formation and Conversion, NREL, Golden, United States of America, 1998.

[187] VDI-Wärmeatlas. Berechnungsblätter für den Wärmeübergang, Verein Deutscher Ingenieure. VDI-Gesellschaft Verfahrenstechnik und Chemieingenieurwesen, Düsseldorf, Germany, 1977.

[188] F. Palazzi, N. Autissier, F. M. A. Marechal, D. Favrat, Appl. Therm. Eng., 27 (2007) 2703-2712.

[189] N. Autissier, F. Palazzi, F. Marechal, J. van Herle, D. Favrat, J. Fuel Cell Sci. Technol., 4 (2007) 123-129.

[190] C. Rechenauer, E. Achenbach, Dreidimensionale mathematische Modellierung des stationären und instationären Verhaltens oxidkeramischer Hochtemperatur-Brennstoffzellen, RWTH Aachen, Jülich, Germany, 1992.

[191] U. Bossel, Facts & Figures, Berne, Switzerland, 1992.

[192] Website, http://dippr.byu.edu/, December 2007.

[193] F. A. Aly, L. L. Lee, Fluid Phase Equilib., 6 (1981) 169-179.

[194] B. E. Poling, J. M. Prausnitz, J. P. O'Connell, The properties of gases and liquids, McGraw-Hill Professional, New York, United States of America, 2000.

[195] E. Schmidt, Einführung in die Technische Thermodynamik, Springer, Berlin, Göttingen, Heidelberg, Germany, 1963.

[196] J. M. Bockris, S. Srinivasan, Fuel cells: Their Electrochemistry, McGraw-Hill, New York, United States of America, 1969.

[197] N. Q. Minh, T. Takahashi, Science and technology of ceramic fuel cells, Elsevier Science, Amsterdam, The Netherlands, 1995.

[198] K. Nisancioglu, Ohmic Losses, in: Proceedings of the Workshop on mathematical modelling: "Natural gas fuelled solide oxide fuel cells and systems", Charmey, Switzerland, 1989, 2nd to 6th July.

[199] E. F. Sverdrup, C. J. Warde, R. L. Eback, Energy Convers., 13 (1973) 129-141.

[200] A. Solheim, K. Nisancioglu, Resistance and Current distribution in Fuel Cell Elements, in: Proceedings of the Second International Symposium on SOFC, Greece, Athens, 1991, 2nd to 5th July.

[201] N. P. Cheremisinoff, Handbook of Heat and Mass Transfer, Butterworth-Heinemann, Houston-London-Paris, 1986.

[202] S. Campanari, P. Iora, J. Power Sources, 132 (2004) 113-126.

[203] S. Campanari, P. Iora, Fuel Cells, 5 (2005) 34-51.

[204] E. Achenbach, E. Riensche, J. Power Sources, 52 (1994) 283-288.

[205] K. Ahmed, K. Foger, Catal. Today, 63 (2000) 479-487.

[206] A. L. Lee, R. F. Zabransky, W. J. Huber, Ind. Eng. Chem. Res., 29 (1990) 766-773.

[207] I. Drescher, Kinetik der Methan-Dampf-Reformierung, Forschungszentrum Jülich, Jülich, Germany, 1999.

[208] M. Pfafferodt, P. Heidebrecht, M. Stelter, K. Sundmacher, J. Power Sources, 149 (2005) 53-62.

[209] P. Costamagna, E. Arato, P. L. Antonucci, V. Antonucci, Chem. Eng. Sci., 51 (1996) 3013-3018.

[210] F. Lange, M. Ise, W. Kleinlein, B. Schricker, Delta 8 - A new cell design for cost optimized generators, in: Proceedings of the Fuel Cell Seminar & Exposition, San Antonio, USA, 2007, 15th to 19th October.

[211] K. Huang, Development of Delta-Type SOFCs at Siemens Stationary Fuel Cells, in: Proceedings of the Fuel Cell Seminar & Exposition, San Antonio, United States of America, 2007, 15th to 19th October.

[212] F. Marechal, F. Palazzi, J. Godat, D. Favrat, Fuel Cells, 5 (2005) 5-24.

[213] R. Turton, R. C. Bailie, W. B. Whiting, J. A. Shaeiwitz, Analysis, Synthesis and Design of Chemical Processes, Pearson Education Inc., Prentice Hall PTR, Upper Saddle River, United States of America, 2003.

[214] D. E. Garrett, Chemical Engineering Economics, Van Nostrand Reinhold, New York, United States of America, 1989.

[215] A. V. Bridgwater, A. J. Toft, J. G. Brammer, Renew. Sust. Energ. Rev., 6 (2002) 181-248.

[216] V. Gnielinski, A. Mersmann, F. Thurner, Verdampfung, Kristallisation, Trocknung, Friedr. Vieweg & Sohn Verlegsgesellschaft mbH, Braunschweig,Wiesbaden, Germany, 1993.

[217] Website, http://www.energychallenge.org/, January 2008.

[218] L. Schneider, Stromgestehungskosten von Grosskraftwerken, Öko-Institut e.V., Freiburg, Germany, 1998.

[219] Website, http://www.carmen-ev.de, January 2008.

[220] W. A. Surdoval, The U. S. Department of Energy Fossil Energy Fuel Cell Program - Solid State Energy Conversion Alliance: Goals and Challenges, in: Proceedings of the 8th SECA Workshop, San Antonio, United States of America, 2007, 7th to 9th August.

[221] Website, http://www.netl.doe.gov/technologies/coalpower/fuelcells/seca.html, January 2008.

[222] S. Jimenez, J. Ballester, Combustion Science And Technology, 178 (2006) 655-683.

[223] M. Seemann, S. Biollaz, C. Aichernig, R. Rauch, H. Hofbauer, R. Koch, Methanation of bio-syngas in a bench scale reactor using a slip stream of the FICFB gasifier in Güssing, in: Proceedings of the 2nd World Conference on Biomass for Energy, Industry, and Climate Protection, Rome, Italy, 2004, 10th to 14th May.

[224] M. C. Seemann, T. J. Schildhauer, S. M. A. Biollaz, S. Stucki, A. Wokaun, Appl. Catal. A-Gen., 313 (2006) 14-21.

[225] R. E. Harth, U. Boltendahl, Interdiscip. Sci. Rev., 6 (1981) 221-228.

[226] C. Aichernig, H. Hofbauer, R. Rauch, R. Koch, RENET Report, (2006).

[227] Website, http://www.ctu.ch/front_content.php?idart=183, May 2008.

[228] J. Karl, Biocellus - Highly efficient SOFC systems with indirect gasification, in: Proceedings of the Bio-energy workshop EU-Russia, Moscow, Russia, 2004, 7th to 8th October.

[229] EEG, "Erneuerbare-Energien-Gesetz vom 21. Juli 2004 (BGBl. I S. 1918), zuletzt geändert durch Artikel 1 des Gesetzes vom 7. November 2006 (BGBl. I S. 2550)".

Curriculum vitae

Personal Data

Surname	Nagel
Given names	Florian-Patrice
Date of birth	5th December 1977
Birthplace	Berlin
Nationality	German

Post-graduate experience

05/2004 – 06/2008	Researcher (LEM Laboratory for Energy and Material cycles, PSI Paul Scherrer Institut, Villigen, Switzerland)
10/2004 – 02/2006	Assistant (Swiss Federal Institute of Technology (ETHZ), Zurich, Switzerland)
10/2003 – 04/2004	Drive train development engineer (DaimlerChrysler Research Center, Ulm, Germany)

Education

05/2004 – 06/2008	Doctorate studies (Swiss Federal Institute of Technology (ETHZ), Zurich, Switzerland)
10/1998 – 10/2003	Diplom- Ingenieur studies (Department of Mechanical Engineering, University of Stuttgart, Stuttgart, Germany)
08/1983 – 07/1996	Elementary and Grammar school (Hochrhein- Gymnasium, Waldshut, Germany)

Under-graduate experience

01/2003 – 03/2003	Intern (LAE Lahmeyer Agua y Energia S.A., Lima, Peru)
12/2002 – 01/2003	Intern (Fundicion Las Rosas S.A., Malloco-Peñaflor, Chile)
11/2002 – 12/2002	Intern (EPS Ltda., Santiago de Chile, Chile)
12/2000 – 04/2002	Junior researcher (IPA Fraunhofergesellschaft, Stuttgart, Germany)
06/1997 – 09/1998	Semi-skilled labor (AWW GmbH, Wutöschingen, Germany)

Publications

Conference proceedings

F. P. Nagel, M. Künstle, S.Biollaz: Link-up of a solid oxide fuel cell with a wood gasifier; Proceedings of the 14th European Biomass Conference and Exhibition: Biomass for Energy, Industry and Climate Protection; Paris, France, 17th-21st October 2005

F. Nagel, M. Jenne, S. Biollaz, S. Stucki: Link-up of a SOFC with an Updraft Wood Gasifier via Hot Gas Processing; Proceedings of the 2006 Fuel Cell Seminar: Fuel Cells in Paradise - 30th Anniversary; Honolulu, HI, United States of America, 13th-17th November 2006

F. P. Nagel, S. Biollaz, M. Jenne, S. Stucki: Link-up of a 1 kW-SOFC with an updraft-wood gasifier via hot gas processing; Proceedings of the 15th European Biomass Conference and Exhibition: From Research to Market Deployment; Berlin, Germany, 7th-11th May 2007

F. P. Nagel, S. Biollaz, M. Jenne, A. Schuler: Long-term tests of a complete biomass integrated gasification fuel cell system (B-IGFC); Proceedings of the 16th European Biomass Conference and Exhibition: From Research to Industry and Markets, Valencia, Spain, 2nd-6th June 2008

S. Biollaz, F.P. Nagel, K. Dennerlein, H. Landes, W. Straub, J. Karl: Results from long term testing of tubular SOFC with woodgas; Proceedings of the 16th European Biomass Conference and Exhibition: From Research to Industry and Markets, Valencia, Spain, 2nd-6th June 2008

S. Biollaz, F. P. Nagel, M. Jenne, A. Schuler: Long-term tests of a complete biomass integrated gasification fuel cell system (B-IGFC); Proceedings of the 8th European SOFC Forum, Lucerne, Switzerland, 30th June-4th July 2008

Oral presentations

"Link-up of a SOFC with an updraft-wood gasifier via hot gas processing (B-IGFC)" held at the 2006 Fuel Cell Seminar in Honolulu, HI, USA, the 16th November 2006

"Link-up of a 1kW-SOFC with an updraft-wood gasifier via hot gas processing" held at the 15th European Biomass Conference and Exhibition in Berlin, Germany,the 8th May 2007

"Verstromung von Holz über die Hochtemperaturbrennstoffzelle" held at the Statusseminar 2008 of the Schweizerische Arbeitsgemeinschaft für Holzforschung (SAH) in Dübendorf, Switzerland, the 19th March 2008

Scientific papers (peer-reviewed)

F.P. Nagel, T.J. Schildhauer, S.M.A. Biollaz, A. Wokaun: Performance comparison of planar, tubular and Delta8 solid oxide fuel cells using a generalized finite volume model; Journal of Power Sources 184 (2008) 143–164

F.P. Nagel, T.J. Schildhauer, S.M.A. Biollaz, S. Stucki: Charge, mass and heat transfer interactions in SOFCs operated with different fuel gases - A Sensitivity analysis; Journal of Power Sources 184 (2008) 129–142

F.P. Nagel, T.J. Schildhauer, S.M.A. Biollaz, A.Schuler: The impact of sulfur on the performance of a SOFC system operated with hydrocarboneous fuel gas; Journal of Power Sources (2009), doi:10.1016/j.jpowsour.2008.12.092

F.P. Nagel, S. Ghosh, C. Pitta, T.J. Schildhauer, S.M.A. Biollaz: Biomass integrated gasification fuel cell systems - Concept development based on experimental results and long-term testing; Biomass and Bioenergy, in internal review process

F.P. Nagel, T.J. Schildhauer, S.M.A. Biollaz: Biomass-Integrated gasification fuel cell systems - Part 1: Definition of systems and technical analysis; International Journal of Hydrogen Energy, submitted

F.P. Nagel, T.J. Schildhauer, N. McCaughey, S.M.A. Biollaz: Biomass-Integrated gasification fuel cell systems - Part 2: Economic analysis; International Journal of Hydrogen Energy, submitted

F.P. Nagel, T.J. Schildhauer: Improving lumped SOFC models for system simulations by parameterization of detailed model results; Journal of Power Sources, in preparation

Patent applications

F.P. Nagel, T.J. Schildhauer, M. Jenne, S. Biollaz, Verfahren und Anlage zur Verstromung fester Biomasse, WO 2008/055591 A2